

Fiber-Reinforced Concrete for the Improved Performance of Transportation Infrastructure



Arizona Department of Transportation Research Center

Fiber Reinforced Concrete for Improved Performance of Transportation Infrastructure

SPR-705

February 2018

Prepared by:

Anna C. Birely, Philip Park, Joshua A. McMahon, Xijun Shi, and Younho Rew
Texas A&M Transportation Institute
The Texas A&M University System
College Station, Texas 77843-3135

Published by:

Arizona Department of Transportation
206 S. 17th Ave.
Phoenix, AZ 85007
In cooperation with
U.S. Department of Transportation
Federal Highway Administration

This report was funded in part through grants from the Federal Highway Administration, U.S. Department of Transportation. The contents of this report reflect the views of the authors, who are responsible for the facts and the accuracy of the data, and for the use or adaptation of previously published material, presented herein. The contents do not necessarily reflect the official views or policies of the Arizona Department of Transportation or the Federal Highway Administration, U.S. Department of Transportation. This report does not constitute a standard, specification, or regulation. Trade or manufacturers' names that may appear herein are cited only because they are considered essential to the objectives of the report. The U.S. government and the State of Arizona do not endorse products or manufacturers.

This report is subject to the provisions of 23 USC § 409. Any intentional or inadvertent release of this material, or any data derived from its use, does not constitute a waiver of privilege pursuant to 23 USC § 409, which reads as follows:

23 USC § 409 — Discovery and admission as evidence of certain reports and surveys

Notwithstanding any other provision of law, reports, surveys, schedules, lists, or data compiled or collected for the purpose of identifying, evaluating, or planning the safety enhancement of potential accident sites, hazardous roadway conditions, or railway-highway crossings, pursuant to sections 130, 144, and 148 of this title or for the purpose of developing any highway safety construction improvement project which may be implemented utilizing Federal-aid highway funds shall not be subject to discovery or admitted into evidence in a Federal or State court proceeding or considered for other purposes in any action for damages arising from any occurrence at a location mentioned or addressed in such reports, surveys, schedules, lists, or data.

1. Report No. FHWA/AZ-18-705		2. Government Accession No.		3. Recipient's Catalog No.	
4. Title and Subtitle Fiber Reinforced Concrete for Improved Performance of Transportation Infrastructure				5. Report Date February 2018	
				6. Performing Organization Code	
7. Author(s) Anna C. Birely, Philip Park, Joshua A. McMahon, Xijun Shi, and Younho Rew				8. Performing Organization Report No.	
9. Performing Organization Name and Address Texas A&M Transportation Institute The Texas A&M University System College Station, Texas 77843-3135				10. Work Unit No. (TRAVIS)	
				11. Contract or Grant No. SPR 000-1(181) 705	
12. Sponsoring Agency Name and Address Arizona Department of Transportation 206 S. 17th Ave. Phoenix, AZ 85007				13. Type of Report and Period Covered FINAL (4/14-12/17)	
				14. Sponsoring Agency Code	
15. Supplementary Notes Project performed in cooperation with the Federal Highway Administration.					
16. Abstract Steel fiber-reinforced concrete (SFRC) provides improved tensile performance of concrete. This improved performance can be used in slabs to reduce the volume of conventional steel reinforcement, create longer spans, or reduce slab thickness. This can lead to a reduction in structure weight and improvements in the safety and speed of construction. These benefits can result in cost savings in both the short term (construction labor) and the long term (improved quality and durability). To maximize the benefits of SFRC, it is necessary to establish optimal mix designs, identify target projects for implementation, and validate design procedures for SFRC. This project investigated the application of SFRC in pavements and bridge decks to reduce the amount of traditional steel used and to improve service level performance. The project consisted of four main tasks. The first was a review of the literature on SFRC applications to elevated slabs and slabs-on-grade. This was followed by case studies on implementation of SFRC for pavement and bridge decks. Results of the case studies informed the development of an experimental test program. Finally, all results were compiled to develop design recommendations and an implementation plan. This report summarizes the project findings and provides recommendations for the implementation of SFRC in Arizona Department of Transportation infrastructure.					
17. Key Words Steel Fiber, Fiber-Reinforced Concrete, Bridge Deck			18. Distribution Statement This document is available to the US public through the National Technical Information Service, Springfield, Virginia 22161		23. Registrant's Seal
19. Security Classif. (of this report) Unclassified	20. Security Classif. (of this page) Unclassified	21. No. of Pages 325	22. Price		

SI* (MODERN METRIC) CONVERSION FACTORS

APPROXIMATE CONVERSIONS TO SI UNITS

Symbol	When You Know	Multiply By	To Find	Symbol
LENGTH				
in	inches	25.4	millimeters	mm
ft	feet	0.305	meters	m
yd	yards	0.914	meters	m
mi	miles	1.61	kilometers	km
AREA				
in ²	square inches	645.2	square millimeters	mm ²
ft ²	square feet	0.093	square meters	m ²
yd ²	square yard	0.836	square meters	m ²
ac	acres	0.405	hectares	ha
mi ²	square miles	2.59	square kilometers	km ²
VOLUME				
fl oz	fluid ounces	29.57	milliliters	mL
gal	gallons	3.785	liters	L
ft ³	cubic feet	0.028	cubic meters	m ³
yd ³	cubic yards	0.765	cubic meters	m ³
NOTE: volumes greater than 1000 L shall be shown in m ³				
MASS				
oz	ounces	28.35	grams	g
lb	pounds	0.454	kilograms	kg
T	short tons (2000 lb)	0.907	megagrams (or "metric ton")	Mg (or "t")
TEMPERATURE (exact degrees)				
°F	Fahrenheit	5 (F-32)/9 or (F-32)/1.8	Celsius	°C
ILLUMINATION				
fc	foot-candles	10.76	lux	lx
fl	foot-Lamberts	3.426	candela/m ²	cd/m ²
FORCE and PRESSURE or STRESS				
lbf	poundforce	4.45	newtons	N
lbf/in ²	poundforce per square inch	6.89	kilopascals	kPa

APPROXIMATE CONVERSIONS FROM SI UNITS

Symbol	When You Know	Multiply By	To Find	Symbol
LENGTH				
mm	millimeters	0.039	inches	in
m	meters	3.28	feet	ft
m	meters	1.09	yards	yd
km	kilometers	0.621	miles	mi
AREA				
mm ²	square millimeters	0.0016	square inches	in ²
m ²	square meters	10.764	square feet	ft ²
m ²	square meters	1.195	square yards	yd ²
ha	hectares	2.47	acres	ac
km ²	square kilometers	0.386	square miles	mi ²
VOLUME				
mL	milliliters	0.034	fluid ounces	fl oz
L	liters	0.264	gallons	gal
m ³	cubic meters	35.314	cubic feet	ft ³
m ³	cubic meters	1.307	cubic yards	yd ³
MASS				
g	grams	0.035	ounces	oz
kg	kilograms	2.202	pounds	lb
Mg (or "t")	megagrams (or "metric ton")	1.103	short tons (2000 lb)	T
TEMPERATURE (exact degrees)				
°C	Celsius	1.8C+32	Fahrenheit	°F
ILLUMINATION				
lx	lux	0.0929	foot-candles	fc
cd/m ²	candela/m ²	0.2919	foot-Lamberts	fl
FORCE and PRESSURE or STRESS				
N	newtons	0.225	poundforce	lbf
kPa	kilopascals	0.145	poundforce per square inch	lbf/in ²

*SI is the symbol for the International System of Units. Appropriate rounding should be made to comply with Section 4 of ASTM E380.
(Revised March 2003)

CONTENTS

	Page
Executive Summary	1
Chapter 1. Introduction	3
Overview.....	3
Overview of Research and Organization of Report.....	3
Phase 1—Background and Preliminary Investigations.....	4
Phase 2—Experimental Test Programs.....	4
Phase 3—Analysis and Design Recommendations.....	4
Chapter 2. Literature Review	5
Characteristics and Classifications of the SFRC Behaviors.....	5
Test Methods and Standards.....	8
Experimental Investigations for SFRC Behavior.....	9
Compression Test.....	10
Tension Test.....	13
Flexural Test.....	17
Reinforcing Effects of SFRC.....	18
Design Methods.....	24
American Concrete Institute.....	24
RILEM TC 162-TDF Method.....	25
Closed Form Solutions.....	26
Round Slabs and Yield Line Theory.....	26
Structural Applications of SFRC.....	27
Seismic Design.....	27
Beams.....	28
Slabs.....	28
Steel-Free and Steel-Reduced Bridge Deck.....	29
Applicability of Literature SFRC Characteristics for ADOT Bridge Decks.....	31
Chapter 3. Slab-on-Grade Case Studies	35
Slab-on-Grade.....	35
Review on the Fiber Reinforced Slab-on-Grade.....	35
Description of the Case at Houston.....	37
Analysis of the Case at Houston.....	40
Summary.....	47
Chapter 4. Bridge Case Studies	49
Introduction.....	49
Modeling Approach.....	49
Slab-Girder Bridges.....	49
Overview.....	49
Strength Results.....	52
Service Results.....	56
Slab Bridges.....	62
Modeling and Analysis.....	62
Results.....	63
Railing.....	66
Summary.....	70

Chapter 5. Material Tests for SFRC	73
Experimental Setups.....	74
Materials and Specimens Preparations.....	74
Compression Test Method.....	81
Tension Test Method.....	81
Flexural Test Method.....	83
Test Results.....	84
Compressive Stress–Strain Curves of the SFRC.....	84
Tensile Stress–Strain Curves of the SFRC.....	88
Flexural Load–Deflection Curves of the SFRC.....	93
Comparisons of Mechanical Parameters.....	100
Compressive Behavior.....	100
Tensile Behavior.....	101
Flexural Behavior.....	104
Summary.....	106
Chapter 6. Slab Strip Test Program	109
Introduction.....	109
Design of Test Matrix.....	109
Design of Conventional Bridge Decks.....	109
Steel Fiber Dosage.....	111
Test Matrix.....	112
Specimen Casting.....	113
First Cast.....	114
Second Cast.....	114
Material Properties.....	116
Steel Fiber Material Properties.....	116
Concrete Material Properties.....	116
Compressive Strength.....	117
Steel Reinforcement Material Properties.....	120
Test Setup and Instrumentation.....	121
Summary of Observed Results.....	122
Comparison of Plain and SFRC Slab Strips (D-series).....	122
Behavior of Beams with Steel at Bottom (S-Series).....	129
Behavior of Beams with Steel at Center (S-Series).....	136
Behavior of Slab Strips with No Steel.....	138
Load-Deflection Response.....	140
Specimens 7.5 in. Deep with Steel Reinforcement.....	140
Specimens 9.0 in. Deep with Steel Reinforcement.....	142
Specimens without Steel Reinforcement.....	144
Discussion.....	146
Service Limit State.....	146
Maximum Girder Spacing Permitted.....	149
Summary.....	151
Chapter 7. Full-Scale Bridge Deck Test	153
Introduction.....	153
Bridge Deck Design.....	153
Test Setup and Instrumentation.....	154
Experimental Test Results.....	157

LP1 – Individual Wheel	157
LP2 – Tandem Axle	161
LP3 – Overhang Single Axle	167
LP4 – Individual Wheel	170
Discussion	173
Overall	173
Comparison to Previous Tests	174
Summary.....	177
Chapter 8. Analysis of Slab Strip Tests.....	178
Introduction.....	178
Experimental Moment Curvature	178
Inverse Analysis to Establish SFRC Tension Model.....	184
Moment-Curvature Analysis of Slab Strips with Steel.....	188
Comparison S- and D-Series Tests	194
Case Study Comparison	196
Summary.....	199
Chapter 9. Analysis of Bridge Deck Tests	200
Introduction.....	200
Yield Line Theory	200
Affinity Theorem	200
Unit Moment Capacities.....	201
LP1 and LP4 – Individual Wheel	202
LP2 – Tandem Axle	204
LP3 – Overhang Single Axle	206
Discussion	207
Two-Way Shear Analysis.....	208
Summary.....	210
Chapter 10. Recommendations for Design And Implementation.....	211
Introduction.....	211
Service Limit State Equations	211
Strength Limit State Equations	212
Evaluation Proposed design equations using Slab strip Test results.....	213
Design Steps	215
Design Examples.....	217
Design Aids	218
Implementation.....	220
Selection, Specifications, and Testing of FRC.....	220
Construction.....	221
Corrosion of SFRC.....	221
Summary.....	221
Chapter 11. Summary and Conclusions	223
Summary.....	223
Case Study: Slab-on-Grade.....	223
Case Study: Bridges	223
Material Test Program.....	224
Structural Test Program	225
Design and Implementation Recommendations.....	226
Recommendations for Future Research.....	227

References.....	229
APPENDIX A: DAMAGE PROFILES OF SLAB STRIP SPECIMENS.....	236
S7505BTM35.....	236
S7505BTM25.....	242
S7505BTM24.....	248
S7505BTM23.....	252
S7505CTR35.....	259
S7505CTR25.....	266
S7505NOS00.....	272
S7520NOS00.....	277
S9005BTM35.....	280
S9005BTM25.....	288
S9005BTM24.....	295
S9005BTM23.....	301
S9005NOS00.....	307
S9020NOS00.....	311
APPENDIX B: SFRC Design Examples	313
Overview.....	313
Design Example with Reinforced Concrete	313
Design Example with SFRC for Service Only	315
Design Example with SFRC for Strength	316

LIST OF FIGURES

	Page
Figure 1. Typical Stress-Strain Curve Response of a Strain Hardening and Strain Softening FRC Composite (Reconstructed Based on Naaman and Reinhardt 2006).....	6
Figure 2. Typical Load-Deflection Response Curve of FRC (Reconstructed Based on Kim et al. 2008).....	6
Figure 3. Classification of FRC Composites Based on the Tensile Strength Response (Reconstructed Based on Naaman and Reinhardt 2006).....	6
Figure 4. Various Steel Fiber Shapes.....	7
Figure 5. Compression Test Data for SFRC with Hooked Fibers (Reproduced from Ezeldin and Balaguru 1992)	11
Figure 6. Compression Test Data for SFRC with Hooked Fibers (Reproduced from Wafa and Ashour 1992)	12
Figure 7. Compression Test Data for SFRC with Hooked Fibers (Reproduced from Hsu and Hsu 1995).....	12
Figure 8. Compression Test Data for SFRC with Hooked Fibers (Reproduced from Bencardino et al. 2008).....	12
Figure 9. Tension Test Data for Straight Steel Fiber-Reinforced Mortar (Reproduced from Walkus et al. 1979).....	14
Figure 10. Tension Test Data for SFRC with Hooked Fibers (Reproduced from Lim et al. 1987)	15
Figure 11. Tension Test Data for SFRC with Straight Fibers (Reproduced from Lim et al. 1987)	15
Figure 12. Tension Test Data for SFRC with Straight Fibers (Reproduced from Li et al. 1996).....	15
Figure 13. Tension Test Data for SFRC with Straight Fibers (Reproduced from Li et al. 1996).....	16
Figure 14. Tension Test Data for Ultra-High-Performance Mortar with Straight Fibers (Reproduced from Wille et al. 2011).....	16
Figure 15. Tension Test Data for Ultra-High-Performance Mortar with Hooked Fibers (Reproduced from Wille et al. 2011).....	16
Figure 16. Tension Test Data for Ultra-High-Performance Mortar with Twisted Fibers (Reproduced from Wille et al. 2011).....	17
Figure 17. Flexural Test Data of SFRC: Aspect Ratio = 57–60 (Soroushian and Bayasi 1991).....	18
Figure 18. Flexural Test Data of SFRC: Aspect Ratio = 72–75 (Soroushian and Bayasi 1991).....	19
Figure 19. Flexural Test Data of SFRC with Hooked Fibers (Balaguru et al. 1992).....	19
Figure 20. Flexural Test Data of SFRC with Hooked Fibers (Balaguru et al. 1992).....	19
Figure 21. Flexural Test Data of SFRC with Various Fibers: 1.2 Percent Fibers by Volume (Kim et al. 2008).....	20
Figure 22. Flexural Test Data of SFRC with Various Fibers: 0.4 Percent Fibers by Volume (Kim et al. 2008).....	20
Figure 23. Flexural Test Data of Steel Fiber Reinforced Mortar with Various Fibers (Kim et al. 2008).....	20
Figure 24. Comparisons of Compressive Properties of SFRC.....	21
Figure 25. Comparisons of Tensile Properties of SFRC	23
Figure 26. MEPDG Iterative Design Process.....	41
Figure 27. The Pavement Structure Used for the Analysis	42
Figure 28. Vehicle Class Distribution Factors.....	43
Figure 29. The Average Crack Width of the CRCP with Fibers (the Houston Case).....	45

Figure 30. The IRI and Punchouts of the CRCP with Fibers (the Houston Case) Predicted by MEPDG	46
Figure 31. The Predicted Average Crack Width of the SFRCs Produced in This Project	46
Figure 32. The Predicted IRI of the SFRCs Produced in This Project	47
Figure 33. The Predicted Punchouts of the SFRCs Produced in This Project	47
Figure 34. Concrete Compression Model for Case Study Moment Curvature Analysis	50
Figure 35. Concrete Tension Model for Case Study Moment Curvature Analysis.....	50
Figure 36. Traditional Slab-Girder Bridge	51
Figure 37. Case Study Reinforcement Layouts (a) Profile 1 and 2, (b) Profile 3-5, (c) Profile 6	51
Figure 38. Moment vs. Curvature Response for SFRC and PC Sections with Conventional Steel Designed in Accordance with AASHTO.....	53
Figure 39. Normalized Moment vs. Curvature for S8-F4500-H80-muALL-Steel1	53
Figure 40. Normalized Moment vs. Curvature for S8-F4500-HALL-muALL-Steel1	54
Figure 41. Normalized Moment vs. Curvature for S8-F4500-H80-muALL-Steel1-3.....	55
Figure 42. Normalized Moment vs. Curvature for S8-F4500-H80-muALL-Steel3-6.....	56
Figure 43. Service Performance S8-F4500-H80-muALL-Steel1-2-Service	57
Figure 44. Service Performance S8-F4500-HALL-muALL-Steel1-2-Service	58
Figure 45. Strain at Extreme Steel Fiber vs. Depth for S8-F4500.....	61
Figure 46. Normalized Moment vs. Curvature for S8-H80 with Varied f'_c , μ , and Steel Profiles.....	62
Figure 47. Normalized Moment vs. Curvature for S30-F4500 with Varied Depth, μ , and Steel Profiles.....	64
Figure 48. Normalized Moment vs. Curvature for S30-H195 with Varied f'_c , μ , and Steel Profiles.....	66
Figure 49. Reference Barrier Design	67
Figure 50. Normalized Collision Load vs. Wall Thickness for F4500 with Varied μ and Steel Profiles.....	69
Figure 51. Normalized Collision Load vs. Concrete Compressive Strength for H100 with Varied μ and Steel Profiles	70
Figure 52. Hooked Steel Fiber (Left) and Straight Steel Fiber (Right)	75
Figure 53. Aggregates Gradation Curves	76
Figure 54. Two Mixers Used in This Project	77
Figure 55. Mixing Quality of the SFRC.....	79
Figure 56. Fresh Concrete Properties	80
Figure 57. Tension Specimen Setup.....	83
Figure 58. A Failed SFRC Specimen after the Compression Test	84
Figure 59. Stress–Strain Curves for Control Specimens under Compression	85
Figure 60. Stress–Strain Curves for the 0.5 Percent Straight SFRCs under Compression.....	85
Figure 61. Stress–Strain Curves for the 1.0 Percent Straight SFRCs under Compression.....	85
Figure 62. Stress–Strain Curves for the 1.5 Percent Straight SFRCs under Compression.....	86
Figure 63. Stress–Strain Curves for the 2.0 Percent Straight SFRCs under Compression.....	86
Figure 64. Stress–Strain Curves for the 3.0 Percent Straight SFRCs under Compression.....	86
Figure 65. Stress–Strain Curves for the 0.5 Percent Hooked SFRCs under Compression.....	87
Figure 66. Stress–Strain Curves for the 1.0 Percent Hooked SFRCs under Compression.....	87
Figure 67. Stress–Strain Curves for the 1.5 Percent Hooked SFRCs under Compression.....	87
Figure 68. Stress–Strain Curves for the 2.0 Percent Hooked SFRCs under Compression.....	88
Figure 69. Stress–Strain Curves for the 3.0 Percent Hooked SFRCs under Compression.....	88
Figure 70. Stress–Strain Curves for the 2.0 Percent Combined SFRCs under Compression.....	88
Figure 71. A Failed SFRC Specimen under Tension.....	89
Figure 72. Stress–Strain Curves for the Control Specimens under Tension	90

Figure 73. Stress–Strain Curves for the 0.5 Percent Straight SFRCs under Tension	90
Figure 74. Stress–Strain Curves for the 1.0 Percent Straight SFRCs under Tension	90
Figure 75. Stress–Strain Curves for the 1.5 Percent Straight SFRCs under Tension	91
Figure 76. Stress–Strain Curves for the 2.0 Percent Straight SFRCs under Tension	91
Figure 77. Stress–Strain Curves for the 0.5 Percent Hooked SFRCs under Tension	91
Figure 78. Stress–Strain Curves for the 1.0 Percent Hooked SFRCs under Tension	92
Figure 79. Stress–Strain Curves for the 1.5 Percent Hooked SFRCs under Tension	92
Figure 80. Stress–Strain Curves for the 2.0 Percent Hooked SFRCs under Tension	92
Figure 81. Stress–Strain Curves for the 2.0 Percent Combined SFRCs under Tension	93
Figure 82. A Failed Flexural Specimen	94
Figure 83. Load–Deflection Curves for the Control Specimens under Bending	94
Figure 84. Load–Deflection Curves for the 0.5 Percent Straight SFRCs under Bending	95
Figure 85. Load–Deflection Curves for the 1.0 Percent Straight SFRCs under Bending	95
Figure 86. Load–Deflection Curves for the 1.5 Percent Straight SFRCs under Bending	95
Figure 87. Load–Deflection Curves for the 2.0 Percent Straight SFRCs under Bending	96
Figure 88. Load–Deflection Curves for the 3.0 Percent Straight SFRCs under Bending	96
Figure 89. Load–Deflection Curves for the 0.5 Percent Hooked SFRCs under Bending	96
Figure 90. Load–Deflection Curves for the 1.0 Percent Hooked SFRCs under Bending	97
Figure 91. Load–Deflection Curves for the 1.5 Percent Hooked SFRCs under Bending	97
Figure 92. Load–Deflection Curves for the 2.0 Percent Hooked SFRCs under Bending	97
Figure 93. Load–Deflection Curves for the 3.0 Percent Hooked SFRCs under Bending	98
Figure 94. Load–Deflection Curves for the 0.5 Percent Combined SFRCs under Bending	98
Figure 95. Load–Deflection Curves for the 1.0 Percent Combined SFRCs under Bending	98
Figure 96. Load–Deflection Curves for the 1.5 Percent Combined SFRCs under Bending	99
Figure 97. Load–Deflection Curves for the 2.0 Percent Combined SFRCs under Bending	99
Figure 98. Load–Deflection Curves for the 3.0 Percent Combined SFRCs under Bending	99
Figure 99. Comparison of Compressive Properties of the Straight SFRCs	100
Figure 100. Comparison of Compressive Properties of the Hooked SFRCs	101
Figure 101. Comparison of Compressive Properties of the Combined SFRCs	101
Figure 102. Comparison of Tensile Properties of the Straight SFRCs	102
Figure 103. Comparison of Tensile Properties of the Hooked SFRCs	102
Figure 104. Comparison of Tensile Properties of the Combined SFRCs	103
Figure 105. Residual Strength of the Straight SFRCs	103
Figure 106. Residual Strength of the Hooked SFRCs.....	104
Figure 107. Residual Strength of the Combined SFRCs.....	104
Figure 108. Comparison of Flexural Properties of the Straight SFRCs.....	105
Figure 109. Comparison of Flexural Properties of the Hooked SFRCs.....	105
Figure 110. Comparison of Flexural Properties of the Combined SFRCs.....	105
Figure 111. Dimensions of Reference Slab-Strip Specimen.....	109
Figure 112. Service State Analysis – Elastic Sections	110
Figure 113. Ultimate State Analysis	111
Figure 114. Naming Scheme. The Letter ‘s’ Indicates Test Series 1, and the Letter ‘d’ Indicates Test Series 2.....	112
Figure 115. Slab Strip Cross Sections	113
Figure 116. 2.0 percent SFRC Lack of.....	114
Figure 117. Significant Clumping in SFRC.....	114
Figure 118. Adding Steel Fibers to Concrete Truck.....	115
Figure 119. Significant Slump of Fresh Mix without Steel Fibers	115

Figure 120. Placing Concrete Directly into Forms.....	115
Figure 121. Five of 12 Completed SFRC Slab Strips.....	116
Figure 122. Casts for ASTM Materials Tests on Way to Curing Room	116
Figure 123. Stress-Strain Curves from ASTM C469	118
Figure 124. Tensile Test Results for (a) M1 and (b) M2	119
Figure 125. ASTM C1609 Test Results for all Mixes.	120
Figure 126. ASTM A370 Test For Steel Reinforcement Bars	121
Figure 127. Experimental Test and Instrumentation Setup.....	122
Figure 128. Crack Maps for Slab strips with Steel at Bottom	123
Figure 129. Average Crack Width vs. Deflection for SFRC (d7505BTM24) and PC Slab (d7500BTM24) Strips.....	124
Figure 130. Maximum Crack Width vs. Deflection for SFRC (d7505BTM24) and PC Slab (d7500BTM24) Strips.....	125
Figure 131. State of Damage for d7505BTM24 and d7500BTM24 at 0.6 in. of Deflection	126
Figure 132. State of Damage for d7505BTM24 and d7500BTM24 at 1.2 in. of Deflection	127
Figure 133. State of Damage for d7505BTM24 and d7500BTM24 at 1.9 in. of Deflection	128
Figure 134. SFRC Crack Behavior (a) Crack Branching—W3 S9005BTM25 and (b) Accessory Cracks—W7 S7505BTM35.....	130
Figure 135. Crack Maps for Slab Strips 7.5 in. Deep with Steel at Bottom	131
Figure 136. Crack Maps for Slab Strips 9.0 in. Deep with Steel at Bottom.....	132
Figure 137. Steel Fiber Failure (a) Spalling at Surface of Concrete—E2 S9005BTM23 (b) Steel Fiber Anchorage Failure	133
Figure 138. General Condition at Failure Criteria (a) Crack Width Greater than 2.5 mm and (b) Onset of Crushing.....	134
Figure 139. Damage for Slab-Strip Specimens 7.5 in. Deep with Steel at the Bottom at 1.2 in. of Deflection	135
Figure 140. Damage for Slab-Strip Specimens 9.0 in. Deep with Steel at the Bottom at 1.2 in. of Deflection	135
Figure 141. Crack Maps for Slab strips with Steel at Center.....	137
Figure 142. Accessory and Branching Cracks of Specimens without Steel Reinforcement S7505NOS00.....	138
Figure 143. Crack Maps for Slab-Strip Specimens without Steel Reinforcement.....	139
Figure 144. Crack Maps for Slab-Strip Specimens without Steel Reinforcement.....	139
Figure 145. Force versus Deflection of 7.5 in Deep SFRC Slab Strips with Steel.....	141
Figure 146. Force vs Deflection for Specimens 9.0 in. Deep with Steel Reinforcement	143
Figure 147. Force vs Deflection for SFRC Specimens without Steel Reinforcement	145
Figure 148. Screen Capture of DAQ during Testing of S9005NOS00	145
Figure 149. Force versus Deflection of Bridge d-Series Specimens	146
Figure 150. Service Performance of S7505BTM## at Maximum Girder Spacing, 7 ft	147
Figure 151. Service Performance of S9005BTM## at Maximum Girder Spacing, 11.5 ft	149
Figure 152. Full-Scale SFRC Bridge Deck Plan	154
Figure 153. Full-Scale Specimen Test Setup – LP2	155
Figure 154. AASHTO Load Patterns Tested on Bridge Deck.....	156
Figure 155. Elevation View of Strain Gauge Locations for Bridge Deck.....	157
Figure 156. SFRC Bridge Deck Failure due to LP1	159
Figure 157. Final Crack Pattern—LP1.....	159
Figure 158. Force vs. Deflection for LP1 Solid for First Session and Dashed Lines for Second Session.....	160

Figure 159. Deflection Profile of LP1—Longitudinal Direction	160
Figure 160. Deflection Profile of LP1—Transverse Direction	161
Figure 161. Final Crack Pattern – LP2	163
Figure 162. Influence of LP1 Cracks on LP2—Crack Extends through LP2.....	163
Figure 163. Crushed Region Extends between Both Load Points	164
Figure 164. Crushing Failure Extends 24 in Passed LP2	164
Figure 165. Turning of Negative Moment Cracks – LP2.....	165
Figure 166. Force vs. Deflection for LP2 Solid for First Session and Dashed Lines for Second Session.....	165
Figure 167. Deflection Profile of LP2—Longitudinal Direction	166
Figure 168. Deflection Profile of LP2—Transverse Direction, West Load Point	166
Figure 169. Deflection Profile of LP2—Transverse Direction, East Load Point.....	167
Figure 170. Damage at End of LP3 Test	168
Figure 171. Final Crack Pattern – LP3	168
Figure 172. Force vs. Deflection for LP3	169
Figure 173. Deflection Profile of LP3—Longitudinal Direction	169
Figure 174. Deflection Profile of LP3—Transverse Direction	170
Figure 175. Final Crack Pattern for LP4.....	171
Figure 176. Force vs. Deflection for LP4	172
Figure 177. Deflection Profile of LP4—Longitudinal Direction	172
Figure 178. Deflection Profile of LP4—Transverse Direction	173
Figure 179. Force vs. Deflection Comparison of SFRC and Others—LP1	175
Figure 180. Force vs. Deflection Comparison of SFRC and Others—LP2	176
Figure 181. Force vs. Deflection Comparison of SFRC and Others—LP3	176
Figure 182. Experimental Moment Curvature Relationship for s7505CTR##.....	179
Figure 183. Experimental Moment Curvature Relationship for s7505BTM##	180
Figure 184. Experimental Moment Curvature Relationship for s9005BTM##	181
Figure 185. Experimental Moment Curvature Relationship for s####NOS00	182
Figure 186. Experimental Moment Curvature Relationship for d-series Slab Strips	183
Figure 187. ASTM C39 Average Compression Results (M2) and Modified Kent Park	184
Figure 188. SFRC Tensile Model—Elastic Region and Initial Residual Stress.....	186
Figure 189. Post-Crack Constitutive Models for SFRC	186
Figure 190. Theoretical and Experimental Moment-Curvature Response—s7505NOS00.....	187
Figure 191. Theoretical and Experimental Moment-Curvature Response—s9005NOS00.....	187
Figure 192. Theoretical and Experimental Moment-Curvature Response for d7505NOS00 and d9005NOS00.....	188
Figure 193. Theoretical and Experimental Moment-Curvature Response for s7520NOS00 and s9020NOS00	188
Figure 194. Theoretical Moment-Curvature Relationship for Slab Strips s7505BTM##.....	190
Figure 195. Theoretical Moment-Curvature Relationship for Slab Strips s9005BTM##.....	191
Figure 196. Steel and SFRC Contribution to Moment Capacity	192
Figure 197. Theoretical Moment-Curvature Relationship for Slab Strips d7505BTM24	193
Figure 198. Theoretical Moment-Curvature Relationship for Slab Strips s7505CTR##.....	193
Figure 199. Average Material Response for S- and D-Series	195
Figure 200. Comparison of S- and D- Series Test Results – x7505NOS00.....	195
Figure 201. Comparison of S- and D- Series Test Results – x7505BTM24	196
Figure 202. Normalized Moment vs. Steel Reinforcement Ratio—6 ft Girder Spacing and Steel at Bottom.....	197

Figure 203. Normalized Moment vs. Steel Reinforcement Ratio—6 ft Girder Spacing and Steel at Center	198
Figure 204. Service Stress vs. Steel Reinforcement Ratio—6 ft Girder Spacing and Steel at Bottom	198
Figure 205. Moment-Curvature Relationship for SFRC Bridge Deck—Both Directions	202
Figure 206. Failure Mechanism for LP1	203
Figure 207. Failure Mechanism for LP4	203
Figure 208. Transformation of Physical Slab to Affine Slab – LP1/LP4	204
Figure 209. Failure Mechanism for LP2	205
Figure 210. Transformation of Physical Slab to Affine Slab – LP2	206
Figure 211. Failure Mechanism and Deflection Profile for LP3	207
Figure 212. Failure Mechanism for LP3	207
Figure 213. Critical Shear Perimeter due to Wheel Load.....	209
Figure 214. Service Limit State—SFRC	211
Figure 215. Strength Limit State – SFRC.....	213
Figure 216. Design Aid—Service Moment vs. Reinforcement Ratio. Shape Indicates Slab Depth: Circle h=6 in.; Square=9 in.; Diamond = 12 in.	219
Figure 217. Design Aid—Strength Moment vs. Reinforcement Ratio	220
Figure 218. S7505BTM35 Crack Profile East Face.....	237
Figure 219. S7505BTM35 East Face Constant Moment Region.....	237
Figure 220. S7505BTM35 Crack Profile West Face	237
Figure 221. S7505BTM35 West Face Constant Moment Region.....	237
Figure 222. S7505BTM35 Crack Opening vs Strip Deflection for (a) East Face and (b) West Face	238
Figure 223. S7505BTM35 Crack Progression of E5 at: (a) 0.2 inches, (b) 0.6 inches, (c) 1.0 inches, and 1.6 inches.....	239
Figure 224. S7505BTM35 Crack Progression of W6 and W7 at: (a) 0.2 inches, (b) 0.3 inches, (c) 0.7 inches, and 1.8 inches.	240
Figure 225. S7505BTM35 Crushing Progression	241
Figure 226. S7505BTM25 Crack Profile East Face.....	243
Figure 227. S7505BTM25 East Face Constant Moment Region.....	243
Figure 228. S7505BTM25 Crack Profile West Face	243
Figure 229. S7505BTM25 West Face Constant Moment Region.....	243
Figure 230. S7505BTM25 Crack Opening vs Strip Deflection for (a) West Face and (b) East Face	244
Figure 231. S7505BTM25 Crack Opening vs Strip Deflection for Primary Crack at Each Reference Line (a) E3 and (b) W5	245
Figure 232. S7505BTM25 Crack Progression of E3 at: (a) 0.1 inches, (b) 0.3 inches, (c) 1.0 inches, and 1.4 inches.....	246
Figure 233. S7505BTM25 Crack Progression of W5 at: (a) 0.2 inches, (b) 0.6 inches, (c) 1.0 inches, and 1.4 inches.....	247
Figure 234. S7505BTM25 Crushing Progression (a) 1.0 inch and (b) 1.4 inch	247
Figure 235. S7505BTM24 Damaged Corner.....	248
Figure 236. S7505BTM24 Crack Progression of E1 and E12 at: (a) 0.1 inches, (b) 0.6 inches, (c) 1.0 inches, and 1.4 inches	249
Figure 237. S7505BTM24 Crack Progression of W4 at: (a) 0.2 inches, (b) 0.7 inches, (c) 1.0 inches, and 1.6 inches.....	250
Figure 238. Crushing Progression of S7505BTM24 at: (a) 1.2 inch, (b) 1.6 inch, (c) After Removal of Instrumentation and (d) Completion of Test	251
Figure 239. S7505BTM23 Crack Profile East Face.....	253
Figure 240. S7505BTM23 East Face Constant Moment Region.....	253

Figure 241. S7505BTM23 Crack Profile West Face	253
Figure 242. S7505BTM23 West Face Constant Moment Region.....	253
Figure 243. S7505BTM23 Crack Opening vs Strip Deflection for (a) East Face and (b) West Face	254
Figure 244. S7505BTM23 Crack Opening vs Strip Deflection for Primary Crack at Each Reference Line (a) E10 and (b) W11	255
Figure 245. S7505BTM23 Crack Progression of E10 at: (a) 0.5 inches, (b) 0.8 inches, (c) 1.0 inches, and 1.6 inches.	256
Figure 246. S7505BTM23 Crack Progression of W11 at: (a) 0.6 inches, (b) 0.7 inches, (c) 1.0 inches, and 1.4 inches.	257
Figure 247. S7505BTM23 Crushing at (a) 1.0 inch and (b) 1.2 inch, (c) 1.6 inches, and (d) Conclusion of Test	258
Figure 248. S7505CTR35 Crack Profile East Face	260
Figure 249. S7505CTR35 East Face Constant Moment Region.....	260
Figure 250. S7505CTR35 Crack Profile West Face	260
Figure 251. S7505CTR35 West Face Constant Moment Region	260
Figure 252. S7505CTR35 Crack Opening vs Strip Deflection for (a) East Face and (b) West Face.....	261
Figure 253. S7505CTR35 Crack Opening vs Strip Deflection for Primary Crack at Each Reference Line (a) E5 and (b) W4	262
Figure 254. S7505CTR35 Crack Progression of E5 at: (a) 0.2 inches, (b) 0.9 inches, (c) 1.2 inches, and 1.6 inches.....	263
Figure 255. S7505CTR35 Crack Progression of W4 at deflection step: (a) 0.2 inches, (b) 0.9 inches, (c) 1.2 inches, and 1.6 inches.	264
Figure 256. S7505CTR35 Crushing Progression	265
Figure 257. S7505CTR35 W4 and Crushed Region at Conclusion of Test.....	265
Figure 258. S7505CTR25 Crack Profile East Face	267
Figure 259. S7505CTR25 East Face Constant Moment Region.....	267
Figure 260. S7505CTR25 Crack Profile West Face	267
Figure 261. S7505CTR25 West Face Constant Moment Region	267
Figure 262. S7505CTR25 Crack Width vs Deflection for (a) East Face and (b) West Face	268
Figure 263. S7505CTR25 Crack Progression of E1 at: (a) 0.2 in deflection, (b) 0.5 in deflection, (c) 0.8 in deflection, and (d) 1.2 in deflection	269
Figure 264. S7505CTR25 Crack Progression of W1 at Deflection Step: (a) 0.3 in deflection, (b) 0.6 in deflection, (c) 1.0 in deflection, and (d) 1.4 in deflection	270
Figure 265. S7505CTR25 Crushing at: (a) 0.7 in Deflection, (b), 1.1 in Deflection, (c) 1.2 in Deflection, (d) Conclusion of Test	271
Figure 266. S7505NOS00 Crack Profile East Face	273
Figure 267. S7505NOS00 Crack Profile West Face.....	273
Figure 268. S7505NOS00 Crack Width Progression of Critical Cracks (a) E1 and (b) W1	273
Figure 269. S7505NOS00 Damage Progression of the Critical Crack on the East Face, E1, at: (a) 0.05 inches, (b) 0.30 inches, (c) 0.80 inches, and (d) Conclusion of Test.....	274
Figure 270. S7505NOS00 Damage Progression of Critical Crack West Face, W1, at (a) 0.05 inches, (b) 0.30 inches, (c) 0.80 inches, and (d) Conclusion of Test	275
Figure 271. S7505NOS00 Concrete Crushing on (a) East Face at 0.70 inches and (b) West Face at Remaining Capacity of 0.050 kips.....	276
Figure 272. S7505NOS00 Collapse of the Specimen Viewed from (a) East Face and (b) West Face	276
Figure 273. S7520NOS00 Damaged Corner	278
Figure 274. S7520NOS00 Crack Progression of E1 and E12 at (a) 0.1 inches, (b) 0.6 inches, (c) 0.8 inches, and 1.1 inches.	278

Figure 275. S7520NOS00 Crack Progression of W2 and W3 at: (a) 0.2 inches, (b) 0.5 inches, (c) 0.8 inches, and 1.1 inches	279
Figure 276. S7520NOS00 Crushing Progression at (a) 1.0 and (b) Completion of Test	279
Figure 277. S9005BTM35 Crack Profile East Face	281
Figure 278. S9005BTM35 East Face Constant Moment Region.....	281
Figure 279. S9005BTM35 Crack Profile West Face	282
Figure 280. West Face Constant Moment Region	282
Figure 281. S9005BTM35 Crack Opening vs Strip Deflection for (a) East Face and (b) West Face	283
Figure 282. S9005BTM35 Crack Opening vs Strip Deflection for Primary Crack at Each Reference Line (a) E6 and (b) W5	284
Figure 283. S9005BTM35 Crack Progression of E6 and E8 at: (a) 0.2 inches, (b) 0.8 inches, (c) 1.4 inches, and Removal of Beam	285
Figure 284. S9005BTM35 Crack Progression of W5 at: (a) 0.2 inches, (b) 0.8 inches, (c) 1.4 inches, and Removal of Beam	286
Figure 285. S9005BTM35 Crushing Progression at (a) 0.7 inch, (b) 0.8 inch, (c) 1.0 inches and (d) 1.6 inches.....	287
Figure 286. S9005BTM35 Severe Crushing Damage above Critical Cracks E6 and E8.....	287
Figure 287. S9005BTM25 Crack Profile East Face.....	289
Figure 288. S9005BTM25 Crack Profile West Face	289
Figure 289. S9005BTM25 Crack Opening vs Strip Deflection for (a) East Face and (b) West Face	290
Figure 290. Crack Opening vs Strip Deflection for Primary Crack at Each Reference Line (a) E1 and (b) W3.....	291
Figure 291. S9005BTM25 Crack Progression of E1 at: (a) 0.05 inches, (b) 0.6 inches, (c) 1.4 inches, and Removal of Beam	292
Figure 292. S9005BTM25 Crack Progression of W3 at: (a) 0.1 inches, (b) 0.6 inches, (c) 1.4 inches, and Removal of Beam	293
Figure 293. S9005BTM25 Crushing Progression at: (a) 0.9 inch, (b) 1.2 inch, (c) 1.6 inches and (d) Completion of Test	294
Figure 294. S9005BTM24 Crack Profile East Face.....	296
Figure 295. S9005BTM24 Crack Profile West Face	296
Figure 296. S9005BTM24 Crack Opening vs Strip Deflection for (a) East Face and (b) West Face	296
Figure 297. S9005BTM24 Crack Opening vs Strip Deflection for Primary Crack at Each Reference Line (a) E1 and (b) W9	297
Figure 298. S9005BTM24 Crack Progression of E1 at: (a) 0.05 inches, (b) 0.6 inches, (c) 1.0 inches, and 1.4 inches	298
Figure 299. S9005BTM24 Crack Progression of W3 at: (a) 0.4 inches, (b) 0.7 inches, (c) 1.0 inches, and (d) 1.4 inches	299
Figure 300. S9005BTM24 Crushing Progression at (a) 0.8 inch, (b) 1.0 inch, (c) 1.4 inches and (d) Completion of Test	300
Figure 301. S9005BTM23 Crack Profile East Face.....	302
Figure 302. S9005BTM23 Crack Profile West Face	302
Figure 303. S9005BTM23 Crack Opening vs Strip Deflection for (a) East Face and (b) West Face	303
Figure 304. S9005BTM23 Crack Opening vs Strip Deflection for Primary Crack at Each Reference Line (a) E2 and (b) W1	303
Figure 305. S9005BTM23 Crack Progression of E2 at Deflection Step: (a) 0.1 inches, (b) 0.4 inches, (c) 0.7 inches, and 1.4 inches	304
Figure 306. S9005BTM23 Crack Progression of W1 at: (a) 0.2 inches, (b) 0.4 inches, (c) 0.7 inches, and 1.4 inches.....	305

Figure 307. S9005BTM23 Crushing Progression at: (a) 0.8 inch, (b) 1.0 inch, (c) 1.4 inches and (d) Completion of Test	306
Figure 308. S9005NOS00 Crack Profile East Face	308
Figure 309. S9005NOS00 Crack Profile West Face	308
Figure 310. S9005NOS00 Crack Width Progression of Critical Cracks (a) E2 and (b) W1	308
Figure 311. S9005NOS00 Damage Progression of the Critical Crack on the East Face, E2, at: (a) 0.1 inches, (b) 0.30 inches, and (c) 0.80 inches. (d) Fiber Bridging	309
Figure 312. S9005NOS00 Damage Progression of the Critical Crack on the West Face, W1, at: (a) 0.1 inches, (b) 0.35 inches, and (c) 0.80 inches. (d) Fiber Bridging	310
Figure 313. S9005NOS00 Concrete Crushing on East Face	310
Figure 314. S9020NOS00 Crack Progression of E1 and E12 at: (a) 0.2 inches, (b) 0.3 inches, (c) 1.2 inches, and 1.6 inches	311
Figure 315. S9020NOS00 Crack Progression of W2 and W3 at: (a) 0.35 inches, (b) 0.9 inches, (c) 1.6 inches, and Removal of Instruments	312
Figure 316. S9020NOS00 Fiber Distribution (a) South Face of Failure Plane and (b) North Face of Failure Plane	312

LIST OF TABLES

	Page
Table 1. Classifications of Experimental Data for SFRC.....	7
Table 2. Comparison of ADOT and TxDOT Standards (ADOT 2008; TxDOT 2008).....	33
Table 3. Coarse Aggregate Gradation Chart (TxDOT 2008)	33
Table 4. Fine Aggregate Gradation Chart (ADOT 2008; TxDOT 2008)	34
Table 5. Mix Design Averages and DOT Requirements.....	34
Table 6. A Summary of the FRC Applications to Slab-on-Grade	36
Table 7. The Fiber Types Used by Folliard et al. (2006)	37
Table 8. The Mixture Design for the Field Application (Folliard et al. 2006)	38
Table 9. Fresh Concrete Properties (Folliard et al. 2006)	38
Table 10. Compression Test Results (Folliard et al. 2006)	39
Table 11. Elastic Modulus Test Results (Folliard et al. 2006).....	39
Table 12. Split Tension Test Results (Folliard et al. 2006).....	39
Table 13. Flexural Test Results (Folliard et al. 2006)	39
Table 14. Summary of On-Site Monitoring (Folliard et al. 2006).....	40
Table 15. General Traffic Input Parameters.....	42
Table 16. Statewide Average Monthly Adjustment Factor.....	43
Table 17. Statewide Hourly Distribution Factor.....	43
Table 18. The CRCP Layer Properties	44
Table 19. The Reinforcement of the CRCP Layer	44
Table 20. The Properties of the Unbound Materials	44
Table 21. The Limit Values for Each Pavement Distresses in MEPDG	45
Table 22. Model Parameters.....	51
Table 23. Steel Profiles.....	51
Table 24. Normalized Moment for S6-F4500.....	59
Table 25. Normalized Moment for S8-F4500.....	59
Table 26. Normalized Moment Capacity for S12-F4500.....	60
Table 27. Normalized Curvature for S6-F4500 with Varied Depth, Mu, and Steel Profiles.....	60
Table 28. Normalized Curvature for S8-F4500 with Varied Depth, Mu, and Steel Profiles.....	60
Table 29. Normalized Curvature for S12-F4500 with Varied Depth, Mu, and Steel Profiles.....	61
Table 30. Slab Bridge Parameters	63
Table 31. Steel Profiles for Slab Bridge	63
Table 32. Normalized Moment Capacity for S15-F4500.....	65
Table 33. Normalized Moment Capacity for S30-F4500.....	66
Table 34. Railing Parameters	68
Table 35. Steel Profiles for Railing	68
Table 36. Material Test Cases and Number of Specimens.....	73
Table 37. Properties of the Raw Materials Used	74
Table 38. SFRC Mix Design	76
Table 39. A Summary of the Mechanical Properties of the SFRCs under Different Loading Conditions	106
Table 40. Steel Area Required to Meet ADOT Limit States.....	111
Table 41. Test Matrix slab strip specimens.....	113
Table 42. TxDOT and ADOT Mix Requirements for Concrete Bridge Decks	117

Table 43. Compressive Strength and Modulus of Elasticity for All Mixes Used	118
Table 44. Summary of Flexural Test Results	120
Table 45. Summary of Steel Reinforcement Properties for All Steel Bars	121
Table 46. Average Properties of Cracks at Maximum Capacity	123
Table 47. Properties of Failure Criteria for Specimens with Steel Reinforcement Located at Bottom.....	125
Table 48. Properties of Non-Critical Cracks for Specimens with Steel Reinforcement Located at the Bottom	130
Table 49. Properties of Failure Criteria for Specimens with Steel Reinforcement Located at Bottom.....	134
Table 50. Properties of Non-Critical Cracks for Specimens with Steel Reinforcement Located at Center.....	136
Table 51. Properties of Failure Criteria for Specimens with Steel Reinforcement Located at Center.....	136
Table 52. Properties of Failure Criteria for Specimens without Steel Reinforcement	138
Table 53. Summary of S7505 Experimental SFRC Service Capacity	141
Table 54. Summary of S7505 Experimental SFRC Maximum Capacity	142
Table 55. Summary of S9005 Experimental Service Capacity	143
Table 56. Summary of S9005 Experimental Maximum Capacity	143
Table 57. Summary of SFRC without Steel Reinforcement Experimental Results.....	144
Table 58. Service Stresses (ksi) of S7505BTM## at Maximum Girder Spacing, 7 ft.....	147
Table 59. Service Stresses (ksi) of S9005BTM## at Maximum Girder Spacing, 11.5 ft.....	148
Table 60. Service and Strength Capacities of PC and SFRC.....	150
Table 61. Maximum Span Permitted for SFRC Slab strips	150
Table 62. Summary of Results from SFRC Bridge Deck Test Program	174
Table 63. Comparison for Full-Scale Specimen and Tests by Others.....	177
Table 64. Summary of ASTM C1609 Results and Tension Models.....	185
Table 65. Percent Difference between Experimental Results and Theoretical model	194
Table 66. Moment Capacities Used for Yield Line Analysis	202
Table 67. Summary of Yield Line Analysis for SFRC Bridge Deck	208
Table 68. Service Moment of Experimental Tests Using Proposed Procedure	214
Table 69. Nominal Moment of Experimental Tests Using Proposed Procedure	215
Table 70. Summary of ADOT LRFD Design Example 4	218
Table 71. Summary of Demands ADOT LRFD Design Example 4	313
Table 72. Summary of Design Values for RC Slab	315
Table 73. Summary of Design Values for SFRC Slab (Service Only)	316
Table 74. Summary of Design Values for SFRC Slab (Strength)	318

LIST OF ACRONYMS

AASHTO	American Association of State Highway and Transportation Officials
ACI	American Concrete Institute
ADOT	Arizona Department of Transportation
AFGC-SETRA	Service d'étude des transports, des routes et leurs aménagement-Association Française de Génie Civil
AFRP	aramid FRP
ARS	average residual strength
ASTM	American Society for Testing and Materials
CMOD	crack mouth opening displacement
CRCP	continuously reinforced concrete pavement
DAQ	data acquisition
DOT	department of transportation
FRC	fiber-reinforced concrete
FRP	fiber-reinforced polymer
HDF	hourly distribution factors
HPFRCC	high-performance fiber-reinforced cementitious composite
IRI	international roughness index
JSCE	Japan Society of Civil Engineers
LOP	limit of proportionality
LRFD	load and resistance factor design
LVDT	linear variable displacement transducer
MEPD	mechanistic-empirical pavement design
MEPDG	mechanistic-empirical pavement design guide
MOR	modulus of rupture
MTS	material testing system
NCHRP	National Cooperative Highway Research Program
PC	plain concrete
PVA	polyvinyl alcohol
RILEM	International Union of Laboratories and Experts in Construction Materials, Systems, and Structures
SFRC	steel fiber-reinforced concrete
TxDOT	Texas Department of Transportation

EXECUTIVE SUMMARY

Implementation of fiber-reinforced concrete in transportation infrastructure necessitates experimental investigation to ensure that the improved tensile response provided by the fibers is effectively used and that appropriate design procedures are adopted to ensure safe, efficient designs are developed. This report documents the findings of a study, sponsored by the Arizona Department of Transportation, on the use of steel fiber reinforced concrete (SFRC) to improve the performance of transportation infrastructure, particularly at the service level.

The project consisted of a preliminary literature review and case studies to guide the development of an experimental test program. Material tests (compression, tension, and bending) were used to establish basic mechanical responses of the two types (straight and hooked) of steel fibers. The following observations were made:

- Increased volume of fiber decreased the workability of the concrete
- Fibers did not significantly influence the compressive behavior, but significantly increased the residual strength and ductility of the concrete in bending and tension.
- Hooked fibers were effective in increasing the modulus of rupture.

The mechanical properties from the material test program were used to design a slab strip test program to investigate the interaction of hooked fiber SFRC at 0.5 percent volume with traditional reinforcement. The slab strip program was used to establish an understanding of the impact of the SFRC on the service performance and strength of the slabs. The test program focused on the ability of the SFRC to reduce the amount of conventional steel reinforcement used in bridge decks, while providing equivalent or improved service level performance. The following was found:

- The use of hooked steel fibers with traditional steel reinforcement resulted in the development of more cracks than in slabs with plain concrete and the same amount of reinforcement. The fibers controlled the width of cracks and reduced the steel strain at service demands.
- In slab strips with 0.5 percent volume hooked fibers and traditional steel designed for the strength limit state satisfied service level stress criteria, whereas the same design without SFRC would not.
- As the amount of traditional steel reinforcement increases, the effect of the steel fibers diminishes.

A full-scale bridge deck was tested to investigate the two-way behavior of SFRC bridge decks with an orthotropic layout of conventional reinforcement. The following was found:

- Crack patterns formed an elliptical yield line pattern as would be expected with a conventional RC deck, however significant multiple cracking effects were observed.
- The performance of the bridge deck satisfied serviceability and strength design requirements, with the experimental strength was as large as 450 percent greater than the factored AASHTO demand for strength design.

- Yield line analysis significantly underpredicted the experimental capacity of load tests, except for overhang load tests.

Finally, equations for strength and service design of SFRC slabs with conventional reinforcement were recommended. Equations for both performance levels use the tensile response of concrete, with the tension response assumed to be the residual tensile strength. Design examples are included

CHAPTER 1. INTRODUCTION

OVERVIEW

Fiber-reinforced concrete (FRC) is concrete containing a small amount of randomly oriented short and discrete fibers. The primary purpose of adding fibers into concrete is to control the cracking resistance of concrete, so improvements in tensile strength and post-cracking ductility are the principal roles of the fibers in the concrete matrix. Reinforcing effects of fibers made of various materials have been investigated by various investigators, and the steel fiber is one of the most popular choices for concrete reinforcement because of its wide availability, good mechanical performances, and cost effectiveness. Improvements to the tensile strength and post-cracking behavior of FRC has led to many successful structural applications, including use in seismic design, as shear reinforcement in beams, and for the construction of slabs-on-grade and elevated slabs. This research is focused on the use of steel fiber reinforced concrete (SFRC) for transportation infrastructure projects.

The implementation of SFRC in transportation infrastructure projects necessitates investigation to ensure that the material benefits are efficiently harnessed and that appropriate design procedures are adopted to ensure safe, efficient designs are developed. The objectives of this research study are 1) to investigate the application of SFRC in transportation projects in Arizona, and 2) to provide recommendations for implementation.

SFRC is a material that has been well studied from materials and structural perspectives; however, there are gaps in the previous research that must be addressed for successful future applications. These gaps include limited data of SFRC with large aggregate, the interaction of SFRC and traditional reinforcement in bridge decks, and the impact of SFRC on service level behavior of bridge decks. This research experimentally tested the use of SFRC using standard Arizona Department of Transportation (ADOT) concrete mixes that include large aggregate. Using one of the mix designs investigated, a structural experimental test program was undertaken to investigate the behavior of bridge decks with a combination of SFRC and traditional reinforcing steel. Specifically, the impact of SFRC on the stiffness, strength, and ductility of the deck was investigated. Experimental investigation included assessment of both one-way and two-way behavior of bridge decks.

OVERVIEW OF RESEARCH AND ORGANIZATION OF REPORT

The research was conducted in three phases. Phase 1 provided background information and preliminary studies to address the project objectives. Phase 2 was an experimental investigation into the application of SFRC to bridge structures. The experimental test program involved three sequential test programs: materials tests, slab-strip beam tests, and a full deck test. In Phase 3, the results of Phase 2 experimental tests were analyzed along with the preliminary investigations to provide design recommendations and preliminary design procedures for the use of SFRC in the ADOT bridge structures.

Phase 1—Background and Preliminary Investigations

The results of Phase 1 are documented in Chapters 2 through 4. Chapter 2 provides a comprehensive literature review to document the state-of-practice and state-of-art on issues related to the use of FRC. Chapter 3 presents case studies for the use of FRC for slab-on-grade. Chapter 4 presents case studies for use of SFRC for bridge structures, specifically slab-girder bridges, slab bridges, and bridge rails.

Phase 2—Experimental Test Programs

The results of the experimental tests are presented in three chapters. Chapter 5 presents the results of a materials testing program. The mix design used was intended to be representative of ADOT standard mixes. Straight, hooked, and a combination of straight and hooked fibers were used in varying volumes to further understanding of the compressive, tensile, and flexural response of these mixes.

Chapter 6 presents the results of a test program investigating the one-way bending behavior of slab strips subjected to four point bending. The beams investigated the impact of fiber content, slab thickness, and steel ratio and placement on the flexural response.

Chapter 7 presents the results of a full-scale bridge deck test used to investigate the two-way behavior of SFRC bridge decks.

Phase 3—Analysis and Design Recommendations

The cumulative results of the background investigations in Phase 1 and the experimental studies in Phase 2 are analyzed in Phase 3 to provide a comprehensive understanding of the use of SFRC in ADOT bridges.

Chapters 8 and 9 provide in-depth analysis of the experimental data from the structural tests (Chapter 6 and 7), including comparison to the findings of the case studies in Chapter 4. Chapter 10 provides recommendations for the use of SFRC in bridge decks, including limits on reinforcement used, design assumptions, and general best practices for implementation. Finally, Chapter 11 provides a summary of the key findings of the research and recommendations for future research.

CHAPTER 2. LITERATURE REVIEW

This literature review provides information on the typical reinforcing effects of smooth and hooked steel fibers and background for structural applications of SFRC. First, the characteristics and classifications of SFRC are summarized, and the standard test methods are provided. Stress–strain curves (compression or tension tests) and load–deflection curves (flexural tests) for coupon size specimens made of SFRC are collected and classified based on the test configuration, matrix type, and reinforcing effect. Next, an overview of the structural applications of SFRC is presented, including a summary of design methods, common applications for SFRC in both buildings and transportation structures. In addition to summarizing applications of SFRC, previous research or application studies for non-steel FRC or other approaches to modifying traditional bridge deck designs are summarized. Finally, to relate the results of previous research to potential application in ADOT structures, characteristics of SFRC used in prior structural application studies are compared to characteristics of standard ADOT mix designs.

CHARACTERISTICS AND CLASSIFICATIONS OF THE SFRC BEHAVIORS

Plain concrete (PC) is a brittle material, and its tensile strength is typically neglected in structural design of concrete. When fibers are added, the increase in tensile strength and ductility are substantial, while the increase in compressive strength is not. Because of the changes in tensile behavior of FRC, the flexural behavior of FRC varies as well. Naaman and Reinhardt (2006) suggested a classification of FRC based on the tensile behavior. According to the behavior after the proportional limit (point 1 in Figure 1), the tensile response of FRC can be divided into tensile strain hardening and tensile strain softening (Figure 1) behaviors. Similarly, the flexural behavior can be classified as deflection hardening and deflection softening (Figure 2). According to Kim et al. (2008), the limit of proportionality (LOP) is the point where a first cracking occurs, and the modulus of rupture (MOR) is the point where softening starts. Therefore, if the force at MOR is higher than the force at LOP, the behavior is considered as deflection-hardening. The deflection-hardening behavior indicates that the beam carries higher loads after the first crack development. This implies that a further propagation of the first crack is retarded by the fiber bridging effect, and the additional cracks can be initiated because of the high bending moment beyond the LOP. Multiple cracking is one of the evidences of the deflection-hardening behavior and has been observed by many previous investigators (Kim et al. 2008). On the other hand, the failure of the deflection-softening FRC is governed by the first crack, and multiple cracking does not occur. The flexural deflection-hardening does not necessarily accompany tensile strain-hardening. Naaman and Reinhardt (2006) stated that the deflection hardening can be observed at both tensile softening and hardening FRCs and suggested a FRC classification shown in Figure 3. FRC showing tensile hardening behavior is often called high-performance fiber-reinforced cementitious composite (HPFRCC). A detailed graphical explanation on stepwise behaviors in tension and bending can be found in Wille et al. (2014).

Table 1 summarizes the key conditions affecting the FRC behavior. These conditions include loading configuration, existence of reinforcing bars, mixture constituents, concrete strength, fiber type, and the reinforcing effects. Figure 4 shows examples of shapes of steel fibers.

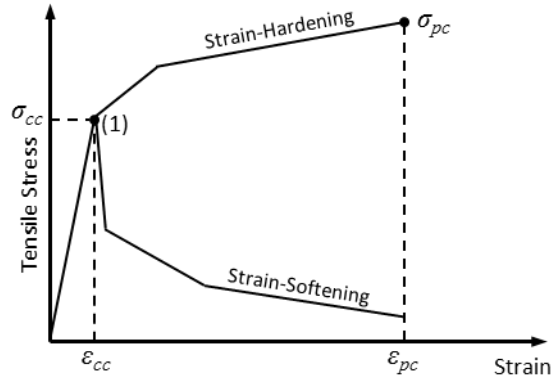


Figure 1. Typical Stress-Strain Curve Response of a Strain Hardening and Strain Softening FRC Composite (Reconstructed Based on Naaman and Reinhardt 2006)

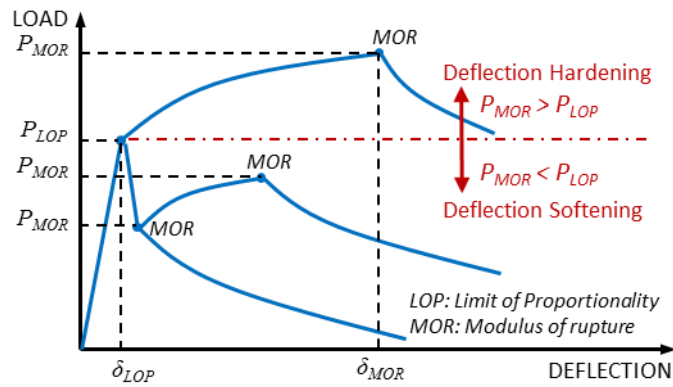


Figure 2. Typical Load-Deflection Response Curve of FRC (Reconstructed Based on Kim et al. 2008)

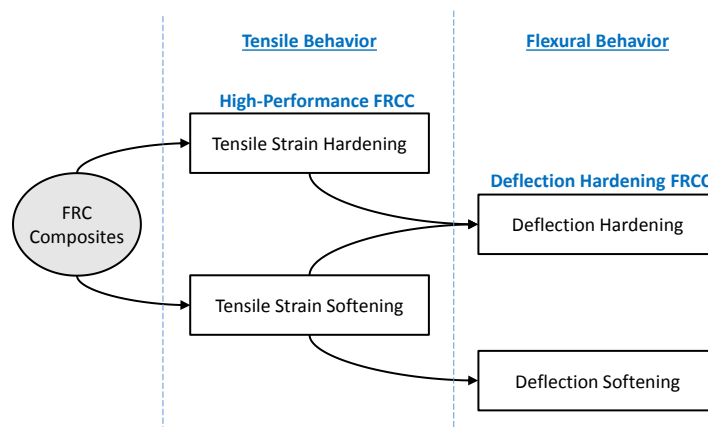


Figure 3. Classification of FRC Composites Based on the Tensile Strength Response (Reconstructed Based on Naaman and Reinhardt 2006)

Table 1. Classifications of Experimental Data for SFRC

Conditions	Classification
Loading configuration	<ol style="list-style-type: none"> 1. Uniaxial compression 2. Uniaxial tension 3. Bending
Reinforcing bars	<ol style="list-style-type: none"> 1. Without reinforcing bars 2. With reinforcing bars
Mixture constituents	<ol style="list-style-type: none"> 1. Cement paste (cement + water) 2. Mortar (cement paste + fine aggregate) 3. Concrete (mortar + coarse aggregate)
Concrete strength	<ol style="list-style-type: none"> 1. Normal strength 2. High strength 3. Ultra-high strength
Fiber types	<ol style="list-style-type: none"> 1. Smooth steel fibers 2. Deformed steel fibers (hooked end) 3. Other fibers (polyvinyl alcohol [PVA] etc.)
Reinforcing effects	<ol style="list-style-type: none"> 1. Tensile hardening/Deflection hardening 2. Tensile softening/Deflection hardening 3. Tensile softening/Deflection softening

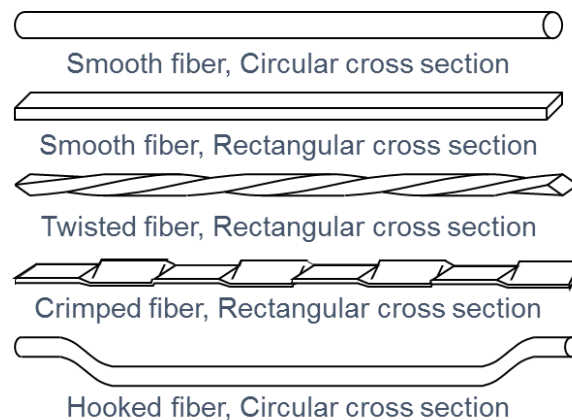


Figure 4. Various Steel Fiber Shapes

Soranakom and Mobasher (2007a; 2007b; 2008) and Mobasher (2012) tried to correlate tensile and flexural responses of strain softening and strain hardening cement composites. They provided the equations predicting the moment-curvature behavior using the uniaxial stress-strain curves or vice versa. Instead of linear stress distribution assumption along with the depth of the beam, they used uniaxial stress-strain model as the stress block. This approach is similar to the method recommended by International Union of Laboratories and Experts in Construction Materials, Systems, and Structures (RILEM) TC 162-TDF (2003).

TEST METHODS AND STANDARDS

The compression test for cylindrical specimen is the most common material test for concrete specimen. Compressive strength of concrete (f'_c) is used for predicting other mechanical properties, such as elastic modulus and MOR. The standard test methods for compressive properties of concrete are:

- American Society for Testing and Materials (ASTM) C39/C39M: Standard Test Method for Compressive Strength of Cylindrical Concrete Specimens (ASTM International 2014a).
- ASTM C469/C469M: Standard Test Method for Static Modulus of Elasticity and Poisson's Ratio of Concrete in Compression (ASTM International 2014b).

The uniaxial tension test is a fundamental test method for evaluating tensile properties of materials, but ASTM International has not adopted a direct tension test method for concrete in general. Instead, alternative test methods simulating the expected conditions of use are recommended. Those are the splitting tensile test and the beam bending test. In the splitting tensile test, diametral compression is applied to a standard cylindrical specimen through two narrow bearing strips along the two opposite sides of the cylinder. ASTM C496/C496M (ASTM International 2011) describes the standard splitting tensile test method. The splitting tensile test simulates the splitting tension failure of concrete subjected to a compressive loading. While splitting tensile strength values are often assumed to be 30–40 percent lower than MOR values and 5–12 percent higher than direct tensile strength values, there are no simple relationships between these values (Mindess et al. 2003).

The beam bending tests simulating loading conditions of flexural members measure another indirect tensile strength, called MOR. Since the flexural loading condition is common in concrete members, MOR values are considered to be more useful than the uniaxial tensile strength. In the case of SFRC, Soranakom and Mobasher (2007a; 2007b) suggested a method of deriving the uniaxial tensile properties from the beam bending test data. The standard test methods for measuring flexural strength are:

- ASTM C293/C293M: Standard Test Method for Flexural Strength of Concrete (Using Simple Beam With Center-Point Loading) (ASTM International 2010a).
- ASTM C78/C78M: Standard Test Method for Flexural Strength of Concrete (Using Simple Beam with Third-Point Loading) (ASTM International 2010b).

The most important benefit of fiber reinforcement is the improvement in tensile strength. Therefore, it is important to evaluate the uniaxial tensile strength of SFRC for modeling and design purpose. While there is no currently available standard for a concrete uniaxial tension test, American Association of State Highway and Transportation Officials (AASHTO) provides a standard test method for cement mortars: AASHTO T 132-87: Standard Method of Test for Tensile Strength of Hydraulic Cement Mortars (AASHTO 2013).

Some foreign institutes provide recommendations for uniaxial tension tests on FRCs that are used for research purpose as follows:

- RILEM TC 162-TDF: Test and Design Methods for Steel Fiber-Reinforced Concrete. Recommendations for Uniaxial Tension Test (RILEM TC 162-TDF 2001).
- Service d'étude des transports, des routes et leurs aménagement-Association Française de Génie Civil (AFGC-SETRA): Ultra High-Performance Fibre-Reinforced Concretes, Interim Recommendations (AFGC-SETRA 2002).
- Japan Society of Civil Engineers (JSCE): Recommendations for Design and Construction of High Performance Fiber Reinforced Cement Composites with Multiple Fine Cracks (HPFRCC) (JSCE 2008).

In addition, Wille et al. (2014) summarizes SFRC specimens for direct tension tests that have been conducted by various researchers.

There exist several standard bending beam test methods tailored for FRCs as follows:

- ASTM C1399/C1399M: Test Method for Obtaining Average Residual-Strength of Fiber-Reinforced Concrete (ASTM International 2010c).
- ASTM C1609/C1609M: Test Method for Flexural Performance of Fiber-Reinforced Concrete (ASTM International 2012a).
- RILEM TC TDF-162: Test and Design Methods for Steel Fiber Reinforced Concrete. Bending Test. (RILEM TC TDF-162 2002).
- BS EN 14651 (British Standards): Test Method for Metallic Fibre Concrete. Measuring the Flexural Tensile Strength (LOP, Residual) (BS 2007).

The loading configurations of ASTM C1399/C1399M and ASTM C1609/C1609M are third-point loading (four-point bending), which is the same as ASTM C78/C78M. While ASTM C78/C78M measures MOR of unnotched specimens, ASTM C1609/C1609M measures first peak loads and residual loads at specific deflections. The specimen toughness and flexural strength ratio are calculated from the residual loads. ASTM C1399/1399M uses a notched specimen. ASTM C1399/1399M describes a method of introducing a pre-crack, and average residual strength (ARS) is calculated from the residual strength at four specified deflections. ARS represents the average stress carrying ability of the cracked FRC beam and is suggested by Banthia and Dubey (1999; 2000). The test method recommended by RILEM TC TDF-162 uses the center-point loading (three-point bending) configuration with a pre-cracked specimen. In the RILEM TC TDF-162 bending test, the deformation of the cracked beam can be described either as deflection or as crack mouth opening displacement (CMOD).

EXPERIMENTAL INVESTIGATIONS FOR SFRC BEHAVIOR

Stress–strain (or load–deflection) curves of SFRC are collected from previous publications. The curves are obtained from direct tension, compression, and flexural tests. The collected stress–strain (and load–deflection) curves are digitalized using computer software. Since the key interest of this literature review is the reinforcing effects of fibers, the stress and strain values for direct tension and compression test data are normalized using the equation below:

$$s_N = \frac{\sigma'_c}{\sigma_{ccN}} \quad (1)$$

$$e_N = \frac{\varepsilon'_c}{\varepsilon_{ccN}} \quad (2)$$

where s_N : Normalized stress.

e_N : Normalized strain.

σ'_c : Stress at arbitrary point in the curve.

σ_{ccN} : Reference first peak stress (obtained from the control specimen of each test set).

ε'_c : Strain at arbitrary point in the curve.

ε_{ccN} : Reference first peak strain (obtained from the control specimen of each test set).

The reference first peak stress and strain, σ_{ccN} and ε_{ccN} , are the stress and strain at the peak point of the stress–strain curves obtained from the control specimen (non-reinforced specimen or specimen with lowest fiber content among the test cases using the same mixture). In the case of non- or low-fiber-reinforced concrete, the stress rapidly drops after the first peak point, and the fracture of the specimen follows. Therefore, σ_{ccN} and ε_{ccN} can be considered as the stress and strain, at the point the damage localization starts for both tension and compression. By this normalization, the improvements in strength and ductility can be compared easily. For example, when the maximum normalized stress is equal to 1.3, the strength increases is 30 percent from addition of the fibers. Because of the diversity in expressions of the beam bending test data, the load-deflection curves are not normalized.

In the previously mentioned publications, different terms were used to indicate the first peak stress and strain of SFRCs, σ_{cc} and ε_{cc} , in tension and compression. Naaman and Reinhardt (2006) defined σ_{cc} and ε_{cc} as the stress and strain at the point where the first deviation from linearity occurs in tensile stress–strain curves. For concretes without fiber reinforcement, this point was considered as the point of first visible cracking (crack localization) during tension tests, but some FRCs such as HPFRCC do not show crack localization at the point of first deviation because of a fiber bridging effect. Kim et al. (2008) denoted the point of first deviation as LOP for load–deflection curves obtained from beam bending tests. On the other hand, for the compression test data, Mobasher (2012) and Soranakom and Mobasher (2008) denoted this point as the yield point. In the sense that a permanent deformation is dominant after the first peak point, this point can be called the yield point. However, the term yield is rarely used for describing the behavior of brittle materials including concrete. In this chapter, σ_{cc} and ε_{cc} are named as first peak stress and strain for both tension and compression.

Compression Test

Ezeldin and Balaguru (1992) investigated the normal- and high-strength FRC under compression. They used steel fibers with hooked ends (hooked fiber). Compressive strength of the specimens ranged from 5 ksi to 12 ksi. The SFRC specimens with three fiber volume fractions—50 lb/yd³ (0.38 percent by volume), 75 lb/yd³ (0.76 percent by volume), and 100 lb/yd³ (1.12 percent by volume)—and three aspect ratios (fiber length, l , divided by fiber diameter, d ; l/d)—60, 75, and 100—were tested. The experimental results showed that the compressive strength, stiffness, and strain at the peak stress are not significantly affected, but the ductility represented by the strain at failure is improved by adding

fibers (Figure 5). They investigated the effect of silica fume on the SFRC behavior and found that adding the silica fume makes the SFRC more brittle.

Wafa and Ashour (1992) investigated the mechanical properties of high-strength FRC. They conducted experiments on a total of 504 specimens to investigate the effect of hooked steel fibers. Fiber contents from 0 percent and 1.5 percent by volume of total mixture were used, and the concrete matrix's compressive strength was 13,600 psi (94 MPa). A small increase in compressive strength (4.6 percent) was observed (Figure 6).

Hsu and Hsu (1994) investigated the stress–strain behavior of steel fiber–reinforced high-strength concrete under compression. They conducted comparative tests with and without tie confinements. The volume fractions of the hooked fiber were 0.0, 0.5, 0.75, and 1.0 percent (Figure 7). They proposed empirical equations to present the complete stress–strain behavior.

Nataraja et al. (1999) conducted compression tests for the specimens with a compressive strength range from 4400 to 7300 psi (30–50 MPa). Round crimped fibers with three different volume fractions (0.5, 0.75, and 1.0 percent) and two aspect ratios (55 and 82) were used. Through the effect of fiber addition, peak stress, strain at peak stress, the toughness of concrete and the characteristics of the stress–strain curve were investigated. As a result, a simple analytical model was proposed that included two portions of stress–strain behavior, ascending and descending parts.

Using two differently shaped specimens (cylindrical and prismatic), Mansur et al. (1999) investigated the effect of casting directions on the compressive stress–strain curves of high-strength (10,200–17,400 psi; 70–120 MPa) concrete and FRC.

Bencardino et al. (2008) conducted compression tests for SFRC. They used cylindrical specimens of PC and SFRC, including 1.0, 1.6, and 3.0 percent fibers by volume (Figure 8). In addition, they evaluated the reliability of the previously published test results. As previous studies showed, the compressive strength is slightly improved, and the ductility significantly increases by adding steel fibers.

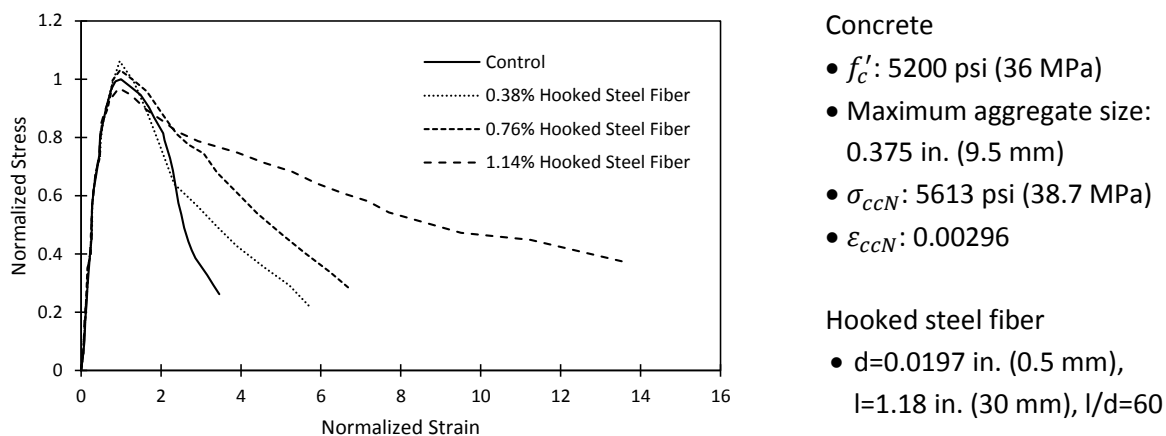


**Figure 5. Compression Test Data for SFRC with Hooked Fibers
(Reproduced from Ezeldin and Balaguru 1992)**

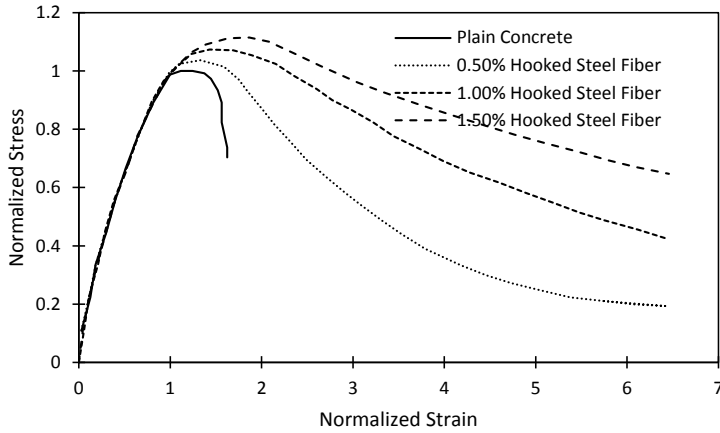


**Figure 6. Compression Test Data for SFRC with Hooked Fibers
(Reproduced from Wafa and Ashour 1992)**

Concrete

- f'_c : 13,600 psi (94 MPa)
- Maximum aggregate size: 0.375 in. (9.5 mm)
- σ_{ccN} : 13,010 psi (89.7 MPa)
- ϵ_{ccN} : 0.00165

Hooked steel fiber

- $d=0.0315$ in. (0.8 mm),
- $l=2.36$ in. (60 mm), $l/d=75$

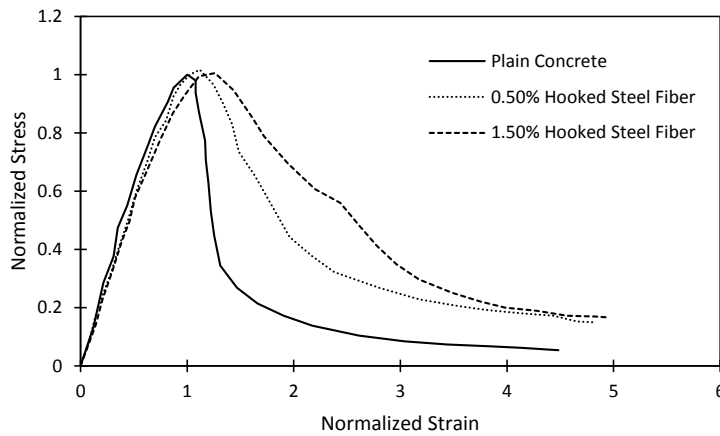


**Figure 7. Compression Test Data for SFRC with Hooked Fibers
(Reproduced from Hsu and Hsu 1995)**

Concrete

- f'_c : 10,600 psi (73.1 MPa at 16 days)
- Maximum aggregate size: 0.375 in. (9.5 mm)
- σ_{ccN} : 11,647 psi (80.3 MPa)
- ϵ_{ccN} : 0.0031

Hooked steel fiber

- $l/d=60$

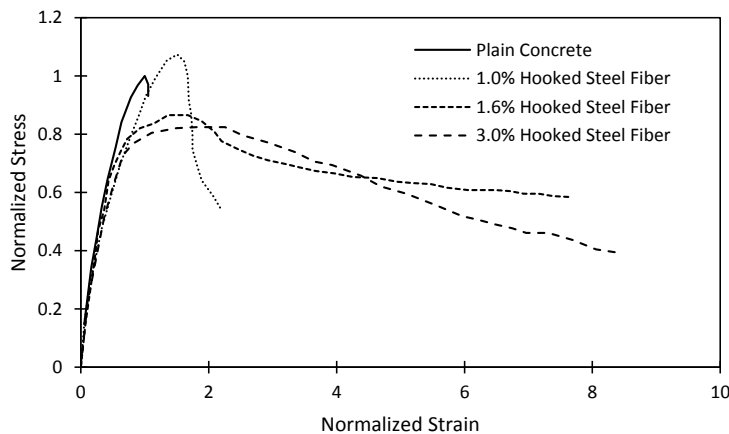


**Figure 8. Compression Test Data for SFRC with Hooked Fibers
(Reproduced from Bencardino et al. 2008)**

Concrete

- f'_c : 9400 psi (65 MPa)
- Maximum aggregate size: 0.625 in. (15 mm)
- σ_{ccN} : 9601 psi (66.2 MPa)
- ϵ_{ccN} : 0.00219

Hooked steel fiber

- $d=0.0217$ in. (0.55 mm),
- $l=0.87$ in. (22 mm), $l/d=40$

Tension Test

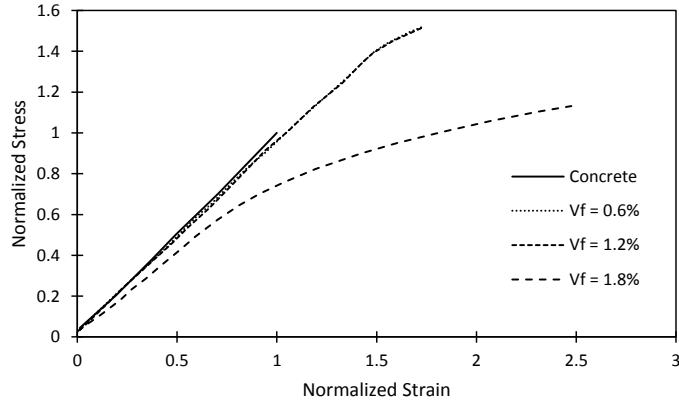
Walkus et al. (1979) studied cracking behavior, strength properties, and deformation properties of mortar with short steel fibers under tension. Specimens containing fibers with different diameter and contents were used. When adding cut steel fibers to the concrete, the strength increased (Figure 9).

Lim et al. (1987) conducted direct tension tests for the concrete reinforced with straight and hooked steel fibers. As compared in Figure 10 and Figure 11, hooked fibers have better reinforcing effect in strength (hooked fiber $\sigma_{ccN} = 408$ psi; straight fiber $\sigma_{ccN} = 352$ psi) and residual strength after the first peak. Using their experimental data, Lim et al. (1987) proposed an idealized tensile stress–strain curve.

Li et al. (1996) studied the tensile properties of cement-based composites including straight steel fibers. The effects of fiber length, interfacial bonding, and processing conditions on composite properties were investigated through direct tension tests. They added fibers into concrete (Figure 12) and cement paste (Figure 13). The experimental results showed that the strength and ductility of SFRC are improved with higher fiber volume, longer fiber length, and improved bond property.

Wille et al. (2011) studied the optimization of strength and ductility of ultra-high-performance FRCs under direct tensile loading. Straight (Figure 14), hooked (Figure 15), and twisted (Figure 16) fibers were used. With an ultra-high-performance concrete that provided high bond strength between fiber and matrix, high-strength deformed steel fibers were used to enhance the ductility and the mechanical bond ductility. Their study showed that a fiber volume fraction of 1 percent was enough to provoke strain hardening behavior and a characteristic essential to satisfy high ductility with proper high-strength steel fibers.

Wille et al. (2014) investigated and analyzed properties of strain hardening ultra-high-performance FRC under direct tensile loading. The objective of this research was to know the uniaxial tensile behavior of the new material through experiments. Through reviewing the tension tests set up in literature, this paper represented revised tension tests set up to obtain reliable results. The variables of their experiments were three types of steel fibers, each in three different volume fractions. According to the test results, they characterized and analyzed the initial cracking stress and strain, elastic and strain hardening modulus, and composite strength.



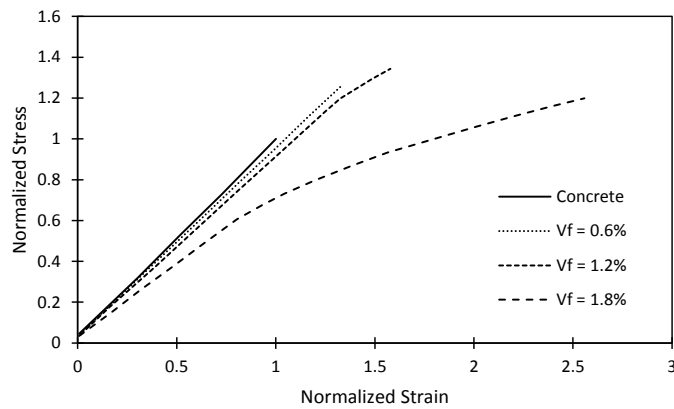
Mortar

- σ_{ccN} : 252 psi (1.74 MPa)
- ϵ_{ccN} : 0.0000839

Straight steel fiber

- $d=0.0098$ in. (0.25 mm),
- $l=0.98$ in. (25 mm), $l/d=100$

(a) Straight Steel Fiber $d=0.25$ mm, $l=25$ mm



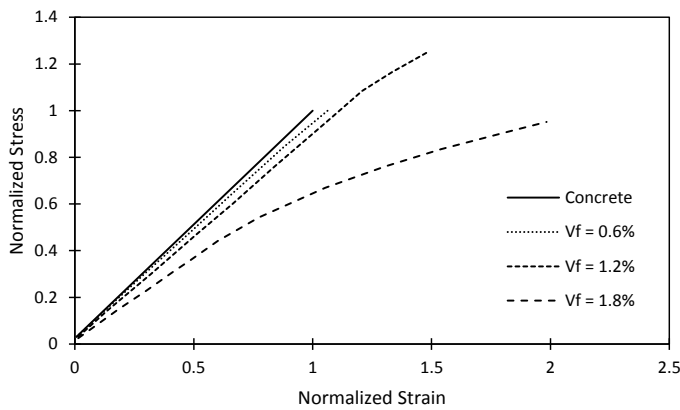
Mortar

- σ_{ccN} : 252 psi (1.74 MPa)
- ϵ_{ccN} : 0.0000839

Straight steel fiber

- $d=0.0138$ in. (0.35 mm),
- $l=0.98$ in. (25 mm), $l/d=71.5$

(b) Straight Steel Fiber $d=0.35$ mm, $l=25$ mm



Mortar

- σ_{ccN} : 252 psi (1.74 MPa)
- ϵ_{ccN} : 0.0000839

Straight steel fiber

- $d=0.0197$ in. (0.50 mm),
- $l=0.98$ in. (25 mm), $l/d=50$

(c) Straight Steel Fiber $d=0.50$ mm, $l=25$ mm

Figure 9. Tension Test Data for Straight Steel Fiber-Reinforced Mortar (Reproduced from Walkus et al. 1979)

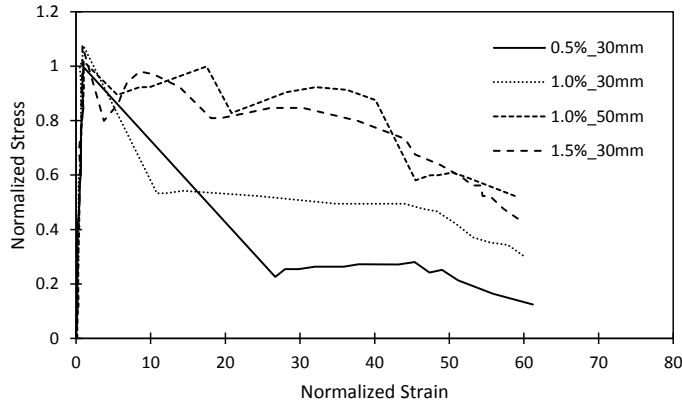


Figure 10. Tension Test Data for SFRC with Hooked Fibers (Reproduced from Lim et al. 1987)

Concrete

- Maximum aggregate size: 0.394 in. (10 mm)
- σ_{ccN} : 408 psi (2.81 MPa)
- ϵ_{ccN} : 0.000245

Hooked steel fiber

- $d=0.0197$ in. (0.50 mm), $l=1.18/1.97$ in. (30/50 mm), $l/d=60/100$

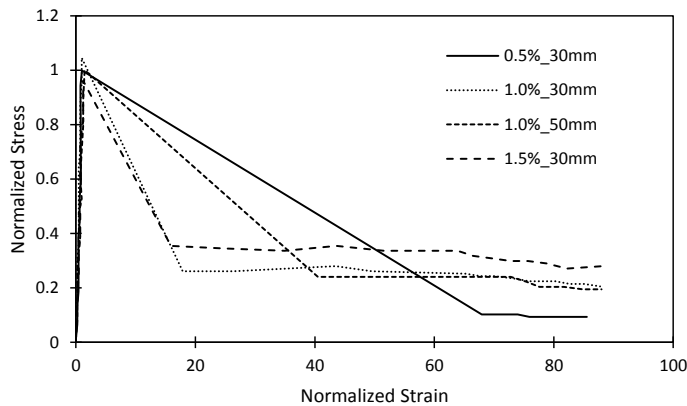


Figure 11. Tension Test Data for SFRC with Straight Fibers (Reproduced from Lim et al. 1987)

Concrete

- Maximum aggregate size: 0.394 in. (10 mm)
- σ_{ccN} : 352 psi (2.43 MPa)
- ϵ_{ccN} : 0.00017

Straight steel fiber

- $d=0.0222$ in. (0.565 mm), $l=1.18/1.97$ in. (30/50 mm), $l/d=53/88.5$

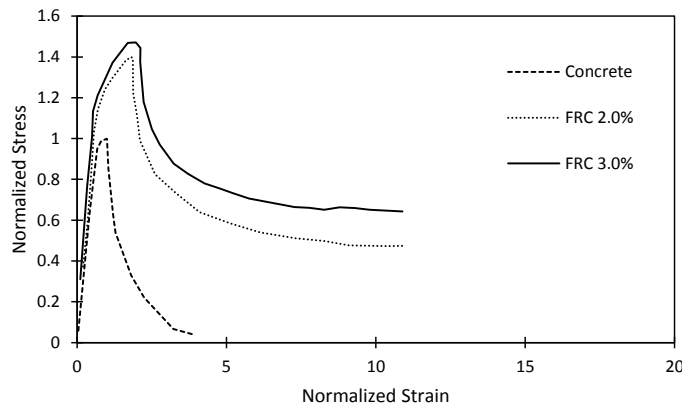


Figure 12. Tension Test Data for SFRC with Straight Fibers (Reproduced from Li et al. 1996)

Concrete

- σ_{ccN} : 421 psi (2.9 MPa)
- ϵ_{ccN} : 0.000551

Straight steel fiber

- $d=0.0059$ in. (0.15 mm), $l=$ inches (16 mm), $l/d=107$

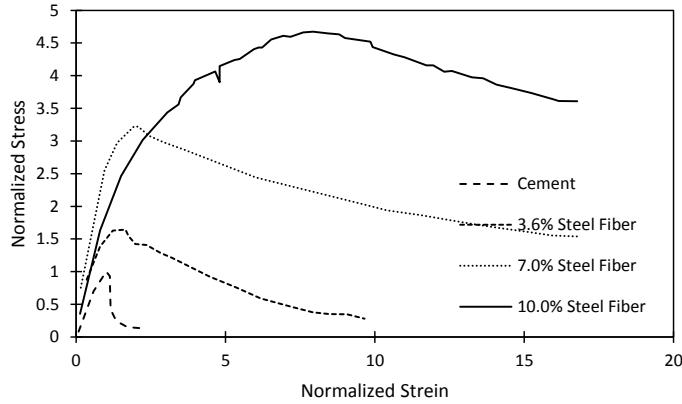


Figure 13. Tension Test Data for SFRC with Straight Fibers (Reproduced from Li et al. 1996)

Cement paste

- σ_{ccN} : 229 psi (1.58 MPa)
- ϵ_{ccN} : 0.000298

Straight steel fiber

- $d=0.0059$ in. (0.15 mm),
- $l=0.236$ in. (6 mm), $l/d=40$

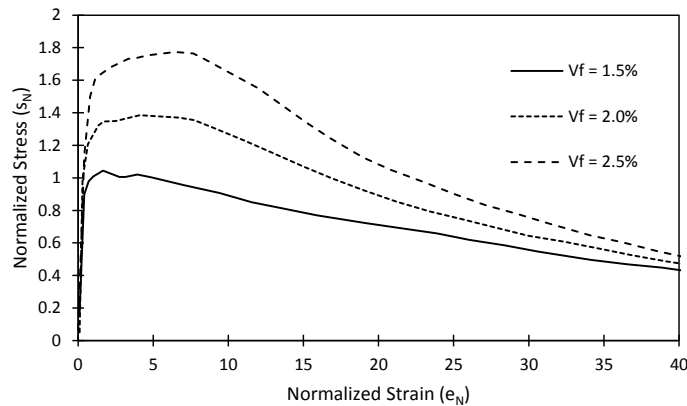


Figure 14. Tension Test Data for Ultra-High-Performance Mortar with Straight Fibers (Reproduced from Wille et al. 2011)

Mortar

- f'_c : 27,800 psi (192 MPa)
- σ_{ccN} : 1208 psi (8.33 MPa)
- ϵ_{ccN} : 0.000575

Straight steel fiber

- $d=0.0079$ in. (0.2 mm),
- $l=0.512$ in. (13 mm), $l/d=65$

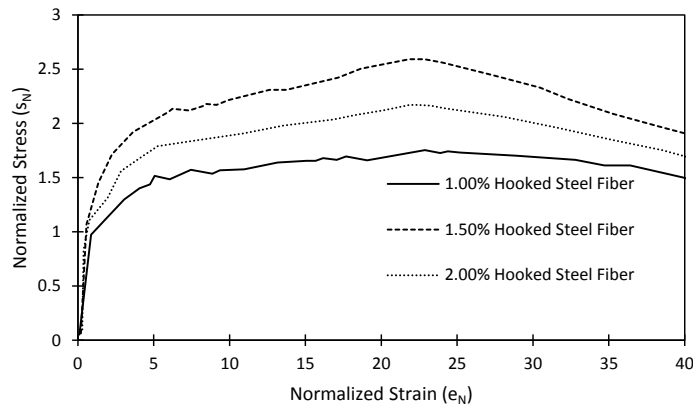


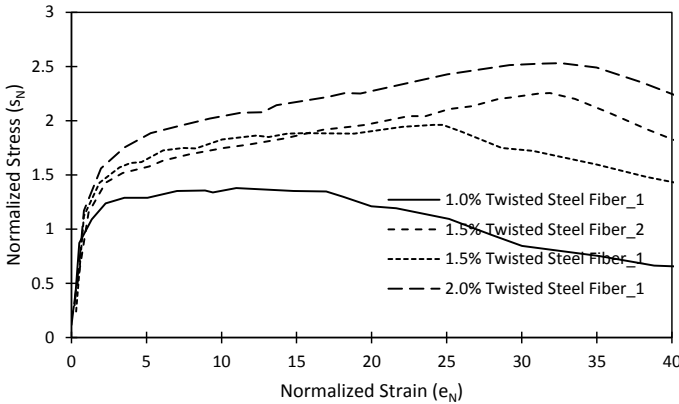
Figure 15. Tension Test Data for Ultra-High-Performance Mortar with Hooked Fibers (Reproduced from Wille et al. 2011)

Mortar

- f'_c : 27,800 psi (192 MPa)
- σ_{ccN} : 1375 psi (9.48 MPa)
- ϵ_{ccN} : 0.00467

Hooked steel fiber

- $d=0.0150$ in. (0.38 mm),
- $l=1.18$ in. (30 mm), $l/d=79$



Mortar

- f'_c : 27,800 psi (192 MPa)
- σ_{ccN} : 1185 psi (8.17 MPa)
- ϵ_{ccN} : 0.0021

Twisted steel fiber

- $d=0.0118$ in. (0.3 mm),
 $l=1.18$ in. (30 mm), $l/d=100$

**Figure 16. Tension Test Data for Ultra-High-Performance Mortar with Twisted Fibers
(Reproduced from Wille et al. 2011)**

Flexural Test

Soroushian and Bayasi (1991) studied the effects of various deformed fibers on the performance of SFRC. The used fibers were straight-round, crimped-round, crimped-rectangular, hooked-single, and hooked-collated with around a 60 aspect ratio, and straight-round and hooked collated fibers with a 75 aspect ratio. They used a constant fiber volume fraction (2 percent). Test results showed that the different fiber types did not influence the workability and slump. Figure 17 and Figure 18 show that the increase in flexural strength is more significant than in the case of tensile strength. The hooked fibers always show higher strength improvements than the straight and crimped fibers.

Balaguru et al. (1992) investigated the flexural toughness of SFRC. The experimental variables were fiber type, length, volume fraction, and matrix composition. The results showed that the specimens with fiber contents ranging from 50 to 100 lb/yd³ (0.38–1.14 percent by total volume) had improved ductility compared to normal strength concrete. Hooked fibers provided better results than corrugated or deformed fibers. Toughness is not significantly affected by the fiber length. Toughness was not affected by addition of silica fume up to 20 percent. Figure 19 and Figure 20 compare the reinforcing effects of hooked fiber contents.

Flexural behaviors of mortars reinforced with four different types of fibers were compared in Kim et al. (2008). The volume fraction of the fibers were 0.4 and 1.2 percent. The mortar matrix had 8122 psi (56 MPa) of nominal compressive strength. The four fibers were twisted steel fiber, hooked steel fiber, polyethylene spectra, and PVA fibers. The twisted fiber specimens exhibited the highest improvements in strength and toughness (Figure 21 and Figure 22). Additional comparative experiments on hooked and twisted fibers in high-strength mortar (12,183 psi; 84 MPa) showed that the twisted fibers have better strength improvement than the hooked fiber (Figure 23).

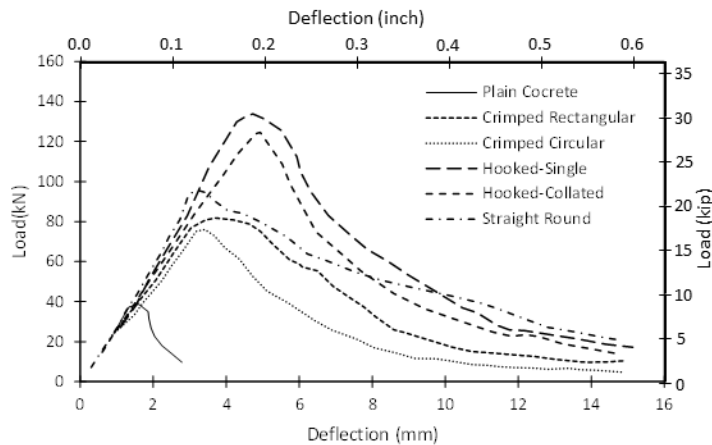
Wafa and Ashour (1992) also conducted beam bending tests and reported that the MOR and the splitting tensile strength improved about 67 percent and 160 percent, respectively.

REINFORCING EFFECTS OF SFRC

Mechanical improvements due to the fibers are compared in this section. Elastic modulus, strength (maximum stress in the stress–strain curve), strain at the maximum stress, and ultimate strain (maximum strain in the stress–strain curve representing ductility) are obtained from the uniaxial tension and compression data above, and plotted against the fiber contents in Figure 24 (compression data) and **Error! Reference source not found.** Figure 25 (tension data).

Figure 24a and Figure 24b show that adding fibers up to 3.0 percent does not bring significant improvement in compressive strength and elastic modulus. On the other hand, the values related to strain show consistent improvements with increase of fiber contents (Figure 24c and Figure 24d).

On the other hand, the tensile properties of concrete are significantly affected by fiber reinforcements. As shown in Figure 25**Error! Reference source not found.**, most results of previous experiments are different according to various fiber contents.



Concrete

- Specimen size: 4×4×20 in.
- Maximum aggregate size: 0.625 in. (10 mm)

Steel fiber

- $V_f = 2.0$ percent
- Crimped-rec: $d=0.035$ in., $l=2$ in., ($l/d=57$)
- Crimped-circular: $d=0.35$ in., $l=2$ in. ($l/d=57$)
- Hooked-single: $d=0.020$ in., $l=1.2$ in., ($l/d=60$)
- Hooked-collated: $d=0.020$ in., $l=1.2$ in., ($l/d=60$)
- Straight-round: $d=0.035$ in., $l=2$ in., ($l/d=57$)

Figure 17. Flexural Test Data of SFRC: Aspect Ratio = 57–60 (Soroushian and Bayasi 1991)

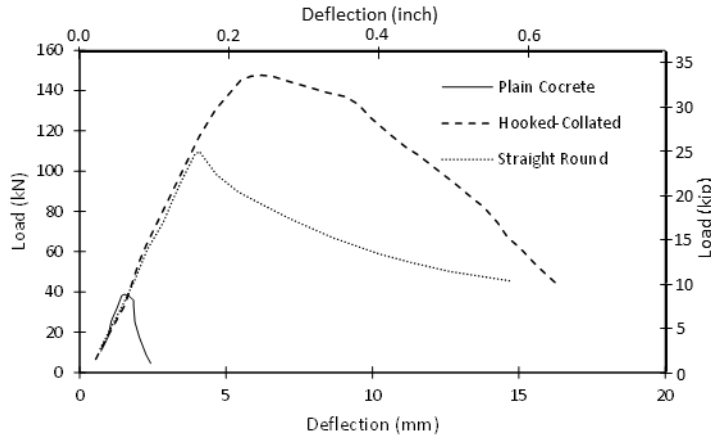


Figure 18. Flexural Test Data of SFRC: Aspect Ratio = 72–75 (Soroushian and Bayasi 1991)

Concrete

- Specimen size: 4×4×20 in.
- Maximum aggregate size: 0.625 in. (10 mm)

Steel fiber

- $V_f = 2.0$ percent
- Hooked-collated: $d=0.0315$ in., $l=2.36$ in., ($l/d=75$)
- Straight-round: $d=0.035$ in., $l=2.5$ in., ($l/d=72$)

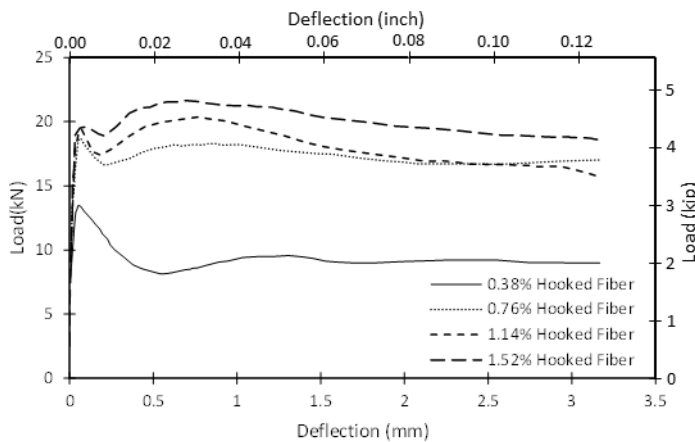


Figure 19. Flexural Test Data of SFRC with Hooked Fibers (Balaguru et al. 1992)

Concrete

- f'_c : 3900 psi (27 MPa)
- Normal maximum agg. size: 0.75 in. (19 mm)
- Specimen size: 4×4×14 in. (100×100×360 mm)

Hooked steel fiber

- $d=0.0079$ in. (0.2 mm), $l=1.18$ in. (30 mm), $l/d=150$

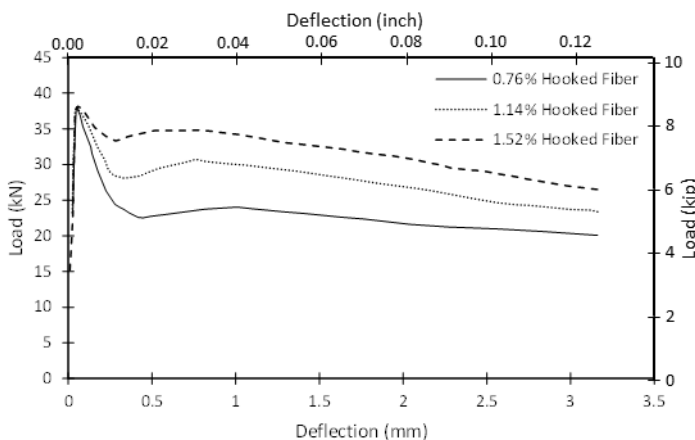


Figure 20. Flexural Test Data of SFRC with Hooked Fibers (Balaguru et al. 1992)

Concrete

- f'_c : 11,700 psi (81 MPa)
- Normal maximum agg. size: 0.75 in. (19 mm)
- Specimen size: 4×4×14 in. (100×100×360 mm)

Hooked steel fiber

- $d=0.0079$ in. (0.2 mm), $l=1.18$ in. (30 mm), $l/d=150$

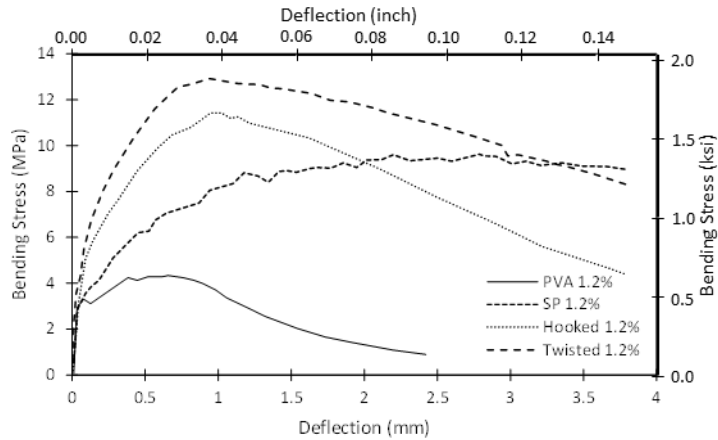


Figure 21. Flexural Test Data of SFRC with Various Fibers: 1.2 Percent Fibers by Volume (Kim et al. 2008)

Mortar

- f'_c : 8100 psi (56 MPa)
- Specimen size: 4x4x14 in. (100x100x350 mm)

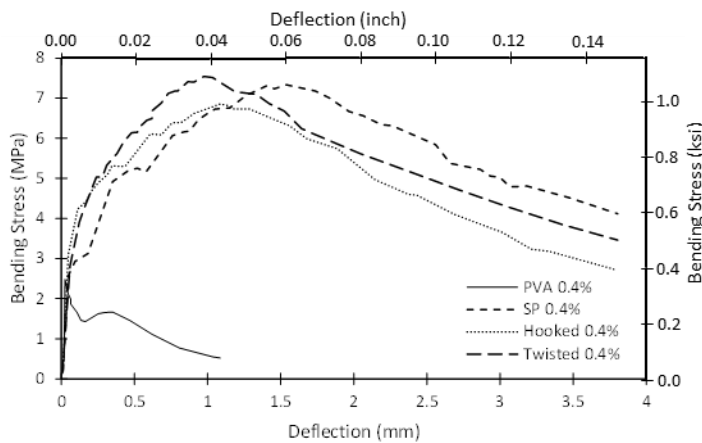


Figure 22. Flexural Test Data of SFRC with Various Fibers: 0.4 Percent Fibers by Volume (Kim et al. 2008)

Mortar

- f'_c : 8100 psi (56 MPa)
- Specimen size: 4x4x14 in. (100x100x350 mm)

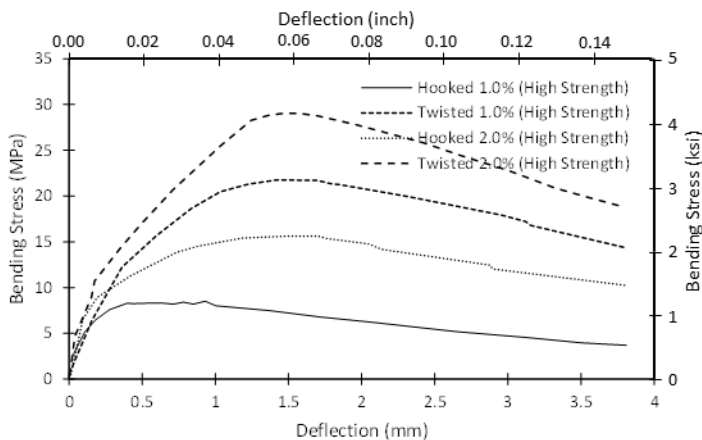
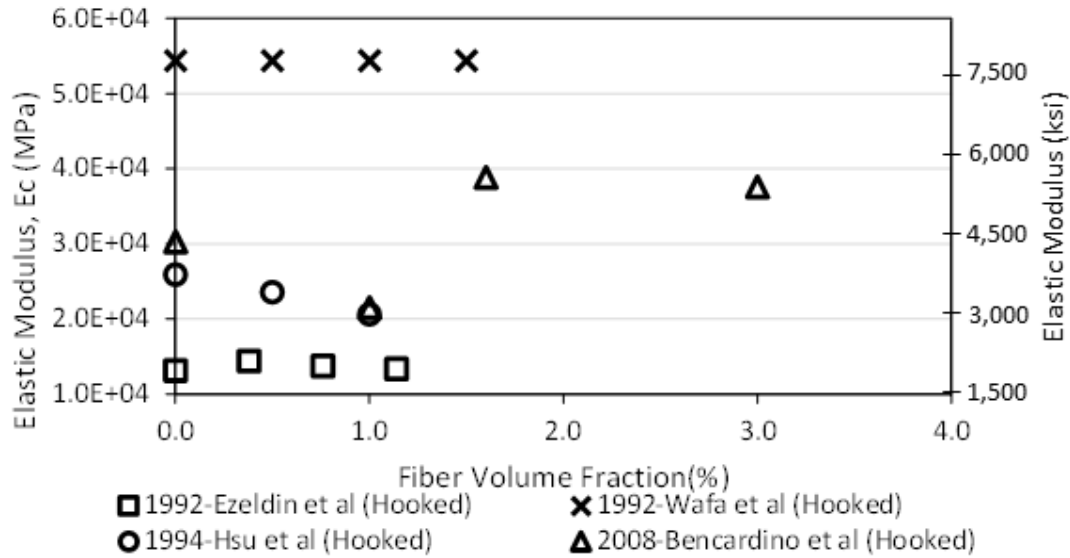


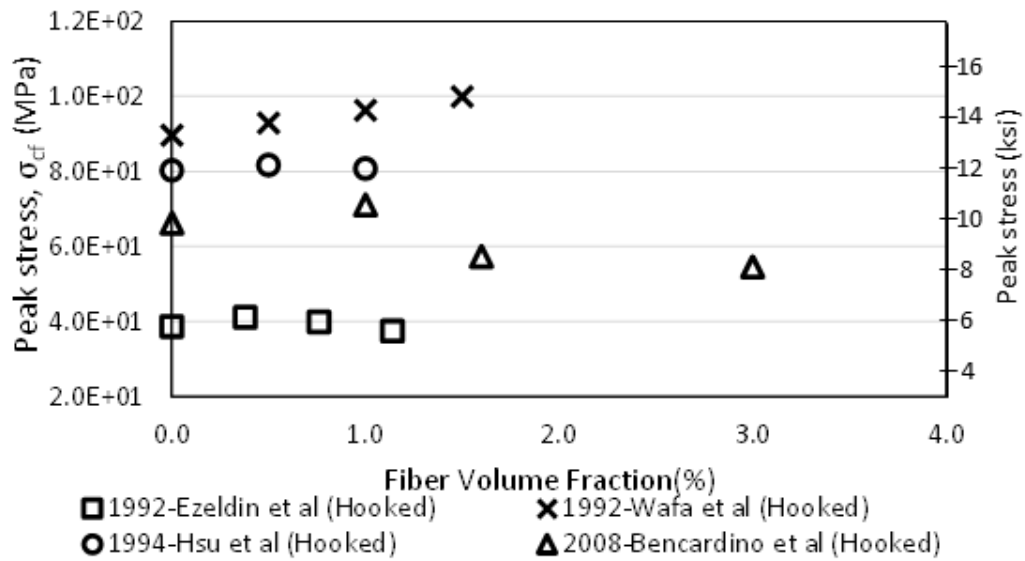
Figure 23. Flexural Test Data of Steel Fiber Reinforced Mortar with Various Fibers (Kim et al. 2008)

Mortar

- f'_c : 12,200 psi (84 MPa)
- Specimen size: 4x4x14 in. (100x100x350 mm)

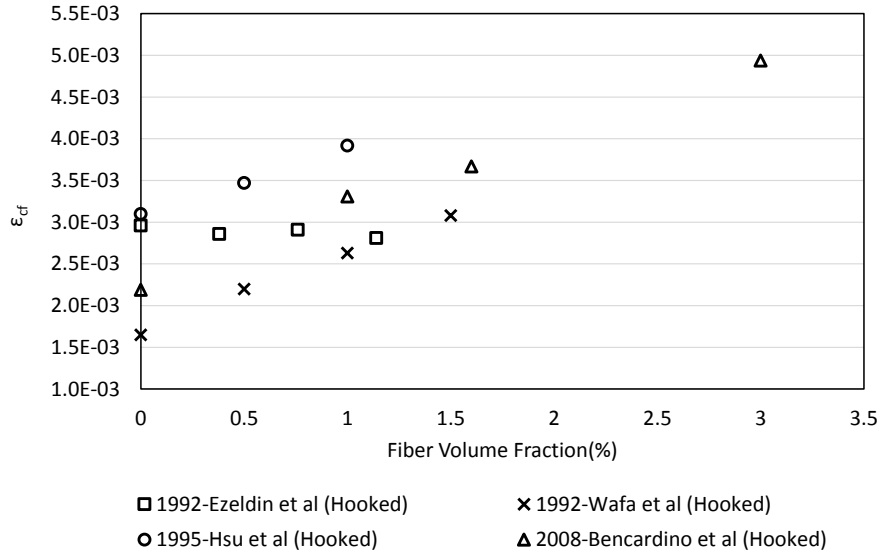


(a) Elastic Modulus in Compression

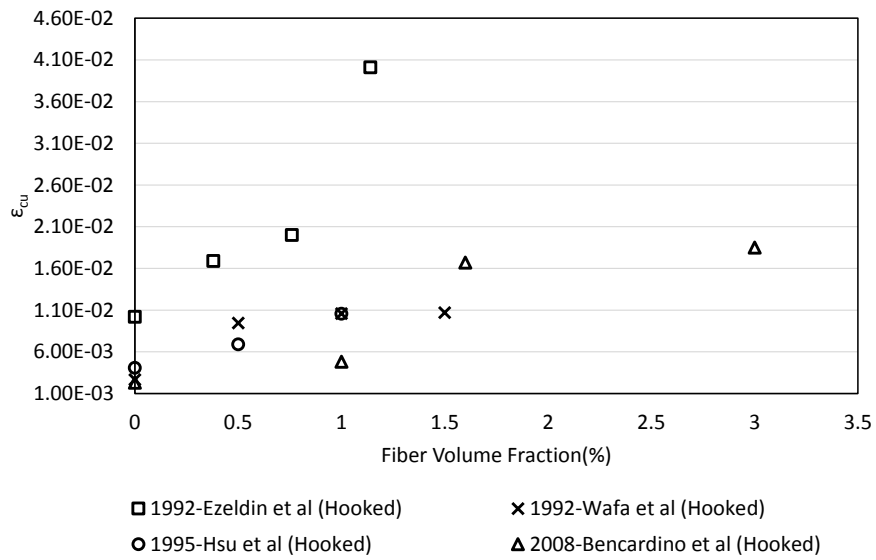


(b) Compressive Strength

Figure 24. Comparisons of Compressive Properties of SFRC

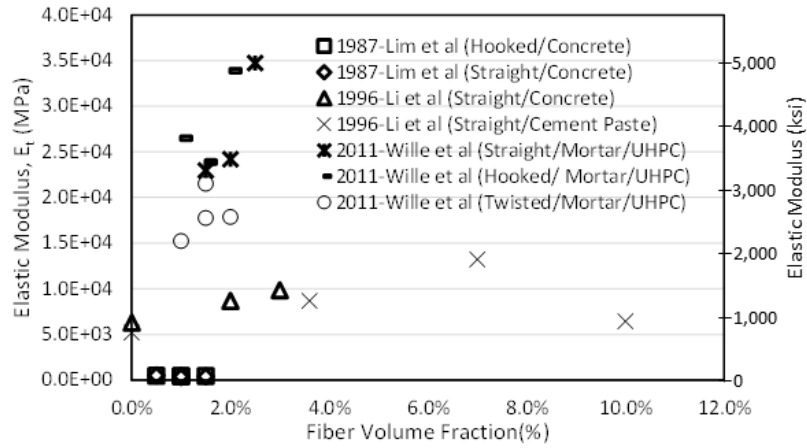


(c) Strain at the Maximum Stress

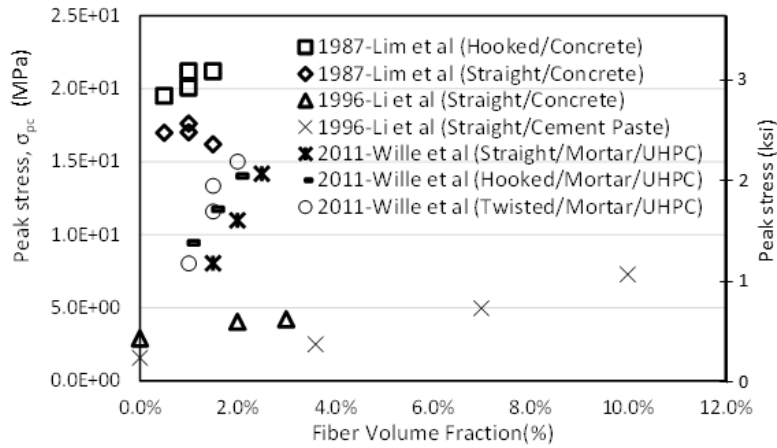


(d) Ultimate Strain

Figure 24. Comparisons of Compressive Properties of SFRC (Continued)

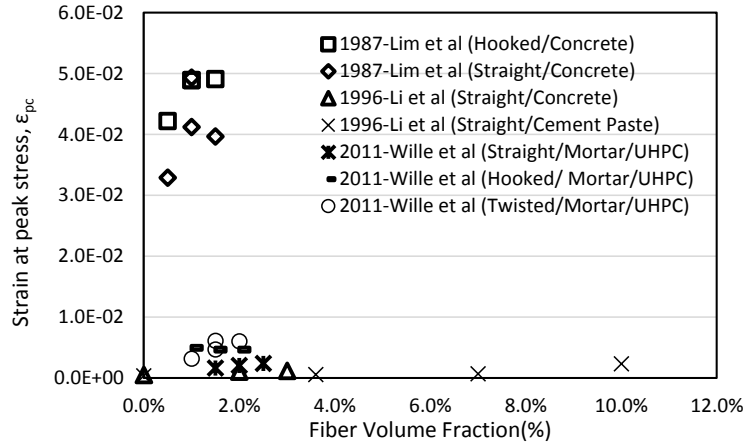


(a) Elastic Modulus in Tension

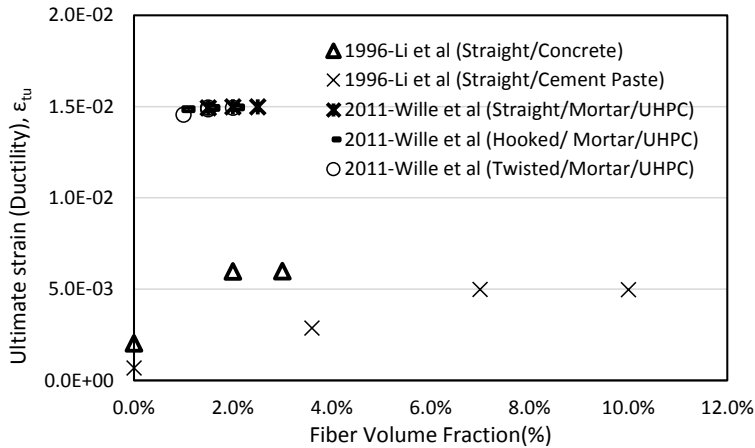


(b) Tensile Strength

Figure 25. Comparisons of Tensile Properties of SFRC



(c) Strain at the Maximum Stress



(d) Ultimate Strain

Figure 25. Comparisons of Tensile Properties of SFRC Error! Reference source not found. (Continued)

DESIGN METHODS

A number of design methods or guidelines are available from a number of organizations including American Concrete Institute (ACI), JSCE, and RILEM. Approaches include empirical, closed-form solutions, fiber section analysis, and yield line analysis. Key methods/guidelines are summarized here as an introduction.

American Concrete Institute

ACI Committee 544 has published several documents concerning FRC. Design Considerations for Steel Fiber Reinforced Concrete (ACI 544.4R) was published in 1988 and was reapproved in 2009. The document does not specify a design procedure. Rather, ACI 544.4R demonstrates methods used in research conducted prior to its original publication date. For example, the flexural design procedure

proposed by Henager and Doherty (1976) is included in ACI 544.4R for FRC beams containing both fibers and reinforcing steel bars.

Other documents published by ACI Committee 544, such as ACI 544.2R Measurement of Properties of Fiber Reinforced Concrete (ACI Committee 544 1988), and ACI 544.3R Guide for Specifying, Proportioning, and Production of Fiber-Reinforced Concrete (ACI Committee 544 1998), provide insight on the effects of adding fibers to the concrete matrix, applications of FRC, and considerations for the mix design.

The ACI 318 Building Code Requirements for Structural Concrete (ACI Committee 318, 2011) does not have provisions for use of FRC as flexural reinforcement; however, the specification does allow for the use of steel fibers to satisfy requirements for minimum shear reinforcement. Specifications for SFRC are based on experimental tests of beams with SFRC as the only shear reinforcement. The ASTM 1609 third-point bending test is used and the following three requirements must be met:

1. The weight of added fibers exceeds 100 lb/ft³.
2. The residual strength corresponding to a midspan deflection of 1/300 of the span length, obtained from flexural testing, is at least 90 percent of the first-peak strength.
3. The residual strength corresponding to a midspan deflection of 1/150 of the span length, obtained from flexural testing, is at least 75 percent of the first-peak strength.

RILEM TC 162-TDF Method

RILEM is an international organization created for the study of construction materials, systems, and structures. The European pre-standard, ENV 1992-1-1, was used as the framework for the design standard.

The method is based upon the fictitious crack model originally proposed by Hillerborg et al. (1976) (RILEM TC 162-TDF 2002). The fictitious crack model divides the crack region developed in concrete members into three zones: the process zone, the aggregate interlock zone, and the traction free zone. Stress can be transferred through the process and aggregate interlock zones, but cannot be transferred through the traction free zone. The stress capacity of each zone is defined by a stress–crack opening relationship determined through standard bending tests with notched prismatic members.

The RILEM technical committee adopted this fictitious crack model concept and modified it to include the contribution of steel fibers (RILEM TC 162-TDF 2002). The steel fibers bridge each zone, including the traction free zone, effectively increasing the stress capacity of the crack. The stress–crack opening relationship can be modeled with a bilinear curve for most SFRC members (RILEM TC 162-TDF 2002). The design of an SFRC member can be achieved with the constitutive models that include post-cracking tensile strength, strain compatibility, and cross-section equilibrium. Through experimental data, the RILEM technical committee developed empirical equations relating the flexural and compressive strengths to the mean and characteristic flexural tensile strength (RILEM TC 162-TDF 2003).

Testing in accordance with the RILEM bending test is achieved by subjecting a 150 mm × 150 mm × 550 mm (6 in. × 6 in. × 22 in.) concrete specimen to a three-point bending test (RILEM TC 162-TDF 2002). The prismatic specimen is notched at its midpoint on the tension face to a depth of 25 mm (1 in.) to simulate a crack in the specimen. As the bending test is conducted, the CMOD is measured until the beam fails. The residual stresses are determined based upon the load at CMOD of 0.5 mm (0.02 in.) and CMOD of 3.5 mm (0.1 in.).

The design standard limits the maximum compressive strain to 0.0035 and the maximum tensile strain in typical steel reinforcement to 0.025. Additionally, the committee discovered that the accuracy of the design method varied with member depth and introduced a size correction factor (RILEM TC 162-TDF 2003).

The RILEM design standard addresses cracking through an equation to calculate the minimum area of traditional steel reinforcement. If the calculated minimum area is less than zero, the steel fibers are sufficient to limit cracking. Additionally, the moment–curvature relationship and moment–area theorems can be used to calculate the deflection of the member.

Closed Form Solutions

Soranakom and Mobasher proposed a design procedure that uses the basis of the RILEM TC-162-TDF design procedure in conjunction with definitions of the ACI 318 for a simplified strain-softening SFRC. Mobasher (2012) extends the RILEM constitutive models to strain hardening FRC using a simplification based upon the stress–strain relationship proposed by Lim et al. (1987) (Soranakom and Mobasher 2007a,b). The post cracking stress, σ_p , corresponds to the residual stress σ_2 of the RILEM TC-162-TDF design method, which is found by the RILEM deflection controlled bending test. The yield compressive strain, σ_{cy} , is defined by the authors as 85 percent of the compressive strength. Both procedures assume that the fibers do not affect the stress or strain prior to the initial cracking of the specimen. Therefore, the cracking stress, strain, and modulus of elasticity are defined by ACI 318 and Hooke’s Law. The stress–strain relationship and subsequent calculations are simplified by normalizing the constitutive relationships by the cracking stress and strain. The method was verified against experimental tests conducted by previous researchers (Soranakom and Mobasher 2009). The comparison demonstrated that the design procedure yielded near experimental values. The authors proposed a strength reduction factor, ϕ_p , of 0.7 to ensure a safe design.

Round Slabs and Yield Line Theory

Researchers investigating the use of SFRC in elevated flat slabs supported on columns have used yield line theory in conjunction with data determined from the testing of round slabs (Destrée and Mandl 2008). The test includes subjecting a simply supported, circular slab to an increasing point load at its center while the deflection is measured.

The load is increased until the typical fan rupture pattern is achieved. Using yield line theory, the ultimate moment capacity can be determined by:

$$P_{ult} = 2\pi M_r \quad (3)$$

The method was compared to several full-scale tests of elevated flat slabs (Destrée and Mandl 2008). The design method resulted in capacities that were significantly less than experimental values leading to safety factors in excess of five. However, when compared to typical prismatic beam procedures, the round slab and yield line theory design method resulted in larger capacities.

STRUCTURAL APPLICATIONS OF SFRC

Researchers have been using the improved strength and performance of FRC in numerous applications. Some of the largest gains have been realized in seismic design, slabs-on-ground and flat elevated slabs, prestressed girders, and bridge decks.

Seismic Design

Several researchers have shown that the addition of up to 2 percent by volume of hooked-end steel fibers is beneficial in seismic design, resulting in increased ductility, damage tolerance, energy dissipation, and confinement (Lequesne et al. 2013; Niwa et al. 2012; Campione 2002; Aviram et al. 2014).

Lequesne et al. (2013) experimented with a strain hardening SFRC in coupling beams and plastic hinge regions of shear walls and found that with the addition of 1.5 percent by volume of steel hook end fibers, the coupling beams failed in flexure, rather than shear, at large drift ratios (Lequesne et al. 2013). The confining properties of the SFRC enabled the researchers to reduce the area of diagonal reinforcement by as much as 70 percent, in addition to eliminating transverse reinforcement after a distance equal to half of the height of the coupling beam away from the wall to beam interface. The study has led to the implementation of SFRC coupling beams in a 440-ft-tall residential building in Seattle, Washington, with shear wall cores (Lequesne et al. 2011).

Researchers at the Tokyo Institute of Technology found that SFRC aided in the anchorage failures of beam-column joints (Niwa et al. 2012). Niwa et al. (2012) determined that the addition of hook-end fibers at 1.5 percent by volume allowed them to reduce the amount of longitudinal reinforcement and transverse reinforcement by as much as 29 percent in beam-column joints while still maintaining the ductility and energy dissipation of code-compliant beam-column joints.

Campione suggested that SFRC used in conjunction with traditional steel reinforcement in columns could lead to a reduction in the amount of transverse reinforcement required to adequately confine a column (Campione 2002). Aviram et al. (2014) used the improved ductility and confinement of SFRC to reduce the amount of transverse steel in bridge columns imposed to bidirectional loading (Aviram et al. 2014). They demonstrated that the SFRC columns did not exhibit significant spalling and could effectively decrease the amount of required transverse reinforcement by one-half.

Ultimately, the use of SFRC has improved the reinforcement congestion in many seismic applications without negatively affecting the ductility and energy dissipation of these systems. These studies have

demonstrated the confining nature and energy dissipation attributed to SFRC; however, these seismic applications generally do not address the supplemental strength provided by the added fibers.

Beams

Kwak et al. (2002) investigated the influence of concrete strength and the volume of fibers on the flexural response of beams. Twelve beams with a cross section of 125 mm (5 in.) × 250 mm (10 in.) were subjected to two point loads 400 mm (16 in.) apart centered at the beam's midpoint. The length of the beams varied from 1548 mm (5 ft) to 2396 mm (8 ft). The specimens included traditional steel reinforcement in the longitudinal direction, but not the transverse.

As the beam increased in length and fiber content, the mode of failure transformed from shear to flexural (Kwak et al. 2002). The addition of steel fibers increased the shear strength of the concrete beams by as much as 180 percent. The largest increases were observed in beams with the lowest shear-span ratios, or shortest length; however, the longer beams failed in flexure and could not achieve their maximum shear strength. Ultimately, researchers evaluated existing methods for determining the shear strength of SFRC members and proposed a new equation to determine the shear strength using their data and data from several other tests.

Dinh et al. (2011) investigated 27 large-scale beams with varying amounts of steel fibers and longitudinal reinforcement. Traditional longitudinal reinforcement was included to ensure that the beams failed in shear rather than flexure. The depth of the SFRC specimens varied from 455 mm (18 in.) to 685 mm (27 in.) to account for size effects. Researchers analyzed the resulting data using a crack width–stress relationship determined from standard four-point bending tests and equilibrium. The stress-profile used a distribution of tensile stresses across a diagonal crack in an SFRC specimen (Dinh et al. 2011). This method resulted in predicted strengths of approximately 80 percent of the actual shear strengths measured during the experiment. The benefit of the stress profile approach is that it does not require direct knowledge of the post-crack strength of SFRC; rather, the information from four-point bending tests is sufficient.

The use of SFRC in prestressed beams has also been investigated. Dhonde et al. (2005) used SFRC in the end regions of prestressed beams in an effort to reduce the amount of cracking and transverse reinforcement (Dhonde et al. 2005). They tested seven prestressed beams with varying volumes of steel fibers and transverse reinforcement. The use of steel fibers successfully reduced or eliminated visible cracking in the end regions of the I-girder. Additionally, the fibers changed the failure from a brittle one to a ductile one. The best performing prestressed girder used 1.5 percent fibers by volume and no transverse steel in the end regions underscoring the effectiveness of SFRC as a crack retarder and shear reinforcement alternative.

Slabs

SFRC has been used in several slab-on-ground and elevated slab applications. As of recent, over 65 multistory buildings use SFRC flat slabs without traditional reinforcement (Destrée 2009). The span-to-

thickness ratio of the slabs range from 25 to 30 and commonly have a depth of approximately 0.2 m (7.9 in.) spanning between 5 m (16 ft) and 8 m (26 ft) in each direction.

Many researchers agree that typical flexural tests and beam analysis resulting from slab strip tests severely underestimate the capacity of SFRC two-way slabs (Roesler et al. 2004; Destrée and Mandl 2008; Destrée 2009; Mobasher and Destrée 2010; Michels et al. 2011). Roesler et al. experimented with SFRC slabs under monotonic loading and found that the slabs' flexural strengths were as much as 30 percent larger than equivalent beam tests (Roesler et al. 2004). Destrée and Mandl investigated the collapse load for four full-scale slabs supported on columns and found that their capacity was five times larger than predicted by round slab tests and yield line theory and 15 times larger than predicted by typical beam flexural tests (Destrée and Mandl 2008). The disparity between the beam flexural test and round slab tests is due to the inability of beam flexural tests to adequately model multiple macro-cracking and load redistribution. SFRC flat slabs benefit from having multiple yield lines, so multiple macro-crack formations that aid in redistributing the load (Mobasher and Destrée 2010). In addition to large factors of safety found in flexural design, numerous studies also show that SFRC elevated slabs can withstand point loads over 600 kN (67 ton) without sustaining punching shear failures.

Fall et al. (2014) tested simply supported two-way slabs with SFRC made with approximately 0.35 percent by volume of double-hooked fibers. Slabs were approximately 80 mm (3.1 in.) thick with a) conventional reinforcement with PC, b) conventional reinforcement with SFRC, or c) SFRC without conventional reinforcement. Slabs with conventional reinforcement and SFRC had larger strengths and more, but narrower, cracks than conventional reinforcement alone. The SFRC-only slab had a limited crack pattern and did not exhibit bending hardening.

Barros and Figueiras (1999) tested 75 mm (3 in.) thick slab strips with wire mesh and SFRC made with three different volumes of hooded-end fibers. Test results demonstrated that SFRC increased the load carrying capacity by nearly two times for SFRC consisting of 0.75 percent of fiber by volume. The crack spacing was also found to be decreased by using SFRC. Moment–curvature analysis demonstrated the ability to predict the flexural response of the SFRC sections.

Steel-Free and Steel-Reduced Bridge Deck

The previous section highlighted the structural benefits of SFRC for structures in general. As this study is focused on the use of SFRC in transportation applications, particularly for the reduction of steel in bridge decks, it is worth reviewing other research related to the reduction or elimination of steel in bridge decks.

Some estimate that over 120,000 bridges in the United States are in need of repair due to steel reinforcement corrosion resulting in damaging concrete spalling (Chandrangsu 2003). The steel-free bridge deck has long been a goal of many designers and researchers. The cost of construction materials may potentially be larger due to the addition of steel fibers; however, the reduction of labor and maintenance in addition to a longer serviceable life could offset this increase.

Mufti et al. (1993) explored the effectiveness of arching, or compressive membrane, action in the flexural design of bridge decks (Mufti et al. 1993). Their goal was to alter the failure mode from flexural failure to a punching shear failure. The experiment involved subjecting quarter scaled bridge decks, supported on two steel girders, to concentrated loads at various locations.

Researchers eliminated all steel reinforcement from the bridge deck and used polypropylene fibers to control temperature and shrinkage cracks. They found that the eliminated internal steel reinforcement contributed significantly to the lateral restraint of the bridge deck that promotes arching action. Their first test resulted in typical flexural failure with a longitudinal crack through the deck due to the lack of lateral restraint. In subsequent tests, Mufti et al. (1993) added an increasing amount of steel straps welded to the top flange of the steel girders supporting the deck and successfully transitioned the mode of failure from flexural to punching shear as desired on the third specimen. Officials in Tama County, Iowa, used this design procedure and successfully built a full-scale bridge that performed adequately under their load testing (Dunn et al. 2005). The bridge consisted of polypropylene fibers and fiber-reinforced polymer (FRP) bars, both intended as temperature and shrinkage reinforcement, in addition to exterior steel straps attached to the top flange of the supporting girders to provide lateral restraint. The addition of steel straps is less than ideal for the bridge superstructure, and this experiment did not take advantage of fibers that improve the strength and performance of concrete.

Naaman and Chandransu (2004) used the basis of the Mufti et al. (1993) experimentation and structurally capable fibers to eliminate only the top layers of reinforcement while keeping the bottom layers to promote arching action and prevent accidental loading and failure. They experimented with bridge decks using a reduced amount of traditional steel reinforcement and three different types of structural fibers: Torex, Spectra, and PVA. Fibers were introduced into the concrete mixes at 2 percent for Torex and PVA, and 1.75 percent for Spectra, by volume based on prior experimental results to best optimize the response of 4 in. by 7 in. FRC beams. The Torex and Spectra FRC beams exhibited increased strength, ductility, and stiffness relative to that of with respect to the control specimen, while the PVA FRC beam exhibited an increased ductility, but comparable strength and stiffness in comparison to the control specimen.

Naaman et al. (2007) expanded this experiment to investigate the punching shear response of FRC bridge decks with reduced steel. They subjected simply supported slabs 810 mm × 810 mm × 180 mm (32 in. × 32 in. × 7 in.) in dimension to a point load at its center. The experiment consisted of Torex, Spectra, and PVA fiber specimens with varying amounts of top and bottom steel. The Torex and Spectra FRC slabs had strengths greater than or equal to that of the control slab. The authors suggested that the punching shear capacity of the FRC slabs can be safely taken as twice the strength recommended by ACI code.

Ostertag and Blunt (2008) performed four-point bending tests on Hybrid FRC beams measuring 6 in. × 6 in. × 24 in. using different mixes to determine their feasibility for use in approach slabs. They chose a hybrid FRC mix to minimize the volume of fibers needed, as the difficulty of placing concrete increases with the volume of fibers has been well documented. The idea of the hybrid mix is to include micro-fibers, PVA fibers, to delay the onset of micro-cracks and macro-fibers, steel hooked-end fibers, to delay

the onset of macro-cracks (Ostertag and Blunt 2008). The addition of fibers into the concrete matrix increased the flexural capacity of the beams; however, the gain diminished as the amount of traditional reinforcement increases, underscoring the larger influence of steel reinforcement over the tension capacity of the FRC.

Throughout all the aforementioned experiments, the addition of fibers into the concrete matrix yields better performance and strength in comparison to the traditionally reinforced counterpart. As suggested by Ostertag and Blunt, the geometry, ratio of steel reinforcement, and fiber volume are means for optimizing the performance and cost of FRCs (Ostertag and Blunt 2008). However, FRC is not the only method being investigated to reduce or eliminate traditional steel reinforcement.

Researchers in Wisconsin have investigated steel-free bridge decks on wide flange concrete girders. Bae et al. (2010) propose using steel rods to connect the webs of adjacent wide flange girders to promote arching action in addition to using polypropylene fibers in the concrete mix to prevent temperature and shrinkage cracking (Bae et al. 2010). Experimental tests have demonstrated that the slab fails in punching shear beneath the wheel load similar to experiments conducted by Mufti et al. (1993). Additionally, Bae et al. found that the reduced clear span of the bridge deck, due to the wide flanges of the girders, and the added lateral restraint cause the bridge deck to behave similar to a D region in short beams (Bae et al. 2011). Through the use of the strut-and-tie method, they were able to accurately determine capacity of the steel-free concrete deck. However, this procedure is limited to decks with a thickness of greater than 7.5 in. and a clear span of less than 5 ft.

Another approach to eliminating traditional steel reinforcement is the use of FRP reinforcement instead. The FRP reinforcement is noncorrosive and has a higher strength-to-weight ratio in comparison to steel; however, it is susceptible to brittle failures due to having a linear stress–strain relationship (Pirayeh Gar et al. 2013). A full-scale test on aramid FRP (AFRP) prestressed concrete panels was tested by Pirayeh Gar et al. to demonstrate the feasibility of using the reinforcement alternative. They found that the AFRP bridge deck performed satisfactorily and exceeded the minimum design loads by a minimum of 40 percent. Additionally, the measured deflections at the maximum load were 1 mm (0.04 in.), well below the maximum allowable deflection.

APPLICABILITY OF LITERATURE SFRC CHARACTERISTICS FOR ADOT BRIDGE DECKS

A large number of published data is available for the mechanical properties of SFRC that could be considered in developing and validating design recommendations for bridge decks. However, material properties are best considered when also demonstrated within structural component tests as demonstrated by the inclusion of SFRC in ACI 318 provisions for minimum shear reinforcement based on experimental tests. Thus, concrete mix data and associated material properties for SFRC used in experimental test programs were gathered and examined for an understanding of challenges of construction and for compliance with standard ADOT and Texas Department of Transportation (TxDOT) mix designs summarized in Table 2 through Table 5. TxDOT mix designs are included for considerations of local materials available for testing by the performing agency. Both departments of transportation (DOTs) require the use of Class S concrete for bridge decks and Class P concrete for pavement.

The addition of fibers to the concrete matrix adversely affects the workability of fresh concrete. The volume percentage and aspect ratio of fibers, coarse aggregate size, and methods of introducing the fibers into the concrete mix are the most influential factors governing the mix workability (ACI 544 1996). As a result, various concrete mixes using admixtures, supplemental cementitious materials, and small coarse aggregate have been found in current literature.

Significant effort has been made to create new mix designs suited for the addition of fibers and to verify the ability of already-established mix designs to accept fibers. Liao et al. (2006) investigated self-consolidating high-performance SFRC mix designs. A total of six designs were tested using direct compression and tension tests. Their goal was to develop a workable mix that could be easily implemented and delivered by ready mix concrete companies. Successful designs were achieved by adjusting the amount of coarse and fine aggregates and the method for creating the concrete mix. Dhonde et al. (2005) also developed a self-consolidating concrete mix in addition to using mix designs already approved by TxDOT. They observed with mechanical vibration that the workability of the TxDOT mixes with steel fibers was adequate and that the rate of placing concrete affected the self-consolidating concrete mix. Aviram et al. (2014) used two mix designs, one similar to the Liao et al. (2006) recommendations and one generic ready mix design. The ready mix design could not be placed without the addition of water, resulting in a significant loss of compressive strength.

The method of introducing the steel fibers to the concrete mix also influences the workability of the concrete mix and tendency of balling for the fibers. There are two general methods for adding fibers to the concrete mix: introducing the fibers after the concrete has already been mixed or introducing them with the coarse aggregates (ACI 544 1998). Liao et al. (2006) added the fibers, at a slow steady rate, after the concrete mix had been formed. Using this method, the concrete mix should have a slump 1 in. to 3 in. greater than the desired final slump before the addition of fibers. Overall, 52 different concrete mixture proportions were recorded from the literature review. Table 5 demonstrates the average water, fine aggregate, and coarse aggregates to cement ratios. Additionally, the average 28-day compressive strength and coarse aggregate size are reported. For comparison, the TxDOT and ADOT requirements for structural concrete have also been included (TxDOT 2008; ADOT 2008).

As demonstrated, the compressive strength of the SFRC used in previous studies significantly exceed the minimum requirements of both TxDOT and ADOT. Furthermore, ADOT requires approval for non-prestressed concrete with a compressive strength above 6000 psi (ADOT 2011). Nine of the 52 mix designs meet the requirements of ADOT. Most failed due to the type of cement used (internationally graded cement). The limited availability of demonstrated applications of steel fibers in concrete similar to bridge deck concrete indicates a need for experimental investigation of potential mixes.

Table 2. Comparison of ADOT and TxDOT Standards (ADOT 2008; TxDOT 2008)

Concrete Class	Class P		Class S	
	ADOT	TxDOT	ADOT	TxDOT
Design Strength, Min 28-day f'_c (psi)	4000	4400	2500 to 4500 and greater	4000
Hydraulic Cement Content (lb/yd ³)	564–658	Less than 700	520 to 752 (if $2500 < f'_c < 4500$) 564 to 752 (if $f'_c > 4500$)	Less than 700
Maximum Water/Cement Ratio	None	0.45	0.55 (if $2500 < f'_c < 4500$) 0.50 (if $f'_c > 4500$)	0.45
Coarse Aggregate Gradation	Size designation No. 467	2 to 3	Chosen by the contractor, maximum size shall not be larger than one-fifth of the narrowest dimension between sides of adjacent forms, or two-thirds of the minimum clear spacing between reinforcing	2 to 5
Slump Range (in.)	0 to 4.5	0 to 4.0	Chosen by the contractor	0 to 4

Table 3. Coarse Aggregate Gradation Chart (TxDOT 2008)

Aggregate Grade No. ¹	Nominal Size	Percent Passing on Each Sieve								
		2- 1/2"	2"	1-1/2"	1"	3/4"	1/2"	3/8"	No. 4	No. 8
1	2"	100	80– 100	50–85		20–40			0–5	
2 (467)	1-1/2"		100	95– 100		35–70		10–30	0–5	
3	1-1/2"		100	95– 100		60–90	25–60		0–5	
4 (57)	1"			100	95–100		25–60		0–10	0–5
5 (67)	3/4"				100	90– 100		20–55	0–10	0–5
6 (7)	1/2"					100	90– 100	40–70	0–15	0–5
7	3/8"					100	100	70–95	0–25	
8	3/8"					100	100	95– 100	20– 65	0–10

1. Corresponding ASTM C33 gradation shown in parentheses.

Table 4. Fine Aggregate Gradation Chart (ADOT 2008; TxDOT 2008)

Nominal Size	Percent Passing	
	ADOT	TxDOT
3/8"	100	100
No. 4	95 to 100	95 to 100
No. 8		80 to 100
No. 16	45 to 80	50 to 85
No. 30		25 to 65
No. 50	0 to 30	10 to 35
No. 100	0 to 10	0 to 10
No. 200	0 to 4.0	0 to 3

Table 5. Mix Design Averages and DOT Requirements

	Literature Average	TxDOT Requirements	ADOT Requirements
Compressive Strength, f'_c (psi)	6270	4000	4500
Maximum Water:Cement	0.45	0.45	0.5
Fine Aggregate:Cement	1.72	N.A.	N.A.
Coarse Aggregate:Cement	1.98	N.A.	N.A.
Coarse Aggregate Size (in.)	0.57	0.75–1.75	N.A.
Most Common Cement Type	Other	N.A.	II, III, V

CHAPTER 3. SLAB-ON-GRADE CASE STUDIES

SLAB-ON-GRADE

A slab-on-grade is a type of foundation having a shape of concrete slab placed on a ground or a bed of crushed gravel. The slab-on-grade is distinguished from a mat foundation by the thickness (several inches thick). The application of the FRC to the slab-on-grade has a history of more than 30 years in Europe and North America (Tatnall and Kuitenbrouwer 1992; Folliard et al. 2006). Industrial floor slabs is one of the common applications of FRC because of the improved resistance to shrinkage and fatigue cracking. The industrial floors are loaded in a more dynamic manner than the residential or office buildings, and FRC slabs are expected to have decreased damage. The structure and loading conditions of rigid pavements are essentially the same as the industrial floor slabs. The typical distresses of rigid pavements are spalling, cracking, faulting, and punchout, and FRCs have been used to improve the pavement performance and to extend the service life.

In this section, the cases of FRC applications to the slab-on-grade are briefly reviewed. A representative case is selected for a detailed review including the mixture design, properties, and monitoring results. Then, a further analysis for the selected case is carried out to compare the distresses of the non-reinforced and FRC.

Review on the Fiber Reinforced Slab-on-Grade

The damage to concrete floors typically originate from slab joints. Alexandre and Bouhon (2010) studied a method to remove saw-cut joints in slabs-on-grade by using SFRC. Alexandre and Bouhon (2010) showed that the post cracking ductility of SFRC can control the micro-cracks induced by flexural and shear stresses combined with restrained shrinkage. To verify the efficiency of SFRC at slabs-on-grade, two different field cases were investigated: 1) Interbake Foods, Front Royal, VA; and 2) Coca-Cola Cald-rack, London, England. The case studies showed that jointless 25,000 ft² slabs can be constructed by using SFRC. Destrée et al. (2011) investigated a suspended foundation slab of the Swedbank arena in Stockholm. Steel fiber reinforcement (40–50 kg/m³) was used for the suspended foundation slabs, which were located on the ground or supported piles. Destrée et al. (2011) concluded that the steel fiber reinforcement was an effective solution for the structural foundation slabs.

MacDonald (2011) summarizes the field applications of synthetic FRC. A long-term monitoring on a thin bonded overlay containing 1.7 percent synthetic fibers, which is located on I-90 in South Dakota, showed that adding fibers is effective on reducing cracking. In another field application, thin concrete overlays containing 0.67 percent synthetic fibers were placed in 2005 and 2006 on a residential asphalt driveway. MacDonald (2011) reported that the crack development in FRC is influenced by the temperature at construction. The synthetic FRC was applied to a pavement north of Pierre, South Dakota, in 1995. Thermal cracks occurred within two weeks of the fall season placement, but no additional crack was observed at the inspection conducted in 2007. Table 6 summarizes the field application cases of FRC to slab-on-grade.

Table 6. A Summary of the FRC Applications to Slab-on-Grade

Name	Location	Purpose	Year	Fiber	References
Pavement	North of Pierre, South Dakota	Pavement full depth	1995	Synthetic fiber	MacDonald (2011)
Pallets floor	Grove City, Pennsylvania	Manufacture pallets in the building	2002	Synthetic fiber (0.25%, 0.5%)	MacDonald (2011)
Roller skating rink	Atlanta, Georgia	Not bonded floor overlay	2003	Synthetic fiber (0.5%)	MacDonald (2011)
Warehouse slab	-	Warehouse slab on ground	2004	Synthetic fiber (0.5%)	MacDonald (2011)
Concrete overlay	-	Concrete overlay of a residential asphalt driveway	2005, 2006	Synthetic fiber (0.67%)	MacDonald (2011)
Sewer lining	London, UK	GFRC panels relining old brick sewer	-	Glass fiber	Jones (2010)
The Sofa Express Warehouse	Portland, Tennessee	Combination of type K shrinkage-compensating concrete and synthetic fiber	-	Synthetic fiber	Flax (2010)
New East High School	Vancouver, Washington	Slab (Combination of type K shrinkage-compensating concrete and synthetic fiber)	-	Synthetic fiber	Flax (2010)
Duncun Aviation Hangar	Grand Rapids, Michigan	Slab without joint (Combination of type K shrinkage-compensating concrete and synthetic fiber)	-	Synthetic fiber	Flax (2010)
I-35 Northern Oklahoma road repair	Oklahoma	I-35 shoulder road repair (Alkaline-Resistant)	-	Cellulose fiber	Brown et al. (2010)
I-40 Central Oklahoma road repair	Muskogee Turnpike, Oklahoma	Bonded overlay project (Alkaline-Resistant)	2006	Cellulose fiber	Brown et al. (2010)
Slab-on-grade projects	Spanish Peaks Golf Course in Big Sky, Montana	Golf cart path (Alkaline-Resistant)	-	Cellulose fiber	Brown et al. (2010)
Slab-on-grade projects	Lavergne, Tennessee	Paving in front of shop complex (Alkaline-Resistant)	2004	Cellulose fiber	Brown et al. (2010)
Slab-on-grade projects	-	A warehouse loading dock (Alkaline-Resistant)	2004	Cellulose fiber	Brown et al. (2010)
Interbake Foods	Front Royal, Virginia	Jointless slab panels (A warehouse for packaged food products)	-	Steel fiber (67-101 lb/yd ³ =40-60kg/m ³)	Alexandre and Bouhon (2010)
Coca-Cola Clad-rack	London, United Kingdom	Jointless slab panels (A warehouse for packaged food products)	-	Steel fiber (Crimped) (76 lb/yd ³ =45kg/m ³)	Alexandre and Bouhon (2010)
Continuously reinforced concrete pavement (CRCP)	Houston, Texas (Kirkwood Drive Exit on Highway 59)	CRCP	2006	Steel fiber (0.5%~1.0%)	Folliard et al. (2006)
Suspended foundation slab	Swedbank Area in Stockholm, Sweden	Ground slab with just steel fiber	2011	Steel fiber	Destrée et al. (2011)

Additional field application cases of FRC can be found in Robinson et al. (1991), Tatnall and Kuitenbrouwer (1992), Folliard et al. (2006), Jones (2010), Flax (2010), and Brown et al. (2010). Among those, Folliard et al. (2006) was selected for a detailed case study in this section because of the full data on materials, lab tests, and pavement field applications.

Description of the Case at Houston

Folliard et al. (2006) conducted a comprehensive study on using fibers for improving the performances of CRCP. CRCP is one of the typical rigid pavements providing a good ride quality, minimal maintenance, and longer service life than jointed PC pavement or flexible pavement. The distresses of the CRCP are surface spalling, cracking, and punchout, and Folliard et al. (2006) expected that the fiber reinforcement can improve the resistances to those distresses. Using synthetic and steel fibers, they conducted: 1) a literature review on CRCP design/performance and the role of fibers, 2) field inspections to confirm constructability and workability of the fiber-reinforced CRCP, and 3) lab experiments to evaluate material properties of the FRCs used in the fields.

The fiber-reinforced CRCP is installed on a frontage road located on the inside lane of a northbound road at the Kirkwood Drive Exit on Highway 59 southwest of Houston, TX. The location had relatively high truck traffic and times of lower traffic flow. The concrete pavement is 10 in. thick, 10 ft wide, and has a total length of 1270 ft. The primary reinforcement is Grade 60 reinforcing steel that was placed at the mid-depth of the pavement. For the longitudinal direction, the reinforcement consists of No. 6 bars spaced at 8.25 in. For the transverse reinforcement, No. 5 bars are spaced at 36 in.

Materials and Mixture Design

The concrete selected by Folliard et al. (2006) was a typical CRCP for the Houston area. Type I/II portland cement and Class C fly ash were used as cementitious materials. The aggregates were the mix of natural river sand and Grade 2 river gravel with the nominal maximum aggregate size of 1.0 in. A water-reducer and an air entraining agent were added as the chemical admixtures. Folliard et al. (2006) selected three types of fibers, including one steel hooked fiber and two synthetic fibers (Table 7). However, the lab tests for the material characterization were made only for SF1 and SnF1. Table 8 shows the mixture design of the FRCs.

Table 7. The Fiber Types Used by Folliard et al. (2006)

Fiber Designation	Description	Length	Aspect ratio
SF1	Steel-Collated Hooked-End	2.56 in. (65 mm)	60
SnF1	Synthetic-Monofilament	3.54 in. (90 mm)	40
SnF2	Synthetic-Collated-Fibrillated	<1.18 in. (30 mm)	NA

Table 8. The Mixture Design for the Field Application (Folliard et al. 2006)

Mixture Designation	Cement (pcy)	Fly Ash (pcy)	Coarse Aggregate (pcy)	Fine Aggregate (pcy)	Water (pcy)	Water Reducer (oz/yd ³)	Air Dosage (oz/yd ³)	Fibers (pcy)
Control	451	96	1936	1132	217	24	2	0
SF1-25	451	96	1842	1265	211	24	2	25
SF1-40	451	96	1842	1265	227	24	2	40
SnF1-4	451	96	1842	1265	221	24	2	4
SnF1-6	451	96	1842	1265	234	24	2	6

(The fiber volume fractions of SF1-25 and SF1-40 are 0.2 percent and 0.3 percent, respectively.)

Material Properties

Concrete specimens were obtained from each pavement section. Fresh concrete properties were evaluated, and compression, splitting tension, and flexural tests were conducted at 7, 28, and 91 days. Table 9 to Table 13 summarize the material property data obtained by Folliard et al. (2006). These data are used as the input data for the distress analysis described in the following section.

Based on the material test results, Folliard et al. (2006) concluded that the addition of fibers has little influence over the material properties before a major crack development such as compressive strength (Table 10), elastic modulus (Table 11), splitting tensile strength (Table 12), and flexural strength (Table 13) because the major improvement due to fibers occurs at the post cracking behavior (i.e., ductility). This can be true for the FRCs with low fiber volume fractions (<1.0 percent), but the other investigators adding moderate (between 1 percent and 2 percent) or high (>2 percent) fiber contents reported the increase in tensile and flexural strengths.

Table 9. Fresh Concrete Properties (Folliard et al. 2006)

Mixture Designation	Slump (in.)	Air Content (%)	Unit Weight (lb/yd ³)
Control	3.5	4.6	140.0
SF1-25	2.75	4.5	144.0
SF1-40	2.25	NA	144.0
SnF1-4	2.75	NA	140.0
SnF1-6	3.25	NA	139.2

Table 10. Compression Test Results (Folliard et al. 2006)

Mixture Designation	Average Compressive Strength (psi)		
	7-day	28-day	91-day
Control	3230	3760	4760
SF1-25	3430	3840	4170
SF1-40	3280	3970	4610
SnF1-4	3200	3960	4310
SnF1-6	2920	3400	4180

Table 11. Elastic Modulus Test Results (Folliard et al. 2006)

Mixture Designation	Average Modulus $\times 10^3$ (psi)		
	7-day	28-day	91-day
Control	4850	5050	5700
SF1-25	4900	4900	6750
SF1-40	4100	4650	5100
SnF1-4	4150	4450	5300
SnF1-6	3900	4650	5150

Table 12. Split Tension Test Results (Folliard et al. 2006)

Mixture Designation	Average Splitting Tensile Strength (psi)		
	7-day	28-day	91-day
Control	370	480	485
SF1-25	365	485	530
SF1-40	360	505	545
SnF1-4	355	445	495
SnF1-6	340	455	495

Table 13. Flexural Test Results (Folliard et al. 2006)

Mixture Designation	Flexural Strength (psi)		
	7-day	28-day	91-day
Control	630	725	665
SF1-25	605	590	620
SF1-40	575	465	640
SnF1-4	630	720	650
SnF1-6	595	560	635

On-Site Monitoring

On-site monitoring was performed to evaluate the condition of the test sections. For each section, the ease of placement and finishability were classified (poor-satisfactory-good) during the construction. The crack spacing, crack width, and spalling were examined at 10, 42, 79, 130, and 235 days after the construction. Table 14 summarizes the field workability and distresses measured at 235 days.

Table 14. Summary of On-Site Monitoring (Folliard et al. 2006)

Section ID	Control	SF1-25	SF1-40	SnF1-4	SnF1-6
Ease of Placement	Good	Satisfactory	Satisfactory	Satisfactory	Poor
Finishability	Good	Satisfactory	Satisfactory	Poor	Poor
Average Crack Spacing (235 days later)	7.5 ft	4.4 ft	3.2 ft	3.4 ft	4.5 ft
Average Crack Width (235 days later)	0.018 in.	0.016 in.	0.014 in.	0.015 in.	0.014 in.
Spalling (235 days later)	Yes	No	No	No	No

Analysis of the Case at Houston

Mechanistic-Empirical Pavement Design Software

The pavement performances of the CRCP with the fiber reinforcement are evaluated using the pavement design/analysis software based on mechanistic-empirical pavement design (MEPD) concept. The MEPD is an advanced design concept combining the mechanistic theories and the huge experimental data obtained through the long-term pavement performance program. As a result of a set of systematic research activities conducted in the National Cooperative Highway Research Program (NCHRP) administered by the Transportation Research Board, a guide for mechanistic-empirical design was developed by NCHRP 1-37A (Witczak et al. 2004). The new design concepts and procedures were implemented in a user-oriented computational software and design guide. Until 2012, both the software and guide were called mechanistic-empirical pavement design guide (MEPDG), and after some upgrade, the software is currently named AASHTOWare Pavement ME Design. Figure 26 shows the iterative design process of MEPDG. The analysis part of MEPDG is composed of three parts: 1) mechanistic pavement analysis using finite element method, 2) damage transfer functions based on empirical data to predict distress, and 3) accumulation of damage throughout the prescribed design life. The iteration will be continued until the accumulated damage (performance indicators) are smaller than the prescribed criteria. The MEPDG analysis assumes a linear elasticity of materials, so the post cracking behavior of FRCs cannot be considered in this analysis.

In this section, the FRC cases are analyzed using the data of Folliard et al. (2006). The official performance indicators for CRCP suggested by MEPDG are international roughness index (IRI) and punchout. Since the crack width data are provided by Folliard et al. (2006), the crack width is also evaluated and compared. In addition to the FRCs used by Folliard et al. (2006), a further analysis is carried out using the material data for the SFRCs with moderate fiber contents produced from the material tests of the presented project.

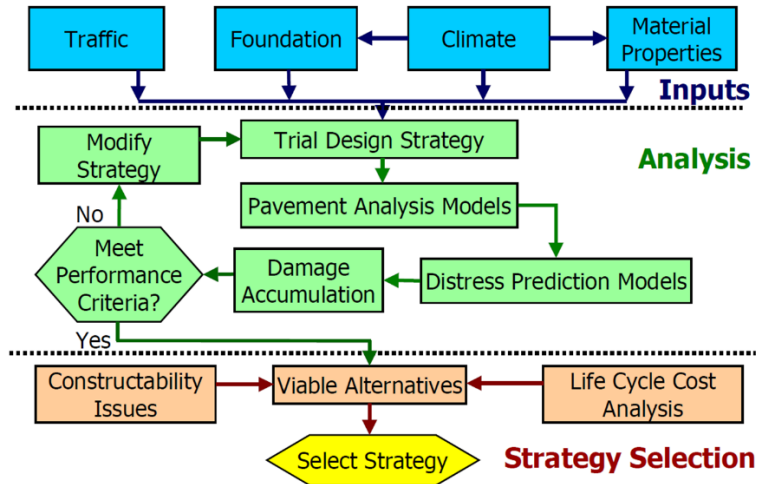


Figure 26. MEPDG Iterative Design Process

Analysis Inputs

As shown in Figure 26, four types of input data are required in MEPDG analysis: structure, traffic, climate, and material properties. Most of the input data are obtained from Folliard et al. (2006). Some input data are assumed based on a typical pavement design when the data are not provided by Folliard et al. (2006).

Figure 27 shows the pavement structure used for the analysis. The general input parameters for the analysis are as follows:

- Design life (years) = 20.
- Existing pavement construction (month, year) = August, 2002.
- Traffic open date (month, year) = September, 2002.
- Type of design = CRCP.

Since Folliard et al. (2006) does not provide the traffic data, level 3 default values were used as the traffic data. Since the default traffic data were obtained from long-term pavement performance program, the data can be considered to be a representative traffic data for general roads in the United States. Table 15 summarizes the assumed traffic input parameters for the analysis. For axle load distribution factors, the default values given in the software are used. The full table for axle load distribution factors can be found in NCHRP 1-37A. Monthly adjustment factors, vehicle class distribution factors, hourly distribution factors (HDF) used for the analysis are shown in Table 16, Figure 28, and Table 17, respectively.

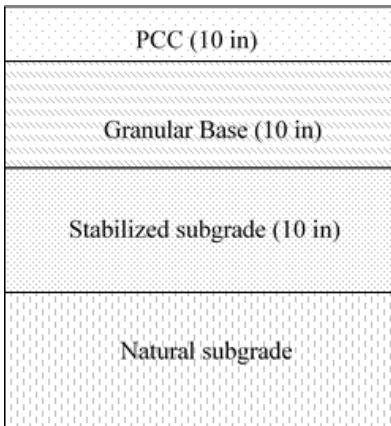


Figure 27. The Pavement Structure Used for the Analysis

Table 15. General Traffic Input Parameters

Initial two-way average annual daily truck traffic	1064 (7% of 15820)
Number of lanes in design direction	2
Percentage of trucks in design direction (%)	60
Percentage of trucks in design lane (%)	90
Operational speed (mph)	55
Mean wheel location (inches from lane marking)	18
Traffic wander standard deviation (inch)	10
Design lane width (ft)	12
Average axle width (ft)	8.5
Dual tire spacing (in.)	12
Tire pressure (psi)	120
Tandem axle spacing (in.)	48.9
Tridem axle spacing (in.)	52.7
Quad axle spacing (in.)	50.0
Average steering axle spacing (ft)	12, 15, 18
Percentage of trucks in each steering axle spacing category	33, 33, 34

Table 16. Statewide Average Monthly Adjustment Factor

Month	Class 4	Class 5	Class 6	Class 7	Class 8	Class 9	Class 10	Class 11	Class 12	Class 13
January	0.9	0.9	0.9	0.9	0.9	0.9	0.9	0.9	0.9	0.9
February	1.0	1.0	1.0	1.0	1.0	1.0	1.0	1.0	1.0	1.0
March	1.0	1.0	1.0	1.0	1.0	1.0	1.0	1.0	1.0	1.0
April	1.0	1.0	1.0	1.0	1.0	1.0	1.0	1.0	1.0	1.0
May	1.0	1.0	1.0	1.0	1.0	1.0	1.0	1.0	1.0	1.0
June	1.1	1.1	1.1	1.1	1.1	1.1	1.1	1.1	1.1	1.1
July	1.0	1.0	1.0	1.0	1.0	1.0	1.0	1.0	1.0	1.0
August	1.0	1.0	1.0	1.0	1.0	1.0	1.0	1.0	1.0	1.0
September	1.0	1.0	1.0	1.0	1.0	1.0	1.0	1.0	1.0	1.0
October	1.0	1.0	1.0	1.0	1.0	1.0	1.0	1.0	1.0	1.0
November	1.0	1.0	1.0	1.0	1.0	1.0	1.0	1.0	1.0	1.0
December	0.9	0.9	0.9	0.9	0.9	0.9	0.9	0.9	0.9	0.9

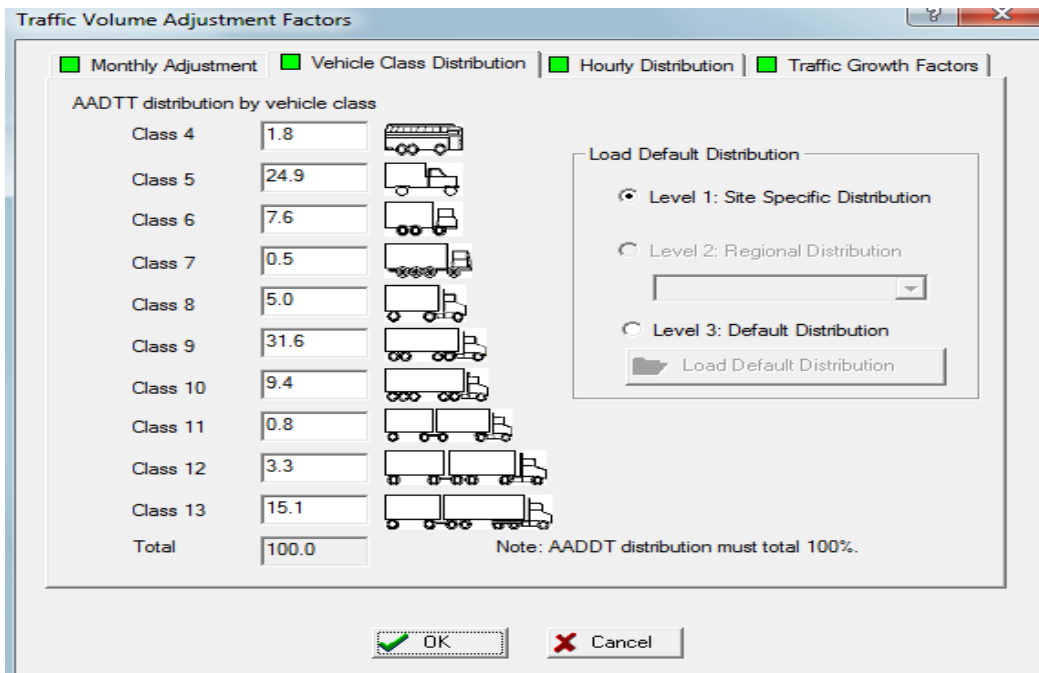


Figure 28. Vehicle Class Distribution Factors

Table 17. Statewide Hourly Distribution Factor

Hour	HDF	Hour	HDF	Hour	HDF	Hour	HDF
Midnight	1.63	6:00 AM	4.65	Noon	6.48	6:00 PM	3.74
1:00 AM	1.51	7:00 AM	5.56	1:00 PM	6.41	7:00 PM	3.15
2:00 AM	1.64	8:00 AM	6.18	2:00 PM	6.23	8:00 PM	2.73
3:00 AM	2.0	9:00 AM	6.53	3:00 PM	5.87	9:00 PM	2.42
4:00 AM	2.63	10:00 AM	6.66	4:00 PM	5.30	10:00 PM	2.12
5:00 AM	3.66	11:00 AM	6.55	5:00 PM	4.55	11:00 PM	1.79

Most of the material data for the surface (CRCP) layer are obtained from Folliard et al. (2006). The unit weight, MOR, compressive strength, and elastic modulus used for the analysis are given in Table 9 to Table 13. For the second set of analysis for the SFRCs with moderate fiber contents, the material data in Table 5 are used. Table 18 and Table 19 show other data for the CRCP layer. Table 20 lists the material properties for the base, subbase, and subgrade are not available, and the assumed values.

Table 18. The CRCP Layer Properties

Thermal Properties		Mix Properties	
Coefficient of thermal expansion (per $F^{\circ} \times 10^{-6}$)	8.5	Cement type	Type 1
Thermal conductivity (BTU/hr-ft- F°)	1.25	Water/cement ratio	0.43
Heat capacity(BTU/lb- F°)	0.28	Aggregate type	Quartzite
		Reversible shrinkage	50%

Table 19. The Reinforcement of the CRCP Layer

Percent steel (%)	0.71
Shoulder type	Gravel
Bar diameter (in.)	0.75
Steel depth (in.)	5
Mean crack spacing	From literature

Table 20. The Properties of the Unbound Materials

Properties	Crushed stone base	Subgrade (A-7-6)	Lime-stabilized subgrade
Poisson's ratio	0.4	0.45	0.25
Coefficient of lateral pressure	0.5	0.5	0.5
Modulus	60,000 psi	7,000 psi	500,000 psi
Gradation and PI	Default	Default	Default

The MEPDG uses a sophisticated climatic modeling tool called the Enhanced Integrated Climatic Model to evaluate the effects of changing temperatures and moisture. The Enhanced Integrated Climatic Model simulates the behavior and characteristics of the pavement and subgrade under heat and moisture flow over the changing climatic conditions. The Enhanced Integrated Climatic Model also has the climate database acquired from the weather stations all over the United States. In this analysis, the climatic data for a weather station in Houston, Texas, are used.

Analysis Results

Table 21 shows the limit values for the pavement distresses defined in MEPDG. When the predicted distresses exceed these limits, the designers have to modify the pavement design and run the analysis to verify the distresses will not reach the limits by the end of the intended pavement design life. Figure 29 compares the average crack width predicted by the MEPDG and that measured from the field. The

values and trend of the predicted crack width agree with the field measurements within a reasonable range. This result validates the MEPDG simulation and the assumptions of the analysis.

As shown in Figure 29, all of the measured crack widths do not exceed the crack width limit, and the crack widths of FRCs are slightly smaller than the control case. In the MEPDG predictions, the control case slightly exceeds the crack width limit, and the similar reduction pattern can be observed with the FRCs except for the SnF1-6. Among the FRCs tested by Folliard et al. (2006), SF1-40 (containing 0.3 percent hooked steel fiber) shows the best performance in crack control. Figure 30a shows that IRI is not significantly influenced by adding fibers. The punchout predictions (Figure 30b) are different from the results on crack width. SF1-40 has more punchout than SF1-25 (0.2 percent hooked steel fibers). However, when the predicted punchouts are compared to the design criterion (10 per mile), the difference in this range is not substantial.

Table 21. The Limit Values for Each Pavement Distresses in MEPDG

Performance	Limit	Reliability
Terminal IRI (in./mile)	172	90
CRCP Punchouts	10	90
Max Crack Width (in.)	0.02	-
Min Crack Spacing (ft)	3.0	-
Maximum Crack Spacing (ft)	6.0	-

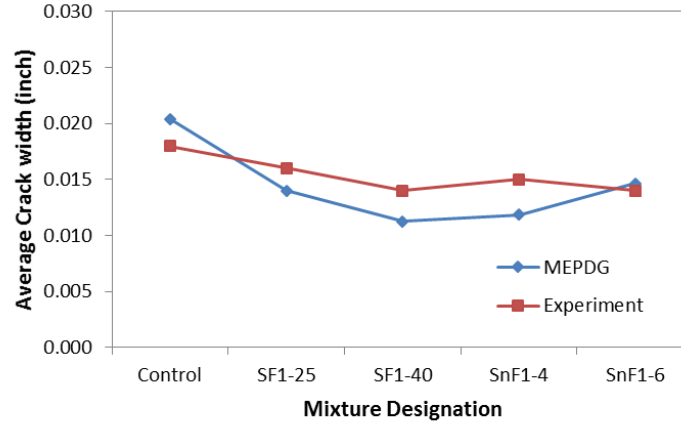
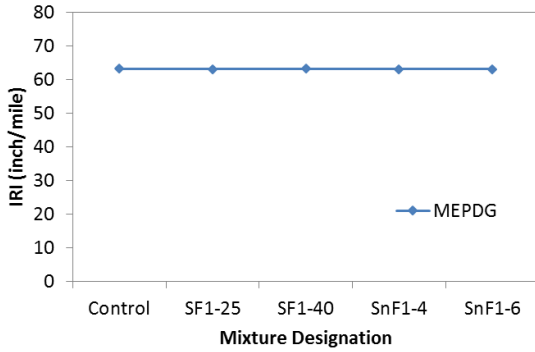
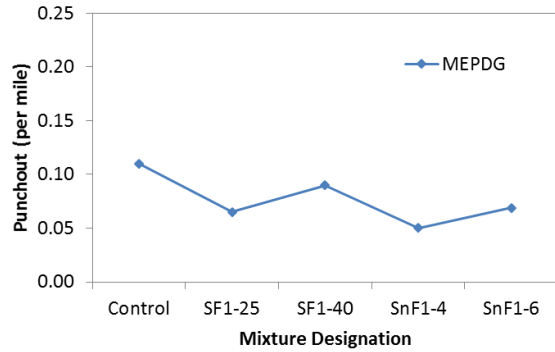


Figure 29. The Average Crack Width of the CRCP with Fibers (the Houston Case)



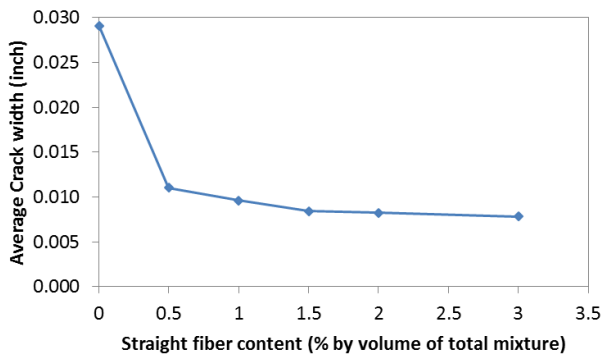
(a) IRI



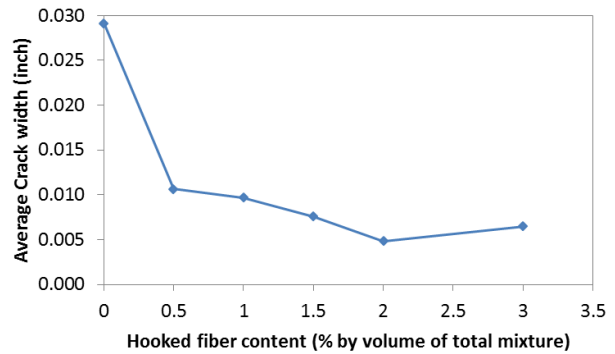
(b) Punchouts

Figure 30. The IRI and Punchouts of the CRCP with Fibers (the Houston Case) Predicted by MEPDG

Figure 31 through Figure 33 compare the crack width, IRI, and punchouts predicted by the MEPDG analysis for the SFRCs containing moderate contents of the straight and hooked steel fibers. Because of the higher fiber contents than from the Folliard et al. (2006) case, the fiber reinforcing effect is obvious in crack width and punchout. The effect on IRI is negligible. The MEPDG analysis indicates that the SFRC containing 2 percent hooked steel fiber has the best reinforcing effect. For both the straight and hooked steel fibers, the performance improvements increase with the fiber content up to 2 percent, but adding more fibers causes the decrease in pavement performances.

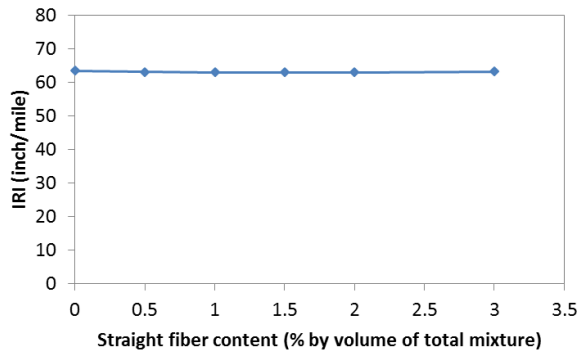


(a) Straight Fibers

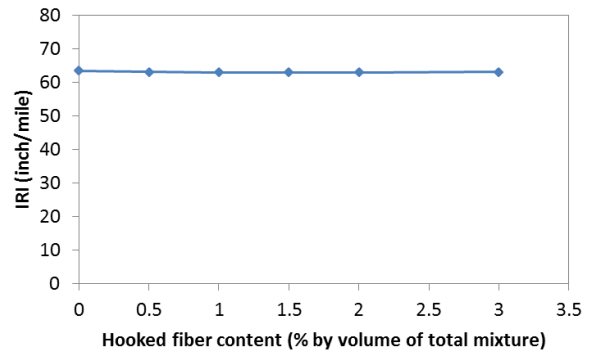


(b) Hooked Fibers

Figure 31. The Predicted Average Crack Width of the SFRCs Produced in This Project

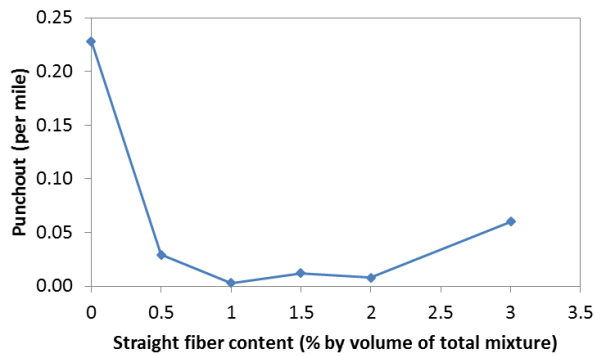


(a) Straight Fibers

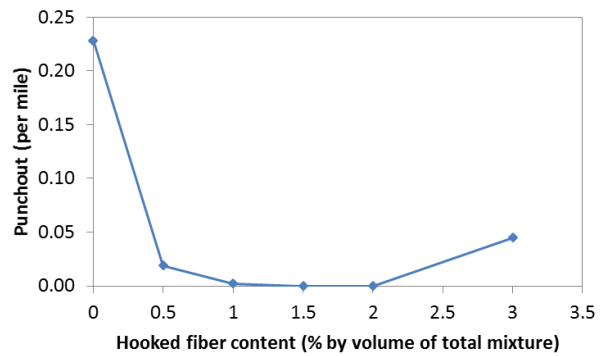


(b) Hooked Fibers

Figure 32. The Predicted IRI of the SFRCs Produced in This Project



(a) Straight Fibers



(b) Hooked Fibers

Figure 33. The Predicted Punchouts of the SFRCs Produced in This Project

SUMMARY

A literature review on the field applications of FRC to slab-on-grade is conducted, and a case at Houston, Texas, is analyzed using a widely used pavement analysis/design software, MEPDG. The fibers used at the slab-on-grade are synthetic fiber (MacDonald 2011; Flax 2010), glass fiber (Jones 2010), cellulose fiber (Brown et al. 2010), and steel fiber (Alexandre and Bouhon 2010; Folliard et al. 2006; Destrée et al. 2011). In most cases, FRC is effective on reducing cracks. For the case of using steel and synthetic fibers for CRCP at Houston, Texas, Folliard et al. (2006) reported that SFRC have better finishability, crack control, and spalling resistance than the un-reinforced (control) and synthetic FRC. A monitoring results after 235 days of concrete placement show that the average crack spacing and crack width of SFRC are smaller than those of un-reinforced and synthetic FRC.

The MEPDG analysis conducted in this case study uses two sets of material test data: 1) given by Folliard et al. (2006, containing 0.2–0.3 percent steel fibers by volume), and 2) produced from material tests of this study (described in Chapter 5, containing 0.5–2.0 percent steel fibers by volume). The average crack width predicted by the MEPDG analysis are 0.020 (control), 0.014 (0.2 percent SFRC), and 0.011 (0.3 percent SFRC) in., and those of the monitoring data (Folliard et al. 2006) are 0.018, 0.016, and

0.014, respectively. The MEPDG predictions slightly overestimate the fiber reinforcing effect, but can be considered to be within a reasonable range (Figure 29). The MEPDG analysis also shows that the SFRC is effective in reducing punchout damage while it has no effect on IRI. The improvements in average crack width and punchout are substantial when the moderate amounts of steel fibers (0.5–2.0 percent by volume) are added. Overall, the average crack width and punchout decrease with the increase of steel fiber contents (both straight and hooked fibers), but the improvements after 0.5 percent fiber content are gradual. Combining the analysis results of these small and moderate fiber contents, it is recommended to use 0.5 percent hooked steel fibers for the slab-on-grade applications.

CHAPTER 4. BRIDGE CASE STUDIES

INTRODUCTION

A parameter study was conducted on two bridge deck structural systems and one structural component to characterize the effect of adding steel fibers to bridge structures. The case studies consisted of a slab-girder bridge deck, a slab bridge, and a structural railing. The goal of each study is to examine the effects of SFRC on the behavior of each system by varying their material and geometric properties, such as the compressive strength of concrete, the post-crack strength of the SFRC and the location and area of traditional steel reinforcement.

MODELING APPROACH

Slab designs were evaluated by generating moment-curvature response curves for each bridge in the case study. Moment-curvature analysis was done using OpenSees, an open-source computer program developed by the University of California at Berkley, OpenSEES. The material response was modeled as a multilinear-elastic curve and the cross-section was subdivided into multiple slices or fibers to achieve the analyses. The results were compiled and normalized to evaluate the effect of SFRC on the strength and service performance of bridges.

Each study used a consistent derivation for the SFRC stress-strain response. The compression response of the SFRC was derived using the same philosophy presented by Lequesne et al. (2011). Specifically, the stress-strain behavior was determined using the Modified Kent Park model with a post-peak descending slope, Z , of 50 (Figure 34). The tension response was determined using the method proposed by Soranakom and Mobasher (2009) (Figure 35).

SLAB-GIRDER BRIDGES

Overview

The three-span rectangular girder system shown in Figure 36 was used for case studies of slab-girder bridges. The capacity requirements of the system were determined using the effective width procedure (AASHTO 2013). The applied wheel load is distributed longitudinally, or parallel to the girders, over an effective width (Equation 4 and Equation 5):

$$EW_{m^+} = 26.6 + 6.6S \quad (4)$$

$$EW_{m^-} = 48 + 3S \quad (5)$$

Where EW_{m^+} , EW_{m^-} = Effective width for the positive and negative moment regions, respectively; S = Girder Spacing.

Parameters investigated were girder spacing, deck thickness, compressive strength, post-crack tensile strength, and the layout and amount of traditional steel.

Table 22 summarizes values used for each parameter. The median deck thickness value for each girder spacing was chosen to be the minimum required depth based upon *ADOT Bridge Design Guidelines* (2011). Figure 37 and Table 23 detail the steel layouts used and how the area of reinforcement was determined. Profile 1 is the amount of steel needed for strength design. Profile 2 is the amount of steel that satisfies the AASHTO empirical design procedure. Profiles 3–5 investigate varying amounts of steel located at mid-depth. Profile 6 has no traditional steel.

A naming pattern using the parameters of each model was created to easily identify the results of each analysis: concrete matrix – girder spacing – compressive strength – deck thickness – post-crack tensile strength ratio – steel profile. For example, FRC-S6-F4500-H75-mu2-steel1 signifies an FRC deck with a girder spacing of 6 ft, compressive strength of 4500 psi, thickness of 7.5 in., post-crack tensile strength ratio of 0.2, and traditional reinforcement layout determined using ultimate strength design.

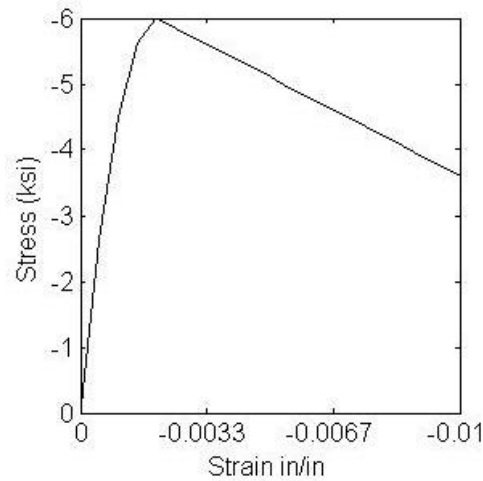


Figure 34. Concrete Compression Model for Case Study Moment Curvature Analysis

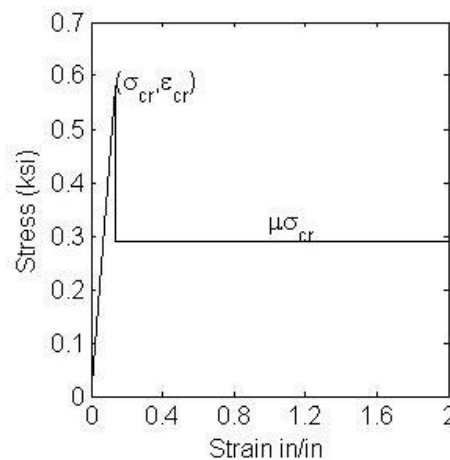


Figure 35. Concrete Tension Model for Case Study Moment Curvature Analysis

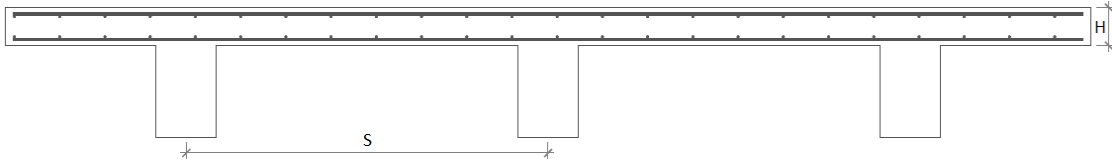


Figure 36. Traditional Slab-Girder Bridge

Table 22. Model Parameters

Girder Spacing – S (ft)	Deck Thickness – H (in.)	f'c (ksi)	μ	Steel Profile
6	5.5	4.5 6 7.5	0.2 0.8 1.4	Steel Profiles 1–6
	7.5			
	9.5			
8	6			
	8			
	10			
12	7.5			
	9.5			
	11.5			

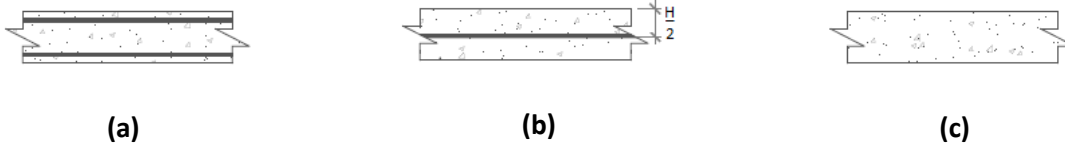


Figure 37. Case Study Reinforcement Layouts (a) Profile 1 and 2, (b) Profile 3-5, (c) Profile 6

Table 23. Steel Profiles

Steel Profile	Steel Location and Design Procedure			Illustration
	Negative Moment Region	Positive Moment Region	Mid-Depth	
1	Strength	Strength	-	Figure 37a
2	0.18	0.27	-	
3	-	-	Strength	Figure 37b
4	-	-	0.27	
5	-	-	0.18	
6	-	-	-	Figure 37c

Strength Results

Figure 38 shows the effect of adding a varying amount of steel fibers to a PC section with conventional steel reinforcement designed in accordance with AASHTO procedures. As shown, the addition of steel fibers increases the moment capacity of the cross section; however, it also decreases the curvature at the nominal moment. The additional tension capacity of the SFRC delays the initial traditional steel reinforcement yielding and reduces its strain at the nominal moment.

The moment and curvature corresponding to the nominal compressive strain of $\epsilon_c = 0.003$ for each SFRC model was extracted from the data set to simplify the analysis and presentation of the case study. Each moment and curvature pair were normalized by the results of a reference section corresponding to PC cross-section with conventional steel reinforcement designed in accordance with AASHTO. Figure 39 provides a sample of this method of presentation for the data. The strength reduction factors (ϕ factor) are accounted for in the secondary axes of each plot. The use of steel fibers for concrete strength design adds uncertainty to the overall concrete design process. Successfully achieving the post-crack tensile strength depends on numerous factors such as the fiber volume, fiber orientation, aggregate size, etc. Accordingly, the strength reduction factor proposed by Soranakom and Mobasher (2009) is 0.70 in comparison to 0.90 specified by AASHTO. Thus, for a SFRC slab to provide nominal values in excess of the reference slab, the ratio of the SFRC value (moment or curvature) to that of the reference slab must be equal to or exceed 1.29. A dashed line is used to indicate this limit.

Reference Concrete Deck with Steel Fibers

Figure 39 shows the normalized moment capacity as a result of the addition of the steel fibers to the reference deck. Adding steel fibers to the reference deck results in an increase in the moment capacity, but a decrease in the curvature at the nominal moment. The magnitude of the change in the strength and curvature correlates with the amount of fibers added to the concrete matrix, or the achieved post-crack tensile strength. The addition of a small amount of fibers changed the moment capacity and curvature by less than 10 percent. The addition of a large amount of fibers resulting in tensile strain hardening, μ_{14} , increased the capacity by more than 100 percent and reduced the curvature by nearly 50 percent.

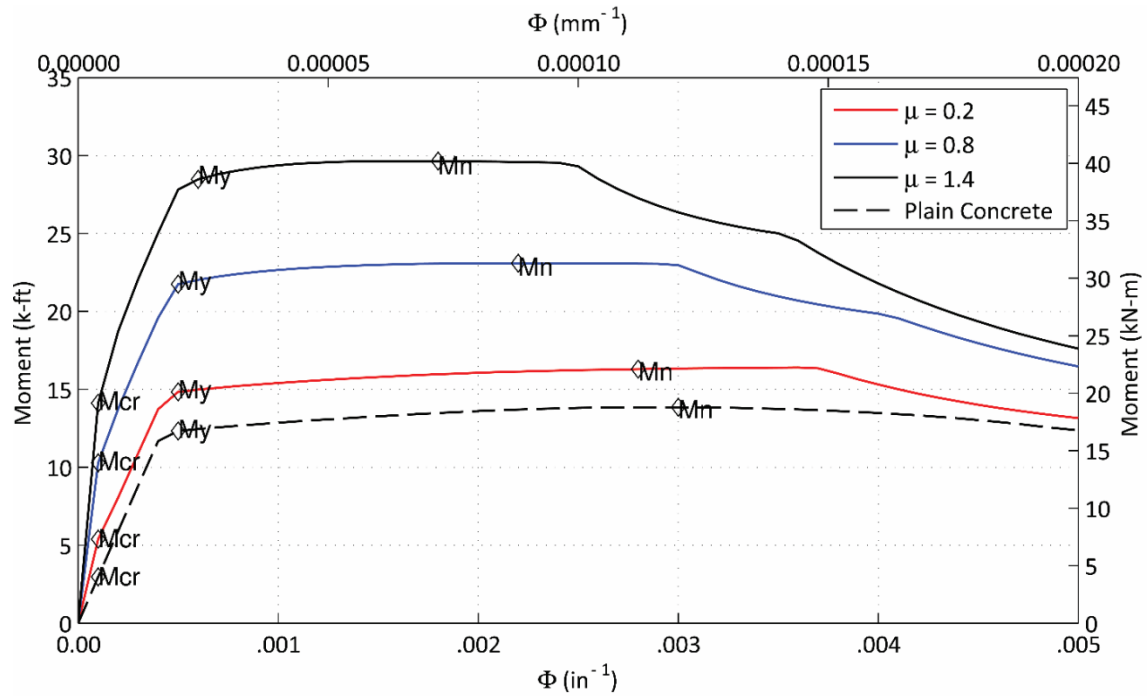


Figure 38. Moment vs. Curvature Response for SFRC and PC Sections with Conventional Steel Designed in Accordance with AASHTO

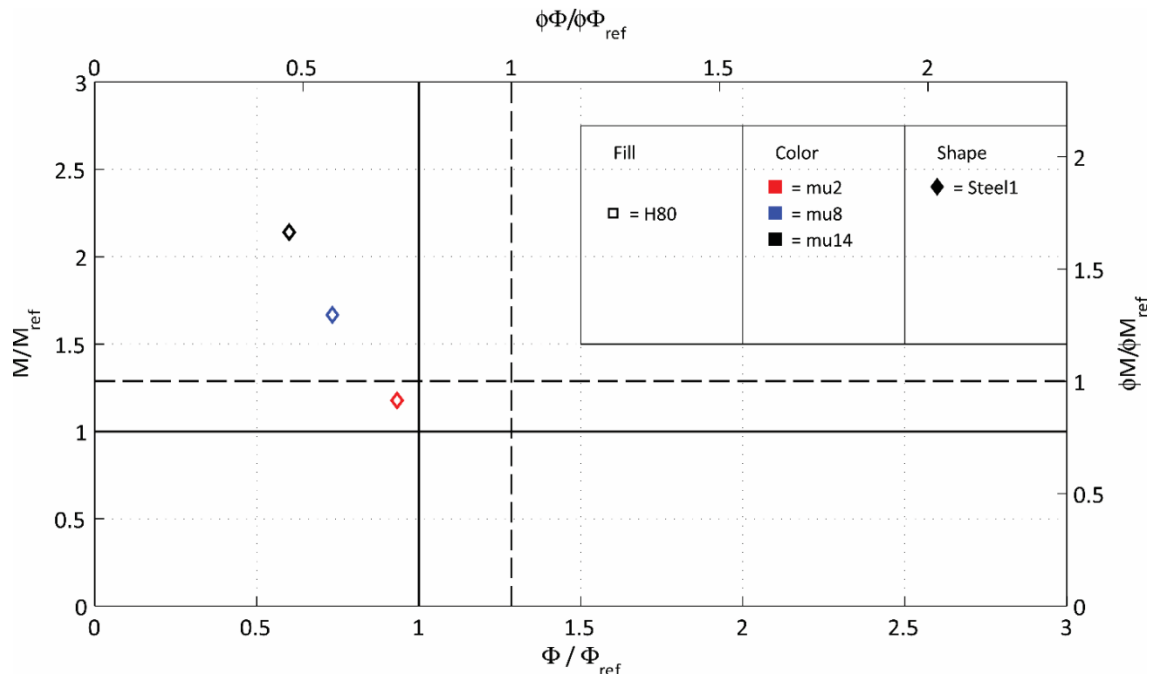


Figure 39. Normalized Moment vs. Curvature for S8-F4500-H80-muALL-Steel1

Varied Depth

Figure 40 shows the relationship between the depth of the member and the reference concrete deck with SFRC. Decreasing the depth of the concrete deck counteracts the decrease in curvature due to the addition of SFRC, but it also decreases the amount of moment capacity gained due to the fibers. The magnitude of this effect correlates to the amount of fibers added. Conversely, increasing the depth of the reference section provides larger moment capacity and reduced curvature. To efficiently use the benefits of SFRC, the depth should be decreased to increase curvature and reduce the design strength back toward unity.

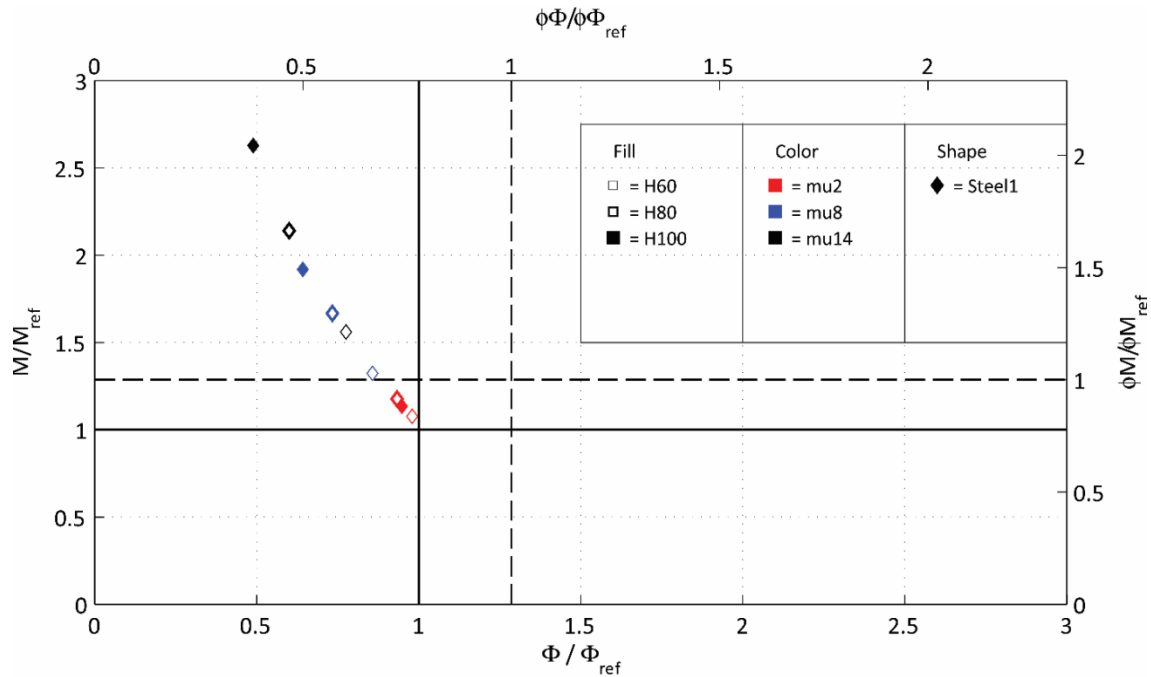


Figure 40. Normalized Moment vs. Curvature for S8-F4500-HALL-muALL-Steel1

Varied Steel Profiles

In addition to modifying the depth to efficiently capture the benefits of SFRC, the amount of steel and/or its location can be changed. Figure 41 shows the effect of reducing the amount of conventional steel to the AASHTO empirical design. Reducing the steel area yields a similar result to reducing the depth of the section; the moment capacity is decreased and the curvature at nominal is increased. The reduced area of steel achieves the required design strength with a moderate addition of steel fibers, mu8.

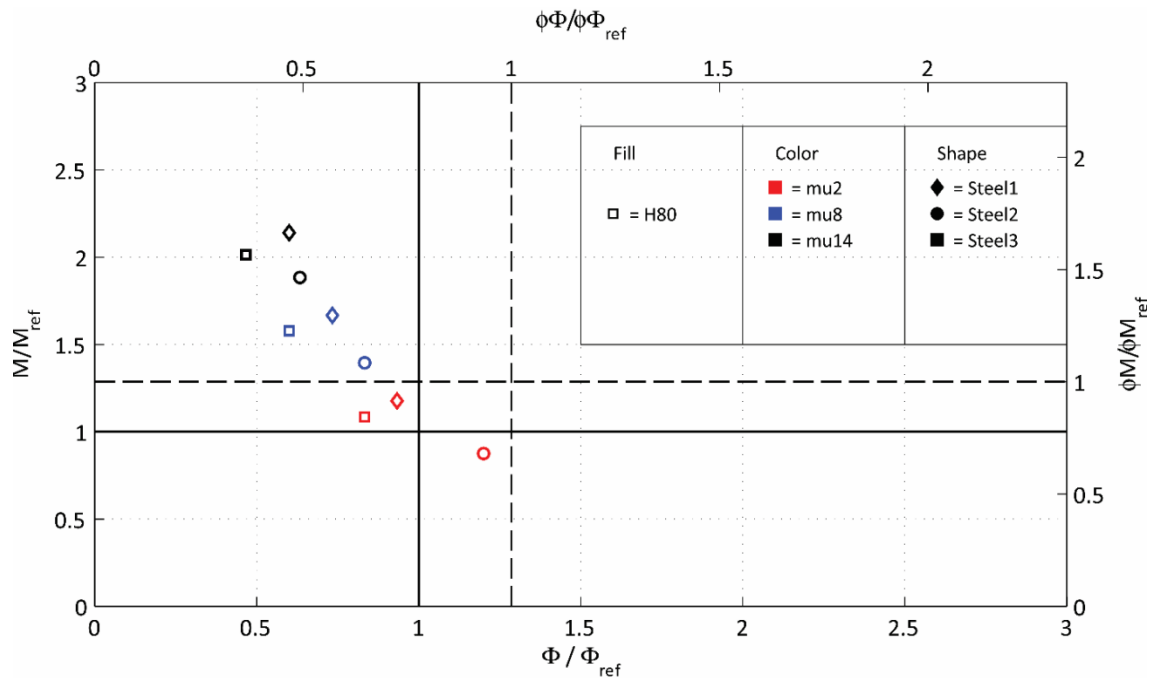


Figure 41. Normalized Moment vs. Curvature for S8-F4500-H80-muALL-Steel1-3

Relocating all conventional steel to the center of the cross-section was also investigated. This configuration is advantageous as it allows the steel reinforcement to provide both negative and positive moment capacity. Designing this section in accordance with AASHTO (Steel3) results in an over-reinforced section with the addition of SFRC. Therefore, a reduction in the area of steel located at mid depth was investigated (Figure 42). Again, reducing the area of conventional steel reinforcement allows the moment and curvature to trend toward unity. Incorporating a moderate amount of steel fibers (mu8) and a reduced steel area at mid depth (Steel4) resulted in an increase in expected strength with a minor decrease in curvature. However, to achieve an appropriate design strength either more steel fibers or more steel reinforcement must be added.

Ultimately, with a significant amount of steel fibers (mu14), all conventional steel may be removed from the section (Steel6) while still being able to achieve the design strength. The case study demonstrates that the use of SFRC allows the designer to both relocate steel reinforcement to advantageous locations and reduce the area of steel reinforcement and section depth.

The stress of the SFRC models mu8 and mu14 are nearly identical suggesting that the post-cracking stiffness of the SFRC specimens increases as the dosage of fiber increases. The increased stiffness aids the models in achieving the service moment sooner after cracking occurs.

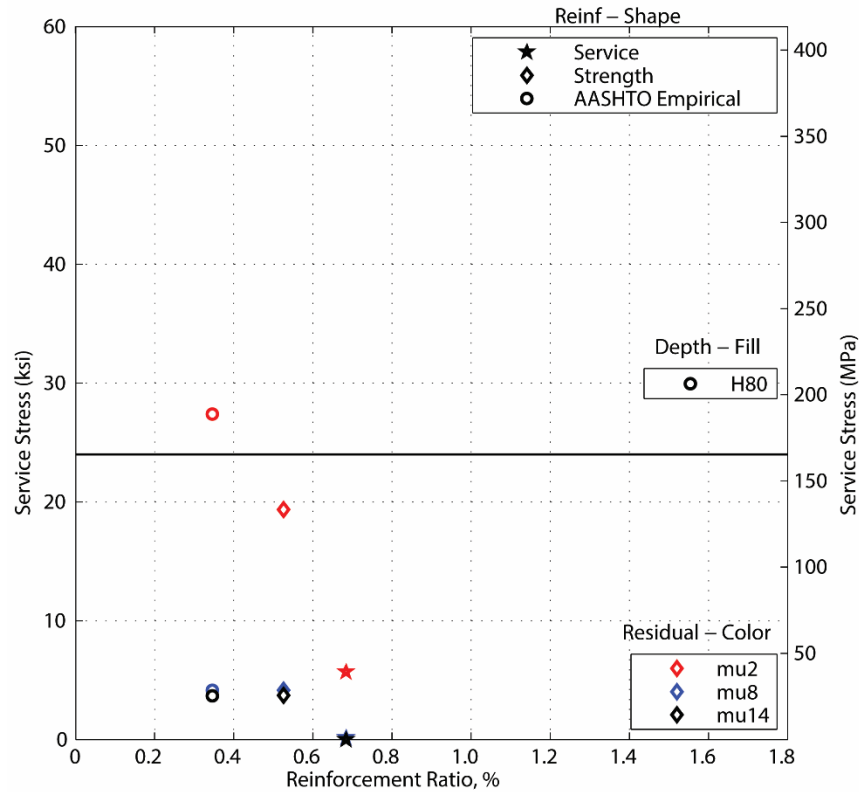


Figure 43. Service Performance S8-F4500-H80-muALL-Steel1-2-Service

Varied Depth

The comparisons made from Figure 43 were expanded to include the effect of different percentages of steel reinforcement, dosage rate of fibers, and depths of concrete (Figure 44). Increasing the depth by 2 in. to 10 in. increases the cracking moment of the models such that they achieve the service moment prior to cracking as shown by the solid points in the figure. Decreasing the depth of the cross-section to 6 in. has a similar effect as decreasing the steel reinforcement. The decreased depth with the strength reinforcement ratio and residual strength of mu2 nearly satisfies the service limit state. Both the steel reinforcement ratio and depth of the section can be decreased with the addition of a moderate amount of steel fibers, mu8. The three models that fail to satisfy the service limit state had either significantly reduced steel, AASHTO empirical, or had a thin cross-section.

As was observed with the strength results, a combination of reduced steel and reduced depth can be used with the addition of fibers. Both the strength and AASHTO empirical designs of a 6 in. deck can satisfy the service limit state with the correct dosage of steel reinforcement.

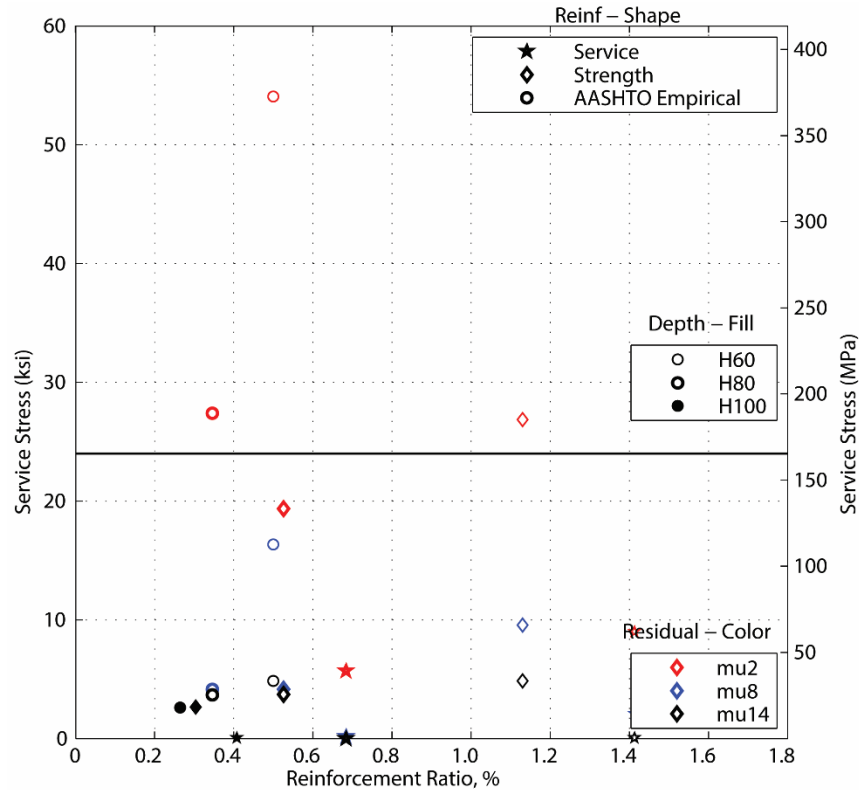


Figure 44. Service Performance S8-F4500-HALL-muALL-Steel1-2-Service

Additional Observations

Table 24–Table 29 summarize the results of the case study for each girder span investigated. The results reflect the appropriate strength reduction factors and highlight the configurations that satisfy the design strength requirements. The tables demonstrate that the trends associated with the SFRC on the capacity and curvature of each deck are maintained for each girder spacing. In most cases, however, the effectiveness of the SFRC decreases with increased girder spacing and moment demand.

Several of the analyses yielded a significantly reduced curvature for acceptable levels of strength. The strain at the extreme steel fiber in each section was calculated to determine the significance in the curvature reduction. As exhibited by Table 28, the largest decrease in curvature was observed in the reference sections (Steel1) and sections with all steel relocated to mid depth (Steel3). Figure 45 shows the strain at the extreme steel fiber for each of these configurations. The majority of analyzed sections maintain a steel strain above the ACI 318 requirements for tension-controlled members. Only the sections with lumped steel resulted in smaller strain and transition members with strength reduction (ϕ) factors less than 0.90.

Figure 46 demonstrates the influence of steel fibers for varying the concrete compressive strength. The data exhibit a clumping corresponding to the compressive strength and steel profile. A slight increase in the moment capacity for larger compressive strengths is observed; however, the compressive strength is overall insignificant in determining the response of SFRC bridge deck. The primary contributors to the

strength of the SFRC deck are the slab depth, post-crack tensile strength, and area of traditional steel reinforcement.

Table 24. Normalized Moment for S6-F4500

		Steel1	Steel2	Steel3	Steel4	Steel5	Steel6
H55	mu2	1.08	0.67	1.00	0.41	NA	NA
	mu8	1.33	0.96	1.23	0.76	0.68	NA
	mu14	1.57	1.22	1.36	1.05	0.98	0.82
H75	mu2	1.13	0.94	1.05	0.49	NA	NA
	mu8	1.63	1.47	1.57	1.19	1.08	NA
	mu14	2.12	1.96	2.02	1.71	1.61	1.41
H95	mu2	1.12	1.15	1.05	0.58	NA	NA
	mu8	2.04	2.06	1.98	1.71	1.57	NA
	mu14	2.83	2.85	2.74	2.50	2.39	2.14

Table 25. Normalized Moment for S8-F4500

		Steel1	Steel2	Steel3	Steel4	Steel5	Steel6
H60	mu2	1.08	0.62	1.00	0.36	NA	NA
	mu8	1.32	0.90	1.20	0.72	0.64	NA
	mu14	1.56	1.16	1.33	1.00	0.94	0.80
H80	mu2	1.18	0.88	1.09	0.45	NA	NA
	mu8	1.67	1.39	1.58	1.14	1.04	NA
	mu14	2.14	1.88	2.01	1.64	1.55	1.37
H100	mu2	1.13	0.97	1.06	0.49	NA	NA
	mu8	1.92	1.82	1.84	1.51	1.40	NA
	mu14	2.63	2.54	2.51	2.23	2.13	1.92

Table 26. Normalized Moment Capacity for S12-F4500

		Steel1	Steel2	Steel3	Steel4	Steel5	Steel6
H75	mu2	1.07	0.56	1.06	0.29	NA	NA
	mu8	1.36	0.88	1.27	0.71	0.65	NA
	mu14	1.63	1.17	1.41	1.02	0.96	0.84
H95	mu2	1.11	0.68	1.09	0.34	NA	NA
	mu8	1.58	1.23	1.54	1.01	0.93	NA
	mu14	2.04	1.70	1.93	1.49	1.42	1.27
H115	mu2	1.11	0.77	1.13	0.39	0.00	0.00
	mu8	1.85	1.61	1.81	1.35	1.26	0.00
	mu14	2.51	2.28	2.41	2.02	1.94	1.77

Table 27. Normalized Curvature for S6-F4500 with Varied Depth, Mu, and Steel Profiles

		Steel1	Steel2	Steel3	Steel4	Steel5	Steel6
H60	mu2	0.98	1.48	0.83	2.22	NA	NA
	mu8	0.87	1.10	0.72	1.25	1.48	NA
	mu14	0.76	0.91	0.64	0.97	1.02	1.25
H75	mu2	0.96	1.11	0.90	1.81	NA	NA
	mu8	0.74	0.77	0.62	0.83	0.97	NA
	mu14	0.59	0.62	0.49	0.60	0.65	0.79
H95	mu2	0.87	0.87	0.87	1.45	NA	NA
	mu8	0.57	0.57	0.50	0.60	0.63	NA
	mu14	0.42	0.42	0.37	0.41	0.45	0.48

Table 28. Normalized Curvature for S8-F4500 with Varied Depth, Mu, and Steel Profiles

		Steel1	Steel2	Steel3	Steel4	Steel5	Steel6
H60	mu2	0.98	1.55	0.78	2.39	NA	NA
	mu8	0.86	1.14	0.69	1.29	1.47	NA
	mu14	0.78	0.94	0.65	0.98	1.04	1.29
H80	mu2	0.93	1.20	0.83	1.95	0.00	0.00
	mu8	0.73	0.83	0.60	0.90	1.00	0.00
	mu14	0.60	0.63	0.47	0.65	0.65	0.80
H100	mu2	0.95	1.07	0.92	1.79	0.00	0.00
	mu8	0.64	0.67	0.55	0.69	0.73	0.00
	mu14	0.49	0.49	0.40	0.50	0.50	0.60

Table 29. Normalized Curvature for S12-F4500 with Varied Depth, Mu, and Steel Profiles

		Steel1	Steel2	Steel3	Steel4	Steel5	Steel6
H75	mu2	0.99	1.55	0.65	2.52	NA	NA
	mu8	0.86	1.08	0.60	1.16	1.36	NA
	mu14	0.73	0.86	0.56	0.84	0.91	1.10
H95	mu2	0.95	1.34	0.76	2.23	NA	NA
	mu8	0.76	0.88	0.53	0.92	0.97	NA
	mu14	0.61	0.65	0.46	0.63	0.69	0.74
H115	mu2	0.94	1.22	0.80	2.03	NA	NA
	mu8	0.66	0.69	0.52	0.73	0.78	NA
	mu14	0.49	0.49	0.38	0.47	0.52	0.57

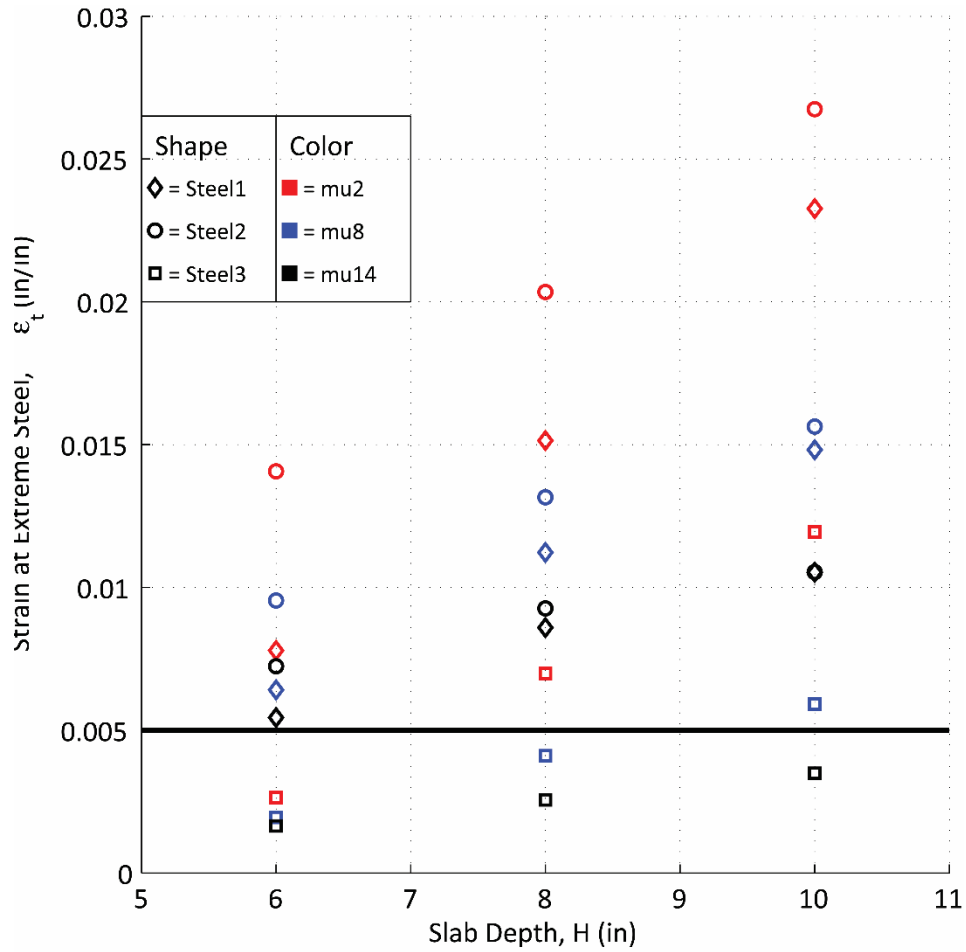


Figure 45. Strain at Extreme Steel Fiber vs. Depth for S8-F4500

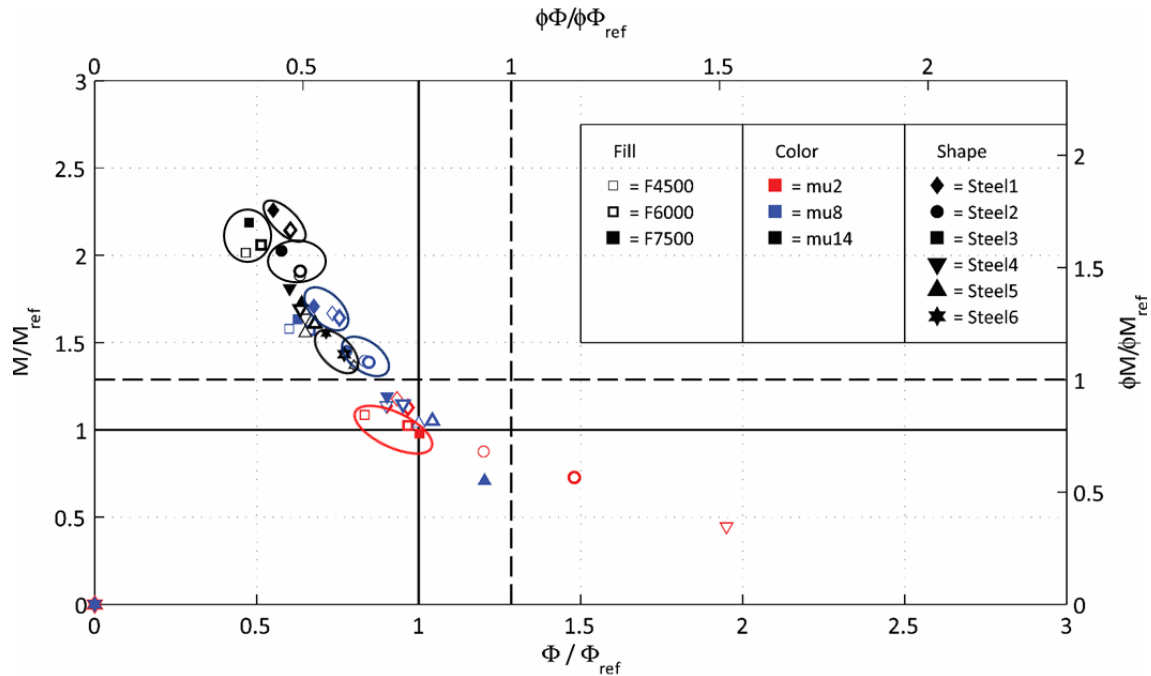


Figure 46. Normalized Moment vs. Curvature for S8-H80 with Varied f'_c , μ , and Steel Profiles

SLAB BRIDGES

Modeling and Analysis

A simply supported slab bridge deck was analyzed in a manner similar to the parameter study conducted for the slab-girder bridge deck. Slab bridge decks use girders that are orientated perpendicular to vehicle traffic and are characterized by short spans and a large thickness in comparison to slab-girder bridge decks. The capacity requirements of the system were determined using the effective width procedure (AASHTO 2014). For a slab bridge spanning less than 30 ft, the effective width is determined the same as slab-girder decks.

Table 30 presents values for each parameter investigated. The median thickness for each girder spacing was chosen as the minimum required depth based on AASHTO requirements. Table 31 details the area of steel reinforcement used near the tension face of the deck. The minimum area of steel required for temperature and shrinkage was used near the compression face of the deck. The same name convention used for the slab-girder deck was used for the slab bridge deck.

Table 30. Slab Bridge Parameters

Span Length (ft)	Deck Thickness (in.)	f'c (ksi)	μ	Steel Profile
15	9.5	4.5	0.2	Steel Profiles 1–4
	12			
	14.5			
30	15.5	6	0.8	
	19.5			
	23.5			
		7.5	1.4	

Table 31. Steel Profiles for Slab Bridge

Steel Profile	Steel Area and Design Procedure	Illustration
1	Strength	Figure 37
2	80% of Strength	
3	50% of Strength	
4	-	

Results

A total of 216 SFRC bridge decks were analyzed as part of this case study. Approximately 20 percent of the decks, 44 total, failed to reach the nominal compressive strain. Each deck was compared to the typical reinforced concrete bridge deck with appropriately designed steel reinforcement to demonstrate the effect of adding steel fibers on the concrete’s strength and serviceability. Figure 47 demonstrates the effects of steel fibers on a bridge deck spanning 30 ft with a varying deck depth.

In a similar manner to the slab-girder bridge case study, the addition of steel fibers to the reference deck, a deck with minimum depth, compressive strength, and ultimate strength design steel, increases the moment capacity while decreasing the curvature at the nominal moment. Adding a small amount of fibers, μ_2 , results in a small increase in the moment capacity. Alternatively, adding a large amount of fibers, μ_{14} , increases the moment capacity by 75 percent, but decreases the curvature at nominal moment by 55 percent.

The depth of the cross-section and area of traditional steel reinforcement can be reduced to increase the ductility back to the ductility observed in the reference deck with steel fibers. Using the ultimate strength design steel with a minimum amount of fibers, μ_2 , the depth of the cross section can be reduced by 20 percent. Alternatively, adding an excessive amount of fibers to the minimum cross section depth allows for the complete exclusion of traditional steel reinforcement. The depth may be reduced by 20 percent and the area of traditional steel reinforcement may be reduced 66 percent with the addition of a moderate amount of steel fibers, μ_8 .

Ultimately, the addition of steel fibers allows the designer to both reduce the depth of the concrete slab and area of steel reinforcement while maintaining the required strength. As a result, the curvature at nominal will also decrease, but can be increased with smaller depths and steel area.

Table 32 and able 33 summarize the results of the case study for the girder spacing and slab depth. Strength reduction factors are considered when evaluating slab bridge configurations. The values in these tables demonstrate that the girder spacing is not a significant factor in the response of the SFRC decks for the ADOT designed decks. Additionally, the concrete compressive strength is insignificant in the response of the SFRC decks (Figure 48). Both of the aforementioned trends were also observed in the slab-girder bridge deck.

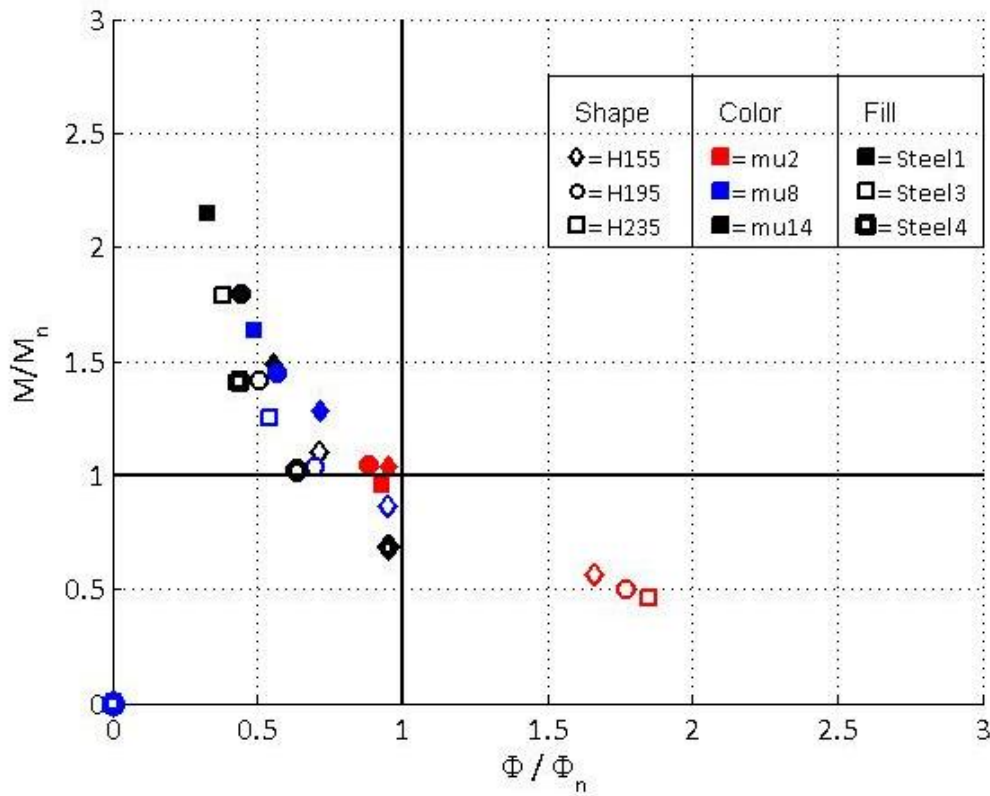


Figure 47. Normalized Moment vs. Curvature for S30-F4500 with Varied Depth, Mu, and Steel Profiles

Table 32. Normalized Moment Capacity for S15-F4500

		Steel1	Steel2	Steel3	Steel4
H95	mu2	1.05	0.87	0.60	NA
	mu8	1.27	1.11	0.85	NA
	mu14	1.46	1.31	1.08	0.65
H120	mu2	1.06	0.87	0.52	NA
	mu8	1.44	1.28	1.03	NA
	mu14	1.77	1.63	1.39	0.99
H145	mu2	1.00	0.78	NA	NA
	mu8	1.63	1.48	1.24	NA
	mu14	2.12	1.98	1.76	1.38

Table 33. Normalized Moment Capacity for S30-F4500

		Steel1	Steel2	Steel3	Steel4
H155	mu2	1.04	0.86	0.57	NA
	mu8	1.28	1.12	0.86	NA
	mu14	1.49	1.34	1.10	0.68
H195	mu2	1.05	0.83	0.50	NA
	mu8	1.45	1.29	1.04	NA
	mu14	1.80	1.65	1.42	1.02
H235	mu2	0.96	0.75	0.46	NA
	mu8	1.64	1.48	1.25	NA
	mu14	2.15	2.00	1.78	1.41

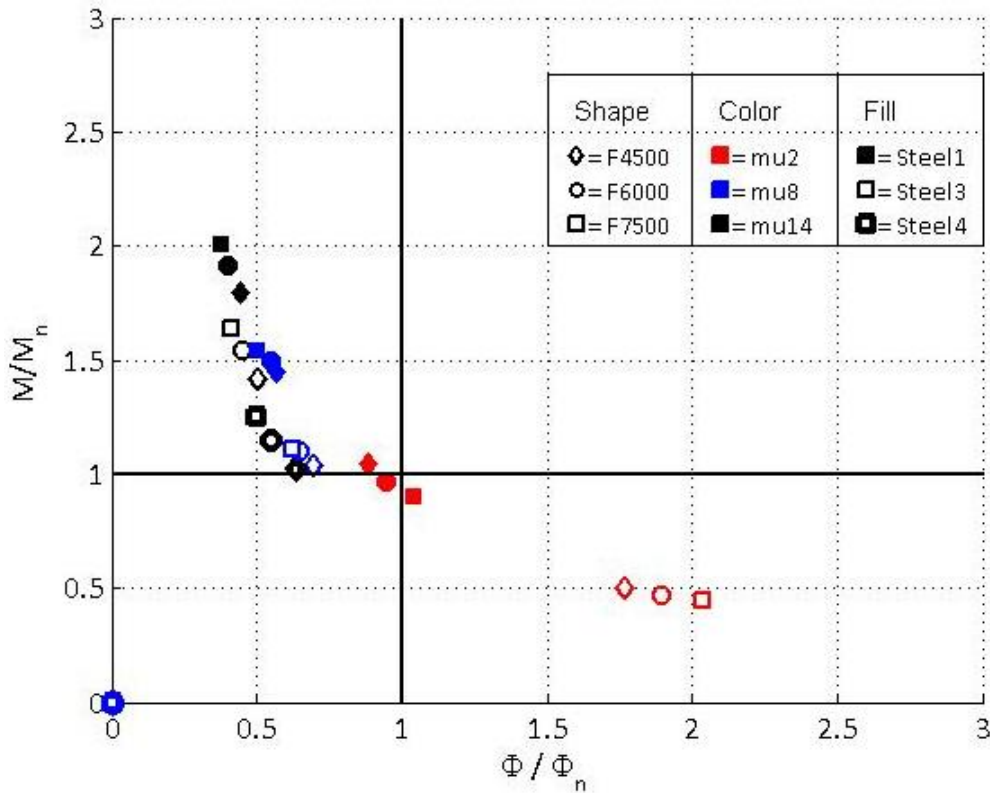


Figure 48. Normalized Moment vs. Curvature for S30-H195 with Varied f'_c , μ , and Steel Profiles

RAILING

The design of bridge railings is based on a yield line theory analysis. A set of equations to determine lateral load capacity for a concrete barrier is presented in AASHTO LRFD (Load and Resistance Factor Design) Bridge Design Specifications (2014). There are six categories for longitudinal bridge railings that correspond to the expected impact loading and barrier strength. The reference barrier dimensions and

steel reinforcement, based on the TL-4 railing category, is shown in Figure 49. Table 34 summaries values used for each parameter investigated, and Table 35 details the area of steel reinforcement used.

$$R_w = \frac{2}{2L_c - L_t} \left(8M_B + 8M_w + \frac{M_c L_c^2}{H} \right) \tag{6}$$

$$L_c = \frac{L_t}{2} + \sqrt{\left(\frac{L_t}{2} \right)^2 + \frac{8H(M_b + M_w)}{M_c}} \tag{7}$$

Where R_w is the transverse railing resistance, L_c is the critical length of yield line, L_t is the length of distributed impact load, M_b is the flexural capacity of beam at top of wall, M_w is the flexural capacity of wall about its vertical axis, and M_c is the flexural capacity of wall about an axis parallel to the wall.

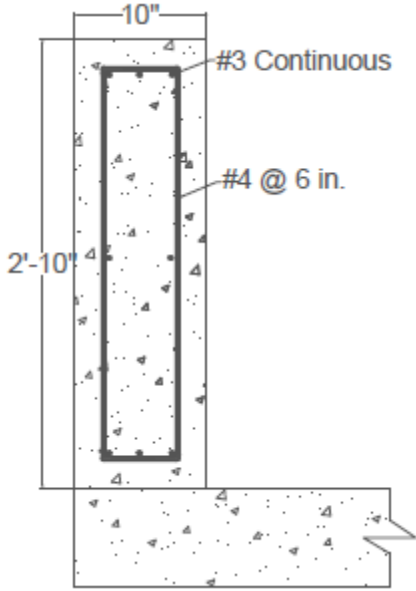


Figure 49. Reference Barrier Design

Table 34. Railing Parameters

Wall Thickness (in.)	f'c (ksi)	μ	Steel Profile
8	4.5	0.2	Steel Profiles 1-4
10	6	.8	
12	7.5	1.4	

Table 35. Steel Profiles for Railing

Steel Profile	Steel Area and Design Procedure	Illustration
1	Reference	Error! eference source not found.
2	66% Reference	
3	33% Reference	
4	-	

Figure 50 and Figure 51 demonstrate the effect of adding fibers to a concrete railing for the reference concrete railing shown above. Without changing the thickness of the wall, the addition a small amount of fibers, μ_2 , allows the steel reinforcement to be reduced by 33 percent. Increasing the amount of added fibers to a moderate amount, μ_8 , allows for the complete exclusion of the steel reinforcement while maintaining the minimum required strength.

Alternatively, both the wall thickness and steel reinforcement may be reduced by 20 percent and 66 percent, respectively, while maintaining the required strength. Both the wall thickness and steel reinforcement can be significantly altered with the use of steel fibers.

As shown in Figure 51, the concrete compressive strength is not as significant as the wall thickness and area of steel reinforcement. This is consistent with the conclusions of both bridge systems case study.

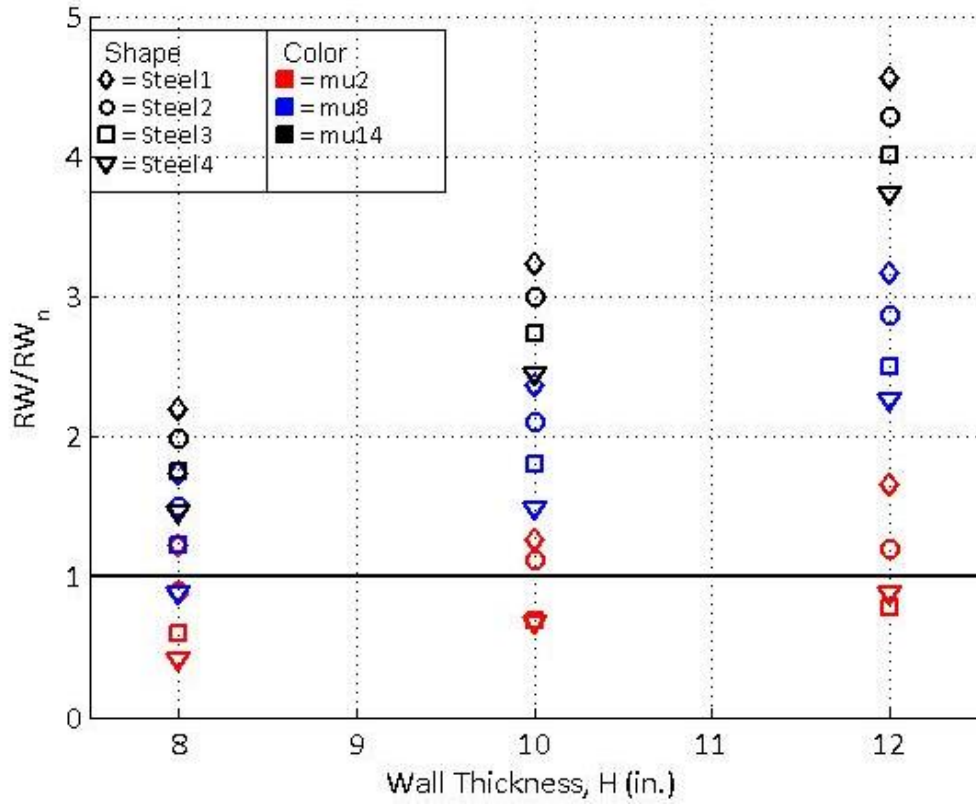


Figure 50. Normalized Collision Load vs. Wall Thickness for F4500 with Varied Mu and Steel Profiles

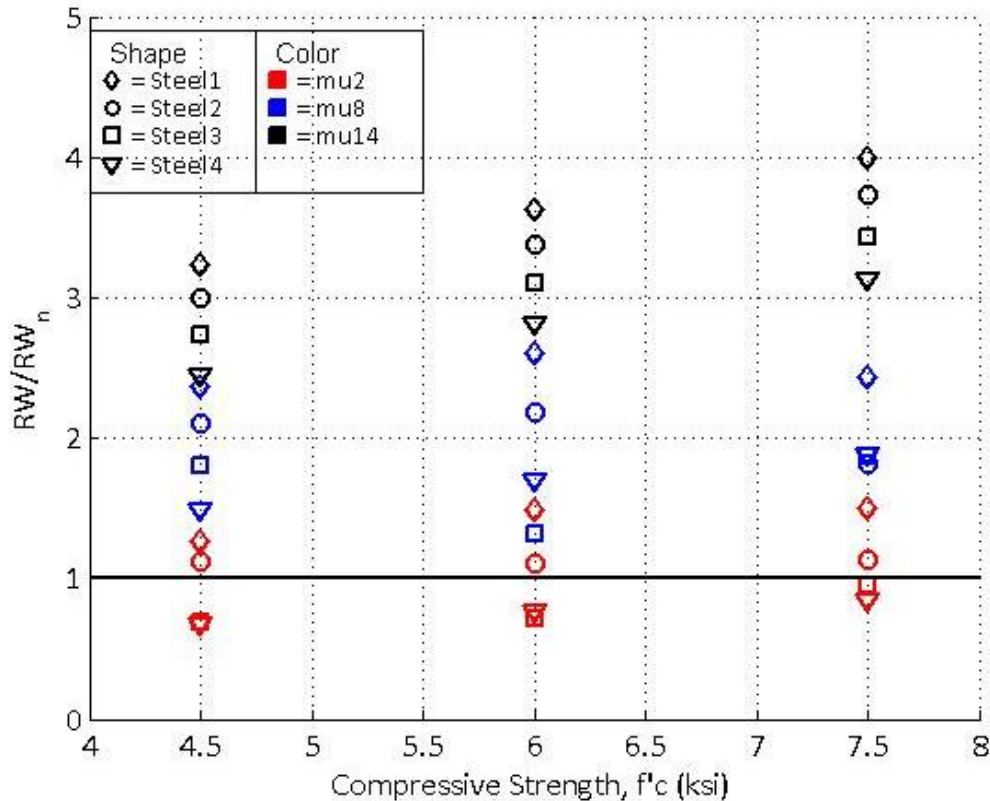


Figure 51. Normalized Collision Load vs. Concrete Compressive Strength for H100 with Varied Mu and Steel Profiles

SUMMARY

The three case studies demonstrated the effects of SFRC on the capacity of different bridge decks and elements. The results of each study yielded similar trends corresponding to the addition of strength due to the steel fibers in relation to conventional steel reinforcement, concrete compressive strength, and section geometry:

- The addition of steel fibers results in an increase in moment capacity and decrease in curvature at the nominal moment.
- Decreasing the depth of the section reduces the moment capacity, but also increases the curvature at nominal.
- With a moderate amount of steel fibers, the amount of conventional steel reinforcement may be reduced or lumped into advantageous locations, such as at mid-depth.
- With an excessive amount of steel fibers, the conventional steel reinforcement may be excluded completely.
- The benefits of SFRC decrease as the moment demand increases for slab-girder bridge decks while the moment demand does not affect the benefits from SFRC.
- The design of concrete railings is based on yield line theory.
- The addition of steel fibers results in an increase in collision failure load.

- Decreasing the thickness of the cross-section reduces the moment capacity, but also increases the curvature at nominal.
- With an excessive amount of steel fibers, the traditional steel may be excluded completely.
- With a moderate amount of steel fibers, both the wall thickness and area of traditional steel may be reduced by 20 percent and 66 percent, respectively.
- The concrete compressive strength slightly increases the capacity of the railing.

Ultimately, the use of SFRC adds to the reinforcement of a section and must be balanced by a reduction in conventional steel or depth. Otherwise, the section will begin to become over-reinforced resulting in a lower curvature at nominal and potentially a brittle failure. This is particularly of concern in the case where reinforcement design is governed by service level criteria. Further exploration of this is presented in Chapters 6 and 8, when such limits are considered along with the experimental performance of slabs.

Further caution must be taken when using the procedure of the case study. Each case study simply selected levels of residual tensile strength without regard to how to achieve the stated levels. Furthermore, each analysis used a strip-method treating each deck as a beam with unit width. While this may be appropriate for decks behaving in a one-way manner, this procedure will result in an underestimation of strength when considering two-way slabs (Destrée and Mandl 2008).

CHAPTER 5. MATERIAL TESTS FOR SFRC

To apply the SFRC for structural design, the mechanical characterization of the material is essential. The required mechanical performances of the SFRC vary with the structural applications, and the requirements including strength, stiffness, and ductility can be fulfilled by changing the type/content of the fibers.

The objective of the material tests is to obtain the basic mechanical properties of typical SFRCs. Uniaxial compression, uniaxial tension, and flexural tests are conducted, and the effects of fiber types (straight and hooked fibers, which are the most widely used for SFRC) and fiber contents (up to 3.0 percent by volume) are investigated. Fundamental material data including a set of stress–strain curves for the uniaxial compression and tension loads and load-deflection curves for the four-point bending are provided in this chapter. In addition, the effect of fibers on the workability of the fresh concrete are described. Table 36 summarizes the test cases and number of specimens. A total of 114 specimens (36 compression, 30 tension, and 48 flexural tests) were tested.

Table 36. Material Test Cases and Number of Specimens

Specimen ID	Description (fiber contents, % by volume)	Number of specimens		
		Compression test	Tension test	Flexural test
CON	Control specimens, No fibers	3	3	3
S05	Straight fibers, 0.5%	3	3	3
S10	Straight fibers, 1.0%	3	3	3
S15	Straight fibers, 1.5%	3	3	3
S20	Straight fibers, 2.0%	3	3	3
S30	Straight fibers, 3.0%	3	-	3
H05	Hooked fibers, 0.5%	3	3	3
H10	Hooked fibers, 1.0%	3	3	3
H15	Hooked fibers, 1.5%	3	3	3
H20	Hooked fibers, 2.0%	3	3	3
H30	Hooked fibers, 3.0%	3	-	3
SH05	Straight fibers, 0.25% and Hooked fibers, 0.25%	-	-	3
SH10	Straight fibers, 0.5% and Hooked fibers, 0.5%	-	-	3
SH15	Straight fibers, 0.75% and Hooked fibers, 0.75%	-	-	3
SH20	Straight fibers, 1.0% and Hooked fibers, 1.0%	3	3	3
SH30	Straight fibers, 1.5% and Hooked fibers, 1.5%	-	-	3

Note: Straight steel fiber , Hooked steel fiber 

EXPERIMENTAL SETUPS

Materials and Specimens Preparations

SFRC is a composite material with different ingredients including cement, fly ash, coarse aggregate, fine aggregate, chemical admixtures, water, and steel fiber. Table 37 shows the properties of each component used in this study.

Table 37. Properties of the Raw Materials Used

Material	Specific Gravity	Typical Size	Other Information
Cement	3.15	N.A.	Type II
Fly ash	2.20	N.A.	Class F
Coarse aggregate	2.58	Meet ASTM #57	Absorption Capacity: 1.7
Fine aggregate	2.63	Meet gradation specified by ADOT	Absorption Capacity: 0.6
Hooked steel fiber	7.8	l=1.3 in. (33 mm), d=0.022 in. (0.55 mm)	Aspect Ratio: l/d=60 Tensile strength: 174 ksi (1200 MPa)
Straight steel fiber	7.8	l=13 mm (0.51 in.), d=0.2 mm (0.0079 in.)	Aspect Ratio: l/d=65 Tensile strength: 386 ksi (2660 MPa)
Water reducer	N.A.	N.A.	Type A
Air entrained agent	N.A.	N.A.	N.A.
Super-plasticizer	N.A.	N.A.	N.A.

Type II Portland cement and Class F fly ash are cementitious materials that react with water to form hydration products, which contribute to most of the strength of the SFRC. Aggregate materials added to the mixture are #57 coarse limestone and concrete river sand. Type A water reducer, super-plasticizer, and air entraining agent are used to increase the workability of the SFRC. All the materials mentioned above are provided from Knife River Inc.

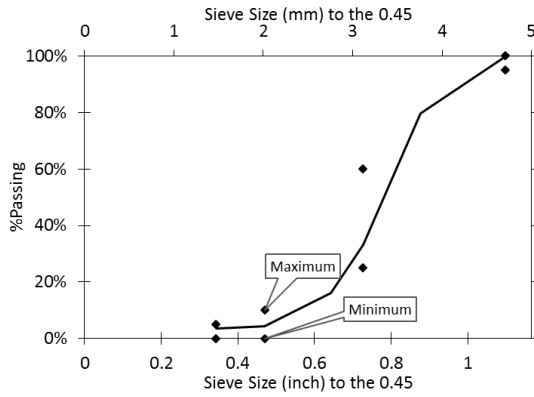
Uncollated hooked steel fiber (provided by Maccaferri Inc.) and straight steel fiber (provided by Nycon Inc.) are employed to reinforce the concrete. The un-collated hooked fiber has an aspect ratio of 60 (length= 1.3 in.=33 mm, diameter=0.022 in.=0.55 mm), while the straight fiber has an aspect ratio of 65 (length=0.51 in. =13 mm, diameter=0.0079 in.=0.2 mm). The straight fiber is coated with copper to prevent corrosion. Figure 52 shows the fibers used for the material tests.



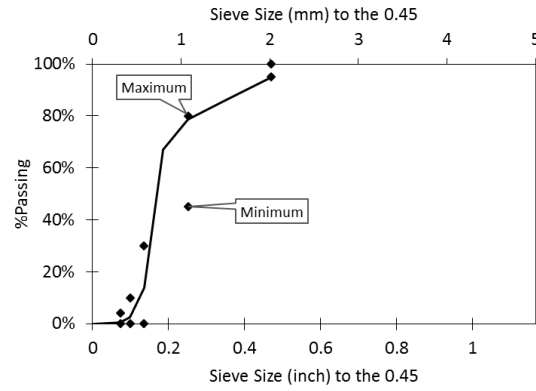
Figure 52. Hooked Steel Fiber (Left) and Straight Steel Fiber (Right)

Mix Design

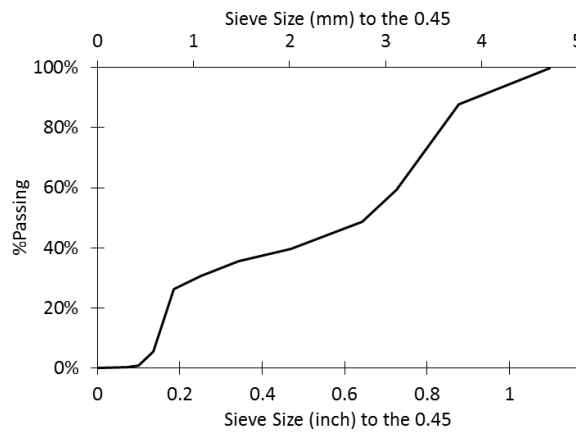
The concrete is designed to meet Class P requirement specified in ADOT Standard (ADOT 2008). The water cement ratio (w/c) is selected as 0.43 to produce a concrete having a minimum 28-day compressive strength of 4000 psi. Twenty-five percent by weight of the cement is replaced by fly ash. Since low workability is a common problem of a SFRC, 3 oz of super-plasticizer per 100 lb of the cementitious material is added in the mix design to make the mixture more workable and to ensure a uniform distribution of fibers. Aggregates of #57 crushed limestone and concrete sand that meet the requirements of gradations specified in ADOT standards are used; their gradation curves, as well as the gradation for aggregate blend are shown in Figure 53. Table 38 **Error! Reference source not found.** lists a summary of mix design of SFRC in this study.



(a) Coarse Aggregate Gradation



(b) Fine Aggregate Gradation



(c) Overall Aggregate Gradation

Figure 53. Aggregates Gradation Curves

Table 38. SFRC Mix Design

Materials	Amount (lb/yd ³ for solid, oz/yd ³ for liquid)
Cement Type II	423
Fly Ash Class F	141
Coarse Aggregate #57 Crushed Limestone	1850
Fine Aggregate Concrete Sand	1184
Water	242.6
Water Reducer Type A/D	23
Air Entraining Agent (5% entrained air content)	1.7
Superplasticizer	16.92

Batching, Mixing, Casting, and Curing of SFRC

A total of 114 SFRC specimens were prepared in this project, including 36 six-inch diameter cylindrical specimens for compression tests, 30 four-inch diameter cylindrical specimens for tension tests, and 48 standard beams (6 in. × 6 in. × 20 in., ASTM C78/C78M) for flexural tests. Fiber volume content (up to 3.0 percent) of the mixture was the only variable controlled in the specimen fabrication.

Materials sufficient for three specimens for the specified tests were prepared as one batch. Each ingredient was weighed precisely according to the mix design shown in Table 38. The aggregates weight in the mix design assumes a saturated surface dry condition. To ensure a consistent moisture condition, the aggregates were dried in the oven for 24 hours before mixing, and the moisture contents were corrected using Equation 8:

$$W_{OD} = \left(\frac{AC}{100} + 1 \right) \times W_{SSD} \quad (8)$$

Where $AC = 100 \times \frac{W_{SSD} - W_{OD}}{W_{OD}}$, W_{SSD} is the aggregate weight in saturated surface dry condition, and W_{OD} is the aggregate weight in oven dry condition.

Two types of mechanical mixers were used in this study (Figure 54). The small mixer was used only to fabricate the tension specimens because mixing a small batch in the big mixer caused a significant loss of the mortar, resulting in a quality control issue.



(a) 4 Cubic Feet Mixer



(b) 6 Cubic Feet Mixer

Figure 54. Two Mixers Used in This Project

The mixing procedure of the SFRC is as follows:

- Add all coarse aggregates, fine aggregates, and $\frac{3}{4}$ of water, and mix for 1 minute.
- Add air entraining agent by using a syringe, and mix for 1 minute.
- Add cementitious materials (cement+fly ash), water reducer, and superplasticizer, and mix for 1 minute.
- Add the rest of the water, and mix for 2 minutes.

- When the mixture becomes consistent and flowing, gradually disperse steel fibers; mix for 3 minutes.
- Stop the mixer and let the mix set for 3 minutes; use a polypropylene sheet to cover the mixer to avoid evaporation of water.
- Restart the mixer and mix for 2 minutes.

After mixing, the fresh SFRC was dumped to a wheelbarrow. A scoop was used to scrape the mortar attached to the mixer out, ensuring the loss of the mortar in the mixture was reduced to a minimum level. The fibers were observed to be uniformly distributed in the mix at low volume contents (vol. % < 1.5 for hooked fiber and vol. % < 1.0 for straight fiber), but some amounts of clumps were found in high fiber content SFRC (Figure 55). The workability of the hooked SFRC was slightly better than that of the straight SFRC. It is presumed that the relatively poor workability of the straight SFRC is caused by the higher aspect ratio and the higher number of straight fibers than hooked fibers (for the same volume, the number of the straight fibers is significantly higher because the straight fibers are shorter and thinner than hooked fibers). The slump and unit weight of the fresh SFRC were measured according to ASTM C143/C143M (2012b) and ASTM C138/C138M (2014c).



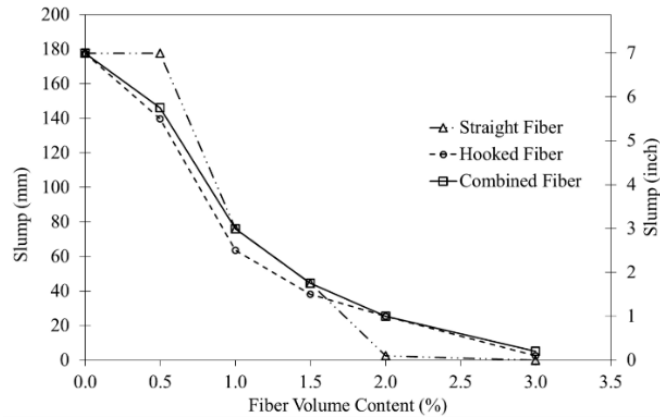
(a) Uniformly Distributed SFRC (H05)



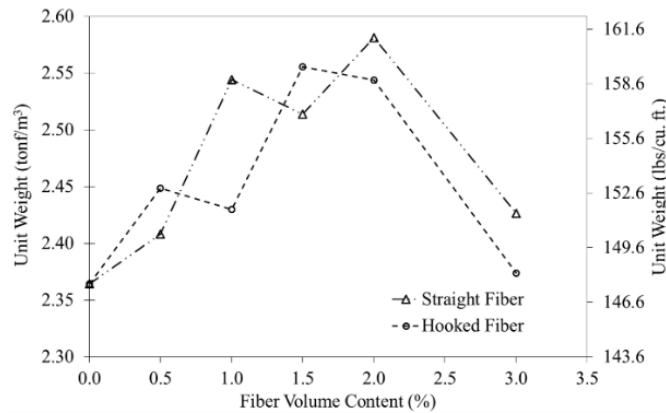
(b) Fiber Clumps (S15)

Figure 55. Mixing Quality of the SFRC

Figure 56 shows the variations of the slump and unit weight with the fiber contents. The slumps of the SFRC decrease with the increase of the fiber contents, indicating a reduction in workability by adding fibers. The drop in the slump values is more rapid with the straight fibers than the hooked and combined fibers. The unit weight of SFRC increases up to the fiber volume fraction of 2.0 percent as the unit weight of fibers is higher than the mixture, and then decreases at the fiber volume fraction of 3.0 percent because the fibers clumping causes lots of air bubbles between the coarse aggregates. The slump and unit weight test results indicate that adding fibers more than 2.0 percent causes serious reduction in workability for this mixture design.



(a) Slump



(b) Unit Weight

Figure 56. Fresh Concrete Properties

All the blended SFRC materials were cast in the molds within 20 minutes after the completion of mixing process. Three types of molds were used to make three different types of specimens. To prevent material segregation, casting of SFRC was completed by tamping and rodding instead of using a vibrating machine.

During the 24 hours of initial curing, the specimens were covered by a plastic sheet to prevent moisture loss. After the initial curing, the specimens were de-molded and placed in water storage tanks, which is located in a room with constant temperature of 25°C, for an additional 26 days. Sufficient lime powder was mixed into the water to prevent leaching of calcium hydroxide from the concrete (ASTM C511 2013). All cured specimens were taken out of the water tank at the age of 27 days, and remained in a dry condition for another 1 day before testing.

Compression Test Method

Compression test using a cylindrical specimen is the most common material test for concrete specimens. Compressive strength (f'_c) can be used for predicting other mechanical properties of concrete, such as elastic modulus (E_c) and MOR. The test method to evaluate compressive properties of concrete are well developed and widely used. The standard test methods are:

- ASTM C39/C39M: Standard Test Method for Compressive Strength of Cylindrical Concrete Specimens (ASTM International 2014a).
- ASTM C469/C469M: Standard Test Method for Static Modulus of Elasticity and Poisson's Ratio of Concrete in Compression (ASTM International 2014b).

Compression tests in this study were conducted in accordance with ASTM C39 and ASTM C469 for determining the constitutive responses of the SFRC under compression. A material testing system (MTS) of 500 kips capacity was used. A ring-type attachment with three linear variable displacement transducers (LVDTs) was used to obtain elastic stress–strain responses of the SFRC specimens, while the post-cracking behavior in a large displacement range was captured by the displacement transducer equipped in the MTS machine. All the tests were completed at a constant displacement rate of 0.05 in./min, and the ring attachment was removed before cracking occurred to prevent damage of the LVDTs.

Tension Test Method

The uniaxial tension test is a fundamental test method for obtaining a tensile stress–strain curve of materials, but ASTM International has not established the uniaxial tension test method for concrete because the tensile strength of concrete is very low, and often is neglected in the structural design of concrete. Instead, alternative test methods simulating the practical loading conditions of concrete are recommended. Those are the splitting tension test and the flexural bending test. In the splitting tension test, a diametral compression is applied to a standard cylindrical specimen through two narrow bearing strips along the two opposite sides of the cylinder. ASTM C496/C496M (ASTM International 2011) describes the standard splitting tension test method. While the splitting tensile strength values are often assumed to be 30–40 percent lower than MOR values and 5–12 percent higher than direct tensile strength values, there is no simple relationships between these values (Mindess et al. 2003).

The most important benefit of the fiber reinforcement is an improvement in tensile strength. Therefore, it is important to obtain the tensile stress–strain curves of the SFRC for modeling and design purposes. While there is no currently available standard for the concrete uniaxial tension test method, AASHTO provides a standard test method for a cement mortar: AASHTO T132-87: Standard Method of Test for Tensile Strength of Hydraulic Cement Mortars (AASHTO 2013).

Some foreign institutes provide recommendations on the uniaxial tension test for FRCs as follows:

- RILEM TC TDF-162: Test and Design Methods for Steel Fiber Reinforced Concrete. Recommendations for Uniaxial Tension Test (RILEM TC 162-TDF 2001).

- AFGC-SETRA: Ultra High Performance Fibre-Reinforced Concretes, Interim Recommendations (AFGC-SETRA 2002).
- JSCE: Recommendations for Design and Construction of High-Performance Fiber-Reinforced Cement Composites with Multiple Fine Cracks (HPFRCC) (JSCE 2008).

Wille et al. (2014) summarized direct tensile test methods for FRCs that have been used by various researchers. Wille et al. (2014) pointed out the existing difficulties in measuring tensile properties of concrete as follows:

- Obtaining evenly distributed stress throughout the cross sections is challenging.
- Specimen shapes and boundary conditions significantly influence the tensile behaviors.
- When a specimen was glued to the jig, a bond failure due to weak bonding and stress concentration at the interface are typical.

Hence, choosing a proper specimen dimension and test procedure to serve a special purpose is one of the biggest challenging for SFRC tension tests. Specimen shapes can be typically classified into unnotched prism or cylinder, notched prism or cylinder, and dog bone shaped. The unnotched prism or cylinder specimen is primarily useful in determining the elastic behavior prior to crack initiation. The notched prism or cylinder specimen is designed to characterize the softening behaviors after cracking, but is not successful in obtaining elastic or strain hardening behaviors. The dog bone shaped specimen is popular for measuring a strain hardening behavior of cement paste or mortar, but is not suitable for a concrete that contains coarse aggregates.

Since the material test aims to obtain stress–strain curves of the SFRCs containing coarse aggregates, it is not suitable to use the notched or dog bone specimen. Based on the recommendations of RILEM TC TDF-162 and Graybeal (2006), the unnotched cylindrical specimen with 4-in. diameter and 8-in. length was used for the tension test of this study. To make the tension test specimens, the top and bottom of the 4-in. diameter concrete cylinders were trimmed by 0.5 in. after 27 days water tank curing. This trimming process is important because the SFRC specimens typically have rugged surfaces that would cause problems in the further specimen preparation. The trimmed specimens were then placed in a ventilated room for another day to remove the moisture on the specimen surfaces so that a better bonding between the jig and concrete can be ensured. As a jig, a retainer ring was welded to a 1¼ thread, which allows connection with an MTS testing machine. A high-strength, high modulus, and rapid setting epoxy was applied to glue the jig to the concrete surface. The epoxy was cured more than five hours to reach the target tensile strength. The concrete tension specimen with both sides attached to the jigs was then connected to a 20 Kips MTS machine, and an adapter that could rotate freely was used to align the specimen. An LVDT of 2-in. gage length was attached to the specimen to record the displacement. The test was performed by controlling the displacement of load cell at a constant rate of 0.025 in./min. Figure 57 shows a photo of the tension specimen setup.



Figure 57. Tension Specimen Setup

Flexural Test Method

Since a bending beam is one of the fundamental structural member, measuring flexural strength is a common test method for concrete. Because the tensile strength of concrete is weaker than the compressive strength, the flexural strength is considered to represent the tensile behavior. The tensile strength obtained from the flexural test is called an MOR, which is one of the basic material parameters for the PC design. In the case of the SFRC, Soranakom and Mobasher (2007a; 2007b) suggested a method of deriving the tensile properties from the flexural test data. The standard test methods for measuring the flexural strength are:

- ASTM C293/C293M: Standard Test Method for Flexural Strength of Concrete (Using Simple Beam with Center-Point Loading) (ASTM International 2010a).
- ASTM C78/C78M: Standard Test Method for Flexural Strength of Concrete (Using Simple Beam with Third-Point Loading) (ASTM International 2010b).

There exist several standard flexural test methods tailored for FRCs as follows:

- ASTM C1399/C1399M: Test Method for Obtaining Average Residual-Strength of Fiber-Reinforced Concrete (ASTM International 2010c).
- ASTM C1609/C1609M: Test Method for Flexural Performance of Fiber-Reinforced Concrete (ASTM International 2012a).
- RILEM TC TDF-162: Test and Design Methods for Steel Fiber Reinforced Concrete. Bending Test (RILEM TC TDF-162 2002).
- BS EN 14651 (British Standards): Test Method for Metallic Fiber Concrete. Measuring the Flexural Tensile Strength (LOP, Residual) (BS 2007).

The loading configurations of ASTM C1399/C1399M and ASTM C1609/C1609M are a third-point loading (four-point bending), which is the same as ASTM C78/C78M. While ASTM C78/C78M measures the MOR of unnotched specimens, ASTM C1609/C1609M measures a first peak load and residual loads at prescribed deflections. The toughness and flexural strength ratio are calculated from the residual loads.

ASTM C1399/1399M uses a notched specimen, and an ARS is calculated from the residual strength at four specified deflections. The ARS represents the load-carrying capacity of the cracked FRC beam, and is suggested by Bantia and Dubey (1999; 2000). The test method recommended by RILEM TC TDF-162 uses a center-point loading (three-point bending) configuration with a pre-cracked specimen. In the RILEM TC TDF-162 bending test, the deformation of the cracked beam can be described by either the deflection or the CMOD.

To obtain full load-deflection curves before and after the crack localization, the flexural tests for the SFRC in this study were conducted in accordance with ASTM C1609/C1609M. Concrete beams of 6 in. × 6 in. × 20 in. were tested by a 20 Kips MTS machine at a displacement rate of 0.05 in./min. The testing stopped when the residual load response reached 10 percent of the maximum load.

TEST RESULTS

Compressive Stress–Strain Curves of the SFRC

As listed in Table 36, 36 specimens with the fiber volume fraction ranging from 0 percent to 3.0 percent were prepared for the compression tests, and the compressive stress–strain curves are obtained. During the test, the SFRC specimens broke silently and remained attached during the test, while the control specimens had explosive failure and always fell into pieces. Figure 58 shows a photo of a failed SFRC specimen after the compression test.



Figure 58. A Failed SFRC Specimen after the Compression Test

Figure 59 through Figure 64 show the stress–strain curves of the SFRC specimens reinforced with the straight steel fibers of different volume fractions. No significant improvement in the compressive strength is observed by adding the straight fibers, but an improvement in post-cracking behavior (residual strength and ductility) is observed in the specimens containing 1.5–3.0 percent straight fibers. The results show that the residual strength and ductility increase with fiber content.

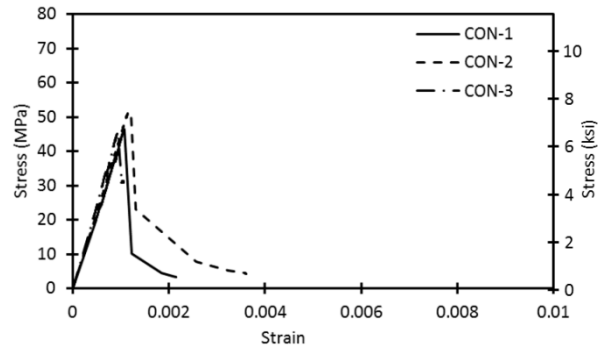


Figure 59. Stress–Strain Curves for Control Specimens under Compression

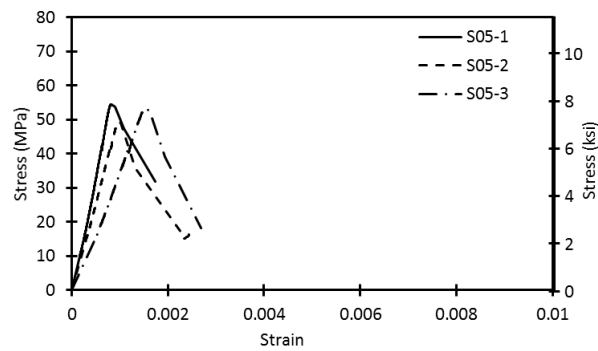


Figure 60. Stress–Strain Curves for the 0.5 Percent Straight SFRCs under Compression

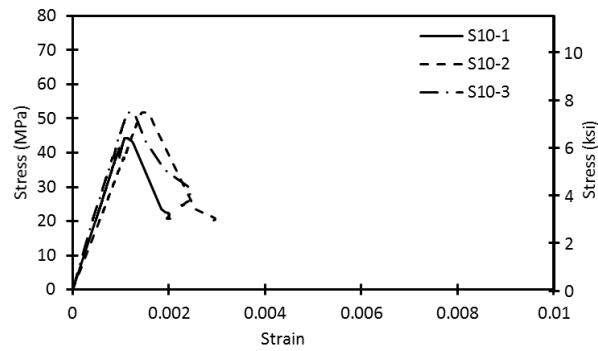


Figure 61. Stress–Strain Curves for the 1.0 Percent Straight SFRCs under Compression

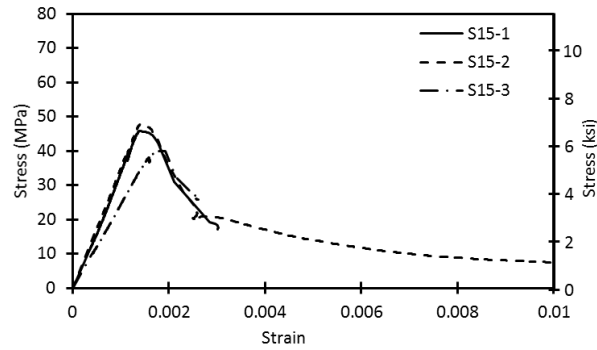


Figure 62. Stress–Strain Curves for the 1.5 Percent Straight SFRCs under Compression

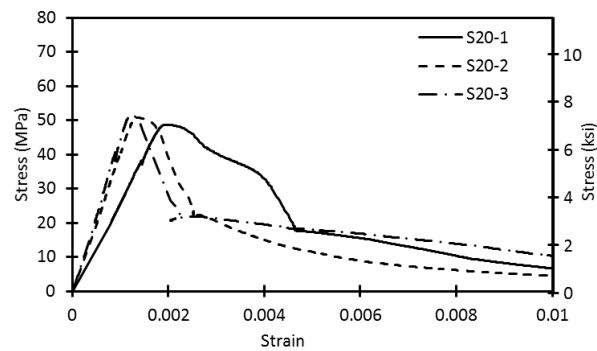


Figure 63. Stress–Strain Curves for the 2.0 Percent Straight SFRCs under Compression

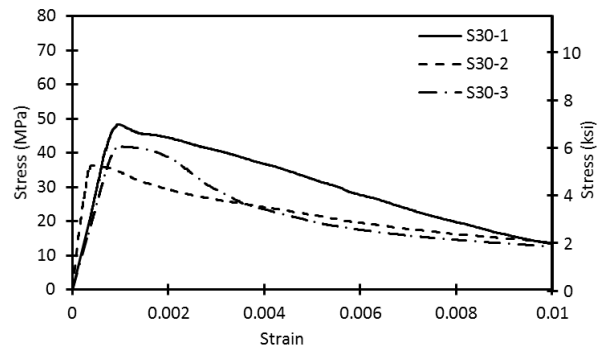


Figure 64. Stress–Strain Curves for the 3.0 Percent Straight SFRCs under Compression

Figure 65 to Figure 70 present the stress–strain curves of the hooked SFRC under compression. Similar to the straight SFRC, adding the hooked fibers up to 2.0 percent does not cause a significant changes in compressive strength. At the higher hooked fiber content (3.0 percent), the compressive strength drops. This is presumed to be the effect of fiber clumping. The specimens containing 2.0 percent and 3.0 percent hooked fibers show a superior post peak behavior. Instead of the abrupt drop of residual

strength, the stress gradually decreases after the first peak stress, where a major crack is developed. When the straight fibers are used, the gradual drop is only observed in the 3.0 percent fiber content.

SH20 specimens were tested to evaluate the effect of the blended fibers (combination of 1.0 percent straight fibers and 1.0 percent hooked fibers). Figure 70 shows the stress–strain curves of SH20 specimens. The post peak behavior of the combined SFRC specimens is in between the straight SFRC and hooked SFRC at the same fiber content.

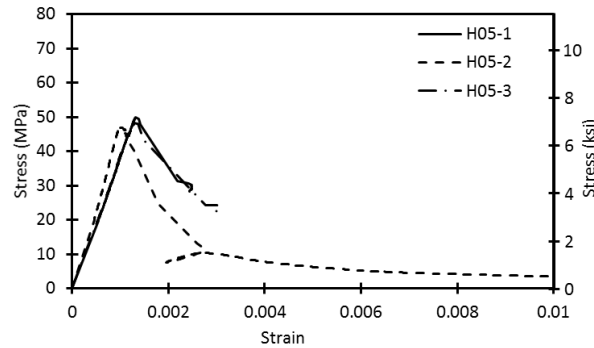


Figure 65. Stress–Strain Curves for the 0.5 Percent Hooked SFRCs under Compression

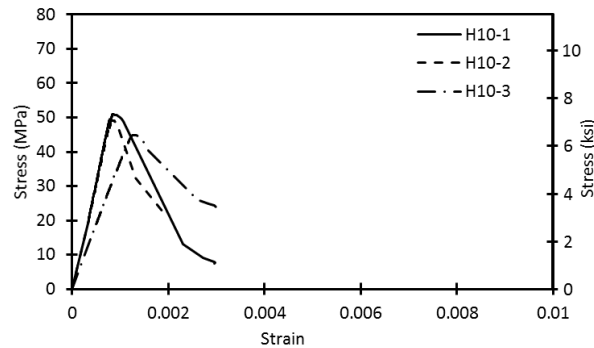


Figure 66. Stress–Strain Curves for the 1.0 Percent Hooked SFRCs under Compression

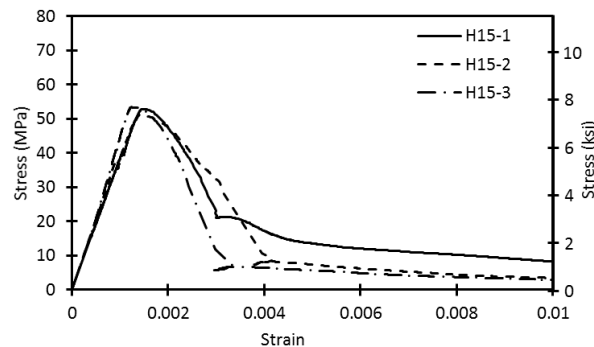


Figure 67. Stress–Strain Curves for the 1.5 Percent Hooked SFRCs under Compression

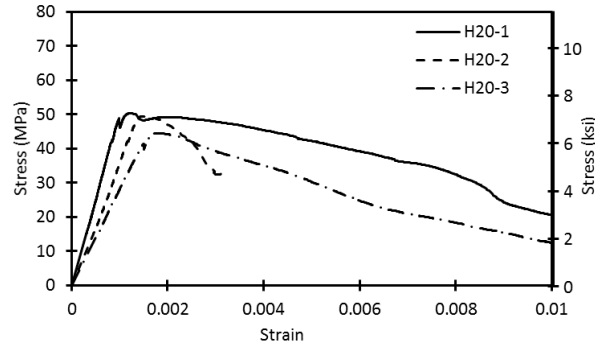


Figure 68. Stress–Strain Curves for the 2.0 Percent Hooked SFRCs under Compression

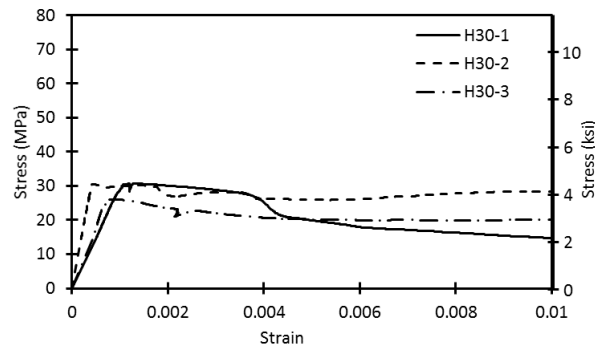


Figure 69. Stress–Strain Curves for the 3.0 Percent Hooked SFRCs under Compression

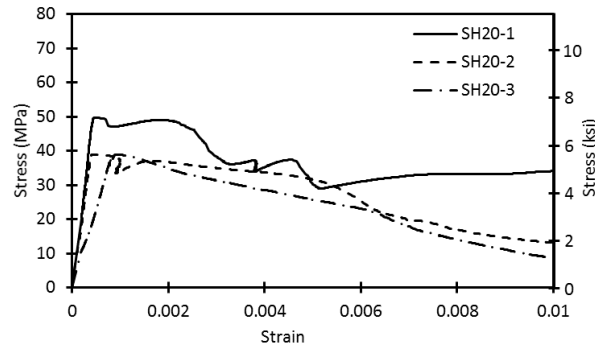


Figure 70. Stress–Strain Curves for the 2.0 Percent Combined SFRCs under Compression

Tensile Stress–Strain Curves of the SFRC

A total of 30 direct tension tests were conducted to obtain the tensile stress–strain curves of the SFRCs. The cases of 3.0 percent fiber content were not included for the tension test because of the poor mixing quality of S30 and H30. Among the tension test results, the data from S05-1 were discarded due to a

failure in epoxy glue. All other specimens failed within the concrete part. Figure 71 shows a failed SFRC specimen during the tension test.

Figure 72 through Figure 76 present the direct tension test results for the straight SFRC. The figures clearly show that the addition of the straight fibers improves tensile properties of concrete, including tensile strength, ductility, and post-cracking residual strength. As shown in Figure 72, the control specimens exhibited a typical brittle fracture: the tensile stress drops to zero right after the peak stress, and the specimens cannot carry any load. However, when the fibers are added, the specimens have residual strength. The specimens containing 1.0–2.0 percent fibers show strain hardening behavior after the proportional limit (around 0.25 ksi), so the peak stresses are higher than the proportional limit. The proportional limit is a stress level at where microcracks are developed, and the peak stress is a stress level at where damage localization occurs. Therefore, the results show that adding 1.0 percent or higher volume fraction of fibers is effective in retarding the damage localization.

Figure 77Error! Reference source not found. through Figure 80Error! Reference source not found. show tensile stress–strain curves of the hooked SFRC with various volume fractions. Overall, the residual strength of the hooked SFRC are higher than the straight SFRC. The strain hardening behavior is observed in some specimens containing fibers of 1.5 percent or higher volume fraction.

Figure 81Error! Reference source not found. shows the stress–strain curves for the specimens containing the combined fibers of 2.0 percent (SH20). The reinforcing effects of the combined fibers are similar to the straight or hooked fibers under tension.



(a) Cracking of SFRC



(b) Pulled Out Fibers

Figure 71. A Failed SFRC Specimen under Tension

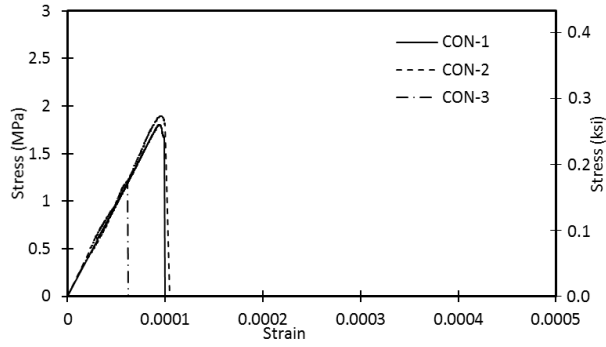


Figure 72. Stress–Strain Curves for the Control Specimens under Tension

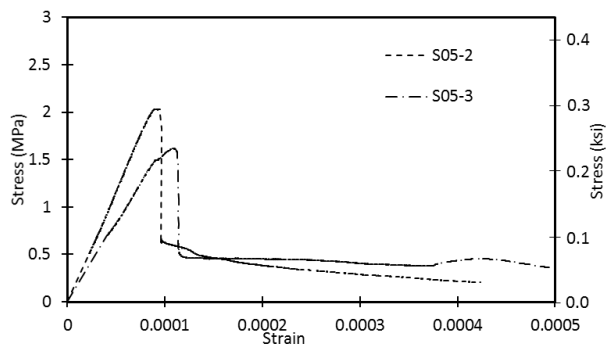


Figure 73. Stress–Strain Curves for the 0.5 Percent Straight SFRCs under Tension

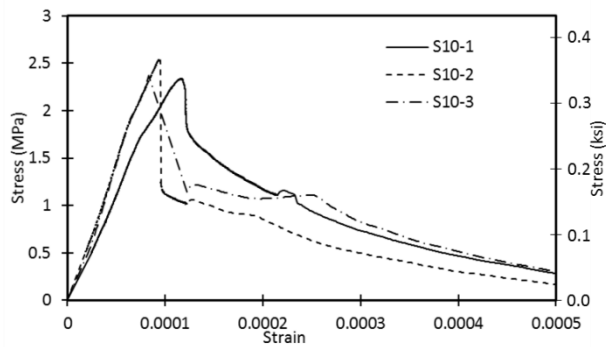


Figure 74. Stress–Strain Curves for the 1.0 Percent Straight SFRCs under Tension

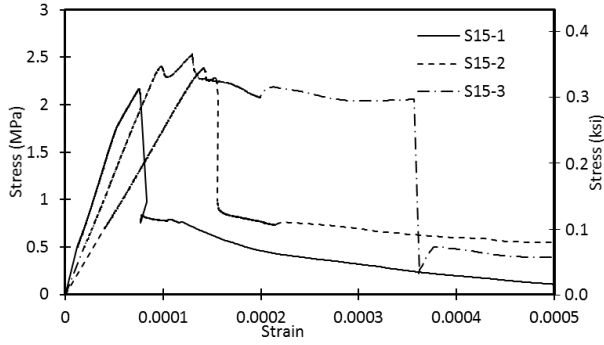


Figure 75. Stress–Strain Curves for the 1.5 Percent Straight SFRCs under Tension

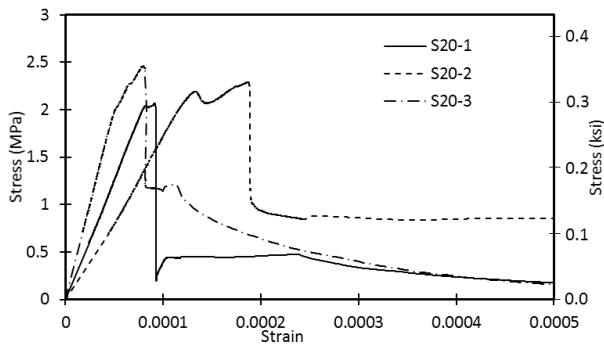


Figure 76. Stress–Strain Curves for the 2.0 Percent Straight SFRCs under Tension

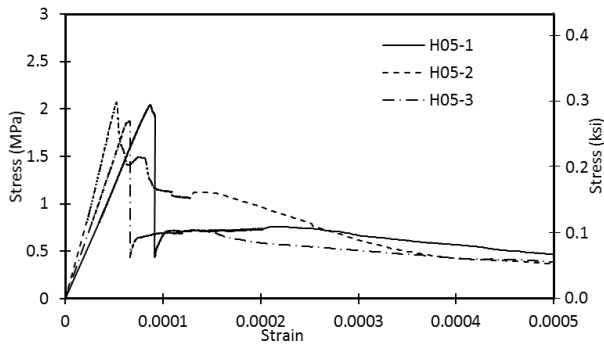


Figure 77. Stress–Strain Curves for the 0.5 Percent Hooked SFRCs under Tension

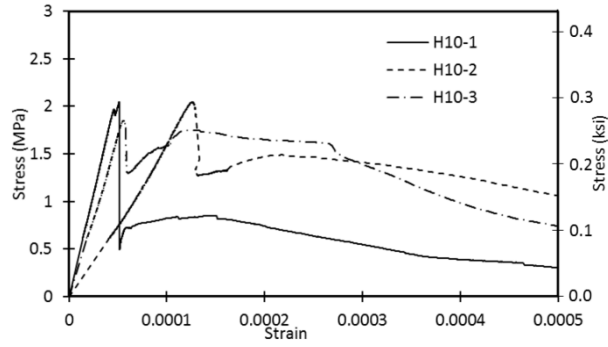


Figure 78. Stress–Strain Curves for the 1.0 Percent Hooked SFRCs under Tension

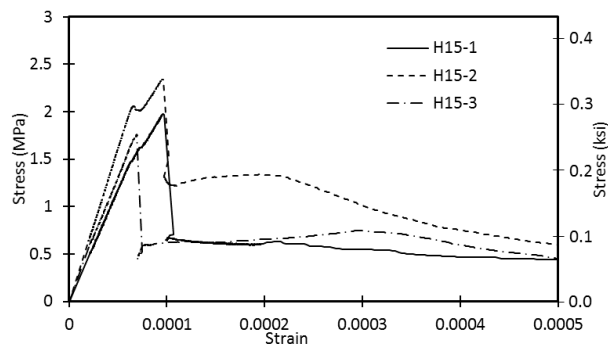


Figure 79. Stress–Strain Curves for the 1.5 Percent Hooked SFRCs under Tension

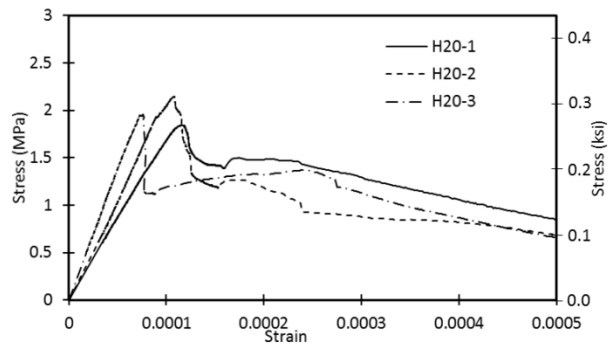


Figure 80. Stress–Strain Curves for the 2.0 Percent Hooked SFRCs under Tension

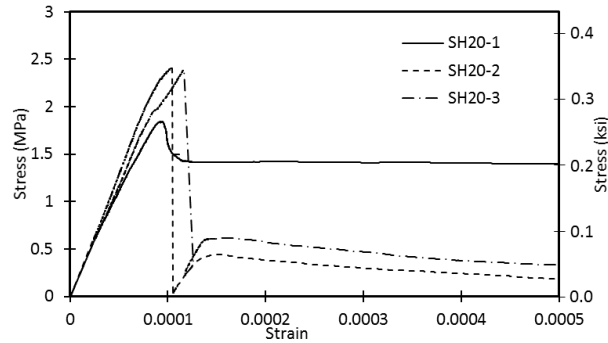


Figure 81. Stress–Strain Curves for the 2.0 Percent Combined SFRCs under Tension

Flexural Load–Deflection Curves of the SFRC

The four-point bending tests were conducted for 48 specimens of the standard dimension (6 in. × 6 in. × 20 in.). Figure 82 is a photo of a cracked flexural specimen showing the fibers between the crack surfaces. Figure 83 shows load-deflection curves of unreinforced specimens. Figure 83 to Figure 88 show the load–deflection curves obtained from the straight SFRC. As indicated in Figure 83, the control specimens show a sudden drop of the load after the peak load, implying a brittle fracture. The flexural responses are changed significantly by adding the straight fibers, and the improvements are: 1) the increase in flexural strength (except for S30), 2) the deflection softening behavior (residual strength) after the peak load, and 3) the increase in ductility. However, a deflection hardening behavior is not observed in the specimens reinforced with the straight fibers.

Figure 89 to Figure 93 plot the load-deflection curves of the hooked SFRCs. As shown in these figures, the reinforcing effect of the hooked fibers is better than the straight fibers. The deflection hardening behavior after the proportional limit is consistently observed from the hooked SFRCs of 1.0 percent, 1.5 percent, 2.0 percent, and 3.0 percent. Correspondingly, the residual strengths of the hooked SFRC specimens are higher than those of the straight SFRC with the same fiber contents. An existence of the deflection hardening behavior is a criterion for an HPRCC because it brings important benefits for structural behavior during failure. The deflection hardening prevents an abrupt failure of material, and the corresponding large deformation gives a warning of structural failure. Figure 94 to Figure 98 **Error! Reference source not found. Error! Reference source not found.** show the load–deflection curves obtained from the combined SFRCs. Similar to the hooked SFRC, the combined fibers caused the deflection hardening behavior when the fiber volume fraction exceeded 1.0 percent. The improvements in the flexural behaviors due to the combined SFRCs are superior to the straight fiber but inferior to the hooked fiber.



Figure 82. A Failed Flexural Specimen

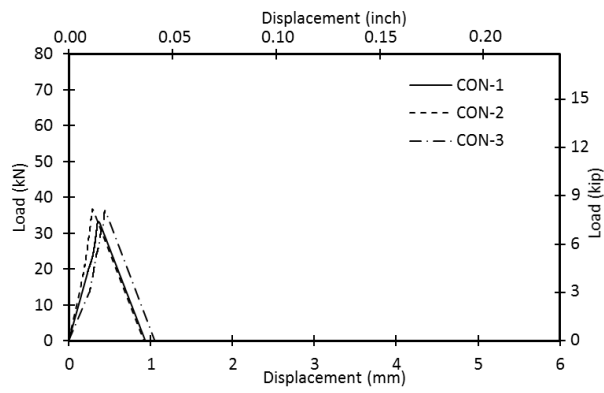


Figure 83. Load-Deflection Curves for the Control Specimens under Bending

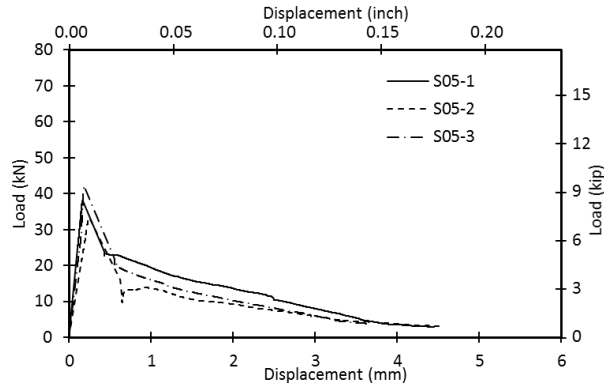


Figure 84. Load–Deflection Curves for the 0.5 Percent Straight SFRCs under Bending

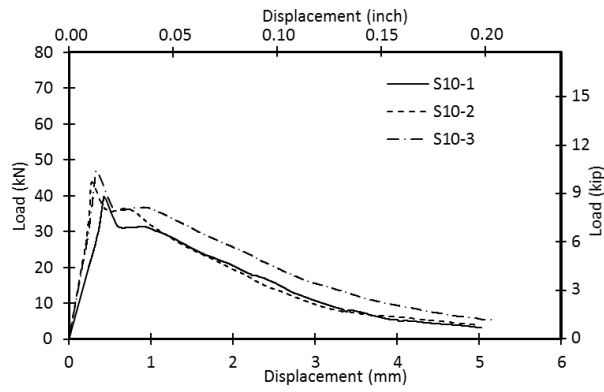


Figure 85. Load–Deflection Curves for the 1.0 Percent Straight SFRCs under Bending

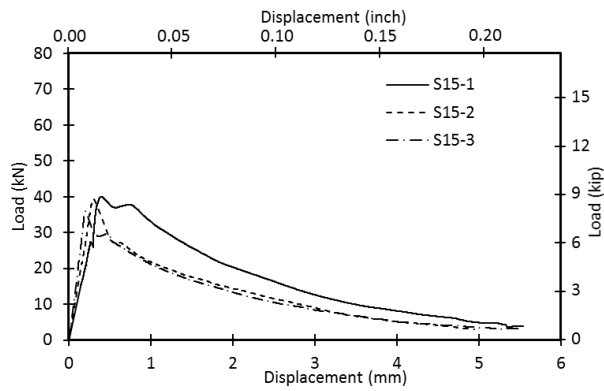


Figure 86. Load–Deflection Curves for the 1.5 Percent Straight SFRCs under Bending

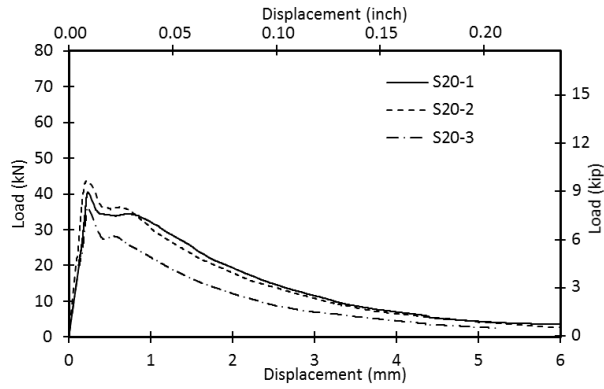


Figure 87. Load–Deflection Curves for the 2.0 Percent Straight SFRCs under Bending

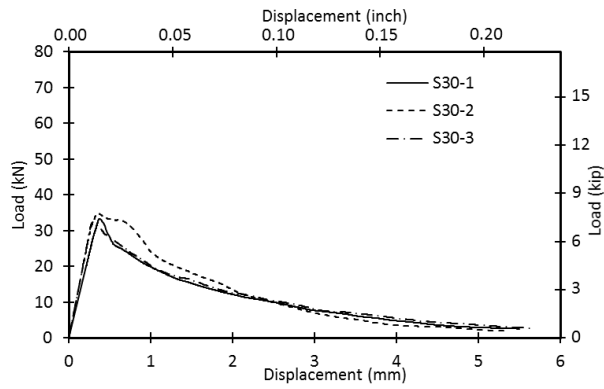


Figure 88. Load–Deflection Curves for the 3.0 Percent Straight SFRCs under Bending

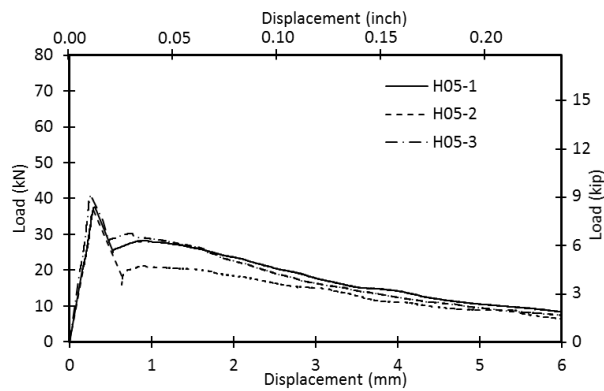


Figure 89. Load–Deflection Curves for the 0.5 Percent Hooked SFRCs under Bending

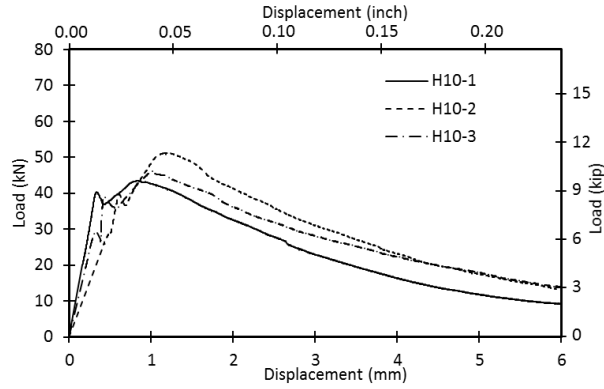


Figure 90. Load–Deflection Curves for the 1.0 Percent Hooked SFRCs under Bending

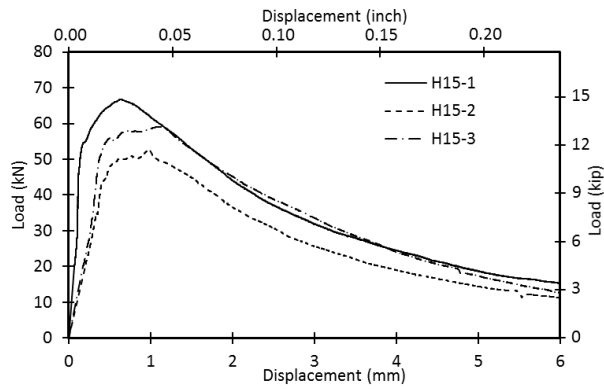


Figure 91. Load–Deflection Curves for the 1.5 Percent Hooked SFRCs under Bending

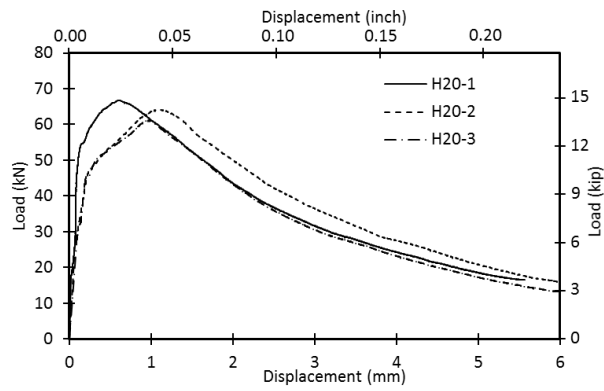


Figure 92. Load–Deflection Curves for the 2.0 Percent Hooked SFRCs under Bending

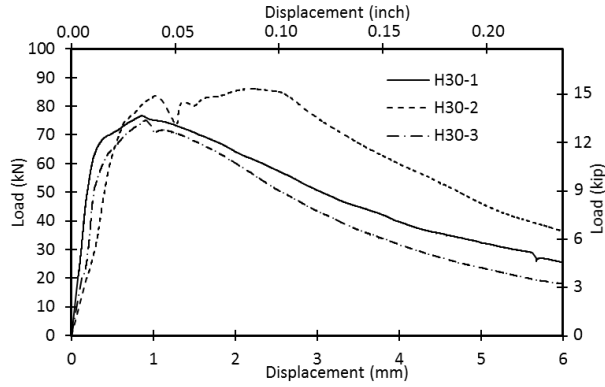


Figure 93. Load–Deflection Curves for the 3.0 Percent Hooked SFRCs under Bending

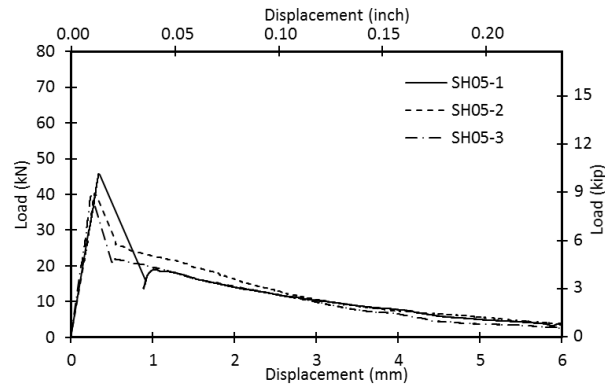


Figure 94. Load–Deflection Curves for the 0.5 Percent Combined SFRCs under Bending

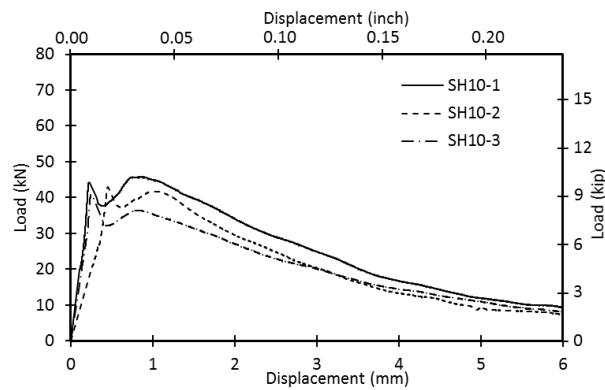


Figure 95. Load–Deflection Curves for the 1.0 Percent Combined SFRCs under Bending

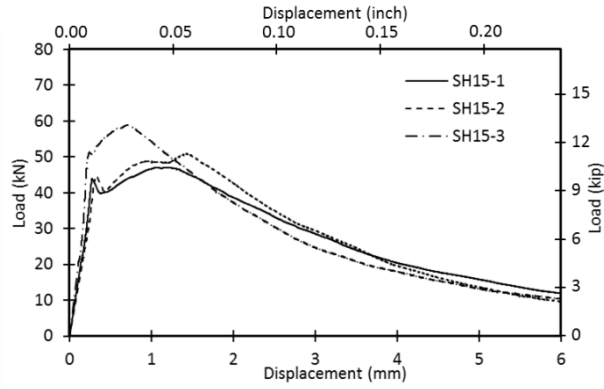


Figure 96. Load–Deflection Curves for the 1.5 Percent Combined SFRCs under Bending

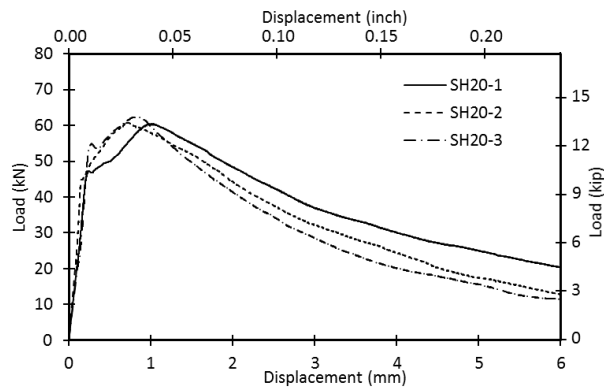


Figure 97. Load–Deflection Curves for the 2.0 Percent Combined SFRCs under Bending

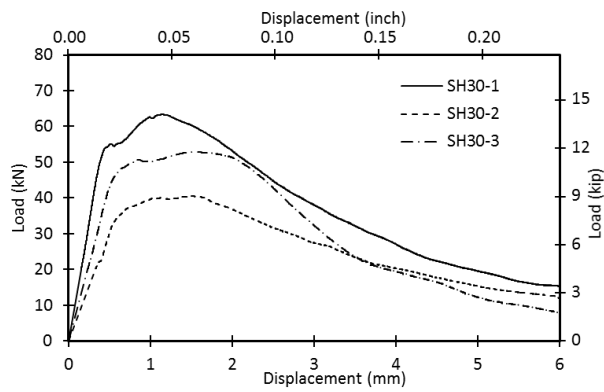


Figure 98. Load–Deflection Curves for the 3.0 Percent Combined SFRCs under Bending

COMPARISONS OF MECHANICAL PARAMETERS

Compressive Behavior

Figure 99 compares the modulus of elasticity in compression and compressive strength of the straight SFRCs at the various volume contents. There exist some fluctuations, but overall, the compressive strength is not significantly affected by adding fibers. The compressive elastic modulus shows some scattering, and has high average value at 3.0 percent fiber content. Figure 100 shows the parameters of the hooked SFRCs. The compressive strength is almost consistent up to 2.0 percent fiber content, and drops at 3.0 percent fiber content. The decrease in the compressive strength at high fiber content (3.0 percent) is caused by the poor mixing condition. The similar level of scattering is observed with the compressive elastic modulus of the hooked SFRC, and the average values do not show specific trend with the increase of fiber content. The specimens with the combined fibers show the increase in the compressive elastic modulus, but the compressive strength is not changed by adding fibers (Figure 101). Overall, it can be concluded that adding steel fibers up to 2.0 percent does not cause a substantial difference in compressive strength, but adding more than 2.0 percent may cause a quality control problem.

The measured compressive elastic moduli of the SFRCs show a high level of scattering by adding fibers. The highest scatter is observed when the fiber volume content is 3.0 percent, while the control specimens have a consistent elastic modulus. It is presumed that the significant differences in the elastic moduli of the SFRCs are caused by the nonuniform distribution of fibers and coarse aggregate. As shown in Figure 56a, the slump values of SFRCs decrease with the increase of fiber content. The high aspect ratio of fibers may cause the entanglement of fibers during the mixing, and may also disturb the uniform distribution of both the fibers and coarse aggregate. Especially, the low unit weight of the SFRCs with 3.0 percent fiber content (Figure 56b) implies that the poor workability due to the fiber clumping causes the increase in air void. The scatter ranges of the compressive elastic moduli are relatively consistent up to 2.0 percent fiber content, which implies that the nonuniform distribution of the fibers and aggregate can be controlled in a specific level. However, the higher scatter in the elastic moduli (Figure 99a and Figure 100a) and lowered unit weight (Figure 56b) of the SFRCs with 3.0 percent fiber content show that the maximum acceptable fiber content should be limited up to 2.0 percent.

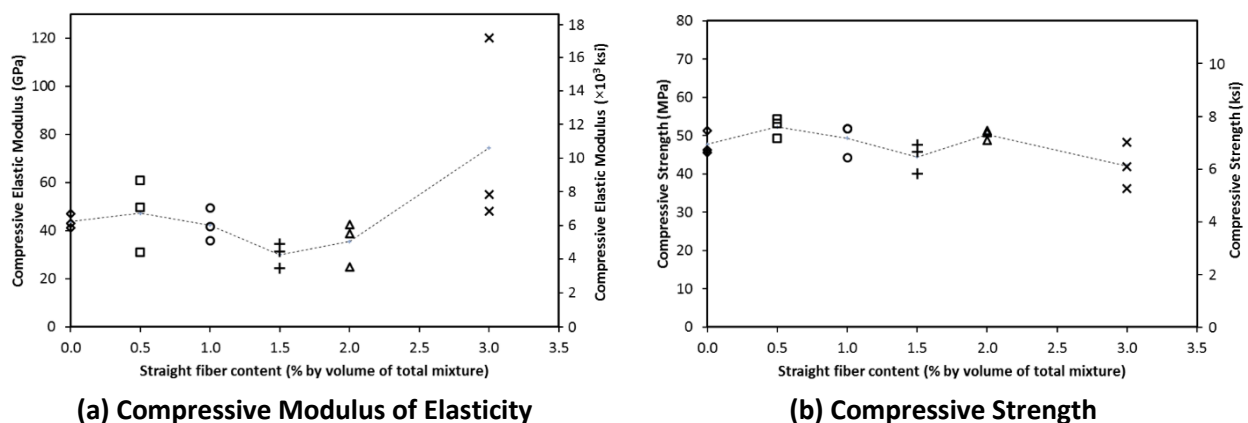
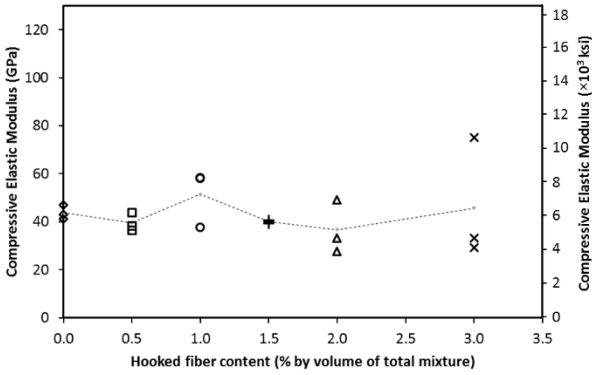
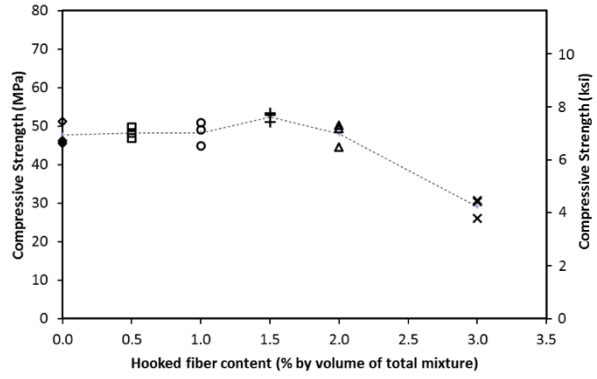


Figure 99. Comparison of Compressive Properties of the Straight SFRCs

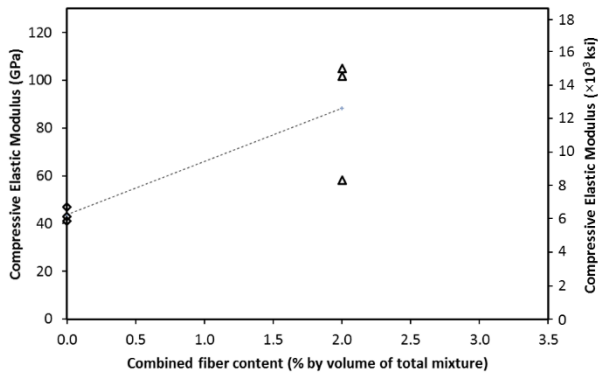


(a) Compressive Modulus of Elasticity

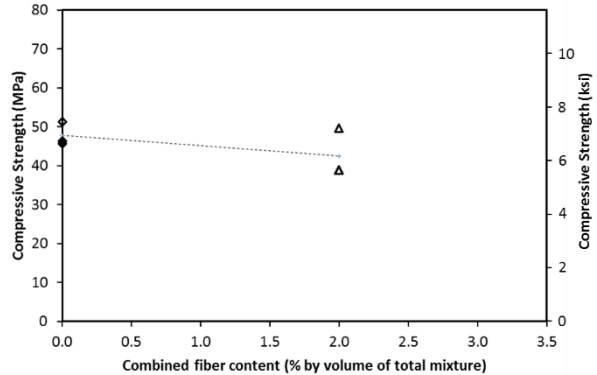


(b) Compressive Strength

Figure 100. Comparison of Compressive Properties of the Hooked SFRCs



(a) Compressive Modulus of Elasticity



(b) Compressive Strength

Figure 101. Comparison of Compressive Properties of the Combined SFRCs

Tensile Behavior

Figure 102 to Figure 104 compare the tensile modulus of elasticity and tensile strength of the SFRCs with various fiber contents. When compared to the control specimens, all the SFRCs have improved tensile strength. The tensile strength of the straight SFRCs increases up to the fiber content of 1.0 percent and then slightly decreases at the fiber contents of 1.5 percent and 2.0 percent, and this is presumed to be the effect of the mixing condition discussed in the earlier section (39–48 percent improvement, Figure 102b). The hooked SFRCs show a consistent improvement in tensile strength ranging from 20 percent to 22 percent (Figure 103b). SH20 shows a highest average tensile strength (352 psi=2.43 MPa, 49 percent improvement; Figure 104b).

The measured tensile elastic moduli (Figure 102a and Figure 103a) have even a higher scatter range than the compressive elastic moduli. The increase in the scatter range of the tension tests can be explained with two reasons: 1) the nonuniform distribution of fibers over the cross section of the specimen influences more in tensile behavior than the compressive behavior, and 2) there exist measurement errors due to the misalignment of tensile specimens because of using one displacement transducer during the tension test. As discussed earlier, the reinforcing effect of adding fibers is significant in the tensile behavior than the compressive behavior, and hence the effect of the nonuniform distribution can

be higher in tensile behavior. Because of the same reason, the scatter range of the tensile strength data is slightly higher than that of the compressive strength data. The scatter due to the measurement set-up was not an issue in compression test because three displacement transducers were used during the compression tests. The misalignment errors can be cancelled each other by averaging the displacements measured by the three displacement transducers (compression tests). However, such setoff does not exist when one displacement transducer is used (tension tests).

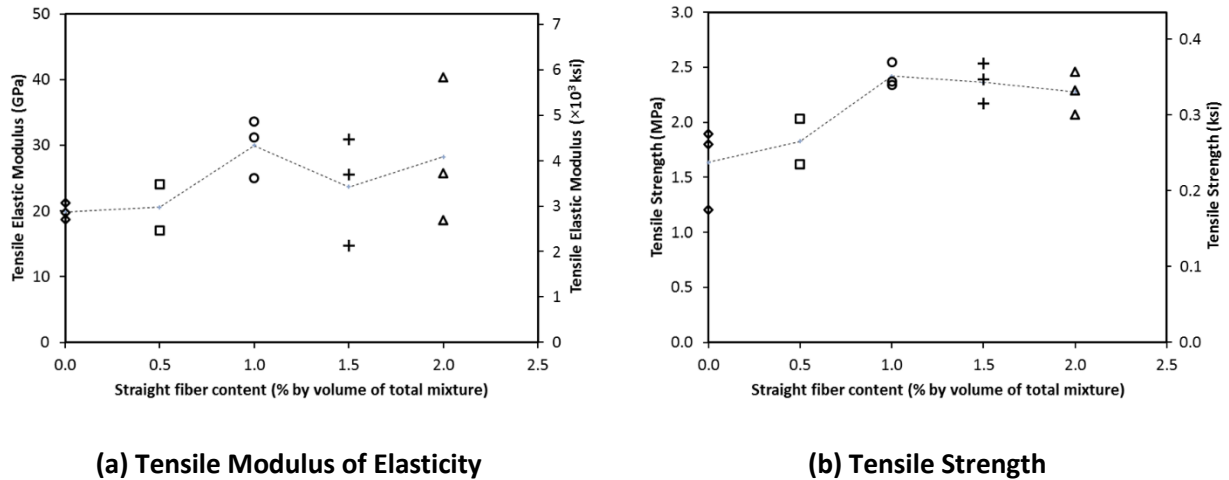


Figure 102. Comparison of Tensile Properties of the Straight SFRCs

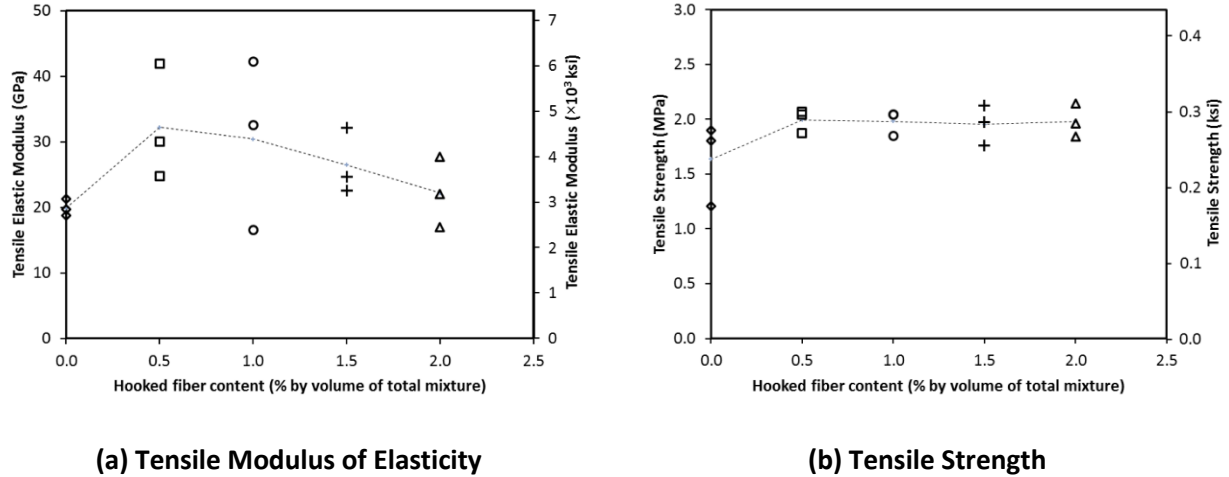
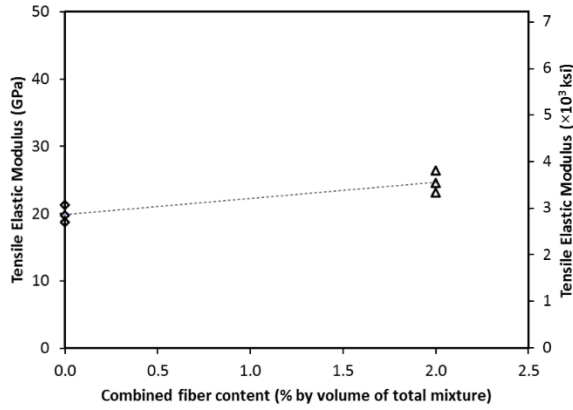
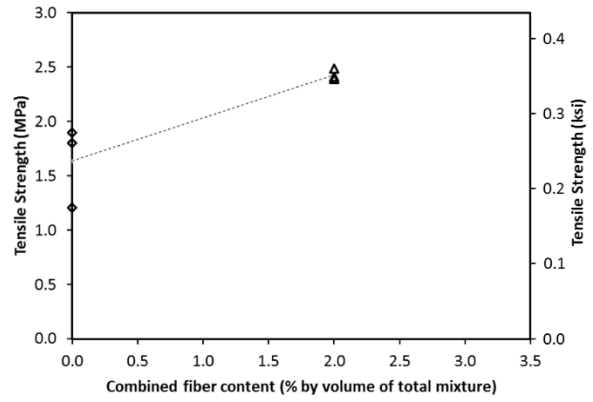


Figure 103. Comparison of Tensile Properties of the Hooked SFRCs



(a) Tensile Modulus of Elasticity



(b) Tensile Strength

Figure 104. Comparison of Tensile Properties of the Combined SFRCs

The primary advantage of the FRC is an improved post-cracking behavior in tension caused by the bridging effect of fibers. To evaluate the post-cracking behavior in tension, the residual strength of the SFRCs are compared in Figure 105 to Figure 107. The tensile residual strength is obtained from the tensile stress–strain curves at the tensile strain of 0.0005. The hooked SFRCs (Figure 106) showed higher residual strengths than the straight or combined SFRCs (Figure 107). The highest ARS at strain of 0.0005 is 106 psi (0.73 MPa) at H20 (2.0 percent hooked fiber), which is 37 percent of the peak tensile strength.

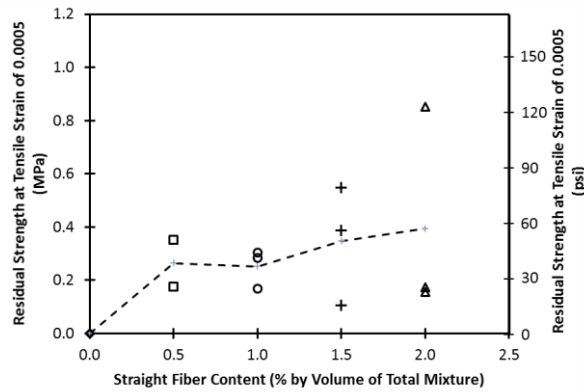


Figure 105. Residual Strength of the Straight SFRCs

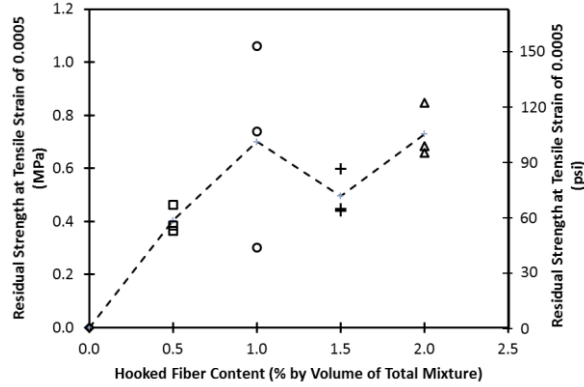


Figure 106. Residual Strength of the Hooked SFRCs

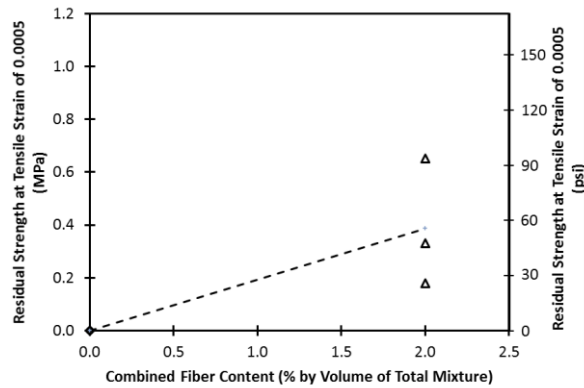
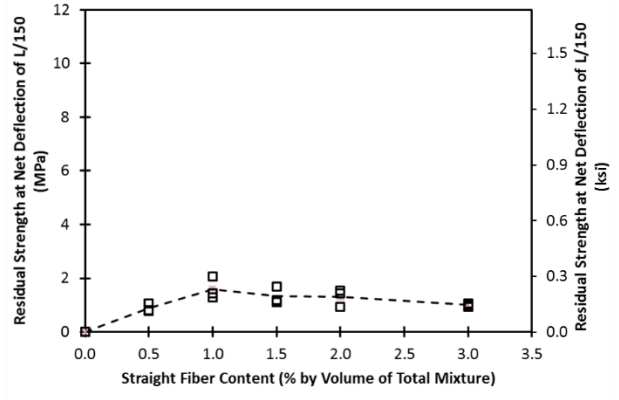
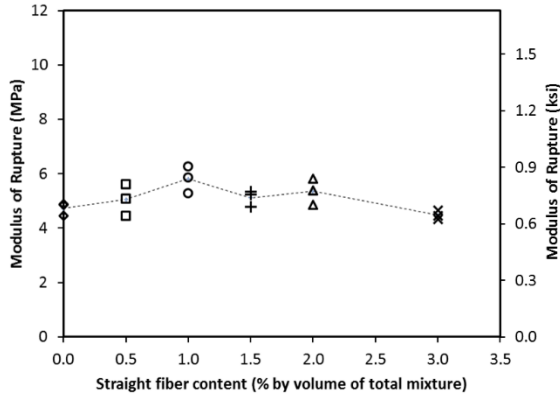


Figure 107. Residual Strength of the Combined SFRCs

Flexural Behavior

Figure 108 to Figure 110 compare MOR and residual strength of the SFRCs obtained from the flexural tests. The residual strengths are obtained when the deflection is 1/150 of the specimen length, L. The results show that the hooked fibers are more efficient in improving the flexural strength (MOR) and the post-cracking behavior (residual strength) than the straight fibers. The highest average MOR of the hooked SFRCs is 1,534 psi (10.6 MPa, 124 percent improvement, H30), while that of the straight SFRCs is 842 psi (5.8 MPa, 23 percent improvement, S10). As expected from the tension test results, the hooked SFRCs show higher residual strengths than the straight SFRCs. The improvements in MOR and residual strength of the combined SFRCs are higher than the straight SFRCs and lower than the hooked SFRCs. Although the H30 case has the highest average MOR and residual strength, adding fibers more than 2.0 percent is not recommended for practical applications because of the workability and quality control issues discussed earlier.

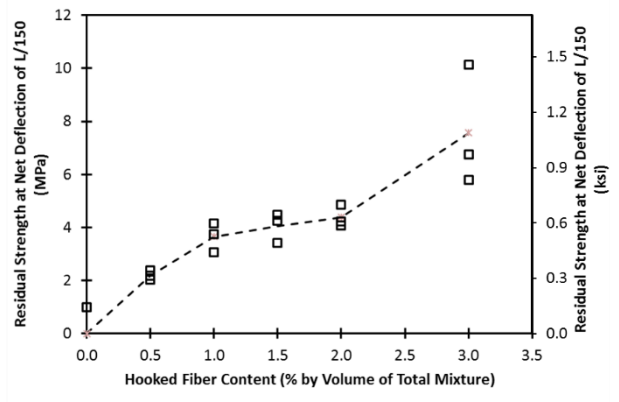
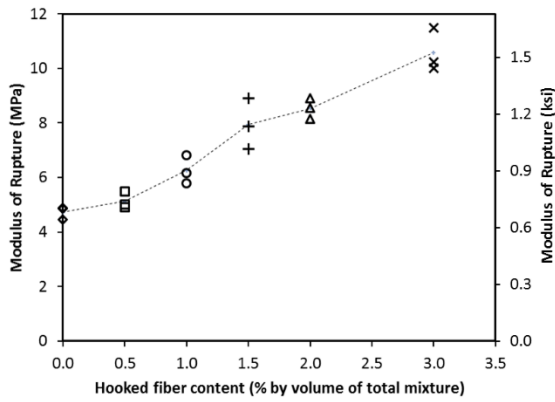
Table 39 lists the average values of three replicates of the mechanical parameters obtained from the material tests.



(a) MOR

(b) Residual Strength

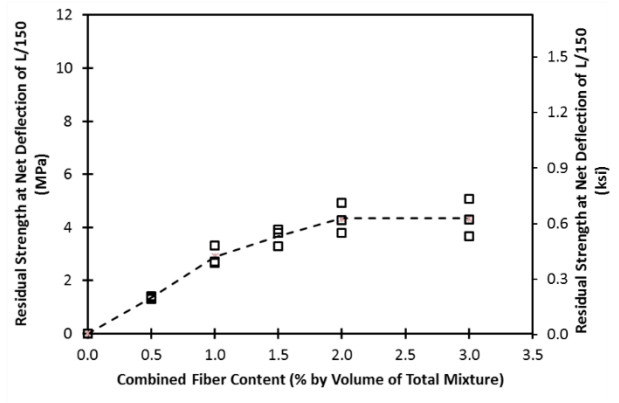
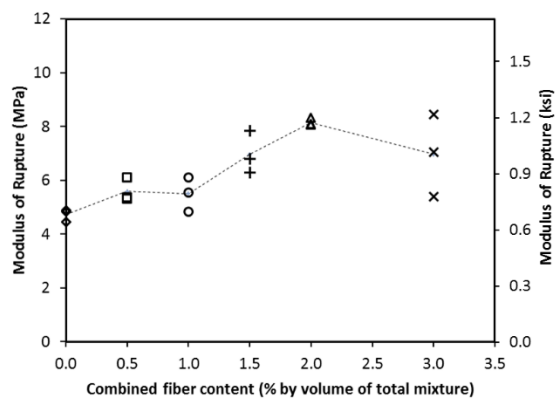
Figure 108. Comparison of Flexural Properties of the Straight SFRCs



(a) MOR

(b) Residual Strength

Figure 109. Comparison of Flexural Properties of the Hooked SFRCs



(a) MOR

(b) Residual Strength

Figure 110. Comparison of Flexural Properties of the Combined SFRCs

Table 39. A Summary of the Mechanical Properties of the SFRCs under Different Loading Conditions

	Compression		Tension			Flexural bending	
	E_c^c (ksi)	f_c' (psi)	E_c^t (ksi)	f_t' (psi)	$f_{0.0005}^t$ (psi)	f_r^f (psi)	f_{150}^f (psi)
CON	6,341	6,924	2,885	237	0.0	686	0
S05	<u>6,841</u>	<u>7,581</u>	2,987	265	38.3	733	129
S10	6,135	7,146	<u>4,350</u>	<u>351</u>	36.6	<u>842</u>	<u>232</u>
S15	4,353	6,446	3,436	343	50.3	742	193
S20	5,137	7,289	4,097	330	<u>57.1</u>	776	189
S30	10,791	6,106	N.A	N.A	N.A	649	146
H05	5,721	7,003	<u>4,673</u>	<u>289</u>	58.6	744	317
H10	<u>7,448</u>	7,002	4,414	287	101.6	907	529
H15	5,802	<u>7,605</u>	3,839	283	71.8	1,151	586
H20	5,319	6,970	3,219	287	<u>105.8</u>	<u>1,238</u>	<u>636</u>
H30	6,636	4,218	N.A	N.A	N.A	1,534	1,096
SH05	N.A	N.A	N.A	N.A	N.A	811	198
SH10	N.A	N.A	N.A	N.A	N.A	798	420
SH15	N.A	N.A	N.A	N.A	N.A	1,011	532
SH20	<u>12,812</u>	<u>6,156</u>	<u>3,581</u>	<u>352</u>	<u>56.2</u>	<u>1,182</u>	<u>629</u>
SH30	N.A	N.A	N.A	N.A	N.A	1,010	630

Note: Highest value among each SFRC type is **bolded** and underscored in the table, the 3.0 percent SFRC is not considered because of mixing and cast problems.

E_c^c : Compressive Modulus of Elasticity

f_c' : Compressive Strength

E_c^t : Tensile Modulus of Elasticity

f_t' : Tensile Strength

$f_{0.0005}^t$: Residual Strength at Tensile Strain of 0.0005

f_r^f : MOR

f_{150}^f : Residual Strength at Net Deflection of L/150

SUMMARY

Aiming to obtain the basic mechanical properties of the SFRCs, a series of materials tests were conducted for a total of 114 specimens including 36 compression, 30 tension, and 48 flexural tests. The straight, hooked, and blending of those fibers were added with the various volume contents ranging from 0.0 to 3.0 percent. Following is the summary of the material test results:

- The compressive behavior of concrete is not significantly influenced by adding the steel fibers up to 2.0 percent. Adding 3.0 percent fibers by volume causes a decrease in the compressive strength due to the poor workability and fiber clumping.
- The strength and residual strength of concrete under tension are remarkably improved by adding the steel fibers. The improvements in tensile strength of the hooked SFRCs are lower than that of the straight SFRCs, but the residual strength of the hooked SFRCs are higher than that of the straight SFRCs.
- The flexural responses of the SFRCs vary with the fiber types. The MOR of the hooked SFRCs significantly increases with the increase of the fiber content, but the improvements in MOR of

the straight SFRCs are not so significant. The improvement in the residual strength is substantial in all the SFRCs resulting in the improved ductility. Moreover the hooked SFRCs show the deflection hardening when the fiber content is equal to or higher than 1.0 percent. The combined SFRCs show a similar trend to the hooked SFRCs.

- Adding too much fibers causes workability issues in mixing and compacting of concrete. The straight fibers are harder to mix than the hooked fibers. The unit weight measurements and slump test results indicate that a fiber content more than 2.0 percent causes a degradation of the concrete quality. This was confirmed by the decreased compressive strength of the SFRCs containing 3.0 percent fibers by volume. Considering the material test results and the observations during the mixing, adding 1.5–2.0 percent of the hooked fibers is recommended for practical applications.
- A wide scatter in the measured elastic moduli is observed in tension and compression tests. The scattering range is higher in tension tests, which use one displacement transducer, due to the misalignment of the specimens than compression tests that use three displacement transducers. The wide scatter in the elastic moduli implies that the mixing of fibers cause a nonuniform distribution of fibers and coarse aggregate. The scatter can be mitigated in larger size members, but an extra care (extended mixing time and compaction) will be needed to improve the uniformity of the fiber-coarse aggregate dispersion. The errors due to the specimen misalignment can be minimized by using two or three displacement transducers around the specimen.
- The good dispersion of fibers in concrete mixtures containing coarse aggregate is one of the topics that requires further investigations. Since most of recent researches for SFRC have focused on high or ultra-high strength FRCs that do not include coarse aggregate, the interaction between fibers and coarse aggregate during mixing has not been actively investigated, yet. The factors of consideration are aggregate gradation, fiber type and aspect ratio, mixing method, and compaction method. The future investigations for the fiber dispersion require a method of measuring the fiber dispersion and a quantified parameter representing the dispersion of fibers.

CHAPTER 6. SLAB STRIP TEST PROGRAM

INTRODUCTION

This chapter summarizes an experimental test program to investigate the behavior of simply supported slab strips to four point bending. Two series of slab strips were tested. The objective of the first was to validate the findings of the case studies and to support the design of the full-scale bridge deck investigated in this research project. The second series was constructed simultaneously with the bridge deck in Chapter 7 to characterize one-way bending response and to compare the performance of SFRC slab strips to slab strips constructed with PC.

First, an overview of the test matrix for both series, is presented. This is followed by summaries of construction and material properties. The results of the tests are presented first as a discussion of damage, followed by analysis of load-deflection behavior. The chapter completes with a discussion of the impact of the results, including a comparison to case studies.

DESIGN OF TEST MATRIX

The geometry and conventional steel reinforcement of the slab strip specimens were chosen to capture the typical reinforced concrete bridge deck design currently used by ADOT. Different depths and percentages of steel reinforcement were investigated to determine the most efficient use of SFRC with conventional steel reinforcement.

A benchmark slab strip with a 6 ft (1829 mm) span was designed as the basis for the experimental test program. This span was chosen to match the girder spacing of the full-scale deck test and is consistent with the smallest spacing in standard ADOT bridge designs. The benchmark slab-strip width is 18 in. to accommodate multiple spacings of steel reinforcement. The minimum deck depth required by ADOT for 6 ft (1829 mm) girder spacing is 8 in. (203 mm). This depth includes a 0.5 in. (12.7 mm) thick wearing surface that is excluded in strength and service analysis. The benchmark slab strip has dimensions 7.5 in. \times 18 in. \times 8 ft long (190.5 mm \times 457 mm \times 2438 mm) (Figure 111). An additional depth, 9 in. (229 mm), is also investigated to demonstrate the effect of SFRC and conventional steel reinforcement ratios in relation to the deck thickness. The deeper section corresponds to the minimum thickness for bridges with girder spacing of 11.5 ft (3505 mm).



Figure 111. Dimensions of Reference Slab-Strip Specimen

Design of Conventional Bridge Decks

The design of conventionally reinforced concrete bridge decks is typically controlled by the service limit state. The service limit state uses the allowable stress design and a maximum allowable tensile stress of

24 ksi (165 Mpa) in the conventional steel. The service condition is assumed to occur after the cross-section has cracked and the concrete does not provide any tension capacity; elastic response is assumed. The service state demand is given by:

$$M_{Service} = 1.0(M_{DC} + M_{DW}) + 1.0(M_{LL+IM}) \quad (9)$$

Where $M_{Service}$ is the design moment at the service limit state, M_{DC} is the moment demand due to both structural and nonstructural components, M_{DW} is the moment demand due to the wearing surface, and M_{LL+IM} is the moment demand due to vehicular loads including impact. Stress in the steel at this demand are shown in Figure 112 and calculated as:

$$f_s = \frac{M_{service}}{A_s j d} \quad (10)$$

$$\rho = \frac{A_s}{b d} \quad (11)$$

$$n = \frac{E_s}{E_c} \quad (12)$$

$$k = \sqrt{(n\rho)^2 + 2n\rho} - n\rho \quad (13)$$

$$j = 1 - \frac{k}{3} \quad (14)$$

Where ρ is the ratio of steel reinforcement area to concrete area; A_s is the area of steel reinforcement; b is the width of concrete beam; d is the depth of bottom layer of steel reinforcement; n is the ratio of steel and concrete modulus of elasticity; k is the ratio of neutral axis depth to depth; j is the ratio of moment arm between resultant forces to depth; f_s is the stress in steel reinforcement at service conditions; and $M_{service}$ is the design moment at the service limit state.

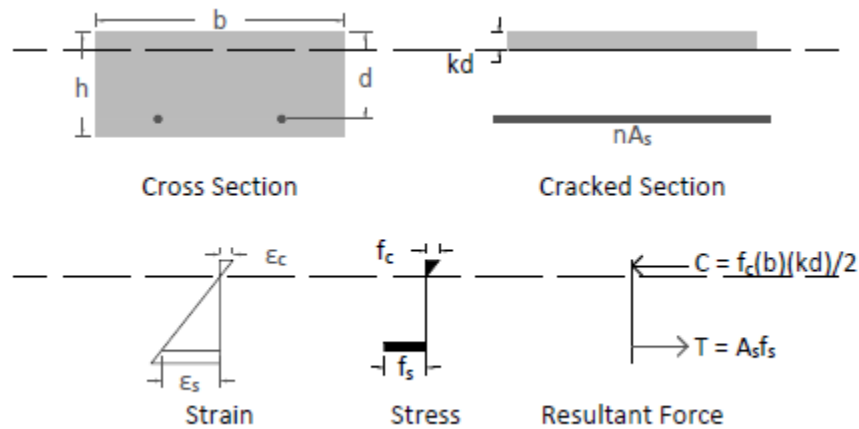


Figure 112. Service State Analysis – Elastic Sections

After the bridge deck has been designed for the service limit state, the ultimate limit state must be checked. The resultant forces and moment capacity of the section are shown in Figure 113 and calculated as:

$$M_{Strength} = 1.25(M_{DC}) + 1.50(M_{DW}) + 1.75(M_{LL+IM}) \quad (15)$$

$$a = \frac{A_s f_y}{0.85 f'_c b} \quad (16)$$

$$M_n = A_s f_y \left(d - \frac{a}{2} \right) \quad (17)$$

Where a is the depth of the compression stress block used for design; and M_n is the nominal moment capacity of the cross-section.

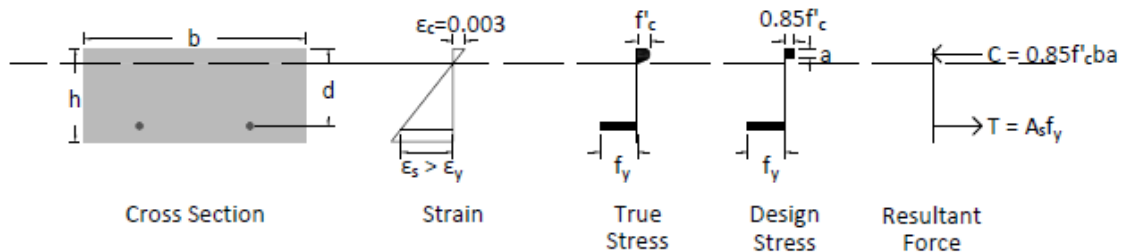


Figure 113. Ultimate State Analysis

The moment demands are determined in accordance with the ADOT Bridge Design Guidelines (2011) and Table A4-1 of AASHTO LRFD Bridge Design Specifications (2014). These demands were used to select the reinforcement provided in Table 40. These designs serve as benchmarks for the development of the test matrix.

Table 40. Steel Area Required to Meet ADOT Limit States

Limit State	Positive		Negative	
	Steel Layout	Steel Ratio, ρ (%)	Steel Layout	Steel Ratio, ρ (%)
Service	#5 @ 8 in.	0.6	#5 @ 6.5 in.	0.76
Strength	#5 @ 11 in.	0.41	#5 @ 10 in.	0.49

Steel Fiber Dosage

Two design philosophies were used for the determination of the volume of fibers used in the experimental program. The first philosophy is to achieve the largest gain in strength and ductility due to the fibers. The second philosophy is to achieve a design that satisfies both the service and strength limit states while using the amount of traditional steel reinforcement required for the strength design. Selection of fiber volume are based on the findings of Chapter 5, with 2.0 percent used for the first philosophy and 0.5 percent used for the second.

Test Matrix

The experimental test was conducted on two series of slab strips, for a total of 18 SFRC slab strips. The first series, indicated by an 's' at the beginning of the name, investigated the impact of percentage of steel reinforcement, steel location, and slab depth. The second series, indicated by a 'd' at the beginning of the name, were built at the same time as the bridge deck specimen to provide baseline strengths for one-way bending. A naming scheme, shown in Figure 114, was developed to easily identify the characteristics of each slab strip. The name consists of the depth (75 = 7.5 in.; 90 = 9.0 in), fiber volume (00 = no fiber; 05 = 0.5 percent; 10 = 1.0 percent), and location (btm = bottom; ctr = center), number (2 or 3), and size of steel reinforcement (3 = #3; 4 = #4; 5 = #5). Table 41 presents the full test matrix.

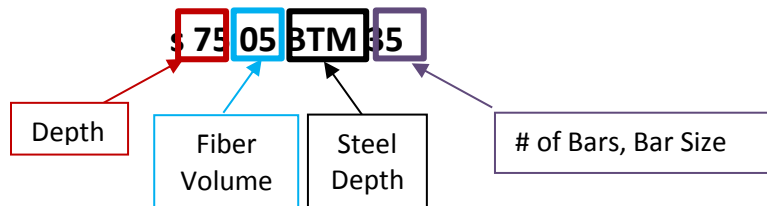


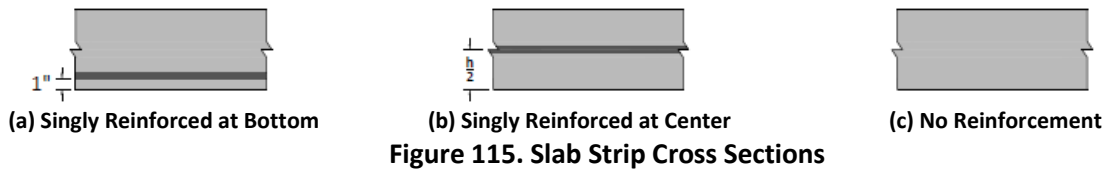
Figure 114. Naming Scheme. The Letter 's' Indicates Test Series 1, and the Letter 'd' Indicates Test Series 2

In the s-series, two slab strips had the amount of conventional steel reinforcement chosen to represent the service (s7505BTM35) and strength (s7505BTM25) limit states. The remaining 12 slab strips in the first series varied to investigate the benefits of SFRC. Based on the results of the case study analysis, adding steel fibers increased the moment capacity of the reinforced concrete section, but also reduced the nominal curvature. Decreasing the area of steel reinforcement with SFRC increased the curvature to the nominal curvature and capacity of PC. Therefore, the location and percentages of steel reinforcement is varied (Figure 115) to investigate the effectiveness of the SFRC on the strength, ductility, and crack management of the slab-strip.

In the d-series, two of the beams (d7505BTM24 and d7500BTM24) have the same steel ratio as the transverse direction steel in the full-scale bridge deck test. Slab strip d7500BTM24 was cast alongside the bridge deck support beams with PC to provide a direct comparison between the strength and behavior of equivalent beams with plain and SFRC reinforcement. Two additional specimens without conventional steel reinforcement were cast to provide a direct comparison between of the SFRC with the first series. Specimen d9005N0S00 was cast to supplement the data not recorded by the data acquisition (DAQ) unit during the s-series test of s9005N0S00.

Table 41. Test Matrix slab strip specimens

Specimen	Depth, in.	Concrete		Steel		
		Mix ID	Fiber Volume (%)	Bars	Location	ρ (%)
s7505BTM35	7.5	M2	0.5	3-#5	Bottom	0.86
s7505BTM25	7.5	M2	0.5	2-#5	Bottom	0.57
s7505BTM24	7.5	M2	0.5	2-#4	Bottom	0.37
s7505BTM23	7.5	M2	0.5	2-#3	Bottom	0.21
s7505CTR35	7.5	M2	0.5	3-#5	Center	0.86
s7505CTR25	7.5	M2	0.5	2-#5	Center	0.57
s7505NOS00	-	M2	0.5	-	-	-
s7520NOS00	-	M1	2.0	-	-	-
s9005BTM35	9	M2	0.5	3-#5	Bottom	0.69
s9005BTM25	9	M2	0.5	2-#5	Bottom	0.46
s9005BTM24	9	M2	0.5	2-#4	Bottom	0.30
s9005BTM23	9	M2	0.5	2-#3	Bottom	0.16
s9005NOS00	9	M2	0.5	-	-	-
s9020NOS00	9	M1	2.0	-	-	-
d7500BTM24	7.5	M3	0.5	2-#4	Bottom	0.57
d7505BTM24	7.5	M4	-	2-#4	Bottom	0.57
d750NOS00	7.5	M3	0.5	-		
d900NOS00	9	M3	0.5	-		



SPECIMEN CASTING

The method of adding the steel fiber to the concrete matrix can significantly affect the workability of the fresh mix. According to the fiber manufacturer, Bekaert, the fibers may either be introduced with the sand and aggregates or into the fresh mixed concrete. Additionally, Bekaert recommends adding the fibers at a continuous rate not to exceed 40 kg/min. Due to restrictions at the ready-mix concrete plant, the steel fibers were added to the fresh mix in accordance with the manufacturer’s recommendations.

Despite efforts in the concrete mix proportions and procedures, issues with the SFRC workability were encountered. As a result, the 14 slab strip specimens in the s-series were cast over two different days

with two different fiber volumes. Details of each is presented in the following sections. Construction of the d-series were done similar to Day 2 of the s-series and thus are not discussed here.

First Cast

At 2.0 percent volume of steel fibers, the workability of the fresh concrete mix was severely reduced. The fresh concrete mix without steel fibers had a slump of approximately 7.5 in. and was measured immediately after the concrete was batched into the truck. After measuring the slump, the fibers were added directly into the concrete truck at the batching plant. The fibers were allowed to mix into the concrete matrix during the transport time to the laboratory, approximately 20 minutes away. Additional water was added to the concrete truck after it arrived to the laboratory elevating the water to cement ratio to 0.48. The concrete was allowed to mix at charging speed for an additional 5 minutes prior to measuring the slump again. Once the fibers were added, the slump was reduced to 0 in. (Figure 116). There was significant clumping of the steel fibers and coarse aggregate (Figure 117). Placement of the concrete required significant amount of internal and external vibration to consolidate the mix and an exceedingly large effort to finish the surface.



Figure 116. 2.0 percent SFRC Lack of



Figure 117. Significant Clumping in SFRC

Second Cast

The fiber dosage rate was reduced to 0.5 percent by volume for the second cast. The percentage was chosen to ensure adequate workability of the SFRC while still providing an improved structural response. The steel fibers were added by a graduate student on-site of the experiment (Figure 118). This procedure was chosen to ensure a slow and consistent addition of steel fibers to the fresh concrete mix and reduce the amount of time between addition of steel fibers and concrete placement:

1. Revolution rate was increased to charging speed.
2. Steel fibers were added at a rate of approximately 24 kg/min.
3. Addition of steel fibers required a total of 5 minutes for 4 yd³ of concrete.
4. Revolution rate of truck was decreased to mixing speed for 5 minutes.

The steel fibers were evenly and randomly distributed using the specified method. The slump of the fresh concrete mix without steel fibers was 9 in. The addition of steel fibers reduced the slump to 7 in. SFRC was placed directly from the concrete truck into the slab strip forms to avoid any flow issues related to the concrete hopper used in first casting attempt (Figure 120). The second cast yielded the remaining 12 slab strips and accompanying cylinders and prisms required for material testing (ASTM C1609, ASTM C39, and ASTM C469) (Figure 121 and Figure 122).



Figure 118. Adding Steel Fibers to Concrete Truck



Figure 119. Significant Slump of Fresh Mix without Steel Fibers



Figure 120. Placing Concrete Directly into Forms



Figure 121. Five of 12 Completed SFRC Slab Strips



Figure 122. Casts for ASTM Materials Tests on Way to Curing Room

MATERIAL PROPERTIES

TxDOT Class S concrete, conventional steel reinforcement with a yield strength of 60 ksi, and Dramix® 3D hooked end fibers were used to design the slab strip specimens. The specified concrete has a minimum compressive strength of 4000 psi.

Steel Fiber Material Properties

Hooked-end steel fiber manufactured by Baekert was used for SFRC. The fiber has a length of 35 mm and a diameter of 0.55 mm. The aspect ratio, ratio of length to the diameter, is 65. The fiber has a tensile strength of 1.345 N/mm² and modulus of elasticity of 210 N/mm².

Concrete Material Properties

Concrete used in the experimental program was provided by a local ready mix concrete plant. The concrete was designed by the supplier to satisfy the requirements for a Class S TxDOT concrete mixture. TxDOT requires Class S concrete to be used in concrete bridge slabs. Table 42 demonstrates the TxDOT and ADOT requirements for concrete used in bridge decks. The lack of workability is a primary concern for SFRC. Accordingly, a high range water reducer, or superplasticizer, was incorporated into the mix design.

Table 42. TxDOT and ADOT Mix Requirements for Concrete Bridge Decks

	TxDOT	ADOT
Compressive Strength, f'c (psi)	4000	4500
Maximum Water:Cement	0.45	0.5
Fine Aggregate:Cement	N.A.	N.A.
Coarse Aggregate:Cement	N.A.	N.A.
Coarse Aggregate Size (in.)	0.75-1.75	N.A. ¹
Allowable Cement Types	N.A.	II, III, V
Max Cementitious Material (lb/yd³)	700	564-752
Slump (in.)	5.5	- ²

¹ "Shall be chosen by the contractor and approved by the Engineer and shall conform to the size designation and grading requirements of AASHTO M 43. In choosing the size designation, the maximum size of coarse aggregate shall not be larger than 1/5 of the narrowest dimension between sides of adjacent forms, or 2/3 of the minimum clear spacing between reinforcing bars, or 1/3 the depth of the slab, whichever is least."

² "The proposed slump shall be chosen by the contractor. Concrete at the proposed slump shall be sufficiently able to allow proper placement without harmful segregation, bleeding, or incomplete consolidation." (ADOT 2008)

Standard tests for compressive (ASTM C39), tensile, and flexural (ASTM C1609) strengths, referenced in Section 3A, were conducted 28 days after the initial casting of the specimens. Additional compressive tests were conducted at 1, 7, and 14 days after the initial casting of the specimens. A total of three specimens were cast for each test. Specimens were prepared in accordance with ASTM C192. The results of these tests are discussed in the following sections.

Compressive Strength

Concrete cylinders 6 by 12 in. (152 by 305 mm) were used for compression tests. In addition to the cylinders cast for compression tests, three 4 by 8 in. (102 by 203 mm) cylinders were cast on each casting date to determine the modulus of elasticity for the SFRC in accordance with ASTM C469M. Figure 123 and Table 43 provide the compressive test results for the concrete mix.

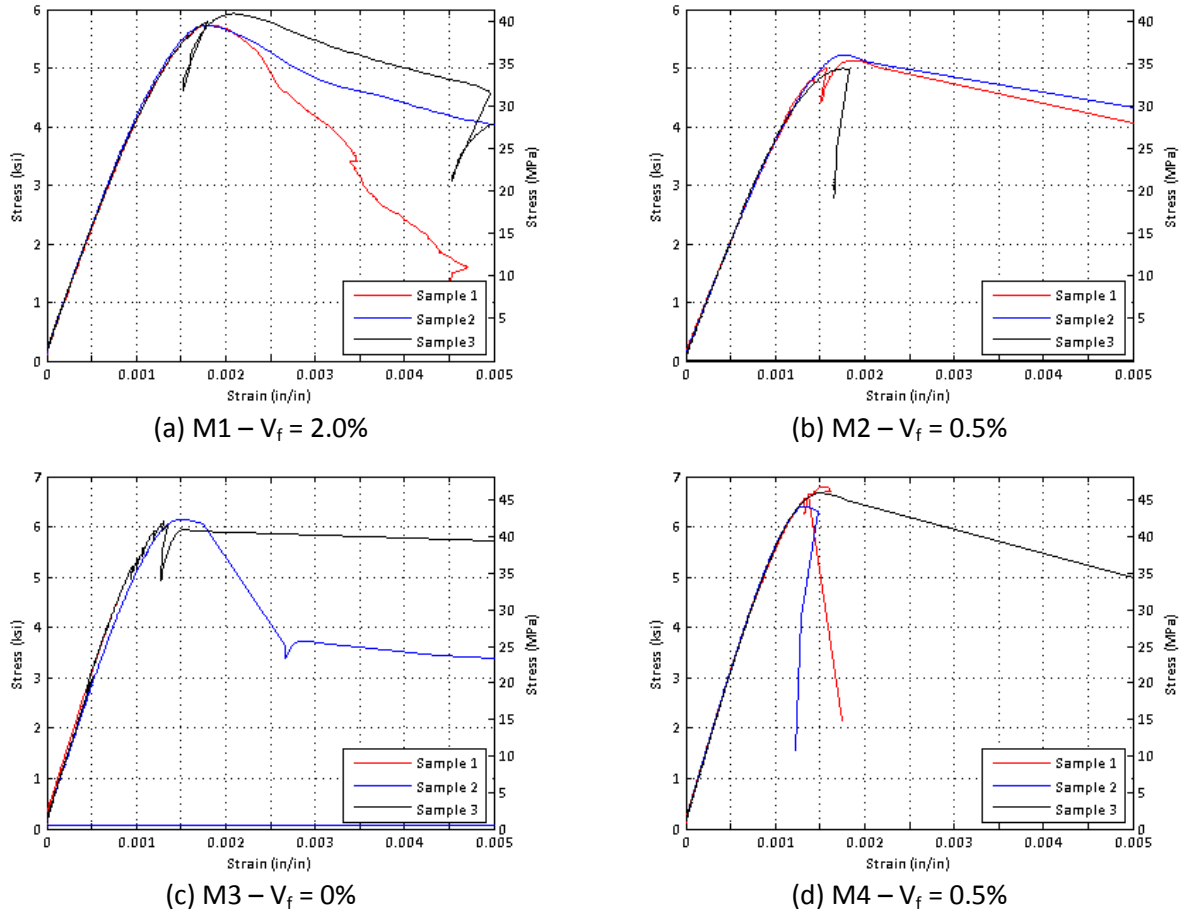


Figure 123. Stress-Strain Curves from ASTM C469

Table 43. Compressive Strength and Modulus of Elasticity for All Mixes Used

Mix ID	Property	Sample 1	Sample 2	Sample 3	Average
M1	E_c (ksi)	4122	4223	4165	4170
	f'_c (ksi)	5.73	5.73	5.93	5.80
M2	E_c (ksi)	3730	3821	4530	4027
	f'_c (ksi)	5.12	5.22	4.99	5.11
M3	E_c (ksi)	-	6530	5572	6051
	f'_c (ksi)	-	6.1	6.1	6.1
M4	E_c (ksi)	6066	6017	5917	5980
	f'_c (ksi)	6.8	6.4	6.7	6.6

Tensile Strength

Currently, there is not an ASTM standard for conducting a uniaxial test of SFRC. Therefore, the same uniaxial tensile test used in the material test program (Chapter 5) was used to measure the tensile properties of the SFRC specimens.

Three tension tests were conducted for mixes M1 and M2. Significant difficulties were encountered using this procedure, thus, no tests were conducted for M3 and M4. Ultimately, the unpredictable failure location of the concrete specimen is less than ideal. A number of the tests failed at the interface between the concrete specimen and epoxy. The crack migrated into the epoxy, allowing the adhesive to contribute to the post-crack response of the specimen. Sample 1 of the concrete with a fiber volume of 2.0 percent was the only test that failed inside the gauge length of the LVDT. Figure 124 presents the results of the test procedure for both fiber dosages.

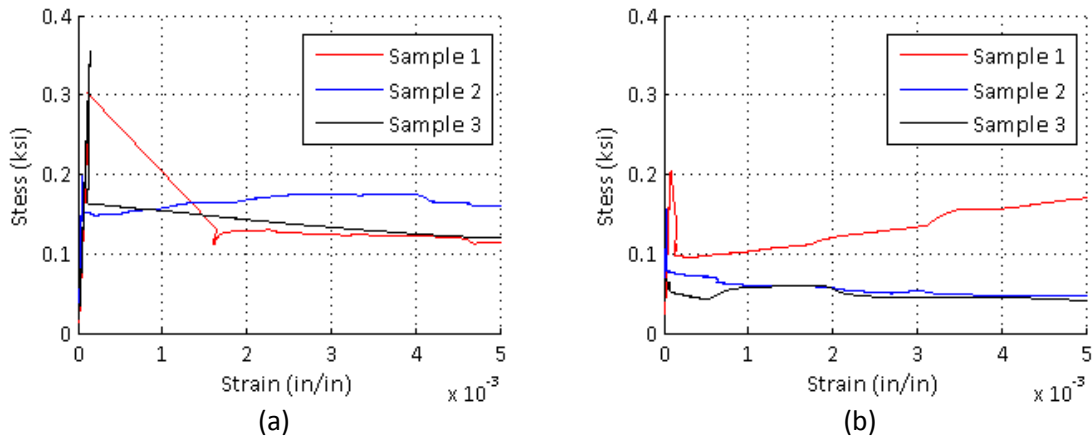


Figure 124. Tensile Test Results for (a) M1 and (b) M2

Flexural Strength

SFRC beams were prepared and tested in accordance with ASTM C1609. Each flexural specimen was subjected to a third-point bending until failure. The tests were conducted using a displacement-control procedure at a rate of 0.025 in./min. Table 44 and Figure 125 present the results of ASTM C1609. Based on ASTM C1609, there are four values of interest in the force vs. deflection plots of the flexural tests:

1. First Peak Load, P_1 : Load at first crack. Corresponds to a slope change in the deflection response.
2. Overall Peak Load, P_p : Maximum achieved load. Also referred to as the MOR.
3. Residual Load $L/600$, P_{600} : Residual capacity at a deflection of $L/600$.
4. Residual Load $L/150$, P_{150} : Residual capacity at a deflection of $L/150$.

The test results for each dosage volume satisfies the strength requirements of ACI 318 to allow for the use of steel fibers as shear reinforcement. However, the dosage volume of 0.5 percent by volume (65 lb/yd^3) is below the minimum specified rate by ACI. The three requirements to use steel fiber reinforcement in lieu of shear reinforcement is as follows:

1. The weight of added fibers exceeds 100 lb/yd^3 .
2. The residual strength corresponding to a midspan deflection of $1/300$ of the span length, obtained from flexural testing, is at least 90 percent of the first-peak strength.
3. The residual strength corresponding to a midspan deflection of $1/150$ of the span length, obtained from flexural testing, is at least 75 percent of the first-peak strength.

Table 44. Summary of Flexural Test Results

Mix ID	P ₁ (kips)	f _{cr} (ksi)	P _p (kips)	f _{MOR} (ksi)	P ₆₀₀ (kips)	f _{r,600} (ksi)	P ₁₅₀ (kips)	f _{r,150} (ksi)
M1	7.4	0.68	13.0	1.20	12.2	1.13	7.5	0.70
M2	5.1	0.48	7.9	0.73	7.7	0.72	5.9	0.54
M3	7.7	0.71	7.7	0.71	-	-	-	-
M4	9.1	0.84	9.1	0.84	8.1	0.75	4.6	0.42

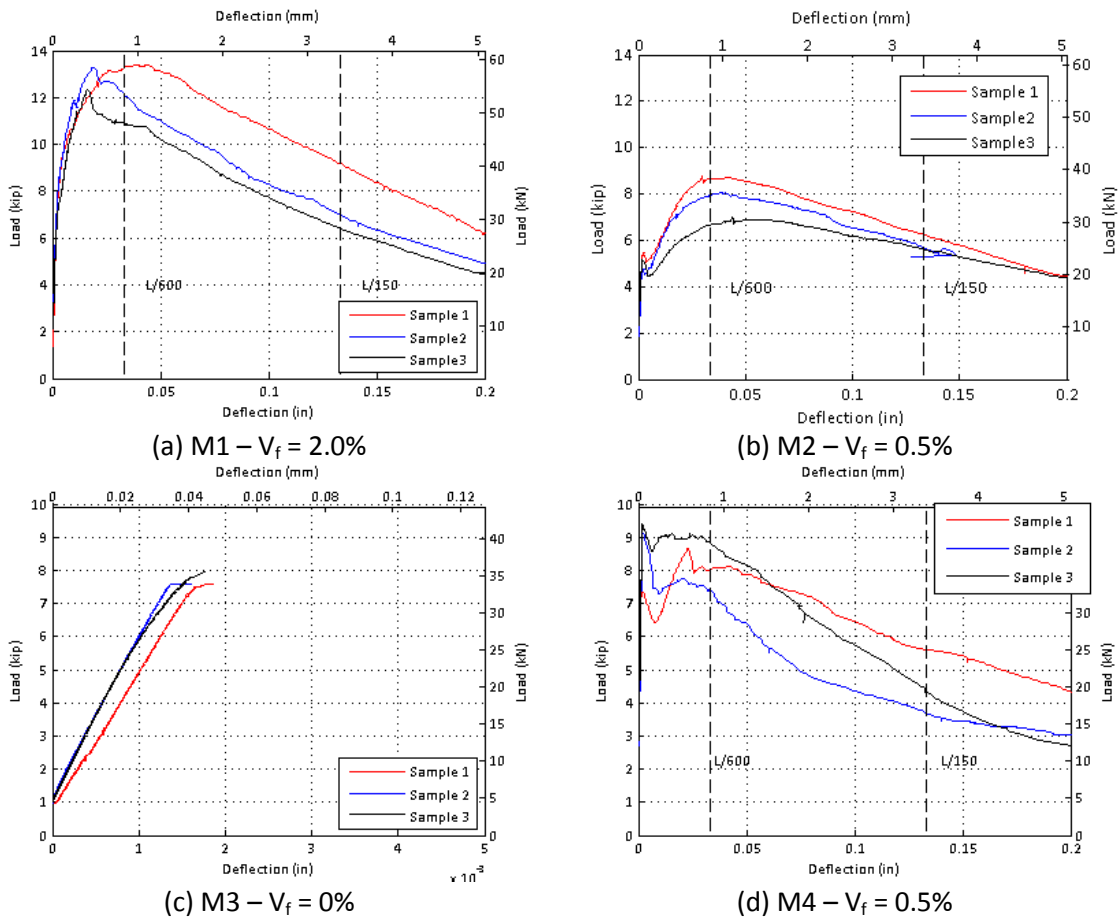


Figure 125. ASTM C1609 Test Results for all Mixes.

Steel Reinforcement Material Properties

Four samples were tested for each steel reinforcement size. The tests were conducted in accordance with ASTM A370, “Standard Test Methods and Definitions for Mechanical Testing of Steel Products.” Elongation data were collected by three LVDTs with a gage length of 8 in. (203 mm). Figure 126 shows the stress-strain relationship measured for each size of steel reinforcement. Table 23 summarizes key values.

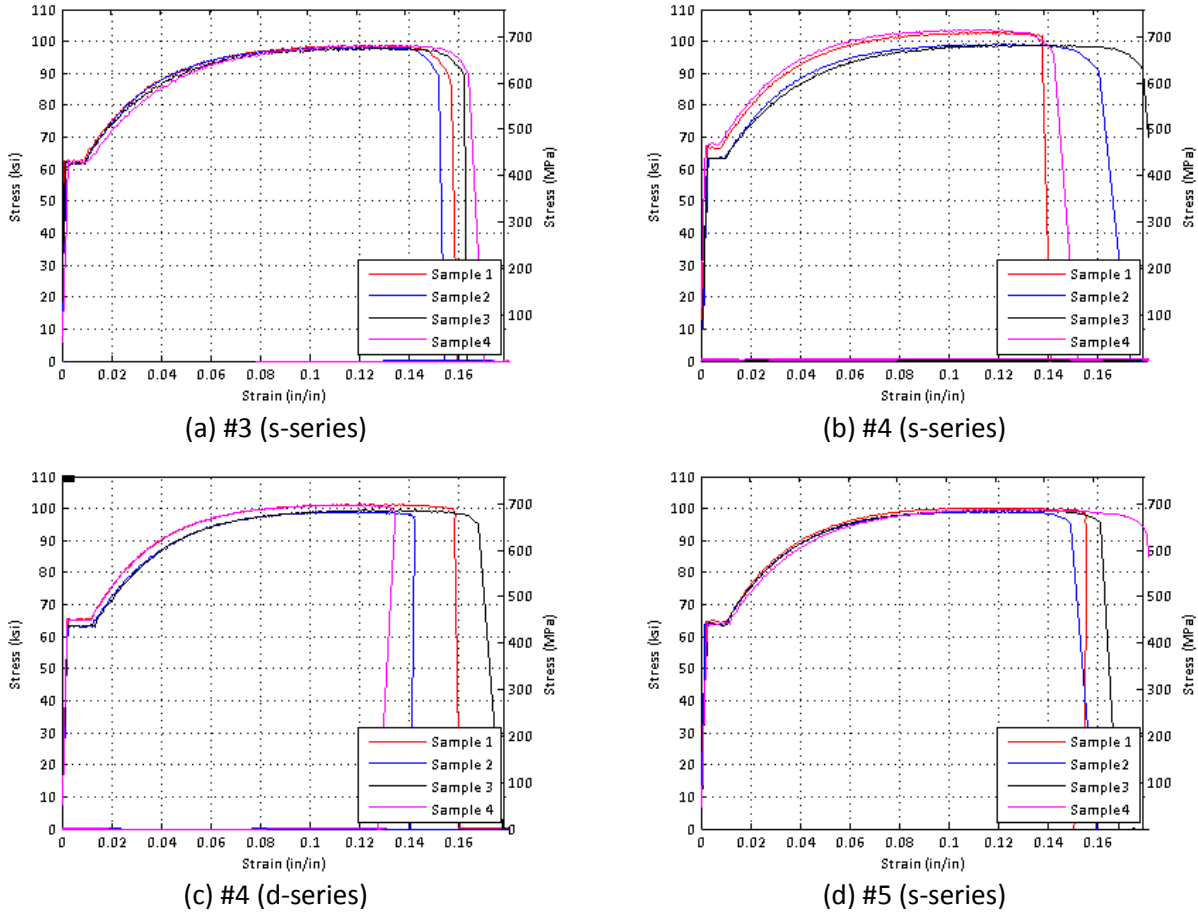


Figure 126. ASTM A370 Test For Steel Reinforcement Bars

Table 45. Summary of Steel Reinforcement Properties for All Steel Bars

	#3		#4 (d-series)		#4 (s-series)		#5	
	f_y (ksi)	f_u (ksi)	f_y (ksi)	f_u (ksi)	f_y (ksi)	f_u (ksi)	f_y (ksi)	f_u (ksi)
Sample 1	63	99	67	103	65	101	65	100
Sample 2	62	99	63	99	63	99	64	99
Sample 3	62	98	63	99	63	99	64	100
Sample 4	62	99	67	104	65	101	64	100
Average	62.3	98.8	65.0	101.3	64	100	64.3	99.8

TEST SETUP AND INSTRUMENTATION

The slab strip specimens were subjected to a four-point bending flexural test (Figure 127). The experimental tests were conducted using a 100 kip (445 kN) actuator. The test was conducted using a deflection-controlled philosophy. The deflection of the beam was increased at a rate of 0.05 in. (1.27 mm) per minute. The test was stopped at regular intervals to document the damage incurred by the beam. Crack locations, width, and height were recorded to document the damage progression of each specimen.

A load cell connected to the actuator recorded the applied load while string potentiometers located at 6 in. (152 mm) intervals recorded the deflection profile of the specimen. An LVDT was installed on the top and bottom of the slab strip specimen to determine the maximum strains and curvature experienced by each specimen. The gauge length of each LVDT was 2 ft (610 mm) to ensure the primary failure plane fell within the readings of the LVDTs. Finally, strain gages were installed on the two outer conventional steel reinforcing bars in each specimen with traditional reinforcing steel.

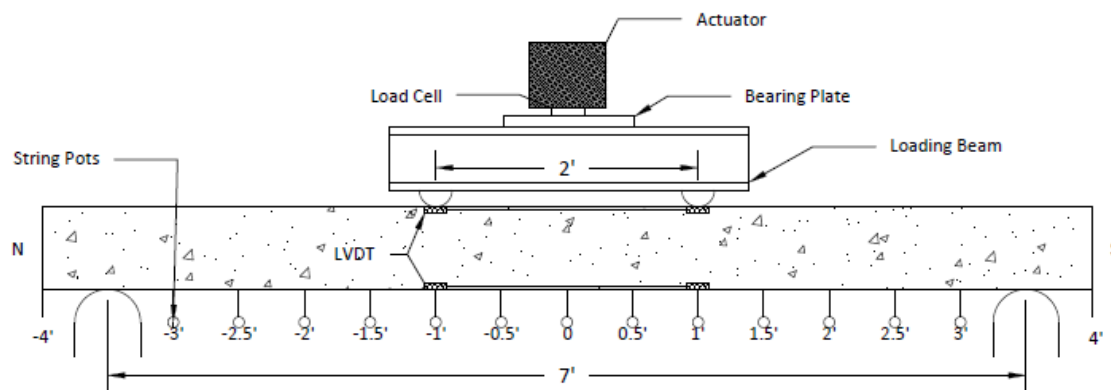


Figure 127. Experimental Test and Instrumentation Setup

SUMMARY OF OBSERVED RESULTS

The objective of this damage profile is to accurately determine the degree of damage to each slab strip and compare each crack's size, width, and location to failure criteria specified by RILEM (2002).

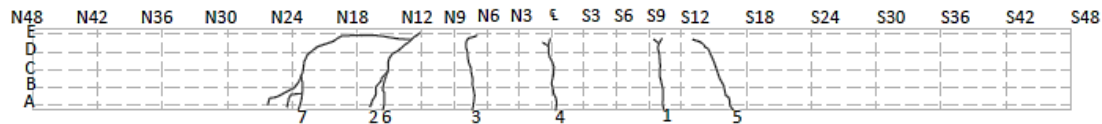
Throughout each experiment, the beams were examined for two failure criteria, the critical crack width and concrete crushing in the compression region. The critical crack width is defined by RILEM (2003) as 2.5 mm (0.1 in.). The failure progression for each SFRC slab-strip behaved in a similar manner. Several cracks would form over the length of the beam. The width of each crack grew as the load was increased on the specimen. Eventually, the progression of damage in the beam localized in an individual crack referred to as the critical crack. Once localization of the failure began, the crack widths of all non-critical cracks remain constant while the critical crack width increased to beyond 10 mm (0.4 in.). The location and amount of steel reinforcement affected the number of cracks that formed and their growth rate.

Comparison of Plain and SFRC Slab Strips (D-series)

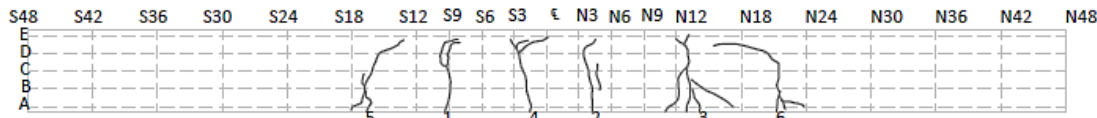
The behavior of the SFRC and PC specimen varied significantly. The SFRC specimen, d7505BTM24, developed a single critical crack on each face of the slab strip. The width of the critical crack continued to increase while all other cracks stopped growing at deflection step 0.5 in. (12.7 mm). In contrast, every crack that formed in the PC specimen continued to grow. Table 46 summarizes the average properties of the cracks inside and outside the constant moment region. Figure 128 shows the final crack map for each slab strip specimen.

Table 46. Average Properties of Cracks at Maximum Capacity

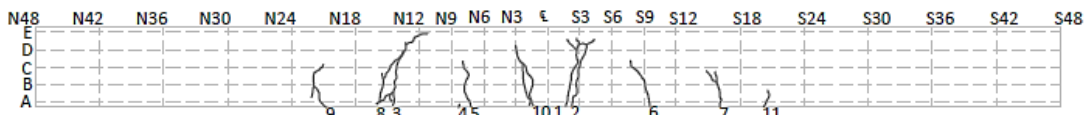
Specimen	Inside Constant Moment Region			Outside Constant Moment Region		
	# of Cracks	$\delta_{\text{first crack}}$ mm (in.)	Width, mm (in.)	# of Cracks	$\delta_{\text{first crack}}$ (in.)	Width, mm (in.)
d7500BTM24	3	1.27 (0.05)	2.96 (0.116)	3.5	7.62 (0.3)	1.29 (0.051)
d7505BTM24	4.5	1.78 (0.07)	1.70 (0.067)	5	5.08 (0.2)	0.15 (0.006)



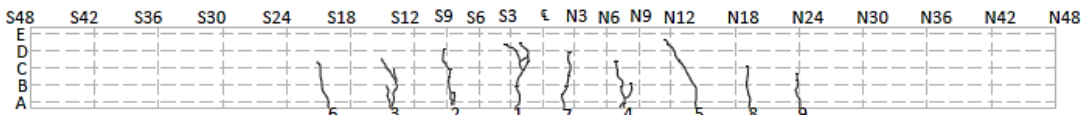
(a) West Face d7500BTM24



(b) East Face d7500BTM24



(c) West Face d7500BTM24



(d) East Face d7505BTM24

Figure 128. Crack Maps for Slab strips with Steel at Bottom

The same number of cracks formed inside and outside the constant moment region for the PC slab strip d7500BTM24. The same behavior occurred in the SFRC specimen. The SFRC specimen developed approximately 1.5 more cracks than its PC counterpart. The average crack width inside and outside the constant moment region is larger in the PC slab strip than the SFRC slab strip. The crack growth of the SFRC slab strip is averaged over a larger number of cracks. The majority of the crack growth for the SFRC specimen occurs in the critical crack that formed in the constant moment region. The SFRC specimen results in one large crack and approximately 9 small cracks while every crack in the PC specimen continues to grow throughout the test.

Figure 129 shows the average crack width measured on the east and west sides for the SFRC and PC strips for each displacement step. The average crack width of the PC beam is significantly larger than the

SFRC specimen due to the number of cracks in each specimen as discussed above. The maximum crack width observed in the SFRC specimen is significantly larger than the PC slab strip (Figure 130). At the beginning of the test, the cracks in the PC slab strip develop much quicker. At deflection step 0.8 in., the failure localization of the SFRC slab strip resulted in maximum crack width greater than the cracks observed in the PC slab strip. Therefore, the addition of SFRC enhances the performance of the slab strip from a damage progression perspective until the failure localization of the SFRC occurs. This transition point is observed after the critical crack width defined by RILEM (2002) of 2.5 mm is achieved.

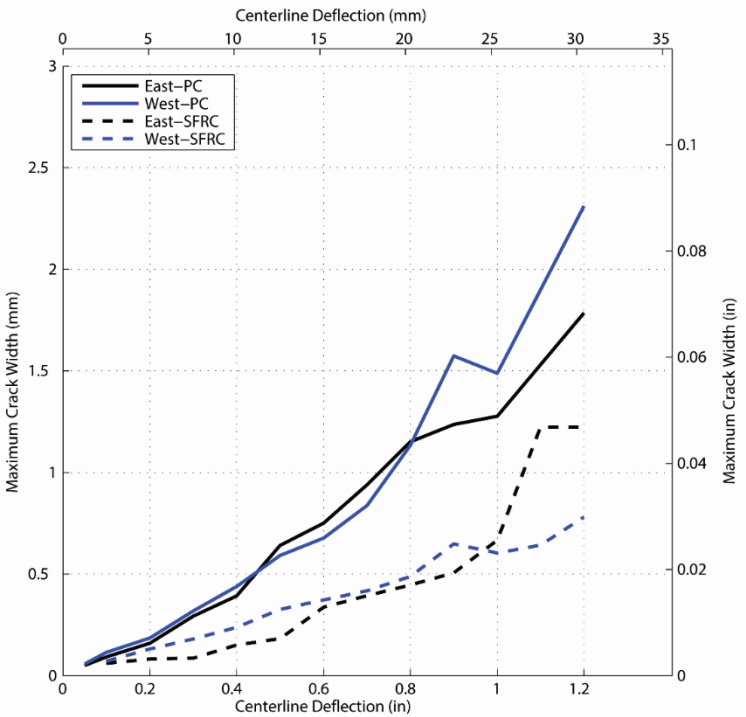


Figure 129. Average Crack Width vs. Deflection for SFRC (d7505BTM24) and PC Slab (d7500BTM24) Strips

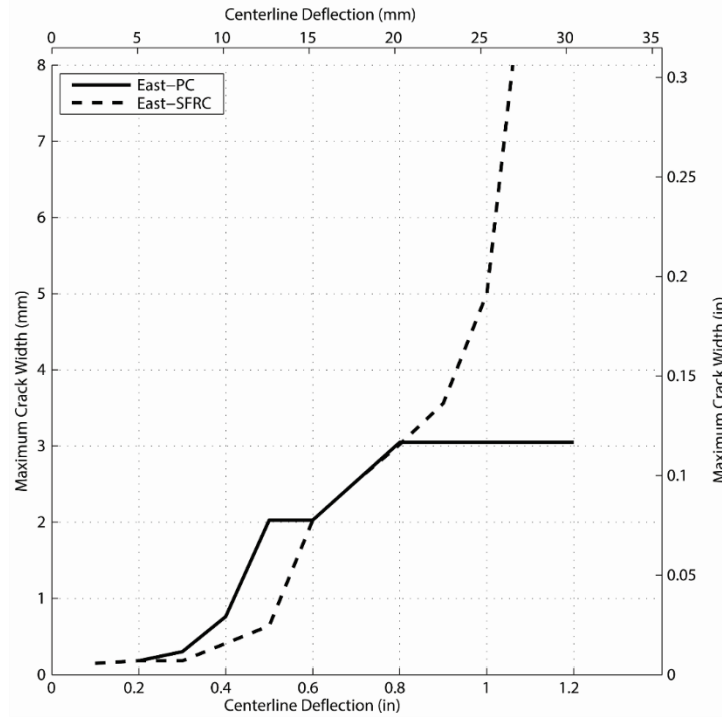


Figure 130. Maximum Crack Width vs. Deflection for SFRC (d7505BTM24) and PC Slab (d7500BTM24) Strips

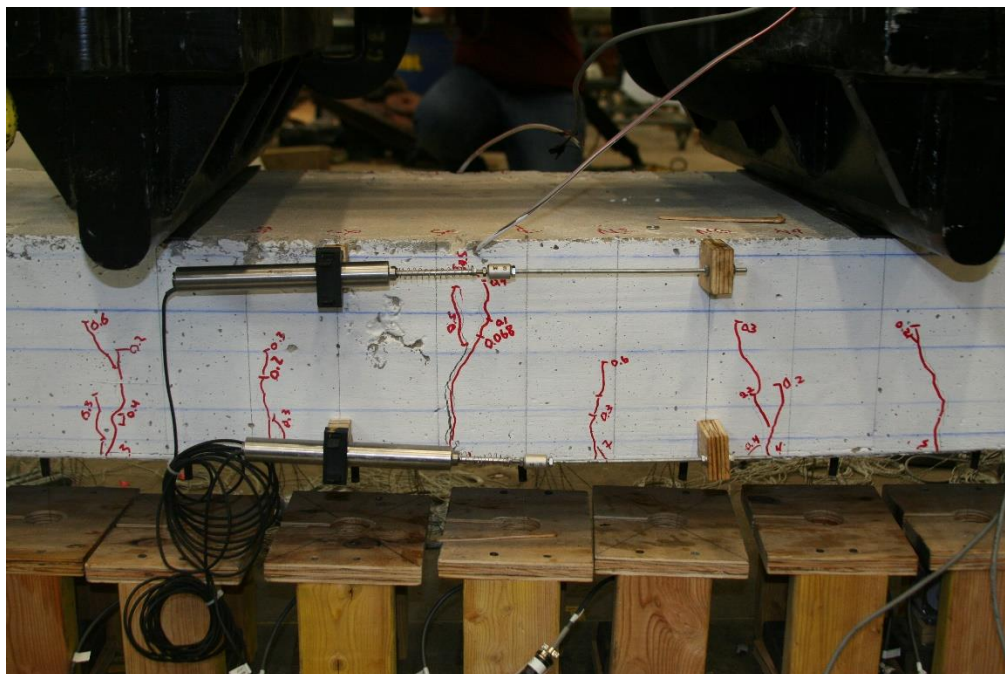
RILEM (2002) and Walraven (2013) classify failure as a maximum crack width of 2.5 mm. This criterion, along with crushing, was used in identifying failure of the tests. Table 49 show the damage properties associated with the failure criteria. Figure 131 through Figure 133 show the condition of the each strip at various deflection steps.

The critical crack for the PC slab strip is defined by the first crack to reach 2.5 mm; however, there was not a single critical crack. A total of four cracks on the east face (E1, E2, E3, and E4) and west face (W1, W3, W4, and W6) approached or exceeded the 2.5 mm limit. The critical crack width was achieved for the PC and SFRC specimens at the same deflection step of 0.7 in.

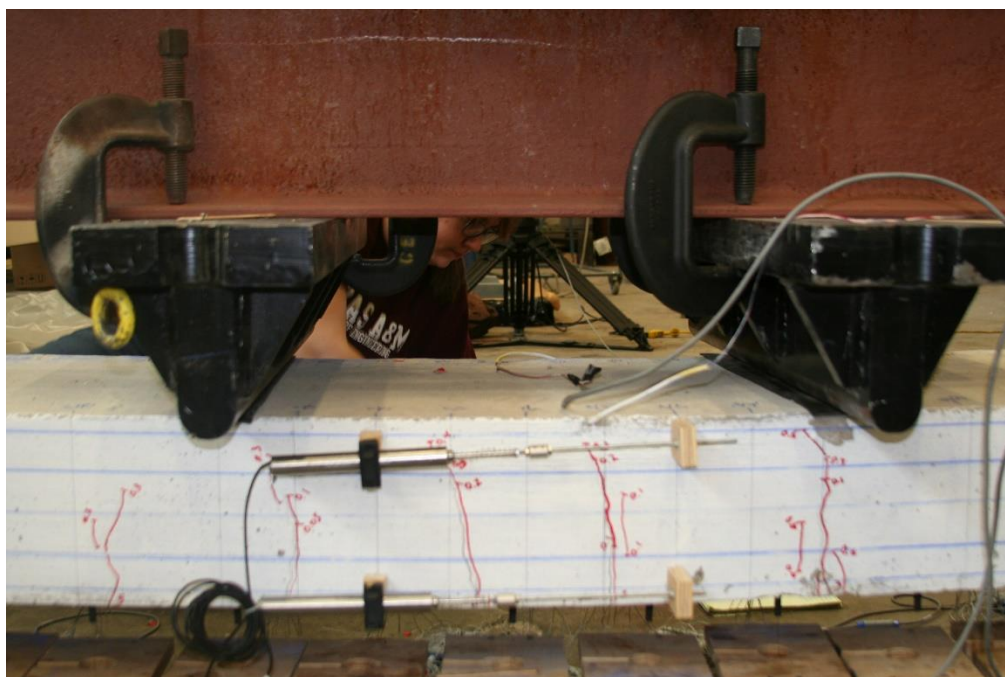
Crushing was not observed until each specimen was largely deflected. The first observation of crushing on the SFRC slab strip, d7505BTM24, occurred a deflection of 1.6 in. Conversely, slab strip s7505BTM24 investigated in the s-series tests exhibited crushing at 1.0 in.

Table 47. Properties of Failure Criteria for Specimens with Steel Reinforcement Located at Bottom

Specimen	Critical Crack				Concrete Crushing		
	Location	#	$\delta_{\text{first obs}}$ (in.)	$\delta_{2.50}$ (in.)	Location	$\delta_{\text{first obs}}$ (in.)	Width (in.)
d7500BTM24	⌀/S12	E4/W5	0.2	0.7	S9 N3-N6	End	6
d7505BTM24	⌀-S3	E1/W2	0.05	0.7	⌀-S3	1.6	3

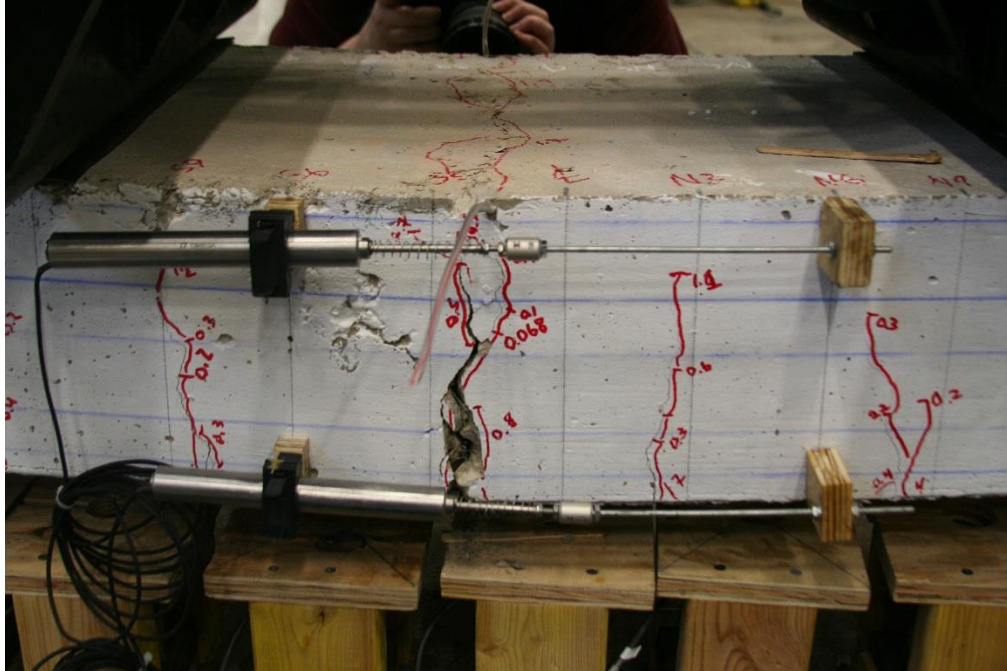


(a) d7505BTM24 – East (SFRC)



(b) d7500BTM24 (PC)

Figure 131. State of Damage for d7505BTM24 and d7500BTM24 at 0.6 in. of Deflection



(a) d7505BTM24 – East (SFRC)



(b) d7500BTM24 – East (PC)

Figure 133. State of Damage for d7505BTM24 and d7500BTM24 at 1.9 in. of Deflection

Behavior of Beams with Steel at Bottom (S-Series)

Overall, the behavior of the slab strips with steel located at the bottom of the specimen was consistent. Trends were observed in the number of cracks both inside and outside the constant moment region and the deflection step of the first crack in each region. The crack width of all non-critical cracks varied significantly between specimens. Table 48 summarizes the number of cracks, the deflection of the first crack, and the average crack width of the non-critical cracks at the time of failure.

Approximately the same number of cracks formed both inside and outside the constant moment region. The total number of cracks for each specimen decreased as the area of steel reinforcement decreased. This is a result of a hinge forming earlier in the lightly reinforced specimens, thus preventing the formation of additional cracks along the strip.

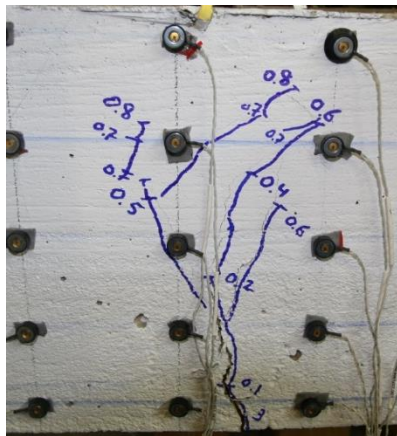
The first crack inside and outside of the constant moment region formed by the second (0.10 in.) and third (0.20 in.) deflection steps, respectively. Generally, the critical crack was not one of the first cracks formed. As the area of steel reinforcement decreased, the formation of the critical crack occurred at an earlier deflection step.

Once the critical crack became obvious, the growth of the majority of the non-critical cracks slowed or stopped completely. No trend was observed in the width of non-critical cracks as shown by the variation in the crack widths reported in Table 48. The majority of the crack width growth for specimen S9005BTM24 occurred in the critical crack as demonstrated by an average constant moment region crack width of 0.19 mm. When the area of steel was smaller, the crack width growth was better distributed among the average number of cracks inside the constant moment region with an average width of 0.41 mm.

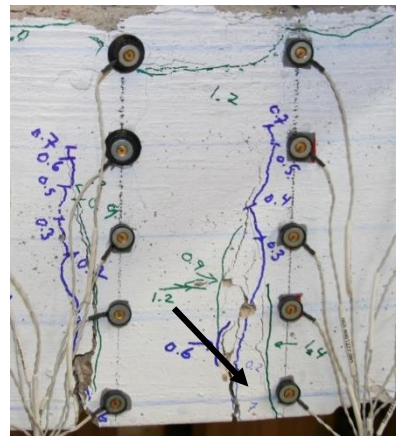
The majority of cracks extended vertically with slight horizontal progressions at locations of steel fibers and coarse aggregates. Branching of cracks was also observed near these locations. Accessory cracks commonly formed adjacent to primary cracks. These cracks formed within a fiber's length horizontally from the primary crack and rarely extended to the bottom of the specimen. Figure 134 shows the horizontal behavior of cracks for the steel fibers and coarse aggregates. Figure 135 shows the crack maps at the conclusion of each test.

Table 48. Properties of Non-Critical Cracks for Specimens with Steel Reinforcement Located at the Bottom

Specimen	Inside Constant Moment Region			Outside Constant Moment Region		
	# of Cracks	$\delta_{\text{first crack}}$ (in.)	Width, mm (in.)	# of Cracks	$\delta_{\text{first crack}}$ (in.)	Width, mm (in.)
s7505BTM35	8.5	0.1	0.41 (0.016)	7	0.2	0.13 (0.005)
s7505BTM25	6.5	0.10	0.40 (0.016)	6	0.15	0.31 (0.012)
s7505BTM23	6.5	0.10	0.60 (0.024)	4.5	0.15	0.17 (0.007)
s9005BTM35	8.5	0.10	0.54 (0.021)	7	0.15	0.15 (0.006)
s9005BTM25	5	0.05	0.98 (0.039)	5.5	0.2	0.31 (0.012)
s9005BTM24	6	0.08	0.19 (0.007)	5	0.15	0.22 (0.009)
s9005BTM23	4.5	0.10	0.41 (0.016)	4	0.15	0.68 (0.027)

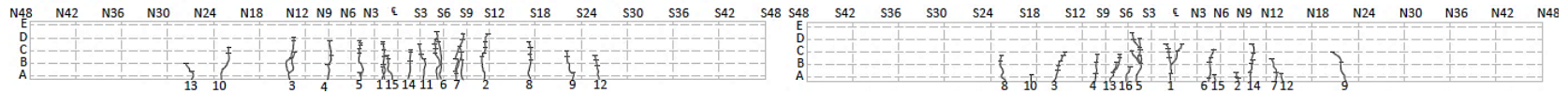


(a)



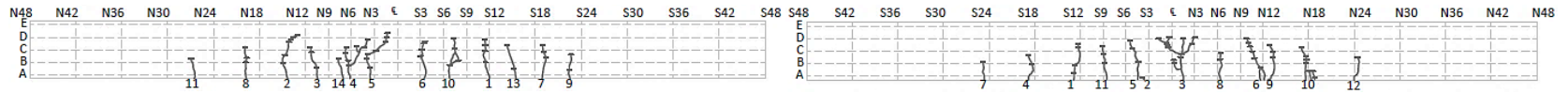
(b)

Figure 134. SFRC Crack Behavior (a) Crack Branching—W3 S9005BTM25 and (b) Accessory Cracks—W7 S7505BTM35



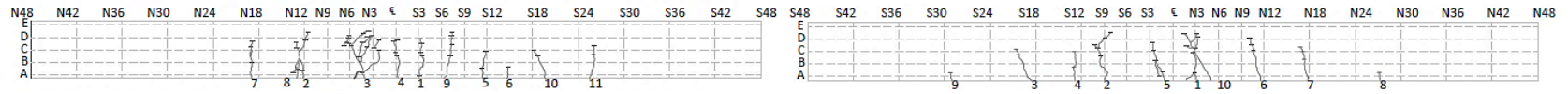
(a) West Face S7505BTM35

(b) East Face S7505BTM35



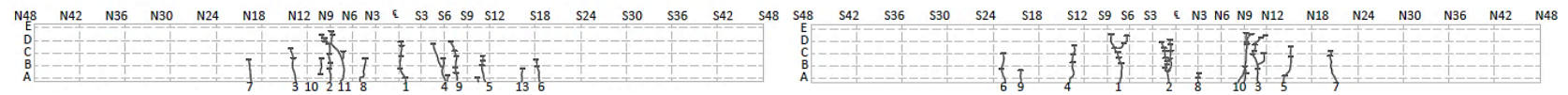
(c) West Face S7505BTM25

(d) East Face S7505BTM25



(e) West Face S7505BTM24

(f) East Face S7505BTM24



(g) West Face S7505BTM23

(h) East Face S7505BTM23

Figure 135. Crack Maps for Slab Strips 7.5 in. Deep with Steel at Bottom

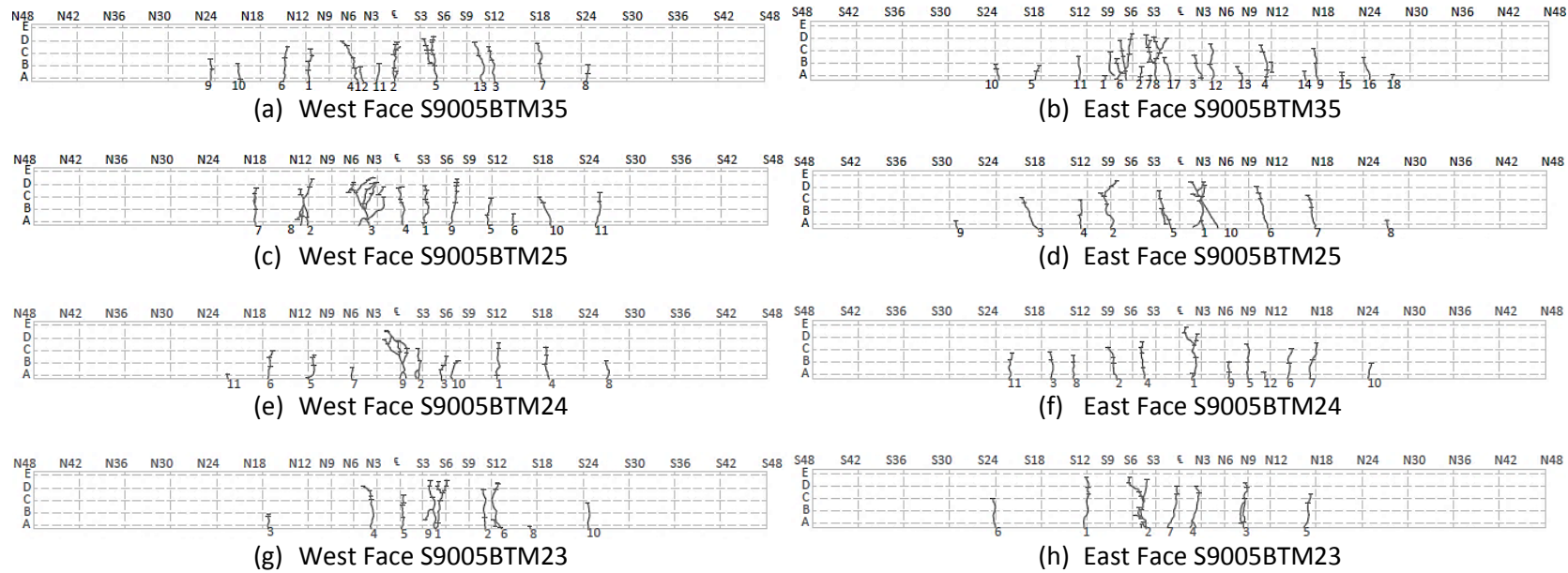


Figure 136. Crack Maps for Slab Strips 9.0 in. Deep with Steel at Bottom

As each test progressed and the damage became more severe, steel fibers were visible bridging widening cracks. Steel fibers located near the surface of the specimen often resulted in spalling of the concrete. Fibers with sufficient coverage resulted in anchorage failure and the straightening of the hooked ends of the fiber. Figure 137 shows the failure of steel fibers. The fibers delayed or prevented the spalling of sizable pieces of concrete.

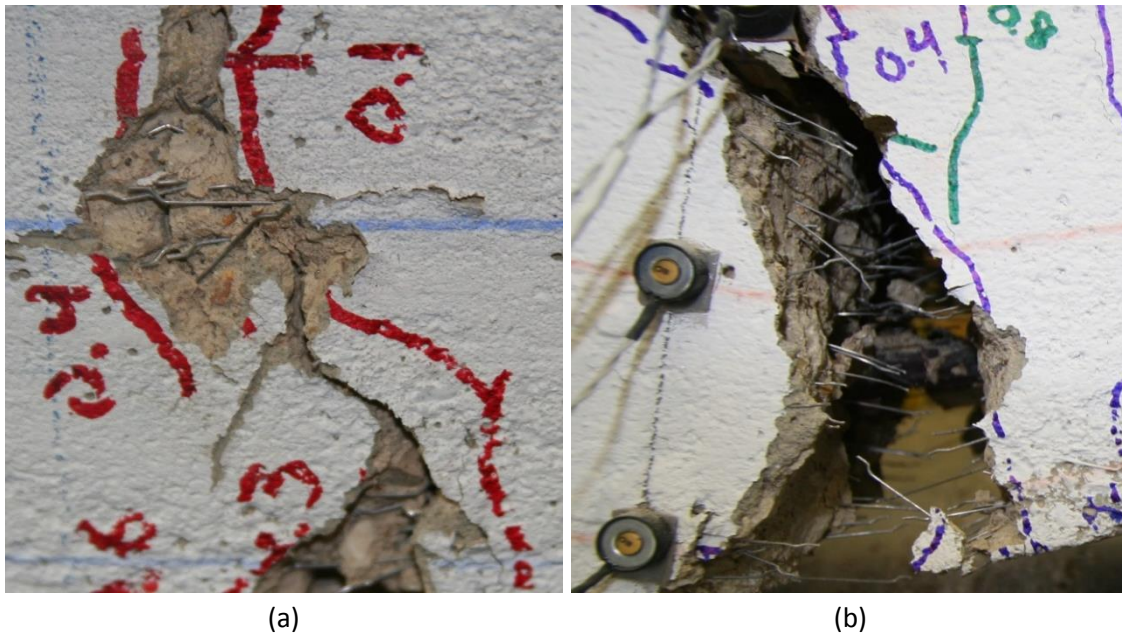


Figure 137. Steel Fiber Failure (a) Spalling at Surface of Concrete—E2 S9005BTM23 (b) Steel Fiber Anchorage Failure

RILEM (2002) and Walraven (2013) classify failure as a maximum crack width of 2.5 mm. This criterion, along with crushing, was used in identifying failure of the tests. Failure is also commonly defined as crushing observed in the top section of the specimen. Table 49 demonstrates the crack characteristics associated with these two failure definitions.

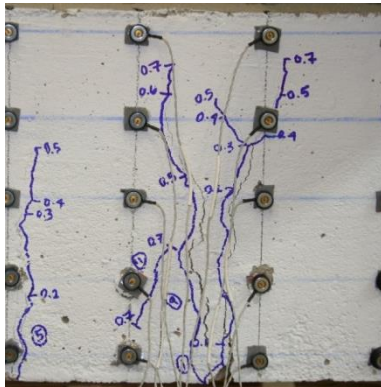
The failure plane for every specimen with steel reinforcement at the bottom formed within 6 in. (152 mm) of the centerline of the specimen, except S7505BTM23 where the failure plane formed near the north loading point. The displacement step reported in Table 49 for the first observation of the critical crack is an average of the east and west faces. The deflection step when the critical crack first formed is inconsistent among the slab specimens. However, the first observation of the maximum crack width occurred at earlier deflection steps for specimens with less steel reinforcement.

The thinner slab specimens, s7505-, exhibited crushing at a consistent displacement of 1.0 in. Concrete crushing for the thicker specimens was not consistent, ranging from displacements of 0.6 to 0.9 in. (15.2 to 22.9 mm). For each specimen the compression region above the critical crack was the first area to exhibit crushing. However, the crushed region extended horizontally as much as 18 in. The specimens with a smaller area of steel reinforcement also had a smaller region of crushed concrete. Figure 139 and

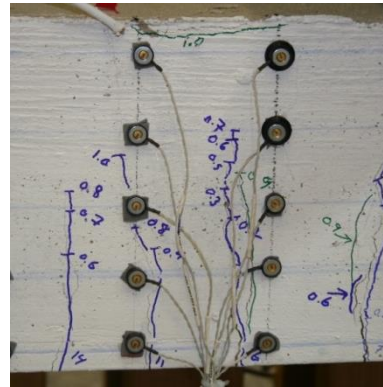
Figure 140 show the condition of each slab-strip specimen with steel located at the bottom at a deflection of 1.2 in. (30.5 mm). Crushing had already begun at this deflection step.

Table 49. Properties of Failure Criteria for Specimens with Steel Reinforcement Located at Bottom

Specimen	Critical Crack				Concrete Crushing		
	Location	Crack #	$\delta_{\text{first obs}}$ (in.)	$\delta_{2.50}$ (in.)	Location	$\delta_{\text{first obs}}$ (in.)	Width (in.)
s7505BTM35	S3-S6	E5/W6	0.2	1.2	S3-S6	1.0	12
s7505BTM25	N3- $\text{\textcircled{C}}$	E3/W5	0.15	0.9	N3- $\text{\textcircled{C}}$	1.0	9
s7505BTM24	S3	E1/W7	0.35	1.2	S3	1.0	6
s7505BTM23	N9	E10/W11	0.38	0.8	N12-N9	0.8	4.5
s9005BTM35	S3-S6	E6/W5	0.20	0.9	N6-S12	0.7	18
s9005BTM25	N6-N3	E1/W3	0.08	0.7	N6- $\text{\textcircled{C}}$	0.9	6
s9005BTM24	N3- $\text{\textcircled{C}}$	E1/W9	0.13	0.8	N3-S3	0.6	6
s9005BTM23	S3-S6	E2/W1	0.10	0.7	S3-S9	0.8	6



(a) S9005BTM23



(b) S7505BTM35 – Crushing
At Top Edge (Green Line)

Figure 138. General Condition at Failure Criteria (a) Crack Width Greater than 2.5 mm and (b) Onset of Crushing

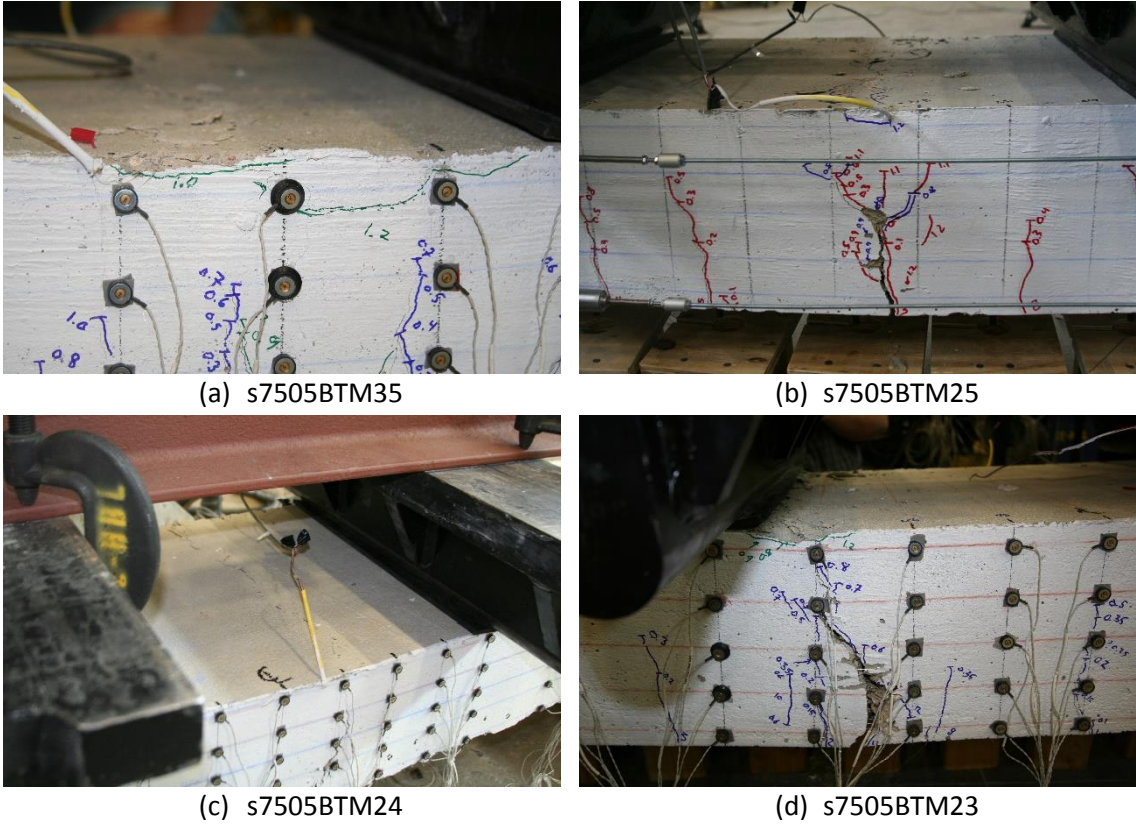


Figure 139. Damage for Slab-Strip Specimens 7.5 in. Deep with Steel at Bottom at 1.2 in. of Deflection

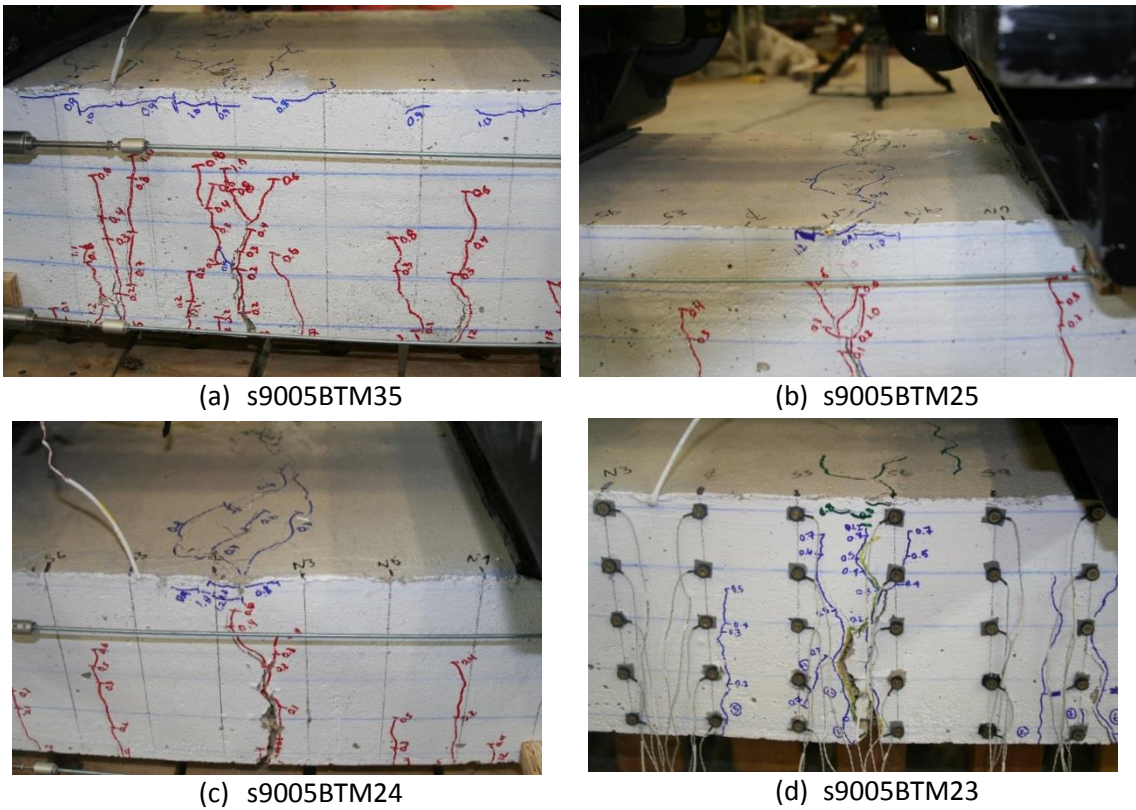


Figure 140. Damage for Slab-Strip Specimens 9.0 in. Deep with Steel at Bottom at 1.2 in. of Deflection

Behavior of Beams with Steel at Center (S-Series)

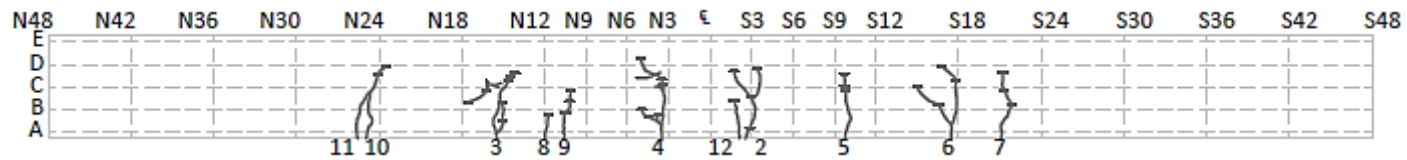
The specimens with steel reinforcement located at mid-depth behaved in a manner similar to the specimens with steel located at the bottom. The number of cracks in the constant moment region matched the number of cracks outside the region. The total number of cracks also decreased with a decrease in the area of steel reinforcement. The average crack width did not adhere to any trend for the locations of the crack, in or out of the constant moment region, nor the area of steel reinforcement in the specimen. The first observance of the critical crack width varied by one deflection step among the two tests. Table 50 and Table 51 display the properties of the non-critical cracks and failure criteria for these specimens. Figure 141 shows the crack maps at the completion of each test. Relocating the steel resulted in fewer total cracks; however, the average crack widths were larger. The deflection step of the failure criteria was not influenced by relocating the steel.

Table 50. Properties of Non-Critical Cracks for Specimens with Steel Reinforcement Located at Center

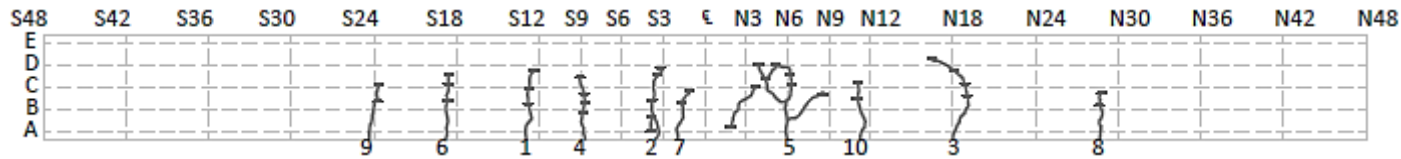
Specimen	Inside Constant Moment Region			Outside Constant Moment Region		
	# Of Cracks	$\delta_{\text{first crack}}$ (in.)	Width (mm)	# Of Cracks	$\delta_{\text{first crack}}$ (in.)	Width (mm)
s7505CTR35	4	0.1	0.53 (0.021)	6	0.15	0.29 (0.011)
s7505CTR25	3	0.13	0.70 (0.028)	3	0.15	0.95 (0.037)

Table 51. Properties of Failure Criteria for Specimens with Steel Reinforcement Located at Center

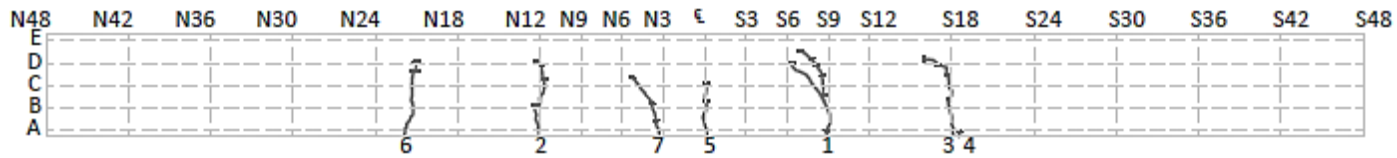
Specimen	Location	Critical Crack			Concrete Crushing		
		Crack #	$\delta_{\text{first obs}}$ (in.)	$\delta_{2.50}$ (in.)	Location	$\delta_{\text{first obs}}$ (in.)	Width (in.)
s7505CTR35	N6-N3	E5/W4	0.2	1	N12- Φ	1.0	12
s7505CTR25	N12-N9	E1/W1	0.10	0.9	N12-N6	0.7	6



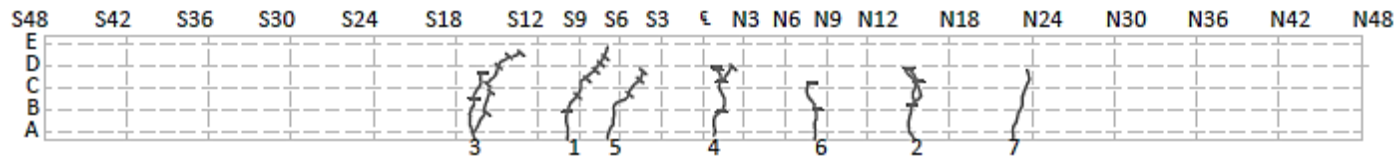
(a) West Face of S7505CTR35



(b) East Face of S7505CTR35



(c) West Face of S7505CTR25



(d) East Face of S7505CTR25

Figure 141. Crack Maps for Slab strips with Steel at Center

Behavior of Slab Strips with No Steel

The specimens without steel reinforcement behaved significantly different in comparison to the specimens with steel reinforcement. Each specimen developed a single crack with accessory cracks adjacent to it (Figure 142). The location of the primary crack varied significantly. In the deeper slab strips, the failure plane occurred directly beneath the loading point.

The slab strips achieved the maximum allowable crack width of 2.5 mm at a very small deflection step relative to the specimens with steel reinforcement. The specimen with a fiber dosage rate of 0.5 percent by volume and thickness of 7.5 in. exhibited the failure criteria by deflection step 0.3 in. (L/280). Increasing the fiber dosage rate to 2.0 percent by volume delayed the failure crack width by one deflection step to 0.4 in. (L/210).

The SFRC specimens with no steel exhibited crushing at approximately deflection step 0.8 in. (L/105) for the s-series tests, which is consistent with the deflection step for crushing in the specimens with steel reinforcement. However, the d-series tests crushed later or did not exhibit crushing at failure. Table 52 details the observance of the failure benchmarks for slab strip specimens without steel reinforcement.

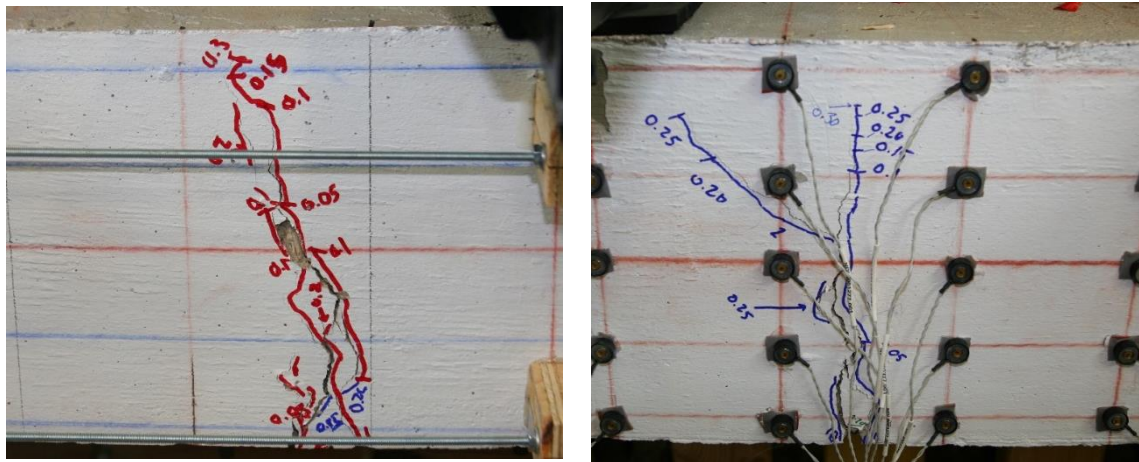
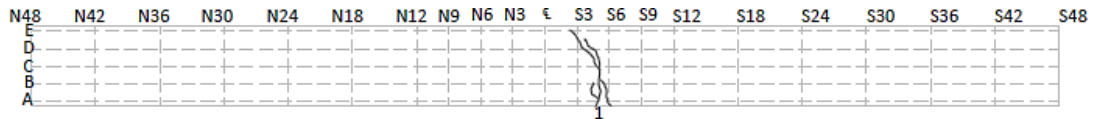


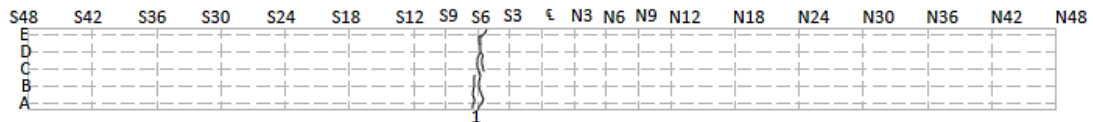
Figure 142. Accessory and Branching Cracks of Specimens without Steel Reinforcement S7505NOS00

Table 52. Properties of Failure Criteria for Specimens without Steel Reinforcement

Specimen	Critical Crack			Concrete Crushing		
	Location	$\delta_{\text{first obs}}$ (in.)	$\delta_{2.50}$ (in.)	Location	$\delta_{\text{first obs}}$ (in.)	Width (in.)
S7505NOS00	N12-N9	0.05	0.3	N12-N9	0.7	1.5
S7520NOS00	S6-S9	0.1	0.4	-	-	-
S9005NOS00	S12-S18	0.05	0.25	N12-N9	0.8	1.5
S9020NOS00	N12	-	-	-	-	-
d7505NOS00	S6	0.05	0.4	-	-	-
d9005NOS00	S9-S6	0.05	0.3	-	-	-



(a) West Face d7505NOS00



(b) East Face d7505NOS00

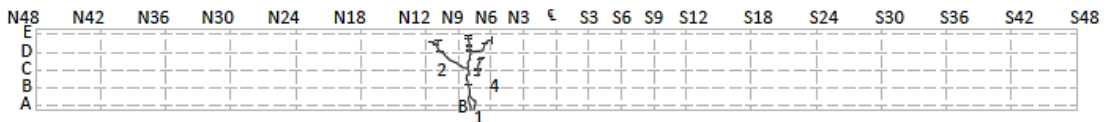


(c) West Face d9005NOS00



(d) East Face d9005NOS00

Figure 143. Crack Maps for Slab-Strip Specimens without Steel Reinforcement



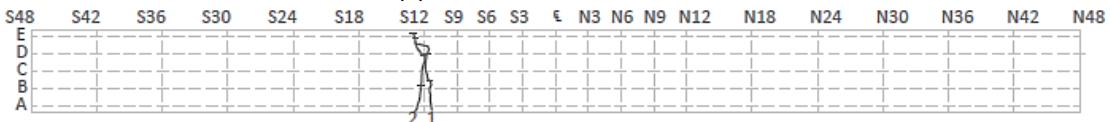
(a) West Face s7505NOS00



(b) East Face s7505NOS00



(c) West Face s9005NOS00



(d) East Face s9005NOS00

Figure 144. Crack Maps for Slab-Strip Specimens without Steel Reinforcement

LOAD-DEFLECTION RESPONSE

The load-deflection response are presented in three categories based on their thickness and steel reinforcement ratio: specimens 7.5 in. deep containing steel reinforcement, specimens 9.0 in. deep with steel reinforcement, and finally specimens of both heights without steel reinforcement. Where applicable, the specimen's performance was characterized by moment capacity at service and ultimate loads.

Specimens 7.5 in. Deep with Steel Reinforcement

Figure 145 exhibits the force versus deflection behavior for 7.5 in. deep strips with steel reinforcement. The deflection is based on the readings of the string potentiometer at the center of the specimen. The string potentiometers were removed prior to the completion of the tests to protect them the collapse of the specimen. The end of the force versus deflection curves does not necessarily signify failure of the specimens.

The initial stiffness of each test was consistent among the specimens. Each specimen cracked at approximately the same centerline deflection, 0.04 in. (1 mm), and applied force, 4.5 kips (20 kN). Using the ACI 318-11 definition for the MOR for concrete and elastic section analysis, the expected cracking load for the SFRC strips is 5.6 kips. The cracking load of the SFRC specimens was approximately 20 percent lower than the ACI prediction.

The post-crack stiffness of the specimens varied based on the amount and location of steel reinforcement. The specimen with the largest area of reinforcement (3-#5 bars) located near the bottom surface had the largest post-crack stiffness. The post-crack stiffness decreased for specimens with less steel reinforcement. Relocating the steel reinforcement to mid-depth of the specimen resulted in a large decrease in post-crack stiffness.

The maximum allowable stress in the steel reinforcement for serviceability, 24 ksi, was achieved after each specimen cracked. The specimens with the steel reinforcement located at mid-depth achieved the largest deflection at this designation. Strip S7505CTR25 has the lowest service load of 5.0 kips while strip S7505BTM35 has the largest service load of 8.3 kips. Relocating the steel reinforcement to the middle, S7505CTR35, decreases the service load to 8.1 kips; however, the specimen with one less steel bar, S7505BTM25, resulted in an even lower service load of 7.4 kips. Table 53 summarizes the service performance of the 7.5 in. deep SFRC slab strips.

A similar trend was observed in the maximum capacity of the SFRC strips. Strip S7505BTM35 has the largest capacity at approximately 24 kips and strip S7505BTM23 has the smallest capacity at approximately 10.2 k-ft. The maximum capacity of the specimens did not correspond with the physical observance of crushing. Additionally, the maximum capacity of each specimen occurred at variable deflections. Strip S7505BTM23 achieved its maximum capacity the earliest at a deflection of 0.55 in. while strip S7505BTM25 achieved its maximum capacity the latest at a deflection of 0.99 in. Table 54 summarizes the maximum capacity of the 7.5 in. deep SFRC slab strips.

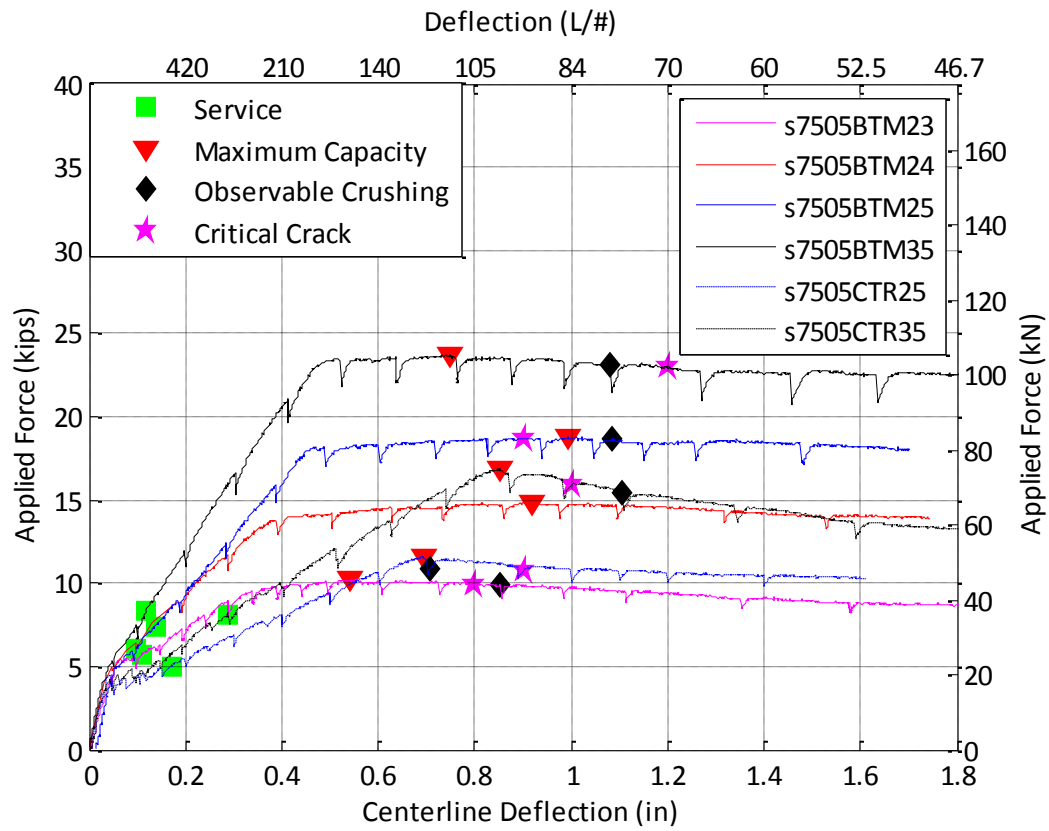


Figure 145. Force versus Deflection of 7.5 in Deep SFRC Slab Strips with Steel

Table 53. Summary of S7505 Experimental SFRC Service Capacity

Specimen	Deflection (in.)	Force (kip)	Moment (k-ft)
s7505BTM23	0.11	5.7	7.1
s7505BTM24	0.1	6.2	7.7
s7505BTM25	0.15	7.4	9.3
s7505BTM35	0.12	8.3	10.4
s7505CTR25	0.17	5.0	6.3
s7505CTR35	0.3	8.2	10.2

Table 54. Summary of S7505 Experimental SFRC Maximum Capacity

Specimen	Deflection (in.)	Force (kip)	Moment (k-ft)
s7505BTM23	0.55	10.2	12.8
s7505BTM24	0.92	14.9	18.59
s7505BTM25	0.99	18.8	23.5
s7505BTM35	0.75	23.7	29.67
s7505CTR25	0.69	11.6	14.48
s7505CTR35	0.85	16.9	21.12

Specimens 9.0 in. Deep with Steel Reinforcement

Figure 146 shows the force versus deflection behavior for each 9.0 in. deep specimen with steel reinforcement. The deeper beams with steel reinforcement exhibited the same trends as observed in the thinner 7.5 in. deep specimens. The deflection is based on the readings of the string potentiometer at the center of the specimen.

The initial and post-crack stiffness of the 9.0 in. (229 mm) deep specimens was similar to the thinner specimens. The initial stiffness of each test was consistent among the specimens while the post-crack stiffness decreased with a decrease in the area of steel reinforcement. Each specimen cracked at approximately the same centerline deflection, 0.035 in. (0.89 mm), and applied force, 6.5 kips (29 kN). The expected cracking load for PC strips with the same dimensions as the tested specimen is 8.15 kips (32.9 kN). Similar to the thinner specimens, the 9.0 in. (229 mm) deep specimens cracked at approximately 20 percent of the ACI prediction.

The maximum allowable stress in the steel reinforcement for serviceability, 24 ksi (165 MPa), was achieved after each specimen cracked. The service stress occurred between deflections 0.07 in. and 0.13 in. (3.3 mm). The service capacity was larger in specimens with a larger area of steel reinforcement with the exception of specimen S9005BTM24. The service capacity ranged from 8.5 kips (37.8 kN) for S9005BTM23 to 12.7 kips (56.5 kN) for S9005BTM35. Table 55 summarizes the service performance of the 9.0 in. deep slab strip specimens.

Strip S9005BTM35 had the largest capacity at approximately 32.0 kips (142.3 kN), and strip S9005BTM23 had the smallest capacity at approximately 12.8 kips (56.9 kN). Unlike the thinner specimens, the maximum capacity of several of the 9.0 in. deep specimens corresponded with the physical observed of crushing noted. The deflection at the maximum capacity was larger in the specimens with a larger area of steel except for strip S9005BTM35. Table 56 summarizes the maximum capacity of the 9.0 in. (229 mm) deep slab strip specimens.

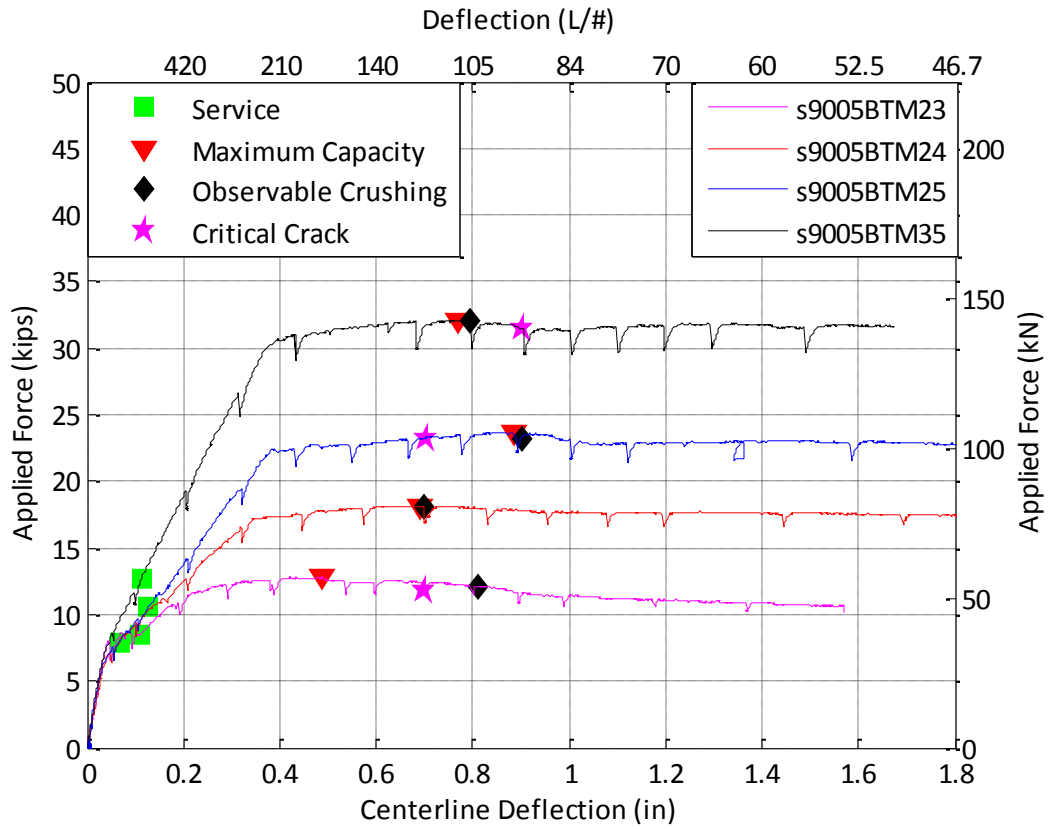


Figure 146. Force vs Deflection for Specimens 9.0 in. Deep with Steel Reinforcement

Table 55. Summary of S9005 Experimental Service Capacity

Specimen	Deflection (in.)	Force (kips)	Moment (k-ft)
s9005BTM23	0.12	8.4	10.6
s9005BTM24	0.07	7.9	9.9
s9005BTM25	0.13	10.6	13.3
s9005BTM35	0.11	12.7	15.9

Table 56. Summary of S9005 Experimental Maximum Capacity

Specimen	Deflection (in.)	Force (kips)	Moment (k-ft)
s9005BTM23	0.50	12.8	16.1
s9005BTM24	0.69	18.2	22.7
s9005BTM25	0.88	23.7	29.6
s9005BTM35	0.77	32.1	40.1

Specimens without Steel Reinforcement

Figure 147 shows the force versus deflection behavior for each specimen without steel reinforcement. The service limit state is determined based on a steel stress and therefore excluded in the analysis of these sections. The deflection used in the figure is the reading of the string potentiometer at the center of the specimen.

The specimens with a fiber dosage volume of 0.5 percent reached maximum capacity at the cracking moment. During the beginning of test S9005NOS00, the DAQ was erroneously set to record data every five minutes rather than every second. As a result, the true maximum load was not captured by the recorder. When the error was noticed, a screen capture of the DAQ system was taken to capture the data in the system's buffer (Figure 148). The cracking and maximum capacity of the 7.0 in. (191 mm) and 9.0 in. (229 mm) deep specimens correspond to the cracking load determined in the sections with steel reinforcement, 4.5 kips (20 kN) and 6.5 kips (28.9 kN), respectively.

The specimens with a fiber dosage volume of 2.0 percent gained capacity after the initial cracking of the specimen. The additional steel fibers increased the specimens' moment capacity to approximately 170 percent and 174 percent of the cracking load. The maximum capacities occurred at 3 approximately the same deflection of 0.10 in. (2.5 mm).

Table 57. Summary of SFRC without Steel Reinforcement Experimental Results

Specimen	Deflection (in.)	Force (kips)	Moment (k-ft)
s7505nos00	0.04	4.6	5.7
s7520nos00	0.13	7.7	9.6
s9005nos00	0.06	4.5	5.6
s9020nos00	0.10	11.3	14.2

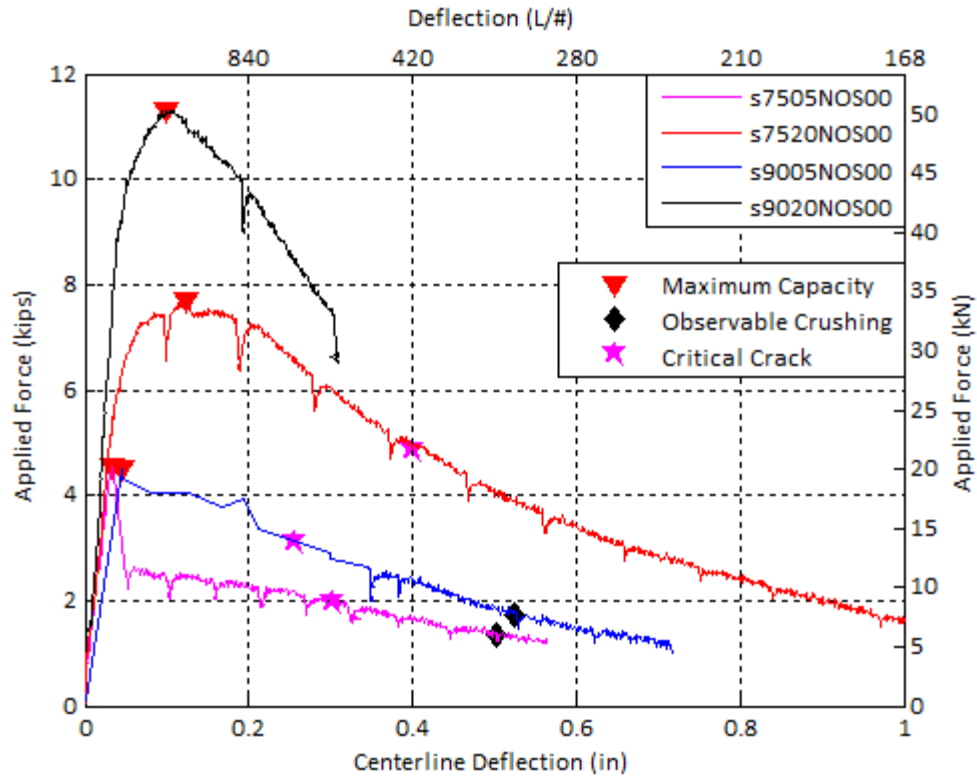


Figure 147. Force vs Deflection for SFRC Specimens without Steel Reinforcement

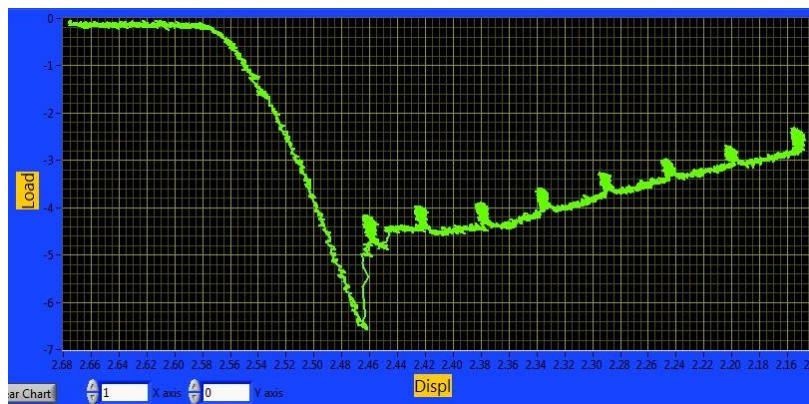


Figure 148. Screen Capture of DAQ during Testing of S9005NOS00

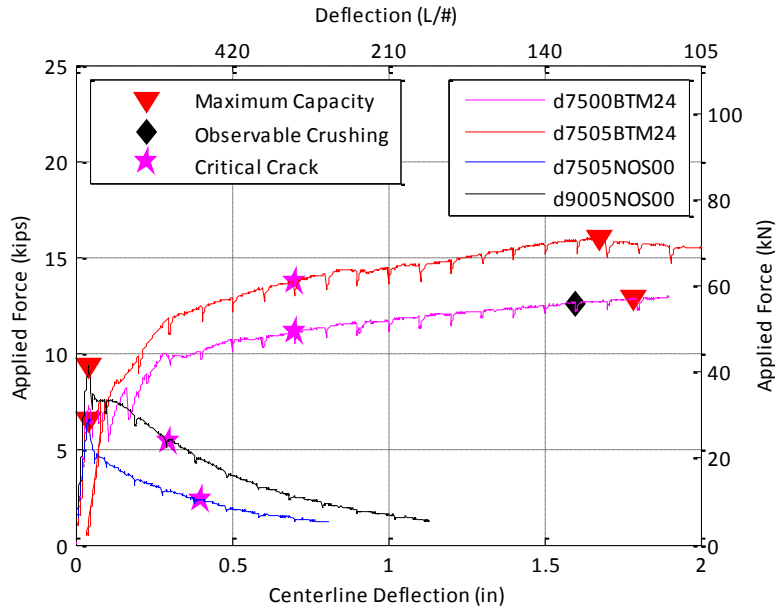


Figure 149. Force versus Deflection of Bridge d-Series Specimens

DISCUSSION

The service capacity of the SFRC strips corresponds to maximum allowable stress of 24 ksi (165 MPa). The following subsection examines the performance of the slab strips based on the maximum girder spacing permitted for each strip depth. This is achieved by determining the steel stress under the service limit state based on the experimental results. Next, the maximum permitted girder spacing for each slab strip based only on the service and maximum capacities is determined.

Service Limit State

The maximum girder spacing corresponding to a 7.5 in. deep deck is 7 ft according to the ADOT design requirements. The service demand for girder spacing of 7 ft is used to evaluate the performance of the 7.5 in. deep specimens. The stress in the steel reinforcement at this limit state was predicted for PC using a moment-curvature analysis. The predicted steel stress for PC specimens is compared to the SFRC experimental stress at the service limit state in Table 58. Figure 150 presents the results of Table 58 graphically. The steel stress at the service limit state is plotted for the SFRC tests and PC to demonstrate the effect of adding steel fibers to PC.

Table 58. Service Stresses (ksi) of S7505BTM## at Maximum Girder Spacing, 7 ft

Specimen	PC (Predicted)	SFRC (Experiment)	$\frac{SFRC_{EXP}}{PC_{PRED}}$
s7505BTM23	65	47	0.72
s7505BTM24	38	31	0.82
s7505BTM25	25	21	0.84
s7505BTM35	17	18	1.05
= Satisfactory steel stress at service limit			

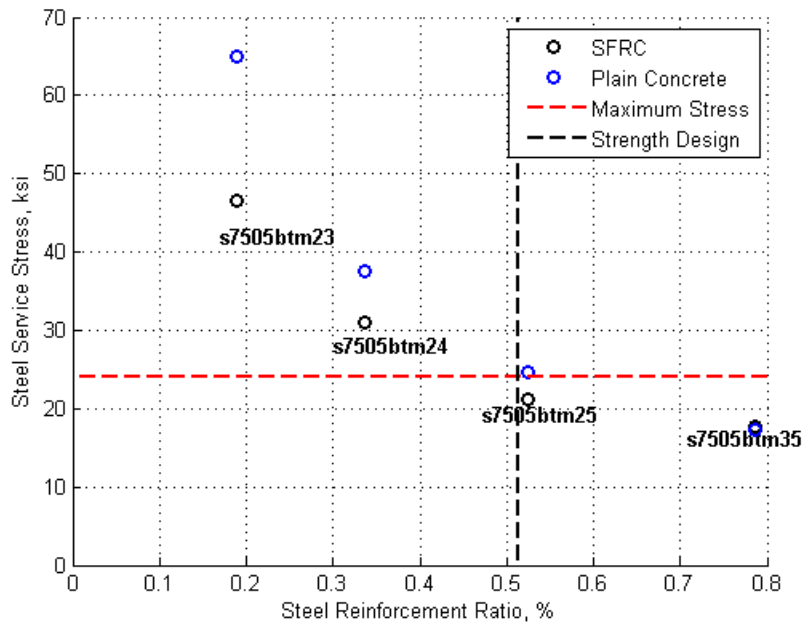


Figure 150. Service Performance of S7505BTM## at Maximum Girder Spacing, 7 ft

The traditional design for the strength limit state of girder spacing of 7 ft is a 7.5 in. deep PC strip with 2-#5 bars. The service limit state is not satisfied by this steel ratio as the predicted stress in the steel reinforcement is 25 ksi. Specimen s7505BTM25 represents the traditional strength design with steel fibers. As observed from the test results, introducing steel fibers to the traditional strength design reduces the stress in the steel reinforcement to an acceptable 21 ksi. The SFRC strips with a steel reinforcement ratio below the traditional strength design performed inadequately at the service limit state. Therefore, the service limit state will control the SFRC bridge deck design.

The service stresses presented shows that the benefit of SFRC in comparison to PC diminishes as the area of steel reinforcement increases. The least reinforced SFRC specimen, s7505BTM23, has a steel stress 28 percent less than the predicted steel stress for a PC strip with the same amount of steel reinforcement. The most reinforced SFRC specimen, s7505BTM35, has a steel stress 5 percent larger

than PC. As the section becomes more heavily reinforced, the steel reinforcement dominates the performance of the specimen. This trend can be observed by the vertical distance between the PC and SFRC data points in Figure 150. The vertical distance between data points decreases until the service stress of the SFRC experiments converge with the predicted service stress of the PC.

The maximum girder spacing corresponding to a 9.0 in. deep deck is 11.5 ft according to the ADOT design requirements. The service demand for girder spacing of 11.5 ft is used to evaluate the performance of the 9.0 in. deep specimens. The stress in the steel reinforcement at this limit state was predicted for PC using a moment-curvature analysis. The predicted steel stress for PC specimens is compared to the SFRC experimental stress at the service limit state in Table 59. Figure 151 presents the results of Table 58 graphically. The steel stress at the service limit state is plotted for the SFRC tests and PC to demonstrate the effect of adding steel fibers to PC.

The thicker slab strips demonstrate the same trends observed in the 7.5 in. deep strips analyzed based on demands of the maximum allowable girder spacing. The addition of steel fibers to a traditionally strength designed PC section improves the service performance and may satisfy the maximum service stress limit of 24 ksi. As demonstrated by Figure 151, the steel reinforcement ratio required for strength design with PC falls between two of the experimental tests. Test s9005BTM25 does not satisfy the service requirement while s9005BTM35 does satisfy the requirement. Interpolating between the two tests results in a service stress of approximately 26 ksi for the traditional strength designed section with SFRC.

The vertical distance between the SFRC and PC data points in Figure 151 does not exhibit the same trend as the 7.5 in. deep slab specimens. The volume of fibers used in the experimental tests does not significantly affect the service stress of the slab strip specimens with the second to least amount of steel reinforcement, s9005BTM24, due to the larger service moment demand.

Table 59. Service Stresses (ksi) of S9005BTM## at Maximum Girder Spacing, 11.5 ft

Specimen	PC (Predicted)	SFRC (Experiment)	$\frac{SFRC_{EXP}}{PC_{Pred}}$
s9005BTM23	-	65	-
s9005BTM24	50	49	0.98
s9005BTM25	33	29	0.76
s9005BTM35	23	21	0.81
	= Satisfactory steel stress at service limit		

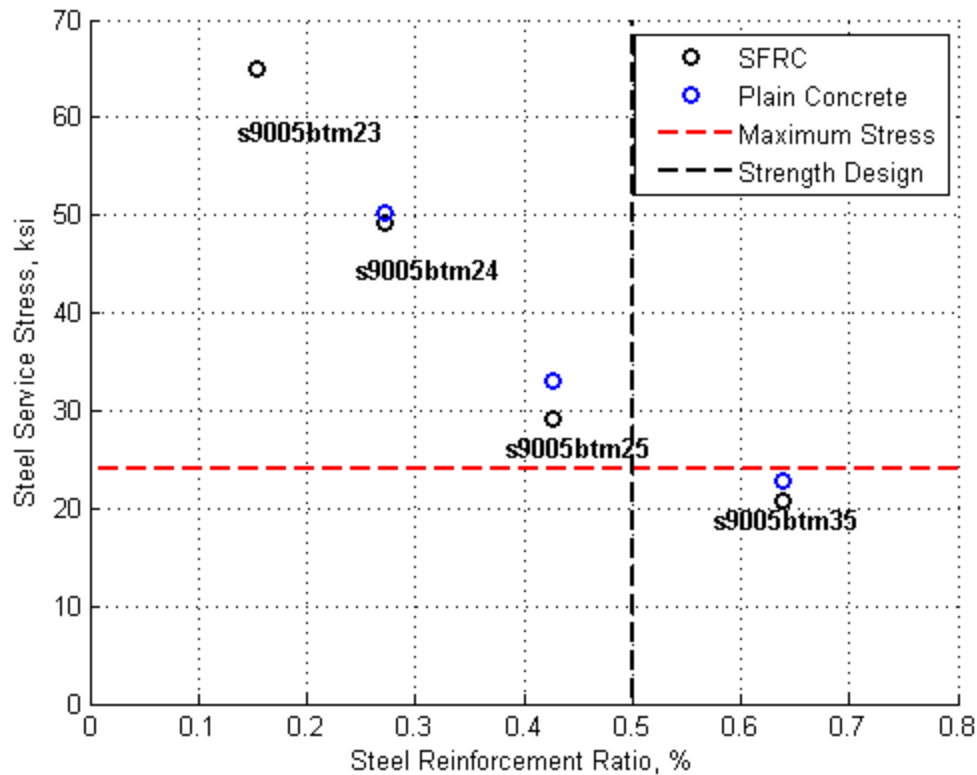


Figure 151. Service Performance of S9005BTM## at Maximum Girder Spacing, 11.5 ft

Maximum Girder Spacing Permitted

SFRC improves the performance of reinforced concrete bridges under both service and strength limit states. An analysis was conducted to determine the maximum permitted girder spacing for the s-series specimens. This was achieved by first calculating the service and strength moment demands for girder spacing between 4 ft and 15 ft based on ADOT design requirements. The moment corresponding to the steel service stress of 24 ksi was extracted from the SFRC experimental results. This moment is referred to as the service strength of the specimen. Additionally, the maximum capacity of the SFRC strips was extracted and is referred to as the ultimate strength of the specimen. The service strength and ultimate strength is then compared to the service and strength demands to determine the maximum permitted girder spacing for each specimen. Table 60 summarize the service and strength capacities of each strip SFRC specimen with steel reinforcement, and Table 61 demonstrate the maximum allowable girder spacing.

Table 60. Service and Strength Capacities of PC and SFRC

Specimen	Moment (k-ft)			
	Service		Strength	
	PC	SFRC	PC	SFRC
s7505BTM23	2.31	7.12	8.29	12.80
s7505BTM24	4.16	7.65	13.48	18.59
s7505BTM25	6.39	9.29	19.50	23.50
s7505BTM35	9.35	10.40	27.58	29.67
s7505CTR25	2.15	6.29	11.38	14.48
s7505CTR35	2.92	10.15	16.04	21.12
s9005BTM23	2.96	10.56	10.89	16.06
s9005BTM24	5.45	9.91	17.51	22.71
s9005BTM25	8.53	13.29	25.22	29.63
s9005BTM35	11.91	15.85	35.60	40.10

Table 61. Maximum Span Permitted for SFRC Slab strips

Specimen	Max Span (Nearest 0.25 ft)			
	Service		Strength	
	PC	SFRC	PC	SFRC
s7505BTM23	-	-	-	5.00
s7505BTM24	-	5.50	6.00	9.00
s7505BTM25	-	7.50	9.50	11.50
s7505BTM35	7.50	8.50	13.75	14.75
s7505CTR25	-	-	-	6.75
s7505CTR35	-	8.25	7.75	10.25
s9005BTM23	-	8.5	-	7.5
s9005BTM24	-	8	8.25	10.75
s9005BTM25	6.50	10.5	12.00	14.25
s9005BTM35	9.50	12.5	15+	15+

The addition of steel fibers at a rate of 0.5 percent by volume to the 7.5 in. deep slab strip sections increases the number of specimens with a maximum allowable girder spacing greater than 4.0 ft to four in comparison to one for a PC section. The increase in capacity allows for the removal of 1-#5 from S7505BTM35 while still maintaining sufficient strength to satisfy the service requirements for a girder spacing of 7.50 ft. Alternatively, the maximum girder spacing can be increased to 8.50 ft without the removal of any steel from S7505BTM35.

The service moment demand controls the design of the specimen, as demonstrated by Table 60. However, the benefits from SFRC are also presented for the ultimate strength capacity. Strip S7505BTM24 with SFRC allows for the maximum girder spacing to be increased by approximately 50 percent from 6.00 ft to 9.00 ft. The increase in ultimate strength capacity is not as great in more

heavily reinforced sections. This is likely a result of the section trending toward the balanced steel reinforcement ratio. As the section becomes more compression controlled, the tensile benefits of SFRC are less significant.

According to the ADOT Bridge Design Guidelines, the maximum girder spacing for a PC deck 9.0 in. deep is 11.50 ft. Only two PC specimens with steel reinforcement ratios tested in the 9.0 in. deep SFRC strips provide sufficient capacity for a girder spacing greater than 4.0 ft.

The addition of steel fibers at a rate of 0.5 percent by volume to the 9.0 in. deep slab strip sections increases the number of specimens with a maximum allowable girder spacing greater than 4.0 ft to include all four tests in comparison to two satisfactory PC sections. SFRC increases the capacity the maximum girder spacing for the service limit by 62 percent and 32 percent for S9005BTM25 and S9005BTM35, respectively.

Similar to the 7.5 in. deep sections, the service moment demand controls the design of the specimen. The ultimate capacity also demonstrates an increase with the addition of SFRC; however, the gains are not as significant as observed in the service moment capacities. The increase in the girder spacing for the ultimate limit state is only 19 percent for S9005BTM25 in comparison to its 62 percent increase in the maximum girder spacing for the service limit state.

Ultimately, a fiber dosage rate of 0.5 percent by volume is less influential at the ultimate limit state than the service limit state. However, the service limit state typically controls the design of reinforced concrete bridge decks. The addition of steel fibers would allow for a decrease in the area of steel reinforcement or the increase in girder spacing while still achieving adequate capacity at both the service and ultimate limit states.

SUMMARY

The purpose of the SFRC slab-strip tests was to confirm the observations made in the case studies and investigate the effect of adding steel fibers to structural concrete members. The program offered insight on the damage progression and strength enhancement of SFRC. This was achieved by constructing 18 slab-strip specimens of two different thicknesses and a varying amount and location of steel reinforcement. The varied parameters allow for identification of the impact of SFRC. Furthermore, the experimental results provide the capacity and service stress of the unit strips to be used in the large-scale bridge deck experiment. The following conclusions are made from the SFRC slab-strip experimental program:

- Steel fibers manage the width of cracks in the concrete prior to the failure criteria. Several cracks developed in the SFRC slab strips, but remained relatively small prior to the onset of crushing in the compression region of the strip and achievement of the specimen's maximum moment.
- The failure of SFRC strips localized in an individual crack. The fibers excel at bridging the cracks and delaying their growth. A hinge forms and the anchorage of the fibers begins to fail. All subsequent rotation and crack opening of the specimen occurs at critical crack.

- SFRC improves the performance of the slab strips under both the service and strength limit states.
- The effect of the steel fibers diminishes at higher ratios of steel reinforcement. The ratio between the residual force of the SFRC and the resultant force of the steel reinforcement decreases as the steel ratio increases. As a result, the influence from the SFRC is smaller.
- The service limit state controls the design of SFRC bridge decks. Adding fibers 0.5 percent by volume improves the service performance of a PC section designed for the strength limit state. The improvement is sufficient to satisfy the service limit state as well.
- The moment-curvature analysis used in the case study analysis accurately predicts service and strength performance of the slab strips.

CHAPTER 7. FULL-SCALE BRIDGE DECK TEST

INTRODUCTION

A full-scale bridge deck was designed and constructed to fully investigate the benefits of adding steel fibers to the concrete matrix when used in a two-way slab. The geometry of the bridge deck is representative of the minimum requirements of the ADOT Bridge Design Guidelines (2011). The reinforcement ratio of the full-scale specimen was chosen to satisfy the ADOT requirements for serviceability and strength capacity. This chapter details the experimental plan used to evaluate the full-scale specimen and analyze its moment capacity, deflection, cracking pattern, and failure mode. First, a summary of the geometry and design philosophy of the bridge deck is presented, followed by an overview of the test setup, instrumentation, and load patterns. Next, a summary of the observed behavior is presented. Finally, conclusions are made for each experiment. Chapter 9 presents analysis of experimental data.

BRIDGE DECK DESIGN

The full-scale specimen is a slab-beam bridge with two equal interior spans and an overhang on each side. Figure 152 shows the geometry and reinforcement details. The specimen has a footprint of 16 ft (4877 mm) by 18 ft (5486 mm) and is supported by three traditionally reinforced concrete beams without steel fibers. The supporting beams are spaced at 6 ft (1829 mm) on center, and the overhangs are 2.5 ft (762 mm) from the outside face of the beams. The overall dimensions of the full-scale specimen were based on the limitations of the testing facility and previous experimental studies (Mander et al. 2010; Pirayeh Gar et al. 2013) that will serve as reference specimens for the evaluation of the SFRC bridge deck. The deck thickness and steel reinforcement was based on current ADOT design practices. The minimum deck thickness for a 6 ft (1829 mm) spacing is 7.5 in. (190.5 mm), excluding a mandatory 0.5 in. (12.7 mm) wearing surface.

The deck is secured to each beam by stirrups spaced at 7.5 in. (190.5 mm). The entire specimen was supported directly on the laboratory's strong floor to decouple the longitudinal bending of the support girders from the response of the bridge deck. Each reinforced concrete beam was secured to the strong floor by threaded rods.

The design of the SFRC bridge deck is based on findings of the tests presented in Chapter 6. A live load factor of 1.75 and impact load factor of 1.33 is applied to the moment demand obtained from AASHTO LRFD Section 4 - Appendix A (2014) to determine the moment demand for the strength limit state, 11.2 k-ft/ft. The strength demand and maximum allowable stress, 24 ksi, for the service limit state were used in selecting the steel reinforcement for the SFRC bridge deck. The ADOT design with traditional reinforced concrete required to satisfy the service stress is #5 bars at 6.5 in. (165.1 mm) in the negative moment region and #5 at 8 in. in the positive moment region. The steel reinforcement ratio for the traditional design in the negative moment region is 0.7 percent. Analysis indicates a lower percentage of traditional reinforcement is possible when 0.5 percent fiber by volume is used. Specimen s7505BTM24 #4 bar at 9 in. (228.6 mm) provides the necessary service and strength performance and was selected

for the design in the transverse direction of the SFRC bridge deck. The SFRC design provides a 53 percent reduction in the amount of traditional reinforcement.

The materials for the bridge deck specimen are the same as those previously presented with the slab strip test program. Support beams were constructed PC (Mix M3). The bridge deck was constructed with 0.5 percent SFRC (Mix M4). All reinforcement was #4 bars. Details of material properties can be found in Chapter 6.

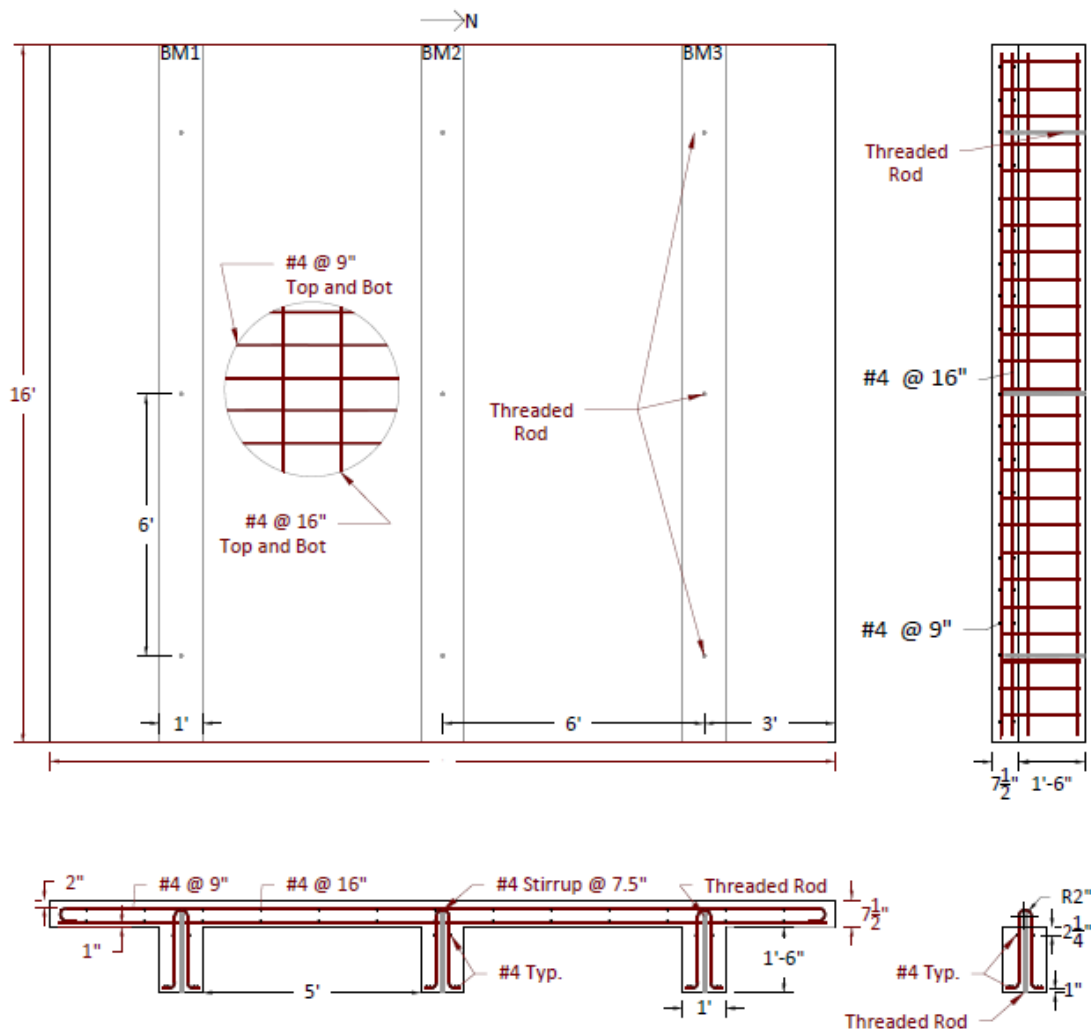


Figure 152. Full-Scale SFRC Bridge Deck Plan

TEST SETUP AND INSTRUMENTATION

Figure 153 shows the experimental test setup. The size and location of the applied loads were determined based on AASHTO LRFD Bridge Design Specifications (2014) and the HS20 design truck. The wheel footprint of an HS20 truck is 10 by 20 in. (254 × 508 mm). Each test was conducted by applying a monotonically increasing load using a 600 kip (2669 kN) hydraulic jack. A load cell was installed in-line with the actuator to record the applied force. Loading was paused at predetermined intervals to

document crack progression on the top of the deck. Cracks on the bottom were only recorded after failure and unloading of the specimen.

The deck was tested in four locations (Figure 154). Both LP1 and LP4 represent an individual wheel applied at the mid span transversely. The loading plate was centered 47 in. (1194 mm) from the free edge of the deck longitudinally. Load pattern LP2 represents a tandem axle with wheel footprints spaced 4 ft (1219 mm) on center. LP2 was centered in both the longitudinal and transverse directions of the bridge deck. Load pattern, LP3, was applied to the south overhang at the longitudinal center of the bridge. LP3, while not an ADOT design requirement, provides an additional comparison to two prior bridge tests (Mander et al. 2010; Pirayeh Gar et al. 2013) with the same dimensions.

String potentiometers were installed below each load point at 12 in. (304.8 mm) intervals in both the longitudinal and transverse directions to record the deflection of the SFRC deck. Strain gauges (locations shown in Figure 155) were installed on the traditional steel reinforcement to determine the steel stress at locations of high positive and negative moments. For LP2, the strain gages are misaligned from the load points due to a change in load plan following construction of the specimen.



Figure 153. Full-Scale Specimen Test Setup – LP2

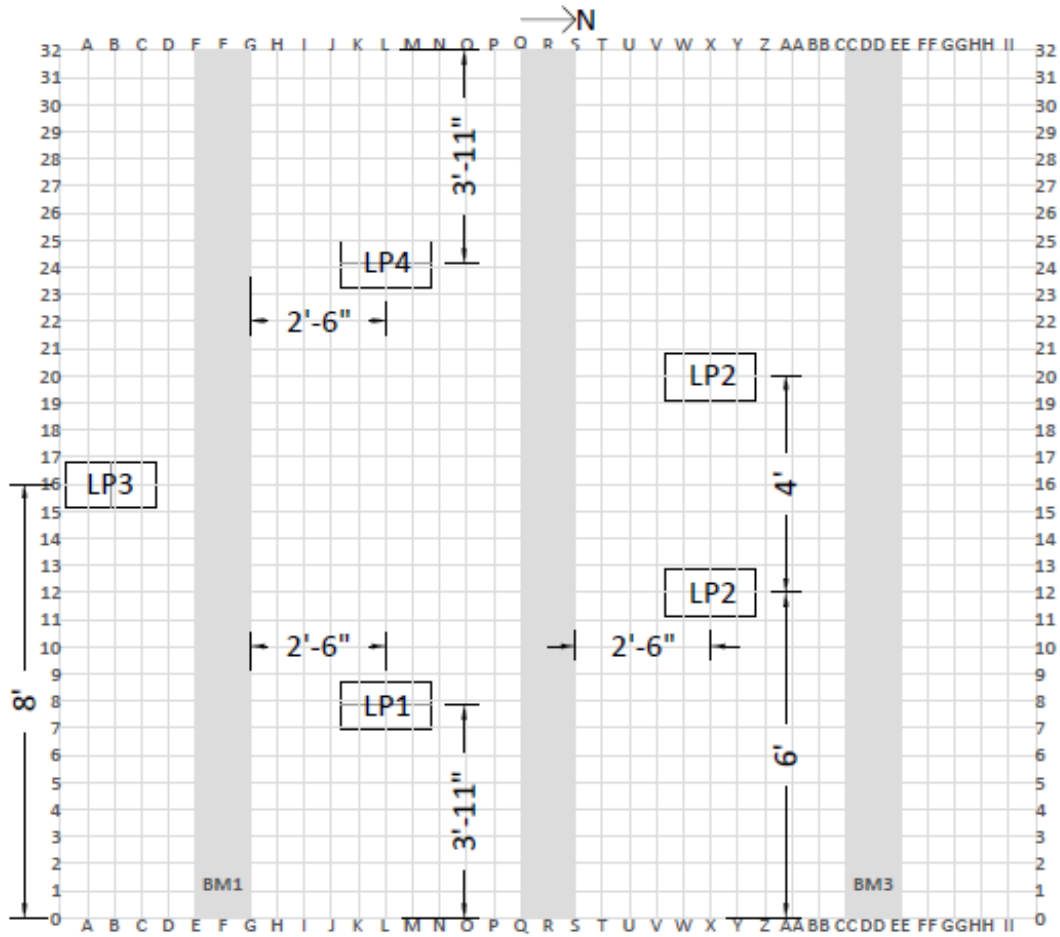


Figure 154. AASHTO Load Patterns Tested on Bridge Deck

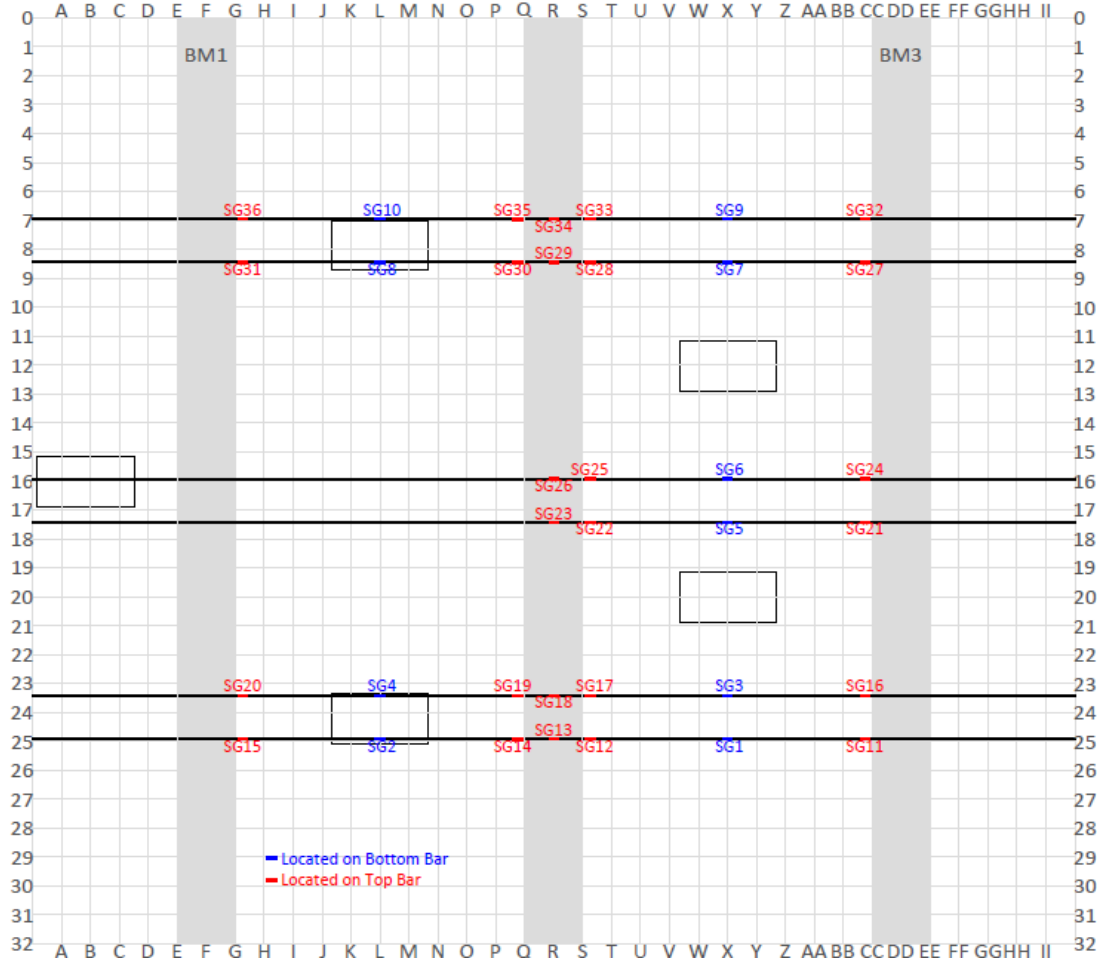


Figure 155. Elevation View of Strain Gauge Locations for Bridge Deck

EXPERIMENTAL TEST RESULTS

LP1 – Individual Wheel

Loading of LP1 was conducted in two sessions. In the first session, the load was increased to 175 kips (778 kN) and then unloaded. In the second, the test was loaded to failure. The first crack was observed at 70 kips (311 kN). As the load increased, additional cracks formed and propagated to create an elongated fan failure mechanism. The specimen achieved a maximum load of 203 kips (903 kN) before sudden failure occurred when the load plate punched through the deck (Figure 156). Figure 157 shows the final crack pattern observed for LP1. Light cracks indicate the cracks on the bottom of the bridge deck.

The first cracks initiated at Grid G (crack South1) and Grid Q (crack North1). The cracks formed on the top surface of the deck above the inside face of the adjacent support beams. They initiated adjacent to the steel plate on Grid 25 and propagated east and west as the load was increased. An additional crack was observed north of crack North1 at 125 kips (556 kN) and extended from the free edge of the deck to

Grid 19. During the final load step of the first session, the crack along Grid S, North2, began to turn south and traverse over the support beam into the loaded span.

No significant changes were observed during the second session prior to reloading the specimen to a load of 160 kips (712 kN). At this interval, a third crack, North3, on Grid P was observed. As the load was further increased, the four primary cracks continued to propagate in the east-west direction. At a load of 190 kips (845 kN), the portion of the primary cracks west of the load point began to turn perpendicular to the support beams. The curving of the cracks toward the north-south direction is consistent with the expected radial-fan mechanism. At the final load step, a crack was observed at Grid 15 and was orientated approximately 90° to the support beam. The portion of the primary cracks to the east side of the load point did not demonstrate this same behavior. They propagated parallel to the support beams until they met the free end of the deck. As a result, the fan mechanism did not occur on the east portion of the failure plane. After the completion of the test, the cracks on the underside of the bridge deck were mapped and recorded. The bottom cracks outlined the loading plate and propagated outward. The cracks on the west side of the load provided the radial cracks for the fan-mechanism while the cracks on the east side of the load continued approximately parallel to the beams as would be expected in a one-way slab.

Figure 158 shows the load-deflection relationship for LP1. Three displacements are shown. The transducer directly below the load disengaged from the deck surface at a displacement of 0.5 in. (12.7 mm). The transducers to the east and west are included to provide data at large displacements. Solid lines in Figure 158 indicate the first loading session of the specimen. Dashed lines indicate the second loading session. Figure 159 and Figure 160 show the deflected shape of the deck in the transverse and longitudinal directions.

The initial stiffness prior to a load of 50 kips (222 kN) is unknown due to a rapid increase in the applied load at the start of the test and the interval at which data were recorded. As a result, the pressure valves used to power the actuator were adjusted to slow the loading rate of the specimen. The force-deflection curve shows a change in its slope at approximately 70 kips (311 kN) indicating a reduction in the specimen's stiffness. This observation is consistent with the first cracks found during the visual inspection of the deck after this load step. The slab deflected approximately 0.1 in. (2.5 mm) prior to the formation of a crack.

At the service demand of 16 kips, the deflection of the specimen is negligible. At the strength demand of 37 kips, the deflection of the specimen is 0.1 in. As the load increases, the stiffness of the bridge is reduced and cracks begin to open resulting in larger deflections. The slope of the deflected shape in the transverse direction is larger due to the restraint provided by the support beams. The stress in the steel reinforcement at the service demand was 1.6 ksi.



Figure 156. SFRC Bridge Deck Failure due to LP1

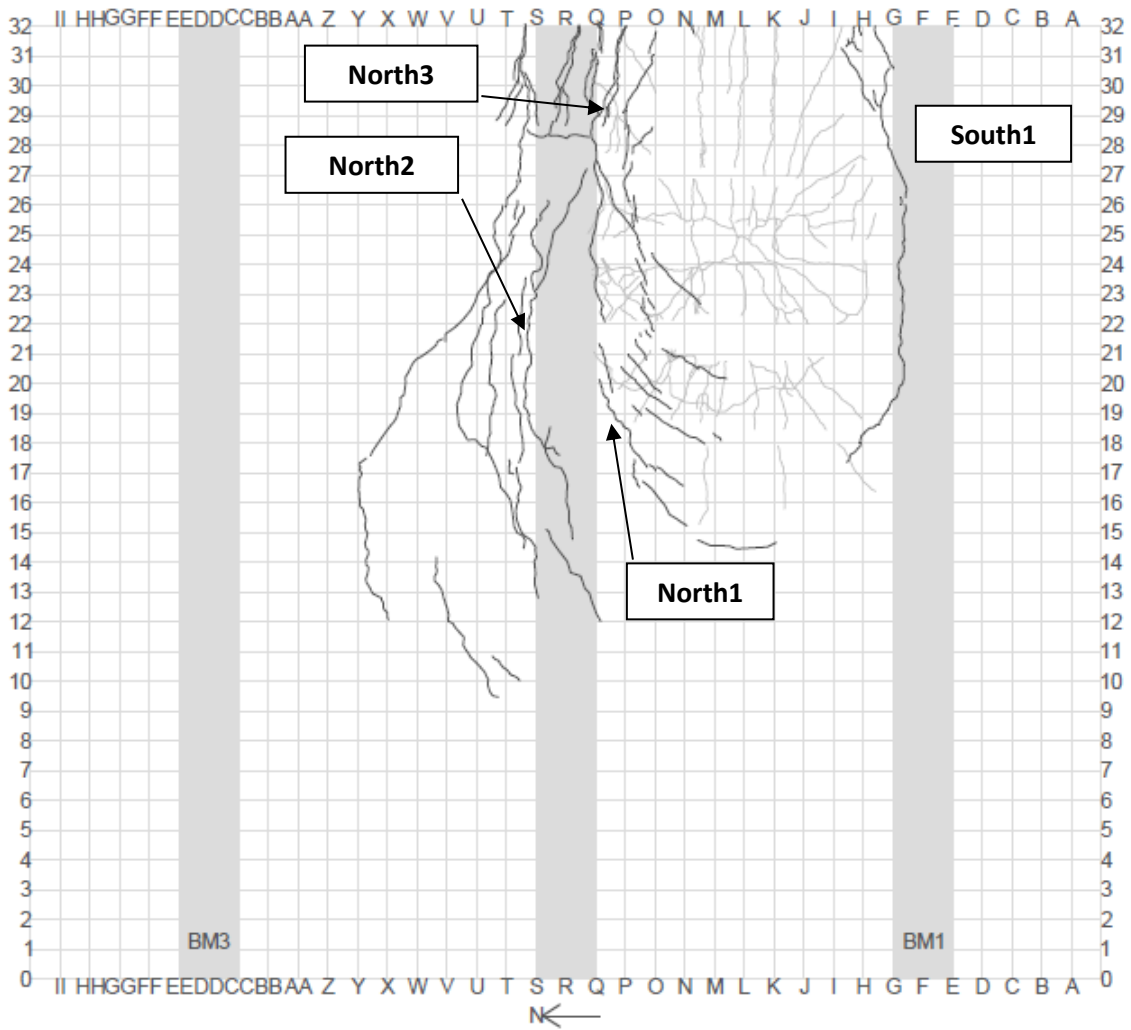


Figure 157. Final Crack Pattern—LP1

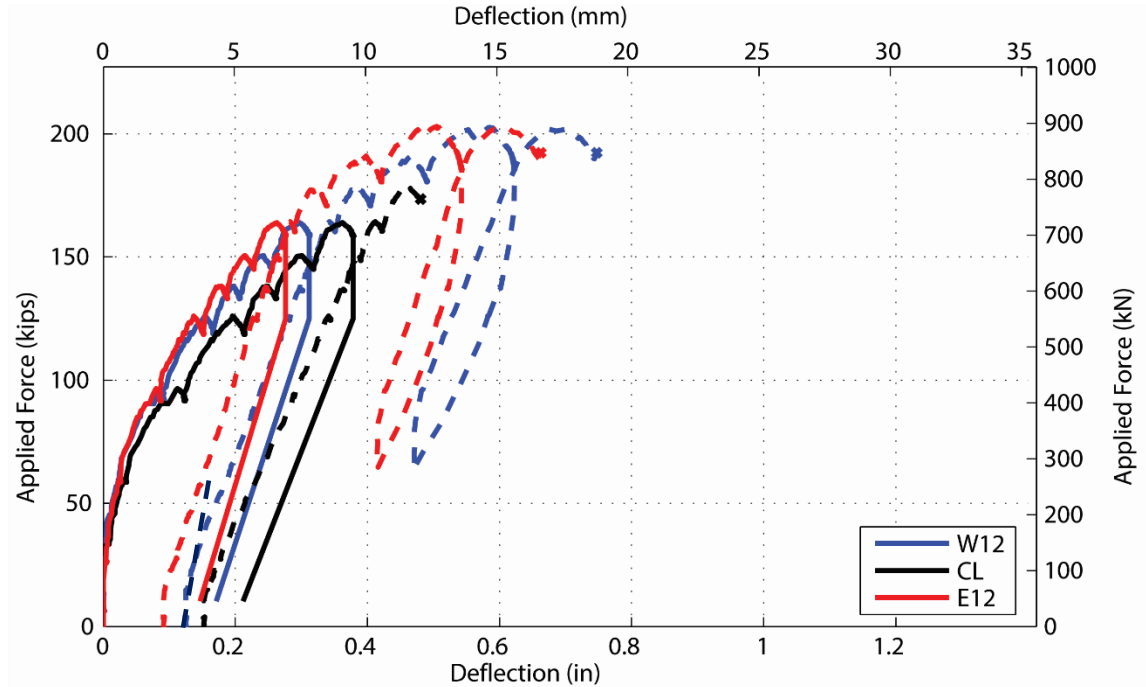


Figure 158. Force vs. Deflection for LP1 Solid for First Session and Dashed Lines for Second Session

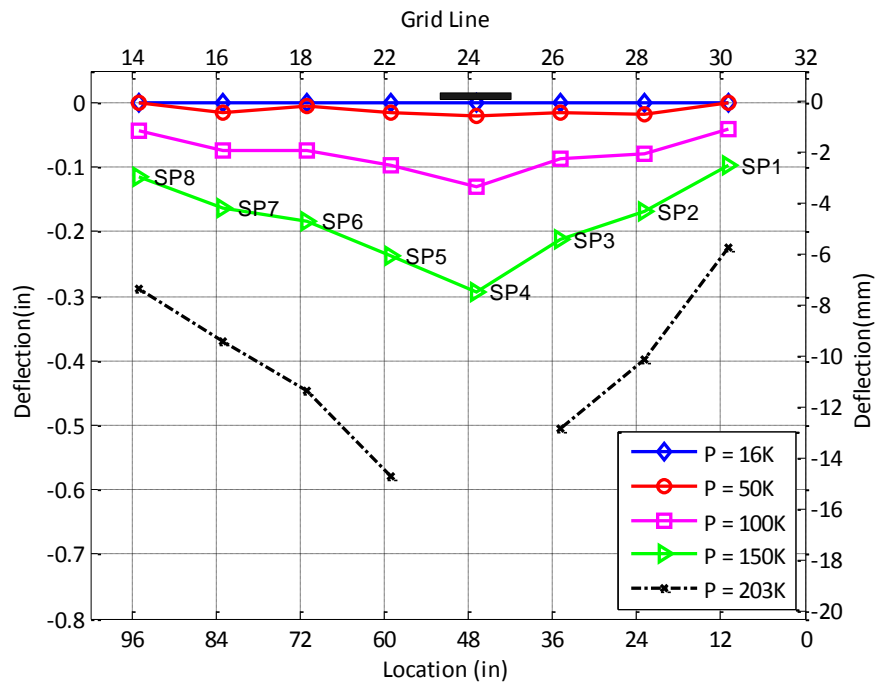


Figure 159. Deflection Profile of LP1—Longitudinal Direction

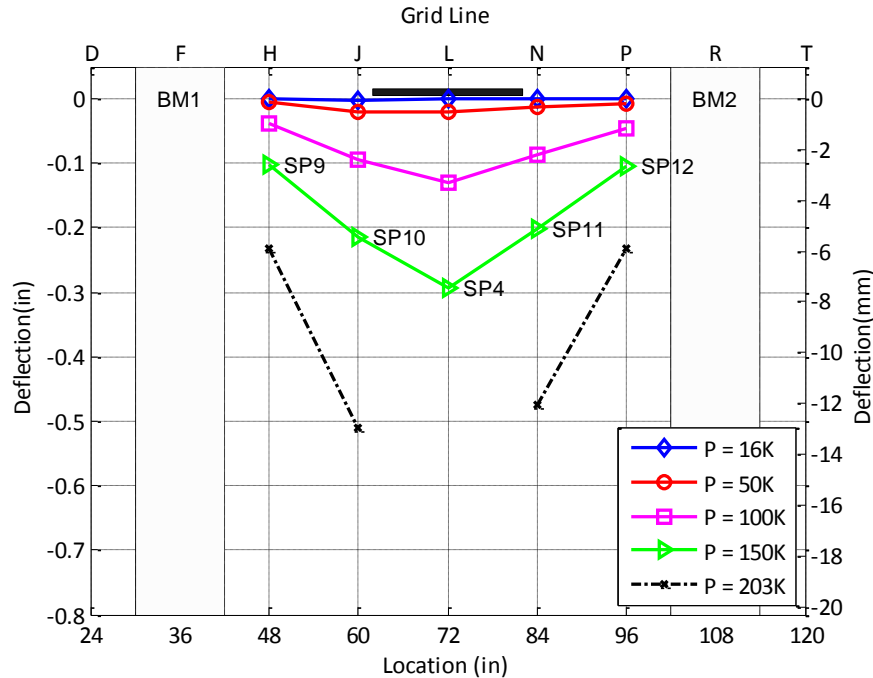


Figure 160. Deflection Profile of LP1—Transverse Direction

LP2 – Tandem Axle

For LP2, the force was applied to a steel wide flange beam that distributed the load between two load points spaced 4 ft apart. All data reported for LP2 is for each individual load point. Test LP2 was divided into two sessions. The first session was concluded at approximately 105 kips and the deck unloaded. The second session loaded the deck until failure occurred when one of the loading plates punched through the deck at a load of 185 kips (823 kN). Figure 161 shows the final crack pattern of LP2; existing cracks from LP1 are not included for clarity.

The extent of cracking from the first test, LP1, impacted the onset of cracking and deflection of LP2. At the conclusion of LP1, a crack on the north side of the middle beam had extended through the mid-point of LP2. In addition, a crack on Grid S, or the north face of beam 2, had extended beyond LP2 (Figure 162). The first new crack on the top surface of the deck, crack South1, was observed at 75 kips and a deflection of 0.27 in. The crack initiated south of the load point at the free edge of the deck and Grid Q and extended 102 in. to Grids M and 17. The first crack north of the load points, North1, was observed at approximately 100 kips (445 kN).

During the second session, no changes to the deck were observed prior to achieving a load of approximately 110 kips (489 kN). A slight extension of the existing cracks was observed at this time. The cracks continued to propagate east-west as the load increased. During the next load step, several string potentiometers adjacent to the loading points began to dislodge from the deck due to damage of the bottom side of the deck. At 130 kips (578 kN), the cracks south of the load point began to turn

perpendicular to the support beams. This behavior became more apparent at 160 kips (712 kN) (Figure 165). Crushing was observed beneath the steel beam at a load of 171 kips (Figure 163). By the conclusion of the test, the crushed region of concrete extended 24 in. west of the west load point.

After the failure of the specimen under LP2, the cracks on the bottom of the deck were mapped. The failure pattern observed on both the top and bottom surfaces are consistent with the expected fan pattern. The negative moment cracks on the top surface propagated parallel to the load points before curving inward to the east and west of the load points forming the outer edge of the fan-mechanism. Radial cracks were observed on the bottom surface east and west of the load points while cracks parallel to the support beams connected the two load points in the positive moment region.

Figure 166 shows the load-deflection relationship for LP2. Three displacements are shown in the figure. The transducer directly below the load, SP6, dislodges from the deck surface at a displacement of 0.5 in. The transducers to the east and west of SP6, SP5, and SP7, respectively, are included to provide data at large displacements. The string potentiometer names are indicated by their direction and distance from the center string potentiometer. Solid lines in Figure 166 indicate the first loading session of the specimen. Dashed lines indicate the second loading session. Figure 167 through Figure 169 present the deflected shape in the transverse and longitudinal directions.

The initial stiffness of the bridge deck is approximately 700 kip/in. and changes at approximately 23 kips (102 kN). As no new cracks had formed, this stiffness change is attributed to the opening of the LP1 cracks. The slope of the force-deflection curve changes again at approximately 70 kips (311 kips) and is consistent with the formation of new cracks. At the service demand of 16 kips (71.2 kN), the deflection of the specimen is approximately 0.03 in. (0.76 mm). As the load increases, the stiffness of the bridge is reduced and cracks begin to open resulting in larger deflections.

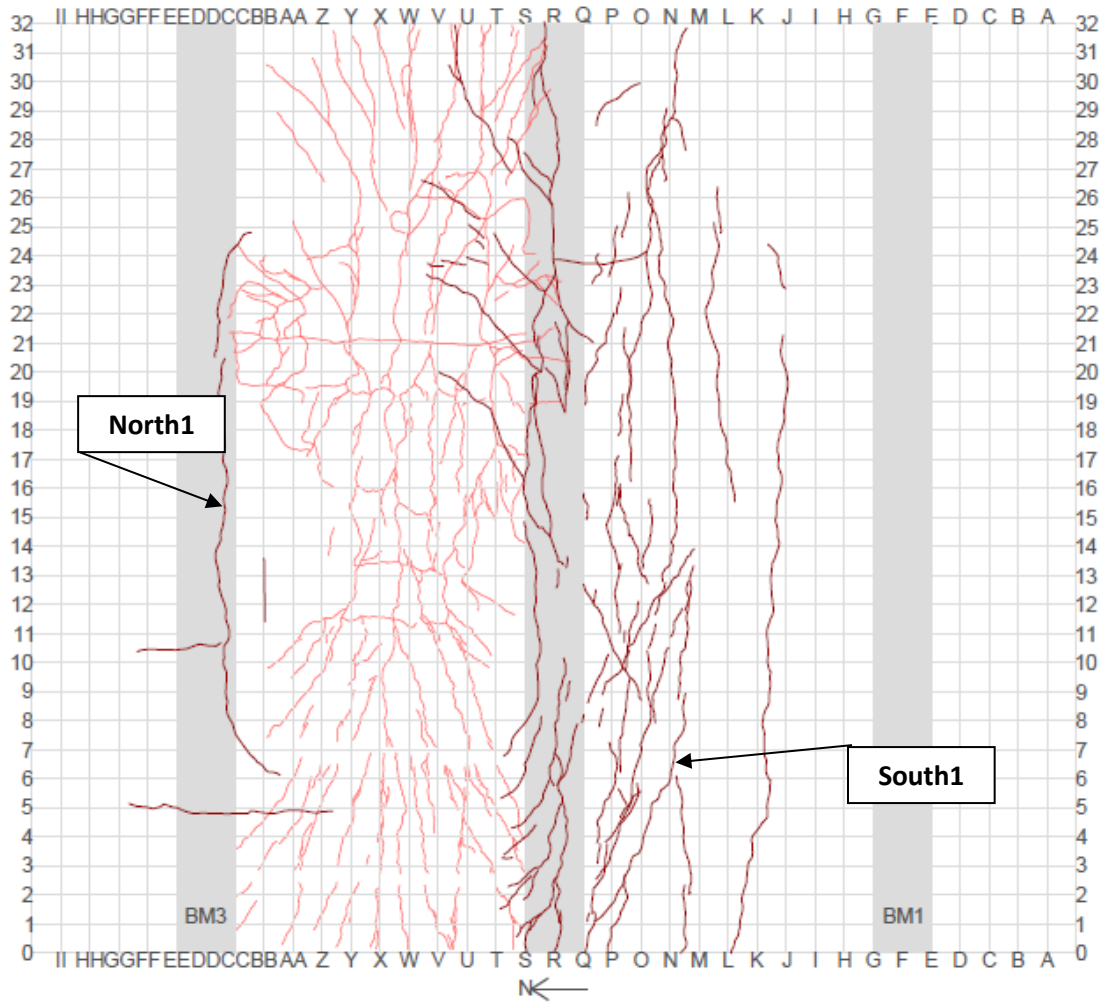


Figure 161. Final Crack Pattern – LP2

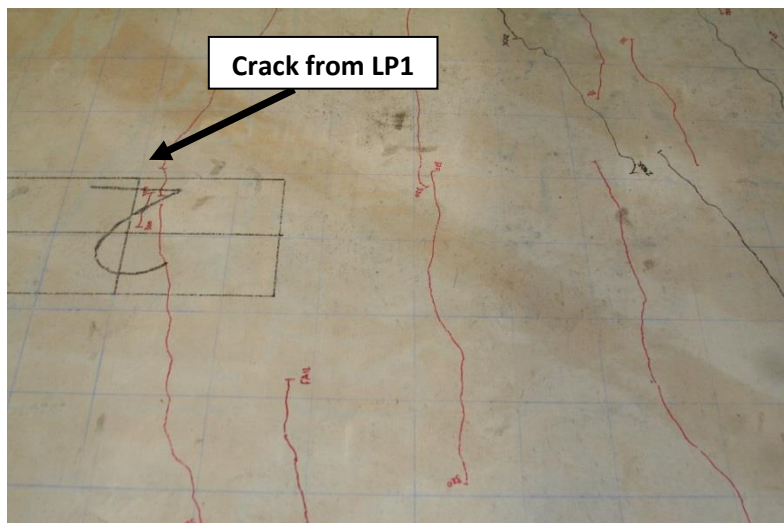


Figure 162. Influence of LP1 Cracks on LP2—Crack Extends through LP2

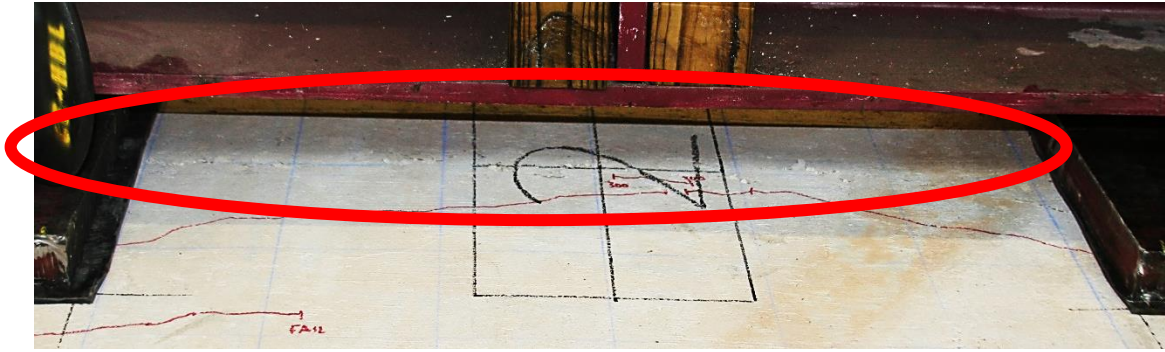


Figure 163. Crushed Region Extends between Both Load Points

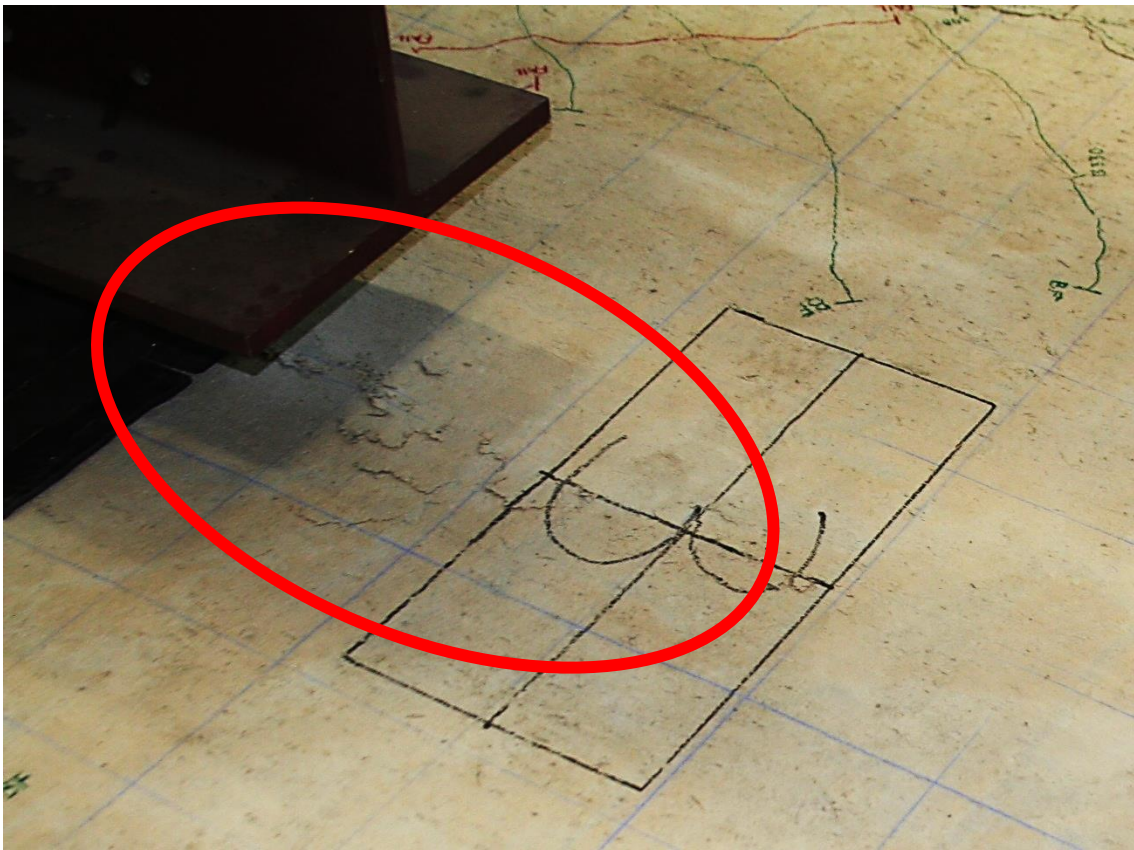


Figure 164. Crushing Failure Extends 24 in Passed LP2

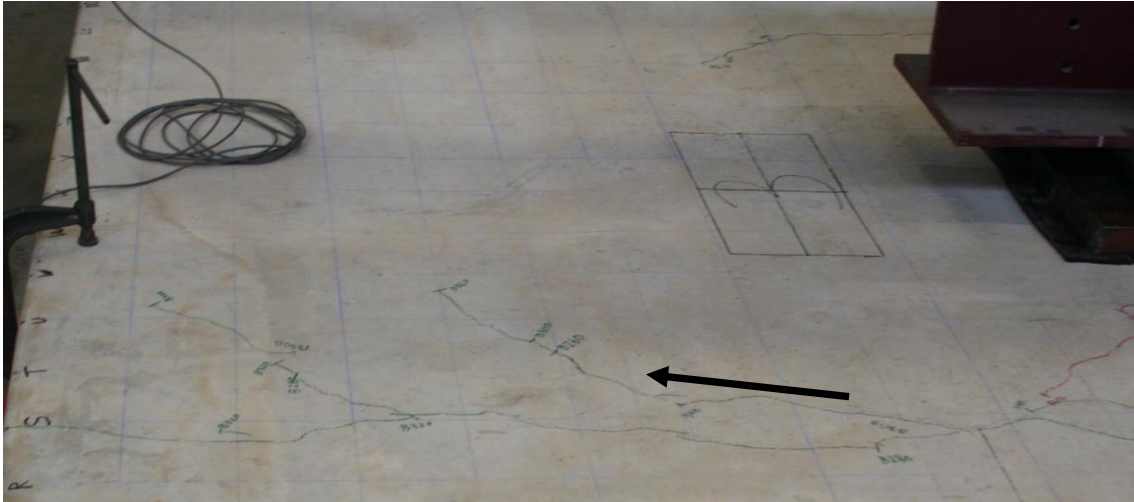


Figure 165. Turning of Negative Moment Cracks – LP2

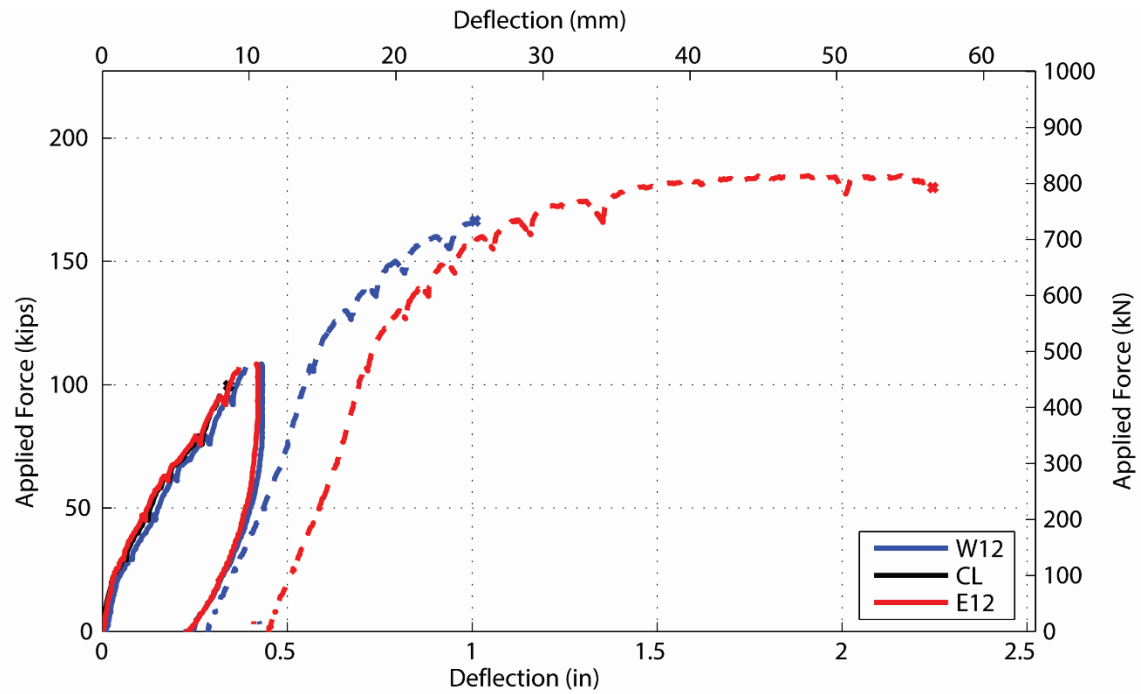


Figure 166. Force vs. Deflection for LP2 Solid for First Session and Dashed Lines for Second Session

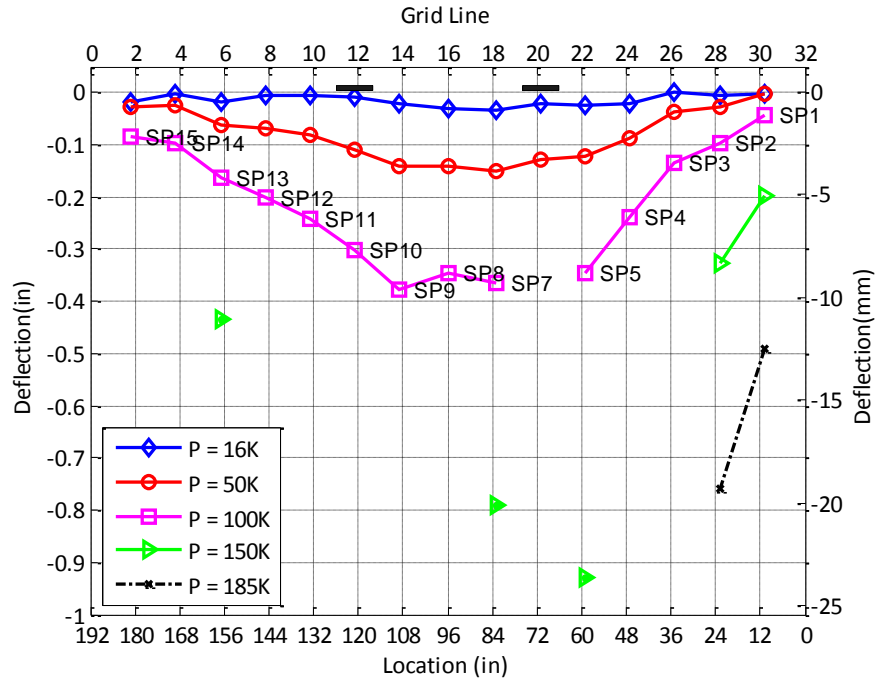


Figure 167. Deflection Profile of LP2—Longitudinal Direction

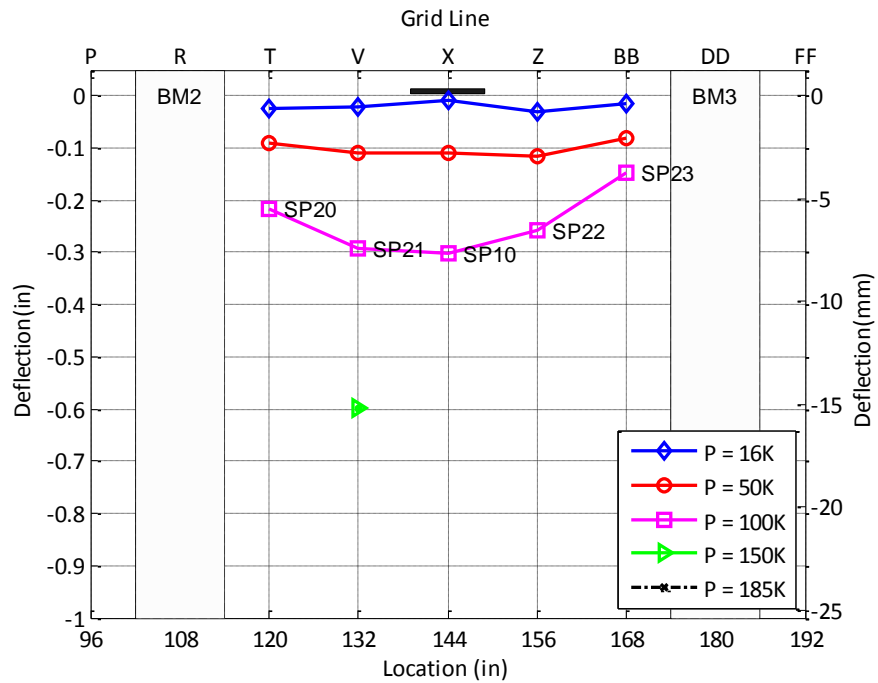


Figure 168. Deflection Profile of LP2—Transverse Direction, West Load Point

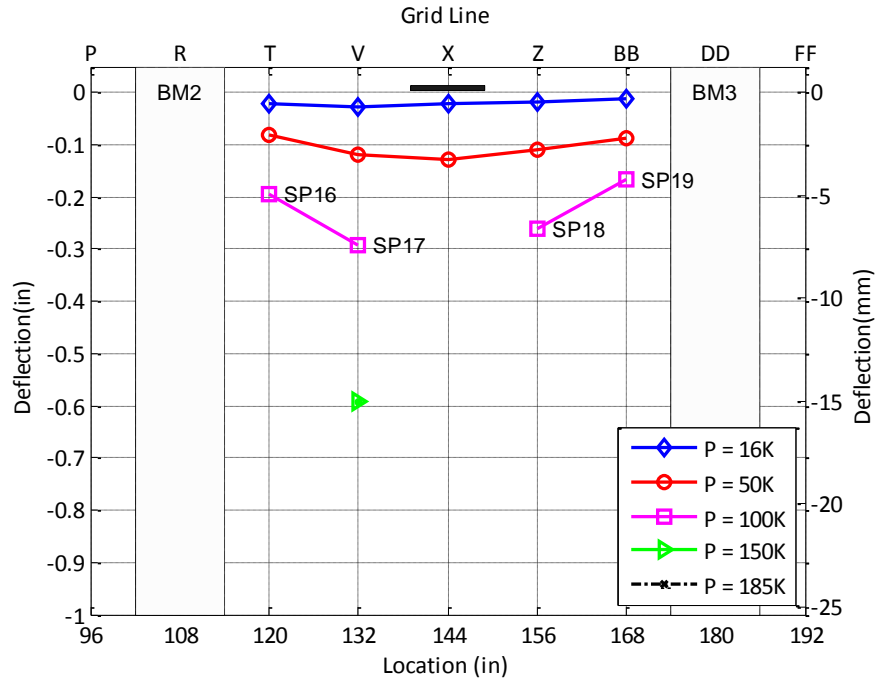


Figure 169. Deflection Profile of LP2—Transverse Direction, East Load Point

LP3 – Overhang Single Axle

Test LP3 was located on the center of the south overhang of the specimen. The test occurred in a single session and continued until 96 kips (427 kN) when the specimen exhibited significant damage (Figure 170). Test LP3 achieved a maximum load of 96 kips (427 kN). The test was concluded due to the extreme damage of the specimen and not a sudden failure of the concrete like in the interior load points.

Figure 171 shows the crack pattern for LP3. Initially, concentric cracks formed at support beam 1 and propagated at approximately 45° toward the free edge of the deck. At failure, cracks on the edge of the deck opened significantly and the panel directly beneath the steel plate was only connected via the steel reinforcement bars.

Figure 172 shows the load-deflection relationship for LP3. Three displacements are shown in the figure: SP5 (E12), SP6 (CL), and W12. The initial stiffness of the full-scale specimen is approximately 225 kip/in. and changes at approximately 30 kips (133 kN). The change in the stiffness at 30 kips (133 kN) is consistent with the observation of the first major cracks observed when the test was paused at 40 kips (178 kN) for inspection. Figure 173 and Figure 174 show the deflected shape in the transverse and longitudinal directions.



Figure 170. Damage at End of LP3 Test

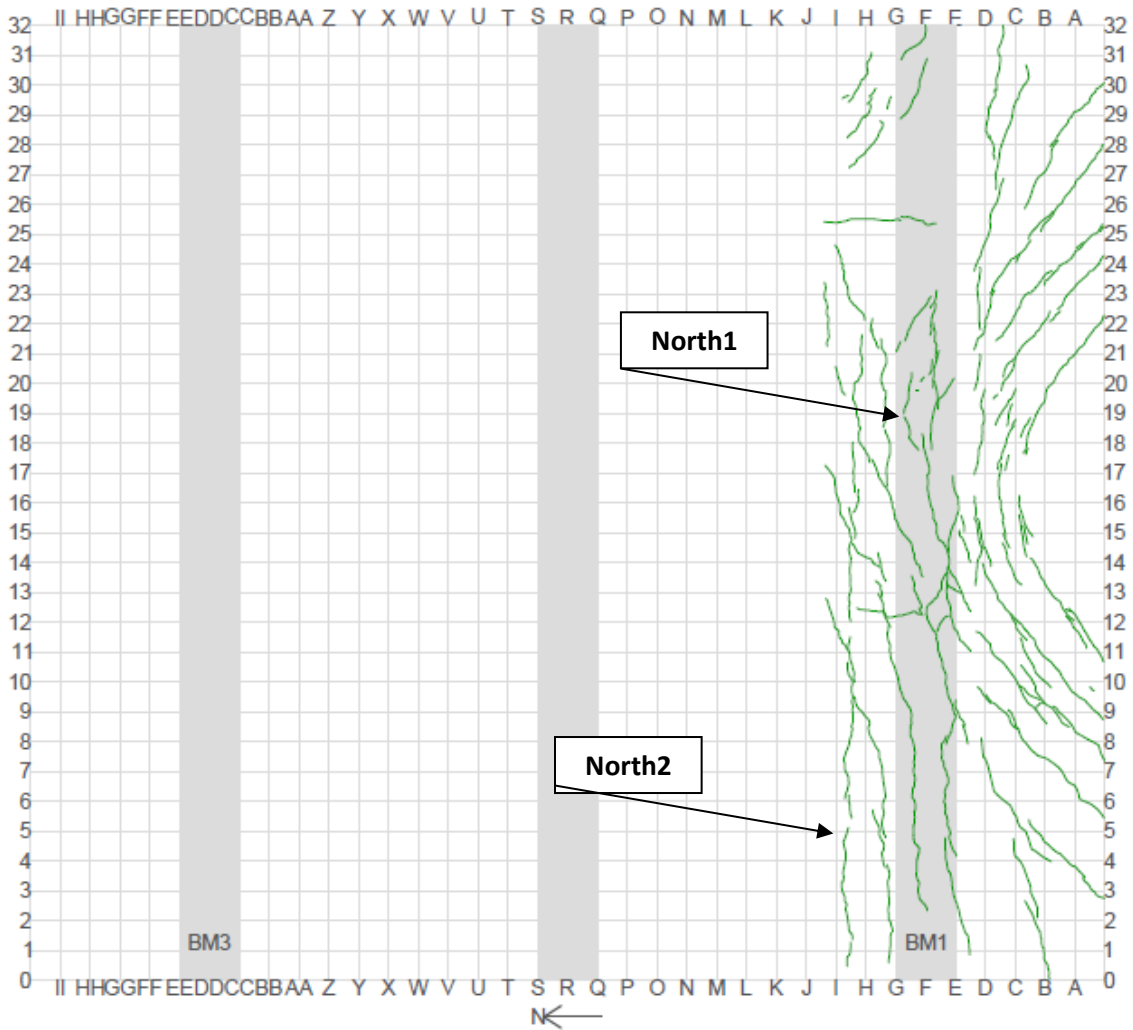


Figure 171. Final Crack Pattern – LP3

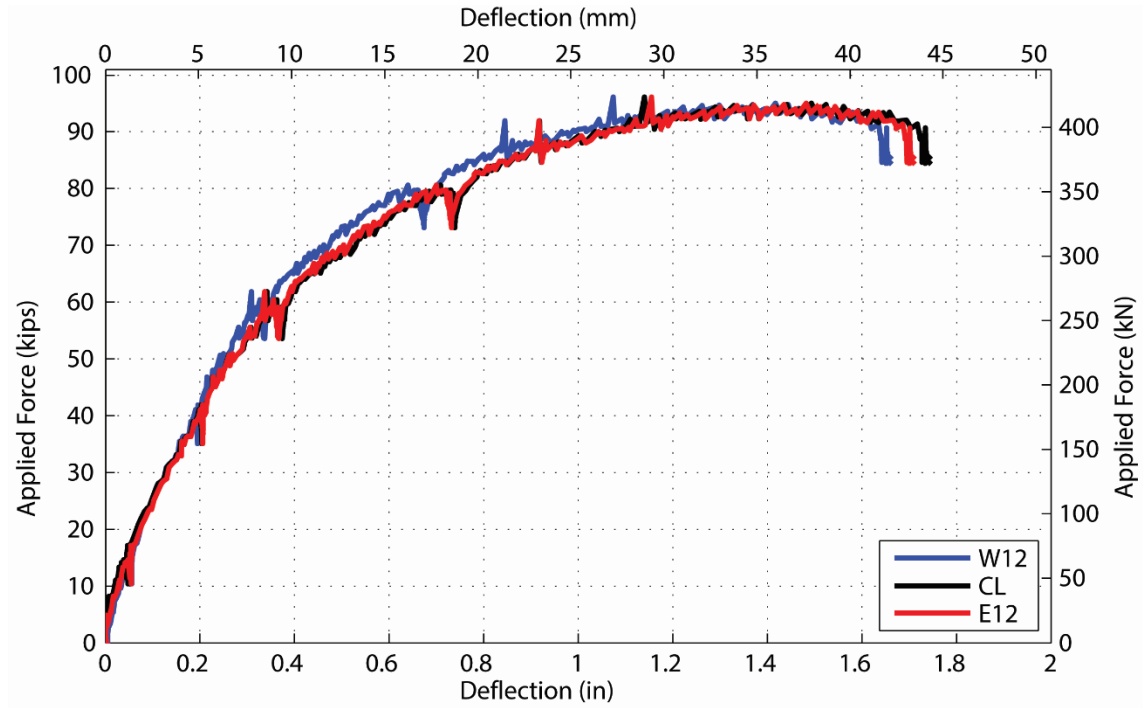


Figure 172. Force vs. Deflection for LP3

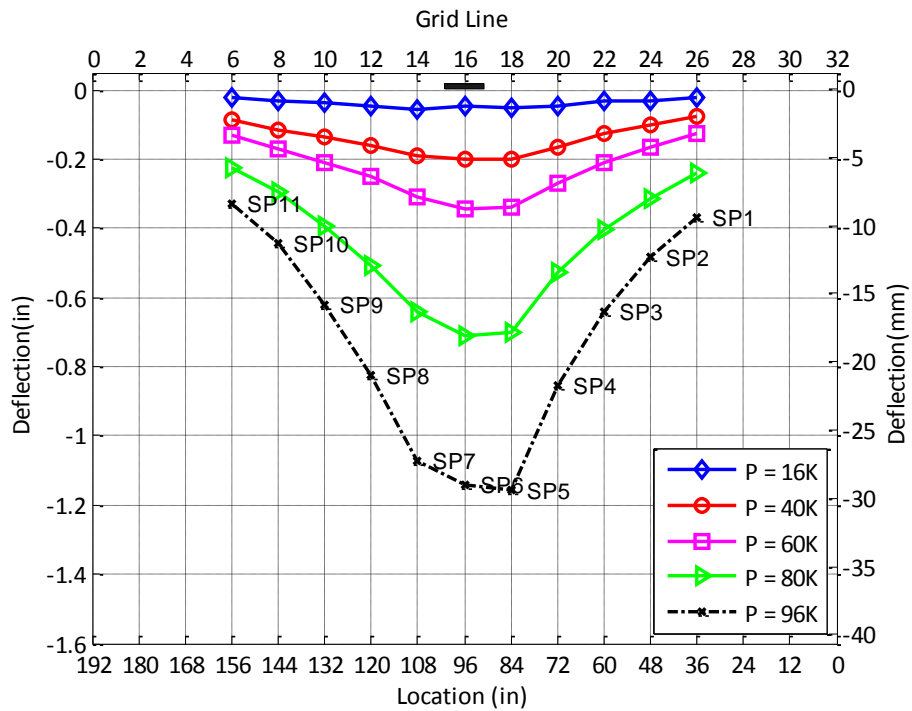


Figure 173. Deflection Profile of LP3—Longitudinal Direction

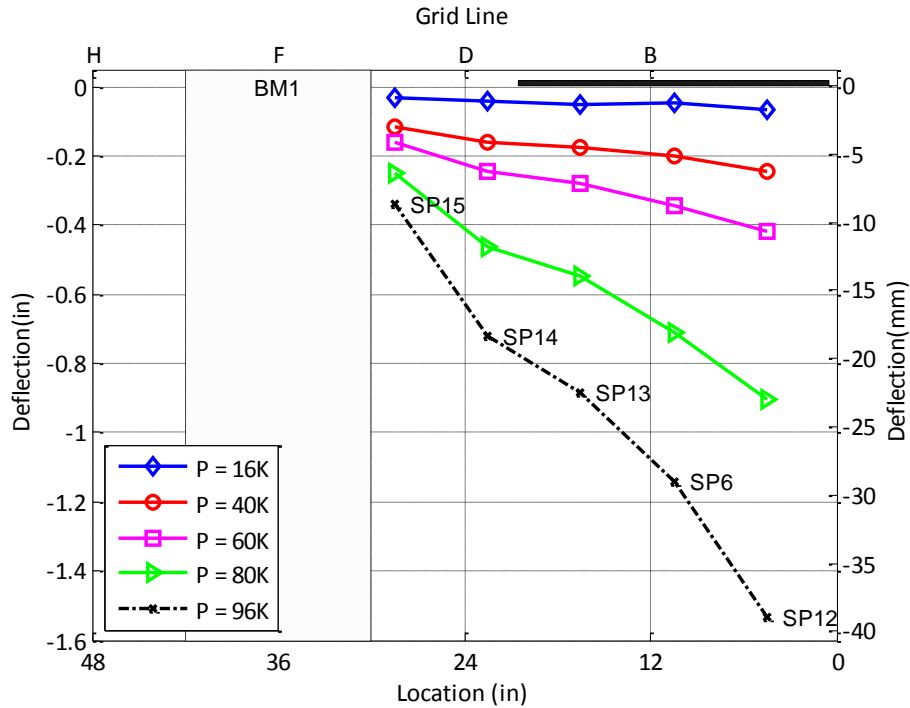


Figure 174. Deflection Profile of LP3—Transverse Direction

LP4 – Individual Wheel

LP4 was the same loading pattern tested in LP1. Loads were applied in a single session. Pre-existing cracks from previous load patterns were located within the influence area of LP4 and opened prior to initiation of new cracks at 100 kips (445 kN). LP4 achieved the same maximum load as LP1, 203 kips, when failure occurred due to punching of the load plate through the deck. Figure 175 shows the final crack pattern.

Figure 176 shows the load-deflection relationship for LP4. Three displacements are shown in the figure: SP7 (E12), SP8 (CL), and SP9 (W12). Figure 177 and Figure 178 show the deflected shape in the transverse and longitudinal directions.

The initial stiffness of the full-scale specimen is approximately 585 kip/in. and changes at approximately 75 kips (333.6 kN). The first extension of existing cracks was observed during the load step to 100 kips (445 kN); however, significant cracking was also present due to the prior tests. At the service demand of 16 kips, the deflection of the specimen is approximately 0.06 in. As the load increases, the stiffness of the structure decreases due to the opening of the cracks resulting in larger deflections. The deflections observed from LP4 are approximately 60 percent larger than those measured during LP1 at the same load points.

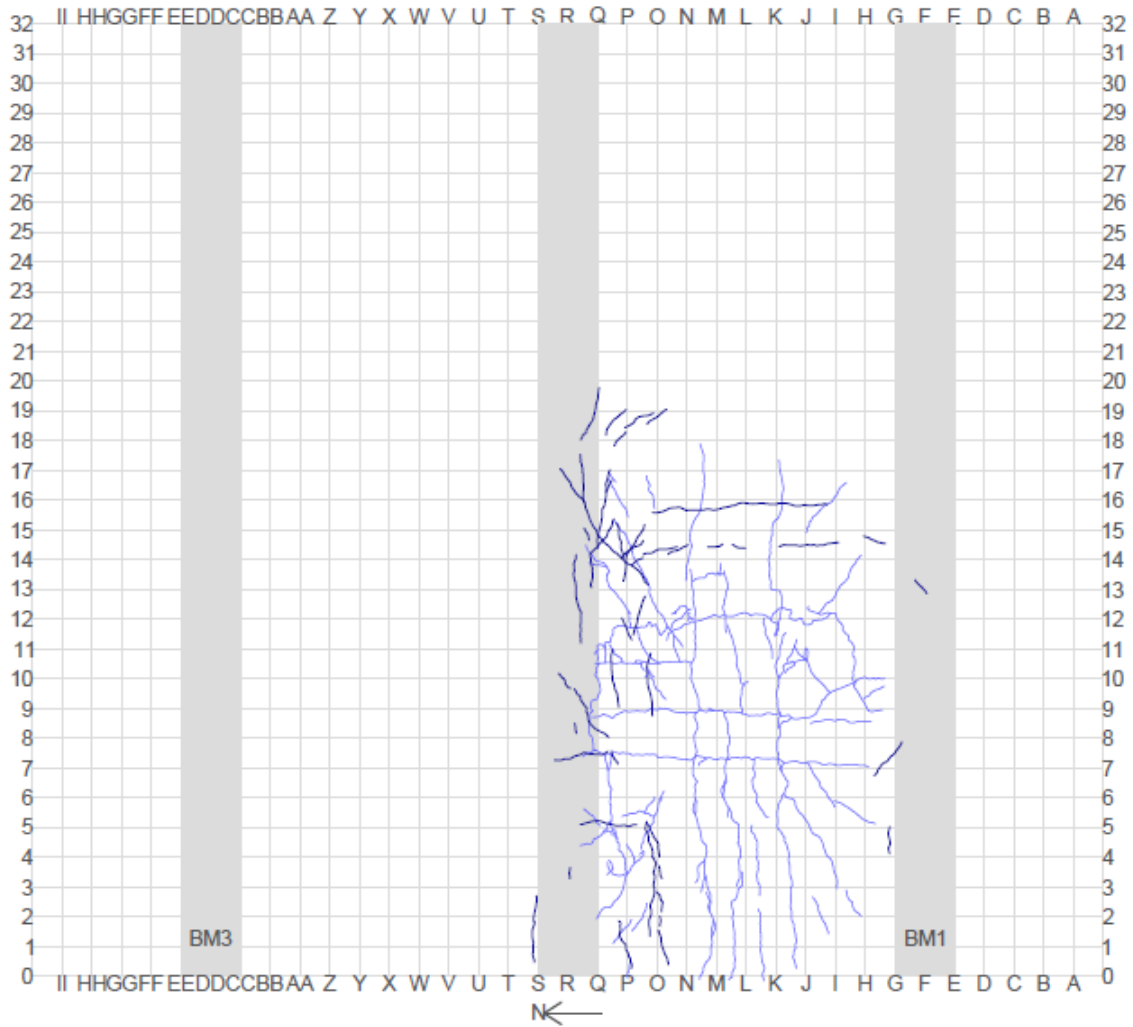


Figure 175. Final Crack Pattern for LP4

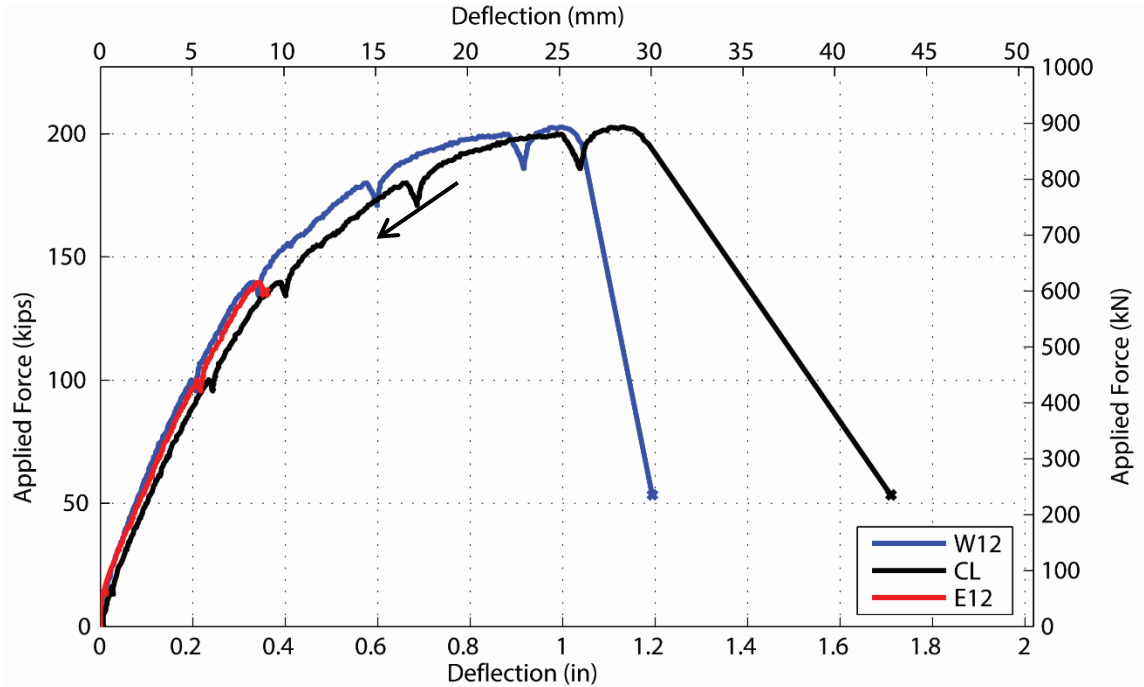


Figure 176. Force vs. Deflection for LP4

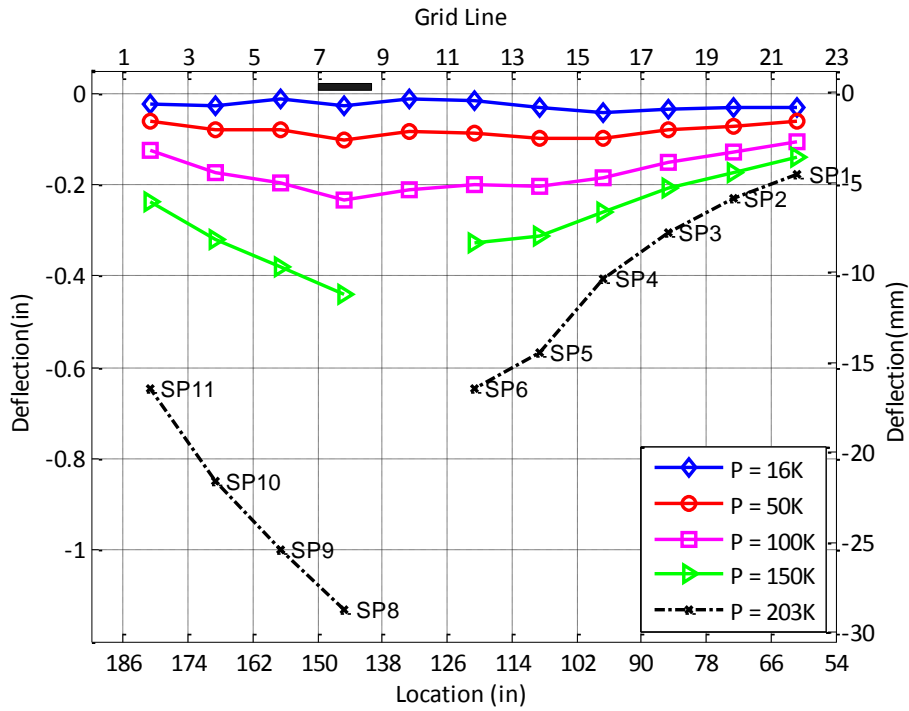


Figure 177. Deflection Profile of LP4—Longitudinal Direction

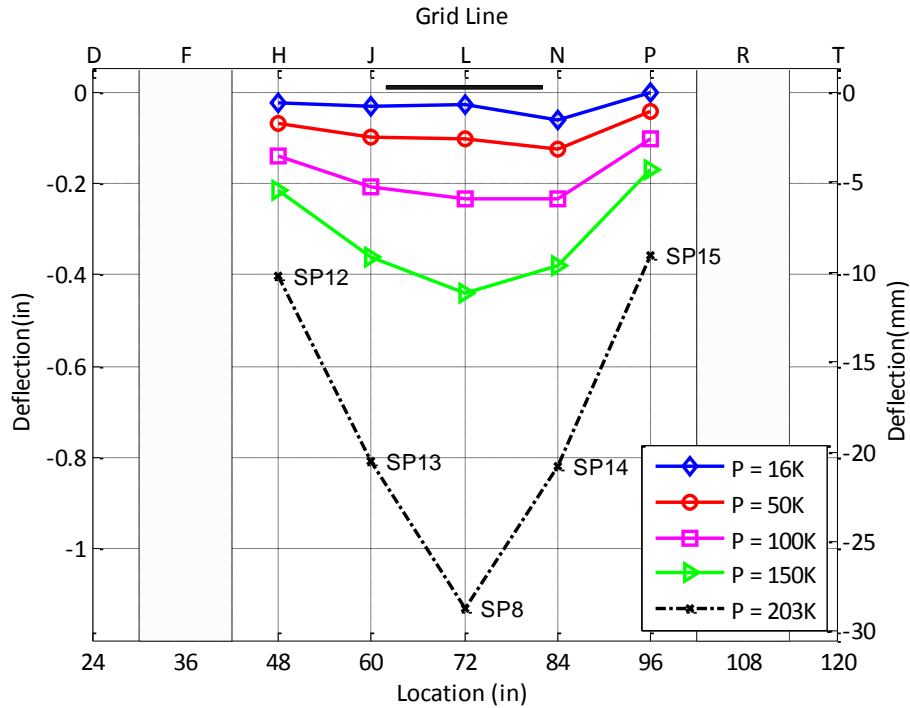


Figure 178. Deflection Profile of LP4—Transverse Direction

DISCUSSION

Overall

Table 62 summarizes the results for each test, including behavior at service and design loads, the loads at which the service stress limit was reached, when cracking occurred, and the maximum loads. All reported strengths represent individual wheel loads.

The SFRC specimen satisfied both the service and strength demands required by ADOT (2011) and AASHTO LRFD (2014). At service loads, the stress must be kept less than the ADOT allowable stress limit of 24 ksi. This was met for all specimens, demonstrating the suitability of SFRC as supplemental reinforcement. For LP1, the full deck was uncracked and the specimen, and the measured strains indicate a stress of approximately 2 ksi (11 MPa). For all load patterns at the service design loads, no preexisting cracks extended and no new cracks initiated, although preexisting cracks did open and affect the stiffness, and thus stress in the deck. This was observed most significantly for LP4, in which the measured strains indicate a maximum stress of 87 percent of the design requirements. In addition to measuring strains at service to indicate stress, the strain gages were monitored to indicate when service stress limits were met. For all interior load patterns, this limit was reached at loads in excess of the ultimate design loads.

The final crack pattern observed from each test is consistent with the expected flexural failure mechanism. The interior loads exhibit the typical fan-radial failure mechanism while the overhang test, LP3, yielded a trapezoidal failure mechanism. Every test, with the exception of the overhang test failed,

in a sudden manner. However, the failures occur beyond the usable limit of the SFRC bridge deck. Furthermore, concrete crushing on the top surface was observed during LP2 and LP3 before the sudden failure occurred. The loads at failure were as large as 500–550 percent of the AASHTO strength design demands for interior loads and 260 percent for the overhang load.

Each test conducted after LP1 presented evidence of their interaction with the initial test. The interaction is evident in the smaller pre-crack stiffness of LP2 through LP4 and the increased ductility observed at both the service and strength limit states. The shared cracked regions did not affect the ultimate capacity of the structure as evident in comparing the capacity of LP1 and LP4.

Table 62. Summary of Results from SFRC Bridge Deck Test Program

	Service (16 kips)		Demand (37 kips)	Service Stress Limit (24 ksi)	Cracking		Maximum Capacity	
	Δ_{service} in.(mm)	σ_{steel} ksi (MPa)	Δ_{demand} in.(mm)	$P_{fs=24\text{ksi}}$ Kips (kN)	P_{crack} kips (kN)	Δ_{crack} in.(mm)	P_u kips (kN)	Δ_u in.(mm)
LP1	0.0 (0.0)	1.6 (11.0)	0.01 (0.25)	64 (284)	70 (311)	0.03 (0.76)	203 (903)	0.58 (14.73)
LP2	0.03 (0.76)	12 (82.7)	0.07 (1.78)	66 (147)	70 (311)	0.21 (5.33)	185 (823)	1.91 (48.51)
LP3	0.05 (1.27)	-	0.18 (4.57)	-	30 (133)	0.13 (3.30)	96 (427)	1.74 (44.20)
LP4	0.01 (0.25)	20.8 (143.4)	0.05 (1.27)	61 (271)	75 (333)	0.14 (3.56)	203 (903)	1.1 (27.94)

Comparison to Previous Tests

Similar deck tests were conducted by others using different reinforcing systems. Mander et al. (2010) constructed a similar specimen using precast, prestressed panels on one half of the bridge while the other half of the bridge was designed as cast-in-place with traditional reinforcement. Pirayeh Gar et al. (2013) tested a deck prestressed AFRP full depth panels. Both investigation teams tested load patterns LP2 and LP3. Load pattern LP1 was tested by only Gar et al. The bridge deck constructed by both research groups had a slightly thicker bridge deck at 200 mm (7.87 in.). Figure 179 through Figure 181 compare the force-deflection curves of each reinforcing system, and Table 63 numerically summarizes the results.

Figure 179 compares the results from Pirayeh Gar et al. (2014) and the SFRC full-scale test program for LP1. The general shape of the SFRC and AFRP specimens are similar; however, the SFRC specimen exhibits a larger pre-cracking stiffness. Additionally, the AFRP specimen cracks at a smaller applied load, 56 kips, than the SFRC specimen, 70 kips. The post-cracking response of each specimen yields a similar

stiffness and peak load, 200 kips. The SFRC specimen achieves a larger deflection than the AFRP specimen before failure, 0.87 in. and 0.5 in., respectively.

Figure 180 compares LP2 for Mander et al. (2010) and Pirayeh Gar et al. (2013). The pre-cracking stiffness for both tests conducted by others are similar while the pre-cracking stiffness of the SFRC specimen is smaller. The reduced stiffness may be a result of the interaction of LP2 and LP1 and the thinner deck. Applying load pattern LP2 resulted in the opening of the existing cracks from LP1 prior to the propagation of new cracks due to LP2. The ultimate capacity of the SFRC specimen, 185 kips, is significantly larger than both prior tests, 127 kips and 157 kips for Mander et al. and Gar et al., respectively.

The response of the SFRC specimen to the single wheel load on the overhang, LP3, is enveloped by the response of the test conducted by Mander et al. and Gar et al. (Figure 181). The pre-crack stiffness of the SFRC and AFRP specimens are similar while the stiffness of the traditionally reinforced specimen is larger. Similar to LP2, an interaction between LP3 and LP1 is likely due to the extent of cracking resulting from LP1. The post-cracking stiffness of the SFRC specimen is larger than both of the other specimens. The SFRC specimen achieved the largest wheel load and deflection under this load pattern at 96 kips and 1.7 in.

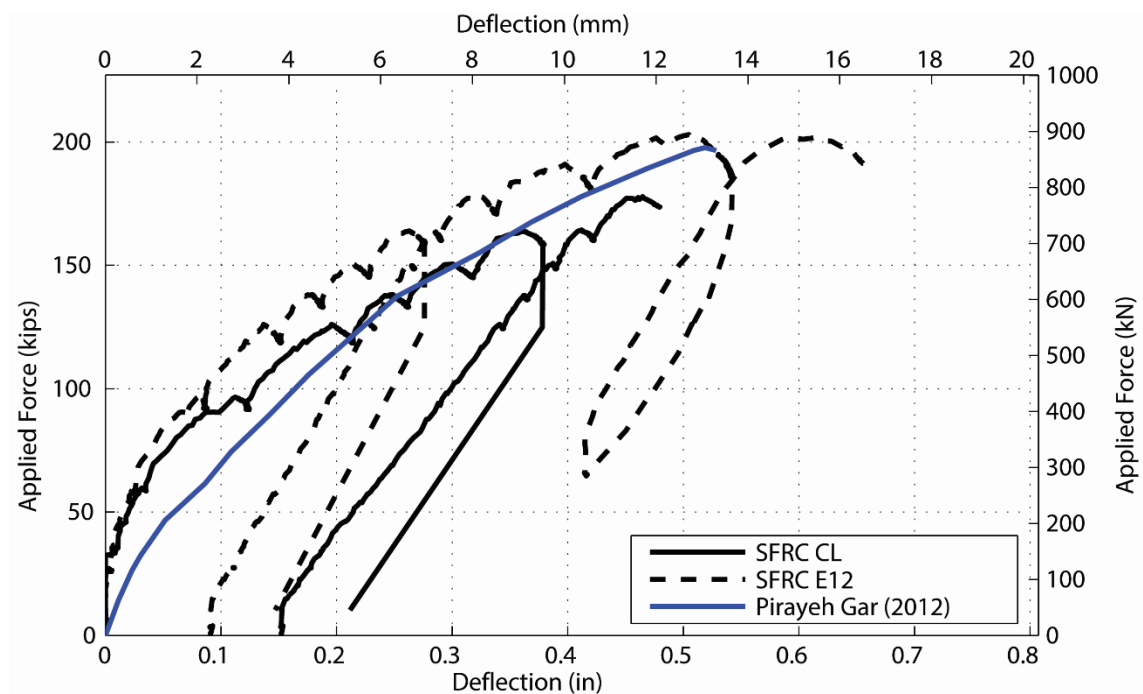


Figure 179. Force vs. Deflection Comparison of SFRC and Others—LP1

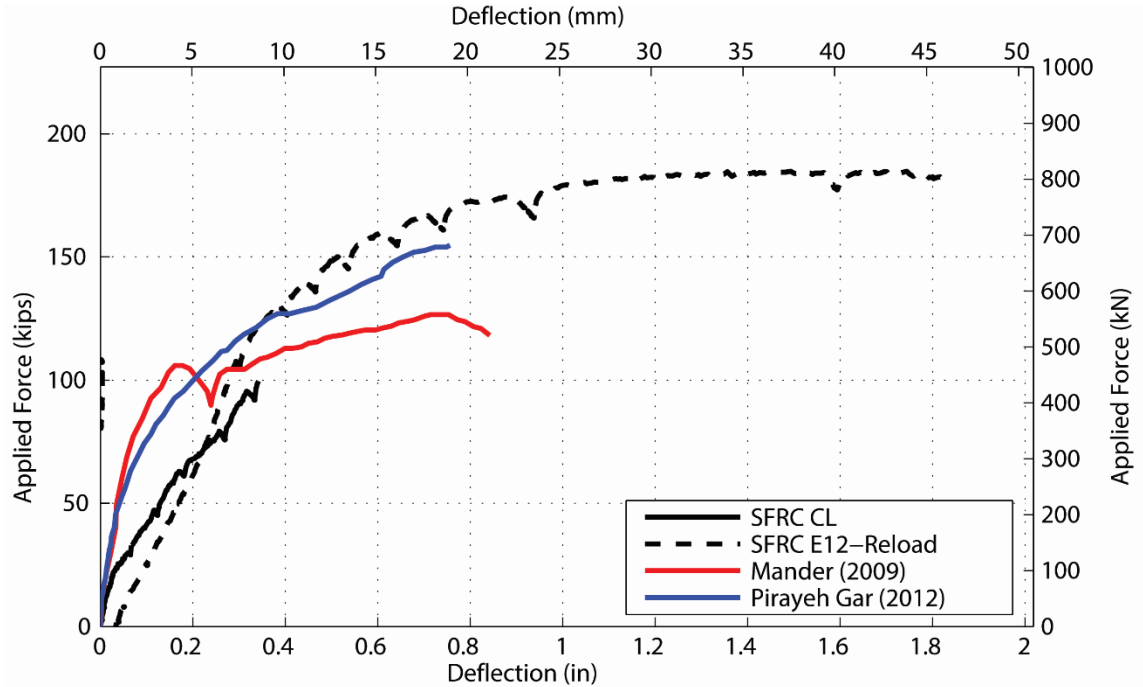


Figure 180. Force vs. Deflection Comparison of SFRC and Others—LP2

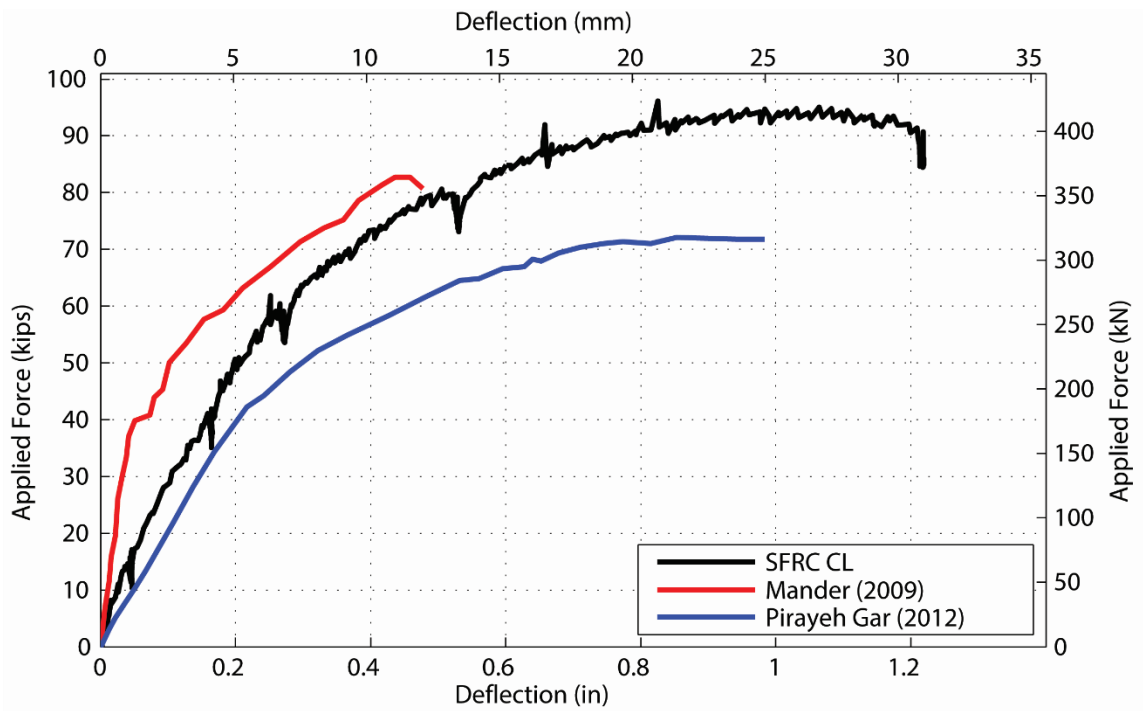


Figure 181. Force vs. Deflection Comparison of SFRC and Others—LP3

Table 63. Comparison for Full-Scale Specimen and Tests by Others

	Failure Capacity kips (kN)			Deflection at Failure in. (mm)		
	LP1/LP4	LP2	LP3	LP1/LP4	LP2	LP3
Mander et al (2009)	-	127 (565)	84 (374)	-	0.8 (21)	0.5 (12)
Gar et al (2014)	197 (880)	157 (700)	71 (320)	0.5 (13.5)	0.7 (19)	1.0 (25)
Full-Scale Specimen	203 (903)	185 (823)	96 (427)	0.84	1.91 (48.5)	1.7 (44.2)

SUMMARY

A full-scale SFRC bridge was tested to demonstrate the effect of adding steel fibers to a two-way slab. The experimental program offered insight on the stiffness, deformability, failure mechanisms, and load capacity of a concrete bridge deck reinforced with steel bars and steel fibers. This was achieved by designing and constructing a full-scale specimen with SFRC and a reduced area of steel reinforcement to achieve a service and ultimate limit state consistent with a traditionally designed reinforced concrete bridge deck. Furthermore, the geometry was chosen to both represent actual bridges in use and conform to tests conducted in the past by other researchers. The similar geometries facilitate the additional comparison to actual data and observations recorded from controlled experiments. The following conclusions are made from the full-scale bridge test program:

- The overall performance of the SFRC bridge deck satisfies the serviceability and strength requirements of ADOT (2011) and AASHTO LRFD (2014). Under the influence of the service limit state, the stress in the steel reinforcement reaches a maximum of 21 ksi, or 87 percent of the stress permitted by ADOT design guidelines. The failure capacity of the SFRC specimen is 500 percent of the ultimate limit state defined by ADOT and AASHTO LRFD (2014).
- Comparing the experimental results to similar tests conducted by others demonstrate the benefits of adding steel fibers to the concrete matrix. The post-cracking stiffness of the SFRC specimen is superior to using prestressed AFRP strands or PC with traditional reinforcement. The larger stiffness is an expected result of the crack-bridging behavior of the steel fibers. Furthermore, the addition of steel fibers resulted in larger ultimate capacities and maximum deflection before failure.
- The failure mechanism of SFRC matches the crack patterns expected from plain reinforced concrete. The only difference in the failure mechanism is the proliferation of cracks. Numerous cracks developed parallel to the interior beam due to the restraint provided and the crack-bridging effect of SFRC.
- The cracks and their location exhibit a flexural failure. Sudden failure of the bridge deck occurred well beyond the usable state of the bridge. Significant cracking and deflection had already been achieved prior to the failure of the specimen.

CHAPTER 8. ANALYSIS OF SLAB STRIP TESTS

INTRODUCTION

This chapter provides an analysis of each slab strip tested. First, the moment-curvature response of the experimental results is computed and evaluated. The analysis will provide the basis for a design procedure using SFRC. Then, material data determined from standard ASTM testing are compared to traditional constitutive models. Next, the theoretical and experimental moment-curvature responses are compared. Finally, a comparison is made between the experimental results and conclusions from the case studies.

EXPERIMENTAL MOMENT CURVATURE

The moment-curvature relationship of the slab-strip specimens were computed at midspan using both string pots and LVDTs. String pots were used to compute curvature with the finite difference method. The second derivative of the deflection profile yields the curvature profile of the specimen:

$$\varphi = \frac{d^2z}{dx^2} \quad (18)$$

$$\varphi_j = \frac{z_{j-1} - 2z_j + z_{j+1}}{\Delta x^2} \quad (19)$$

Where φ is the curvature at string potentiometer j , z is the vertical deflection measured by string potentiometer j , and Δx is the horizontal spacing of string potentiometers.

The curvature was also computed using the strain profile inferred from the LVDTs attached to the east face of the specimen. The strain at the top and bottom of the specimen is determined based on the horizontal displacement measured by each LVDT and the gauge length of the LVDTs. The slope of the strain profile is used to compute the curvature of the specimen at the midspan. This method provides the average curvature over the entire gauge length of the LVDT.

$$\varepsilon_j = \frac{\Delta x_j}{x} \quad (20)$$

$$\varphi = \tan \frac{y}{\varepsilon_1 + \varepsilon_2} \quad (21)$$

Where ε_j is the strain at LVDT j , x is the LVDT gauge length, and y is the vertical distance between top and bottom LVDTs.

Figure 182 through Figure 186 show the moment-curvature relationship for the slab strip tests. The experimental moment-curvature relationships are consistent with physical observations and the measured force-deflection relationships. The curves show a change in stiffness at the cracking moment and plateau when the steel yields and failure localizes in the critical crack. After yielding occurs, the moment capacity of the specimens with steel reinforcement located at the bottom of the specimen remains nearly constant with a very slight decrease. The moment capacity of the specimens with steel reinforcement located at the center gradually declines as the curvature increases. The decrease in the moment capacity is likely a result of the decrease in the tension capacity of the SFRC. The effect is more

pronounced in the specimens with the steel reinforcement located at the center than the specimens with steel at the bottom due to the smaller moment arm to the center of the specimen. The end of the moment-curvature relationships signifies the removal of the string potentiometers from the slab-strips to prevent them from damage.

The experimental moment-curvature relationship determined by both methods show an overall consistency between each other. The curves from both methods show agreement in the pre-crack and plateau portion of the curves. However, a slight difference is observed in the post-crack stiffness between the two methods. The LVDT curve resulted in a smaller post-crack stiffness in five specimens: s7505BTM24, s7505BTM25, s7505BTM35, s9005BTM25, and s9005BTM35. The LVDT response for specimen s9005BTM23 resulted in a larger post-crack stiffness compared to the string pot response.

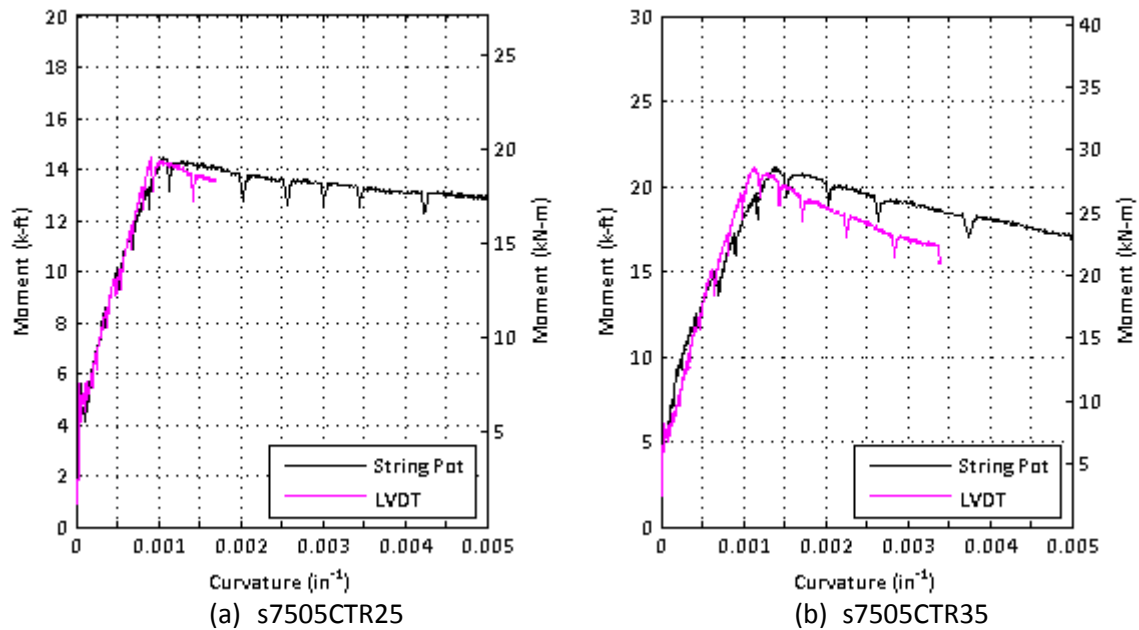
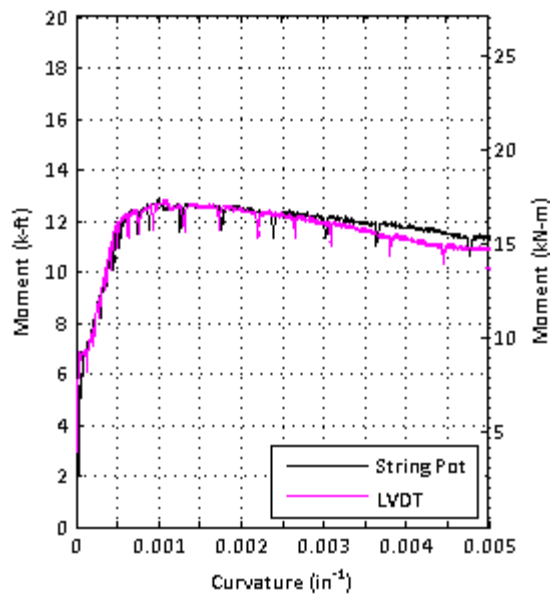
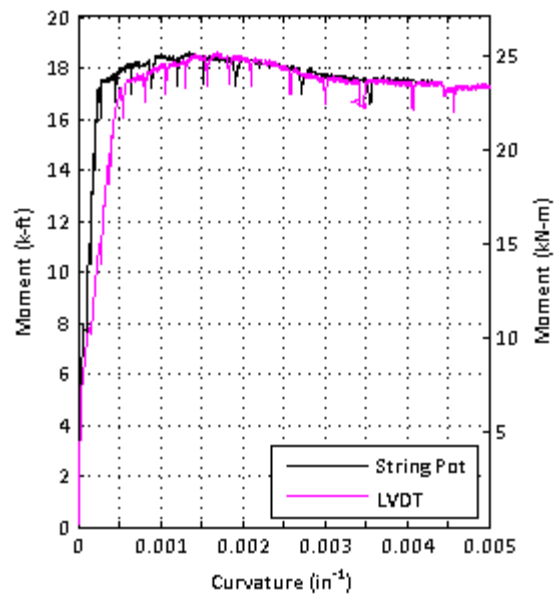


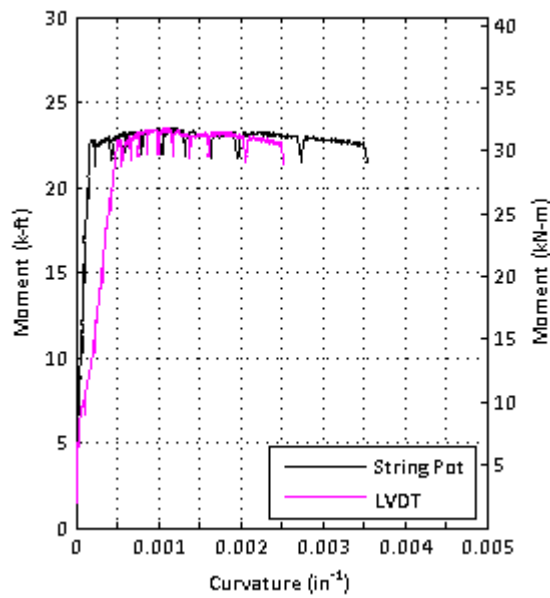
Figure 182. Experimental Moment Curvature Relationship for s7505CTR##



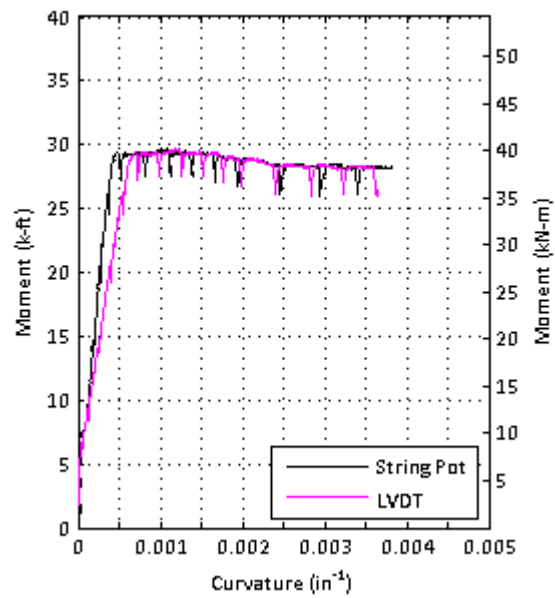
(a) s7505BTM23



(b) s7505BTM24

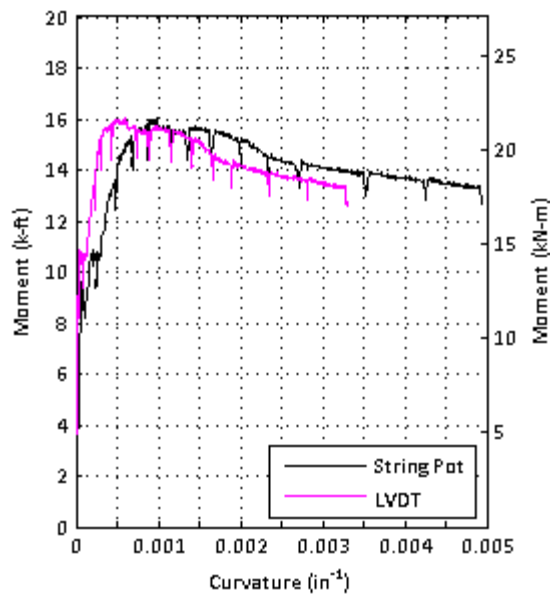


(c) s7505BTM25

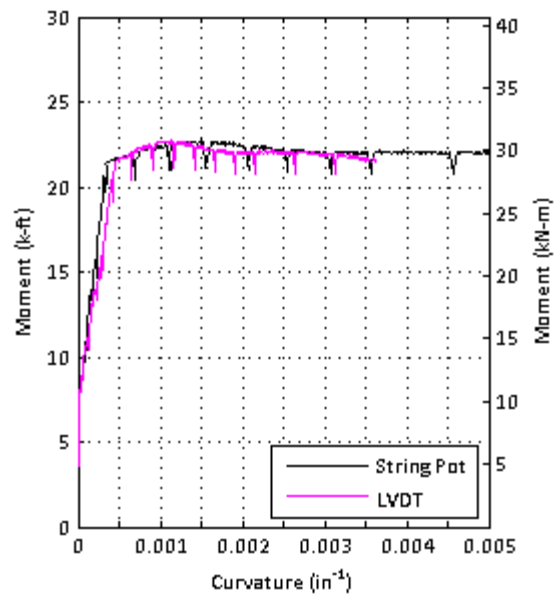


(d) s7505BTM35

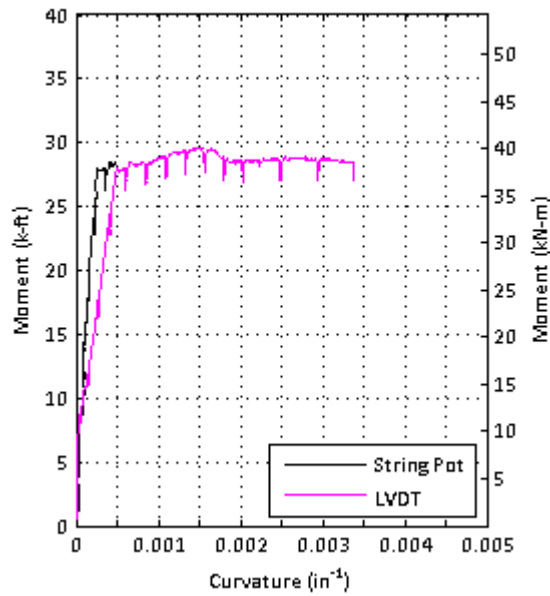
Figure 183. Experimental Moment Curvature Relationship for s7505BTM##



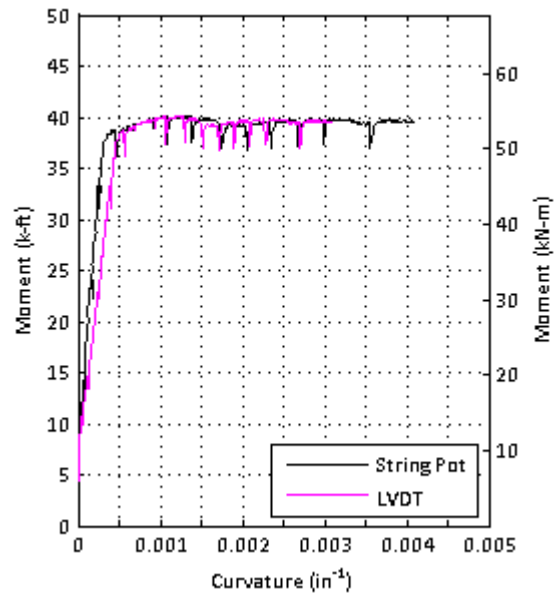
(a) s9005BTM23



(b) s9005BTM24

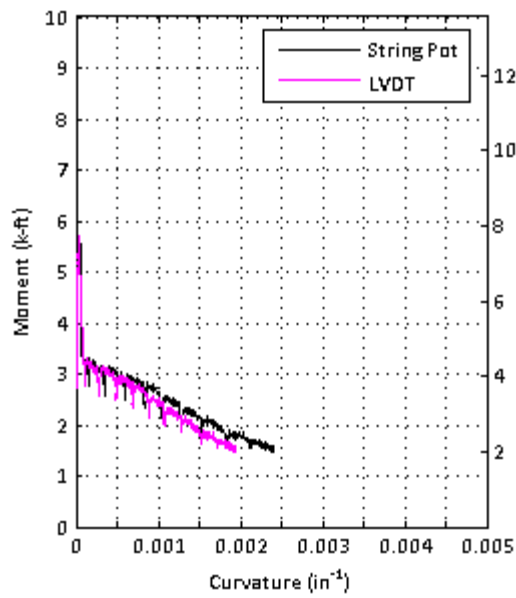


(c) s9005BTM25

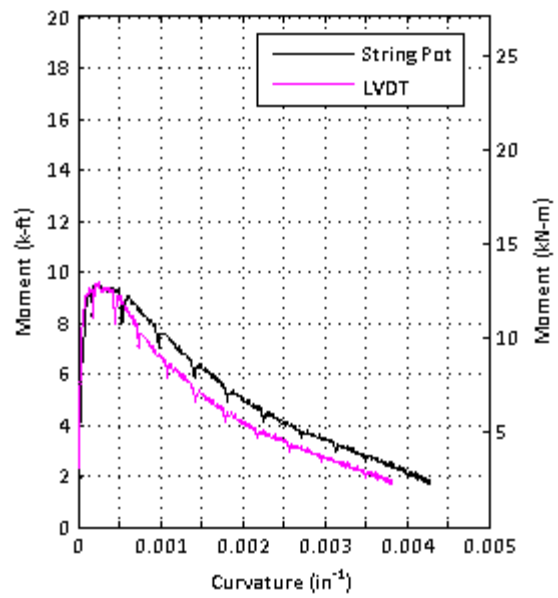


(d) s9005BTM35

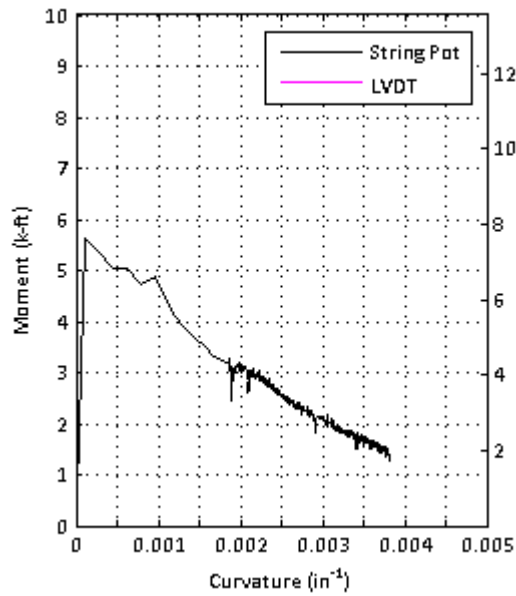
Figure 184. Experimental Moment Curvature Relationship for s9005BTM##



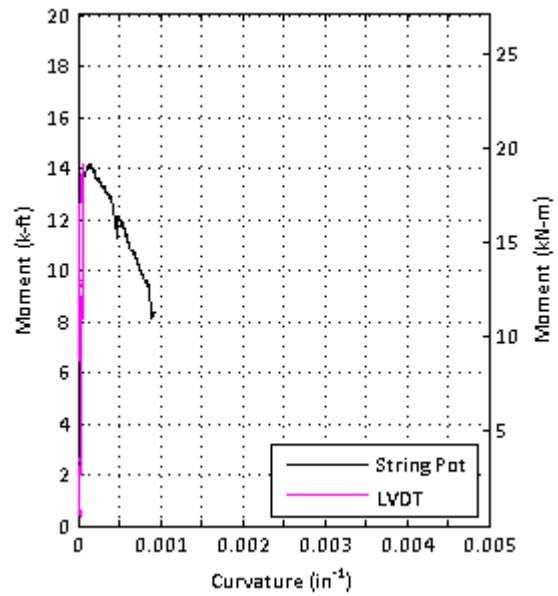
(a) s7505NOS00



(b) s7520NOS00

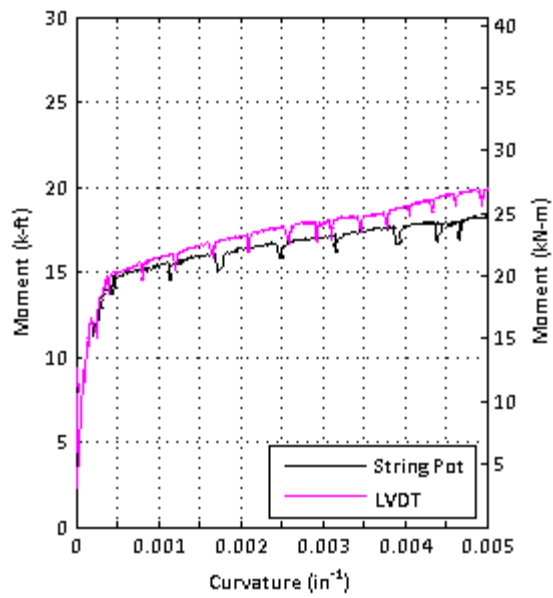


(c) s9005NOS00

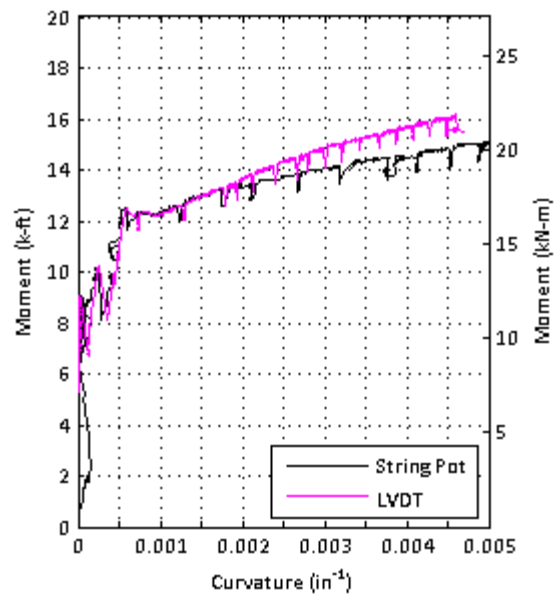


(d) s9020NOS00

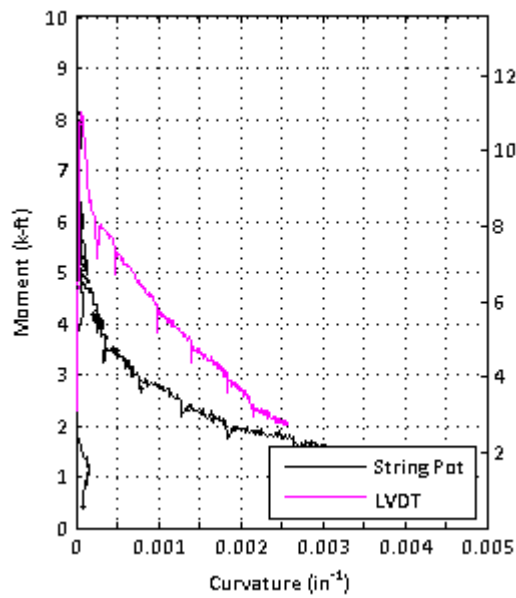
Figure 185. Experimental Moment Curvature Relationship for s####NOS00



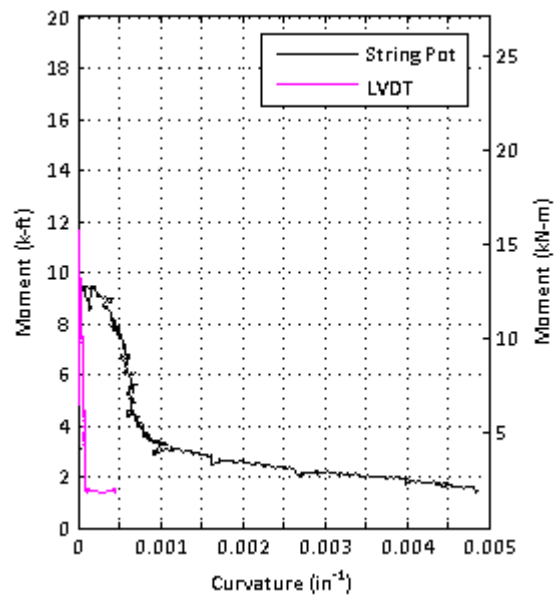
(a) d7505BTM24



(b) d7500BTM24



(c) d7505NOS00



(d) d9005NOS00

Figure 186. Experimental Moment Curvature Relationship for d-series Slab Strips

INVERSE ANALYSIS TO ESTABLISH SFRC TENSION MODEL

Prediction of flexural behavior of SFRC slab strips requires the use of accurate material models for compression and tension response. Since a standard tension test does not exist and there is not established procedure for determining tensile response from ASTM C78 bending tests, tensile stress-strain response was characterized using an inverse analysis (RILEM 2003; Soranakom and Mobasher 2007b).

In an inverse analysis, the desired response is adjusted until the experimental results are reproduced. For the slab strips, moment-curvature analysis the desired response is the post-peak tensile response of the SFRC. The slab strips without reinforcing bars was used to conduct the inverse analysis to eliminate any effects of tension stiffening.

Compressive response of the SFRC was based on measured material properties. Figure 187 summarizes the results of test ASTM C39 for each SFRC and PC mixture used in the experimental programs. Figure 187 compares the measured compression response of SFRC to the modified Kent-Park model for PC with a post-peak descending slope, Z , of 50 computed as follows:

$$f_c = f'_c \left(\frac{2\varepsilon_c}{\varepsilon_0} - \left(\frac{\varepsilon_c}{\varepsilon_0} \right)^2 \right) \text{ for } \varepsilon_c < \varepsilon_0, \quad (22)$$

$$f_c = f'_c (1 - Z(\varepsilon_c - \varepsilon_0)) \text{ for } \varepsilon_c > \varepsilon_0 \quad (23)$$

Where ε_c is the strain at any point, f_c is the stress at any point, ε_0 is the strain at maximum compressive strength, f'_c is the maximum compressive strength, and Z is the slope of descending branch of the stress-strain response.

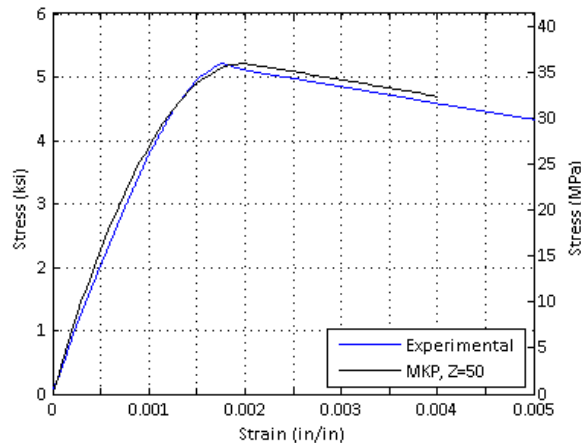


Figure 187. ASTM C39 Average Compression Results (M2) and Modified Kent Park

The tensile model used in the moment-curvature analysis is defined by the three parameters, modulus of elasticity, cracking stress, and residual stress. Standard test ASTM C1609 provides the modulus of elasticity and cracking stress for the SFRC mix. After cracking, the residual stress of the SFRC decreases linearly. The residual stress decreases until it has lost all capacity at 0.025.

Figure 188 and Figure 189 show example tensile models for the SFRC used for the inverse analysis. The inverse analysis was conducted by changing the initial residual stress of the SFRC model and performing a theoretical moment-curvature analysis of the SFRC specimens without steel reinforcement. The fit of the tensile model was evaluated based on the moment curvature response after cracking occurs. The theoretical moment capacity was compared to the experimental moment capacity at 15 different curvatures following the peak moment.

Table 64 summarizes the tensile model and residual strength used to determine the theoretical moment-curvature relationship. Figure 190 and Figure 191 show the theoretical moment-curvature response for s-series tests with 0.5 percent fiber (s7505NOS00 and s9005NOS00). A residual tensile stress of 90 psi minimized the error of the portion of the curve bound by the red lines in the figures. The same volume of fiber was used in the d-series tests, and although the initial cracking stress was larger, the residual tensile stress was approximately the same using inverse analysis. Figure 192 shows the moment-curvature for these tests. For the s-series tests with 2.0 percent fiber, the residual stress was found to be 230 psi; Figure 193 shows the computed moment curvature response.

Table 64. Summary of ASTM C1609 Results and Tension Models

Dosage Rate	E (ksi)	f_{cr} (ksi)	f_r (ksi)	μ
s-series				
0.5%	4027	0.48	0.09	0.19
2.0%	4170	0.68	0.23	0.34
d-series				
0.5%	5980	0.81	0.09	0.11

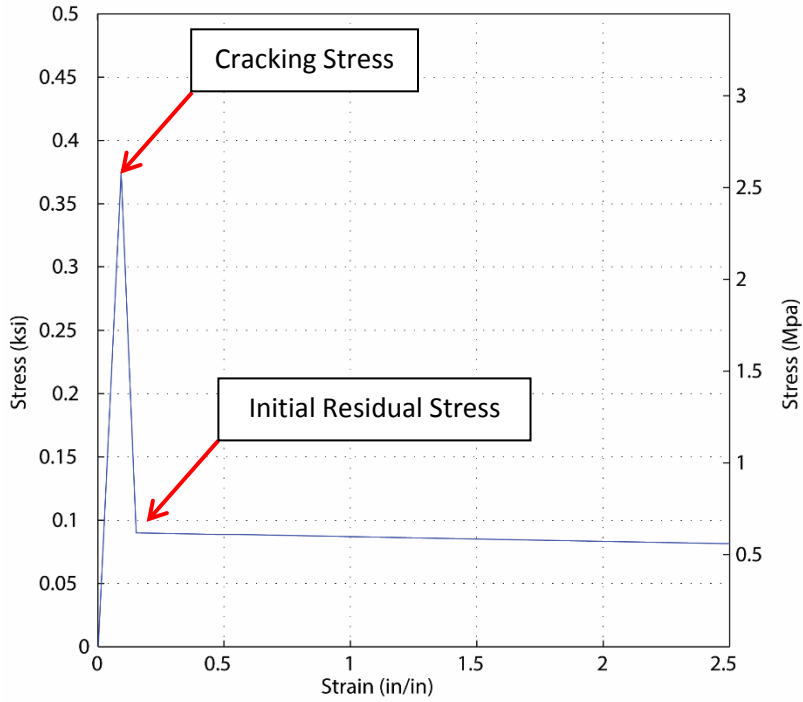


Figure 188. SFRC Tensile Model—Elastic Region and Initial Residual Stress

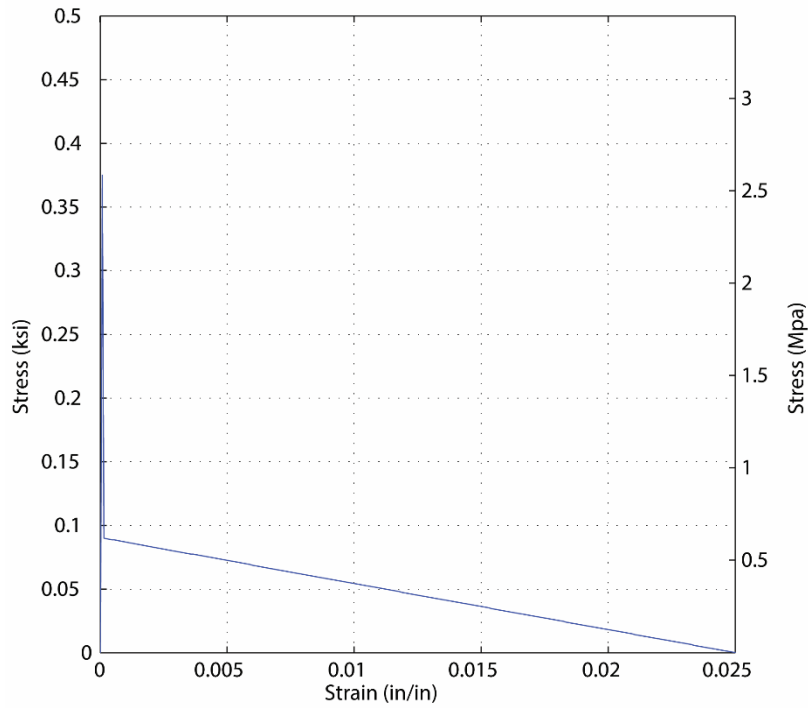


Figure 189. Post-Crack Constitutive Models for SFRC

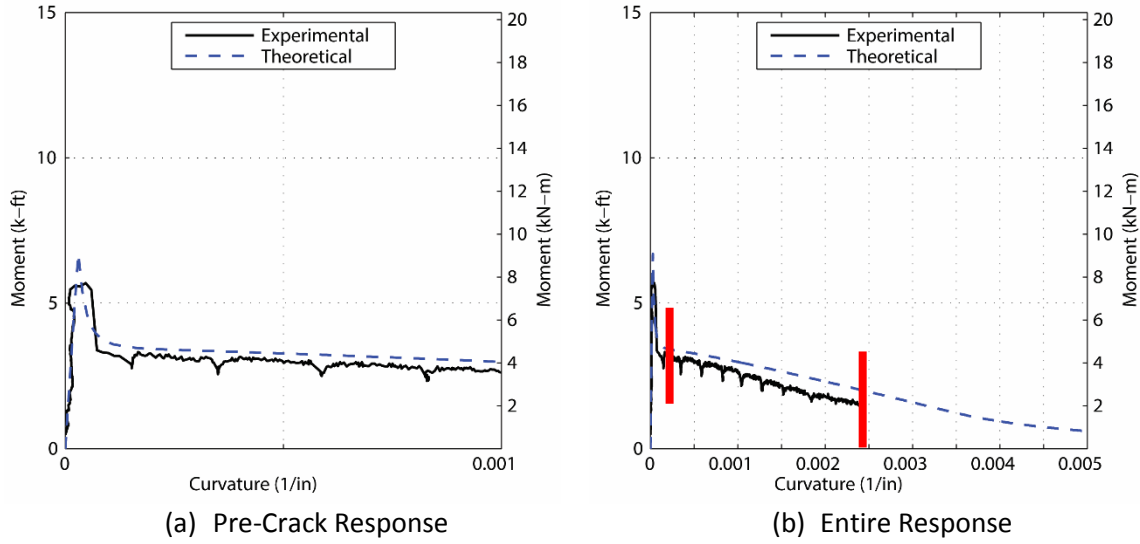


Figure 190. Theoretical and Experimental Moment-Curvature Response—s7505NOS00

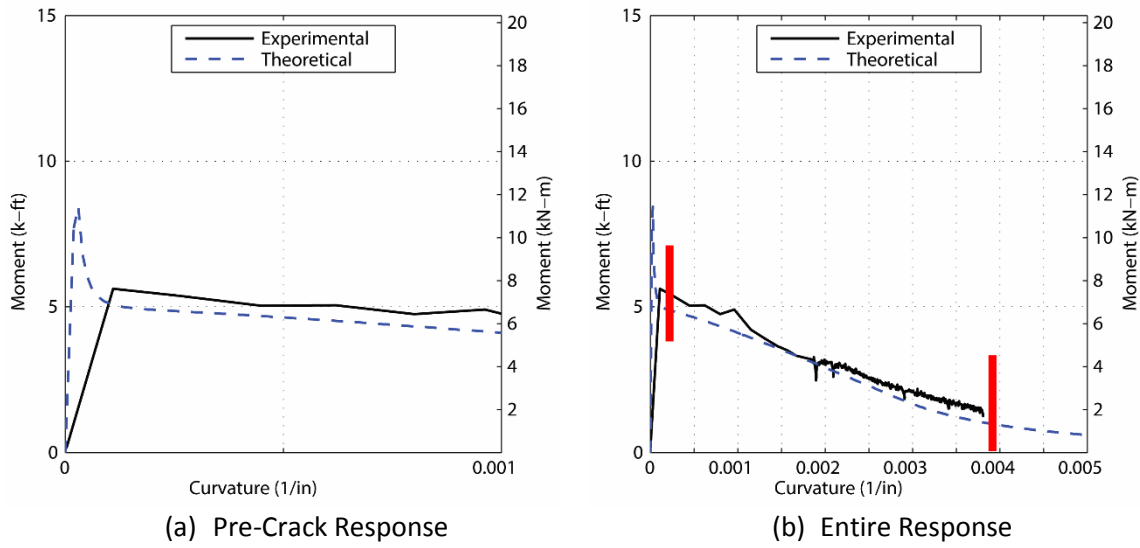


Figure 191. Theoretical and Experimental Moment-Curvature Response—s9005NOS00

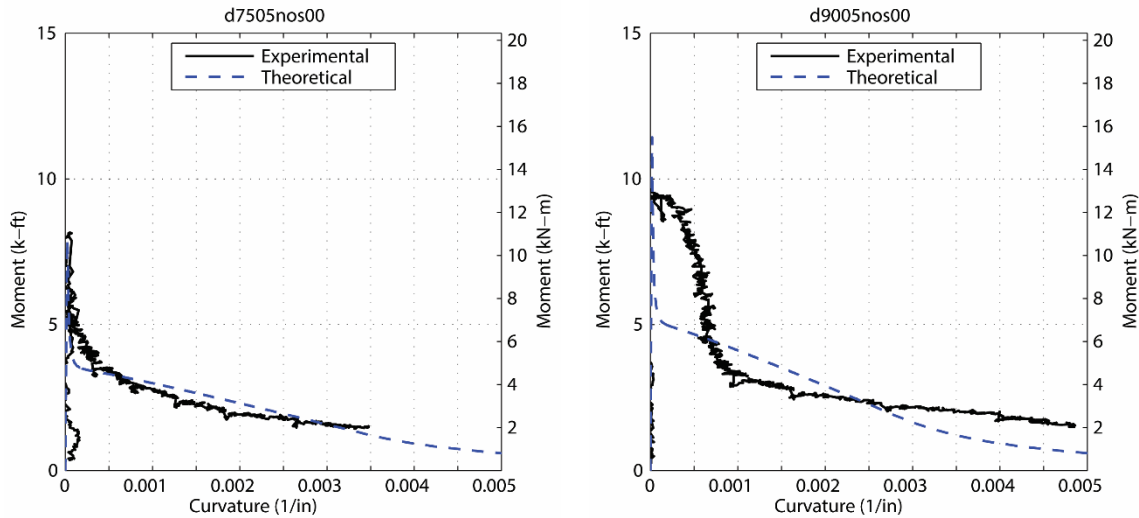


Figure 192. Theoretical and Experimental Moment-Curvature Response for d7505NOS00 and d9005NOS00

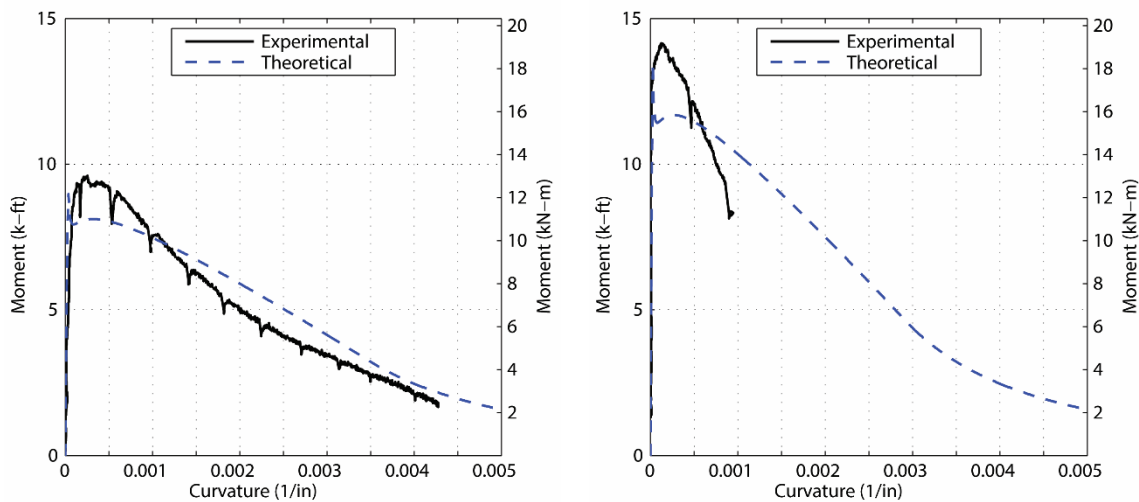


Figure 193. Theoretical and Experimental Moment-Curvature Response for s7520NOS00 and s9020NOS00

MOMENT-CURVATURE ANALYSIS OF SLAB STRIPS WITH STEEL

The tensile models determined in the previous section were used in moment-curvature response of the slab strips with steel. Figure 194 through Figure 197 present these results, along with the experimental results and theoretical moment-curvature response with PC. The experimental moment-curvature relationship determined based on the string potentiometers.

Figure 194 and Figure 195 show the theoretical and experimental moment-curvature response for the slab-strip specimens with 0.5 percent fiber by volume and steel reinforcement at the bottom of the specimen. The theoretical model accurately captures the experimental behavior of each slab strip prior

to the moment plateau with the exception of s7505BTM24 and s7505BTM25, in which the experimental stiffness is larger than the models. This was also observed between the moment-curvature response determined from string potentiometers and the LVDT. Uneven bending of the specimen is the probable cause for the increased stiffness reported by the string potentiometers.

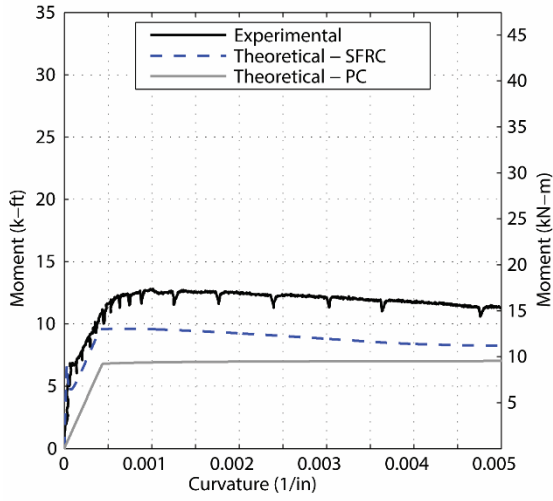
The behavior, or shape, of the theoretical moment-curvature response after yielding occurs is consistent with the behavior of the experimental results. The moment in the theoretical model gradually declines as the curvature of the specimen increases. At a large curvature, the tension capacity in the theoretical model achieves the maximum tensile strain for SFRC and the moment begins to decline ultimately converging with the PC model.

While the general behavior of the theoretical responses adheres to the behavior of the experimental results, the moment at yield and beyond is different. The theoretical models under predict the moment capacity of the SFRC specimens with a low steel reinforcement ratio. The under prediction of the capacity decreases as the reinforcement ratio increases. As demonstrated by specimen s7505BTM35, a critical reinforcement ratio exists at which point the theoretical models begin to over predict the moment capacity of the specimen. At low reinforcement ratios, the steel fibers contribute significantly to the moment-curvature response of the specimen increasing its yield and nominal moment. As the reinforcement ratio increases, the benefits of the steel fibers diminish as the moment-curvature response is dominated by the steel reinforcement ratio.

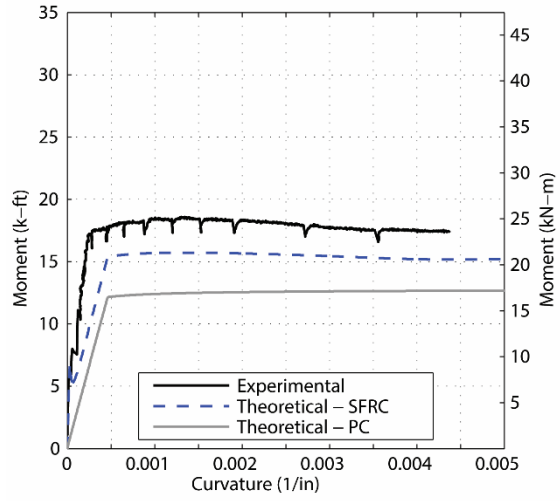
This trend can be explained by examining the resultant tension force and moment contributions of the SFRC and steel reinforcement (Figure 196) for 7.5-in. deep slabs. The neutral axis depth is not largely affected by adding steel reinforcement resulting in a near constant SFRC resultant force while the steel resultant force sees a significant increase. Therefore, the moment-curvature response of the SFRC specimen will begin to converge to the response of a PC specimen as the steel reinforcement ratio increases.

Figure 197 shows the theoretical and experimental moment-curvature response for the SFRC deck strip with steel reinforcement, d7505BTM24. The SFRC strip had the same reinforcement and fiber dosage as s7505BTM24 tested during the first experimental program of the project. As expected, the theoretical response of d7505BTM24 in comparison to the experimental results is consistent with the comparisons made for s7505BTM24. The theoretical model captures initial stiffness and capacity up to yield. Afterward, the theoretical model continues to under predict the response of the SFRC specimens.

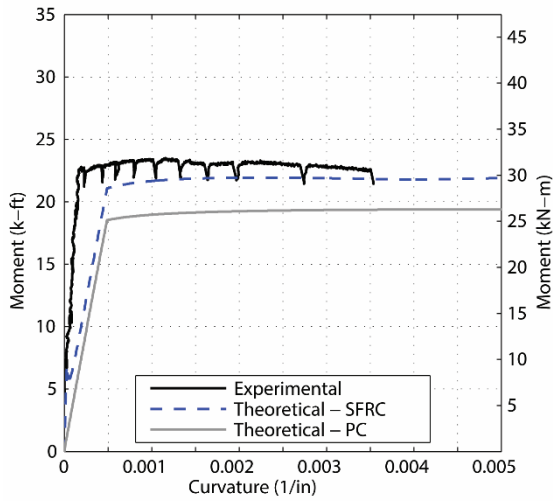
Figure 198 compares the moment curvature results for the slab strips with steel reinforcement located at the center. The decreased moment-arm for the steel reinforcement decreases its influence in the overall response of the specimen. Additionally, the SFRC in the lower half of the specimen is free to act more like the specimens without steel reinforcement that was used in determining the steel tensile properties.



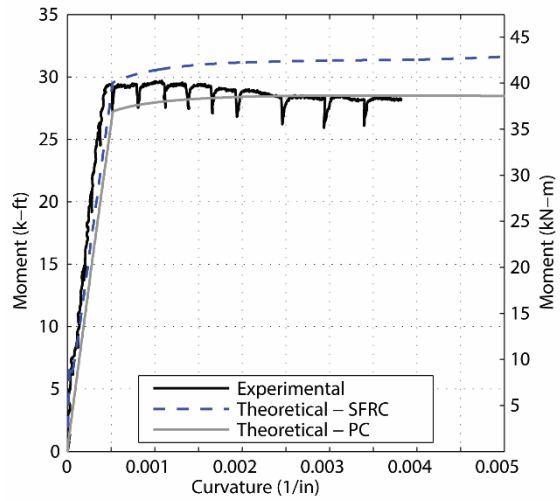
(a) s7505BTM23



(b) s7505BTM24

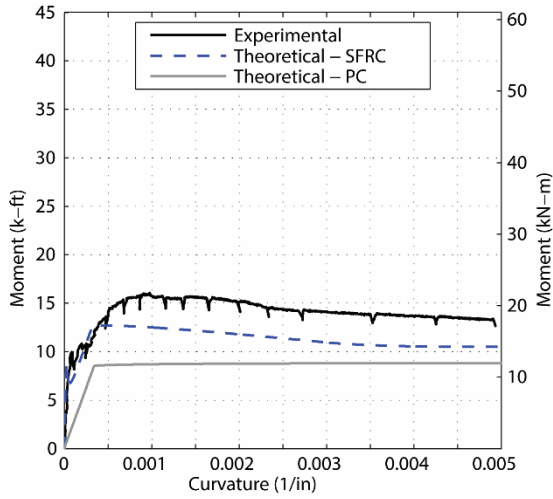


(c) s7505BTM25

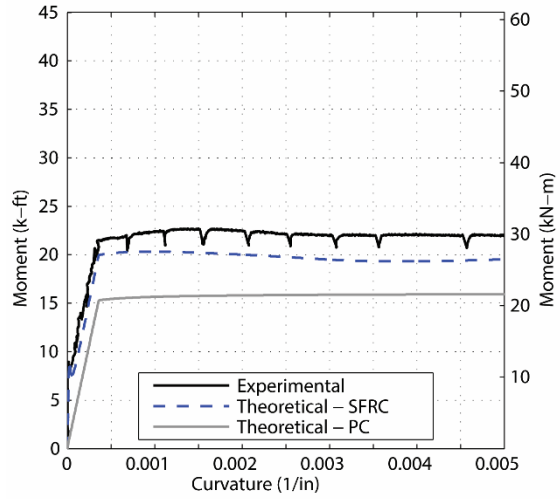


(d) s7505BTM35

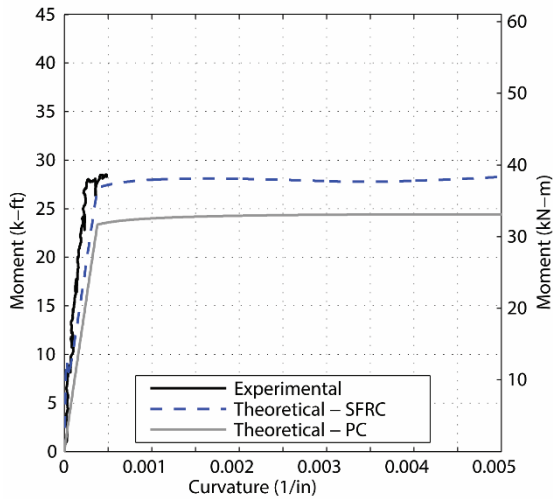
Figure 194. Theoretical Moment-Curvature Relationship for Slab Strips s7505BTM##



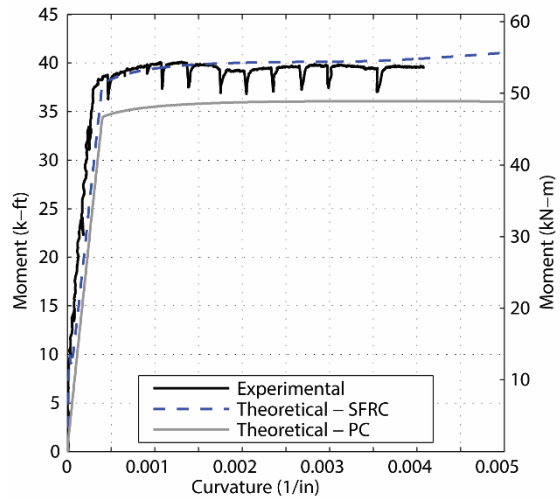
(a) s9005BTM23



(b) s9005BTM24

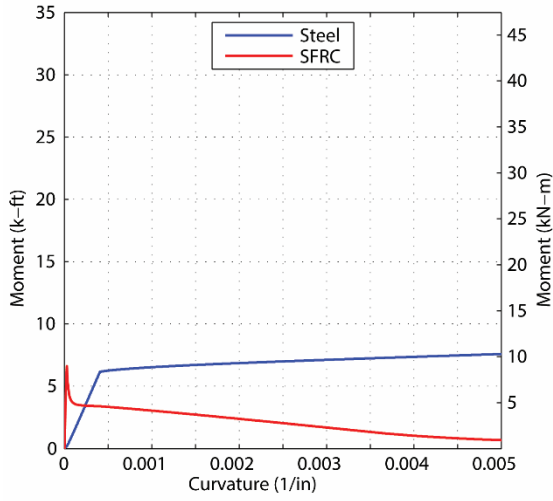


(c) s9005BTM25

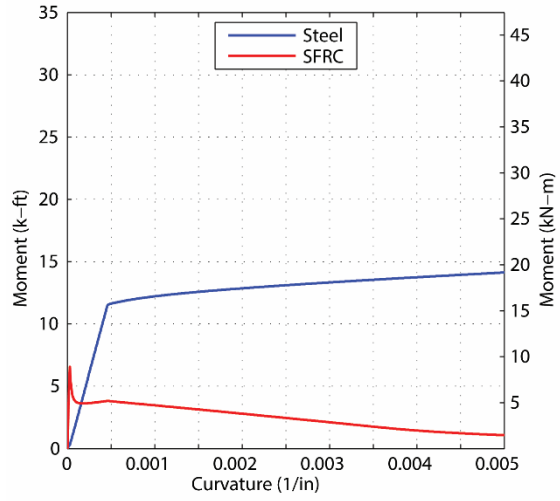


(d) s9005BTM35

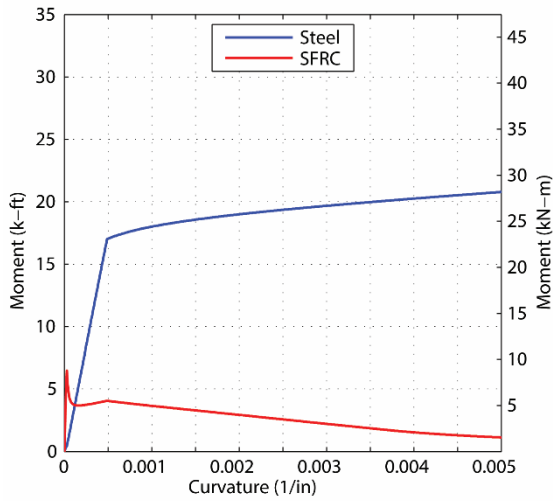
Figure 195. Theoretical Moment-Curvature Relationship for Slab Strips s9005BTM##



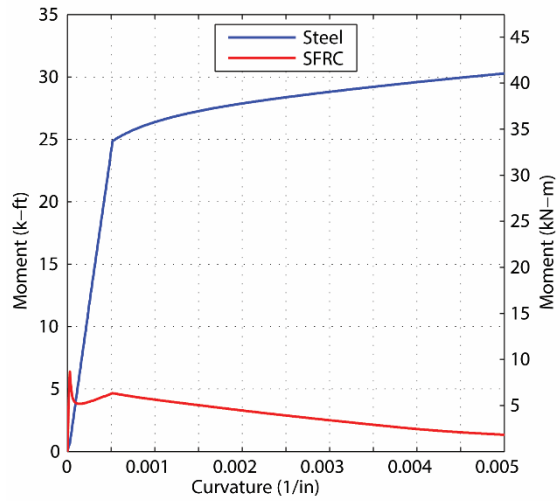
(a) s7505BTM23



(b) s7505BTM24



(c) s7505BTM25



(d) s7505BTM35

Figure 196. Steel and SFRC Contribution to Moment Capacity

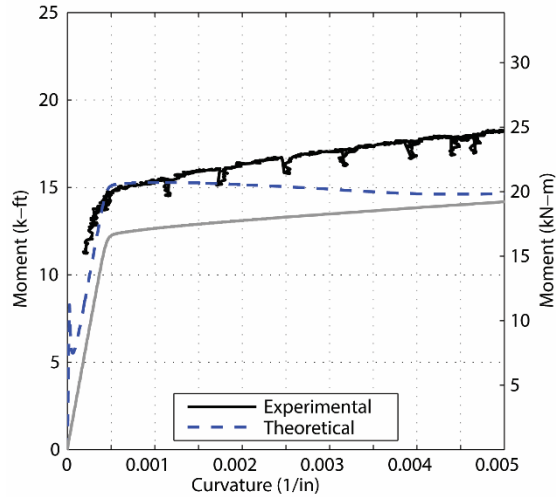


Figure 197. Theoretical Moment-Curvature Relationship for Slab Strips d7505BTM24

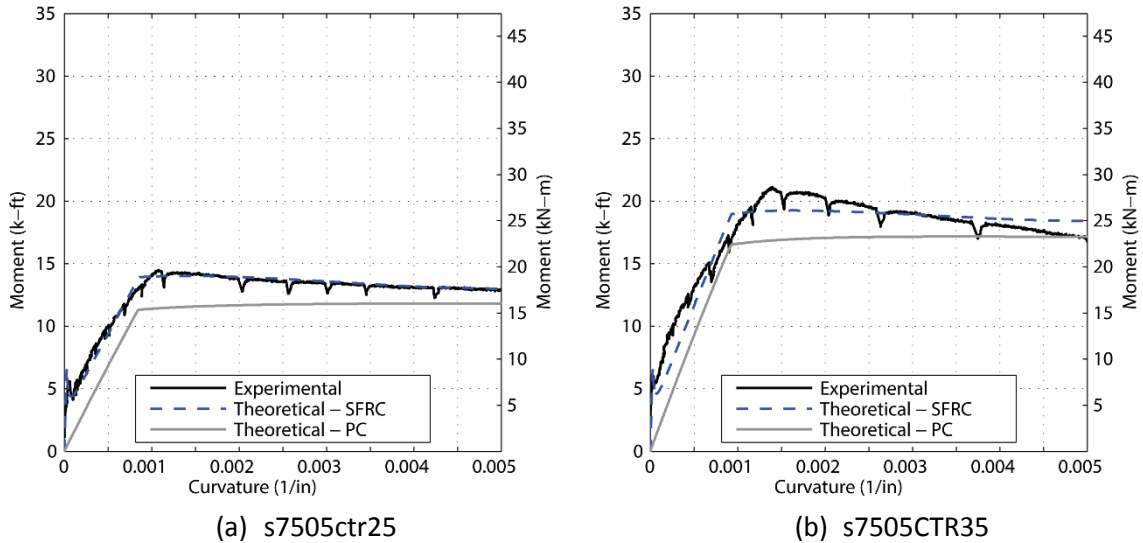


Figure 198. Theoretical Moment-Curvature Relationship for Slab Strips s7505CTR##

The moment capacity of the theoretical and experimental models was compared to each other to determine the accuracy of the theoretical models. Table 65 shows the difference in the theoretical and experimental models. The theoretical model under predicts the capacity specimen with the smallest reinforcement ratio, s9005BTM23, by 27 percent and over predicts the capacity of the specimen with the largest reinforcement ratio, s7505BTM35, by 11.3 percent. Both specimens with steel reinforcement at the center are over predicted by as much as 10 percent.

Table 65. Percent Difference between Experimental Results and Theoretical model

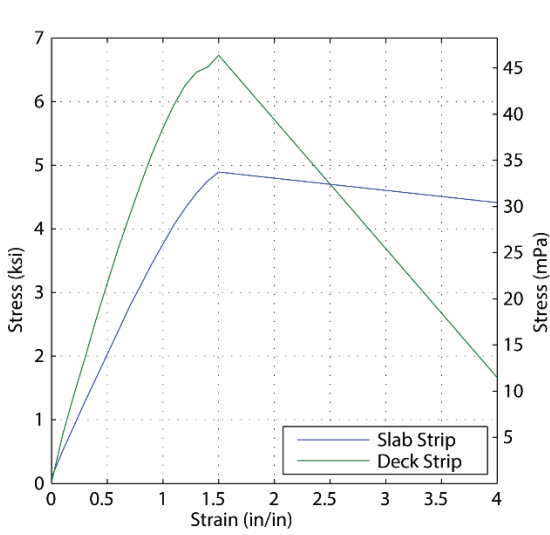
Slab-Strip	P (%)	% Difference
s7505BTM23	0.20	-33.1
s7505BTM24	0.37	-13.4
s7505BTM25	0.57	0.4
s7505BTM35	0.86	11.3
s9005BTM23	0.16	-26.6
s9005BTM24	0.30	-4.6
s9005BTM25	0.46	3.5
s9005BTM35	0.69	10.0
s7505CTR25	0.92	3.3
s7505CTR35	1.4	9.7

COMPARISON S- AND D-SERIES TESTS

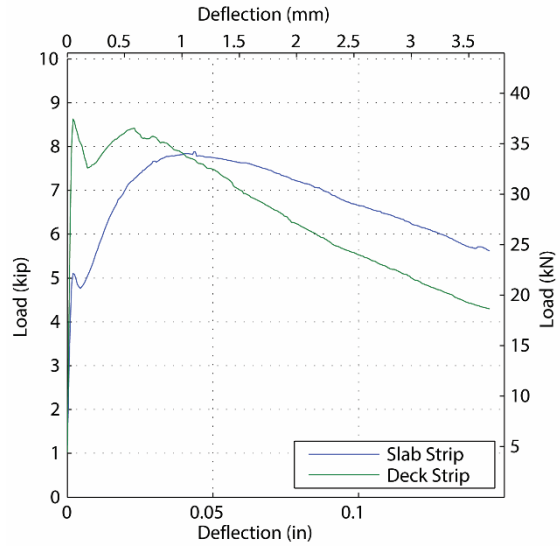
Three cross-section designs were used in both the s- and d-series. The similarity of the results tests show the repeatability of the experimental results with SFRC. Figure 199 shows the average response of the standard ASTM material tests conducted for each series. The SFRC for the d-series had a larger compressive strength and cracking stress. The increased cracking stress is evident in the flexural response of the material samples. The average response of the s-series SFRC samples become larger than the d-series response at larger strains and deflections.

Figure 200 shows the force-deflection and moment-curvature responses for s-series specimens 7.5-in. deep without steel reinforcement, d7505NOS00 and s7505NOS00. The strip from both series have the same initial stiffness. The increased cracking stress is prominent in both the force-deflection and moment-curvature response of the d-series. The slope of the post-crack response of the d7505NOS00 is larger than the slope of s7505NOS00. This is consistent with flexural material test ASTM C1609. The behavior of both slab strips with the same dosage of fibers is similar; however, the compressive strength and cracking stress are significant in the response SFRC specimens without steel reinforcement.

Figure 201 shows the force-deflection and moment-curvature responses for strip specimens 7.5-in. deep with two #4 bars, d7505BTM24 and s7505BTM24. Both strips have the same stiffness prior to cracking. However, after cracking occurs d7505BTM24 is less stiff and has a shallow force-deflection and moment-curvature response. The yield moment for the for the d-series is lower as a result of the smaller stiffness. As the deflection and curvature increases, the moment capacity of the d-series surpasses that of the s-series. The improved compression strength and larger MOR shown by the SFRC material tests provide the enhancement in the d-series. The maximum moment capacity of the strips from each series is comparable, but the overall behavior, or shape, of the force-deflection and moment-curvature relationships is not. The difference in their behavior is manifested in the ASTM material tests.

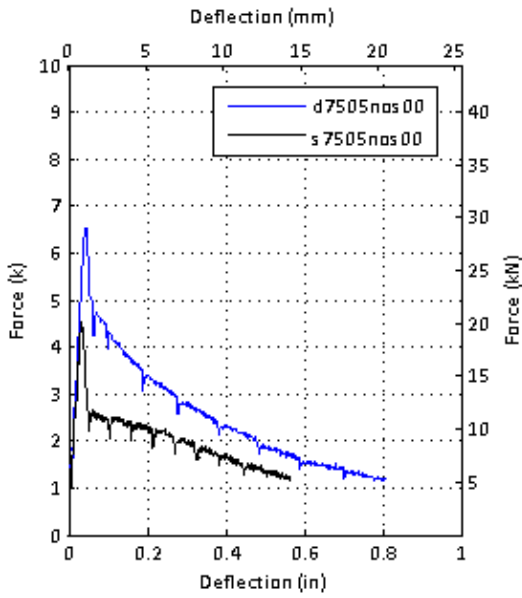


(a) ASTM C39 – Compression

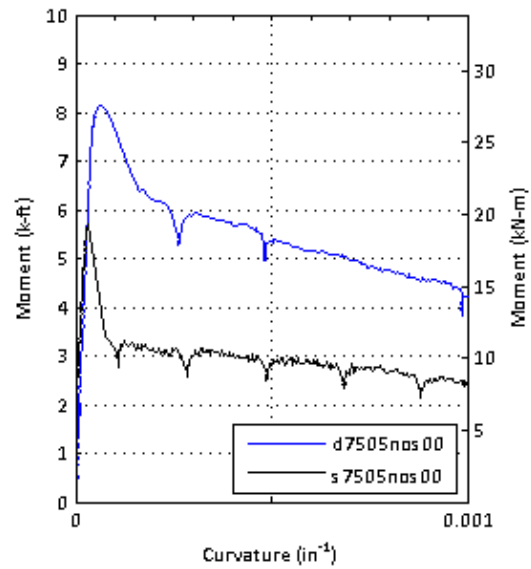


(c) ASTM C1609 – Flexural

Figure 199. Average Material Response for S- and D-Series



(a) Force vs Deflection



(b) Moment vs Curvature

Figure 200. Comparison of S- and D- Series Test Results – x7505NOS00

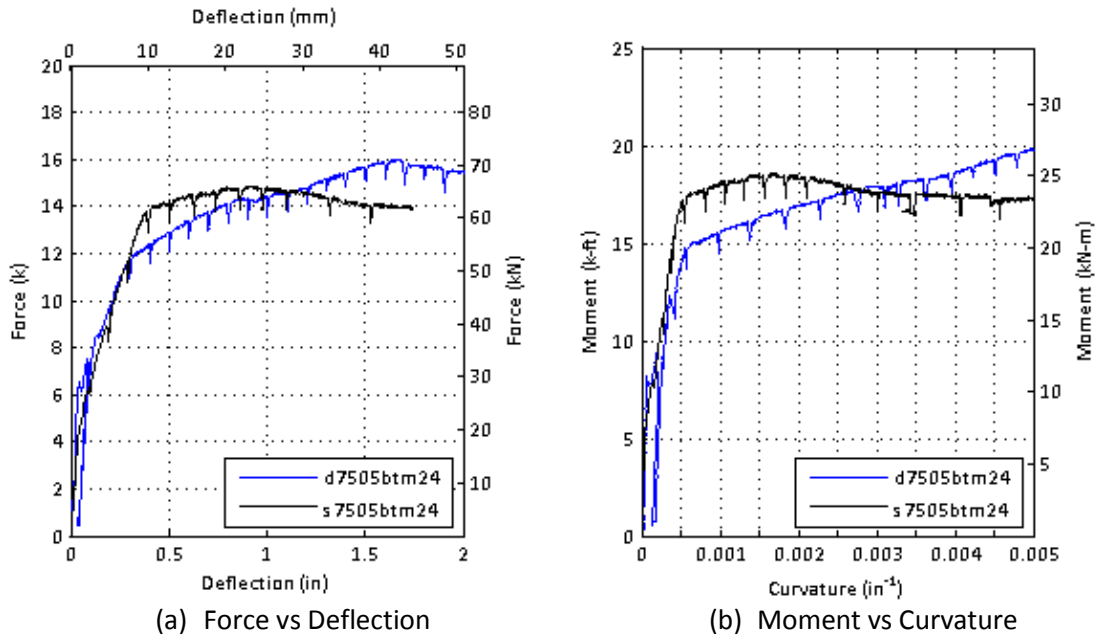


Figure 201. Comparison of S- and D- Series Test Results – x7505BTM24

CASE STUDY COMPARISON

Several case studies were conducted and presented in Chapter 4. The goal of the parameter studies was to examine the effects of SFRC on the behavior of each system by varying their material and geometric properties, such as the compressive strength of concrete, the post-crack strength of the SFRC, and the location and area of traditional steel reinforcement.

The slab strip experimental program recreated the case study analysis with fewer parameters, specifically, the area of traditional steel reinforcement and the depth of the section. The maximum recorded moment for the experimental program is normalized by the moment demand for a 6 ft span. Figure 202 through Figure 203 show the relationship between the steel reinforcement ratio and the sections moment capacity and service stress. Each figure has a vertical line representing the steel reinforcement ratio for the traditional strength and service designs. Figure 202 and Figure 203 have horizontal lines signifying a ratio of capacity to demand of 1. The black horizontal line does not take into account strength reduction factors while the red horizontal line does. The trends observed in the slab strip program are consistent with the trends noted in the theoretical case study analysis:

- Increasing the area of traditional steel reinforcement results in a proportional increase in the moment capacity. The effect of the SFRC is more pronounced in the deeper section as shown by the steeper trend line for the 9-in. sections. The increased effectiveness is a result of a larger area of concrete being in tension for the deeper section and therefore a larger resultant force and moment arm.

- The case study showed that a moderate amount of steel fibers and the AASHTO empirical steel design may be used to satisfy the moment demand. The AASHTO empirical steel is equivalent to #4 rebar spaced at 9 in.
- Figure 202 shows that the a section with 0.5 percent fibers by volume and less steel than the AASHTO empirical design, #3 spaced at 9 in. (s7505btm23), provides sufficient strength to satisfy the moment demands of a 6-ft girder spacing.
- The case study concluded that a large amount of fibers may be used instead of steel reinforcement to satisfy the moment demand. According to the case study analysis, a section using SFRC with a significant amount of strain hardening provided approximately 40 percent more strength than required by the ultimate strength design. This trend was also observed in the slab strip program. Section s9020nos00 provided sufficient strength to meet the strength moment demands; however, the section did not produce as large of an over strength as observed in the case study. Including fiber 2.0 percent by volume is not sufficient to achieve the levels of strain hardening used in the case study.
- Current ADOT design procedures for concrete bridge decks is based on the elastic analysis of the deck under service loads. This design is accomplished by limiting the stress in the steel reinforcement to 24 ksi. Based on the case study analysis and the slab strip program, the use of strength design with 0.5 percent fibers by volume satisfies the service design (Figure 204). Additionally, the amount of steel reinforcement may further be decreased as shown by section s7505btm23.

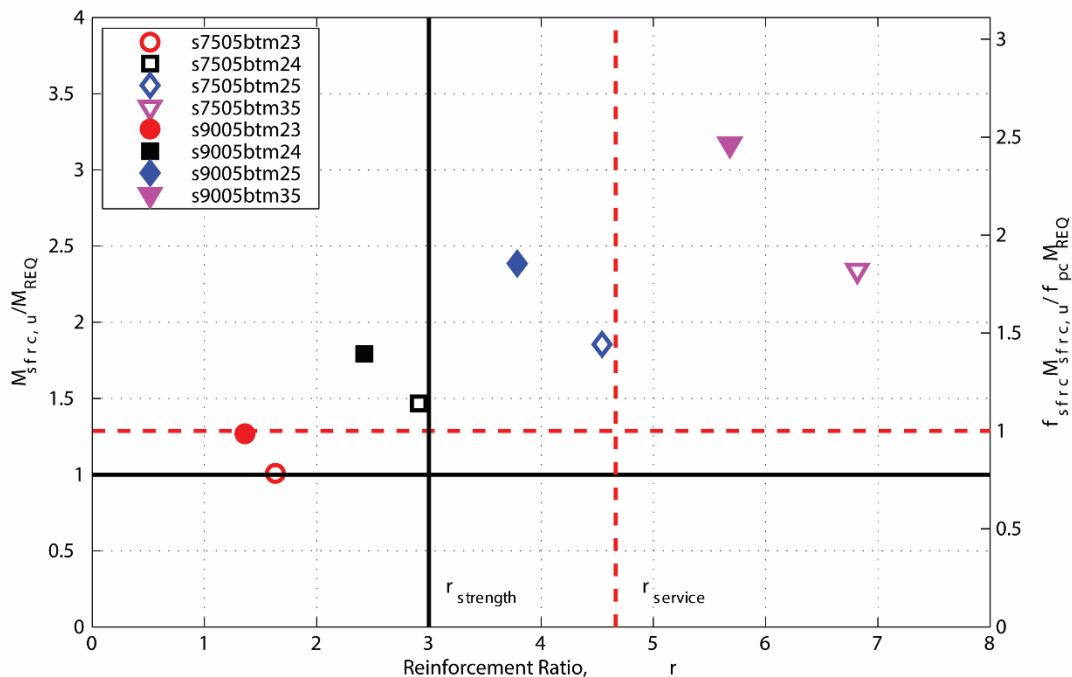


Figure 202. Normalized Moment vs. Steel Reinforcement Ratio—6 ft Girder Spacing and Steel at Bottom

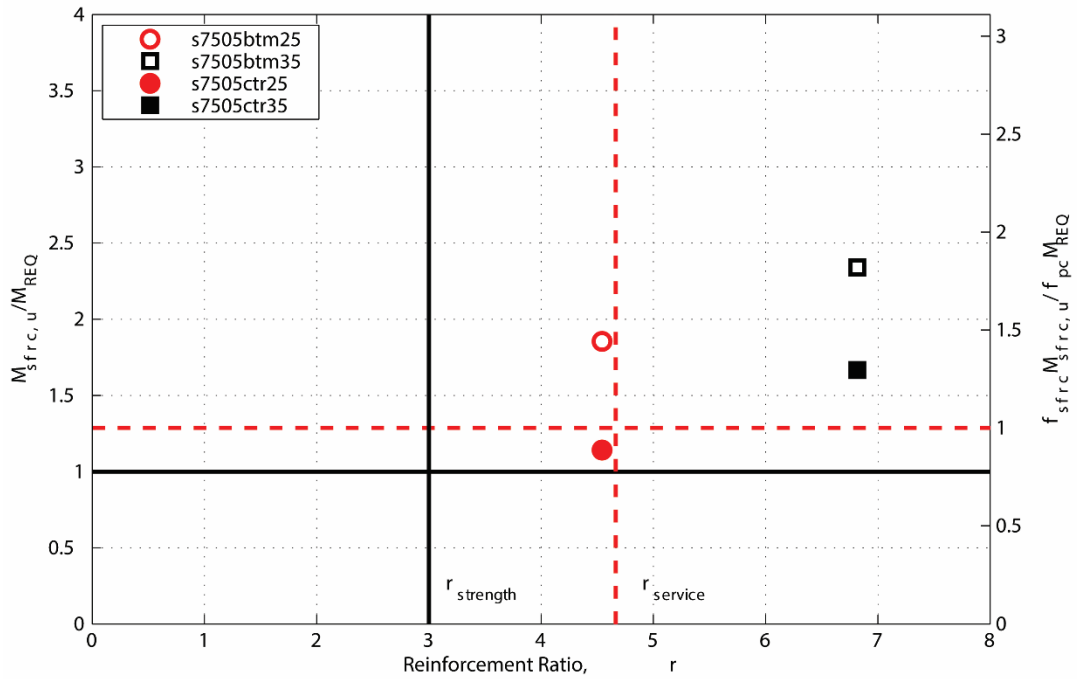


Figure 203. Normalized Moment vs. Steel Reinforcement Ratio—6 ft Girder Spacing and Steel at Center

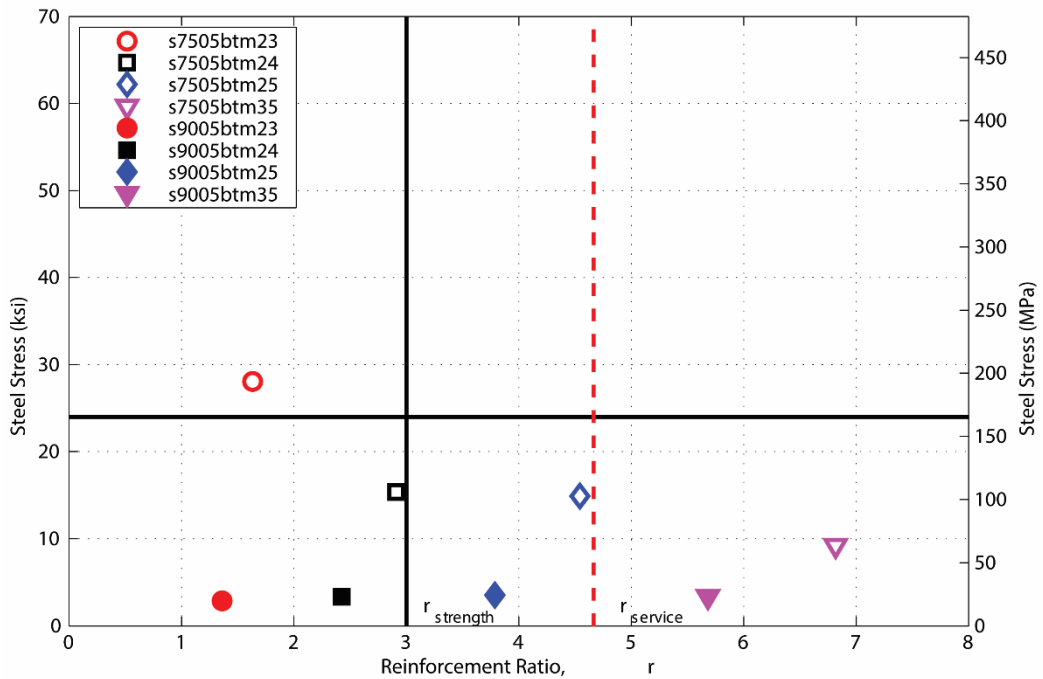


Figure 204. Service Stress vs. Steel Reinforcement Ratio—6 ft Girder Spacing and Steel at Bottom

SUMMARY

The moment-curvature analysis presented in this chapter is intended for the development of design procedures for SFRC in concrete bridge decks. The analysis provides a means to inversely determine the constitutive model for the tensile response of SFRC after the initial crack occurs. Furthermore, the analysis presents a comparison between the theoretical and experimental moment-curvature relationships and overall behavior. Verification of trends observed in the parameter study presented in Chapter 4 is also made. Finally, the repeatability of SFRC structural members is examined in the two experimental programs. The following conclusions are made from the moment-curvature analysis:

- The compression response is not affected by the presence of steel fibers in the concrete matrix. The modified Kent-Park model with a post-peak slope, Z , of 50 closely models the response of SFRC.
- The tension response can be modeled with a piecewise curve. An elastic response is used prior to the formation of the first crack. Following cracking, the response can be modeled with a linearly decreasing curve or a constant stress until the maximum strain of 0.025. The post-crack models are consistent with responses presented by others.
- The residual stress used in the tension response can be determined using an inverse analysis to create the best-fit curve of the moment-curvature response.
- The effectiveness of the steel fibers decreases as the area of steel reinforcement increases. Increasing the area of steel reinforcement directly increases the tension force carried by steel reinforcement; however, the maximum tension force carried by the fibers remains unchanged. Therefore, at low levels of steel reinforcement, the tension capacity of the fibers and the steel reinforcement are similar.
- The response of the companion beams cast alongside the bridge deck varied slightly from the slab strip specimens cast during the original experimental program. Further research needs to be conducted on the repeatability of SFRC experiments and the development of the post-crack tension response from standard ASTM C1609.
- The results of the slab strip experimental program are consistent with the trends observed in the parameter study conducted in Chapter 4.
 - Increasing the area of traditional steel reinforcement results in a proportional increase in the moment capacity.
 - Add fibers 0.5 percent by volume to the AASHTO empirical design satisfies both strength and service criteria.
 - Traditional steel reinforcement can be excluded from a SFRC section with 2.0 percent by volume fibers while satisfying strength requirements.

CHAPTER 9. ANALYSIS OF BRIDGE DECK TESTS

INTRODUCTION

The experimental results of the SFRC bridge deck presented in Chapter 7 are evaluated using a yield line analysis and a two-way shear analysis. The analyses are based on the results of the slab-strip experiments presented in Chapter 8. The yield line analysis is presented first and evaluates the flexural capacity of the bridge deck based on crack patterns and the moment capacity of a unit strip. The two-way shear analysis is next and is based on design equations formulated by other researchers.

YIELD LINE THEORY

Yield line theory is an upper-bound method that determines the failure load of a slab system. The method assumes that regions of plastic deformation, or hinges, form in the slab to create a failure pattern or mechanism. The failure pattern forms slab panels that rotate as a unit about each yield line or axis of rotation. Because the theory is an upper-bound method, all possible failure mechanisms must be investigated, with the lowest providing the true collapse load. The method uses the conservation of work and energy principle. The internal and external work of the slab are calculated and equated to each other to determine the failure capacity of the specimen. The internal and external work are calculated by:

$$IW = \sum ml\theta \quad (24)$$

$$EW = \sum P\delta + w_d A_d \delta_c \quad (25)$$

Where IW and EW are the internal and external work, respectively, m is the moment capacity per linear foot, θ is the angle of rotation for deflected shape, P is the externally applied load, δ is the deflection measured at the applied load, w_d is the self-weight of concrete slab, A_d is the area encompassed by failure mechanism, and δ_c is the deflection measured at the centroid of the failure mechanism.

Affinity Theorem

The affinity theorem is a transformation of an orthotropic failure mechanism to an isotropic mechanism (Park and Gamble 2000). The transformation modifies the length and external loads of the failure mechanism using a ratio, denoted μ , of the moment capacities in the strong and weak direction. The affinity transformation ratio is:

$$\mu = \frac{m_y}{m_x} \quad (26)$$

Where μ is the affinity transformation ratio of moment capacity in the strong and weak directions and m_x and m_y are the moment capacity per linear foot in the strong and weak directions.

The length in the weak direction and external load is normalized by the square root of the affinity transformation ratio to determine the equivalent isotropic mechanism, or affine slab. The transformed length and load for the affine slab is determined as follows:

$$l_{y,a} = \frac{l_y}{\sqrt{\mu}} \quad (27)$$

$$P_{u,a} = \frac{P_u}{\sqrt{\mu}} \quad (28)$$

Where $l_{y,a}$ is the length of affine slab in the weak direction, l_y is the length of real slab in the weak direction, $P_{u,a}$ is the external load for the affine slab, and P_u is the external load for the real slab.

The affinity theorem is particularly useful for fan failure mechanisms in orthotropic slabs. A circular fan is a common failure mechanism for an isotopically reinforced slab. The circular failure mechanism is stretched into an ellipse in the orthotropic slab due to the unequal moment capacities. Applying the affinity theorem to the orthotropic slab transforms the ellipse failure mechanism to a circular fan. The affine slab is solved by the simple equation for the internal and external work of a circular fan mechanism with the following affine transformation:

$$P_{u,a} = \frac{P_u}{\sqrt{\mu}} = 2\pi(m_x^+ + m_x^-) \quad (29)$$

Unit Moment Capacities

The unit moments used for the yield line analysis were determined based on the moment-curvature relationship for d7505BTM24. The constitutive model used for the SFRC post-crack response was the plastic model with a residual strength of 0.14 ksi. The nominal moment was extracted from the theoretical moment-curvature relationship determined for each direction of the SFRC bridge deck. Figure 205 and Table 66 show the theoretical moment curvature relationships and summarize the unit capacities.

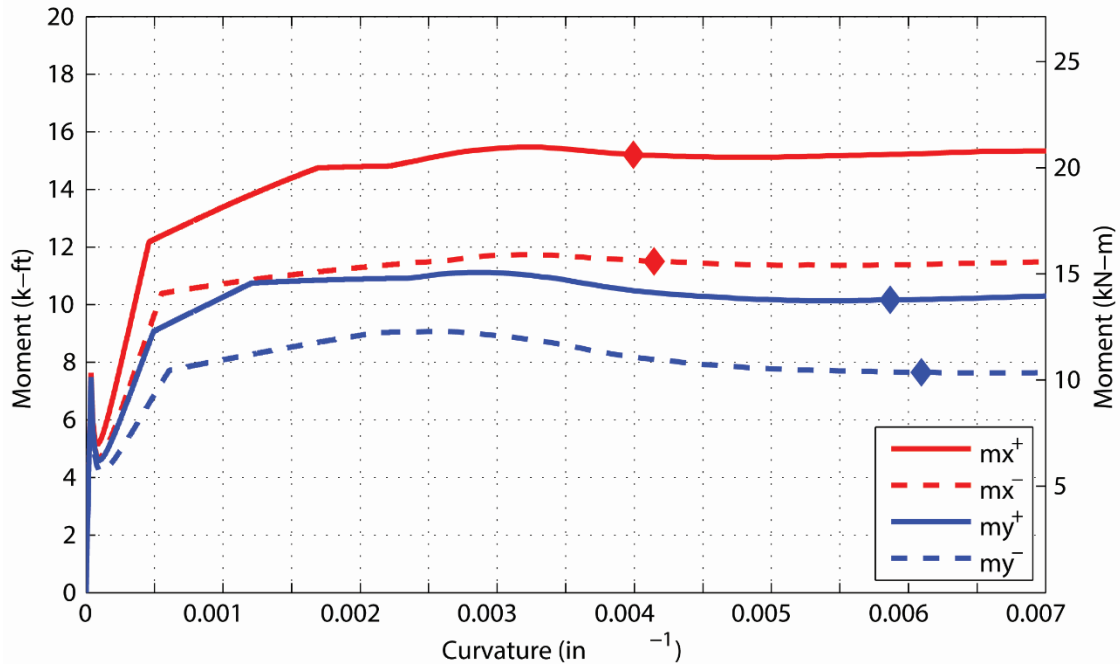


Figure 205. Moment-Curvature Relationship for SFRC Bridge Deck—Both Directions

Table 66. Moment Capacities Used for Yield Line Analysis

	Positive (k-ft)	Negative (k-ft)
m_x	15.21	11.51
m_y	10.16	7.65

LP1 and LP4 – Individual Wheel

Figure 206 and Figure 207 show the crack pattern observed at the conclusion of testing for LP1 and LP4. Tests LP1 and LP4 achieved the same maximum capacity and failure pattern. Negative yield lines originated on the top surface of the deck adjacent to the support beams and propagated east and west. Both load cases had negative yield lines that propagated toward the longitudinal middle of the deck prior to orientating perpendicular to the support beams extending north and south. The portion of the bridge deck between the load point and the free edge of the deck behaved in a one-way manner. The negative yield lines extended directly toward the free edge of the deck with very minimal signs of re-orientating perpendicular to the support beams. Positive yield lines form on the bottom surface of the deck adjacent to the wheel load and propagate east and west parallel to the support beams. After extending beyond the load point the positive yield lines radiate outward diagonal completing the formation of the elliptical fan failure pattern at the longitudinal middle of the deck. The yield pattern consists of half of an elliptical fan mechanism and four rectangular panels. These regions are labeled in Figure 206 and Figure 207. The darker lines in each of these figures are the cracks that were observed on the top surface of the deck and the lighter lines are the cracks observed on the bottom surface.

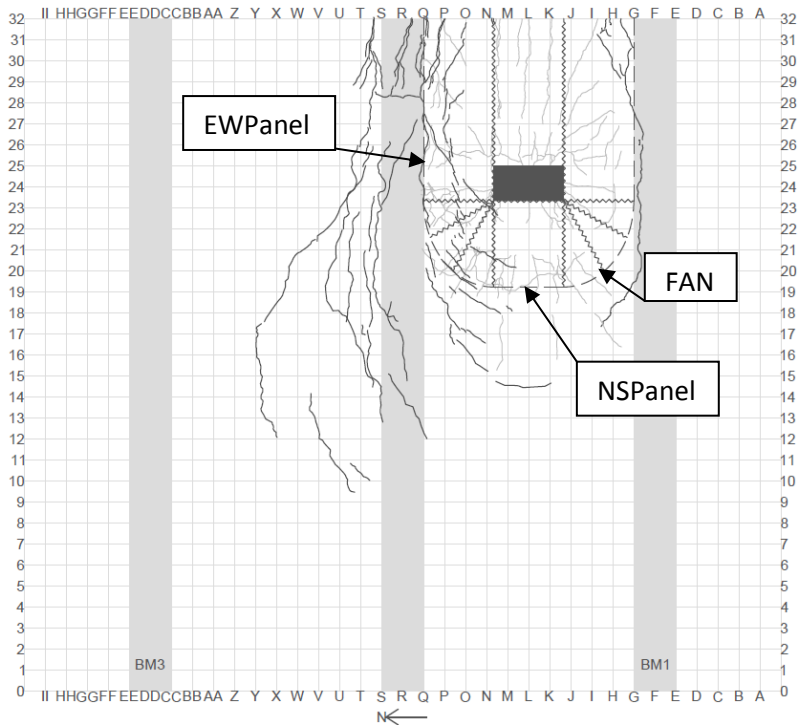


Figure 206. Failure Mechanism for LP1

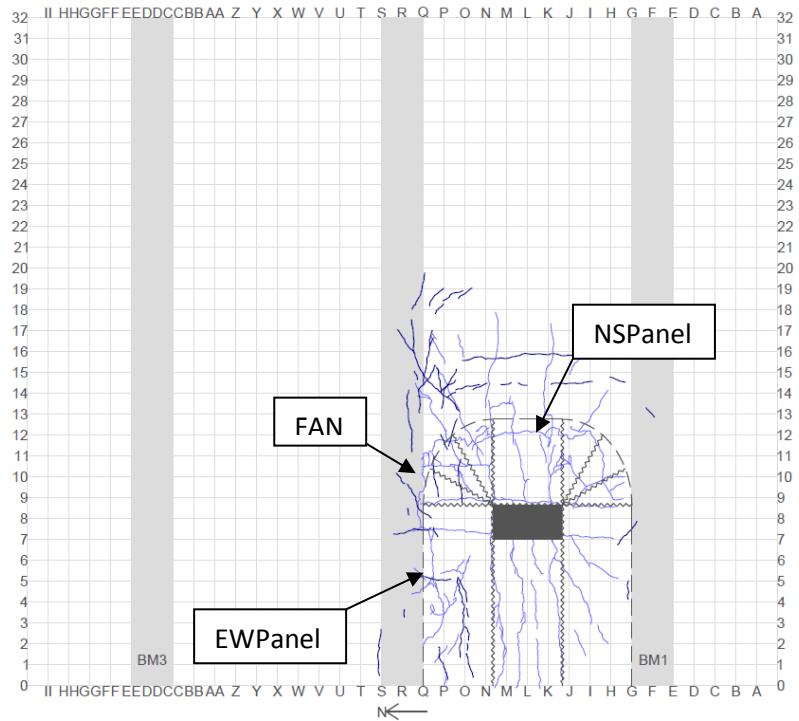


Figure 207. Failure Mechanism for LP4

An elliptical fan mechanism formed as a result of the concentrated load and orthotropic reinforcement. An affinity transformation is applied to the deck to simplify the elliptical fan mechanism into a circular fan (Figure 208). The deck is transformed by the following:

$$EW = \underbrace{\frac{P}{\sqrt{\mu}}\delta}_{\text{FAN}} + \underbrace{q\left(\frac{\pi r^2}{3}\right)\delta}_{\text{EWPanel}} + \underbrace{3(52qr^2\delta) + \frac{20}{\sqrt{\mu}}qr^2\delta}_{\text{NSPanel}} \quad (30)$$

$$IW = \underbrace{2\pi\delta(m_x^- + m_x^+)}_{\text{FAN}} + \underbrace{\frac{20}{\sqrt{\mu}}\frac{\delta}{r}(m_x^- + m_x^+)}_{\text{EWPanel}} + \underbrace{2\left(52\frac{\delta}{r}(m_x^- + m_x^+)\right)}_{\text{NSPanel}} \quad (31)$$

Where m_x is the moment capacity in the strong direction, r is the radius of circular fan pattern, μ is the affine ratio of moment capacity in weak direction to moment capacity in the strong direction, q is the self-weight of concrete, and P_u is the external load.

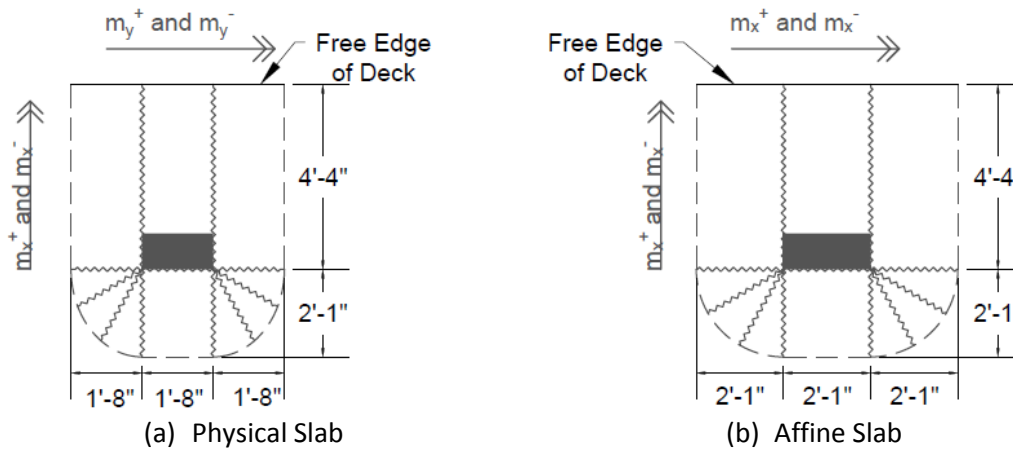


Figure 208. Transformation of Physical Slab to Affine Slab – LP1/LP4

LP2 – Tandem Axle

Figure 209 shows the crack pattern observed at the conclusion of testing for LP2 and its associated failure mechanism or yield line. Negative yield lines originated on the top surface of the deck adjacent to the support beams and propagated east and west. After extending beyond each loading point, the yield line curves forming the outside edge of an elliptical failure pattern. Positive yield lines form on the bottom surface of the deck adjacent to the wheel loads and propagate east and west parallel to the support beams. After extending beyond the load points the positive yield lines radiate outward diagonal completing the formation of the elliptical fan failure pattern. The yield pattern consists of a complete

elliptical fan mechanism and four rectangular panels. These regions are labeled in Figure 209. The darker lines in the figure are the cracks that were observed on the top surface of the deck and the lighter lines are the cracks observed on the bottom surface.

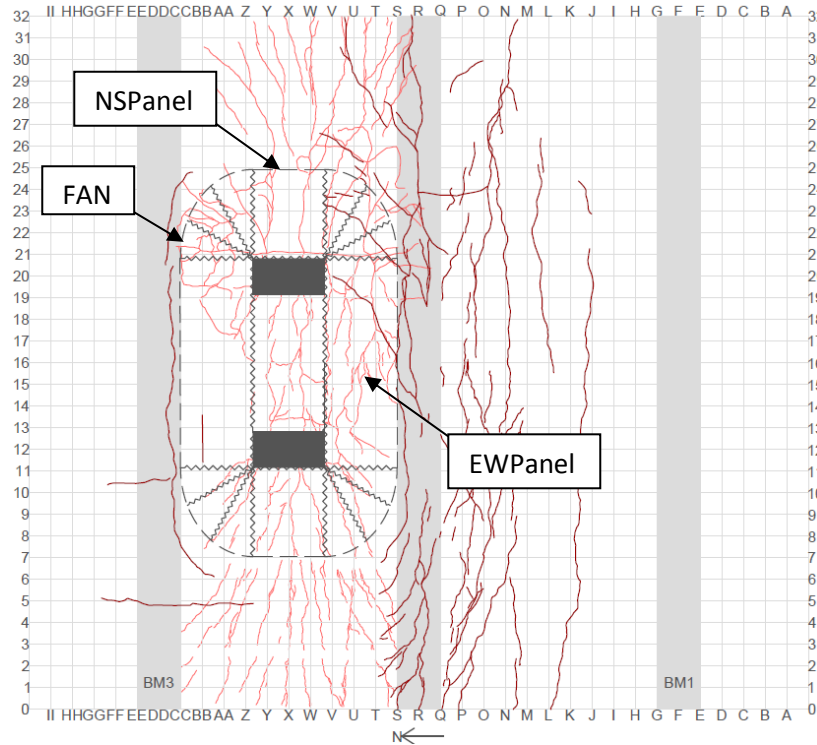


Figure 209. Failure Mechanism for LP2

An elliptical fan mechanism formed as a result of the concentrated load and orthotropic reinforcement. An affinity transformation is applied to the deck to simplify the elliptical fan mechanism into a circular fan (Figure 210). The deck is transformed by the following:

$$EW = \frac{P}{\sqrt{\mu}} \delta + \underbrace{q \left(\frac{\pi r^2}{3} \right) \delta}_{\text{FAN}} + \underbrace{3(58qr^2 \delta)}_{\text{EWPanel}} + \underbrace{\frac{20}{\sqrt{\mu}} qr^2 \delta}_{\text{NSPanel}} \quad (32)$$

$$IW = \underbrace{2\pi\delta(m_x^- + m_x^+)}_{\text{FAN}} + 2 \underbrace{\left(\frac{20}{\sqrt{\mu}} \frac{\delta}{r} (m_y^- + m_y^+) \right)}_{\text{EWPanel}} + 2 \underbrace{\left(58 \frac{\delta}{r} (m_x^- + m_x^+) \right)}_{\text{NSPanel}} \quad (33)$$

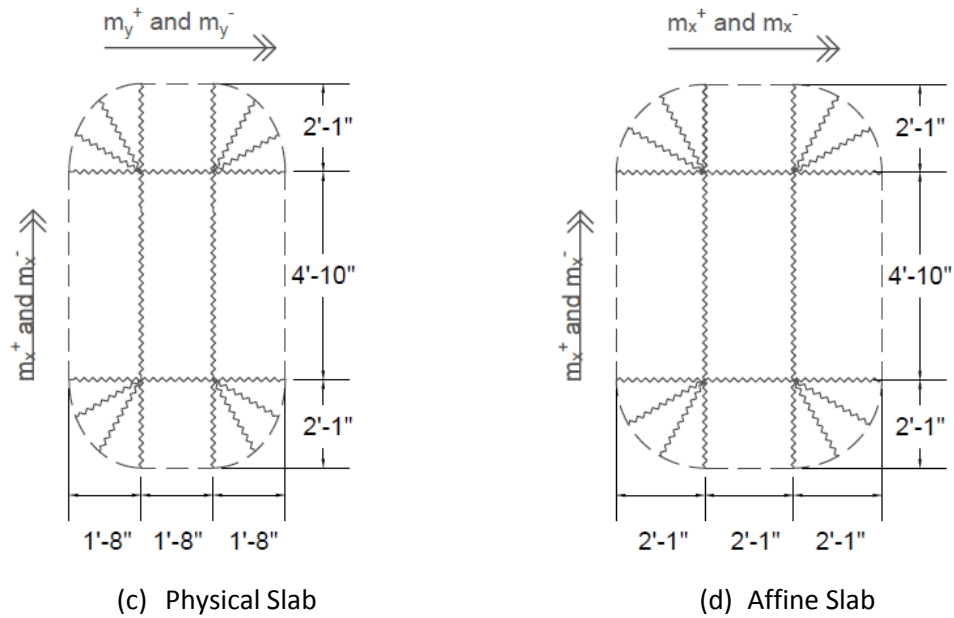


Figure 210. Transformation of Physical Slab to Affine Slab – LP2

LP3 – Overhang Single Axle

Figure 211 shows the crack pattern observed at the conclusion of testing for LP3 and its associated failure mechanism or yield line. Negative yield lines originated on the top surface of the deck adjacent to the support beams and propagated diagonally southwest and southeast. Positive yield lines form on the bottom surface of the deck adjacent to the wheel loads and propagated north until extending to the support beams. The yield pattern consists of two triangular panels and one rectangular panel. An affinity transformation was not necessary for this load pattern. The conservation of work was determined by the following (Mander et al. 2010):

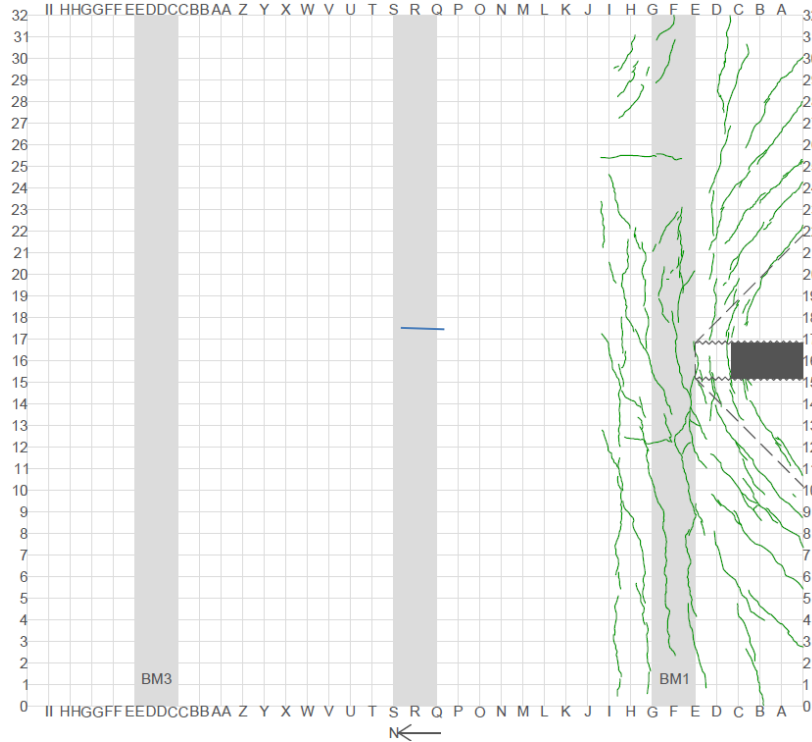


Figure 211. Failure Mechanism and Deflection Profile for LP3

$$EW = P\delta + q \left(l_x l_y \frac{\delta}{3} + b_1 l_x \frac{\delta}{2} \right) \quad (34)$$

$$IW = \frac{2m_x^-}{l_x - .5(20)} (l_y + 0.5(10)) \delta + 2(m_y^+ + m_y^-) \frac{l_x^2}{l_y(l_x - .5(20))} \quad (35)$$

Where l_x and l_y are the length of yield lines in the strong and weak directions.

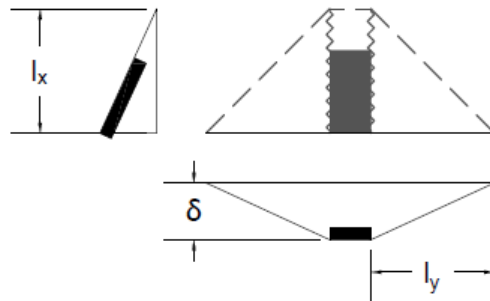


Figure 212. Failure Mechanism for LP3

Discussion

Table 67 summarizes the results for the yield line analysis conducted on the SFRC bridge deck. The theoretical strength of the SFRC bridge deck is approximately 11 percent larger than the theoretical strength of a PC bridge deck with the same area of traditional steel reinforcement. The addition of fibers

increases the unit moment capacity of the bridge deck and allows for a redistribution of the stresses in the bridge deck. The theoretical strength for the SFRC and PC bridge deck was computed using an identical failure mechanism; therefore, only the increase moment capacity of the SFRC is accounted for in the theoretical values reported in Table 67. As a result, the experimental results vary significantly from the theoretical strength.

Table 67. Summary of Yield Line Analysis for SFRC Bridge Deck

	P_{SFRC}^{Exp} , kips	P_{SFRC}^{Theory} , kips	$\frac{P_{SFRC}^{Exp}}{P_{SFRC}^{Theory}}$	P_{PC}^{Theory} , kips	$\frac{P_{SFRC}^{Theory}}{P_{PC}^{Theory}}$
LP1/LP4	203	161	1.26	145	1.11
LP2	185	128	1.44	122	1.05
LP3	96	91	1.06	83	1.09

*All collapse loads are for individual wheels.

The experimental failure capacity of the interior load patterns, LP1, LP2, and LP4, is approximately 35 percent larger than the theoretical capacity determined using the yield line analysis. Numerous other potential failure patterns were investigated based on the observed crack patterns. The failure pattern presented here resulted in the lowest collapse load. The under-prediction of the failure capacity is not observed in LP3. The south overhang lacks the restraint necessary to redistribute the load and provide membrane action.

The significant under-prediction of yield line analysis for SFRC slabs has been observed by other researchers. Fall et al. (2014) tested simply supported two-way slabs with SFRC made with approximately 0.35 percent by volume of double-hooked that performed significantly better than the yield line analysis predicted. Destrée and Mandl (2008) investigated elevated flat slabs with SFRC. The flat slab had a maximum capacity of up to five times the yield line capacity.

The under-prediction of the collapse load is a factor of the redistribution of the load. The indeterminacy and restraint of the structure allows the SFRC to significantly spread the load as observed by the larger areas of cracking on the SFRC bridge deck. Compressive and tension membrane action has been demonstrated to also play a significant role. Mufti et al. (1993) investigated the use of exterior struts and synthetic fibers on bridge decks. Researchers reduced the area of steel reinforcement to a single layer due to the restraint provided by the exterior struts and the resulting compressive membrane action.

TWO-WAY SHEAR ANALYSIS

The concentrated footprint of the applied wheel load and restraints of the supporting concrete beams can result in a two-way or punching shear failure. The shear capacity of the bridge deck must also be evaluated.

Naaman et al. (2007) evaluated the shear capacity of HPRCC slabs and found that FRC had nearly double the capacity of plain reinforced concrete. The slabs evaluated by Naaman et al. had fiber

percentages between 1.75 percent and 2.0 percent. Nguyen-Minh et al. (2011) evaluated the existing equations proposed by Harajili et al. (1995), and Choi (2007) for the two-way shear capacity of FRC. Nguyen-Minh et al. concluded that the proposed methods are inadequate because they do not account for the length, shape, or aspect ratio of the fibers included in the concrete matrix. Furthermore, the authors found that the scatter of the proposed equations was significant with a coefficient of variance of greater than 24 percent.

The design philosophy proposed by Harajili et al. is used to determine the two-way shear capacity of the SFRC used in this test program due to the lack of a code approved method for calculating the capacity of SFRC. The method proposed by Harajili et al. is currently the most accurate method as demonstrated by Nguyen-Minh et al. (2011). The additional two-way shear capacity of an SFRC slab can be accounted for by adding an additional term to the existing equation for punching shear of a plain reinforced concrete slab as follows:

$$V = V_{PC} + V_{FRC} \quad (36)$$

$$V_{FRC} = 1.15v_f b_0 d \sqrt{f'_c} \quad (37)$$

$$= \left(0.063 + \frac{0.126}{\beta_c} \right) b_0 d \sqrt{f'_c} \quad (38)$$

Where V the total shear strength of composite material is, V_{PC} is the shear strength of PC for critical failure plane in accordance with AASHTO (2014); V_{FRC} is the shear strength of FRC for critical failure plane (Harajili et al. 1994); v_f is the dosage of fiber by volume; b_0 is the perimeter of critical failure plane shown in Figure 213; d is the depth to bottom layer of steel; f'_c is the compressive strength of concrete; and β_c is the ratio of long side to short side of concentrated load.

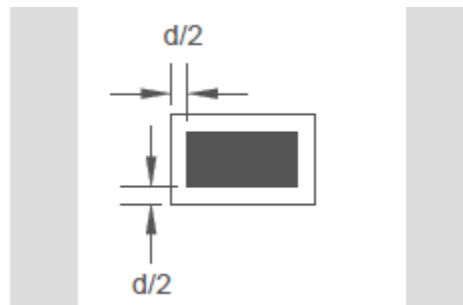


Figure 213. Critical Shear Perimeter due to Wheel Load

The two-way shear capacity was calculated using Equations 36 through 38 for plate used for the bridge deck tests. The SFRC bridge deck has a shear capacity of 243 kips, approximately 40 kips larger than the failure load recorded for LP1 and LP4.

SUMMARY

The analyses performed in this section are intended to demonstrate and predict the two-way behavior of an orthotropic SFRC bridge deck. The analysis provides a means to predict the failure capacity of the SFRC bridge deck based on its moment capacity and shear strength. The yield line analysis is compared to the experimental tests of the bridge deck. A two-way shear analysis was conducted to relate the moment capacity of the SFRC to its shear capacity. The following conclusions are made from the two-way analysis:

- The failure capacity of the SFRC specimen is significantly under predicted by the yield line theory. This result is consistent with conclusions made by other researchers (Fall et al. 2014; Destrée and Mandl 2008). The membrane action and load redistribution provided by the steel fibers adds significant strength to the ultimate limit state of the structure not accounted for by yield line analysis.
- The predicted failure capacity from yield line analysis is five times larger than the AASHTO HS20 design truck wheel load with strength limit state load factors.

A satisfactory method for determining the two-way, or punching shear strength of SFRC has not been developed. Using the design philosophy proposed by Harajili et al. (1995), the punching shear capacity of the SFRC bridge deck is 243 kips. The punching shear strength is 40 kips larger than the highest experimental collapse load and 80 kips larger than the highest theoretical collapse load from yield line analysis.

CHAPTER 10. RECOMMENDATIONS FOR DESIGN AND IMPLEMENTATION

INTRODUCTION

The experimental tests have shown the benefits of SFRC on the performance of reinforced concrete bridge decks. This chapter provides insight and recommendations for design and implementation of SFRC for slabs. First, equations for service and nominal strength are presented. This is followed by use of the proposed equations for design, including a discussion of design examples. Finally, potential obstacles to implementation are put forward and discussed.

SERVICE LIMIT STATE EQUATIONS

The design of conventionally reinforced concrete bridge decks is typically controlled by the service limit state. The service limit state uses the allowable stress design and a maximum allowable tensile stress of 24 ksi (165 Mpa) in the conventional steel. This design is achieved using Hooke's law in an elastic analysis of the cross-section. The steel area is transformed into an equivalent concrete area to permit the analysis. The service condition is assumed to occur after the cross-section has cracked, and the tension capacity of the PC is ignored.

The proposed service state design procedure for SFRC uses the same principles as the traditional design for PC, but the use of FRC eliminates ability to use a transformed section. An additional component (Figure 214) is added to the stress and strain profiles to account for the contribution of the SFRC. The residual tensile force of the SFRC will be accounted for in a manner similar to the traditional steel reinforcement by lumping the resultant force at the mid-depth of the cracked region.

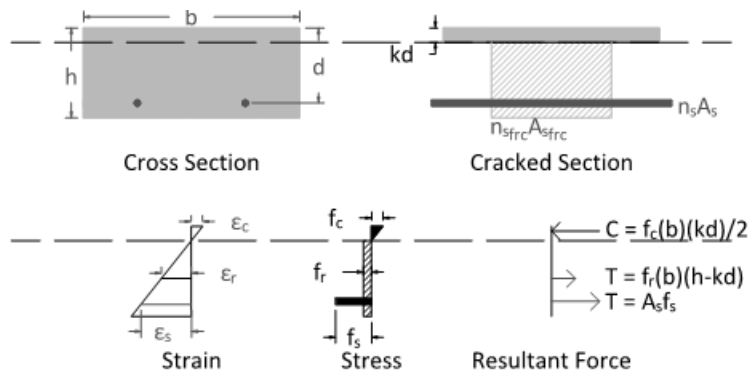


Figure 214. Service Limit State—SFRC

Tension resultant forces from the steel and FRC can be calculated as:

$$T_s = A_s f_s \quad (39)$$

$$T_{FRC} = f_{resid} b (h - kd) \quad (40)$$

Where f_s is the stress in the steel; A_s is the area of conventional steel; f_{resid} is the residual tension stress (assumed constant in tension region); b is the width of the slab; h is the slab thickness; kd is the depth of

the neutral axis measured from the extreme compression face; and d is the effective flexural depth to the centroid of the steel.

The stress in the concrete, f_c , can be found from the neutral axis depth kd and the steel stress:

$$f_c = E_c \varepsilon_c = E_c \frac{f_s}{E_s} \frac{kd}{d - kd} = \frac{f_s}{n} \frac{kd}{d - kd} \quad (41)$$

Where E_c is the concrete modulus of elasticity; E_s is the steel modulus of elasticity; and n is the modular ratio. The concrete stress is used to calculate the concrete resultant force:

$$C = \frac{f_c kd}{2} b = \frac{f_s b}{2n} \frac{kd^2}{d - kd} \quad (42)$$

The neutral axis can be found by setting the steel stress to the maximum allowable stress and solving the equilibrium of forces equation:

$$0 = A_s f_s + f_{resid} b (h - kd) - \frac{f_s b}{2n} \frac{kd^2}{d - kd} \quad (43)$$

Once the neutral axis is known, the allowable service moment can be found:

$$j = 1 - \frac{k}{3} \quad (44)$$

$$M_{sa} = f_s A_s j d + f_{resid} b (h - kd) \left(\frac{2kd}{3} + \frac{h - kd}{2} \right) \quad (45)$$

The proposed procedure has all of the same components of the traditional service analysis for SFRC. Determining the depth of the neutral axis is more involved than PC design due to the SFRC tension stress block. However, once the neutral axis is known, the procedure returns to the traditional service equation with the addition of a single term for the SFRC contributions to the service capacity. The proposed method is also different in that it uses the maximum allowable service stress to find the maximum allowable service moment, whereas the traditional procedure uses the service moment demand to check the stress in the steel reinforcement. This is necessary because, unlike a PC reinforced beam, the neutral axis depth after cracking cannot be calculated independent of the strains in the steel and concrete.

STRENGTH LIMIT STATE EQUATIONS

The proposed procedure to verify the strength of an SFRC specimen uses the traditional approach for PC with the addition of a component to account for the SFRC. Figure 215 shows the stress and strain profiles for an SFRC section at the strength limit state. A simplification is made to both the compression and tension stress blocks of the SFRC consistent with current practice. The compression block is identical to current design for PC while the tensile stress block is represented by a constant residual stress the entire height of the tensile region of the cross section.

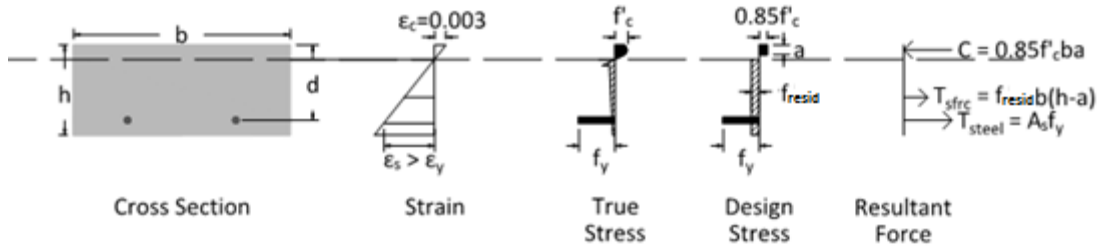


Figure 215. Strength Limit State – SFRC

The depth of the neutral axis is calculated based on static equilibrium of the cross-section:

$$T_s = A_s f_y \quad (46)$$

$$C_c = 0.85 f'_c b a \quad (47)$$

$$T_{sfrc} = (h - c) f_{resid} b \quad (48)$$

$$a = \frac{A_s f_y + h f_{resid} b}{0.85 f'_c b + \frac{f_{resid} b}{\beta_1}} \quad (49)$$

Once the depth of the neutral axis is determined, the moment capacity of the section is determined by:

$$M_n = A_s f_y j d + f_{resid} (h - c) b \alpha d \quad (50)$$

Where αd is the lever arm between the concrete compression and concrete tension resultant forces and $j d$ is the lever arm between the concrete compression and steel tension resultant forces. The lever arms can be calculated by:

$$j = d - \frac{a}{2} \quad (51)$$

$$\alpha d = h - \frac{h - c}{2} - \frac{a}{2} \quad (52)$$

The procedure for determining the strength capacity of an SFRC section is nearly identical to the traditional design equation with the exception of an additional term in the equation to determine the depth of the neutral axis and moment capacity.

EVALUATION PROPOSED DESIGN EQUATIONS USING SLAB STRIP TEST RESULTS

The proposed equations for service and nominal strengths were used to calculate the measured values of the s-series slab strips. Calculations were done using a residual tensile strength of 0.090 ksi, determined during the inverse analysis presented in Chapter 8. Table 68 and Table 69 provide the results for service and nominal strength, respectively.

For service, the proposed equations have large scatter in the error. Although many are with 10 percent of the observed experimental value, there is no consistent over or under prediction. For slab strips with steel at the bottom, there is a trend in that the design equations under predict at lower reinforcement

ratios and over predict at higher strength levels. The low prediction of service moments for s7505btm23 and s9005tm23 are consistent with the observed difference between the measured and predicted experimental capacity; insufficient data are available to determine if this is a trend applicable to all slabs with low reinforcement ratios or if it is a phenomena of the small #3 bars used in these two tests. For slab strips with the steel at the center, there is wide range of error, but stress in the steel may not be the most appropriate method to establish acceptable service level performance.

Table 69 summarizes the error of the proposed method for calculating the nominal strength. The theoretical model under predicts the experimental moment capacity for every slab-strip specimen, with an average error of 4 percent and a maximum error of 11 percent. If the proposed equations were used for design, the resulting design could be considered to be conservative.

Table 68. Service Moment of Experimental Tests Using Proposed Procedure

	Experimental (k-ft)	Design Equations (k-ft)	Error
s7505BTM23	7.1	5.8	-0.18
s7505BTM24	7.7	7.8	0.01
s7505BTM25	9.3	10.1	0.09
s7505BTM35	10.4	13.3	0.28
s9005BTM23	10.6	7.9	-0.25
s9005BTM24	9.9	10.3	0.04
s9005BTM25	13.3	13.2	-0.01
s9005BTM35	15.9	17.2	0.08
s7505CTR25	6.3	7.5	0.19
s7505CTR35	10.2	9.4	-0.08
Max Error, %		28	
Min Error, %		0.1	
Average , %		12.1	
Average, %		2.0	
STD, %		16.0	

Table 69. Nominal Moment of Experimental Tests Using Proposed Procedure

	Experimental (k-ft)	Design Equations (k-ft)	Error
s7505BTM23	12.2	11.0	-0.102
s7505BTM24	17.6	16.6	-0.058
s7505BTM25	23.5	23.1	-0.016
s7505BTM35	32.8	32.2	-0.018
s9005BTM23	16.1	14.3	-0.109
s9005BTM24	22.7	21.4	-0.057
s9005BTM25	29.6	29.7	0.004
s9005BTM35	40.1	41.2	0.029
s7505CTR25	15.1	14.9	-0.010
s7505CTR35	20.2	19.9	-0.014
Max Error, %		10.9	
Min Error, %		0.4	
Average , %		4.2	
Average, %		-4.0	
STD, %		5	

DESIGN STEPS

Two approaches for the design of slabs using SFRC are recommended here. The first ignores the contribution of SFRC in tension at nominal strength, but uses the tensile strength for calculating the serviceability limit.

1. Computer design demands for ultimate and service loads.
2. Establish material strengths, including SFRC post-peak tensile strength.

$$f_{resid} = \mu f_r \quad (53)$$

3. Design amount of steel needed to provide adequate nominal strength.
4. Solve for the elastic neutral axis depth, k_d , using Equation 43.
5. Compute the allowable service moment M_{sa} using Equations 45 and the allowable service stress, f_s .
6. If M_{sa} is less than or equal to the service demands, M_s , design is complete.
7. If M_{sa} is greater than the service demands, M_s , additional reinforcement is needed to satisfy the limits:

$$k = 3(1 - j) \quad (54)$$

$$A_{s,reqd} \geq \frac{1}{f_s j d} (M_s - f_{resid} b (h - kd) \left(\frac{2kd}{3} + \frac{h - kd}{2} \right)) \quad (55)$$

The second design approach is to consider the SFRC to contribute tensile strength to the nominal strength. This is practical only with higher residual tensile strengths than that used in the experimental test program of this report. This is due not only to relatively small strength, but the need to use a lower strength reduction factor recommended by previous researchers. The steps for design are as follows:

1. Compute design demands for ultimate and service loads.
2. Establish material strengths, including SFRC post-peak tensile strength.

$$f_{resid} = \mu f_r \quad (56)$$

3. Assume a value of the lever arm jd . Based on the experimental tests, a recommended value for j is 0.95 for steel at the top or bottom and 0.9 for steel at the center.
4. Calculate the compressive stress block height by rearranging Equation 51:

$$a = 2d(1 - j) \quad (57)$$

5. Calculate the required area of steel by rearranging Equation 50 and replacing M_n with M_u/ϕ , where $\phi=0.7$.

$$A_{s,reqd} \geq \frac{\frac{M_u}{\phi} - f_{resid}(h - c)ba d}{f_y j d} \quad (58)$$

$$c = a/\beta_1 \quad (59)$$

$$j = d - \frac{a}{2} \quad (60)$$

$$\alpha d = h - \frac{h - c}{2} - \frac{a}{2} \quad (61)$$

6. Select reinforcing steel size and spacing to satisfy the required area.
7. Verify strength design using Equations 49-52.
8. Verify service design using Equations 43-45.

These proposed design approaches are for steel reinforced SFRC slabs and should not be applied to SFRC only slabs, which is beyond the scope of this report.

DESIGN EXAMPLES

Example designs implementing the proposed design equations for SFRC are provided here. The design examples are modified from the deck design portion of ADOT LRFD Example 4 (2-span Precast Pretensioned I-Girder) to allow a direct comparison of conventional and FRC designs. Relevant characteristics for the bridge deck design include:

- 8 in. slab thickness, including 0.5 in. wearing surface.
- Reinforcing steel: Yield strength 60 ksi; Modulus of Elasticity 29,000 ksi.
- Deck concrete: Compressive strength 4.5 ksi; Modulus of Elasticity 3861 ksi; MOR (service level calculations), $f_r = 0.509$ ksi; MOR (cracking moment), $f_r = 0.785$ ksi.
- Modular ratio, $n = 7.51$ ($n = 8$ used for design).
- #5 bars.

Four different designs are compared: RC with service limits, RC without service limits, SFRC design for service, and SFRC design for strength. The first two are to provide a baseline for the SFRC designs.

For the SFRC service design, residual tensile strength is computed using $\mu = 0.12$. This is the same value as was determined for the slab-strip experimental tests in Chapter 8. Such a value is ineffective for strength design due to the small value in comparison to the steel yield stress and when the lower strength reduction factor is taken into account. Thus, for the SFRC strength design example, a larger value of $\mu = 0.40$ is used. Such a value is reasonable for a SFRC mix, but would require a different fiber type than is used in this report.

Table 70 summarizes the resulting four designs; Appendix B provides calculations. A comparison of the two RC designs highlights the fact that service limits control the design of slabs and leads to an increase of steel over that needed for strength. In the SFRC service design example, the SFRC is able to provide reduced steel stresses at service and thus the spacing of reinforcing bars is nearly the same as for RC strength design. For SFRC strength design, less steel is needed than for the strength design of RC slabs.

The service design procedure presented includes a conservative assumption that all concrete on the tension side of the neutral axis has the residual concrete strength. In reality, the concrete near the neutral axis will have a greater stress, thus reducing the service stresses. A more accurate calculation for the service moment can be obtained through implementation of a more detailed tensile concrete stress block such as that proposed by Soranakom and Mobashar, although this would require significantly more computational effort.

Implementation of the proposed equations for the slab strip s-series tests indicates that the prediction of the allowable service moment is more conservative as the amount of conventional steel decreases. Caution should be used at low ratios; it is tempting to assume service stress may be acceptable, but more experimental data are needed to verify this observation is not an outlier. While the equations yield unconservative results at higher reinforcement ratios, service behavior is unlikely to be affected as the higher reinforcement ratio with generally satisfy service independent of the FRC. Care must be exercised if the proposed service level equations are to be used for the design of slabs thinner than would typically

be used for design. In such cases, a more detailed stress block is recommended, as is the use of an SFRC with a well-defined and easily repeatable μ .

In addition to modifications of the nominal strength, M_n , strength design dependent on SFRC tension response requires modification of the strength reduction factor used. Previous researchers have recommended a value of 0.70 in the absence of sufficient experimental data to support a higher value; although the proposed design equations applied to the s-series slab strips indicate the design equations are appropriate, the conservative recommendation of 0.70 will be used in this example. When the lower strength reduction factor is used, slab design using low residual strengths will result in a design that requires more steel than is required for design for the service limit. Thus, a larger design capacity ϕM_n will be obtained by ignoring the contributions of FRC. Strength design using FRC becomes practical only at larger residual tensile strengths.

Table 70. Summary of ADOT LRFD Design Example 4

	Positive Bending	Negative Bending
Demands and Constant Values		
M_{cr} , k-ft	8.37	8.37
M_s , k-ft	6.01	6.82
M_u , k-ft	10.21	11.62
d_s , in.	6.19	5.19
RC Design (w/ service limits)		
Reinforcement	#5 @ 6.5"	#5 @ 5"
$f_s^{service}$, ksi	22.58	24.00
$M_r = \phi M_n$, k-ft	14.97	15.75
RC Design (w/out service limits)		
Reinforcement	#5 @ 9"	#5 @ 6.5"
M_{sa} , k-ft	4.45	5.33
SFRC Service Design ($\mu = 0.12$)		
Reinforcement	#5 @ 9.0"	#5 @ 6"
SFRC Strength Design ($\mu = 0.40$)		
Reinforcement	#5 @ 9.0"	#5 @ 6"

DESIGN AIDS

Design aids can be developed by researchers and fiber manufacturers to facilitate the empirical design with SFRC. Soranakom and Mobasher (2009) presented design aids relating the capacity of PC with SFRC sections.

Figure 216 and Figure 217 provide service and strength capacities for three levels of residual strength and three different depths. Designers with a required moment demand, known residual stress, and

depth of the section may use the design aid to determine the area of steel reinforcement necessary to satisfy both the service and strength demands.

The proposed design aids does not solve the issue of obtaining the residual stress for SFRC. The aids simplify the design procedure once the material properties are known. Additional research to relate the tension response of SFRC to repeatable material tests is crucial to the adoption of SFRC as supplemental reinforcement.

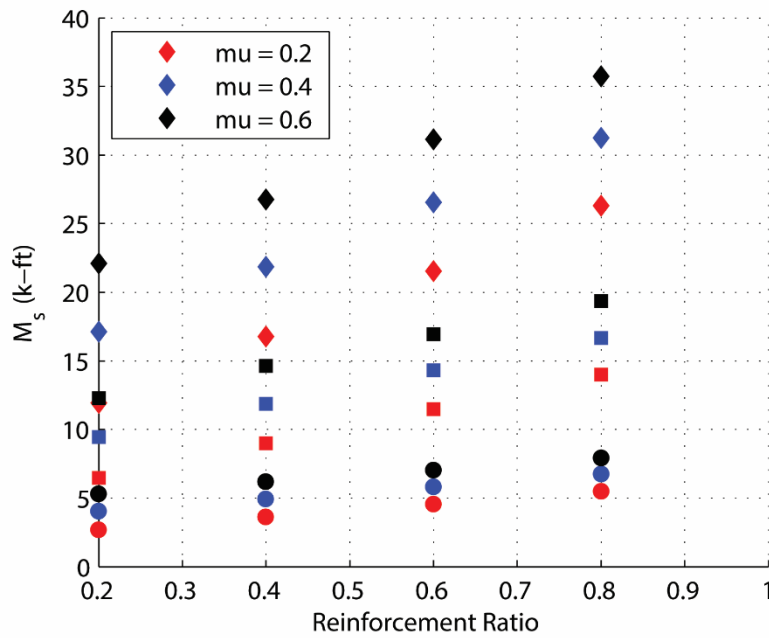


Figure 216. Design Aid—Service Moment vs. Reinforcement Ratio. Shape Indicates Slab Depth: Circle h=6 in.; Square=9 in.; Diamond = 12 in.

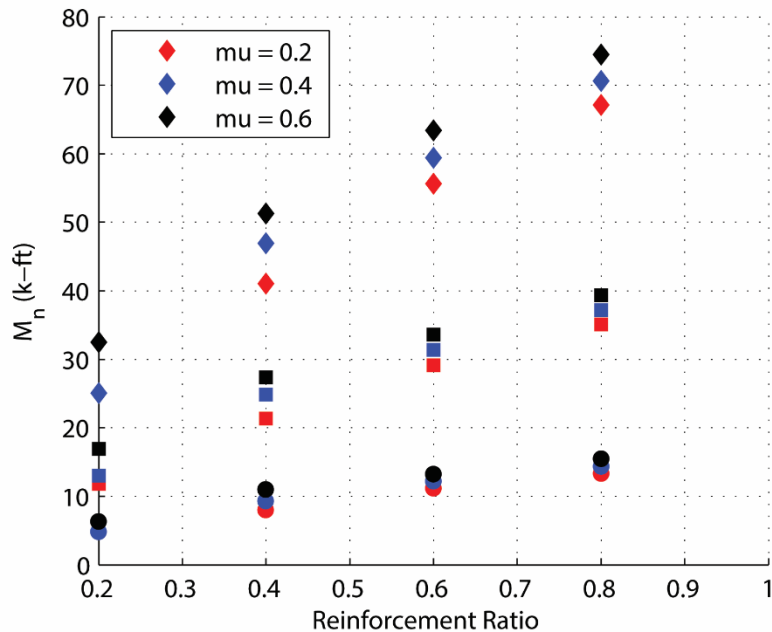


Figure 217. Design Aid—Strength Moment vs. Reinforcement Ratio

IMPLEMENTATION

Selection, Specifications, and Testing of FRC

Critical to the implementation of FRC is the selection, specification, and testing of the appropriate material properties.

Selection of the material properties can take a two basic approaches:

1. Selection of FRC with minimum material properties, with the material properties used by the structural engineer to determine the amount of conventional steel.
2. Calculation of minimum material properties to meet desired objectives. For example, the structural engineer may choose to design conventional reinforcement to satisfy strength criteria and specify the residual strength needed to satisfy service criteria.

Specification of the material properties should include the following:

1. Characteristics of fibers (ASTM standards, length-to-diameter ratios).
2. Dosage of fibers (traditionally specified as a weight per cubic volume).
3. Compliance requirements for residual strength of beam samples based on ASTM C1609 test.

As an example, ACI 31 permits use of SFRC with characteristics, volume, and residual flexural strengths. Such specifications exceed the properties of the FRC used in the s-series slab strips discussed in the design evaluations.

Testing of the SFRC should be done to verify the strength of the concrete in compression and tension. Whenever possible, test should be done in accordance with ASTM standards. For compression, ASTM

C39/C39M and C469/C469M should be used. Direct tension tests are not advised due to difficulties in gripping the sample and size effects. Instead, flexural tests are available to characterize the residual tensile response. The ASTM option for flexural strength tests for FRC is ASTM C1609/C1609M; this is a four point bending test that measures the displacement to characterize residual strength. At the present time, there is no direct method to calculate the residual tensile strength from the C1609 flexural strength tests. International institutes use a notched beam test that is similar to ASTM C1609 but has a notch in the constant moment region that forces the crack to form at that location. The opening of the notch is measured and used to establish the tensile strength. Such a test has been demonstrated to provide reliable data for design, thus, should be adopted in the future if a notched beam standard becomes available from ASTM.

Construction

The decision to use FRC in a project should factor in the method of construction. Fiber is best added to concrete with the aggregate as the first component at the batch plant or on-site to the fresh mix. Addition at the batch plant requires a partnership with the ready-mix company to facilitate this, but can enable large scale use of FRC in transportation infrastructure. Addition on-site to the concrete truck can be effective in small projects, but the time involved with adding the fibers at the specified rate can be time consuming (approximately 10 minutes was need for a half truck of concrete). This additional time should be factored in to the decision to use FRC.

Corrosion of SFRC

Although concerns about corrosion of steel fibers are warranted, research has shown that durability requirements can be met at small crack widths. Concerns about corrosion can be best addressed by using non-steel fibers when a low residual strength is needed. When steel fibers are preferred for strength and/or stiffness, zinc-coated steel fibers should be used. ACI 544.5R considers crack widths up to 0.15 mm to have no adverse effects of corrosion; at service level demands, the maximum crack width in the 7.5 in. thick slab does not exceed this limit. In the deeper slabs and slabs with reinforcement at the center, the crack widths are no larger than 0.2 mm and 0.38 mm, respectively. The crack widths at service increase with increasing ratio of conventional steel. When crack widths are larger than 0.2 mm, research has shown that corrosion will be limited to a thin layer of the concrete. For such slabs, it would be prudent to replace h with d for service and ultimate strength calculations, effectively ignoring the contribution of cover concrete in tension.

SUMMARY

Design equations for service and strength were presented, evaluated using experimental results, and applied with a design example:

- The contributions of SFRC to the service and strength limit states can be accounted for by adding an additional stress block to the traditional design. The tension response of the SFRC is lumped at its mid-depth. For service, this method results in an average error of 12 percent, with scatter of results sensitive to amount of conventional steel. For nominal, the proposed methods

have an average error of 4 percent and are conservative regardless of the amount or location of conventional steel.

- Proposed service level design approaches indicate that FRC can be used to reduce that amount of conventional steel used for design, although the service limit state will likely govern the amount of steel needed.
- The proposed design approaches focus on using a conservative value for the residual concrete strength in tension. Additional research is needed to improve confidence in and prediction of material properties of FRC. This can enable design with larger values and therefore enable further reduction of the amount of conventional steel needed.
- The effectiveness of FRC for strength design is limited to large residual strength values, due in large part to the recommendation for a lower strength reduction factor. With the conservative material properties recommended, this service design is a more effective approach at the time of this report. Additional research is needed to support the use of less conservative strength reduction factors.
- Design aids proposed by manufacturers and other researchers can be used to design with SFRC. Two design aids are presented relating the service and strength performance of SFRC. Designers with a known residual strength and section depth can use the design aids to determine the required steel reinforcement to satisfy their moment demands.
- The decision to use and the implementation of FRC should consider the material tests needed and the method of adding fibers to the concrete.

CHAPTER 11. SUMMARY AND CONCLUSIONS

SUMMARY

The research was conducted in three phases. Phase 1 provided background information and preliminary studies to address the project objectives. Phase 2 was an experimental investigation into the application of SFRC to bridge structures. The experimental test program involved three sequential test programs: materials tests, slab-strip beam tests, and a full deck test. In Phase 3, the results of Phase 2 experimental tests were analyzed along with the preliminary investigations to provide design recommendations and preliminary design procedures for the use of SFRC in the ADOT bridge structures.

Case Study: Slab-on-Grade

A literature review on the field applications of FRC to slab-on-grade is conducted, and a case at Houston, Texas, is analyzed using a widely used pavement analysis/design software, MEPDG. The fibers used at the slab-on-grade are synthetic fiber (MacDonald 2011; Flax 2010), glass fiber (Jones 2010), cellulose fiber (Brown et al. 2010), and steel fiber (Alexandre and Bouhon 2010; Folliard et al. 2006; Destrée et al. 2011). In most cases, FRC is effective on reducing cracks. For the case of using steel and synthetic fibers for CRCP at Houston, Texas, Folliard et al. (2006) reported that SFRC have better finishability, crack control, and spalling resistance than the un-reinforced (control) and synthetic FRC. A monitoring results after 235 days of concrete placement show that the average crack spacing and crack width of SFRC are smaller than those of un-reinforced and synthetic FRC.

The MEPDG analysis conducted in this case study uses two sets of material test data: 1) given by Folliard et al. (2006), containing 0.2–0.3 percent steel fibers by volume, and 2) produced from material tests of this study (described in Chapter 5, containing 0.5–2.0 percent steel fibers by volume). The average crack width predicted by the MEPDG analysis are 0.020 (control), 0.014 (0.2 percent SFRC), and 0.011 (0.3 percent SFRC) in., and those of the monitoring data (Folliard et al. 2006) are 0.018, 0.016, and 0.014, respectively. The MEPDG predictions slightly overestimate the fiber reinforcing effect, but can be considered to be within a reasonable range (Figure 29). The MEPDG analysis also shows that the SFRC is effective in reducing punchout damage while has no effect on IRI. The improvements in average crack width and punchout are substantial when the moderate amounts of steel fibers (0.5–2.0 percent by volume) are added. Overall, the average crack width and punchout decrease with the increase of steel fiber contents (both straight and hooked fibers), but the improvements after 0.5 percent fiber content are gradual. Combining the analysis results of these small and moderate fiber contents, it is recommended to use 0.5 percent hooked steel fibers for the slab-on-grade applications.

Case Study: Bridges

The case study analysis investigated the effectiveness of SFRC using a fiber model and a moment-curvature analysis. The constitutive relationships used in the case studies were based upon the literature. The modified Kent-Park compression model was used in the case study analysis as the additional of steel fibers does not affect the compression response of concrete significantly. The tension model used was a bilinear curve proposed by Soranakom and Mobasher (2009). The case study

investigated the relationship between SFRC and the girder spacing, thickness of the concrete deck, the concrete compressive strength, the post-crack tensile strength, and the traditional steel reinforcing layout. A total of 486 models were investigated.

The models were evaluated based on their service performance and nominal moment. The service performance is characterized by the stress in the steel reinforcement at the service limit state. Both the service stress and nominal moment of each model was normalized by a traditionally designed reinforced concrete section.

The addition of steel fiber to the traditional design resulted in a service performance enhancement and a strength increase, but also a reduced curvature at the nominal moment. The use of SFRC adds to the reinforcement of a section and must be balanced by a reduction in conventional steel or depth. Otherwise, the section will begin to become over-reinforced resulting in a lower curvature at nominal and potentially a brittle failure.

Material Test Program

Aiming to obtain the basic mechanical properties of the SFRCs, a series of materials tests were conducted for a total of 114 specimens including 36 compression, 30 tension, and 48 flexural tests. The straight, hooked, and blending of those fibers were added with the various volume contents ranging from 0.0 to 3.0 percent. Following is the summary of the material test results:

- The compressive behavior of concrete is not significantly influenced by adding the steel fibers up to 2.0 percent. Adding 3.0 percent fibers by volume causes a decrease in the compressive strength due to the poor workability and fiber clumping.
- The strength, and residual strength of concrete under tension are remarkably improved by adding the steel fibers. The improvements in tensile strength of the hooked SFRCs are lower than that of the straight SFRCs, but the residual strength of the hooked SFRCs are higher than that of the straight SFRCs.
- The flexural responses of the SFRCs vary with the fiber types. The MOR of the hooked SFRCs significantly increases with the increase of the fiber content, but the improvements in MOR of the straight SFRCs are not so significant. The improvement in the residual strength is substantial in all the SFRCs resulting in the improved ductility. Moreover the hooked SFRCs show the deflection hardening when the fiber content is equal to or higher than 1.0 percent. The combined SFRCs show a similar trend to the hooked SFRCs.
- Adding too much fibers causes workability issues in mixing and compacting of concrete. The straight fibers are harder to mix than the hooked fibers. The unit weight measurements and slump test results indicate that a fiber content more than 2.0 percent causes a degradation of the concrete quality. This was confirmed by the decreased compressive strength of the SFRCs containing 3.0 percent fibers by volume. Considering the material test results and the observations during the mixing, adding 1.5–2.0 percent of the hooked fibers is recommended for practical applications.

- A wide scatter in the measured elastic moduli is observed in tension and compression tests. The scattering range is higher in tension tests, which use one displacement transducer, due to the misalignment of the specimens than compression tests that use three displacement transducers. The wide scatter in the elastic moduli implies that the mixing of fibers cause a nonuniform distribution of fibers and coarse aggregate. The scatter can be mitigated in larger size members, but an extra care (extended mixing time and compaction) will be needed to improve the uniformity of the fiber-coarse aggregate dispersion. The errors due to the specimen misalignment can be minimized by using two or three displacement transducers around the specimen.
- The good dispersion of fibers in concrete mixtures containing coarse aggregate is one of the topics that requires further investigations. Since most of recent researches for SFRC have focused on high or ultra-high strength FRCs that do not include coarse aggregate, the interaction between fibers and coarse aggregate during mixing has not been actively investigated, yet. The factors of consideration are aggregate gradation, fiber type and aspect ratio, mixing method, and compaction method. The future investigations for the fiber dispersion require a method of measuring the fiber dispersion and a quantified parameter representing the dispersion of fibers.

Structural Test Program

The slab-strip experimental program investigated the relationship between SFRC and ratio of steel reinforcement in a specimen. The program was conducted by constructing 18 unique slab-strips using two different depths, two volume dosages of steel fibers, and four different amounts of steel reinforcement. The objective was to identify the failure progression of SFRC and determine the effect of SFRC on the performance of reinforced concrete bridge decks under the service and strength demands.

Steel fibers controlled the width of cracks in the concrete prior to the crushing or crack width failure criteria. Several cracks developed in the SFRC slab strips, but remained relatively small prior to the onset of crushing in the compression region of the strip and achievement of the specimen's maximum moment. Eventually, the anchorage of the steel fibers failed in a single crack creating a hinge allowing all subsequent rotation and crack opening of the specimen occurs in the critical crack.

The tests provided information on the service and strength performance of SFRC sections. SFRC improves the performance of the slab strips under both the service and strength limit states. Adding 0.5 percent fibers to a section with traditional reinforcement and concrete designed for the strength limit state elevates the performance of the concrete bridge deck to satisfy the service limit state.

An inverse analysis was conducted for the slab-strip specimens without steel reinforcement. The theoretical tensile model was used in a moment-curvature analysis. The residual stress in the tensile model used in the analysis was adjusted to reduce the error between the theoretical and experimental moment-curvature relationships after cracking occurs. The theoretical models showed that the effect of the steel fibers diminishes at higher ratios of steel reinforcement. The ratio between the residual force of the SFRC and the resultant force of the steel reinforcement decreases as the steel ratio increases. As a result, the influence from the SFRC is smaller.

Ultimately, the conclusions of the slab-strip experimental program were consistent with the findings of the case study analysis. An increase in the area of traditional steel reinforcement in a concrete specimen results in a proportional increase in the moment capacity. Adding fibers 0.5 percent by volume to the AASHTO empirical design satisfies both strength and service criteria. Traditional steel reinforcement can be excluded from a SFRC section with 2.0 percent by volume fibers while satisfying strength requirements.

The purpose of the full-scale SFRC bridge test was to demonstrate the effect of adding steel fibers to a two-way slab. The experimental program offered insight on the stiffness, deformability, failure mechanisms, and load capacity of a concrete bridge deck reinforced with steel bars and steel fibers. The geometry was chosen to both represent actual bridges in use and conform to tests conducted in the past by other researchers.

The deck was subjected to four tests consistent with traditional AASHTO (2014) load patterns: a single wheel load, a trailing axle design truck, and a single axle on the overhang of the bridge deck. The tests failed in a flexural manner with several cracks forming on the top surface parallel to the supporting girders. These cracks are consistent with negative bending experienced by the SFRC bridge deck at the girders. Directly under the load point, cracks formed on the bottom surface that radiated outward in an elliptical radial fan mechanism. Multiple negative and positive bending cracks formed for each load pattern exhibiting the load redistribution of the SFRC. The SFRC bridge deck achieved deflections of up to 2 in. prior to the failure of the bridge deck. In comparison, similar tests conducted by others using either traditionally designed and reinforced concrete or prestressed concrete with AFRP tendons achieved a deflection of 1 in. prior failure.

The overall performance of the SFRC bridge deck satisfies the serviceability and strength requirements of ADOT and AASHTO LRFD (2014). The bridge's maximum strength was 450 percent greater than the factored AASHTO demand. The largest stress measured in the steel reinforcement at the service limit state was 21 ksi.

Yield line and punching shear analysis was conducted to determine the theoretical collapse load of the SFRC specimens. The slab-strips cast and tested alongside the large scale specimen were used in determining the unit moment capacity for the analyses. The yield line analysis did not significantly underpredict the load in the overhang. The theoretical collapse load was 6 percent smaller than the experimental failure. Test LP3 was conducted on the overhang without restraint on one side. The lack of restraint prevents membrane action from occurring and increasing its moment capacity similar to the results for the other tests.

Design and Implementation Recommendations

Design equations for service and strength were presented, evaluated using experimental results, and applied with a design example:

- The contributions of SFRC to the service and strength limit states can be accounted for by adding an additional stress block to the traditional design. The tension response of the SFRC is

lumped at its mid-depth. For service, this method results in an average error of 12 percent, with scatter of results sensitive to amount of conventional steel. For nominal, the proposed methods have an average error of 4 percent and are conservative regardless of the amount or location of conventional steel.

- Proposed service level design approaches indicate that FRC can be used to reduce that amount of conventional steel used for design, although the service limit state will likely govern the amount of steel needed.
- The proposed design approaches focus on using a conservative value for the residual concrete strength in tension. Additional research is needed to improve confidence in and prediction of material properties of FRC. This can enable design with larger values and therefore enable further reduction of the amount of conventional steel needed.
- The effectiveness of FRC for strength design is limited to large residual strength values, due in large part to the recommendation for a lower strength reduction factor. With the conservative material properties recommended, this service design is a more effective approach at the time of this report. Additional research is needed to support the use of less conservative strength reduction factors.
- Design aids proposed by manufacturers and other researchers can be used to design with SFRC. Two design aids are presented relating the service and strength performance of SFRC. Designers with a known residual strength and section depth can use the design aids to determine the required steel reinforcement to satisfy their moment demands.
- The decision to use and the implementation of FRC should consider the material tests needed and the method of adding fibers to the concrete.

RECOMMENDATIONS FOR FUTURE RESEARCH

A design guideline has not yet been adopted in the United States for SFRC. Currently there is not a way to accurately determine the residual stress associated with SFRC. Material tests proposed adopted by ASTM provide information on the post-crack behavior of SFRC; however, a direct translation of the force-deflection data to stress-strain data has not been developed. An inverse analysis similar to the one used in this thesis have been shown by other researchers to provide adequate information to design. The lack of a material test with a direct correlation to the tensile stress-strain response prevents the widespread use and adoption of a design procedure for FRC in the United States. Future work to develop and adopt material test to determine the stress-strain response of FRC is critical to the use of enhanced concrete.

Additional research needs to be conducted for concrete systems using both fibers and traditional steel reinforcement. An inverse analysis with a generally accepted SFRC tensile model and unreinforced concrete beams can be used to determine the tensile constitutive relationship for strain-softening SFRC. However, the interaction of the steel fibers and steel reinforcement results in theoretical models that under predict the capacity of lightly reinforced sections and over predict heavily reinforced sections. Further experimentation of the dual reinforcement system will provide insight on the tension hardening of the SFRC and its contribution to the capacity of the section.

The yield line analysis under predicted the capacity of the SFRC bridge deck. In particular, the under prediction was observed in the portions of the bridge that were the most restrained. The yield line analysis failed to capture 26 percent capacity of the individual wheel load patterns. Further work investigating the effect of membrane action and the significant redistribution of load due to the excessive cracking can allow for designers to use the full potential of SFRC.

REFERENCES

- Alexandre, E. and B. Bouhon. 2010. "Jointless Steel Fiber-Reinforced Concrete Slabs-on-Grade and on Piles." *ACI Special Publication*, 268, 89–102.
- American Association of State Highway and Transportation Officials (AASHTO). 2014. AASHTO LRFD Bridge Design Specifications, U.S. Customary Units. Washington, DC: Print.
- American Association of State Highway and Transportation Officials (AASHTO). 2013. "Standard Method of Test for Tensile Strength of Hydraulic Cement Mortars." AASHTO T132-87. Washington, D.C.
- American Concrete Institute (ACI) Committee 544.4R. 1988. *Design Considerations for Steel Fiber Reinforced Concrete*. ACI 544-4R. Farmington Hills, MI: American Concrete Institute.
- American Concrete Institute (ACI) Committee 544.3R. 1998. *Guide for Specifying, Proportioning, Mixing, Placing, and Finishing Steel Fiber Reinforced Concrete*. Farmington Hills, MI: American Concrete Institute.
- American Concrete Institute (ACI) Committee 544. 1996. *Report on Fiber Reinforced Concrete*. ACI 544.R1. Farmington Hills, MI: American Concrete Institute.
- American Concrete Institute (ACI) Committee 544. 1999. *Measurement of Properties of Fiber Reinforced Concrete*. ACI 544.2R. Farmington Hills, MI: American Concrete Institute.
- American Concrete Institute (ACI) Committee 318. 2011. *Building Code Requirements for Structural Concrete (ACI 318-11) and Commentary*. Farmington Hills, MI: American Concrete Institute.
- American Society for Testing and Materials International (ASTM International). 2006. "Standard Specification for Steel Fibers for Fiber-Reinforced Concrete." ASTM Standard A820. West Conshohocken, PA.
- American Society for Testing and Materials International (ASTM International). 2010a. "Standard Test Method for Flexural Strength of Concrete (Using Simple Beam With Center-Point Loading)." ASTM Standard C293/C293M. West Conshohocken, PA.
- American Society for Testing and Materials International (ASTM International). 2010b. "Standard Test Method for Flexural Strength of Concrete (Using Simple Beam with Third-Point Loading)." ASTM Standard C78/C78M. West Conshohocken, PA.
- American Society for Testing and Materials International (ASTM International). 2010c. "Standard Test Method for Obtaining Average Residual-Strength of Fiber-Reinforced Concrete." ASTM Standard C1399/C1399M. West Conshohocken, PA.
- American Society for Testing and Materials International (ASTM International). 2011. "Standard Test Method for Splitting Tensile Strength of Cylindrical Concrete Specimens." ASTM Standard C496/C496M. West Conshohocken, PA.

- American Society for Testing and Materials International (ASTM International). 2012a. "Standard Test Method for Flexural Performance of Fiber-Reinforced Concrete (Using Beam With Third-Point Loading)." ASTM Standard C1609/C1609M. West Conshohocken, PA.
- American Society for Testing and Materials International (ASTM International). 2012b. "Standard Test Method for Slump of Hydraulic-Cement Concrete." ASTM Standard C143/C143M. West Conshohocken, PA.
- American Society for Testing and Materials International (ASTM International). 2013. "Standard Specification for Mixing Rooms, Moist Cabinets, Moist Rooms, and Water Storage Tanks Used in the Testing of Hydraulic Cements and Concretes." ASTM Standard C511. West Conshohocken, PA.
- American Society for Testing and Materials International (ASTM International). 2014a. "Standard Test Method for Compressive Strength of Cylindrical Concrete Specimens." ASTM Standard C39/C39M. West Conshohocken, PA.
- American Society for Testing and Materials International (ASTM International). 2014b. "Standard Test Method for Static Modulus of Elasticity and Poisson's Ratio of Concrete in Compression." ASTM Standard C469/C469M. West Conshohocken, PA.
- American Society for Testing and Materials International (ASTM International). 2014c. "Standard Test Method for Density (Unit Weight), Yield, and Air Content (Gravimetric) of Concrete." ASTM Standard C138/C138M. West Conshohocken, PA.
- Arizona Department of Transportation (ADOT). 2008. *Standard Specifications for Road and Bridge Construction*. Phoenix: Arizona Department of Transportation.
- Arizona Department of Transportation (ADOT). 2011. ADOT Bridge Design Guidelines – Section 5: Concrete Structures.
- Association Francaise de Genie Civil (AFGC) – Service d'études techniques des routes et autoroutes (SETRA). 2002. Bétons fibrés à ultra-hautes performances – ultra high performance fibre-reinforced concretes, recommandations provisoires – Interim recommendations.
- Aviram, A., B. Stojadinovic, and G. J. Parra-Montesinos. 2014. "High-Performance Fiber-Reinforced Concrete Bridge Columns under Bidirectional Cyclic Loading." *ACI Structural Journal* 111 (2): 303–312.
- Bae, H. U., M. G. Oliva, and L. C. Bank. 2011. "Reinforcement-Free Decks Using Modified Strut-and-Tie Model." *ACI Structural Journal* 108 (5): 562–571.
- Bae, Han-Ug, Michael G. Oliva, and Lawrence C. Bank. 2010. "Obtaining Optimal Performance with Reinforcement-Free Concrete Highway Bridge Decks." *Engineering Structures* 32 (2010): 2300–2309.

- Balaguru, P., R. Narahari, and M. Patel. 1992. "Flexural Toughness of Steel Fiber Reinforced Concrete." *ACI Materials Journal* 89 (6): 541–546.
- Banthia, N. and A. Dubey. 1999. "Measurement of Flexural Toughness of Fiber-Reinforced Concrete Using a Novel Technique – Part 1: Assessment and Calibration." *ACI Materials Journal* 96 (6): 651–656.
- Banthia, N. and A. Dubey. 2000. "Measurement of Flexural Toughness of Fiber-Reinforced Concrete Using a Novel Technique – Part 2: Performance of Various Composites." *ACI Materials Journal* 97 (1): 3–11.
- Barros, J.A. and Figueiras, J.A. 1999. "Flexural Behavior of SFRC: Testing and Modeling." *Journal of Materials in Civil Engineering* 11 (4): 331-339.
- Bencardino, F., L. Rizzuti, G. Spadea, and R. N. Swamy. 2008. "Stress–Strain Behavior of Steel Fiber-Reinforced Concrete in Compression." *Journal of Materials in Civil Engineering* 20 (3): 255–263.
- British Standards (BS). 2007. "Test Method for Metallic Fibre Concrete. Measuring the Flexural 790 Tensile Strength (Limit of Proportionality [LOP], Residual)." BS EN 14651.
- Brown, H., J. Speakman, and J. Morton. 2010. "Applications of Alkaline-Resistant Cellulose Polymer Fiber in Ready Mixed Concrete." *ACI Special Publication*, 268, 55–62.
- Campione, G. 2002. "The Effects of Fibers on the Confinement Models for Concrete Columns." *Canadian Journal of Civil Engineering* 29: 742–750.
- Chandrangsu, Kulsiri. 2003. *Innovative Bridge Deck with Reduced Reinforcement and Strain-Hardening Fiber Reinforced Cementitious Composites*, Department of Civil and Environmental Engineering, University of Michigan, Ann Arbor.
- Choi KK, Reda Taha MM, Park HG, and Maji AK. 2007. Punching shear strength of interior concrete slab–column connections reinforced with steel fibers. *Cement & Concrete Composites*. 29, pp. 409–420.
- Destrée, X. 2009. "Steel-Fibre-Only Reinforced Concrete in Free Suspended Elevated Slabs." *Concrete Engineering International* 13 (1): 47–49.
- Destrée, Xavier, and Jürgen Mandl. 2008. "Steel Fibre Only Reinforced Concrete in Free Suspended Elevated Slabs." In *Tailor Made Concrete Structures*, 437–443. London, UK: CRC Press.
- Destrée, X., H. Oscarsson, and M. Pettersson. 2011. "The Suspended Foundation Slab of the Swedbank Arena in Stockholm (Sweden): 16,000 m³ (21,000 cu yd) of Steel Fiber Reinforced Concrete." *ACI Special Publication*, 280, 1–12.
- Dhonde, Hemant B., Y. L. Mo, Thomas T. C. Hsu. 2005. *Fiber Reinforcement in Prestressed Concrete Beams*. FHWA/TX-06/0-4819-1. Houston, TX: University of Houston.

- Dinh, Hai H., Gustavo J. Parra-Montesinos, and James K. Wight. 2011. "Shear Strength Model for Steel Fiber Reinforced Concrete Beams without Stirrup Reinforcement." *Journal of Structural Engineering* 137 (10): 1039–1051.
- Dunn, Mark, Lyle Brehm, F. Wayne Klaiber, Brent M. Phares, and Douglas L. Wood. 2005. *Tama County's Steel Free Bridge Deck*. Paper read at Proc., Mid-Continent Transportation Research Symposium, Ames, Iowa.
- Ezeldin, A. S. and P. N. Balaguru. 1992. "Normal- and High-Strength Fiber-Reinforced Concrete under Compression." *Journal of Materials in Civil Engineering* 4 (4): 415–429.
- Fall, D., J. Shu, R. Rempling, K. Lundgren, and K. Zandi. 2014. "Two-Way Slabs: Experimental Investigation of Load Redistributions in Steel Fibre Reinforced Concrete." *Engineering Structures* 80: 61-74.
- Flax, D. 2010. "When You Want Concrete without Cracks, Joints, Curling, and Reinforcing Bars." *ACI Special Publication*, 268, 45–54.
- Folliard, K. J., D. Sutfin, R. Turner, and D. P. Whitney. 2006. *Fiber in Continuously Reinforced Concrete Pavements*, Technical Report FHWA/TX-07/0-4392-2.
- Graybeal, B. A. 2006. *Material Property Characterization of Ultra-High Performance Concrete*, FHWA Project Report FHWA-HRT-06-103.
- Harajli, M.H., D. Maalouf, and H. Khatib. 1995. Effect of fibers on the punching shear strength of slab-column connections. *Cement and Concrete Composites*, 17(2), pp.161-170.
- Henager, C.H. and Doherty, T.J. 1976. "Analysis of Reinforced Fibrous Concrete Beams." *Journal of the Structural Division*. 102 (1): 177-188.
- Hillerborg, M. Mod er, P.-E. Petersson. 1976. "Analysis of crack formation and crack growth in concrete by means of fracture mechanics and finite elements." *Cement Concrete Res.*, 6 (6) (1976), pp. 773–782
- Hsu, L. S. and C. T. Hsu. 1994. "Stress–Strain Behavior of Steel-Fiber High-Strength Concrete under Compression." *ACI Structural Journal* 91 (4): 448–457.
- Japan Society of Civil Engineers (JSCE). 2008. Recommendations for Design and Construction of High Performance Fiber Reinforced Cement Composites with Multiple Fine Cracks (HPFRCC).
- Jones, J. 2010. "Case Studies of Glass Fiber-Reinforced Concrete (GFRC) Applications." *ACI Special Publication*, 268, 29–44.
- Kim, D., A. E. Naaman, and S. El-Tawil. 2008. "Comparative Flexural Behavior of Four Fiber Reinforced Cementitious Composites." *Cement and Concrete Composites* 30: 917–918.
- Kwak, Yoon-Keun, Mark O. Eberhard, Woo-Suk Kim, and Jubum Kim. 2002. "Shear Strength of Steel Fiber-Reinforced Concrete Beams without Stirrups." *ACI Structural Journal* 99 (4): 530–538.

- Lequesne R, M. Setkit, G. Parra-Montesinos, J. K. Wight, C. Kopczynski, J. Ferzli, and M. Y. Cheng. Advances in Fiber Reinforced Concrete Durability, and A. C. I. Convention Field Applications at the Spring. 2011. "Implementation of High-Performance Fiber Reinforced Concrete Coupling Beams in High-Rise Core-Wall Structures." *ACI Special Publication 280*: 94–105.
- Lequesne, R. D., G. J. Parra-Montesinos, and J. K. Wight. 2013. "Seismic Behavior and Detailing of High-Performance Fiber-Reinforced Concrete Coupling Beams and Coupled Wall Systems." *Journal of Structural Engineering* 139 (8): 1362–1370.
- Li, V. C., H. C. Wu, M. Maalej, D. K. Mishra, and T. Hashida. 1996. "Tensile Behavior of Cement-Based Composites with Random Discontinuous Steel Fibers." *Journal of the American Ceramic Society* 79 (1): 74–78.
- Liao, W.-C., Chao, Shih-Ho, Park, Sang-Yeol, and Naaman, Antoine E. (2006). Self-Consolidating High Performance Fiber Reinforced Concrete - Preliminary Investigation. Ann Arbor, MI, University of Michigan.
- Lim, T., P. Paramasivam, and S. Lee. 1987. "Analytical Model for Tensile Behavior of Steel-Fiber Concrete." *ACI Materials Journal* 84 (4): 286–298.
- MacDonald, C. N. 2011. "Cracking Histories of Synthetic Fiber Reinforced Concrete Applications." *ACI Special Publication 276*, 1–10.
- Mander, T., Henley, M., Scott, R., Head, M., Mander, J., and Trejo, D. (2010). "Experimental Performance of Full-Depth Precast, Prestressed Concrete Overhang, Bridge Deck Panels." *J. Bridge Eng.*, 10.1061/(ASCE)
- Mansur, M., M. Chin, and T. Wee. 1999. "Stress–Strain Relationship of High-Strength Fiber Concrete in Compression." *Journal of Materials in Civil Engineering* 11 (1): 21–29.
- Michels, Julien, Daniele Waldmann, Stefan Maas, and Arno Zurbes. 2011. "Steel Fibers as only Reinforcement for Flat Slab Construction—Experimental Investigation and Design." *Construction and Building Materials* 26 (2012): 145–155.
- Mindess, S., J. F. Young, and D. Darwin. 2003. *Concrete: Second Edition*. New Jersey: Pearson Education, Inc.
- Mobasher, B. 2012. *Mechanics of Fiber and Textile Reinforced Cement Composites*. New York: CRC Press, Taylor and Francis Group, LLC.
- Mobasher, B. and X. Destrée. 2010. "Design and Construction Aspects of Steel Fiber-Reinforced Concrete Elevated Slabs." *ACI Special Publication 274*: 95–107.
- Mufti, Aftab A., Leslie G. Jaeger, Baidar Bakht, and Leon D. Wegner. 1993. "Experimental Investigation of Fibre-Reinforced Concrete Deck Slabs without Internal Steel Reinforcement." *Canadian Journal of Civil Engineering* 20: 398–406.

- Naaman, A. E. and H. W. Reinhardt. 2006. "Proposed Classification of HPFRC Composites Based on Their Tensile Response." *Materials and Structures* 39 (5): 547–555.
- Naaman, Antoine E., and Kulsiri Chandrangsu. 2004. "Innovative Bridge Deck System Using High-Performance Fiber-Reinforced Cement Composites." *ACI Structural Journal* 101 (1): 57–64.
- Naaman, Antoine E., Visit Likhitrungsilp, and Gustavo Parra-Montesinos. 2007. "Punching Shear Response of High-Performance Fiber-Reinforced Cementitious Composite Slabs." *ACI Structural Journal* 104 (2): 170–179.
- Nataraja, M., N. Dhang, and A. Gupta. 1999. "Stress–Strain Curves for Steel-Fiber Reinforced Concrete under Compression." *Cement and Concrete Composites* 21 (5): 383–390.
- Niwa, Junichiro, Kabir Shakya, Koji Matsumoto, and Ken Watanabe. 2012. "Experimental Study on the Possibility of Using Steel Fiber-Reinforced Concrete to Reduce Conventional Rebars in Beam-Column Joints." *Journal of Materials in Civil Engineering* 24 (12): 1461–1473.
- Nguyen-Minh, L., Rovňák, M., Tran-Quoc, T., Nguyen kim, K. 2011. "Punching Shear Resistance of Steel Fiber Reinforced Concrete Flat Slabs." *Procedia Engineering* 14: 1830-1837.
- Ostertag, C. P. and J. Blunt. 2008. *Use of Fiber Reinforced Concrete in Bridge Approach Slabs*. CA09-0632. Berkeley: University of California.
- Park, R. and W.L. Gamble. 2000. *Reinforced concrete slabs*. John Wiley & Sons.
- Pirayeh Gar, S., Head, M., Hurlebaus, S., and Mander, J. 2013. "Experimental Performance of AFRP Concrete Bridge Deck Slab with Full-Depth Precast Prestressed Panels." *Journal of Bridge Engineering* 19 (4): 04013018.
- Reunion Internationale des Laboratoires et Experts des Materiaux Technical Committee 162 – Test and Design Methods for Steel Fibre Reinforced Concrete. (RILEM TC 162-TDF). 2001. "Test and Design Methods for Steel Fiber Reinforced Concrete. Recommendations for Uniaxial Tension Test." *Materials and Structures* 34: 3–6.
- Reunion Internationale des Laboratoires et Experts des Materiaux Technical Committee 162 – Test and Design Methods for Steel Fibre Reinforced Concrete. (RILEM TC 162-TDF). 2002. "Test and Design Methods for Steel Fiber Reinforced Concrete. Bending Test." *Materials and Structures* 34: 579–582.
- Reunion Internationale des Laboratoires et Experts des Materiaux Technical Committee 162 – Test and Design Methods for Steel Fibre Reinforced Concrete. (RILEM TC 162-TDF). 2003. "Test and Design Methods for Steel Fiber Reinforced Concrete. σ - ϵ Design Method Final Recommendation" *Materials and Structures* 36: 560–567.
- Robinson, C., A. Colasanti, and G. Boyd. 1991. "Steel Fibers Reinforce Auto Assembly Plant Floor." *Concrete International* 13 (4), 30–35.

- Roesler, Jeffery R., David A. Lange, Salah A. Altoubat, Klaus-Alexander Reider, and Gregory R. Ulrich. 2004. "Fracture of Plain and Fiber-Reinforced Concrete Slabs under Monotonic Loading." *Journal of Materials in Civil Engineering* 16 (5): 452–460.
- Soranakom, C. and B. Mobasher. 2007a. "Closed-Form Moment-Curvature Expressions For Homogenized Fiber Reinforced Concrete." *ACI Materials Journal* 104 (4): 351–359.
- Soranakom, C. and B. Mobasher. 2007b. "Closed Form Solutions for Flexural Response of Fiber Reinforced Concrete Beams." *Journal of Engineering Mechanics* 133(8): 933–941.
- Soranakom, C. and B. Mobasher. 2008. "Correlation of Tensile and Flexural Responses of Strain Softening and Strain Hardening Cement Composites." *Cement and Concrete Composites* 30 (6): 465–477.
- Soranakom, C. and B. Mobasher. 2009. "Flexural Design of Fiber-Reinforced Concrete." *ACI Materials Journal* 106 (5): 461–469.
- Soroushian, P. and Z. Bayasi. 1991. "Fiber Type Effects on the Performance of Steel Fiber Reinforced Concrete." *ACI Materials Journal* 88 (2): 129–134.
- Tatnall, P. C. and L. Kuitenbouwer. 1992. "Steel Fiber Reinforced Concrete in Industrial Floors." *Concrete International*, 14 (2), 43–47.
- Texas Department of Transportation (TxDOT). 2008. *Standard Specifications for Construction and Maintenance of Highways, Streets, and Bridges*. Austin: Texas Department of Transportation.
- Wafa, F. F. and S. A. Ashour. 1992. "Mechanical Properties of High-Strength Fiber Reinforced Concrete." *ACI Materials Journal* 89 (5): 449–455.
- Walkus, B., A. Januszkiewicz, and J. Jeruzal. 1979. "Concrete Composites with Cut Steel Fiber Reinforcement Subjected to Uniaxial Tension." *ACI Journal* 76 (10): 1079–1092.
- Walraven, J. 2013. "fib Model Code for Concrete Structures 2010: mastering challenges and encountering new ones." *Structural Concrete*, 14: 3–9. doi:10.1002/suco.201200062
- Wille, K., D. J. Kim, and A. E. Naaman. 2011. "Strain-Hardening UHP-FRC with Low Fiber Contents." *Materials and Structures* 44 (3): 583–598.
- Wille, K., S. El-Tawil, and A. E. Naaman. 2014. "Properties of Strain Hardening Ultra High Performance Fiber Reinforced Concrete (UHP-FRC) under Direct Tensile Loading." *Cement and Concrete Composites* 48: 53–66.
- Witczak, M.W., D. Andrei, and W.N. Houston. 2004. Guide for mechanistic-empirical design of new and rehabilitated pavement structures. *Transportation Research Board of the National Research Council*, pp.1-91.

APPENDIX A: DAMAGE PROFILES OF SLAB STRIP SPECIMENS

S7505BTM35

Slab strip specimen S7505BTM35 was 7.5 inches deep with, 3-#5 bars located at the bottom (1 inch clear cover), and a fiber volume of 0.5 percent. The specimen achieved a maximum capacity of 23.55 kips at a deflection of 0.7 inches (L/120).

Fourteen cracks formed on the east face, with eight inside the constant moment region. Fifteen cracks formed on the west face, nine inside the constant moment region. The first crack for each side occurred at a deflection of 0.1 inches (L/840). The majority of the cracks extended to the mid-depth of the specimen by a deflection of 0.3 inches (L/280). Beyond this deflection, little upward extension occurred for the cracks outside the constant moment region. At 0.7 inches (L/120) of deflection, the extension of cracks in the constant moment region slowed or stopped. The cracks approached but did not pass reference line E. Figure 218 through Figure 221 show the vertical progression of the cracks on the east and west faces.

The average non-critical crack width on the east and west face were 0.19 mm 0.37 mm, respectively. Ultimately, cracks E5 and W7 created the primary failure plane of the specimen. At 0.8 inches of deflection, E5 was 1.27 mm. The next largest crack on the east face, E1, had a width of 0.64 mm. On the west face, adjacent cracks W6 and W7 were the widest. At a deflection of 1.2 inches and load of 22.6 kips, E5 surpassed the maximum crack width allowed by RILEM (2002) and fib (2010), 2.5 mm. Figure 222 shows the relationship between crack opening and deflection for each face.

Figure 223 and Figure 224 show the progression of critical cracks on the east and west faces. E5 and W6 first formed at deflection step 0.2 inches (L/480). By 0.3 inches, they both extended to mid-depth of the section. At deflection step 1.0 inch each crack had reached its highest point above reference point D. As shown, both E5 and W6 shown spalling related to the crack, aggregate, and fibers. A “wedge” of concrete corresponding to a small coarse aggregate was dislodged from both E5 and W6 while fibers near the surface of the specimen resulted in spalling at reference line B on W7.

Crushing was first observed on both sides at a deflection of 1.0 inch and load of 23.1 kips. The crushing occurred between references S3 and S6. At the conclusion of the test, the crushed region had expanded to include the entire south region of the constant moment region and approached vertical reference D. At the completion of the test, the specimen had not collapsed. Figure 225 shows the progression of crushing damage in specimen S7505BTM35.

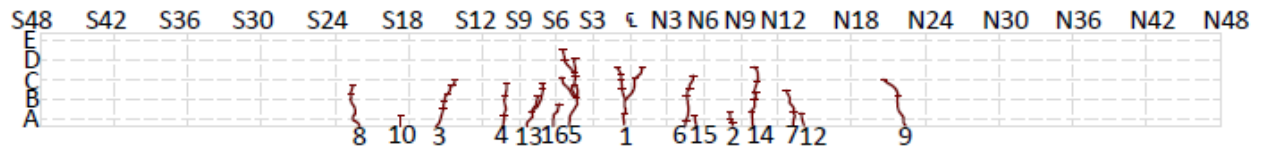


Figure 218. S7505BTM35 Crack Profile East Face

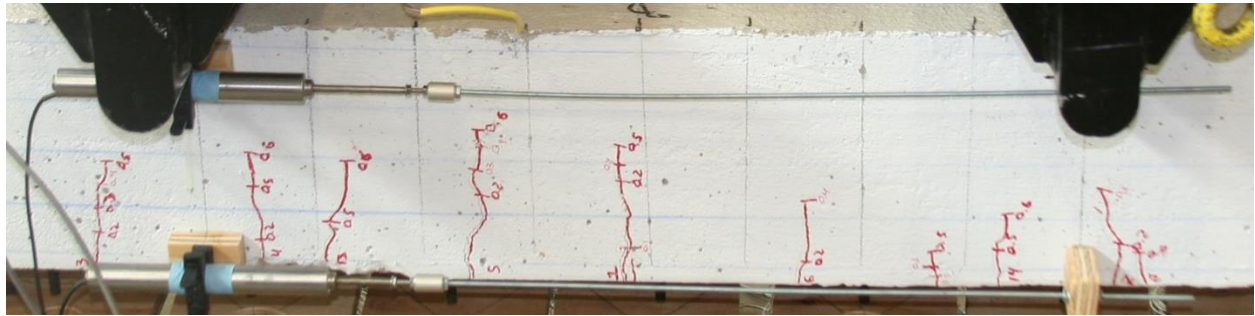


Figure 219. S7505BTM35 East Face Constant Moment Region

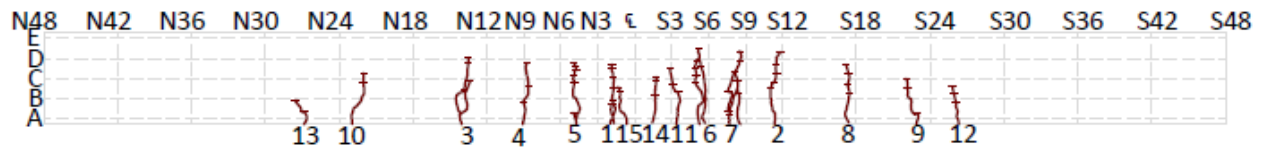


Figure 220. S7505BTM35 Crack Profile West Face

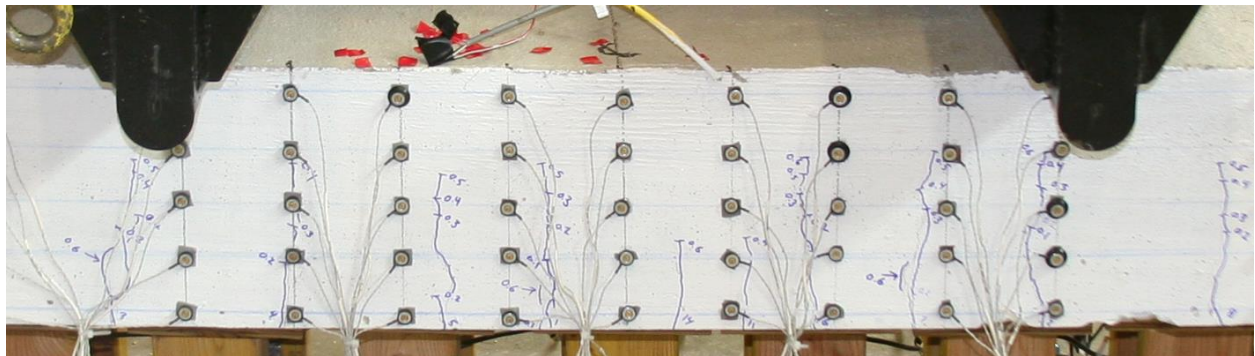
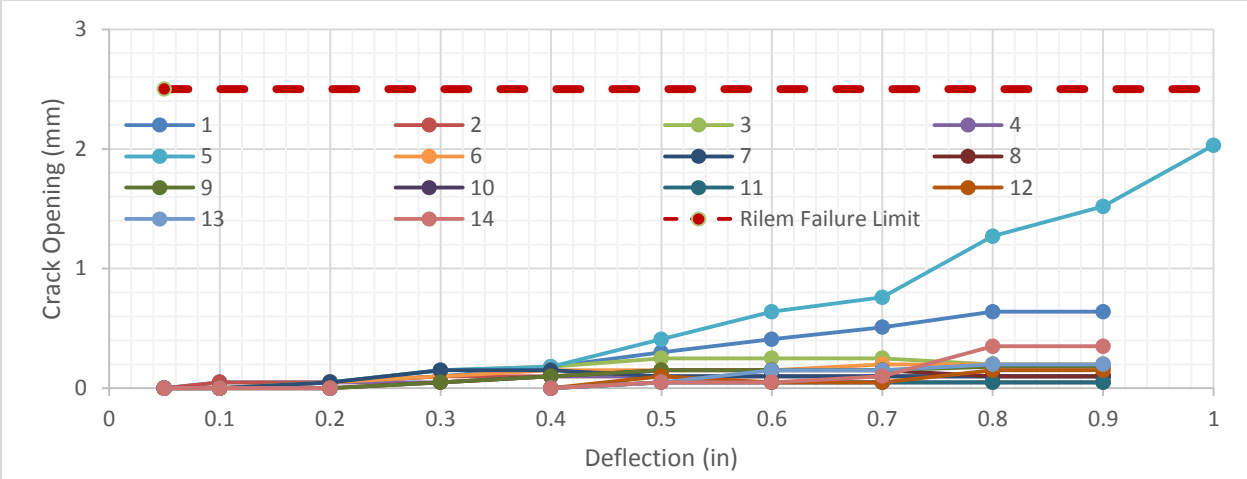
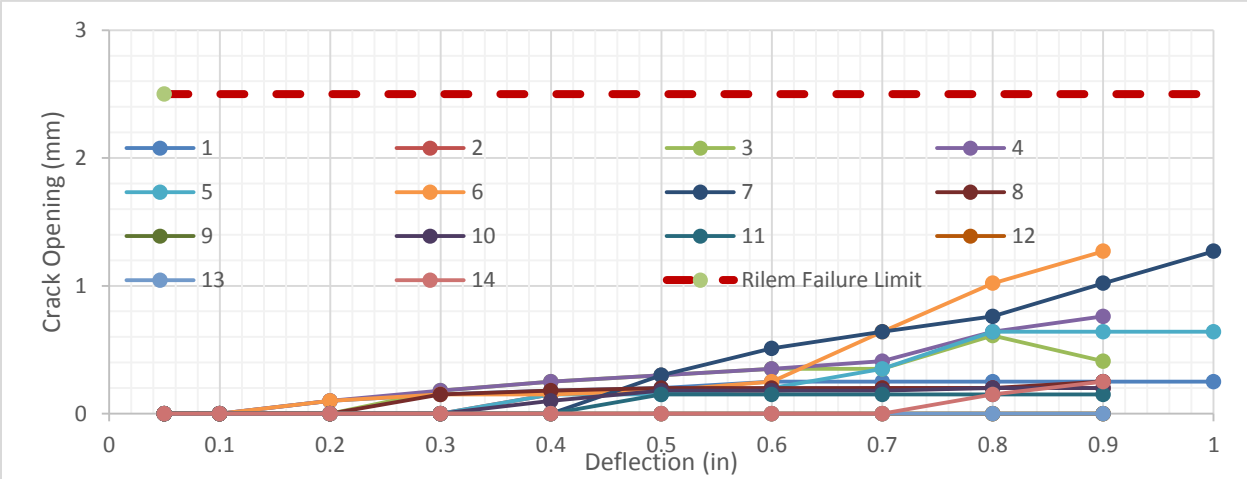


Figure 221. S7505BTM35 West Face Constant Moment Region

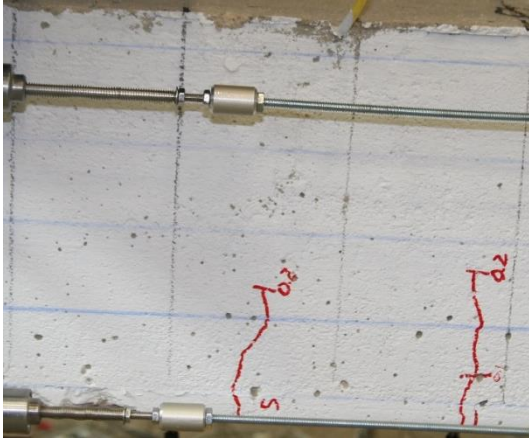


(a)

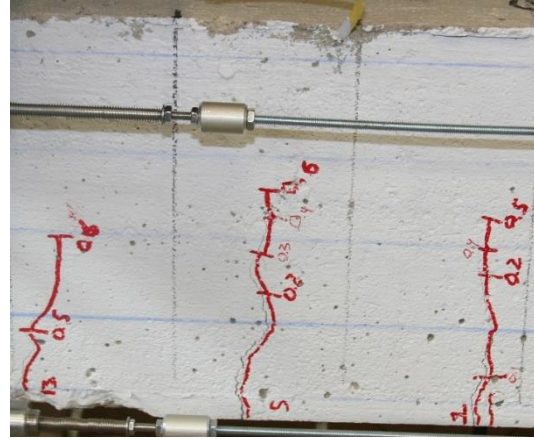


(b)

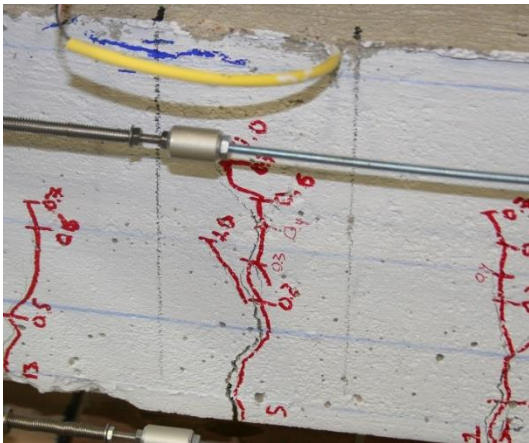
Figure 222. S7505BTM35 Crack Opening vs Strip Deflection for (a) East Face and (b) West Face



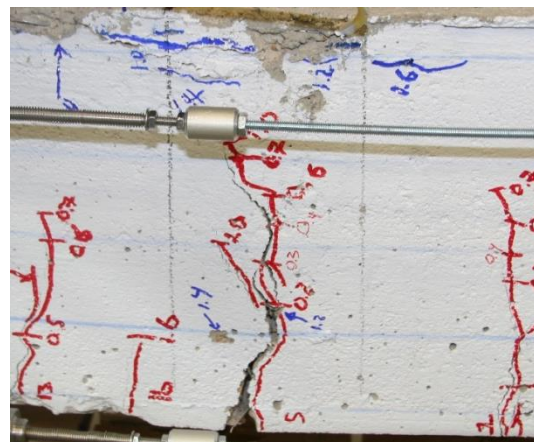
(a)



(b)

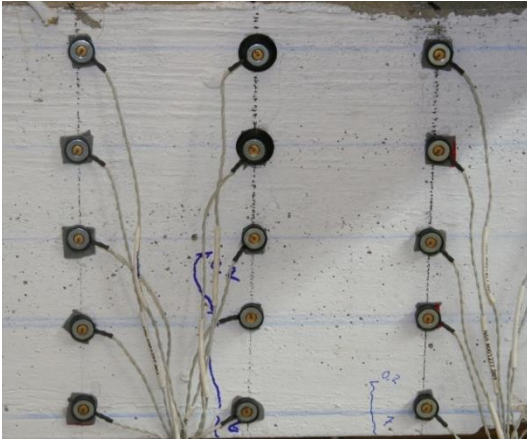


(c)

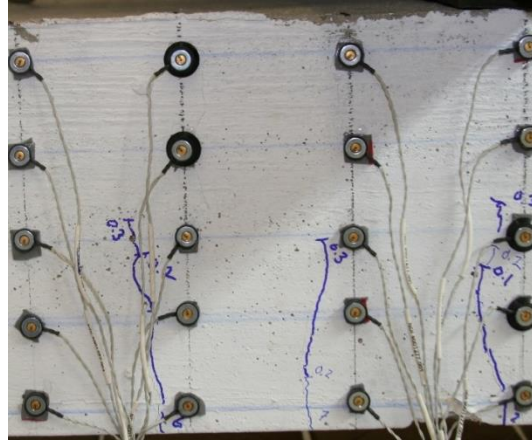


(d)

Figure 223. S7505BTM35 Crack Progression of E5 at: (a) 0.2 inches, (b) 0.6 inches, (c) 1.0 inches, and 1.6 inches.



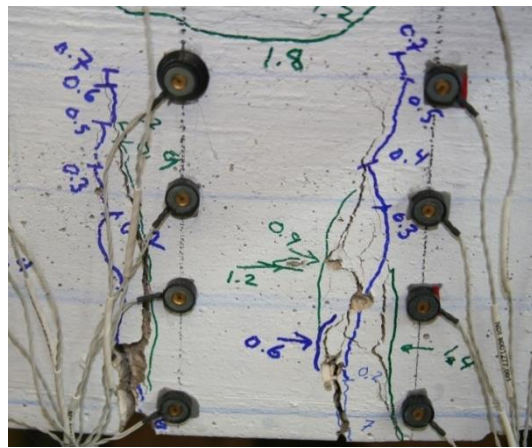
(a)



(b)

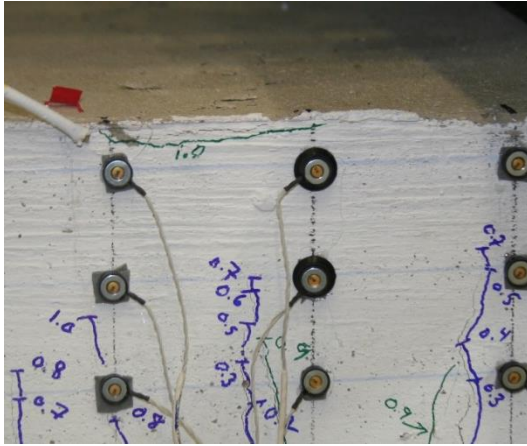


(c)

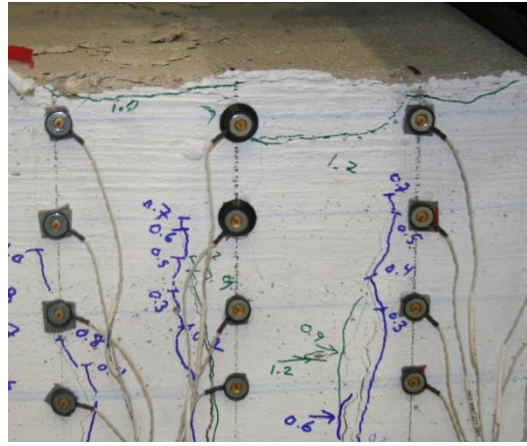


(d)

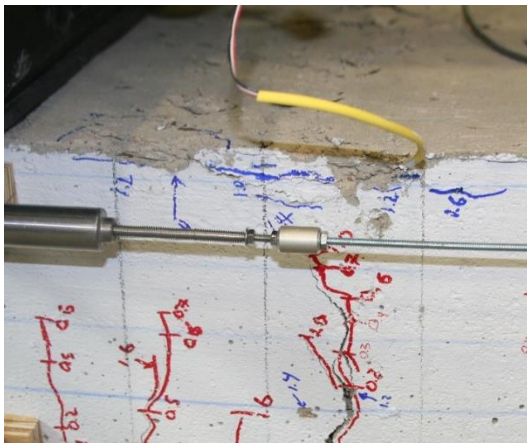
Figure 224. S7505BTM35 Crack Progression of W6 and W7 at: (a) 0.2 inches, (b) 0.3 inches, (c) 0.7 inches, and 1.8 inches.



(a)



(b)



(c)



(d)

Figure 225. S7505BTM35 Crushing Progression

S7505BTM25

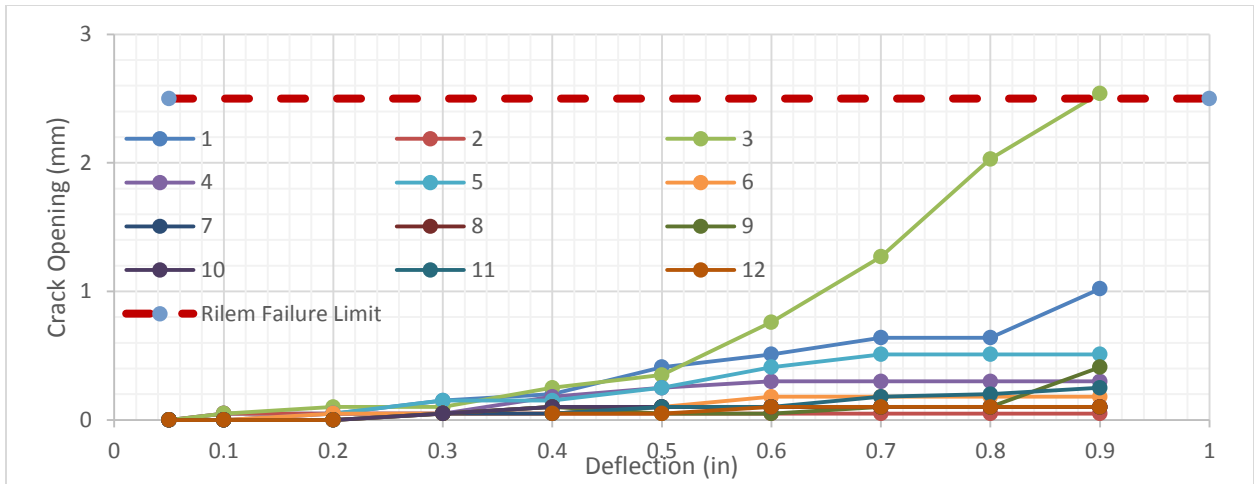
Slab strip specimen S7505BTM25 was 7.5 inches deep, with 2-#5 bars located at the bottom (clear cover of 1 inch), and a fiber volume of 0.5 percent. The specimen achieved a maximum capacity of 18.58 kips at a deflection of 0.8 inches (L/105).

Twelve cracks formed on the east face, six inside the constant moment region. Thirteen cracks formed on the west face of the specimen, seven inside the constant moment region. The first crack for each side occurred at a deflection of 0.1 inches (L/840). The majority of the cracks extended to the mid-depth of the specimen by a deflection of 0.6 inches (L/140). Beyond this deflection, little upward extensions were observed in the cracks outside of the constant moment region. At 0.8 inches (L/105), the extension of cracks in the constant moment region slowed or stopped. Between 0.8 and 1.1 inches, some cracks in the constant moment region extended beyond reference line D. Figure 226 through Figure 229 show the vertical progression of the cracks on the east and west faces.

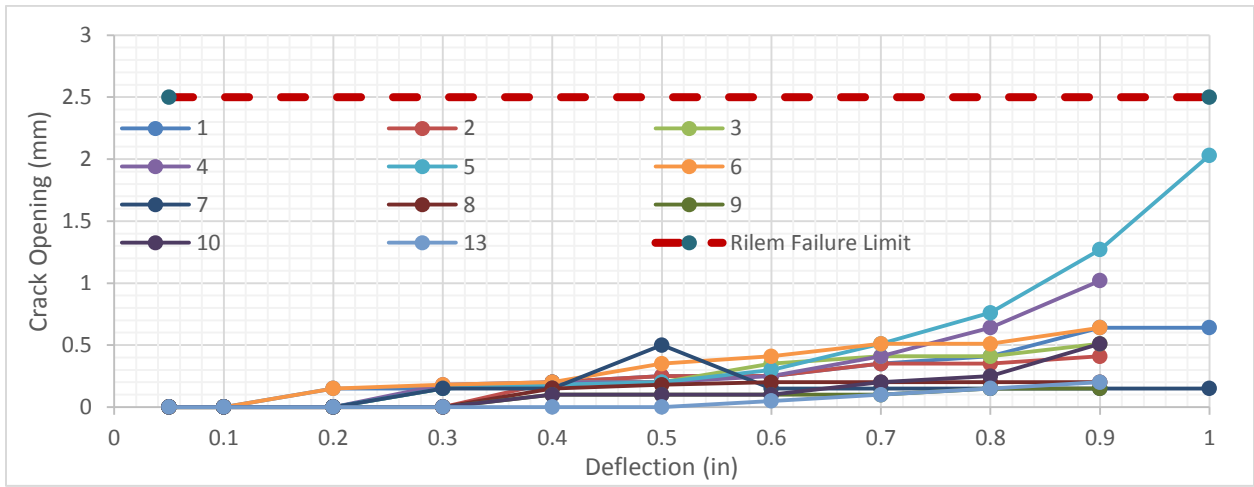
The average non-critical crack width on the east and west face was 0.28 mm 0.47 mm, respectively. Ultimately, cracks E3 and W5 created the primary failure plane of the specimen. At a deflection of 0.8 inches, the width of E3 was 2.54 mm while the next largest crack on the east face, E1, had a width of 1.02 mm. On the west face, adjacent cracks W4 and W5 were the largest. At a deflection of 0.9 inches and load of 18.55 kips, E3 surpassed the maximum crack width allowed by RILEM (2002) and fib (2010), 2.5 mm. Figure 230**Error! Reference source not found.** and Figure 231**Error! Reference source not found.** show the relationship between crack opening and deflection for each face.

Figure 232**Error! Reference source not found.** and Figure 233 show the progression of critical cracks on the east and west faces. E3 first formed at deflection step 0.1 inches (L/840) while W3 did not form until the next deflection step, 0.2 inches (L/420). By 0.3 inches, they both extended to the mid-depth of the section. At deflection step 1.1 inches (L/76), both cracks had extended beyond reference line D. Severe spalling was observed in E3 at reference line C. The spalling was directly related to steel fibers located near the surface due to their hooked ends not having sufficient cover.

Crushing was first observed on both sides at a deflection of 1.0 inch (L/84) and load of 18.63 kips. The crushing occurred between references centerline and N3. By the conclusion of the test, the crushed region expanded south to include S3 to N3, approximately 6 inches wide. At the conclusion of testing, the specimen had not collapsed. Figure 234 shows the crushed region of concrete for specimen S7505BTM25.

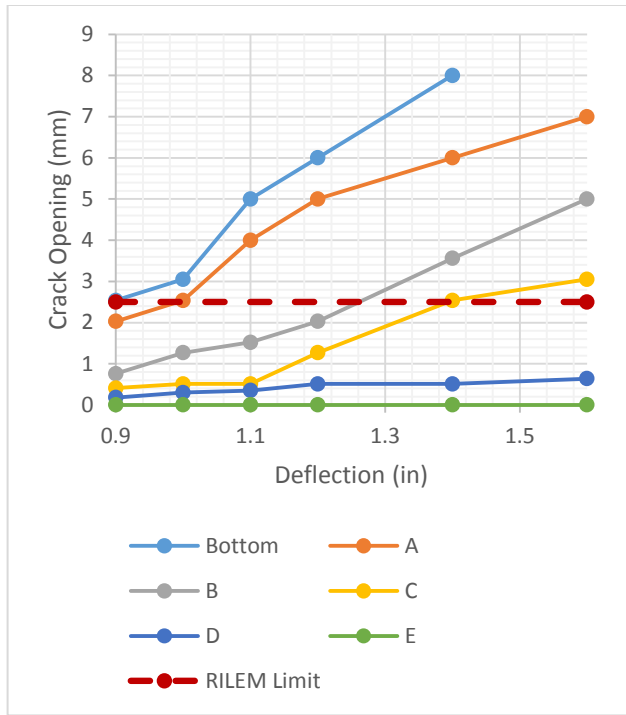


(a)

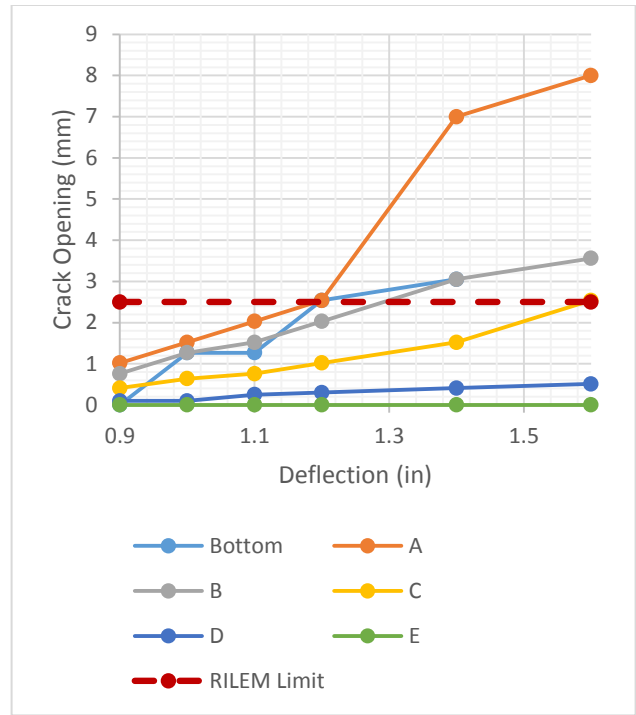


(b)

Figure 230. S7505BTM25 Crack Opening vs Strip Deflection for (a) West Face and (b) East Face

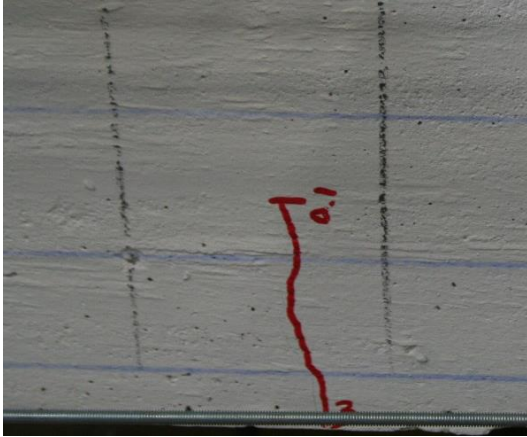


(a)

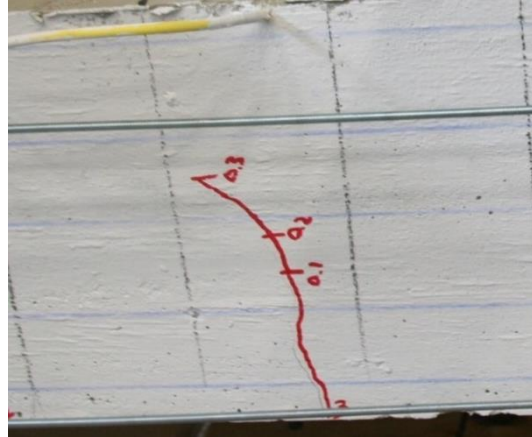


(b)

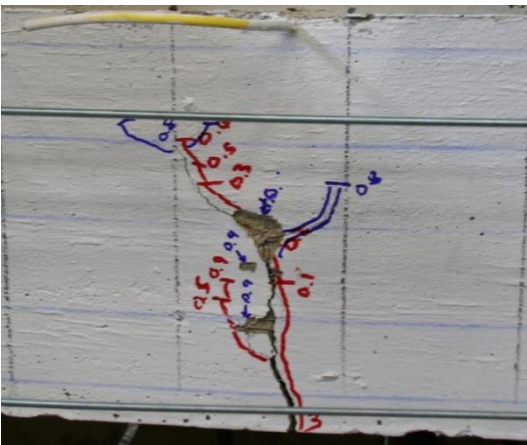
Figure 231. S7505BTM25 Crack Opening vs Strip Deflection for Primary Crack at Each Reference Line (a) E3 and (b) W5



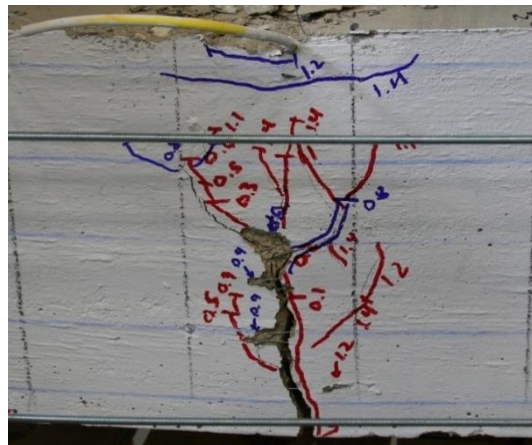
(a)



(b)



(c)



(d)

Figure 232. S7505BTM25 Crack Progression of E3 at: (a) 0.1 inches, (b) 0.3 inches, (c) 1.0 inches, and 1.4 inches.

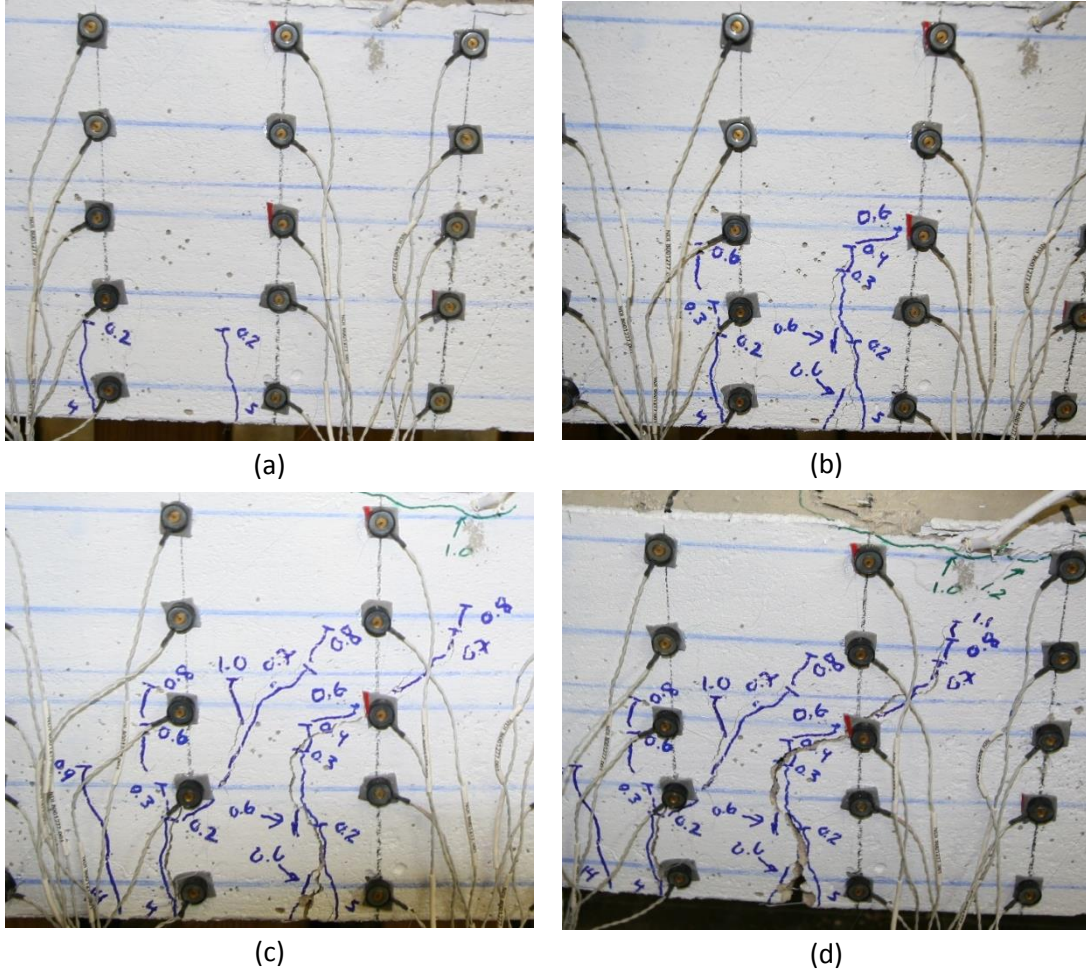


Figure 233. S7505BTM25 Crack Progression of W5 at: (a) 0.2 inches, (b) 0.6 inches, (c) 1.0 inches, and 1.4 inches.

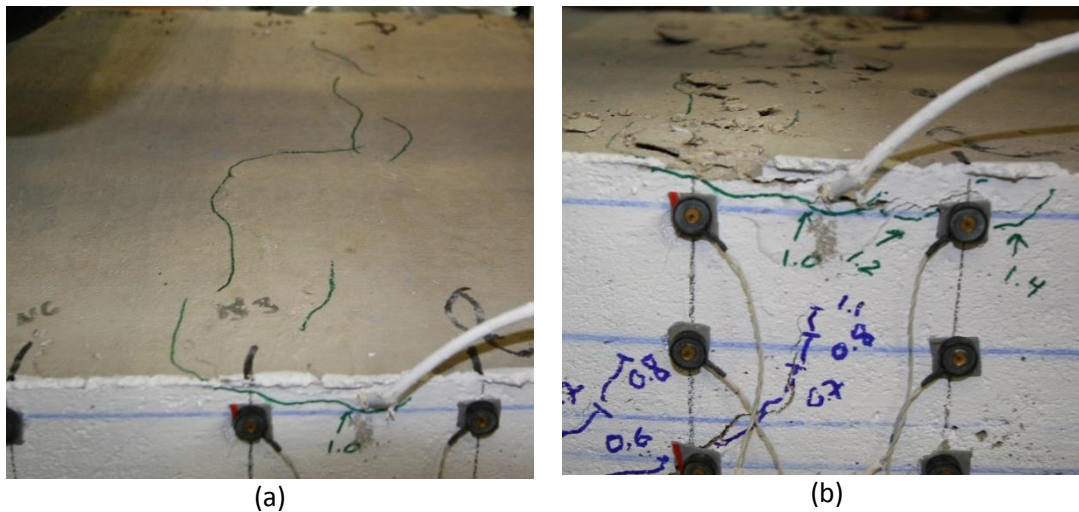


Figure 234. S7505BTM25 Crushing Progression (a) 1.0 inch and (b) 1.4 inch

S7505BTM24

Slab strip specimen S7505BTM24 was 7.5 inches deep with 2-#4 bars located at the bottom of the specimen (1 inch clear cover) and a fiber volume of 0.5 percent. The specimen achieved a maximum capacity of 14.70 kips at a deflection of 0.9 inches (L/93).

The bottom edge on the east face was damaged in the demolding of the specimen between N3 and S9. Cracks E1, E5, and E10 formed at the base of this damaged region as shown in Figure 235.

Twelve cracks formed on the east face, with seven inside the constant moment region. Thirteen cracks formed on the west face, with five inside the constant moment region. The first crack for both the east and west face occurred during the 0.1 inch deflection step, (L/840). All cracks formed by the 0.50 inch deflection step (L/168). Cracks outside the constant moment region progressed vertically to reference line D. Cracks inside the constant moment region progressed vertically to reference line E. Vertical progression of cracks ceased at deflection step 0.7 inches (L/120). Further increasing the deflection of the specimen resulted in widening of the primary crack and crack branching.

The critical cracks on the east face and west face were E12 and W7. Crack E1 formed during the 0.5 inch deflection step (L/168) while crack W7 formed during the 0.2 inch deflection step (L/420). Both cracks formed between the centerline and horizontal reference S3. The maximum allowable crack width, 2.5 mm, for each crack was observed at deflection step 1.0 inches (L/84). Critical crack E12 formed a wedge with crack E1 at the bottom edge allowing a large piece of concrete to fall away. Figure 236 and Figure 237 show the progression of each crack throughout the test.

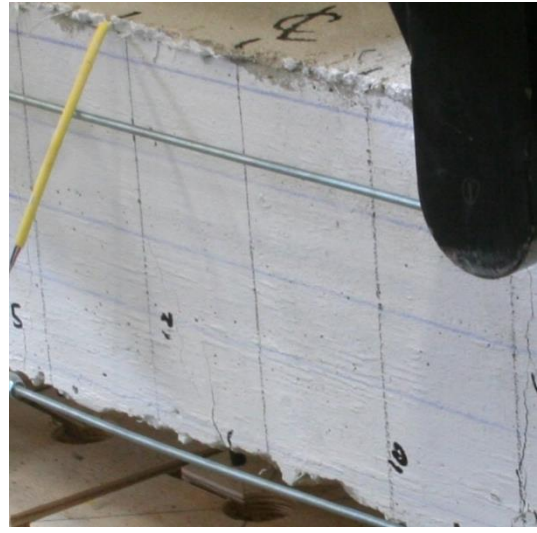
Crushing was first observed on the east, west, and top surface at deflection step 1.0 inches (L/84). The crushing began at horizontal reference S3 above each critical crack. As the test continued, the crushing extended horizontally extending to centerline and S6. The crushed concrete region extended downward and joined the tension cracks prior to completion of the test. The specimen did not collapse due to the steel reinforcement; however, a complete fracture plane of the concrete was observed. Figure 238 shows the progression of concrete crushing and the extent of the damage prior to removal of the specimen.



Figure 235. S7505BTM24 Damaged Corner



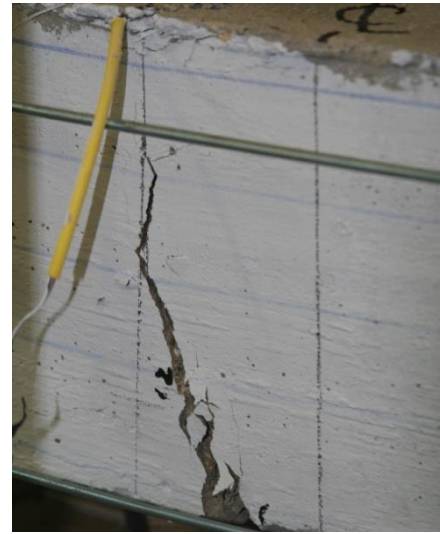
(a)



(b)

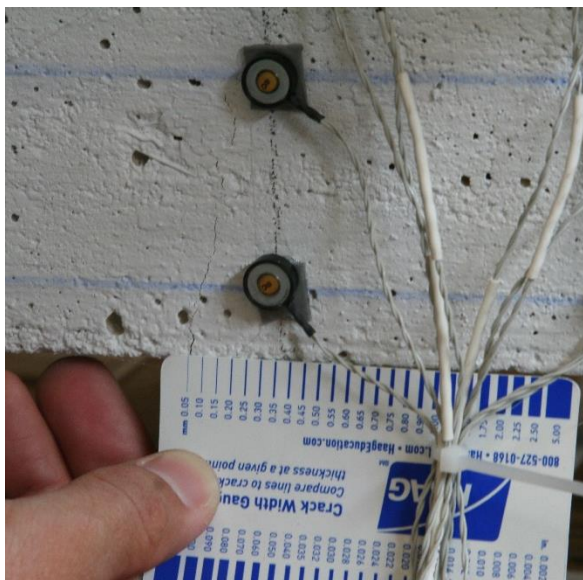


(c)



(d)

Figure 236. S7505BTM24 Crack Progression of E1 and E12 at: (a) 0.1 inches, (b) 0.6 inches, (c) 1.0 inches, and 1.4 inches



(a)



(b)



(c)

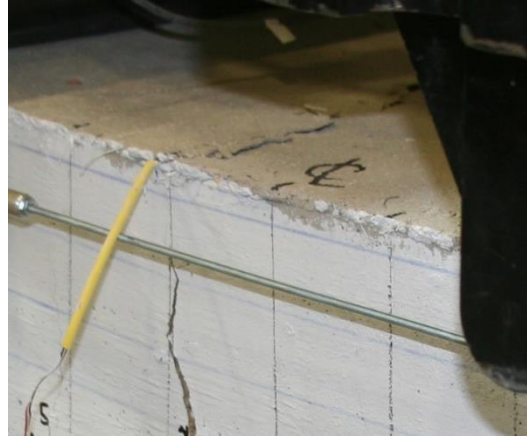


(d)

Figure 237. S7505BTM24 Crack Progression of W4 at: (a) 0.2 inches, (b) 0.7 inches, (c) 1.0 inches, and 1.6 inches



(a)



(b)



(c)



(d)

Figure 238. Crushing Progression of S7505BTM24 at: (a) 1.2 inch, (b) 1.6 inch, (c) After Removal of Instrumentation and (d) Completion of Test

S7505BTM23

Slab strip specimen S7505BTM23 was 7.5 inches deep with 2-#3 bars located at the bottom (1 inch clear cover) and a fiber volume of 0.5 percent. The specimen achieved a maximum capacity of 10.0 kips at a deflection of 0.5 inches (L/168). During construction, the bottom corner of the east face was damaged along the constant moment region. Cracks E1, E2, E8, and E10 formed in this damaged region.

Ten cracks formed on the east face, with four inside the constant moment region. Eleven cracks formed on the west face, with six inside the constant moment region. The first crack for both the east and west face occurred during the 0.1 inch deflection step, (L/840). At the 0.35 inch deflection step, (L/240), the majority of the formed cracks had extended to the mid-depth of the specimen. Cracks outside of the constant moment region had little to no vertical extensions after the 0.35 inch deflection step. Cracks inside the constant moment region continued to extend vertically until the 0.7 inch deflection step, (L/120). At this deflection, further deflections resulted in minor vertical extensions and significant widening of the critical cracks. The critical cracks approached reference line E while non-critical cracks extended slightly beyond reference line D. Figure 239 through Figure 242 show the progression of each crack throughout the test.

The average non-critical crack width on the east and west face was 0.4 mm 0.36 mm respectively. Ultimately, cracks E10 and W11 created the critical failure plane of the specimen. From deflection step 0.7 inches to 0.8 inches (L/150), the crack width of E10 doubled to 2.54. In comparison, all other cracks on the east face did not change in width except the second largest crack, E3 with a width of 1.27mm. The same behavior was observed on the west face; W11 doubled in width to 3.05. **Error! Reference source not found.** displays the critical crack on each side of the specimen. Both E10 and W11 surpassed the maximum allowed crack width at the 0.8 inch deflection step, capacity of 9.82 kips. (RILEM 2002, fib 2010). Figure 243 and Figure 244 show the relationship between the crack opening and strip deflection for each face.

Figure 245 and Figure 246 show the progression of critical cracks on the east and west faces. The crack on the west face, W11, first formed at deflection step 0.6 inches. In comparison, the critical crack, E10, on the east face formed at deflection step 0.45 inches. Each critical crack became the widest crack on their respective face by deflection step 0.7 inches. Critical crack W11 extended vertically for the final time at the next deflection step, 0.8 inches. Significant spalling at reference line B and C was observed where the hooked end of several fibers were near the surface of the concrete. However; steel fibers were clearly seen bridging W11 until the anchorage of the hooked ends failed.

Crushing was first observed on both sides at the deflection step 0.8 inches (L/105) or a capacity of 9.82 kips. The crushing occurred between references N9 and N12. The crushed region of concrete did not extend significantly north or south. At the conclusion of the test, the steel reinforcement fractured preventing an extended crushing region. The progression of the crushed region is shown by Figure 247.

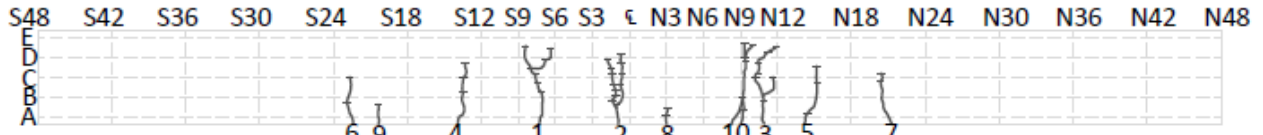


Figure 239. S7505BTM23 Crack Profile East Face

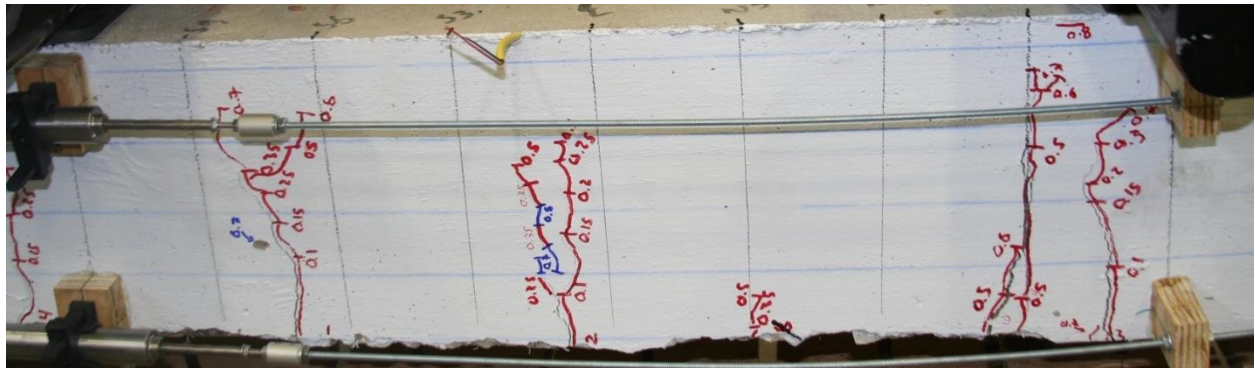


Figure 240. S7505BTM23 East Face Constant Moment Region

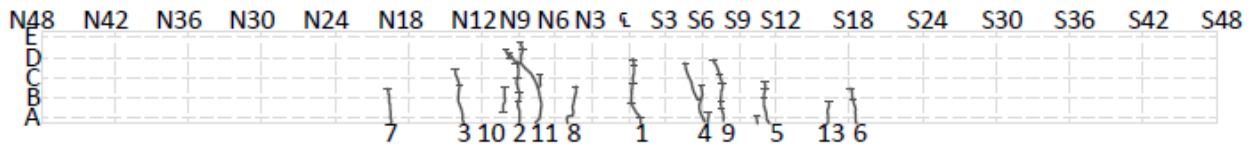


Figure 241. S7505BTM23 Crack Profile West Face

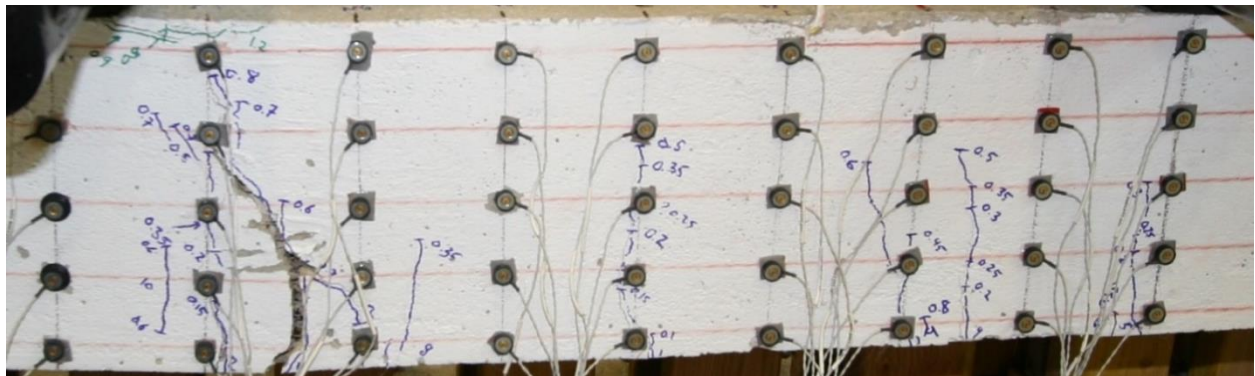
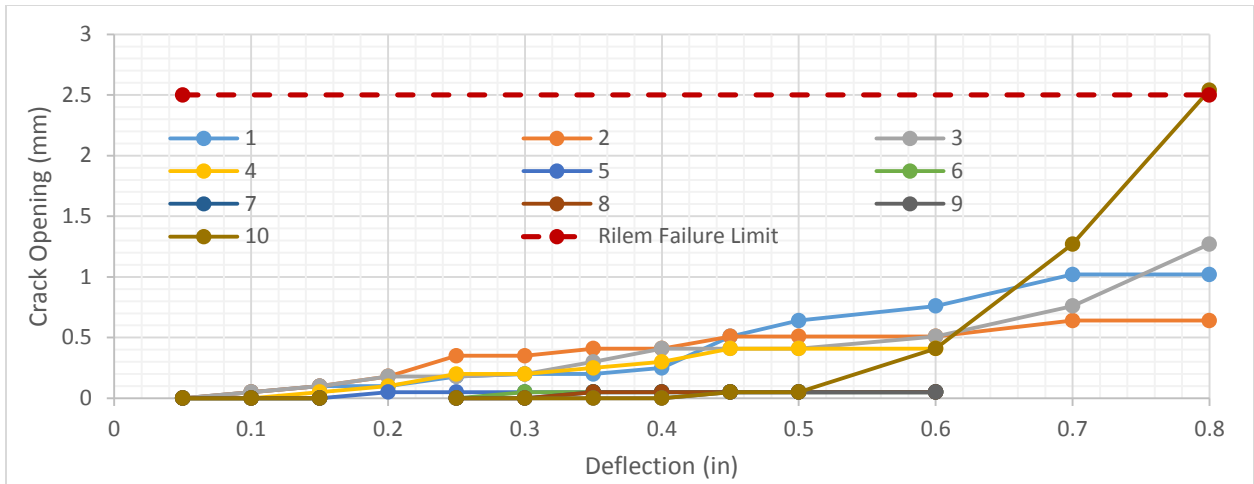
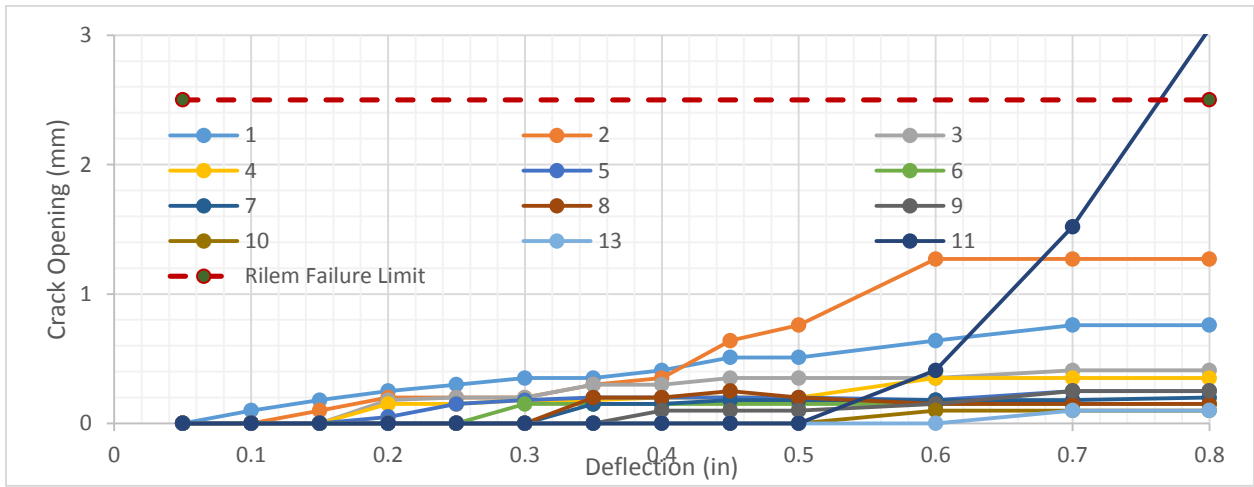


Figure 242. S7505BTM23 West Face Constant Moment Region

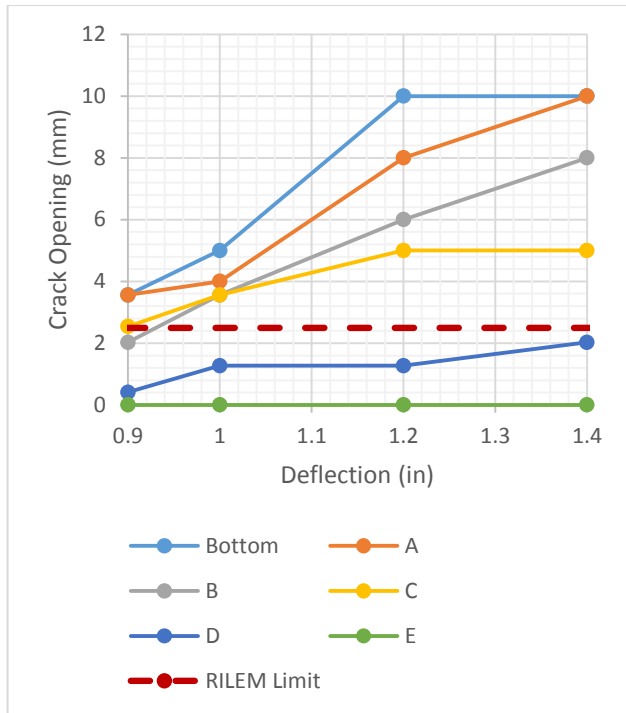


(a)

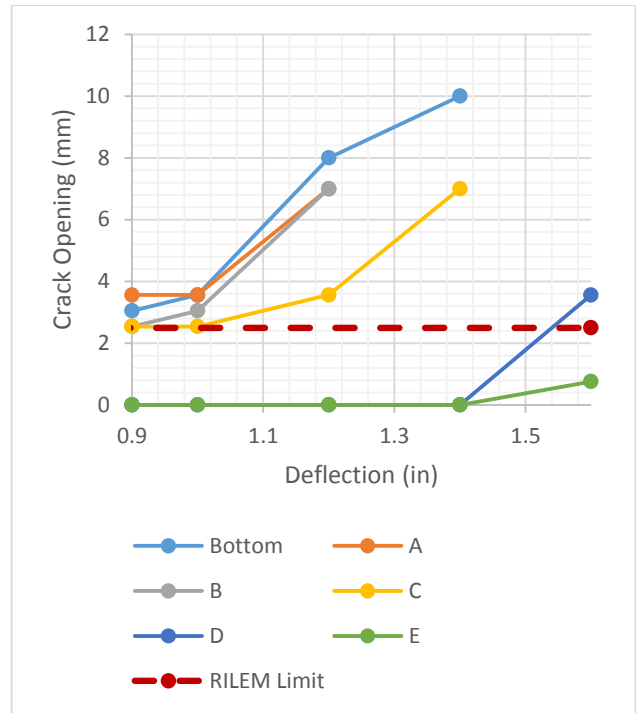


(b)

Figure 243. S7505BTM23 Crack Opening vs Strip Deflection for (a) East Face and (b) West Face

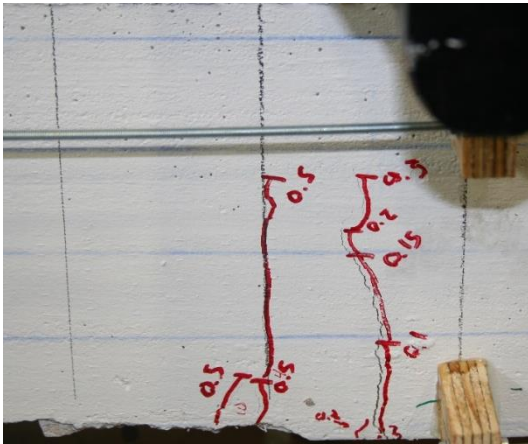


(a)

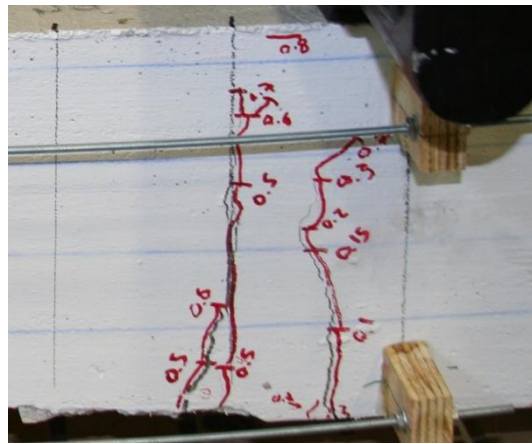


(b)

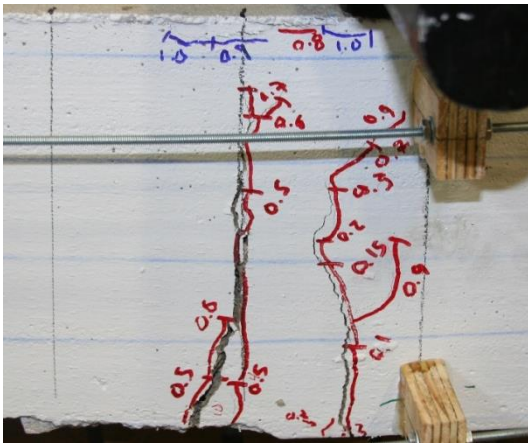
**Figure 244. S7505BTM23 Crack Opening vs Strip Deflection for Primary Crack at Each Reference Line
(a) E10 and (b) W11**



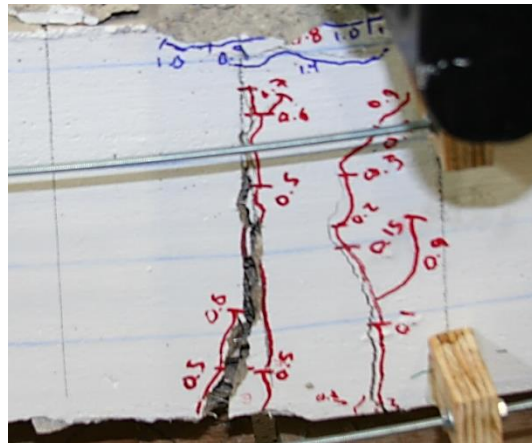
(a)



(b)

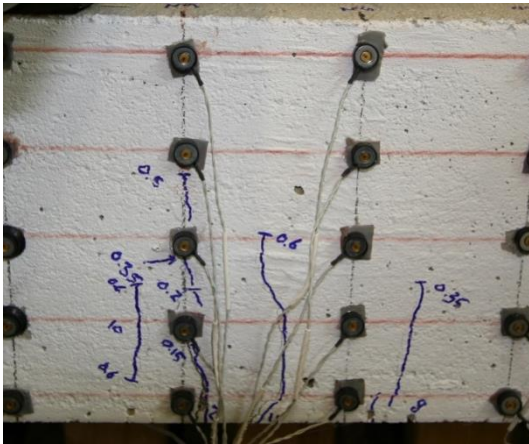


(c)

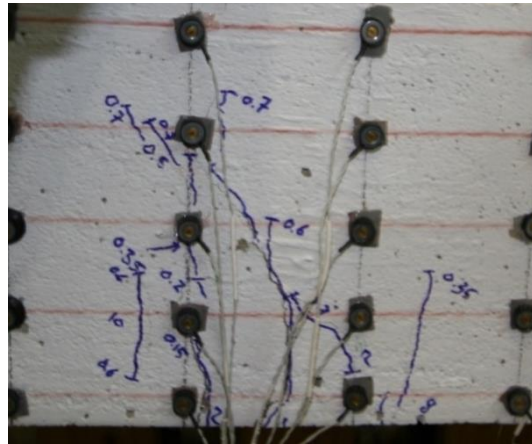


(d)

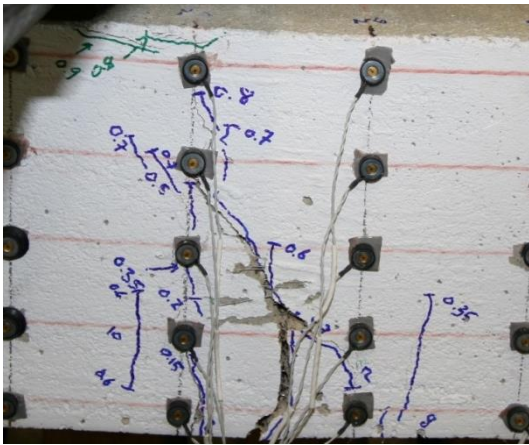
Figure 245. S7505BTM23 Crack Progression of E10 at: (a) 0.5 inches, (b) 0.8 inches, (c) 1.0 inches, and 1.6 inches.



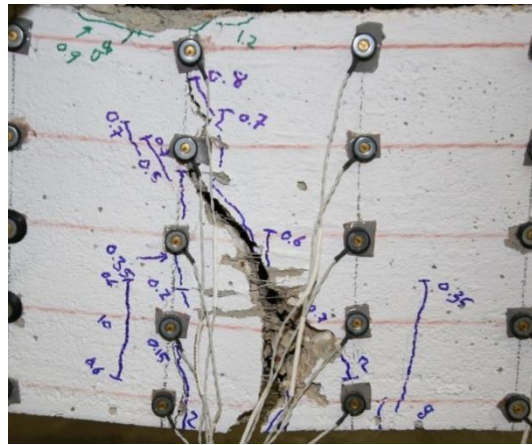
(a)



(b)

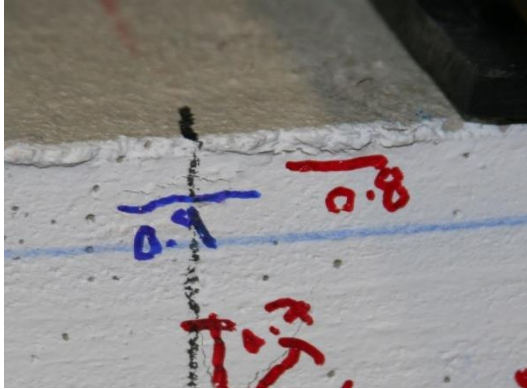


(c)



(d)

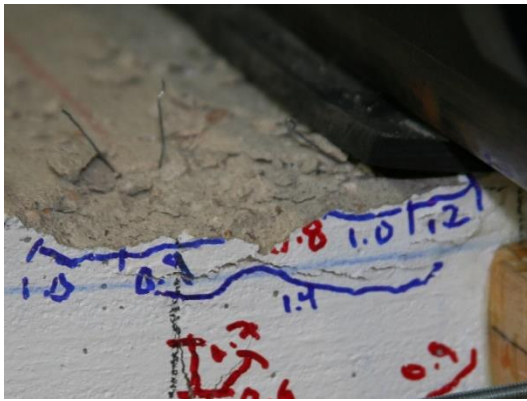
Figure 246. S7505BTM23 Crack Progression of W11 at: (a) 0.6 inches, (b) 0.7 inches, (c) 1.0 inches, and 1.4 inches.



(a)



(b)



(c)



(d)

Figure 247. S7505BTM23 Crushing at (a) 1.0 inch and (b) 1.2 inch, (c) 1.6 inches, and (d) Conclusion of Test

S7505CTR35

Slab strip specimen S7505CTR35 was 7.5 inches deep with 3-#5 bars located at the mid-depth of the specimen and a fiber volume of 0.5 percent. The specimen achieved a maximum capacity of 16.52 kips at a deflection of 0.8 inches (L/105). During construction, the bottom edge on the west face was damaged centerline and N3. Cracks W2 and W12 formed at the base of this damaged region.

Ten cracks formed on the east face, with five inside the constant moment region. Twelve cracks formed on the west face of the specimen, with six inside the constant moment region. The first crack for both the east and west face occurred during the 0.1 inch deflection step, (L/840). At the 0.30 inch deflection step, (L/280), the majority of the formed cracks had extended to the mid-depth of the specimen. Cracks outside of the constant moment region had little to no vertical extensions beyond the 0.40 inch deflection step. However, new cracks continued to form outside of the constant moment region up to the deflection step 0.7 inches (L/120). Cracks inside the constant moment region continued to extend vertically until the deflection step 0.9 inches, (L/93). At this deflection, additional deflections resulted in minor vertical extensions and significant widening of the critical cracks. The critical cracks exceeded reference line D by approximately one inch while non-critical cracks extended slightly below reference line D. Figure 248 through Figure 251 show the progression of each crack throughout the test.

The average non-critical crack width on the east and west face was 0.43 mm 0.66 mm respectively. Ultimately, cracks E3 and W4 created the critical failure plane of the specimen. From deflection step 0.9 inches to 1.0 inches (L/84), the crack width of E3 doubled to 2.54. In comparison, all other cracks on the east face did not change in width. The second largest crack, E3 with a width of 1.27mm. The same behavior was observed on the west face; W4 width increased by 150 percent to 3.05. Both E5 and W4 surpassed the maximum allowed crack width at the 1.0 inch deflection step, load of 15.51 kips. (RILEM 2002, fib 2010) The crack width at the location of the steel, mid-depth, did not exceed the allowable limit on the east face; however, by deflection step 1.2 inches, W4 had the maximum allowed crack width at reference line C. Figure 252 and Figure 253 show the relationship between the crack opening and strip deflection for each face.

Figure 254 and Figure 255 show the progression of cracks E5 and W4. Both critical cracks formed at deflection step 0.2 inches. Each critical crack became the widest crack on their respective face by deflection step 0.8 inches. With the exception of associated crack branching, each critical crack extended vertically for the final time at the next deflection step, 0.9 inches. Both E5 and W4 resulted in multiple "branch" cracks and steel fiber anchorage failure.

Crushing was first observed on both sides at the deflection step 1.0 inches (L/84) and load of 15.51 kips. The crushing occurred between references N3 and N9. During the next deflection step, the crushing region expanded north 3 inches to include N3 through N12. As the test continued, the crushing region continue to descend vertically until diagonal cracks began to form originating at the crushed region orientated downward away from the critical cracks. The progression of the crushed region is shown in Figure 256.

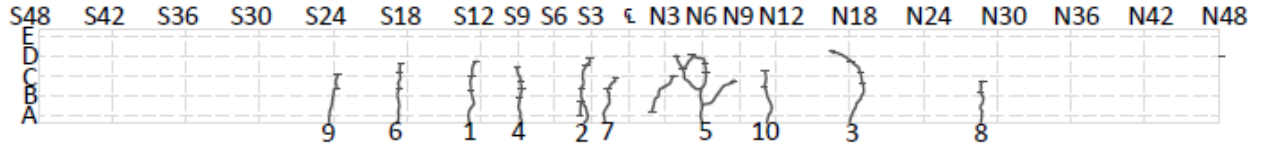


Figure 248. S7505CTR35 Crack Profile East Face

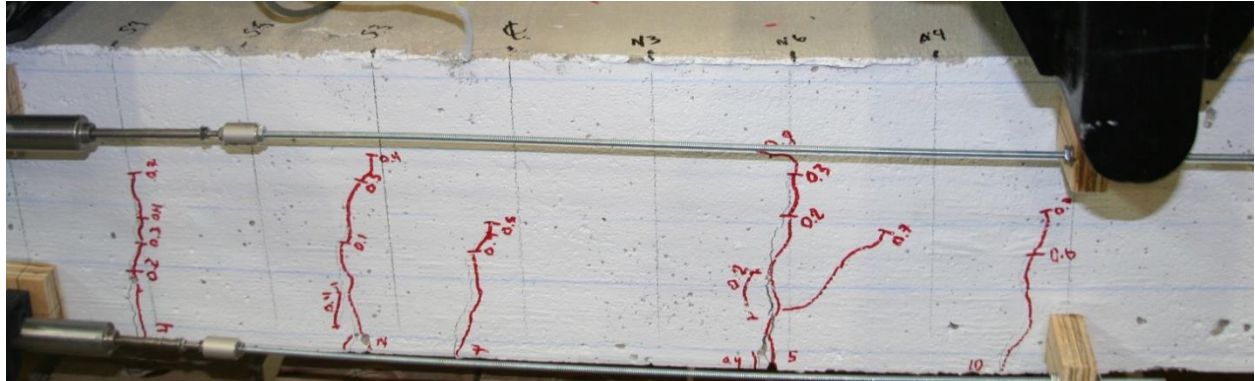


Figure 249. S7505CTR35 East Face Constant Moment Region

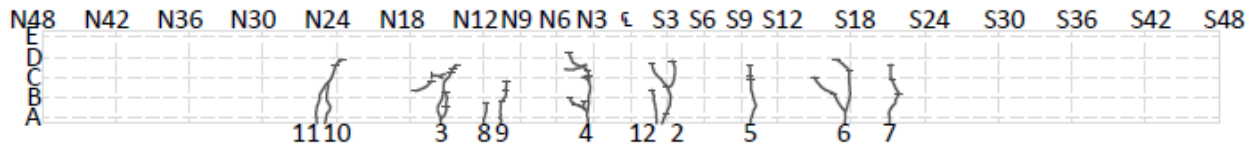


Figure 250. S7505CTR35 Crack Profile West Face

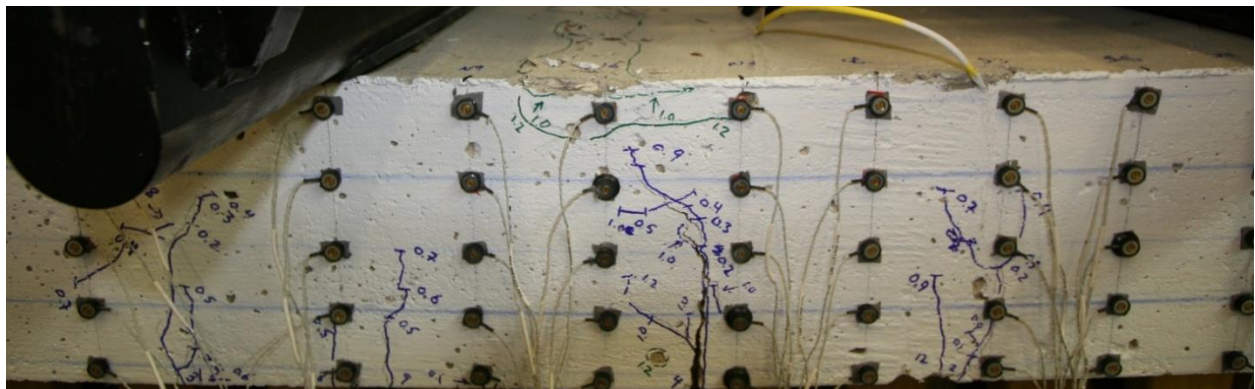
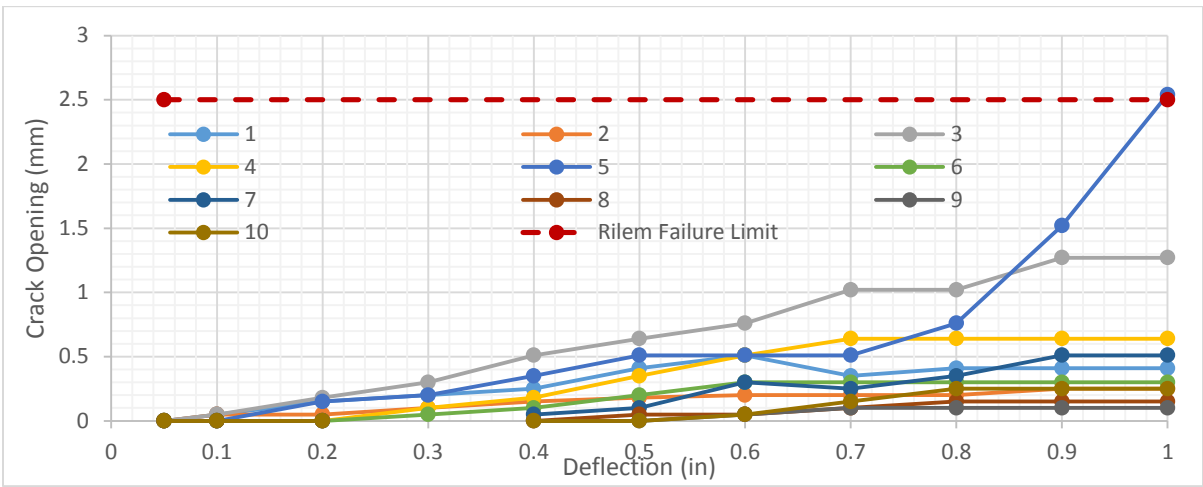
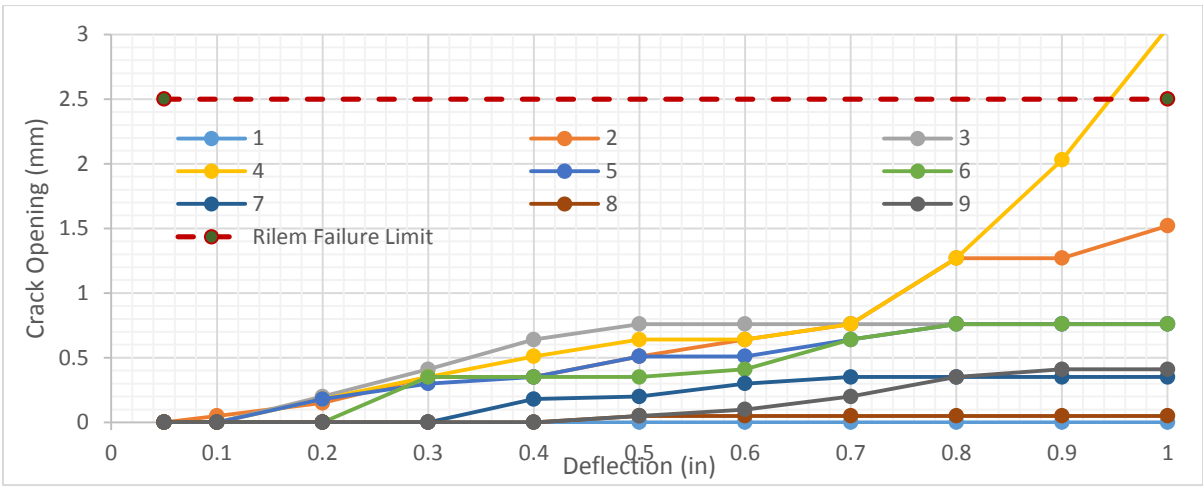


Figure 251. S7505CTR35 West Face Constant Moment Region

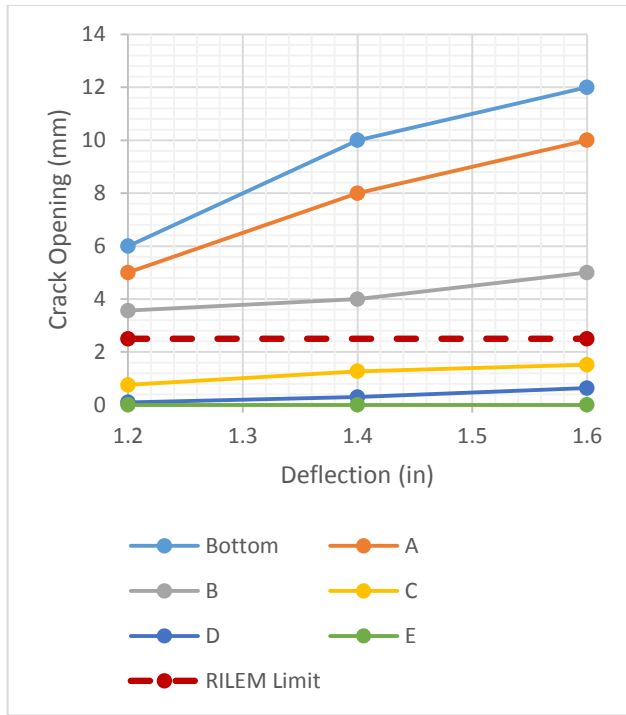


(a)

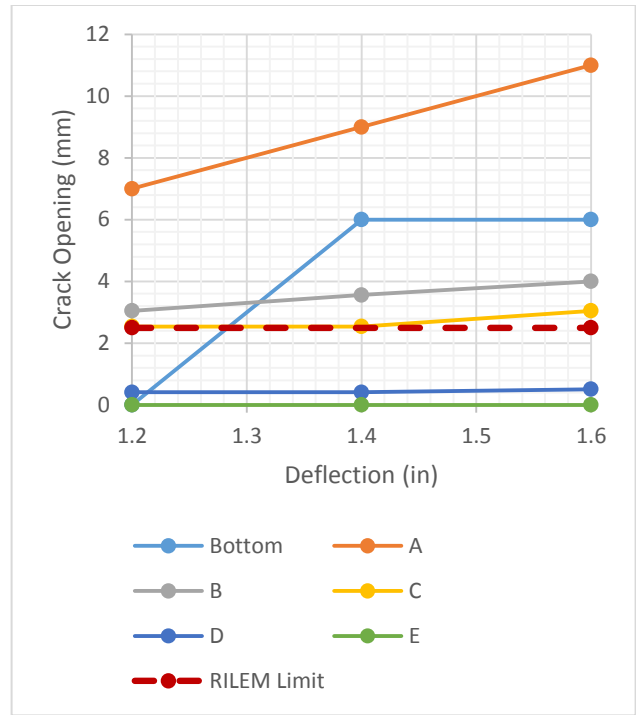


(b)

Figure 252. S7505CTR35 Crack Opening vs Strip Deflection for (a) East Face and (b) West Face

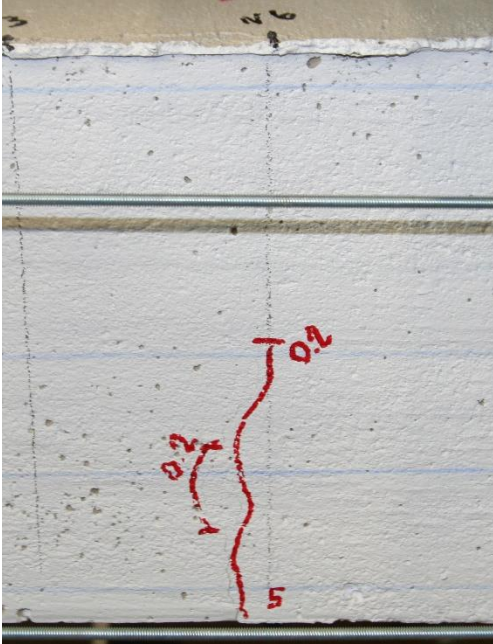


(a)

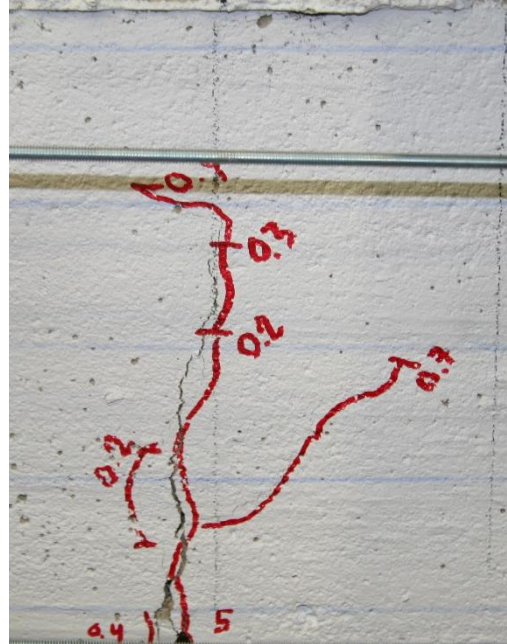


(b)

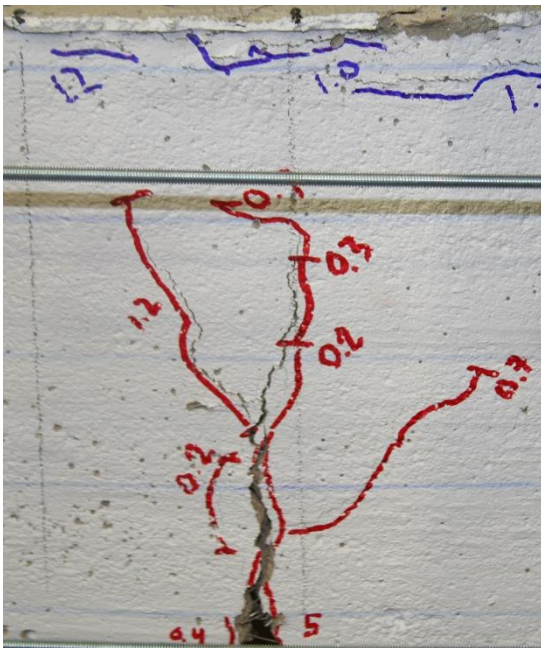
Figure 253. S7505CTR35 Crack Opening vs Strip Deflection for Primary Crack at Each Reference Line (a) E5 and (b) W4



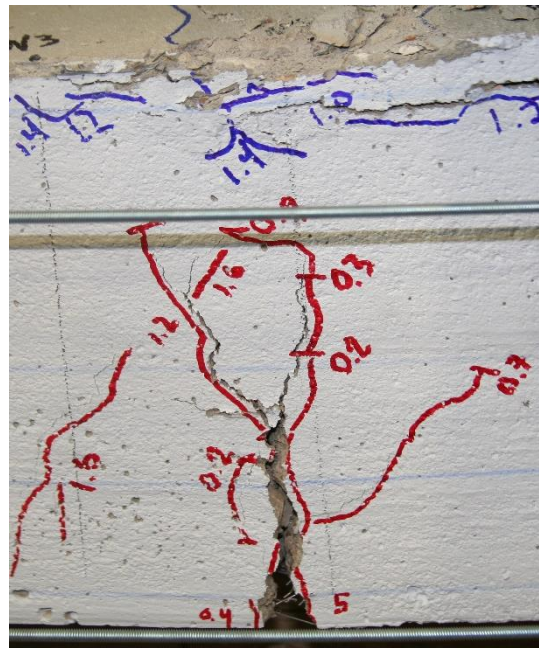
(a)



(b)

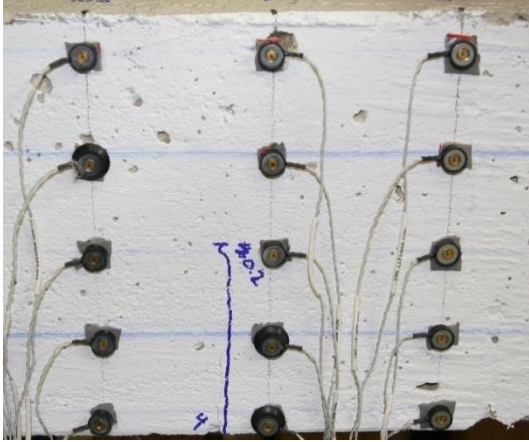


(c)

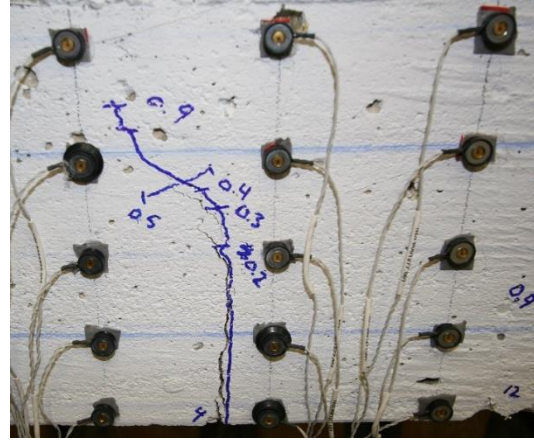


(d)

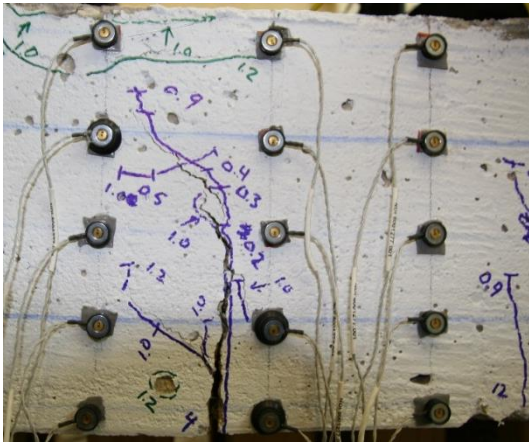
Figure 254. S7505CTR35 Crack Progression of E5 at: (a) 0.2 inches, (b) 0.9 inches, (c) 1.2 inches, and 1.6 inches.



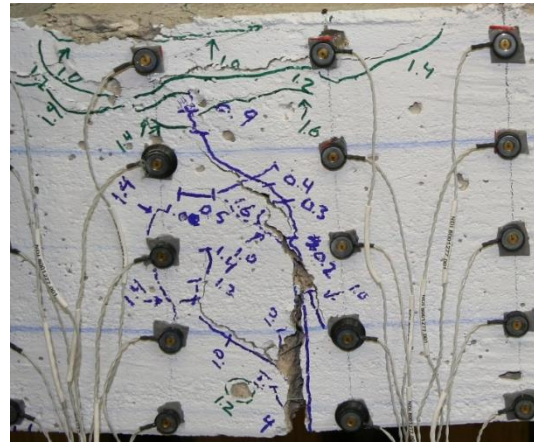
(a)



(b)

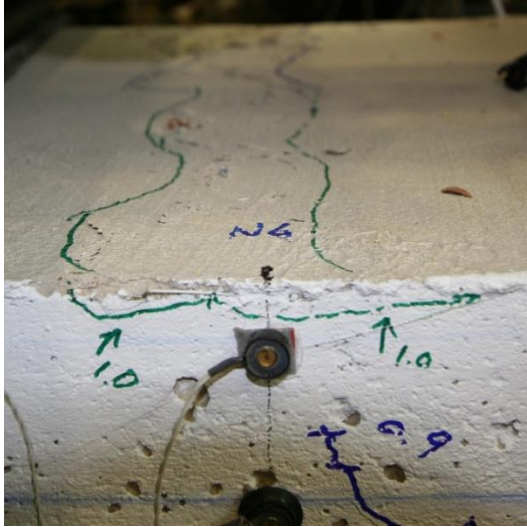


(c)

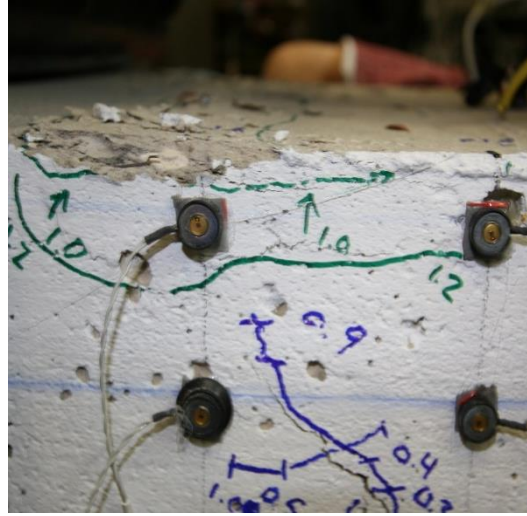


(d)

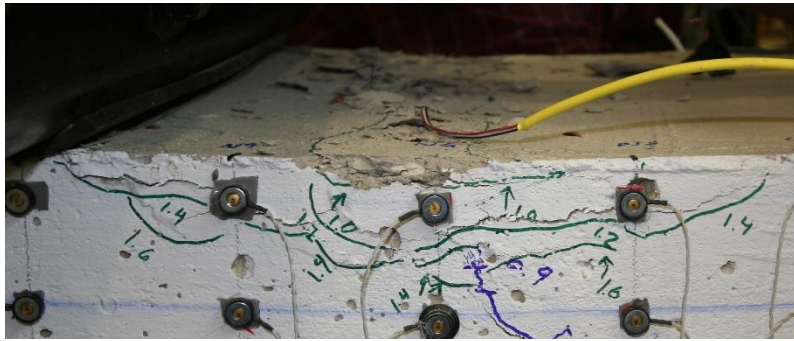
Figure 255. S7505CTR35 Crack Progression of W4 at deflection step: (a) 0.2 inches, (b) 0.9 inches, (c) 1.2 inches, and 1.6 inches.



(a)



(b)



(c)

Figure 256. S7505CTR35 Crushing Progression



Figure 257. S7505CTR35 W4 and Crushed Region at Conclusion of Test.

S7505CTR25

Slab strip specimen S7505CTR25 was 7.5 inches deep with 2-#5 bars located at mid-depth and a fiber volume of 0.5 percent. The specimen achieved a maximum capacity of 11.46 kips at a deflection of 0.7 inches (L/120). During construction, the bottom edge of the west face was damaged near the center line of the beam between N3 and S3. One crack, E5, formed in this damaged region of the specimen; the crack was not the primary failure plane of the test.

Seven cracks formed on the east face, with four inside the constant moment region. Seven cracks formed on the west face, with four inside the constant moment region. The first crack on the east face formed at deflection step 0.05 inches (L/1680). The first crack on the west face occurred during the next deflection step, 0.1 inches (L/840). At the 0.30 inch deflection step, (L/280), the majority of the cracks had extended to the mid-depth of the specimen. Cracks outside of the constant moment region extended vertical to reference by deflection step 0.7 inches. At this point, the extension of all non-critical cracks ceased. Cracks inside the constant moment region continued to extend vertically until the deflection step 1.0 inches, (L/84). Further deflecting the specimen resulted in significant widening of the critical cracks. Figure 258 through Figure 261 show the progression of each crack throughout the test.

The average non-critical crack width on the east and west face was 0.89 mm 0.76 mm, respectively. Ultimately, cracks E1 and W1 created the critical failure plane of the specimen. From deflection step 0.4 inches to 0.5 inches, the crack width of E1 doubled to 1.02 mm. The second largest crack at this step was E3 with a width of 0.64 mm. The same behavior was observed on the west face; the width of W1 increased by 300 percent to 1.02 mm. Critical crack E1 surpassed the maximum allowed crack width at the 0.9 inch deflection step. (RILEM 2002, fib 2010). W1 exceeded the maximum allowed width during the next deflection step of 1.0 inches. Figure 262 shows the relationship between the crack opening and strip deflection for each face. Figure 263 and Figure 264 displays the critical crack progression on each side of the specimen.

Crushing began a deflection of 0.7 inches. The crushing occurred adjacent to the north loading point and directly above the critical crack on both faces of the specimen. At the onset of crushing failure, the maximum crack width had grown to 1.52 mm. A continuous crushing failure plane along the top face of the beam formed by a deflection of 1.2 inches. At the conclusion of the test, significant spalling and damage was noted on the top surface. At this time, the beam maintained a capacity of 76 percent of the peak load. Figure 265 shows the progression of the crushing failure of the specimen.

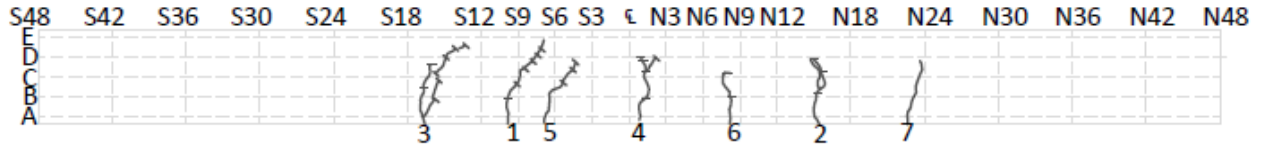


Figure 258. S7505CTR25 Crack Profile East Face

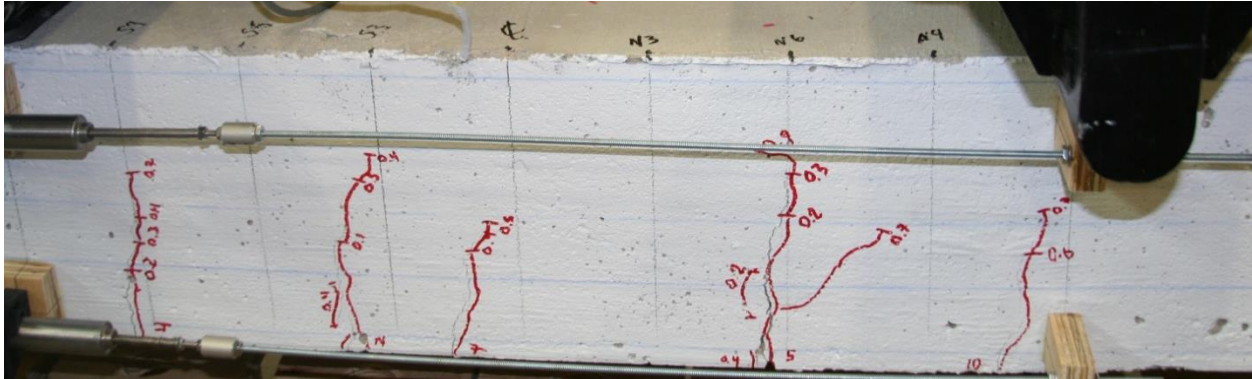


Figure 259. S7505CTR25 East Face Constant Moment Region

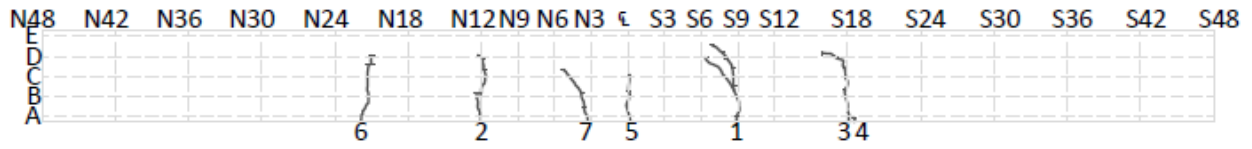


Figure 260. S7505CTR25 Crack Profile West Face

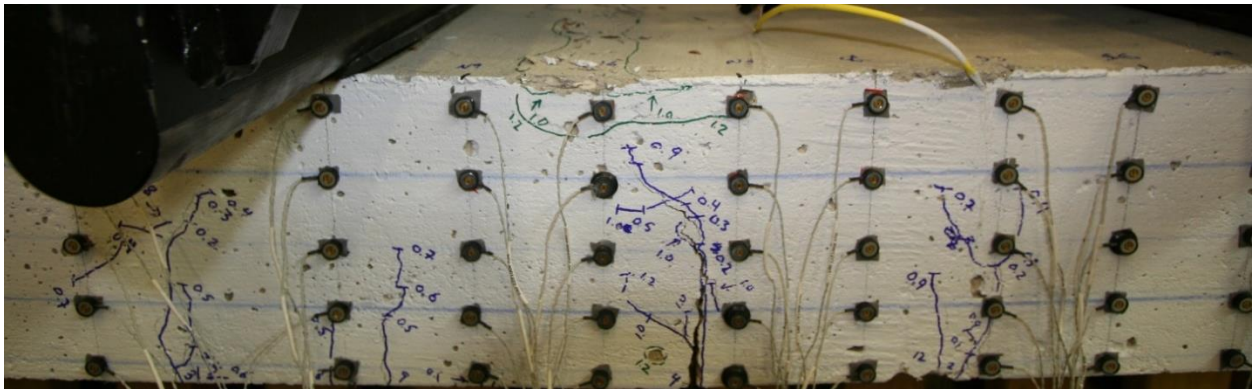
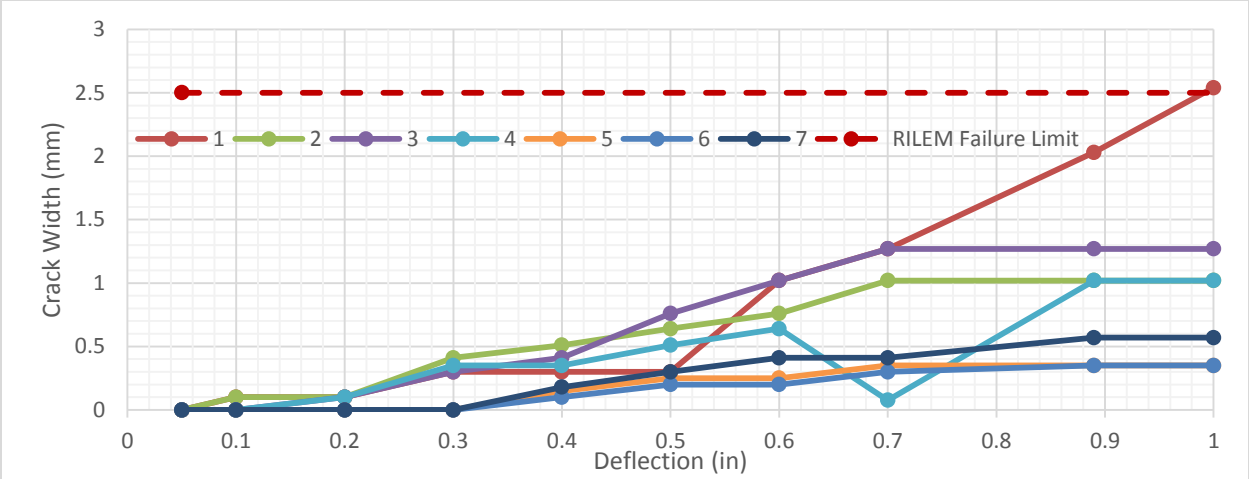
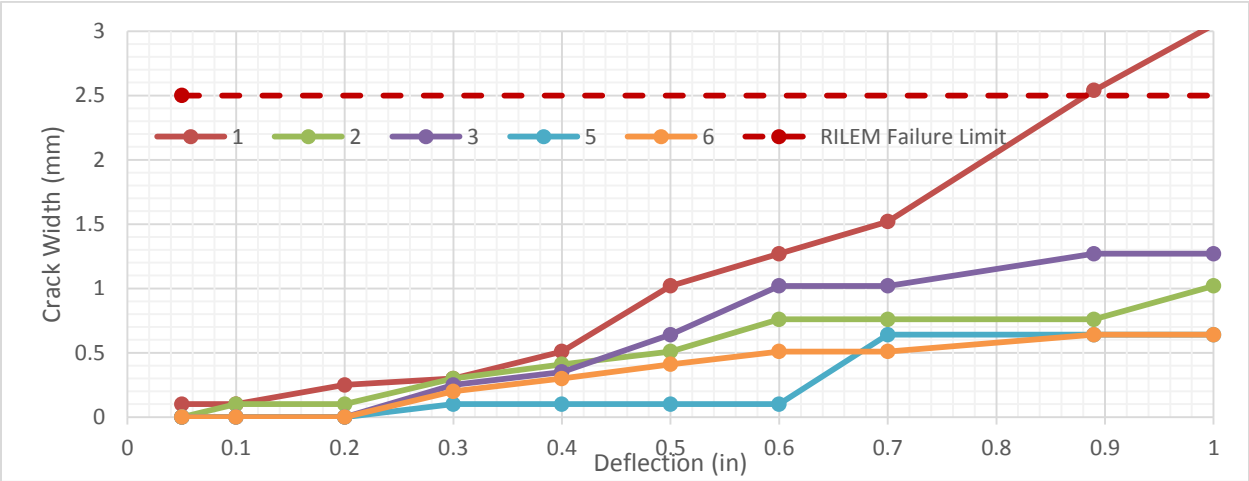


Figure 261. S7505CTR25 West Face Constant Moment Region

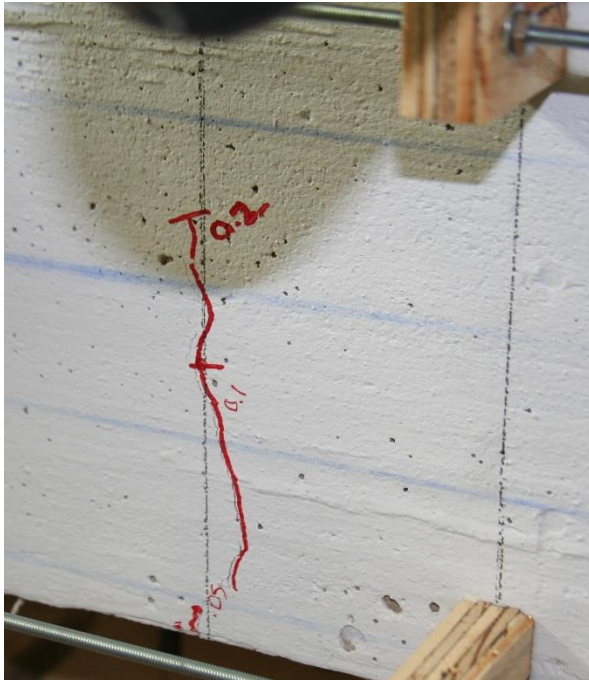


(a)

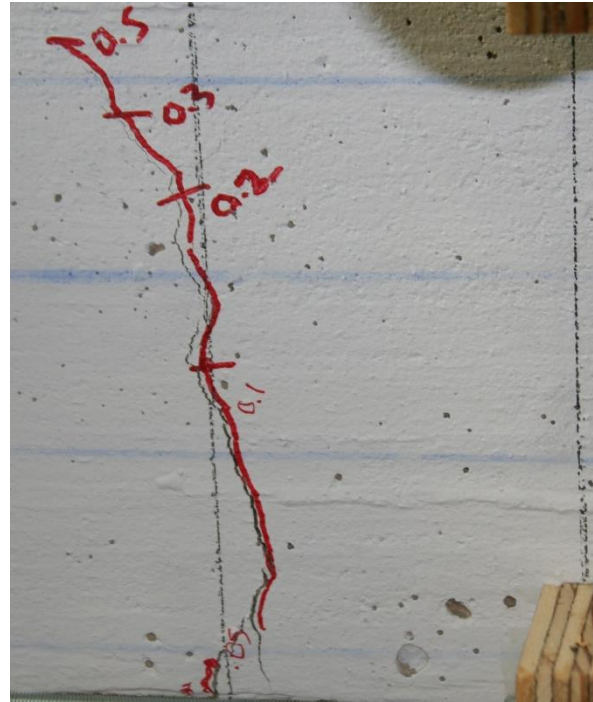


(b)

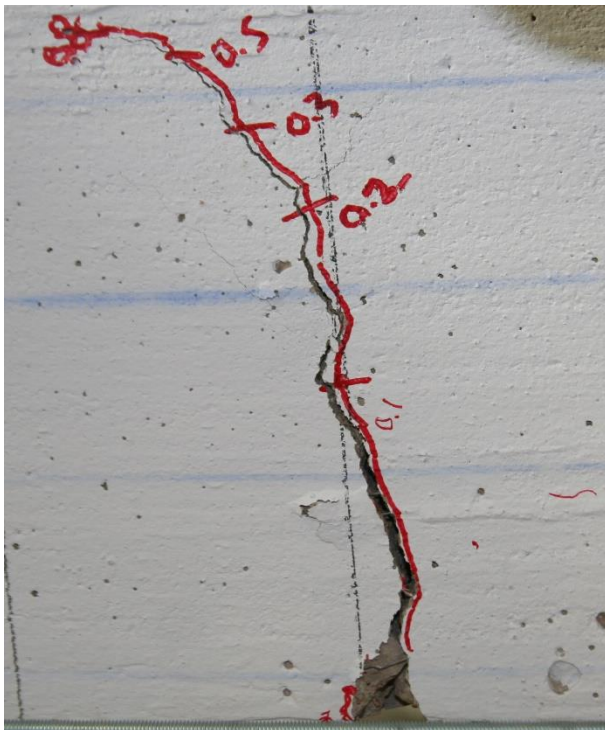
Figure 262. S7505CTR25 Crack Width vs Deflection for (a) East Face and (b) West Face



(a)



(b)

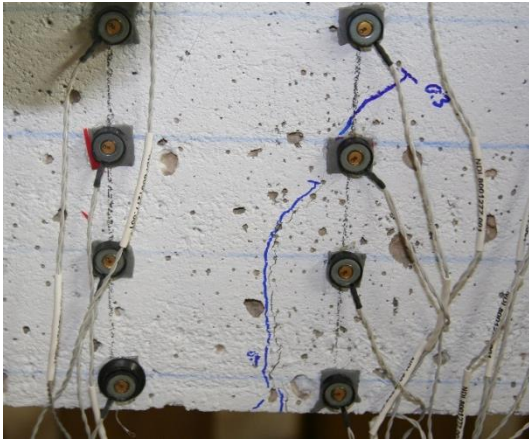


(c)



(d)

Figure 263. S7505CTR25 Crack Progression of E1 at: (a) 0.2 in deflection, (b) 0.5 in deflection, (c) 0.8 in deflection, and (d) 1.2 in deflection



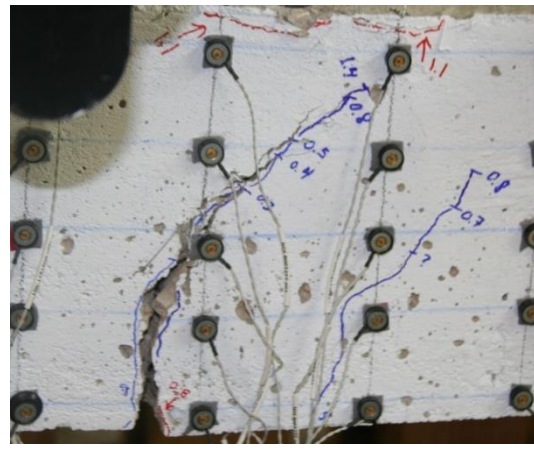
(a)



(b)

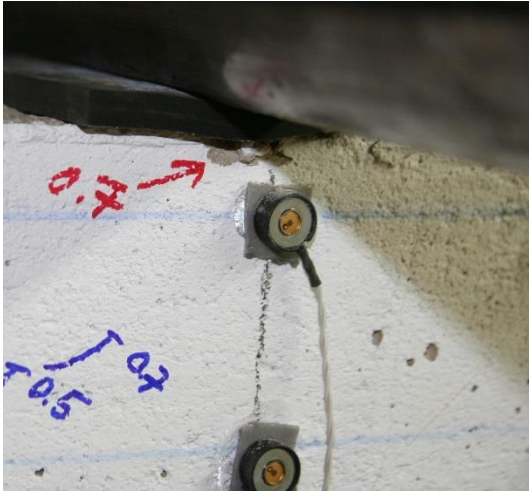


(c)



(d)

Figure 264. S7505CTR25 Crack Progression of W1 at Deflection Step: (a) 0.3 in deflection, (b) 0.6 in deflection, (c) 1.0 in deflection, and (d) 1.4 in deflection



(a)



(b)



(c)



(d)

Figure 265. S7505CTR25 Crushing at: (a) 0.7 in Deflection, (b), 1.1 in Deflection, (c) 1.2 in Deflection, (d) Conclusion of Test

S7505NOS00

Slab strip specimen S7505NOS00 was 7.5 inches deep with no traditional reinforcement and a fiber volume of 0.5 percent. The specimen achieved a maximum capacity of 2.54 kips at a deflection of 0.05 inches ($L/1680$). Without steel reinforcement, the specimen's peak capacity corresponded to its cracking strength.

A single crack developed on both the east and west face during the first deflection step, 0.05 inches. As the deflection of the specimen increased, accessory cracks formed on either side of the main cracks. The accessory cracks often formed within a steel fiber's length of the main crack. As the test continued and spalling began to occur, fibers were observed connecting the accessory cracks to the primary crack.

The critical crack on the east face, E1, extended to vertical reference E by the third deflection step, 0.15 inches. In contrast, W1 did not extend to reference E until the ninth deflection step, 0.70 inches. During the fourth deflection step, 0.20 inches, W1 developed a branching crack that ultimately formed a large wedge at the top of the specimen. Figure 266 and Figure 267 show the vertical progression of the cracks on the east and west faces respectively.

The crack width was measured at each reference line throughout the entirety of the test except where excessive spalling prohibited it. The critical crack on each side achieved the maximum allowable crack width at the bottom of the specimen by the sixth deflection step, 0.3 inches. The maximum allowable crack width was achieved at a new reference line with each successive deflection step for E1. The width of the critical crack on the west face, W1, did not progress upwards as quickly as E1. This is consistent with the behavior of the vertical progression of the two critical cracks. The maximum allowable crack width was not observed at mid-depth, reference line C, for W1 until the eighth load step, 0.5 inches. Fibers were visibly bridging the widening cracks at later deflection steps. Figure 268 through Figure 270 show the crack width progression of both critical cracks.

All instrumentation was removed from the specimen at deflection step 0.70 inches to prevent damage to the equipment. Concrete crushing was observed at this deflection step on the east face. Concrete crushing was not observed on the top or west face at that time. Prior to the collapse of the specimen, crushing damage was observed on the west face. Extension of the crushed region of concrete was not observed on either face before collapse of the specimen. Figure 271 shows the first observance of crushing on each face. Figure 272 shows the failure of the specimen.

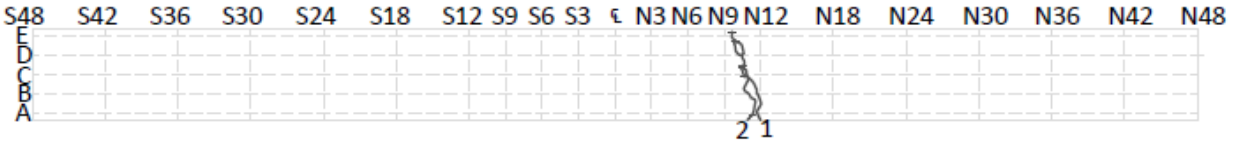


Figure 266. S7505NOS00 Crack Profile East Face

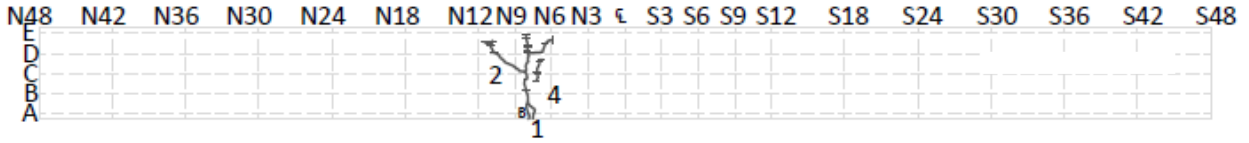
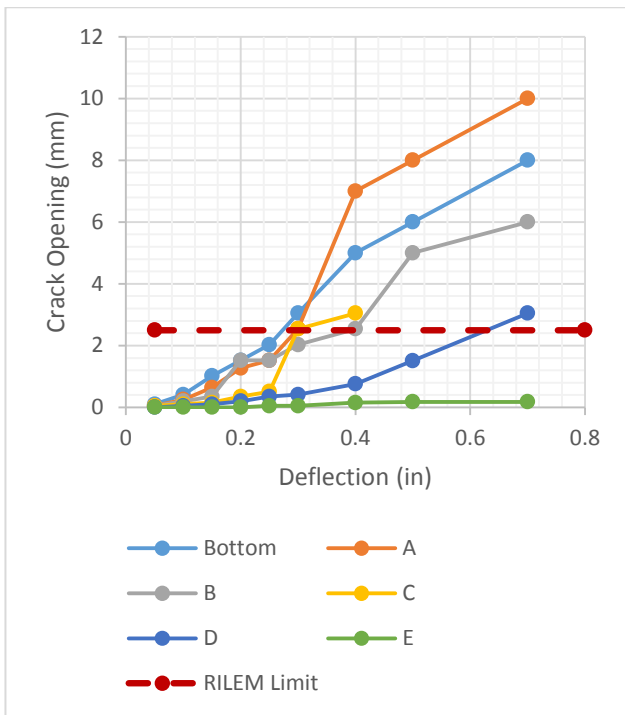
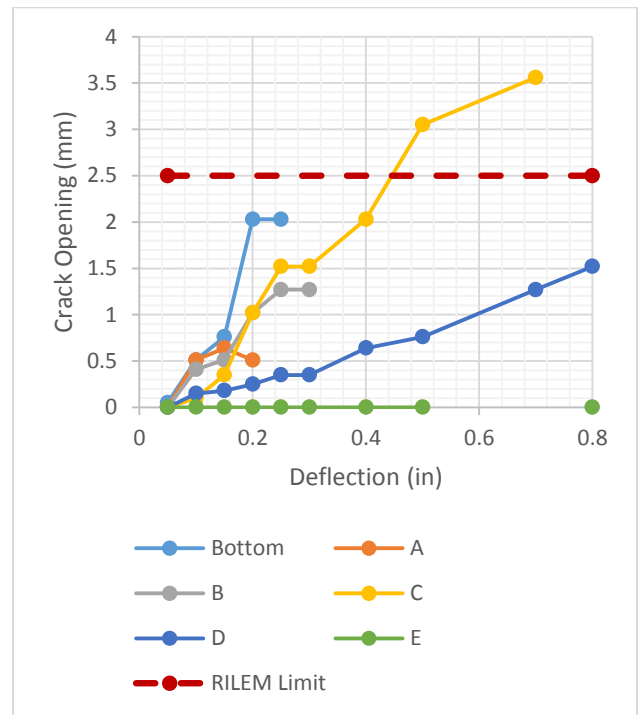


Figure 267. S7505NOS00 Crack Profile West Face

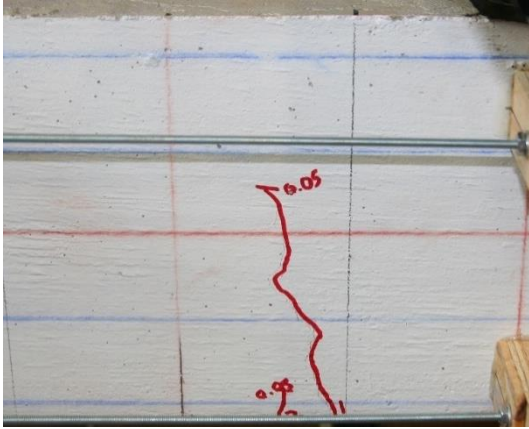


(a)



(b)

Figure 268. S7505NOS00 Crack Width Progression of Critical Cracks (a) E1 and (b) W1



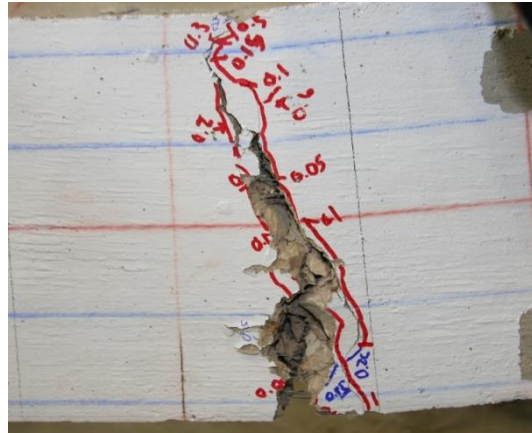
(a)



(b)

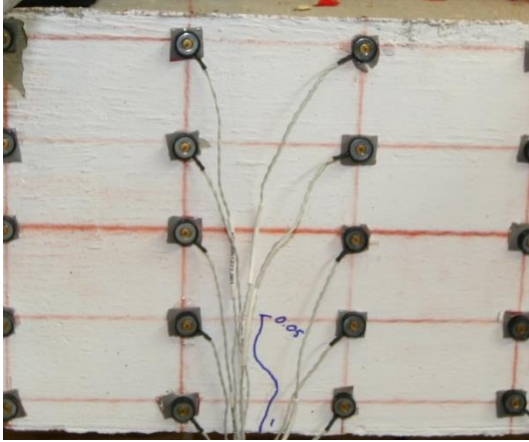


(c)

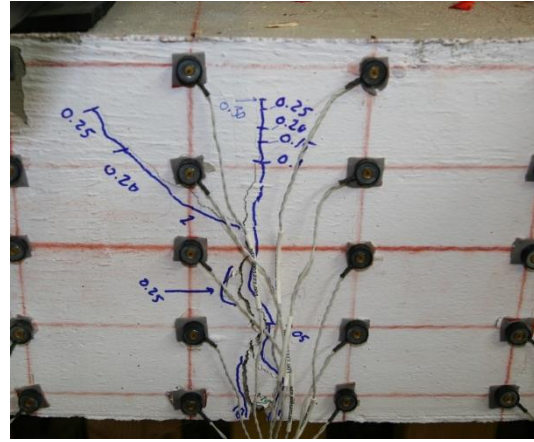


(d)

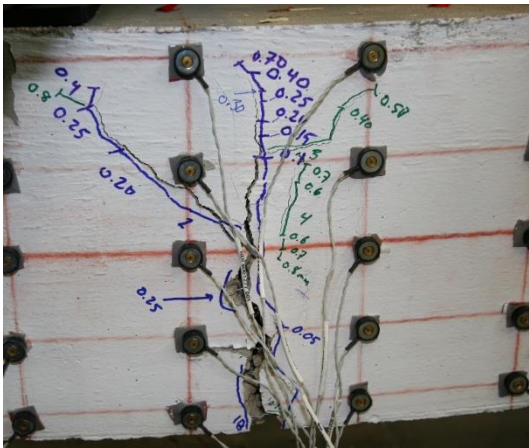
Figure 269. S7505NOS00 Damage Progression of the Critical Crack on the East Face, E1, at: (a) 0.05 inches, (b) 0.30 inches, (c) 0.80 inches, and (d) Conclusion of Test



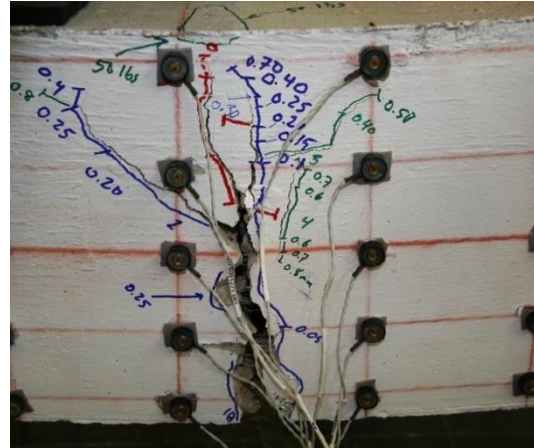
(a)



(b)



(c)



(d)

Figure 270. S7505NOS00 Damage Progression of Critical Crack West Face, W1, at (a) 0.05 inches, (b) 0.30 inches, (c) 0.80 inches, and (d) Conclusion of Test

S7520NOS00

Slab strip specimen S7520NOS00 was 7.5 inches deep with no traditional reinforcement and a fiber volume of 2.0 percent. The specimen achieved a maximum capacity of 7.3 kips at a deflection of 0.1 inches (L/840).

The bottom edge on the east face was damaged in the demolding of the specimen between S3 and S6. Crack E1 formed at the base of this damaged region as shown in Figure 273.

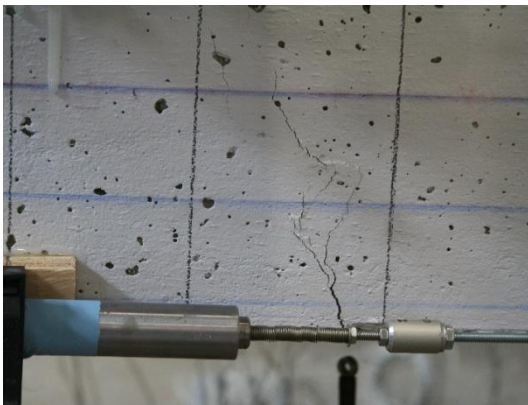
On the east face, two cracks formed in the constant moment region. On the west face, three cracks formed in the constant moment region. The first east face crack occurred at deflection step 0.1 inches (L/840). The first west face crack did not form until deflection step 0.2 inches (L/24). All cracks formed by the 0.20 inch deflection step (L/240). Cracks inside the constant moment region progressed vertically passed reference line E, to approximately 0.25 inches from the top surface. Vertical progression of cracks ceased at deflection step 1.0 inches (L/84). Further increasing the deflection of the specimen resulted in widening of the primary crack and crack branching.

The critical cracks on the east face and west face were E1 and W2. Crack E1 formed during the 0.1 inch deflection step (L/840). Crack W3 formed during the 0.2 inch deflection step (L/420). The critical crack on the east face formed between S6 and S9. The critical crack on the west face formed between S9 and S12. The maximum allowable crack width, 2.5 mm, was observed at deflection step 0.4 inches (L/210) for each crack. Critical crack W2 formed a large wedge with adjacent crack W3. The wedge remained intact and did not fall away. At the bottom of W2 and W3, fibers visibly joined the two cracks. Crack E1 branched at reference line D. Spalling of the concrete occurred at the apex of the branch, revealing fibers joining the two branches. Figure 274 and Figure 275 show the progression of each crack throughout the test.

Crushing was first observed on the west face at deflection step 1.0 inches (L/84). The crushing began directly below the south load point at horizontal reference S12 above each critical crack. Crushing was not observed on the east face or top surface. Extension of the crushing region on the west face was not observed. The test was concluded after the residual strength fell to 20 percent of the maximum applied load. Figure 276 shows the progression of concrete crushing and the specimen at the completion of the test.



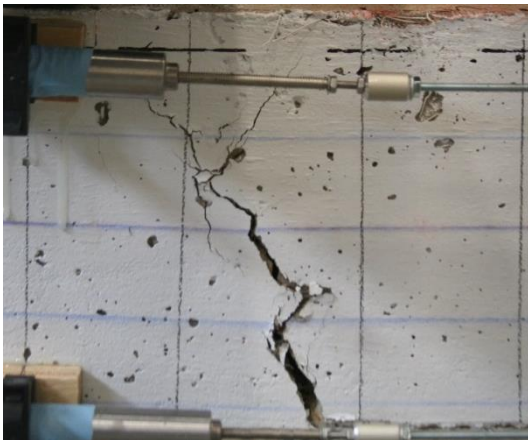
Figure 273. S7520NOS00 Damaged Corner



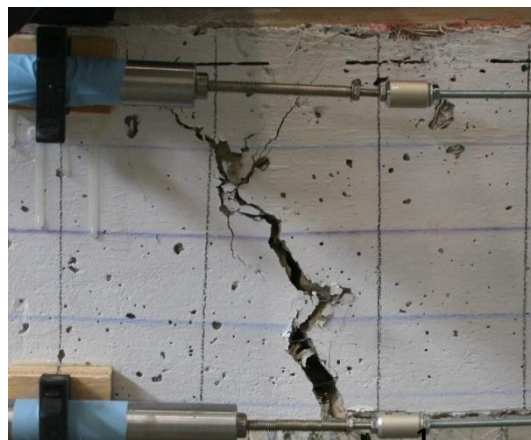
(a)



(b)



(c)

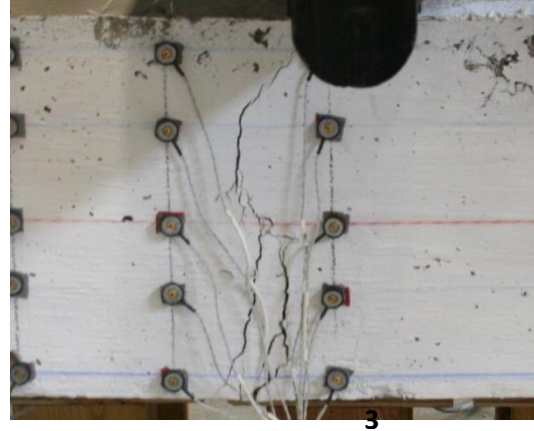


(d)

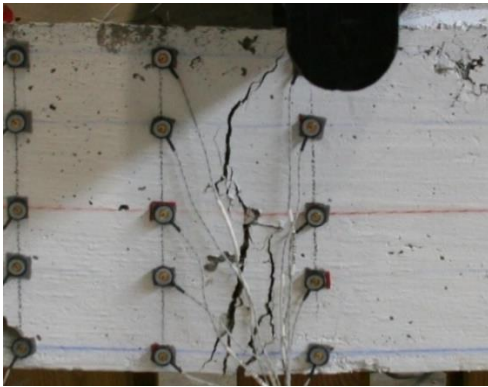
Figure 274. S7520NOS00 Crack Progression of E1 and E2 at (a) 0.1 inches, (b) 0.6 inches, (c) 0.8 inches, and 1.1 inches.



(a)



(b)



(c)



(d)

Figure 275. S7520NOS00 Crack Progression of W2 and W3 at: (a) 0.2 inches, (b) 0.5 inches, (c) 0.8 inches, and 1.1 inches



(a)



(b)

Figure 276. S7520NOS00 Crushing Progression at (a) 1.0 and (b) Completion of Test

S9005BTM35

Slab strip specimen S9005CTR35 was 9.0 inches deep with 3-#5 bars located at the bottom (1 inch clear cover) and a fiber volume of 0.5 percent. The specimen achieved a maximum capacity of 31.97 kips at a deflection of 0.7 inches (L/120). Additional flexural cracks formed beyond this deflection step.

Eighteen cracks formed on the east face, with 10 inside the constant moment region. Twelve cracks formed on the west face, with six inside the constant moment region. The first crack for both the east and west face occurred during the 0.1 inch deflection step, (L/840). At the 0.40 inch deflection step, (L/210), all but three cracks on the west face and one on the east face had formed. The majority of the cracks in the constant moment region extended to or beyond the mid-depth of the specimen by deflection step 0.6 inches (L/140). The majority of the cracks outside of the constant moment region did not reach mid-depth. The maximum vertical line was achieved by deflection step 0.8 inches (L/105) to approximately 0.5 inches above reference D. Further increasing the deflection of the specimen resulted in widening and formation of “branch” and accessory cracks, such as E8 and W5. Figure 277 through Figure 280 show the vertical progression of cracks on each face.

The average non-critical crack width on the east and west face was 0.19 mm and 0.48 mm, respectively. The east face developed two critical cracks, E6 and E8 that continued to widen with each deflection step. Crack E6 was approximately 4.5 inches south of E8. The two cracks joined on the bottom face of the specimen to meet the critical crack on the west face, W5. Figure 282 shows the critical cracks on each face.

The critical cracks on the east face were twice the size of the next largest crack by deflection step 0.9 inches (L/93). At that time, each crack was approximately 1.52 mm in width. In comparison, the critical crack on the west face was 2.54 mm wide. The growth of the individual cracks on the east face was slower than the growth of the critical crack on the west face. However, the combined growth of the cracks on the east face was comparable to the growth of the crack on the west face.

The maximum allowable crack width was observed on the east face after the deflection step 1.2 inches (L/70). In contrast, crack W5 had achieved the maximum crack width two steps earlier at 0.90 inches (L/93). The crack width limit was observed at reference line B on both faces, but was not observed any higher prior to the removal of all instrumentation. Figure 281 and Figure 282 show the crack width growth observed throughout the test.

Figure 283 and Figure 284 show the progression of cracks E6 and W5 respectively. Both cracks first formed at deflection step 0.2 inches. Crack E6 was the widest crack on the east face by deflection step 0.6 inches. Crack W5 did not gain that distinction until deflection step 0.9 inches. Each critical crack became the widest crack on their respective face by deflection step 0.8 inches. With the exception of associated crack branching, each critical crack extended vertically for the final time at deflection step, 0.8 inches. Both E6 and W5 resulted in multiple “branch” cracks and steel fiber anchorage failure.

Crushing was first observed between horizontal reference S3 and S6 on the top surface at deflection step 0.70 inches (L/120). The crushing was observed above the critical cracks on either face. After the

next step, crushing was also visible on both faces between N3 and S6. As the test continued, the crushing extended horizontally to include the entire constant moment region; however, the significant damage was focused above the critical cracks on each face. The crushed concrete region extended downward to meet the tension cracks by deflection step 1.60 inches ($L/52.5$). The slab strip specimen did not collapse during the test, yet the concrete experienced severe crushing damage. Figure 285 and Figure 286 show the progression of concrete crushing and the extent of the damage after the specimen was removed from the test.

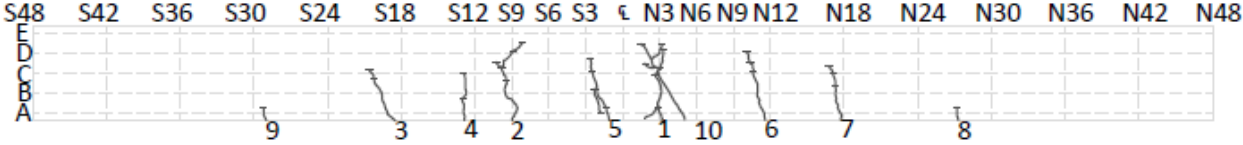


Figure 277. S9005BTM35 Crack Profile East Face

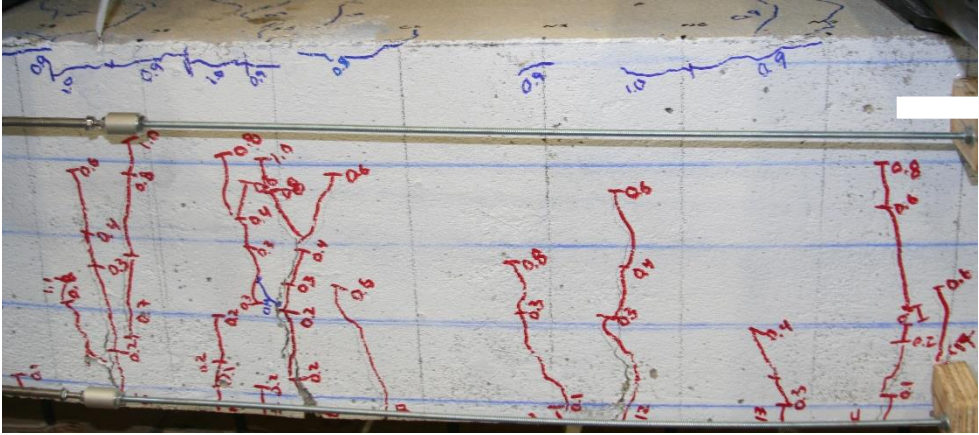
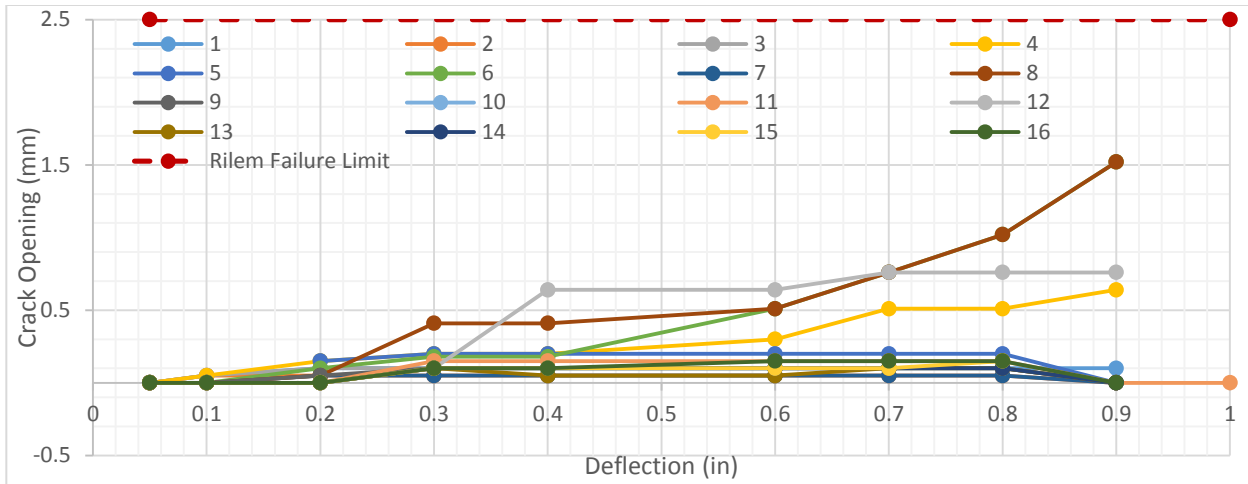
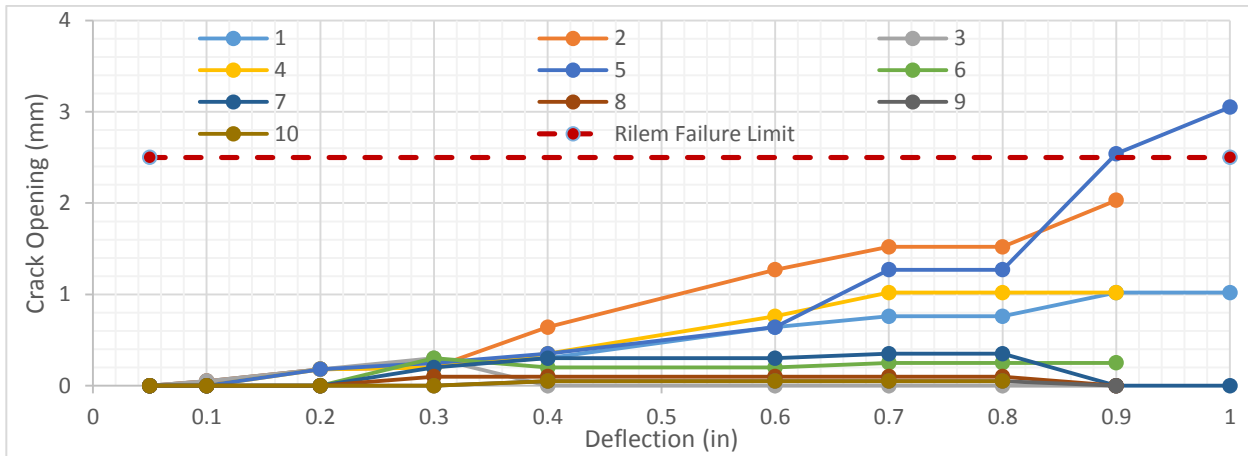


Figure 278. S9005BTM35 East Face Constant Moment Region

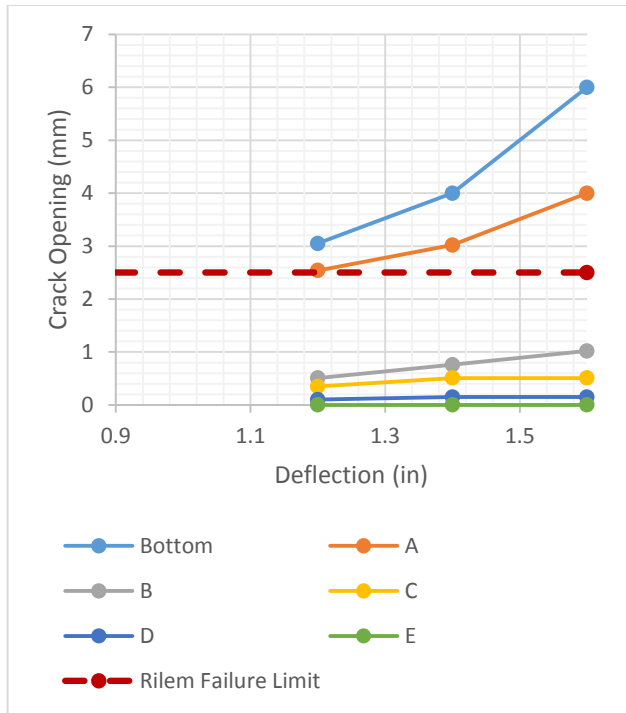


(a)

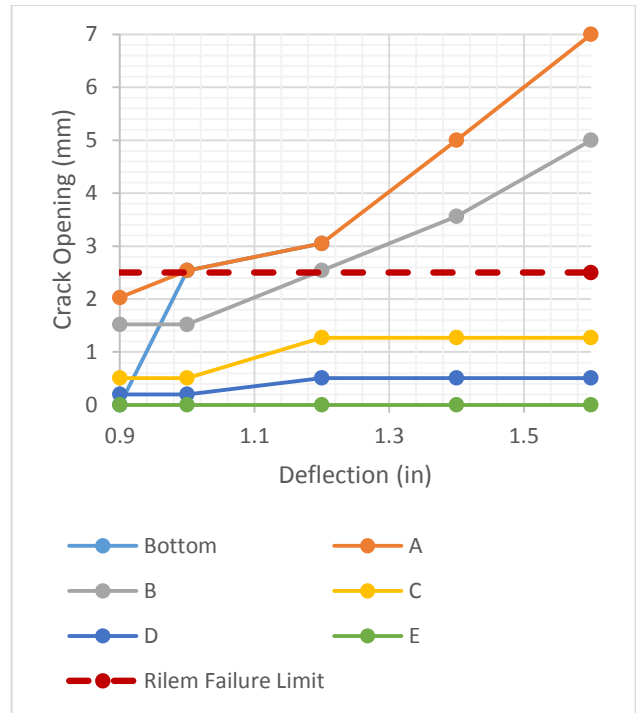


(b)

Figure 281. S9005BTM35 Crack Opening vs Strip Deflection for (a) East Face and (b) West Face

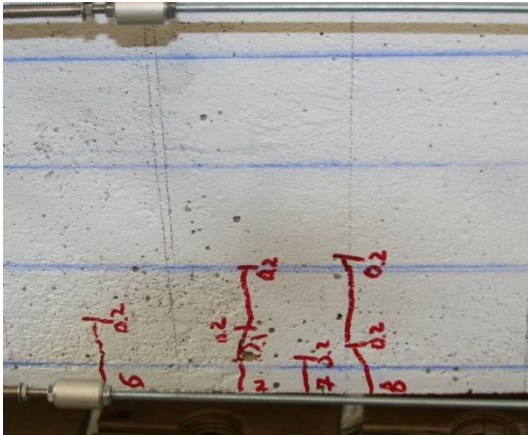


(a)

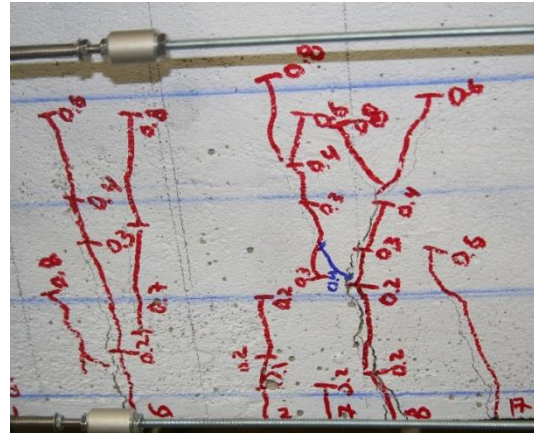


(b)

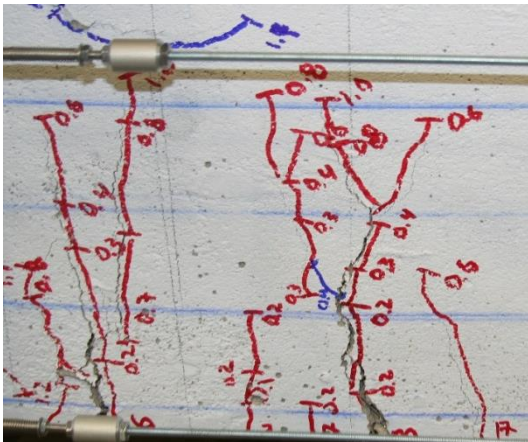
Figure 282. S9005BTM35 Crack Opening vs Strip Deflection for Primary Crack at Each Reference Line (a) E6 and (b) W5



(a)



(b)



(c)

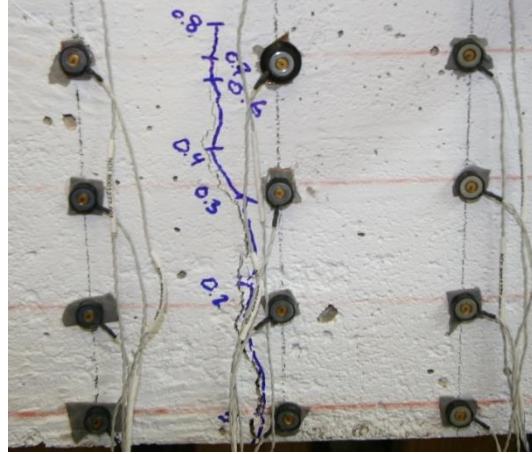


(d)

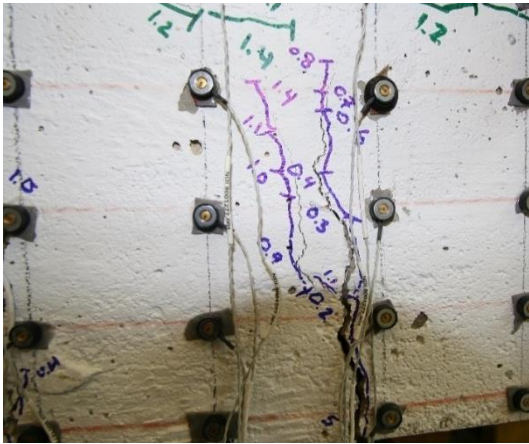
Figure 283. S9005BTM35 Crack Progression of E6 and E8 at: (a) 0.2 inches, (b) 0.8 inches, (c) 1.4 inches, and Removal of Beam



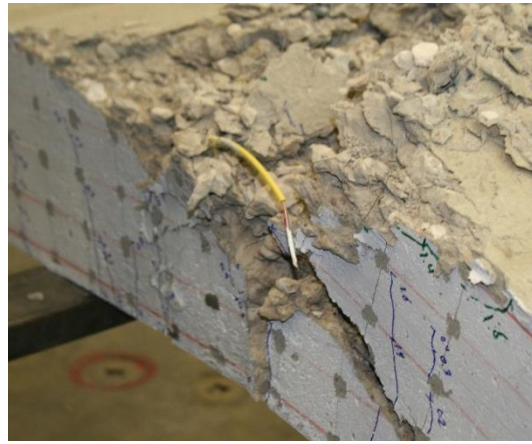
(a)



(b)



(c)

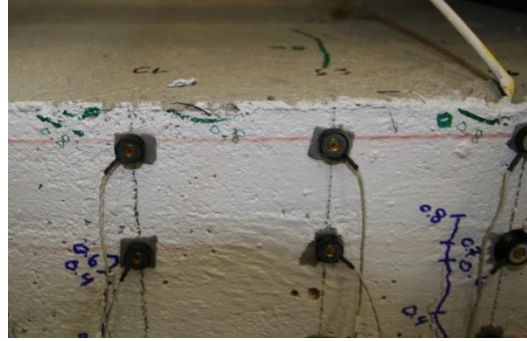


(d)

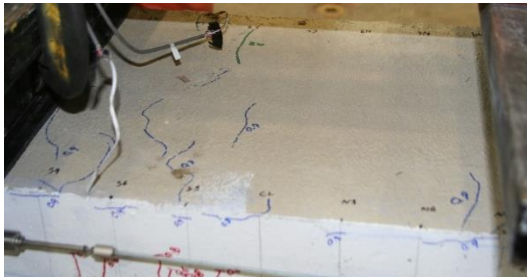
Figure 284. S9005BTM35 Crack Progression of W5 at: (a) 0.2 inches, (b) 0.8 inches, (c) 1.4 inches, and Removal of Beam



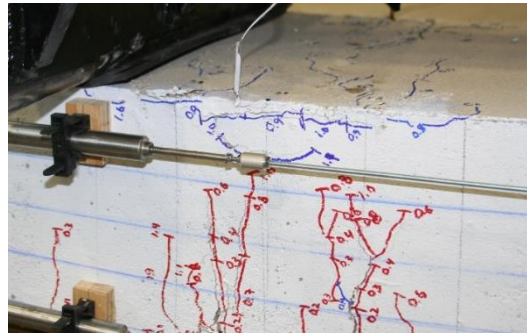
(a)



(b)



(c)



(d)

Figure 285. S9005BTM35 Crushing Progression at (a) 0.7 inch, (b) 0.8 inch, (c) 1.0 inches and (d) 1.6 inches

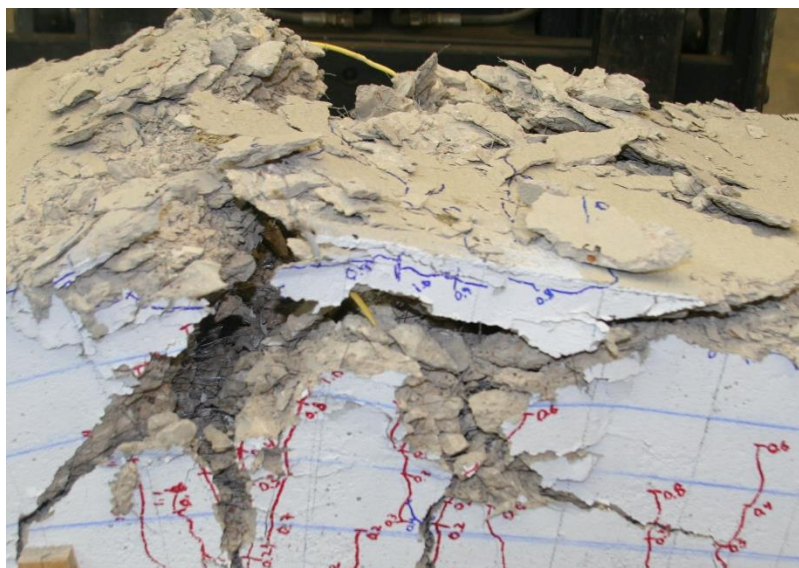


Figure 286. S9005BTM35 Severe Crushing Damage above Critical Cracks E6 and E8

S9005BTM25

Slab strip specimen S9005BTM25 was 9.0 inches deep with 2-#5 bars located at the bottom (1 inch clear cover) and a fiber volume of 0.5 percent. The specimen achieved a maximum capacity of 22.87 kips at a deflection of 0.9 inches (L/93).

Ten cracks formed on the east face, with five inside the constant moment region. Eleven cracks formed on the west face, with 6 inside the constant moment region. The first crack for both the east and west face occurred during the 0.05 inch deflection step, (L/1680). All cracks formed by the 0.40 inch deflection step (L/210). The majority of the formed cracks extended to or beyond the mid-depth of the specimen by deflection step 0.3 inches (L/280). The cracks in the constant moment region extended halfway between reference lines D and E, reaching a maximum length by the 0.6 inch deflection step on the east face and 0.8 inch deflection step on the west face. Further deflection resulted in widening and formation of “branch” and accessory cracks, such as E1 and W3. Figure 287 and Figure 288 show the vertical progression of cracks on each face.

The average non-critical crack width on the east and west face was 0.41 mm and 0.34 mm, respectively. The critical crack on the east face, E1, was clearly identified by deflection step 0.7 inches (L/120). The critical crack on the west face, W3, was identified by deflection step 0.4 inches (L/210). The maximum allowable crack width was observed on the east face after the deflection step 0.9 inches (L/93). Crack W3 had achieved the maximum crack width two steps earlier at 0.7 inches (L/120). The crack width limit was observed at reference line C on both faces, but was not observed any higher prior to the removal of all instrumentation. Figure 289 and Figure 290 show the crack width growth observed throughout the test.

Error! Reference source not found. Figure 291 and Figure 292 show the progression of cracks E1 and W3, respectively. Crack E1 formed during the first deflection step, 0.05 inches. Crack W3 formed at the subsequent deflection step. With the exception of associated crack branching, critical crack E1 extended vertically for the final time at deflection step, 0.6 inches, and W3 at 0.8 inches. Both E6 and W5 resulted in multiple “branch” cracks and steel fiber anchorage failure.

Crushing was first observed at N3 on both faces at deflection step 0.90 inches (L/93). The crushing was observed above the critical cracks on either face. As the test continued, the crushing extended horizontally to include the portion of the constant moment region between the centerline and N3. The crushed concrete region extended downward but did not meet the tension cracks prior to removal of testing instrumentation. The slab strip specimen did not collapse during the test, yet the concrete experienced severe crushing damage. Figure 293 shows the progression of concrete crushing and the extent of the damage prior to removal of the specimen.

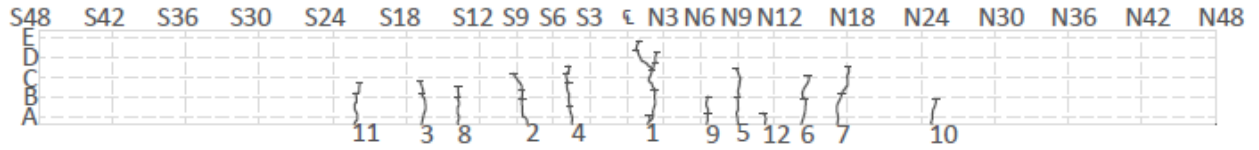


Figure 287. S9005BTM25 Crack Profile East Face

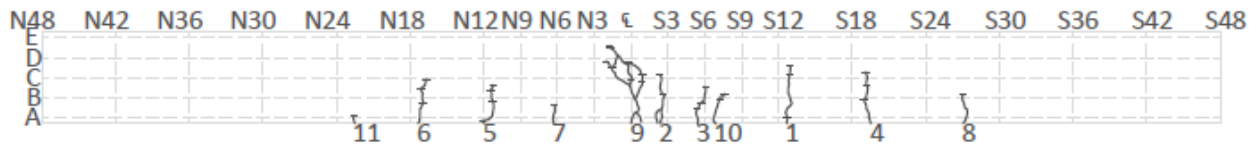
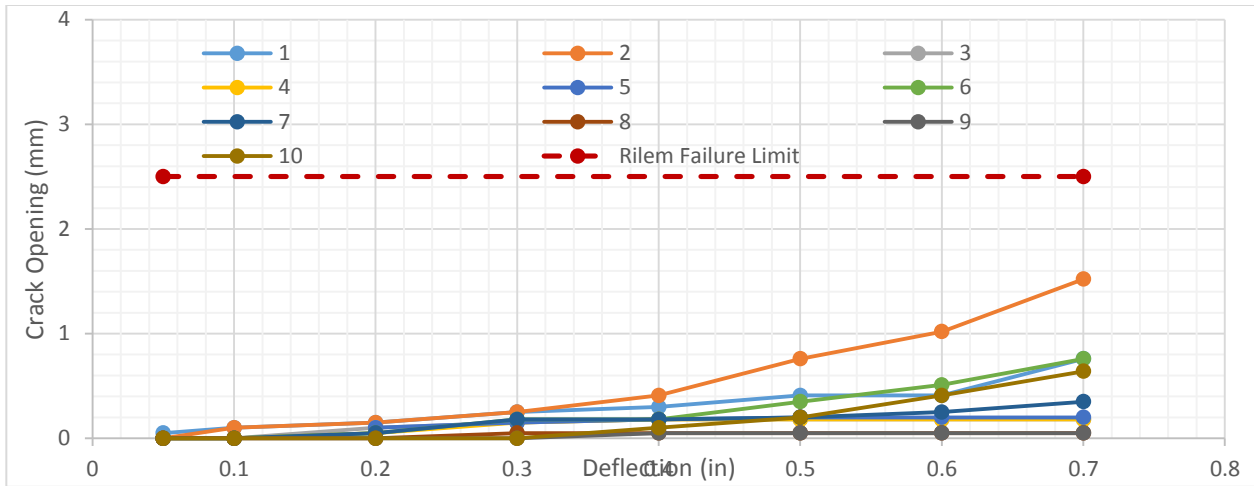
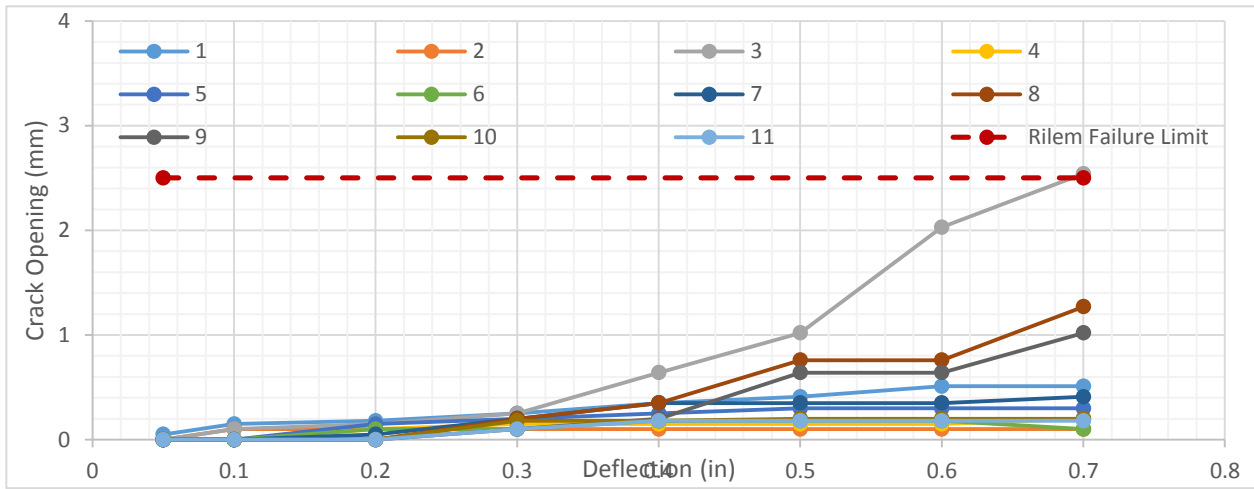


Figure 288. S9005BTM25 Crack Profile West Face

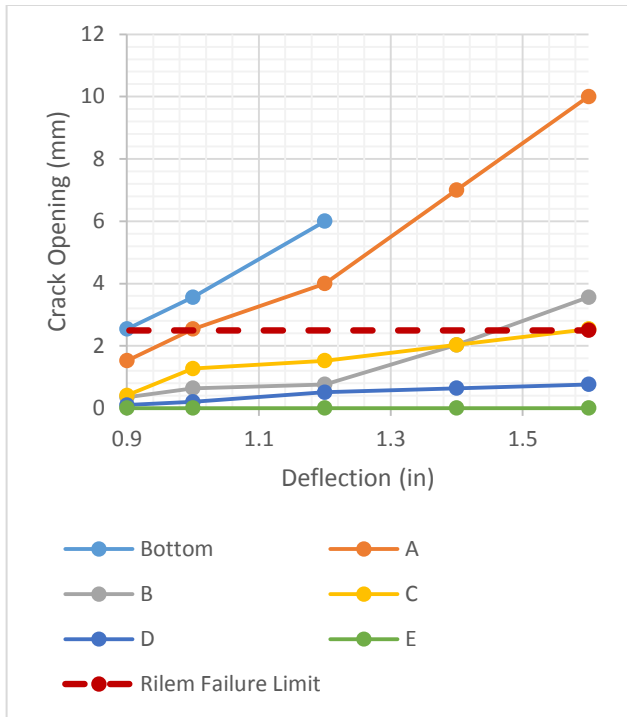


(a)

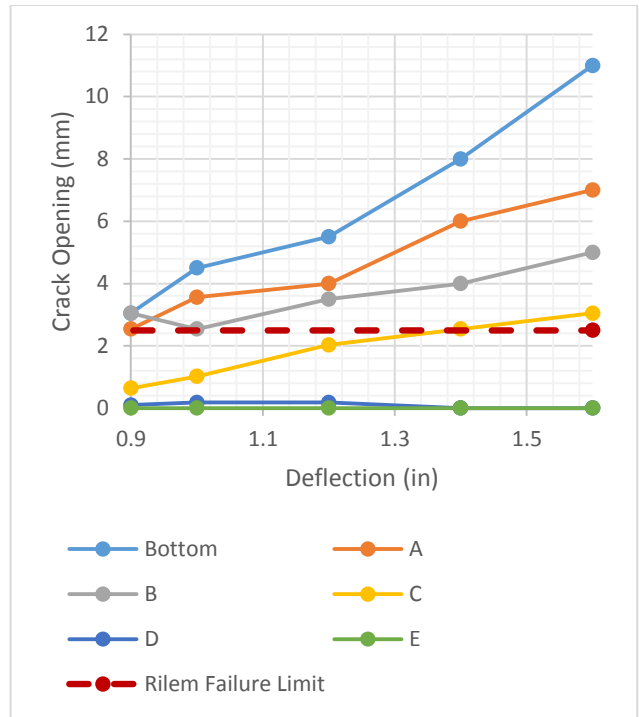


(b)

Figure 289. S9005BTM25 Crack Opening vs Strip Deflection for (a) East Face and (b) West Face

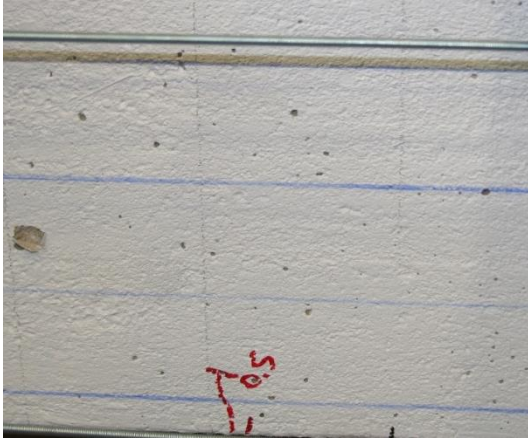


(a)

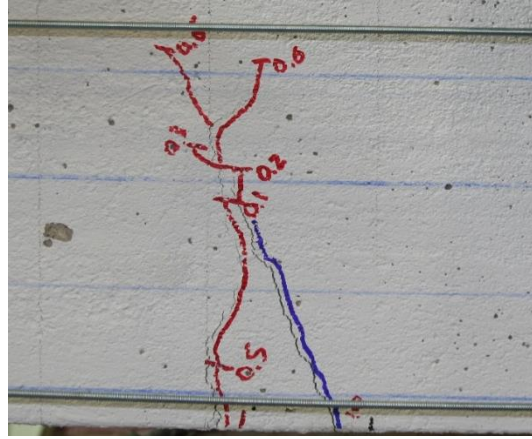


(b)

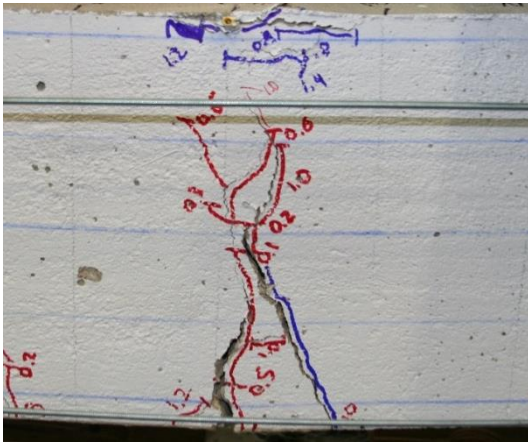
Figure 290. Crack Opening vs Strip Deflection for Primary Crack at Each Reference Line (a) E1 and (b) W3



(a)



(b)



(c)

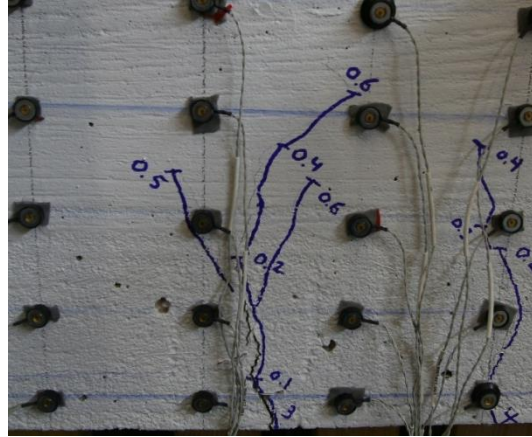


(d)

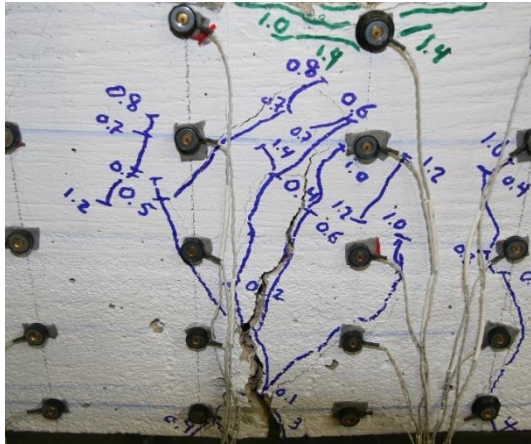
Figure 291. S9005BTM25 Crack Progression of E1 at: (a) 0.05 inches, (b) 0.6 inches, (c) 1.4 inches, and Removal of Beam



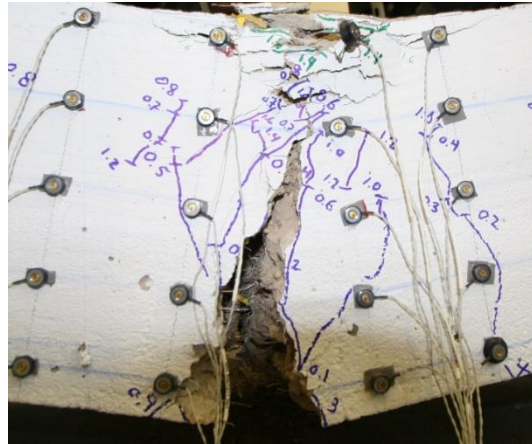
(a)



(b)

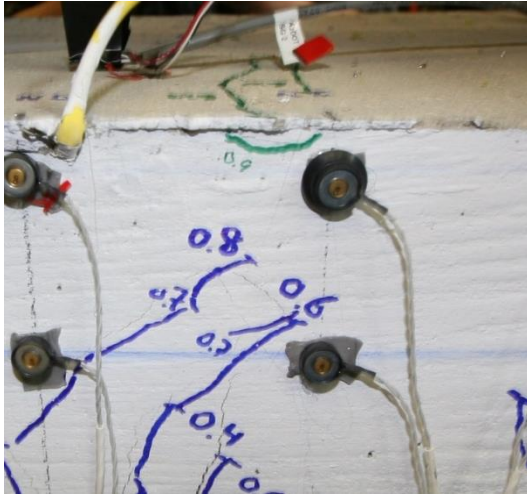


(c)

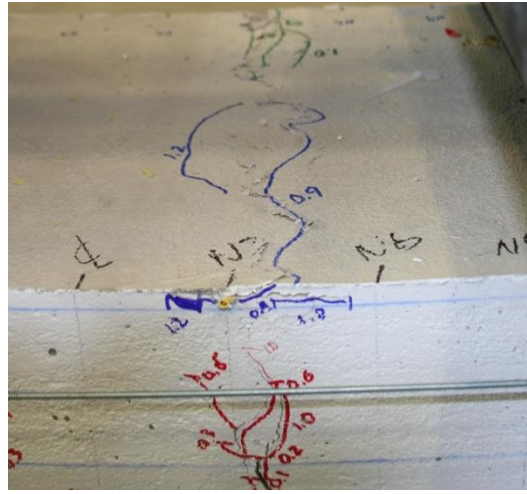


(d)

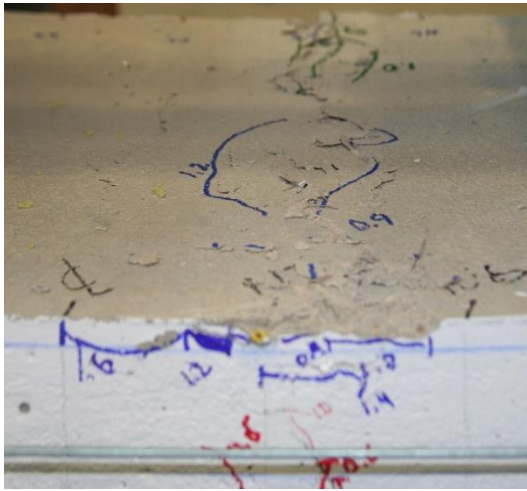
Figure 292. S9005BTM25 Crack Progression of W3 at: (a) 0.1 inches, (b) 0.6 inches, (c) 1.4 inches, and Removal of Beam



(a)



(b)



(c)



(d)

Figure 293. S9005BTM25 Crushing Progression at: (a) 0.9 inch, (b) 1.2 inch, (c) 1.6 inches and (d) Completion of Test

S9005BTM24

Slab strip specimen S9005BTM24 was 9.0 inches deep with 2-#4 bars located at the bottom (1 inch clear cover) and a fiber volume of 0.5 percent. The specimen achieved a maximum capacity of 17.93 kips at a deflection of 0.6 inches (L/140).

Twelve cracks formed on the east face, with six inside the constant moment region. Eleven cracks formed on the west face, with six inside the constant moment region. The first crack formed on the east face at the first deflection step, 0.05 inches. The first crack on the west face formed at the next deflection step, 0.1 inches. All cracks formed by the 0.50 inch deflection step (L/168). Cracks outside the constant moment region extended to reference line D. Vertical progression of cracks outside the moment region ceased at deflection step 0.7 inches. Cracks inside the constant moment region extended to reference line E. Vertical progression of cracks inside the moment region ceased at deflection step 0.6 inches on the east face and 1.4 inches on the west face. Further deflection resulted in widening of the primary crack. Figure 294 and Figure 295 show the final crack map for each face.

The average non-critical crack width on the east and west face was 0.17 mm and 0.22 mm, respectively. The critical crack on the east face, E1, became the largest crack on its face by deflection step 0.5 inches (L/168). The critical crack on the west face, W9, achieved this distinction at deflection step 0.4 inches (L/140). The maximum allowable crack width was observed on both the east and west face after the deflection step 0.6 inches (L/93). The crack width limit was observed at reference line C on both faces. Figure 296 and Figure 297 show the crack width growth observed throughout the test.

Figure 298 and Figure 299 show the progression of cracks E1 and W9 respectively. Crack E1 formed during the first deflection step, 0.05 inches, while W9 did not form until deflection step 0.4 inches (L/210). With the exception of associated crack branching, critical crack E1 extended vertically for the final time at deflection step, 0.6 inches, and W9 at 1.4 inches.

Crushing was first observed on the top surface at deflection step 0.6 inches (L/140). At step 0.70 inches (L/120), crushing was also observed on the east and west faces between the centerline and reference N3. The crushing was observed above the critical cracks on either face. As the test continued, the crushing extended horizontally to include the portion of the constant moment region between S3 and N3. The crushed concrete region extended downward to connect to the tension cracks by the completion of the test. The slab strip specimen did not collapse during the test, yet the concrete experienced severe crushing damage. Figure 300 shows the progression of concrete crushing and the extent of the damage prior to removal of the specimen.

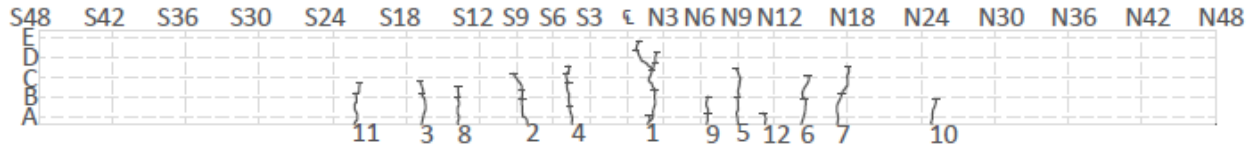


Figure 294. S9005BTM24 Crack Profile East Face

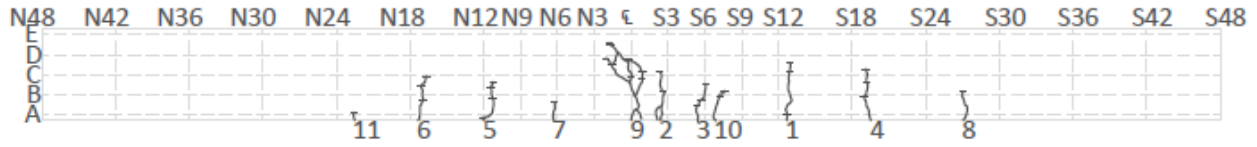
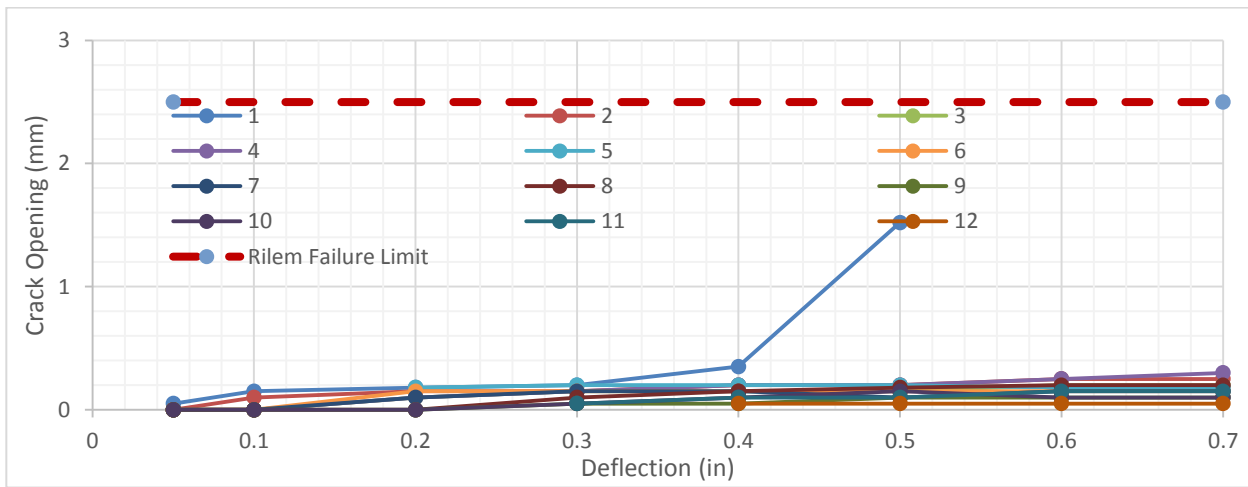
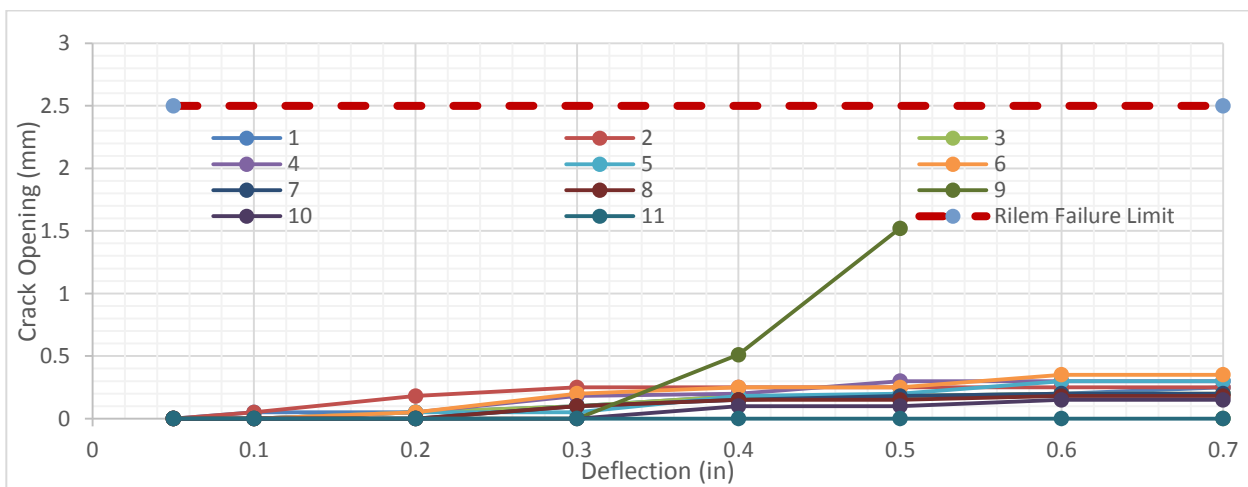


Figure 295. S9005BTM24 Crack Profile West Face

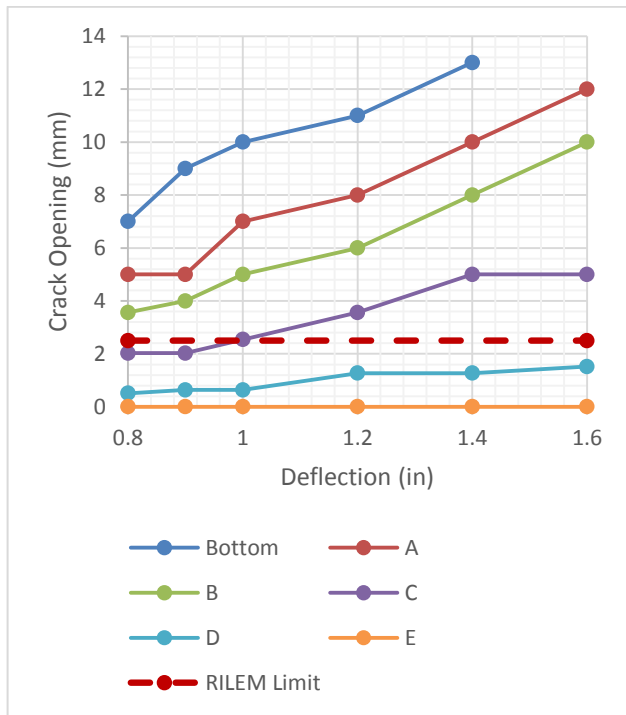


(a)

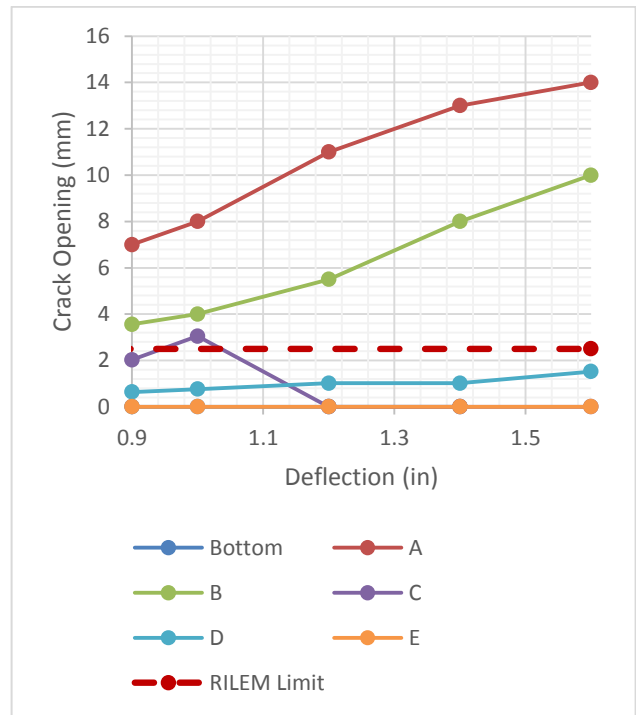


(b)

Figure 296. S9005BTM24 Crack Opening vs Strip Deflection for (a) East Face and (b) West Face

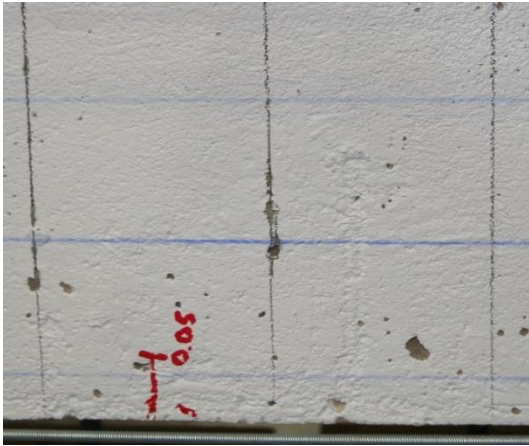


(a)

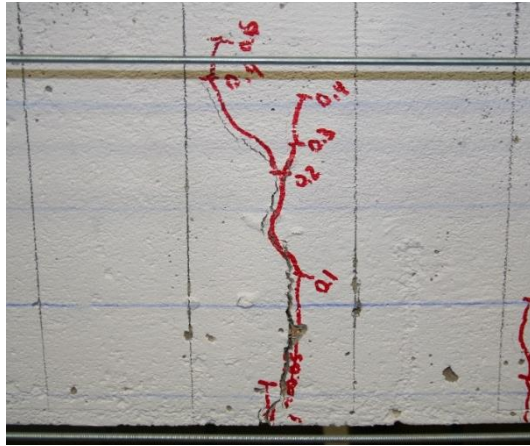


(b)

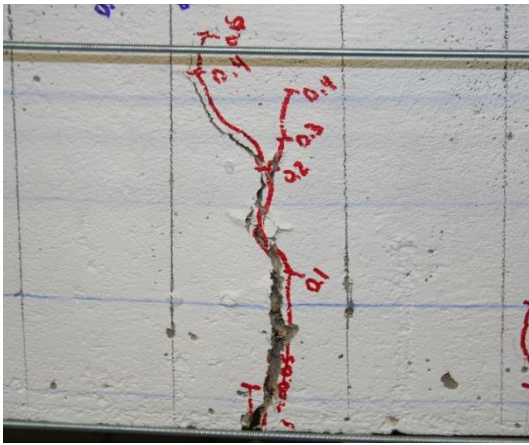
Figure 297. S9005BTM24 Crack Opening vs Strip Deflection for Primary Crack at Each Reference Line (a) E1 and (b) W9



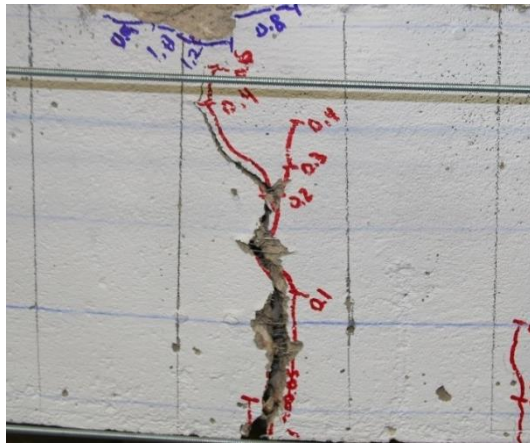
(a)



(b)

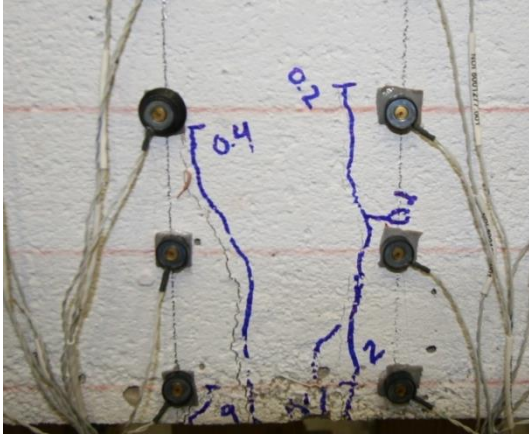


(c)

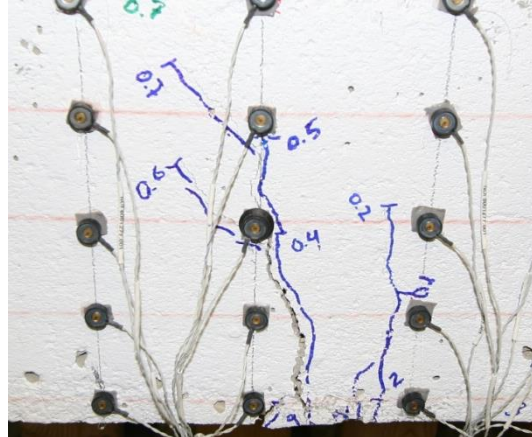


(d)

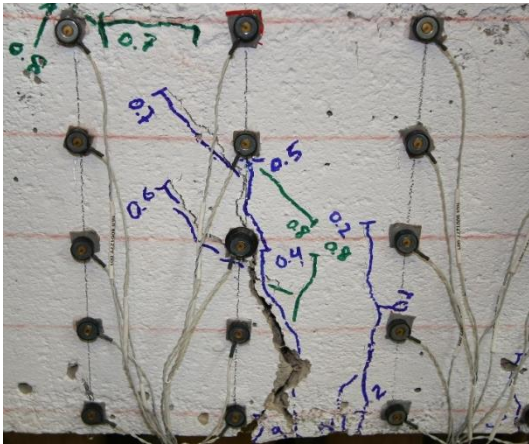
Figure 298. S9005BTM24 Crack Progression of E1 at: (a) 0.05 inches, (b) 0.6 inches, (c) 1.0 inches, and 1.4 inches



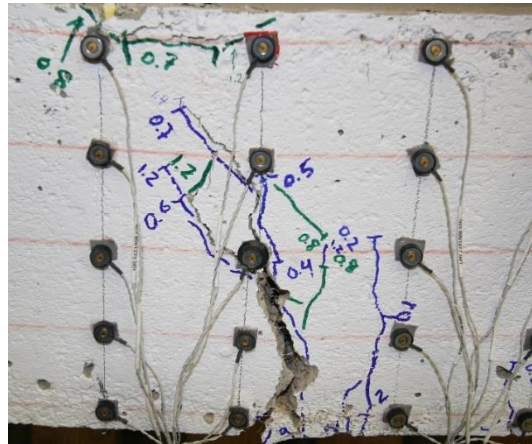
(a)



(b)

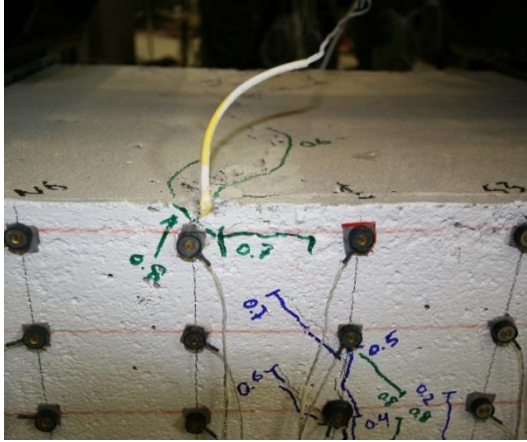


(c)

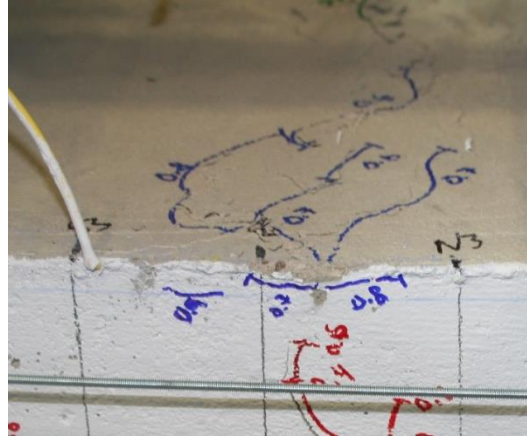


(d)

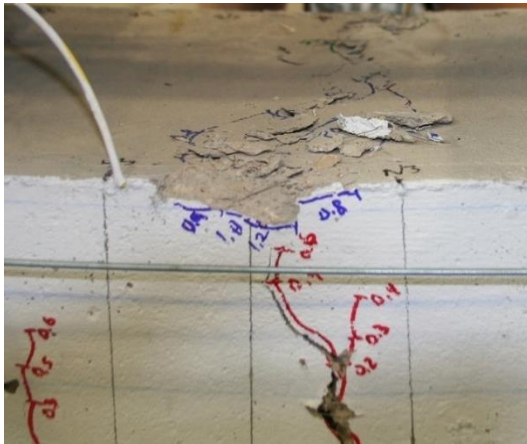
Figure 299. S9005BTM24 Crack Progression of W3 at: (a) 0.4 inches, (b) 0.7 inches, (c) 1.0 inches, and (d) 1.4 inches



(a)



(b)



(c)



(d)

Figure 300. S9005BTM24 Crushing Progression at (a) 0.8 inch, (b) 1.0 inch, (c) 1.4 inches and (d) Completion of Test

S9005BTM23

Slab strip specimen S9005BTM23 was 9.0 inches deep with 2-#3 bars located at the bottom (1 inch clear cover) and a fiber volume of 0.5 percent. The specimen achieved a maximum capacity of 12.58 kips at a deflection of 0.5 inches (L/168).

Seven cracks formed on the east face, with four inside the constant moment region. Ten cracks formed on the west face, with five inside the constant moment region. The first crack formed on both faces at the deflection step 0.1 inches. All cracks formed by the 0.50 inch deflection step (L/168). Cracks outside the constant moment region extended to between reference lines D and E (approximately 1.5 inches from the top). Vertical progression of cracks outside the moment region ceased at deflection step 0.6 inches. Cracks inside the constant moment region extended to reference line E. Vertical progression of cracks inside the moment region ceased at deflection step 0.7 inches. Further deflection resulted in widening of the primary crack and crack branching. Figure 301 and Figure 302 show the final crack map for each face.

The average non-critical crack width on the east and west face was 0.53 mm and 0.57 mm respectively. The critical cracks on the east face and west face, E2 and W1 respectively, became the largest cracks on each face by deflection step 0.7 inches (L/120). The maximum allowable crack width for each crack was also observed at this deflection step. The crack width limit was observed at reference line D on the east face and reference line C on the west face, but was not observed any higher prior to the removal of all instrumentation. Figure 303 and Figure 304 show the crack width growth observed throughout the test.

Figure 305 and Figure 306 shows the progression of cracks E1 and W9 respectively. With the exception of associated crack branching, both critical cracks reached the final length at deflection step, 0.7 inches.

Crushing was first observed on the east, west, and top surface at deflection step 0.8 inches (L/105). The crushing began between horizontal references S6 and S9 above each critical crack. As the test continued, the crushing extended horizontally, but did not extend beyond S6 and S9. The crushed concrete region extended downward and joined the tension cracks prior to collapse of the specimen. Figure 307 shows the progression of concrete crushing and the extent of the damage prior to removal of the specimen.

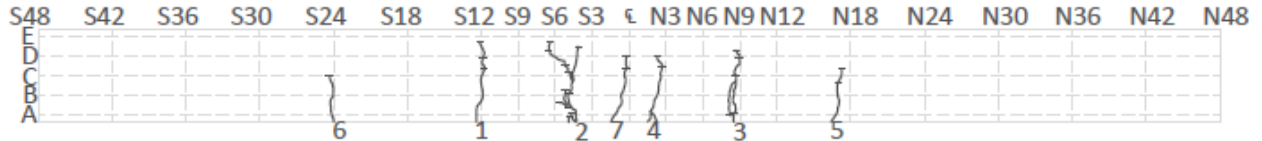


Figure 301. S9005BTM23 Crack Profile East Face

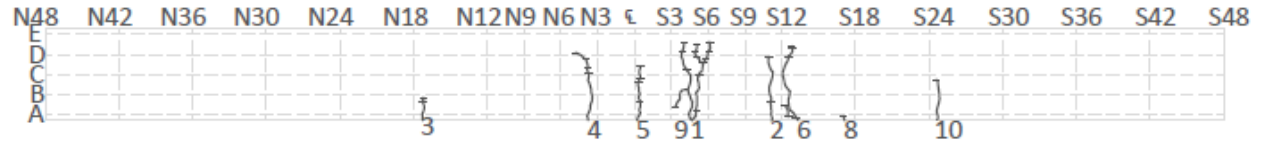
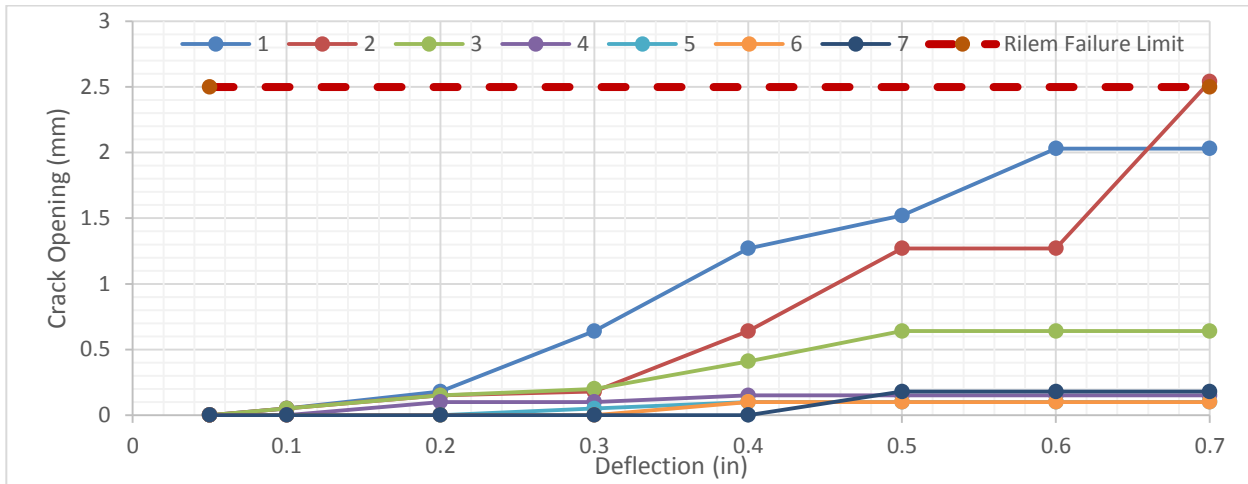
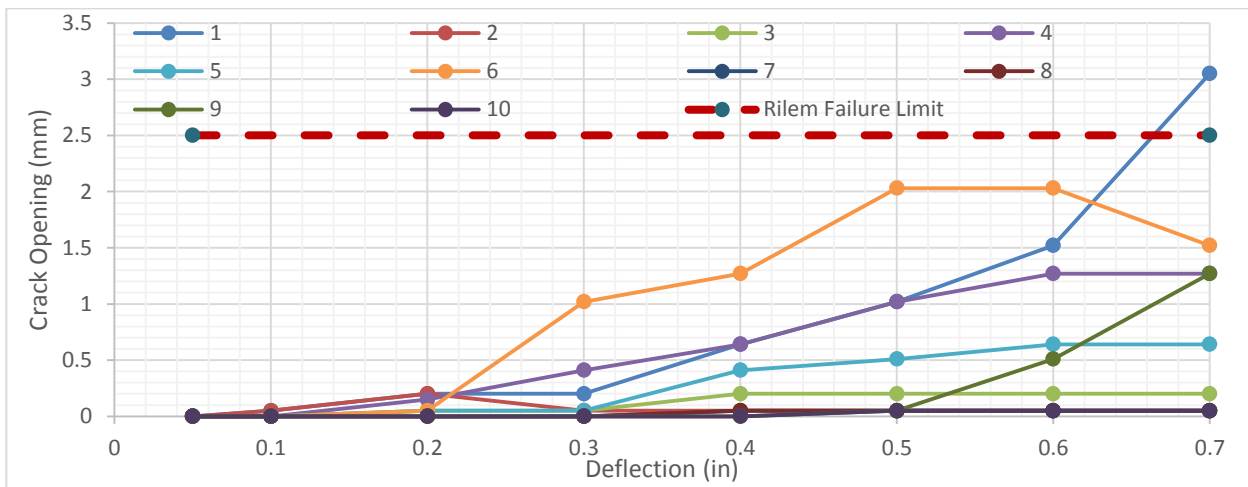


Figure 302. S9005BTM23 Crack Profile West Face

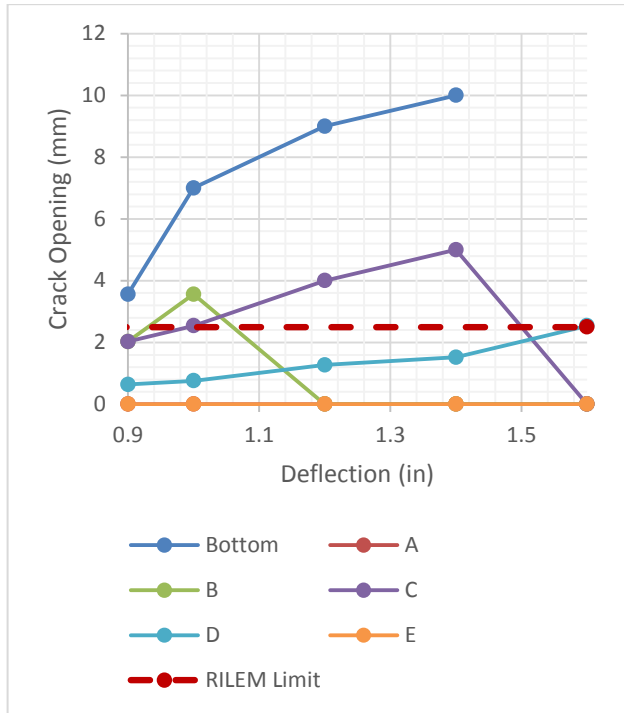


(a)

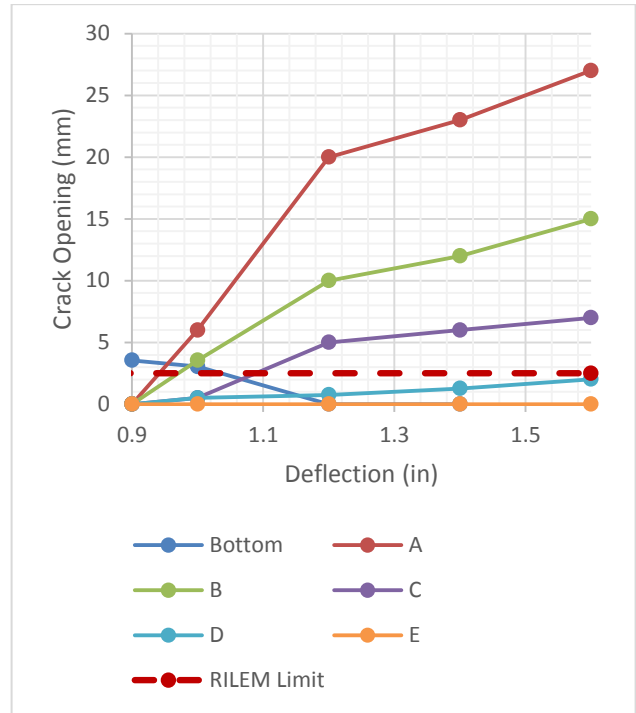


(b)

Figure 303. S9005BTM23 Crack Opening vs Strip Deflection for (a) East Face and (b) West Face

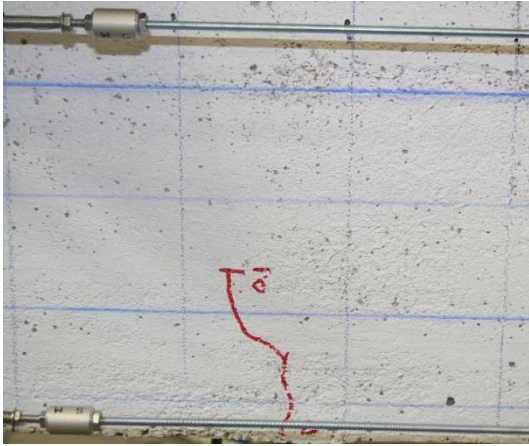


(a)

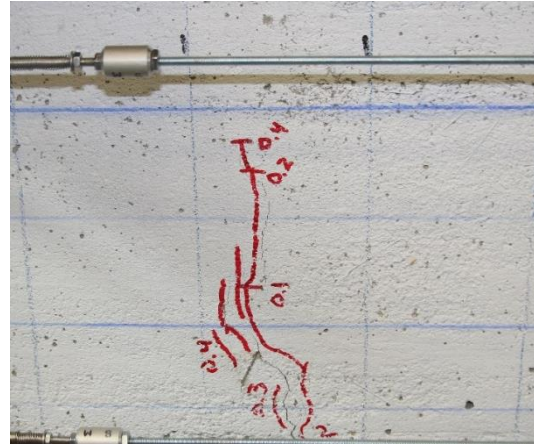


(b)

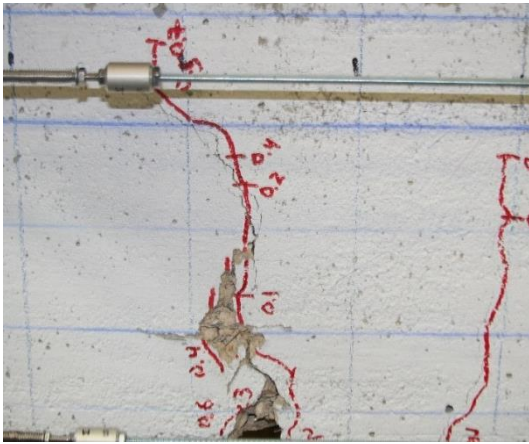
Figure 304. S9005BTM23 Crack Opening vs Strip Deflection for Primary Crack at Each Reference Line (a) E2 and (b) W1



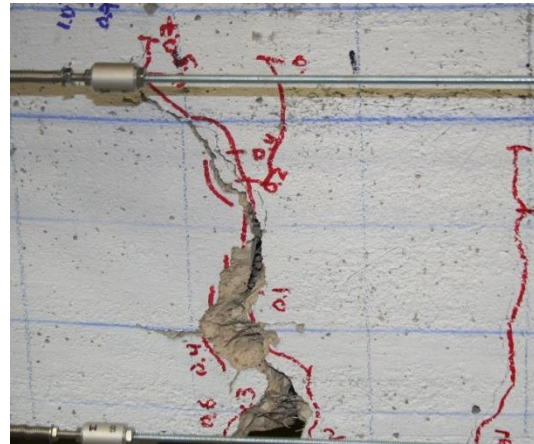
(a)



(b)

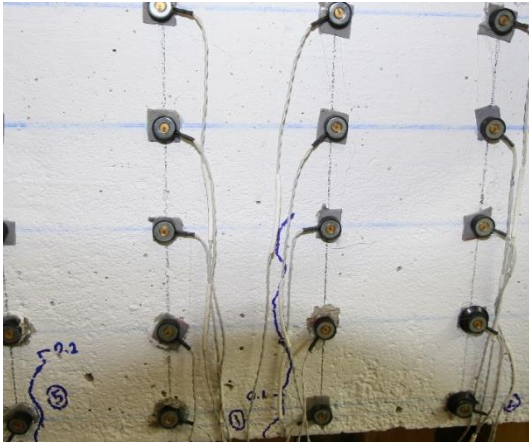


(c)

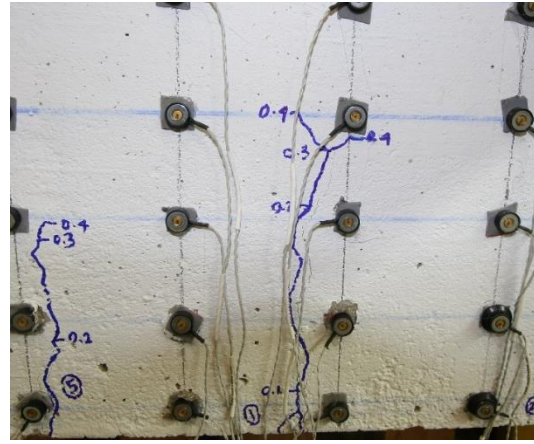


(d)

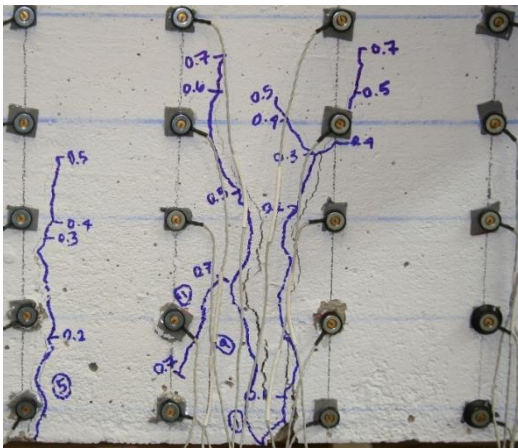
Figure 305. S9005BTM23 Crack Progression of E2 at Deflection Step: (a) 0.1 inches, (b) 0.4 inches, (c) 0.7 inches, and 1.4 inches



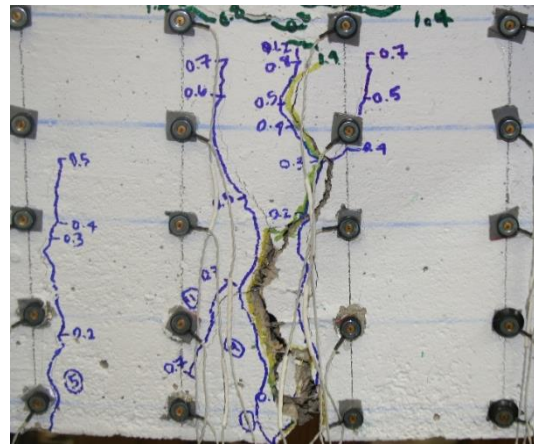
(a)



(b)

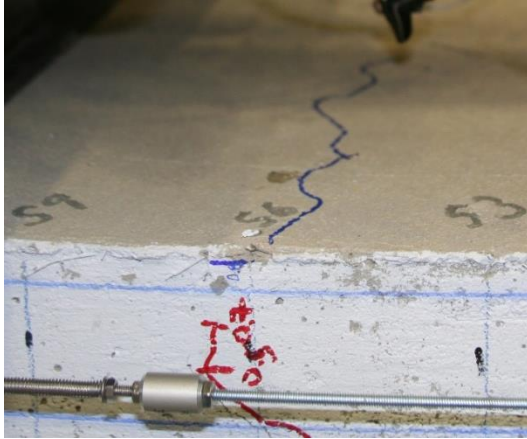


(c)

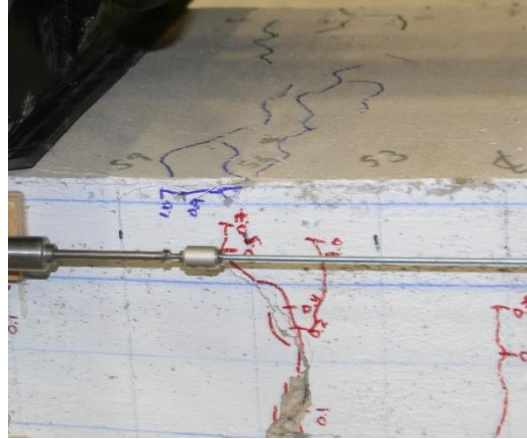


(d)

Figure 306. S9005BTM23 Crack Progression of W1 at: (a) 0.2 inches, (b) 0.4 inches, (c) 0.7 inches, and 1.4 inches



(a)



(b)



(c)



(d)

Figure 307. S9005BTM23 Crushing Progression at: (a) 0.8 inch, (b) 1.0 inch, (c) 1.4 inches and (d) Completion of Test

S9005NOS00

Slab strip specimen S9005NOS00 was 9.0 inches deep with no traditional reinforcement and a fiber volume of 0.5 percent. The specimen achieved a maximum capacity of 4.56 kips at a deflection of 0.05 inches (L/1680). Without steel reinforcement, the specimen's peak capacity corresponded to its cracking strength.

A single crack formed on both faces of the specimen at the first deflection step (0.05 inches). The east face formed a second crack approximately 1 inch to the south of the first crack during the next deflection step, but neither face developed additional cracks. The failure plane developed beneath the south load point at horizontal reference S12.

The critical crack on both faces extended beyond the vertical reference E at deflection step 0.35 inches (L/240). Crack W1 extended vertically slightly during deflection step 0.5 inches (L/168), otherwise, neither critical crack extended further. Both cracks rose to approximately 0.25 inches from the top surface of the slab strip specimen. Both cracks "branched" at vertical reference D. Figure 308 and Figure 309 show the vertical progression of the cracks on the east and west faces respectively.

The crack width was measured at each reference line throughout the entirety of the test except where excessive spalling prohibited it. The critical crack on each side achieved the maximum allowable crack width at the bottom of the specimen by the sixth deflection step (0.3 inches (L/280)). The maximum allowable crack width was achieved at a new reference line with each successive deflection step until reference line C. The crack reached the maximum allowable crack width at reference line D at the final deflection step (0.8 inches (L/105)). Fibers visibly bridged the cracks at later deflection steps. Figure 310 through Figure 312 shows the crack width progression of both critical cracks.

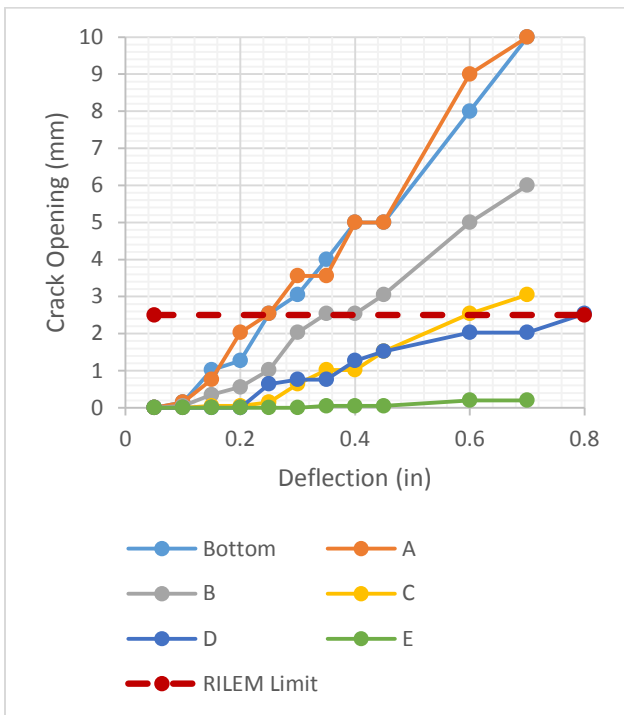
All instrumentation was removed from the specimen at deflection step 0.80 inches (L/105) to prevent damage to the equipment. Concrete crushing was observed on the east face at this deflection step on the east face. Concrete crushing was not observed on the top or west face at that time. Crushing was not observed on the west face prior to the collapse of the specimen. Figure 313 shows the first observance of crushing on east face.



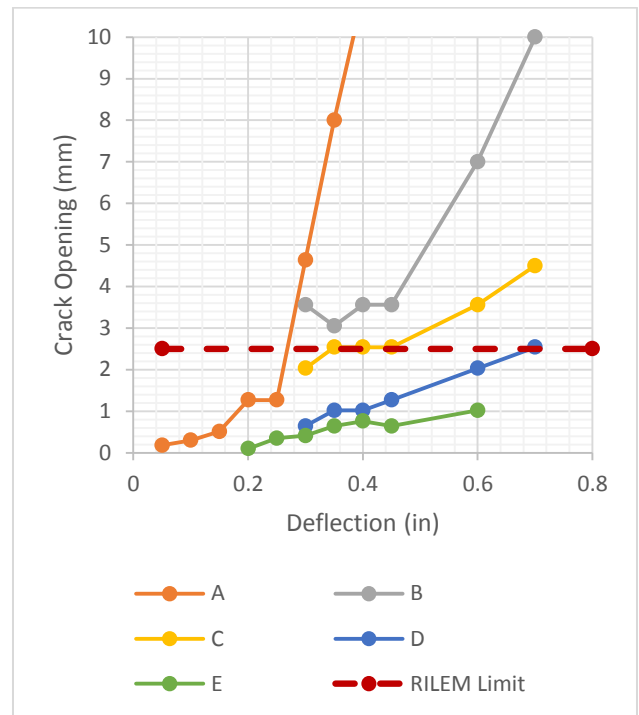
Figure 308. S9005NOS00 Crack Profile East Face



Figure 309. S9005NOS00 Crack Profile West Face

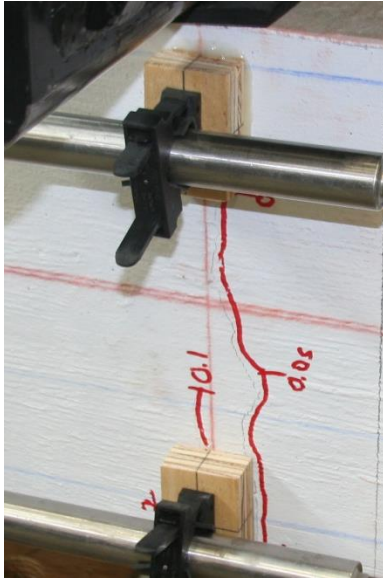


(a)

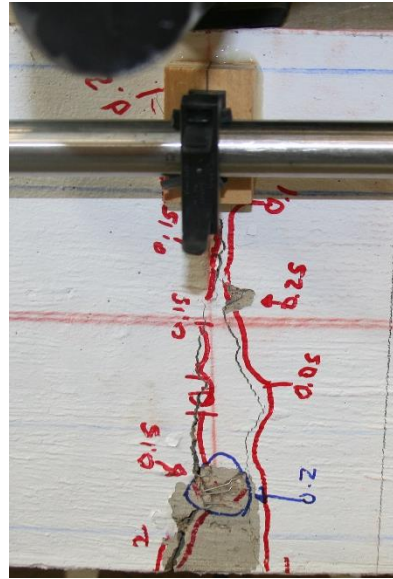


(b)

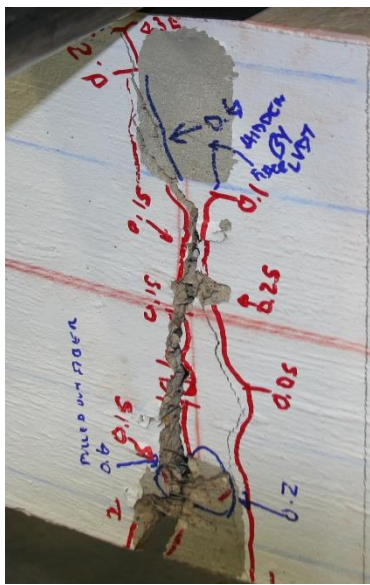
Figure 310. S9005NOS00 Crack Width Progression of Critical Cracks (a) E2 and (b) W1



(a)



(b)

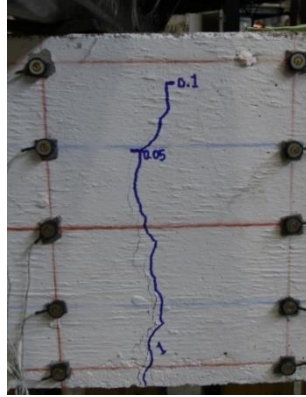


(c)

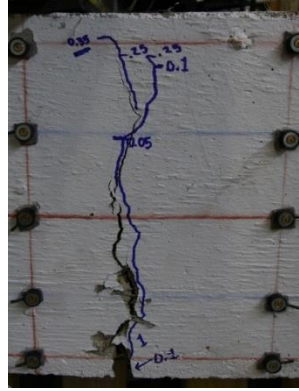


(d)

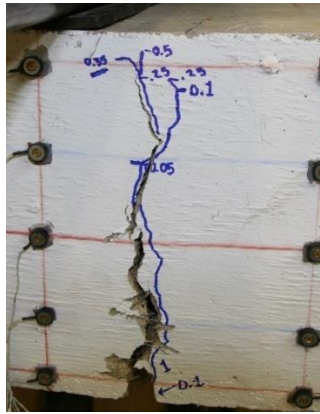
Figure 311. S9005NOS00 Damage Progression of the Critical Crack on the East Face, E2, at: (a) 0.1 inches, (b) 0.30 inches, and (c) 0.80 inches. (d) Fiber Bridging



(a)



(b)



(c)



(d)

Figure 312. S9005NOS00 Damage Progression of the Critical Crack on the West Face, W1, at: (a) 0.1 inches, (b) 0.35 inches, and (c) 0.80 inches. (d) Fiber Bridging

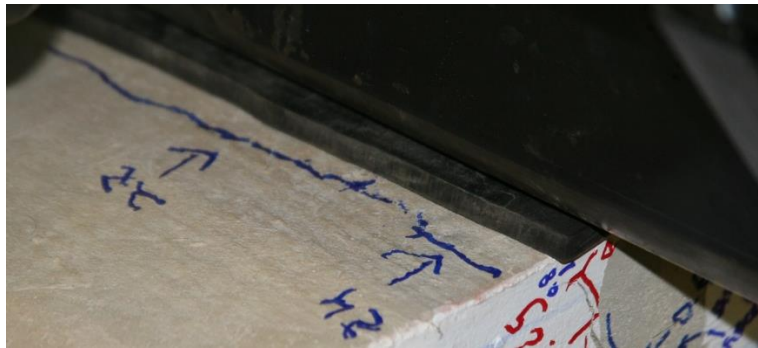


Figure 313. S9005NOS00 Concrete Crushing on East Face

S9020NOS00

Slab strip specimen S9020NOS00 was 9.0 inches deep with no traditional reinforcement and a fiber volume of 2.0 percent. The specimen achieved a maximum capacity of 11.5 kips at a deflection of 0.1 inches ($L/840$). At that time all observed cracks had already formed.

A single crack formed on both the east and west face. The critical cracks formed prior to the first deflection step (0.2 inches ($L/420$)). The crack on the east face formed between horizontal references N6 and N9. The crack on the west faced formed between N3 and N6. The cracks extended beyond reference line E to approximately 0.25 inches from the top surface. The maximum allowable crack width, 2.5 mm, for each crack was observed at deflection step 0.3 inches ($L/280$). Figure 314 and Figure 315 show the progression of each crack throughout the test.

Crushing was not documented during the test. The test was continued until collapse of the specimen. Figure 316 shows the failed specimen and its fiber distribution in the cross-section.

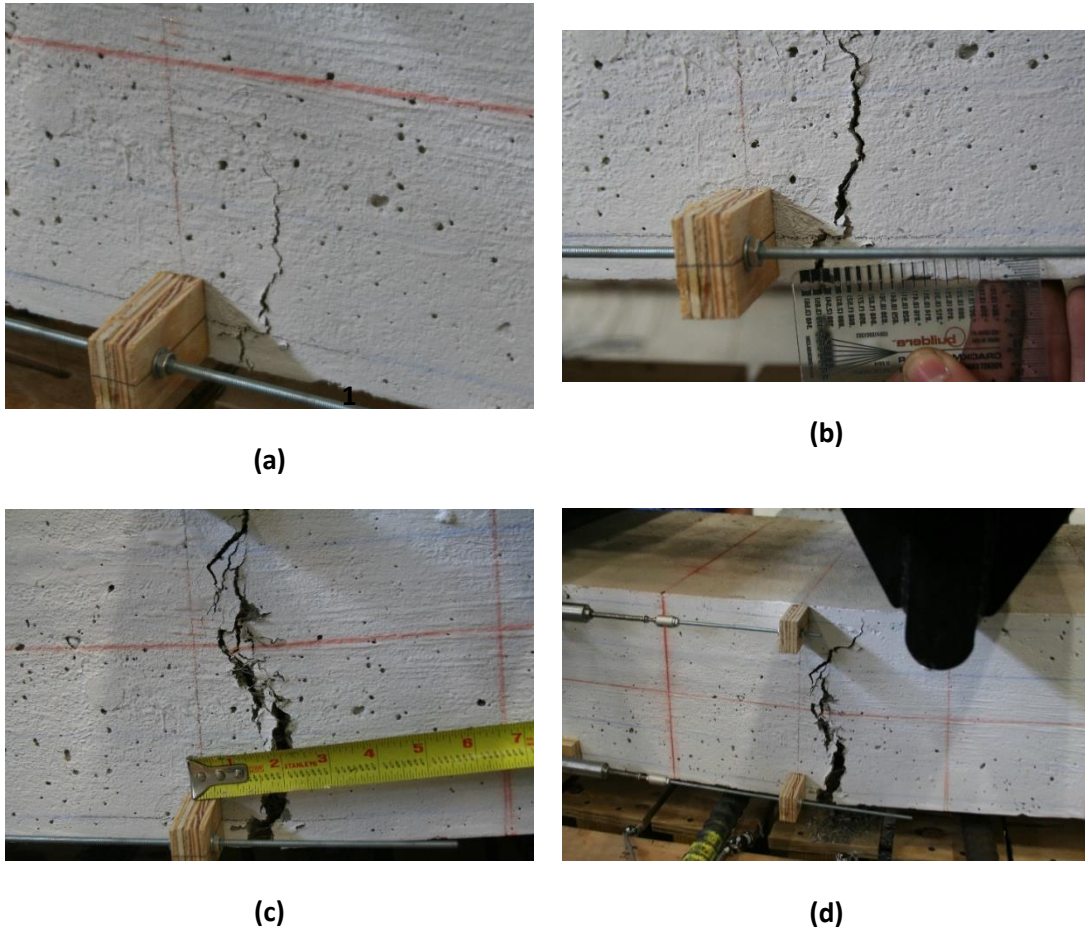
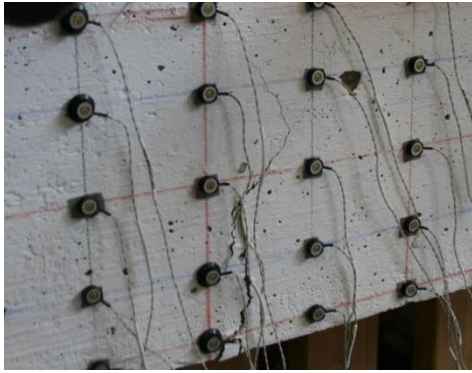


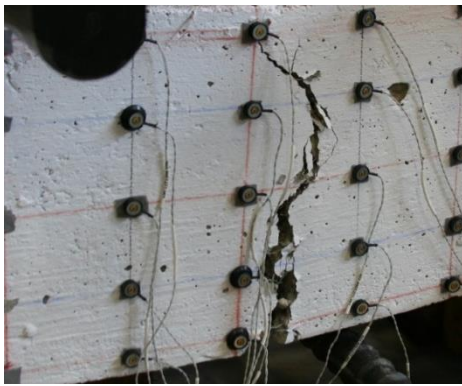
Figure 314. S9020NOS00 Crack Progression of E1 and E12 at: (a) 0.2 inches, (b) 0.3 inches, (c) 1.2 inches, and 1.6 inches



(a)¹



(b)



(c)



(d)

Figure 315. S9020NOS00 Crack Progression of W2 and W3 at: (a) 0.35 inches, (b) 0.9 inches, (c) 1.6 inches, and Removal of Instruments



(a)



(b)

Figure 316. S9020NOS00 Fiber Distribution (a) South Face of Failure Plane and (b) North Face of Failure Plane

APPENDIX B: SFRC DESIGN EXAMPLES

OVERVIEW

Design examples are modified from the ADOT bridge design examples to provide for a comparison to conventional RC design. The design example is modified from the deck design portion of ADOT LRFD Example 4 (2-span Precast Pretensioned I-Girder) to allow for a direct comparison of conventional and SFRC designs. Relevant characteristics for the bridge deck include:

- 8 inch slab thickness, including 0.5 inch wearing surface
- Reinforcing steel: Yield strength, $f_y = 60$ ksi; Modulus of Elasticity, $E_s = 29,000$ ksi
- Deck concrete: Compressive strength, $f'_c = 4.5$ ksi; Modulus of Elasticity, $E_c = 3861$ ksi; Modulus of Rupture (service level calculations), $f_r = 0.509$ ksi; Modulus of Rupture (cracking moment), $f_r = 0.785$ ksi
- Modular ratio, $n = 7.51$ ($n = 8$ used for conventional design)
- Effective flexural depth, d_s , based on the use of #5 bars with adequate coverage

Table 1 summarizes the design demands for positive bending and interior negative bending. Here, calculations are provided for positive bending. In strength design calculations, verification of steel yield assumption is not included to keep the length manageable, but should be done in all design calculations.

Table 71. Summary of Demands ADOT LRFD Design Example 4

	Positive Bending	Negative Bending
M_{cr} , k-ft	8.37	8.37
$1.2M_{cr}$, k-ft	10.05	10.05
M_s , k-ft	6.01	6.82
M_u , k-ft	10.21	11.62
d_s , in	6.19	5.19

DESIGN EXAMPLE WITH REINFORCED CONCRETE

The design steps in the design presented here differ from the ADOT example, but the resulting designs are the same. The ADOT design example designs for service, and verifies strength criteria are satisfied. Here, the steel needed for strength is designed first and then checked for service, with adjustments made if needed. This provides consistency with the proposed design procedures for SFRC slabs.

The flexural resistance of a reinforced concrete section is given by:

$$M_r = \phi M_n = \phi A_s f_y \left(d - \frac{a}{2} \right) \quad (62)$$

Since the neutral axis depth is unknown, the lever arm $d-a/2$ can be approximated by jd , where $j = 0.95$ for slabs. From this, the required area of steel is calculated:

$$A_{s,reqd} \geq \frac{M_u/\phi}{f_y j d} = \frac{10.21(12)/0.9}{60(0.95)(6.19)} = 0.39 \text{ in}^2/\text{ft} \quad (63)$$

$$a = \frac{A_{s,reqd} f_y}{0.85 f'_c b} = \frac{0.39(60)}{0.85(4.5)(12)} = 0.51 \text{ in} \quad (64)$$

$$A_{s,reqd} \geq \frac{M_u/\phi}{f_y (d - a/2)} = \frac{10.21(12)/0.9}{60(6.19 - 0.51/2)} = 0.38 \text{ in}^2/\text{ft} \quad (65)$$

Using #5 bars, the required spacing is:

$$s \leq \frac{12 A_b}{A_{s,reqd}} = \frac{12(0.31)}{0.38} = 9.79 \text{ in} \quad (66)$$

Using #5 @ 9.5" spacing provides $A_s = 0.392$. Verifying strength design:

$$a = \frac{A_s f_y}{0.85 f'_c b} = \frac{0.392(60)}{0.85(4.5)(12)} = 0.51 \text{ in} \quad (67)$$

$$c = \frac{a}{\beta_1} = \frac{0.61}{0.825} = 0.62 \text{ in} \quad (68)$$

$$\varepsilon_t = 0.003 \left(\frac{d_t}{c} - 1 \right) = 0.003 \left(\frac{6.19}{0.62} - 1 \right) = 0.027 \quad (69)$$

$$M_n = A_s f_y \left(d - \frac{a}{2} \right) = \frac{1}{12} (0.392)(60) \left(6.19 - \frac{0.51}{2} \right) = 11.63 \text{ k} - \text{ft} \quad (70)$$

$$M_r = \phi M_n = 0.9(11.63) = 10.46 \text{ k} - \text{ft} > (M_u = 10.21) \quad (71)$$

Adequate strength is therefore provided. Checking the adequacy of design for service demands can be done in two ways. The first is to calculate the stress in the steel and verify it does not exceed the allowable stress. The second is to calculate the allowable service moment and ensure that it does not exceed the service demand, M_s . The second approach is used here.

For the slab with #5 @ 9.5", the allowable service moment is:

$$M_{sa} = \frac{f_s A_s j d}{12} = \frac{24(0.392)(0.916)(6.19)}{12} = 4.45 \text{ k} - \text{ft} < M_s = 6 \text{ k} - \text{ft} \quad (72)$$

Since the allowable service moment is less than the service demand, the design is inadequate and the amount of steel must be increased. To calculate the required area of steel, a service stress of $f_s = 24$ ksi is used and j is assumed equal to 0.9:

$$A_s \geq \frac{M_s}{f_s j d_s} = \frac{6.01(12)}{24(0.9)(6.19)} = 0.539 \text{ in}^2 \quad (73)$$

This can be satisfied by providing #5 @ 6.5" ($A_s = 0.572 \text{ in}^2$). This is the same area of steel provided by the ADOT design example. A summary of all values for positive and negative bending are provided in Table 2.

Table 72. Summary of Design Values for RC Slab

	Positive Bending	Negative Bending
Strength Design		
Reinforcement	#5 @ 9.5"	#5 @ 6.5"
Service Design (Final)		
Reinforcement	#5 @ 6.5"	#5 @ 5.0"

DESIGN EXAMPLE WITH SFRC FOR SERVICE ONLY

In this example, the same slab as the previous example is designed, but with the post-cracking tensile strength considered at service level loads. The initial step of this design is to calculate the steel required to satisfy strength criteria while ignoring contributions of the SFRC in tension. This example picks up with checking the allowable service moment. For this, the residual tensile capacity of the concrete, f_{resid} , is needed:

$$f_{resid} = \mu f_r \quad (74)$$

Where f_r is the cracking strength and μ is the ratio of the residual stress to the cracking stress. Using the recommended value of $\mu = 0.12$:

$$f_{resid} = \mu f_r = 0.12(0.509) = 0.0611 \text{ksi} \quad (75)$$

The neutral axis depth, kd , can be found by solving:

$$0 = A_s f_s + f_{resid} b h - f_{resid} b k d - \frac{f_s b}{n} \frac{k d}{d - k d} \quad (76)$$

$$0 = (0.392)(24) + 0.0611(12)(6.91)k - \frac{24(12)}{8} \frac{6.91k}{6.91 - 6.91k} \quad (77)$$

A design spreadsheet is used to solve for $k = 0.285$. The allowable service moment is then found by:

$$j = 1 - \frac{k}{3} = 1 - \frac{0.285}{3} = 0.905 \quad (78)$$

$$k d = 0.285(0.619) = 0.176 \quad (79)$$

$$M_{sa} = \frac{1}{12} \left(f_s A_s j d + f_{resid} b (h - k d) \left(\frac{2k d}{3} + \frac{h - k d}{2} \right) \right) \quad (80)$$

$$M_{sa} = \frac{1}{12} \left(24(0.392)(5.60) + 0.0611(12)(7.5 - 0.176) \left(\frac{2(0.176)}{3} + \frac{7.5 - 0.176}{2} \right) \right) \quad (81)$$

$$M_{sa} = 5.6k - ft \quad (82)$$

The allowable service moment is still less than the service demand of 6 k-ft and the area of reinforcement must be increased beyond that used for strength design. The area required for service is computed as:

$$A_s \geq \frac{1}{f_s j d} \left(12M_s a - f_{resid} b (h - kd) \left(\frac{2kd}{3} + \frac{h - kd}{2} \right) \right) \quad (83)$$

$$A_s \geq \frac{1}{24(5.60)} \left(12(6) - 0.0611(12)(7.5 - 0.176) \left(\frac{2(0.176)}{3} + \frac{7.5 - 0.176}{2} \right) \right) \quad (84)$$

$$= 0.409$$

Decreasing the spacing of the steel from 9.5" to 9.0 will satisfy the design. Table 3 provides a summary of the design using this revised spacing, along with a design for negative bending.

Table 73. Summary of Design Values for SFRC Slab (Service Only)

	Positive Bending	Negative Bending
Strength Design		
Reinforcement	#5 @ 9.5"	#5 @ 6.5"
M _{sa} , k-ft	4.45	5.33
Service Design (w/ μ = 0.12)		
Reinforcement	#5 @ 9.0"	#5 @ 6.0"

DESIGN EXAMPLE WITH SFRC FOR STRENGTH

In this example, the tensile strength of the SFRC is considered to contribute to the nominal strength.

To consider SFRC in strength design, a residual strength, f_{resid} , is needed:

$$f_{resid} = \mu f_r \quad (85)$$

Where f_r is the cracking strength and μ is the ratio of the residual stress to the cracking stress. Here, a larger value of $\mu = 0.40$ is used. Such a value is a reasonable value for a SFRC mix, but would require a different fiber type than is used in this report, and is thus a hypothetical value if an appropriate fiber type and dosage were identified.

$$f_{resid} = \mu f_r = 0.4(0.509) = 0.204 \text{ksi} \quad (86)$$

The first step is to assume a value of the lever arm jd :

$$j = 0.95 \quad (87)$$

$$jd = 0.95(6.19) = 5.88 \quad (88)$$

From this, the stress block depth, a , and the neutral axis depth, c , are calculated:

$$a = 2d(1 - j) = 2(6.19)(1 - 0.95) = 0.619 \quad (89)$$

$$c = a/\beta_1 = 0.619/0.825 = 0.75 \quad (90)$$

$$\alpha d = h - \frac{h - c}{2} - \frac{a}{2} = 7.5 - \frac{7.5 - 0.75}{2} - \frac{0.619}{2} = 3.82 \quad (91)$$

The required area of steel is then computed by:

$$A_{s,reqd} \geq \frac{\frac{M_u}{\phi} - f_{resid}(h - c)b\alpha d}{f_y j d} \quad (92)$$

$$A_{s,reqd} \geq \frac{\frac{10.2(10)}{0.7} - 0.20(7.5 - 0.75)(12)(3.82)}{60(5.88)} \quad (93)$$

$$A_{s,reqd} \geq \frac{\frac{M_u}{\phi} - f_{resid}(h - c)b\alpha d}{f_y j d} \quad A_{s,reqd} \geq 0.318 \quad (94)$$

Using #5 bars, the required spacing is:

$$s \leq \frac{12A_b}{A_{s,reqd}} = \frac{12(0.31)}{0.318} = 11.71in \quad (95)$$

Using #5 @ 11.5" spacing provides $A_s = 0.32$. Verifying strength design:

$$a = \frac{A_s f_y + h f_{resid} b}{0.85 f'_c b + \frac{f_{resid} b}{\beta_1}} \quad (96)$$

$$a = \frac{(0.32)(60) + 7.5(0.20)(12)}{0.85(4.5)(12) + \frac{0.2(12)}{0.825}} = 0.73 \quad (97)$$

$$c = a/\beta_1 \quad (98)$$

$$c = 0.73/0.825 = 0.89 \quad (99)$$

$$\alpha d = h - \frac{h - c}{2} - \frac{a}{2} \quad (100)$$

$$\alpha d = 7.5 - \frac{7.5 - 0.89}{2} - \frac{0.73}{2} = 3.83 \quad (101)$$

$$j = d - \frac{a}{2} \quad (102)$$

$$j = 6.19 - \frac{0.73}{2} = 0.94 \quad (103)$$

$$M_n = A_s f_y j d + f_{resid}(h - c)b\alpha d \quad (104)$$

$$M_n = \frac{1}{12} (0.32(60)(0.94)(6.19) + 0.20(7.5 - 0.89)(12)(3.83)) = 14.6 \quad (105)$$

$$\phi M_n = 0.70(14.6) = 10.2k - ft (= M_u) \quad (106)$$

The design is satisfactory. Table 4 provides a summary of the design using this revised spacing, along with a design for negative bending.

Table 74. Summary of Design Values for SFRC Slab (Strength)

	Positive Bending	Negative Bending
Strength Design		
Reinforcement	#5 @ 9.5"	#5 @ 6.5"
Service Design (w/ $\mu = 0.40$)		
Reinforcement	#5 @ 11.5"	#5 @ 8.0"

